LBL-28085

Lawrence Berkeley Laboratory
UNIVERSITY OF CALIFORNIA

Materials & Chemical Sciences Division

An *In Situ* Study of the Anodic Film Formation of Cu, Ag, and Zn in Alkaline Media

S.T. Mayer* and R.H. Muller

*(Ph.D. Thesis)

December 1989

LOAN COPY
Circulates
for 2 weeks
Bldg. 50 Library.
LBL-28085
Copy 2

Prepared for the U.S. Department of Energy under Contract Number DE-AC03-76SF00098.

DISCLAIMER

This document was prepared as an account of work sponsored by the United States Government. While this document is believed to contain correct information, neither the United States Government nor any agency thereof, nor the Regents of the University of California, nor any of their employees, makes any warranty, express or implied, or assumes any legal responsibility for the accuracy, completeness, or usefulness of any information, apparatus, product, or process disclosed, or represents that its use would not infringe privately owned rights. Reference herein to any specific commercial product, process, or service by its trade name, trademark, manufacturer, or otherwise, does not necessarily constitute or imply its endorsement, recommendation, or favoring by the United States Government or any agency thereof, or the Regents of the University of California. The views and opinions of authors expressed herein do not necessarily state or reflect those of the United States Government or any agency thereof or the Regents of the University of California.

LBL-28085

AN *IN SITU* STUDY OF THE ANODIC FILM FORMATION OF Cu, Ag, AND Zn IN ALKALINE MEDIA

Steven T. Mayer* and Rolf H. Muller

*Ph.D. Thesis

Department of Chemical Engineering
University of California

and

Materials and Chemical Sciences Division
Lawrence Berkeley Laboratory
1 Cyclotron Road
Berkeley, CA 94720

December 1989

AN *IN SITU* STUDY OF THE ANODIC FILM FORMATION OF Cu, Ag, AND Zn IN ALKALINE MEDIA

STEVEN THOMAS MAYER

Materials and Chemical Sciences Division

Lawrence Berkeley Laboratory

and

Department of Chemical Engineering

University of California

Berkeley, California 94720

ABSTRACT

The anodic film formation of Cu, Ag, and Zn in alkaline solutions was investigated using several *in situ* as well as *ex situ* techniques. These included angular resolved elastic light scattering, Raman spectroscopy, spectroscopic ellipsometry, scanning tunneling microscopy, scanning electron microscopy, and x-ray diffraction. A discussion of the apparatus and theory of *in situ* elastic light scattering and Raman spectroscopy for studying thin-film nucleation and growth is presented.

The mechanisms of film formation were inferred from the observations. The solubility and conductivity of the oxides/hydroxides formed strongly influence the morphology and reversibility of the electrochemical reactions. Low solubility

tends to favor solid-state, planar film growth. However, planar film growth was generally accompanied by some concurrent formation of soluble reaction products.

Ag_2O formation begins with the production of a planar precursor layer (primary layer) in which nucleation of three-dimensional crystals occurs after a critical thickness is reached. The wavelength-dependent optical properties of the primary layer have been derived from the measurements. After nucleation, a redistribution of material among the growing crystals (Ostwald ripening) causes the number density of growth sites to decrease. The redistribution occurs via the transport of oxide material through the electrolyte (by diffusion of the soluble species) from small crystals to larger ones.

Strong illumination causes the photoelectrochemical transformation of Ag_2O to AgO at potentials where the monovalent oxide is known to form. This transformation is not a strong function of illumination, and a threshold illumination energy for the process was not observed. At potentials cathodic of the (dark) Ag_2O to AgO reduction, photoelectrochemically produced AgO is not reduced to Ag_2O when illumination is terminated. The photochemically produced AgO film is chemically or structurally different from electrochemically produced AgO in that its reduction occurs preferentially via a soluble monovalent intermediate.

The formation of cuprous oxide is controlled by diffusion. Cu_2O is less soluble than Ag_2O and forms a compact layer that does not exhibit three-dimensional

nucleation. The optical properties of this layer have been derived. At higher potentials, the formation of the divalent cuprite ion from the Cu_2O film results in the precipitation of $Cu(OH)_2$. When the electrolyte near the interface becomes supersaturated with the cuprite ion, $Cu(OH)_2$ precipitates as a fine, needle-like, porous film. The more thermodynamically favored CuO is formed only at higher potentials and longer periods of time from the underlying Cu_2O layer. At potentials near oxygen evolution, a broad Raman band, which we associate with the formation of a trivalent copper species, is observed at around 550 cm^{-1}. Cathodic reduction of the surface layers is hindered by the limited conductivity of the semiconductive Cu_2O film. This layer acts as a Schottky barrier whose resistance decreases with illumination.

The oxides of zinc are much more soluble than those of silver and copper. The major soluble zinc species at all concentrations (including supersaturated solutions) is the tetrahedral $Zn(OH)_4^{-2}$ ion. This ion does not polymerize or form polynuclear aggregates at higher concentrations. Solutions containing silicate show no new Raman bands, and therefore silicate does not radically alter the $Zn(OH)_4^{-2}$ environment. The stability of the supersaturated zincate solution is associated with the slow kinetics of ZnO nucleation, with silicate further hindering the process.

The formation of a ZnO film by corrosion in deoxygenated, zincate-saturated solution follows a limiting-thickness growth law whose exact form is unclear. We suggest that film growth is controlled by the simultaneous diffusion and migration of ions within the films' space- charge layer and by the dissolution of the

oxide into the electrolyte.

During the active anodic polarization of zinc in alkaline solutions, a film of ϵ–$Zn(OH)_2$ is formed. The rate of film formation is balanced by its rate of dissolution into the electrolyte, and therefore most of the charge ends up as products in the electrolyte and not in the film. Near the active/passive transition potential, the diffusion of hydroxide to the metal/film interface becomes rate limiting, and a film containing kinetically less favored ZnO is formed. The conductivity of this layer is small and therefore causes a marked decrease in the observed current once the layer is formed. The ϵ–$Zn(OH)_2$ layer is removed from the interface by dissolution beyond the transition potential. The slow rate of dissolution of ZnO is balanced by its rate of formation at higher potentials.

To the memory of my grandfather,

Michael J. Stewart

Contents

Introduction 1

1. Anodic Copper Films in Alkaline Solutions: Literature 5

1.1 Copper in Alkaline Media: Thermodynamics 5

1.2 Copper in Alkaline Media: Kinetics 7

1.3 CuOH and Oxygen Adsorption on Copper 8

1.4 Cuprous Oxide Film Formation 9

1.5 Nucleation and Growth Mechanism of Cuprous Oxide 13

1.6 Semiconductive Properties of Cuprous Oxide 18

1.7 Divalent Copper Oxide Formation 21

1.8 Formation of Divalent Copper Surface Species 24

1.9 Trivalent Copper Species 28

1.10 Literature Summary and Conclusions 29

References for Chapter 1 31

Figure Captions for Chapter 1 36

Figures for Chapter 1 37

2. Anodic Silver Films in Alkaline Solutions: Literature 41

2.1 Introduction 41

2.2 Thermodynamics 41

2.3 Film Composition and Structure 45

2.4 Kinetics 48

2.5 Literature Summary and Conclusions 51

References for Chapter 2 52

Figure Captions for Chapter 2 56

Figures for Chapter 2 57

3. Zinc in Alkaline Solutions: Literature 59

3.1 Thermodynamics 59

3.2 Dissolved Zinc in Alkaline Solutions 59

3.3 The Hydrogen Overpotential in Zinc 62

3.4 Zinc Anodic Film Formation 63

3.5 Literature Summary and Conclusions 65

References for Chapter 3 67

4. Theories of Nucleation and Growth by Electrocrystallization 71

4.1 Introduction 71

4.2 The Mechanism of Crystal Growth 72

4.3 The Nucleation Growth Site 74

4.4 Thermodynamics of the Anodic Nucleation Process 76

4.5 Geometric Nucleation and Growth Models 78

4.6 Models for Diffusion-Controlled Nucleation and Growth 82

4.7 Electrocrystallization Growth Theory 87

4.8 Literature Summary and Conclusions 90

References for Chapter 4 92

Figure Caption for Chapter 4 96

Figure for Chapter 4 97

5. Review of Alkaline Battery Systems Using Zinc, Copper, and Silver 99

5.1 Energy Storage in Electrochemical Systems 99

5.2 The Zinc/Silver Oxide Alkaline Battery 102

5.3 The Cadmium/Silver Oxide Alkaline Battery 103

5.4 The Zinc/Nickel Oxide Alkaline Battery 104

5.5 The Zinc/Mercury (II) Oxide Alkaline Battery 105

5.6 The Zinc/Manganese Dioxide Alkaline Battery 106

5.7 The Zinc/Air Alkaline Battery 107

5.8 The Zinc/Copper (II) Oxide Alkaline Battery 109

References for Chapter 5 112

Table for Chapter 5 115

6. Experimental Procedures for Surface Preparations and Electrochemical Measurements 117

6.1 Introduction 117

6.2 Crystal Preparation and Mounting 117

6.3 Electrolyte Preparation 118

6.4 Electrode Surface Preparation 120

6.5 Hg/HgO Reference Electrode 123

6.6 Electrochemical Measurements 124

References for Chapter 6 126

Figure Captions for Chapter 6 128

Figures for Chapter 6 129

7. *In Situ* Elastic Light-Scattering Measurements Made During the Anodization of Metals 131

7.1 Introduction 131

7.2 Light-Scattering Principles and Theory 132

7.2.1 Introduction 132

7.2.2 Diffraction by N Identical Apertures 132

7.2.3 Scattering from Random and Semiordered Surface Particles 135

7.2.4 Surface Spectral Analysis 143

7.2.5 Scalar Scattering Theory 145

7.2.6 Vector Scattering Theory 147

7.3 Equipment Design and Operation 151

7.3.1 System Specifications and Requirements 151

7.3.2 Equipment Description 153

7.3.3 Computer Data Acquisition Hardware and Software 155

7.4 Calibration 157

7.5 Anodic Oxidation of Silver 159

7.5.1 Potential-Sweep Experiments 160

7.5.2 Calculations of RMS Roughness 162

7.5.3 Calculation of the Near-to-Far-Angle SPDF Ratio 163

7.5.4 Potential-Step Measurements 166

7.5.5 Current-Step Measurements 169

7.6 Effects of Size and Number Density on RMS Roughness 171

7.7 Anodic Oxidation of Copper 175

7.7.1 Potential-Sweep Measurements 175

7.7.2 Potential-Step Measurements 179

7.8 Conclusions 181

References for Chapter 7 184

Figure Captions for Chapter 7 187

Figures for Chapter 7 195

8. Observations of the Anodization of Metals Using *in situ* Laser Raman Spectroscopy 233

8.1 Introduction 233

8.2 Principles of Raman Spectroscopy 235

8.2.1 Electromagnetic Waves 235

8.2.2 Sources of Electromagnetic Radiation 239

8.2.3 A Classical Theory of Raman Scattering 240

8.3 Raman Equipment Design and Operation 245

8.3.1 Argon-Ion Laser 245

8.3.2 Laser Focusing System 247

8.3.3 Electrochemical Cell 249

8.3.4 The Monochromator and Optical Filters 251

8.3.5 Intensified Photodiode Array Detector 252

8.4 Calibration 257

8.5 Anodic Oxidation of Silver 258

8.5.1 Introduction 258

8.5.2 Potential-Sweep Experiments 259

8.5.3 Silver Photochemical Transformations 264

8.6 Anodic Oxidation of Copper 266

8.6.1 Introduction 266

8.6.2 Copper Oxide Reference Spectra 267

8.6.3 Effect of Illumination on Raman Standards 269

8.6.4 Potential-Sweep Experiments 270

8.6.5 Potential-Step Oxidation of Copper in 1M KOH 285

8.6.6 Soluble Copper Species 287

8.7 Anodic Oxidation of Zinc 288

8.7.1 Introduction 288

8.7.2 Raman Spectra of Zinc Dissolved in Alkali 290

8.7.3 Zinc Oxide and Hydroxide Reference Spectra 293

8.7.4 Potential-Sweep Oxidation of Zinc 294

8.8 Conclusions 299

References for Chapter 8 306

Figure Captions for Chapter 8 313

Figures for Chapter 8 322

Tables for Chapter 8 383

9. Observations of the Anodization of Metals Using Spectroscopic Ellipsometry 391

9.1 Introduction 391

9.2 Anodic Oxidation of Silver 400

9.2.1 Introduction 400

9.2.2 Slow Potential-Sweep Measurements 403

9.2.3 Single Potential-Step Measurements 404

9.2.4 Double Potential-Step Experiments 405

9.3 Anodic Oxidation of Copper 408

9.3.1 Introduction 408

9.3.2 Potential-Sweep Experiments 410

9.3.3 Constant-Current Experiments 414

9.3.4 Potential-Step Experiments 416

9.3.5 Cuprous Oxide Optical Properties 416

9.4 Anodic Oxidation of Zinc 418

9.5 Conclusion 423

References for Chapter 9 428

Figure Captions for Chapter 9 431

Figures for Chapter 9 436

10. *Ex situ* Measurements of Anodic Films Formed in Alkaline Media 463

10.1 Introduction 463

10.2 Scanning Electron Microscopy of Anodic Films 463

10.2.1 Introduction 463

10.2.2 SEM of Silver 464

10.2.3 SEM of Copper 465

10.2.4 SEM of Zinc 466

10.3 X-Ray Diffraction Measurements of Anodic Films 467

10.3.1 Introduction 467

10.3.2 XRD of Copper 467

10.3.3 XRD of Zinc 469

10.4 Scanning Tunneling Microscopy of Ag_2O Nucleation 469

10.5 Conclusions 474

References for Chapter 10 476

Figure Captions for Chapter 10 477

Figures for Cahpter 10 481

Index 501

INTRODUCTION

The formation of surface layers has a significant effect on the chemical properties of most metals in contact with a liquid phase. Depending on their physical and chemical properties, films can exhibit desirable or undesirable properties. In many batteries, surface layers are formed as a result of an electrochemical reaction and are used as an energy storage medium. These films may be porous or electrically conducting, and they may provide both a stable potential and a high rate of charge and discharge. Inert, compact thin oxide films can offer a significant resistance to corrosion, but their formation on an electrode can be detrimental to the operation of a battery. An improved understanding of the processes involved in the formation of anodic surface layers is necessary to predict and control the film properties important to the storage and conversion of electrical energy or the corrosion resistance of cell components.

In this study the physical and chemical mechanism of the anodic formation of metal oxide/hydroxide films in alkaline media has been investigated. The anodic oxidations of zinc, copper, and silver were chosen because these systems are of practical interest, are used in a number of battery systems, and vary widely in their oxidation potential and the solubility of their reaction products, and because film formation plays a central role in controlling the behavior of the metals. Good physical data pertaining to the chemical and morphological

transformations that occur during anodic film formation on these metals is still limited. While much of the information on electrochemically formed anodic films has been derived from electrochemical measurements, our aim was to carry out *in situ* measurements in order to gain insight into the principal film growth processes and to relate the electrochemical behavior to the film growth characteristics.

In the first part of this thesis, a literature review is presented. This part includes a review of (1) the anodic behavior of copper, silver, and zinc in alkaline solutions, (2) present electrocrystalization theories, and (3) alkaline battery systems that use copper, silver and zinc as electrodes. In the second part of the thesis, experimental procedure, apparatus, optical theory, and experimental results are presented. In the third part of the thesis, the results are interpreted and some conclusions are presented

We have chosen to study the anodic oxidations of zinc, copper, and silver because these systems have practical interest and encompass the solubilized-material and surface-film mechanisms described in Chapter 5. These metals vary widely in their standard electrode potential of formation and solubility of their respective oxides and/or hydroxides. Despite the fact that many electrochemical studies have been reported, there is still little concrete physical data pertaining to the chemical and morphological transformations that occur during anodic film formation on these metals. Since film formation plays such a central role in controlling the behavior of these electrochemical systems, our aim was to gather *in situ* optical measurements to gain insight into the the important film-growth

processes and to interpret the electrochemical behavior of these systems in terms of the film-growth characteristics.

CHAPTER 1

ANODIC COPPER FILMS IN ALKALINE SOLUTIONS: LITERATURE

Section 1.1: Copper in Alkaline Media: Thermodynamics

Thermodynamic data for copper in alkaline media are most conveniently presented in a so-called "Pourbaix diagram"[A1]. In creating these aqueous pH/potential diagrams, one must often restrict the number of solid substances being considered to make the diagram tractable. Furthermore, the most thermodynamically stable species may not be formed because of kinetic limitations. Figure 1-1 shows the Pourbaix diagram with Cu, Cu_2O, and CuO treated as possible solid substances, whereas Figure 1-2 exchanges $Cu(OH)_2$ with CuO. $Cu(OH)_2$ is less stable than CuO and will tend to be converted into the oxide. The free-energy difference between these two compounds is 1.79 kcal/mole, corresponding to 3.88 mV for a two-electron-transfer process.

There is a minimum in the solubility of both CuO and $Cu(OH)_2$ at a pH of around 9.0. $Cu(OH)_2$ is the more soluble compound at all values of pH by more than an order of magnitude, with a solubility of approximately 2.1×10^{-3} M at pH 14. The CuO solubility is around 1.1×10^{-5} M at the same pH. Though it is known that the solubility of cuprous oxide is very low, no values have been reported in the literature. The only soluble monovalent copper species considered in the construction of the Pourbaix diagram (Figures 1-1 and 1-2) is the cuprous

ion, which is known to be colorless. Various divalent copper species have been considered, but the blue cuprite (CuO_2^{-2}) and bicuprite ($HCuO_2^{-1}$) ions predominate at higher pH. For instance, the cuprite ion is 16 orders of magnitude more soluble than the cupric ion (Cu^{+2}) at pH 14. However, the cuprite ion is only six times more soluble than bicuprite at the same pH [A1-A3].

The redox reactions that occur in 1M caustic as the potential is increased are shown in Figure 1-3. The reduction of water to molecular hydrogen will occur at a potential of -826 mV vs NHE (line a, Figure 1-1). All potential measurements in this study were made with reference to a Hg/HgO in 1M KOH electrode. Since the potential of the Hg/HgO in 1M KOH reference electrode is 98.6 mV vs NHE, hydrogen reduction occurs at a potential of -924 mV vs this Hg/HgO reference electrode. The hydrogen evolution reaction is impeded by the reaction overpotential on the copper electrode. Copper exhibits an average (with respect to all metals) overpotential for this reaction, and so overpotentials on the order of 100 mV for reasonable currents might be expected. At a potential of -898 mV vs Hg/HgO in 1M KOH, the cuprite ion, CuO_2^{-2}, is in equilibrium with an equimolar concentration of cuprous ion (line 6′, Figure 1-1), but both species have been reduced to negligible concentration at this pH. The oxidation of copper to cuprous oxide occurs at -455 mV vs Hg/HgO in 1M KOH (line 7). Cuprous oxide can react with water and lose an electron to form cupric ion, and this reaction will be in equilibrium with a saturated solution of cupric ion at a potential of -257 mV (line 20). Cuprous oxide will react to form cupric oxide at -257 mV or cupric hydroxide at -179 mV (line 9). Finally, water will decompose to molecular

oxygen at 301 mV vs Hg/HgO in 1M KOH [A1-A3].

The effects of oxygen on this system are believed to be the cause of the differences of several millivolts in values reported by different authors for a number of reactions discussed above [A3]. Molecular oxygen will oxidize Cu^+ ions, changing the relative concentrations of the cuprous and cupric ions. This reaction can cause a slow dissolution of the metal. Dissolved oxygen has also been found to significantly increase the rate of cuprous oxide dissolution [A4,A5]. Under anodic conditions a potential shift associated with this reaction will make the interpretation of current-voltage measurements difficult. Therefore, thorough deaeration of the solutions is imperative.

Section 1.2: Copper in Alkaline Media: Kinetics

The oxidation of copper in basic solutions has been studied by voltammetry for a number of years. Yet, despite the relative simplicity of a voltammetric experiment, there is a fair amount of disagreement concerning the physical and chemical processes that cause the voltammetric features. Therefore, it is necessary to discuss the literature as a whole to ascertain which aspects of copper oxidation voltammetry are clear and which aspects need further clarification.

Cyclic voltammetry of copper has been noted to be sensitive to electrode history [A8]. There are generally two major anodic oxidation peaks observed for copper in alkaline solutions (see Figure 1-4). Most authors show the first oxidation peak, referred in this work as the A1 peak, at around -350 mV vs Hg/HgO in 1M KOH. This peak has been associated with a monovalent oxidation process

[A2,A3]. The second anodic peak, A2, associated with a divalent oxidation process, has a peak current at around 0 mV vs Hg/HgO in 1M KOH and is more than an order of magnitude larger than the A1 peak at pH 14.

Section 1.3: CuOH and Oxygen Adsorption on Copper

A number of authors have suggested the formation of a CuOH layer prior to, or concurrent with, the first anodic peak [A6-A9]. CuOH is apparently an unstable compound in air because no data are available on its properties. Some investigators have assumed the existence of this compound in chemical mechanisms to explain how copper is transformed from bare metal to Cu_2O. The literature is also unclear as to whether this layer exists as an adsorption monolayer on copper (and perhaps an intermediate to a dissolution product), or as a bulk film. The following reactions have been proposed by Haleem and Ateya [A9] to account for the formation of CuOH and the transformation of CuOH into Cu_2O:

$$Cu + OH^- \rightleftarrows Cu(OH) + e^- \ , \qquad 1.1$$

$$2\ Cu(OH) \rightleftarrows Cu_2O + H_2O \ . \qquad 1.2$$

Because a photocurrent was not observed prior to the production of Cu(II) species and an unidentified optical absorption maximum was observed in their reflectance measurements in the region where the Cu(I) surface species is believed to exist, Pyun and Park [A8] stated that a film of CuOH exists in equilibrium with the

Cu_2O film after CuOH is initially formed. Droog *et. al.* have studied the adsorption of oxygen on polycrystalline [A6] and single-crystal [A10] copper surfaces. They found that the reaction was highly reversible and that it can be detected by ellipsometry at around -700 mV vs Ag/AgCl sat. KCl (Ag/AgCl sat. KCl is +207 mV vs NHE). Two unique adsorption peaks were found and were assigned to the adsorption of oxygen on the (110) (at -610 mV vs Ag/AgCl) and (100) (at -670 mV vs Ag/AgCl) crystal planes. The (111) surface was found to be the least reactive in the underpotential range, yielding only a broad increase in current prior to bulk oxidation. The size of the changes in the ellipsometer parameters Δ and Ψ were both shown to be small, consistent with the adsorption of a submonolayer. Therefore, the results of Droog *et al.* [A6,A10] support the notion that CuOH may form as an adsorption layer, but not as a bulk film.

Section 1.4: Cuprous Oxide Film Formation

The first major cyclic voltammetry (CV) anodic peak, A1, has a number of interesting characteristics, which depend on sweep rate, concentration, and disk rotation rate. Anodic current associated with this peak is first observed at around -400 mV vs Hg/HgO in 1M KOH, approximately 50 mV anodic of the theoretical reversal potential for the Cu/Cu_2O reaction. For sweep reversals slightly above the peak potential, hysteresis between the ascending and descending scans has been observed [A11]. The value of the peak current was found to increase with the rotating disk electrode's (RDE) rotation rate, indicating that some solution-side diffusion process occurs during film formation. This peak

becomes more anodic with increased rotation rate. According to Strehblow, the peak is not observed at low pH and slow sweep rates [A12].

Based on the potential at which the A1 peak appears, it has been attributed to the formation of cuprous oxide. *Ex-situ* x-ray and electron diffraction measurements of the copper films formed at constant current indicate that the films are totally cuprous oxide at current densities below 0.2 mA/cm^2 [A13]. However, while Raman spectroscopy has identified Cu_2O *in situ* in 0.1 M KOH, the species could not be detected until well beyond the A1 peak [A14]. Cu_2O was observed in the potential range of +50 to +500 mV vs saturated calomel electrode (SCE) on the anodic sweep. It was observed in this work that Cu_2O could be observed around the A1 peak potential when the potential was stepped into the A1 peak potential range (around -400 mV vs Hg/HgO in 1M KOH). A reason for this inconsistency between the potential step and potential sweep experiments was not given. Furthermore, this finding is perplexing, since the relatively slow sweep rate of 1 mV/sec used in this experiment might be expected to facilitate a pseudo-steady-state potential condition. Therefore, while it is generally agreed that the A1 peak is at least partially associated with Cu_2O film formation, the necessary conditions and potential for film formation are not clear. MacDonald [A11] has suggested that above the A1 peak potential the surface is completely covered by a resistive film.

By increasing the reversal potential for each subsequent sweep in a CV (referred to as a "window-opening" experiment), anodic and cathodic peaks can be corrolated. One of the problems in the literature assignment of peaks by this

procedure is that the peak potentials are not necessarily independent of the sweep reversal potential. The reduction peak C1 associated with the A1 peak is seen to move progressively to lower potentials and to increase as the anodic reversal potential is increased from -350 to -50 mV vs Hg/HgO in 1M KOH [A8]. Once the sweep reversal potential passes the A2 peak potential (0 mV vs Hg/HgO in 1M KOH), the C1 peak potential becomes independent of further increases in reversal potential. It should be noted that another reduction peak, C2 (associated by most authors with the reduction of the species formed at the A2 peak), occurs near the potential of the A1 peak and can be mistaken as being associated with the A1 process. Therefore, the reduction of the material formed at A1 becomes increasingly irreversible as the reversal potential is increased up to the potential where divalent oxide is formed. Galvanostatic reduction of films also shows an increase (more cathodic) in the reduction potential of the monovalent species as a divalent species is formed on an anodic cycle [A16]. It may be that the wave becomes increasingly negative solely as a result of the increase in charge associated with the anodic sweep. Pyun and Parks' data [A8] indicated that there is an increase in the C1 peak width with anodic charge in the A1 peak, but the potential at which cathodic current becomes significant remains the same (around -500 mV vs Hg/HgO). If the reduction process is initially limited by the migration of charge though the p-type semiconducting oxide, linear I/E behavior might be expected on the rising portion of the cathodic wave. This type of linear I/E behavior is shown in the data of Pyun and Park [A8]. The initial portion of the cathodic wave is nearly retraced in each subsequent window-opening wave.

Even under the condition where the C1 peak becomes independent of sweep reversal, its location varies from author to author. The peak potential has been reported to shift by -60 mV/pH [A9]. Hampson *et al.* [A15] show the C1 peak at around -460 mV vs Hg/HgO in 1M KOH at pH 14 and a sweep rate of 1.25 mV/sec, whereas Haleem and Ateya's voltammograms show the peak to be at -700 mV vs Hg/HgO at 25 mV/sec. Both of these authors used the same type of reference electrode (SCE) in their studies. Pyun and Park [A8] show the C1 peak at -670 mV vs Hg/HgO in 1M KOH at pH 13 with a sweep rate of 10 mV/sec, close to the value shown by Becerra *et al.* (-620 mV) with a sweep rate of 1/2 mV/sec. Furthermore, Haleem and Ateya's results [A9] at pH 13.7 (0.5 M NaOH) showed only slight variations of the C1 peak location with sweep rate. The location of the other peaks (i.e., A1, A2, C2) published by Hampson *et al.* [A15] are also more positive by about 250 mV, compared to those of other authors. With this understanding, we can say that the C1 reduction peak is found around -670 mV +/- 50 mV. Most importantly, this peak is some 320 mV cathodic of the corresponding anodic peak, demonstrating the irreversibility of the reaction.

When the CV peak reversal does not extend into the A2 region, the C1 peak is clean (i.e., appears as a single peak), but it becomes complex when the A2 peak is passed (see Figure 1-4). Because of the complex peak structure in the C1 region of reduction, some authors have suggested that a composite reaction or process is occurring [A9,A11]. The explanation generally given is that a number of different reactions and reaction paths are occurring in this potential range.

The reappearance of Cu_2O during the cathodic sweep of a CV was observed by Raman spectroscopy at a potential of -400 mV [A14]. There was a significant increase in signal at potentials around 0 mV vs SCE. The signal from the Cu_2O phase completely disappeared around -700 mV vs SCE (past the C1 reduction peak). Therefore, the previous Raman result did little to clarify that relationship between the CV reduction waves and the chemical transformations involved. X-ray photoelectron spectroscopy (XPS†) measurement [A12] suggested the continued presence of cuprous oxide at potentials greater than the A1 peak potential.

Section 1.5: Nucleation and Growth Mechanism of Cuprous Oxide

At potentials above -400 mV vs Hg/HgO in 1M KOH, an anodic current associated with cuprous oxide is first seen; we know from this study that bulk formation of cuprous oxide begins at this potential. The mechanism of film formation is still highly controversial. The structure has been described variously as porous [A5,A13,A17], growing two- or three-dimensional crystals [A18,A19], compact and homogeneous layers [A12,A20], and a compact underlayer with a precipitated upper layer of cuprous oxide [A21]. Haleem and Ateya [A9] state that only a monolayer of cuprous oxide is formed prior to divalent oxide formation at pH 13, and that only two monolayers are formed at pH 14.

These structure suggestions are largely influenced by the two schools of thought regarding the physical mechanism of the process. Some authors suggest

† XPS is also known as Electron Spectroscopy for Chemical Analysis or ESCA.

that the films are formed simply by a solid-state mechanism, presumably with oxygen ion O^{-2} diffusing into the copper lattice; whereas others favor the role of dissolved products as intermediates to film formation. The overall reaction for a direct solid-state reaction of copper to form cuprous oxide in alkaline solution might be represented by

$$2\,Cu + 2\,OH^- \rightleftarrows Cu_2O + H_2O + 2\,e^- \;, \qquad 1.3$$

but this equation clearly does not represent the elementary reaction steps involved in this process. Shoesmith [A13,A17,A20] has stated that the cuprous oxide film forms via a solid-state mechanism but that the structure is porous. While not clearly stated, these authors believe that the layer has holes or canals perpendicular to the film/metal interphase. Soluble products are said to dissolve from these pores. Solid-state-mechanism proponents point out that cuprous ion is virtually insoluble and taht this fact should eliminate any solution-side effects. Indeed, soluble cuprous ion is known to change rapidly to Cu_2O in alkali [A22]. Primarily because of the thinness of the oxide layers formed at (10-20 Å) pH < 10, Strehblow and Titze [A12] rejected film formation by "precipitation from a supersaturated electrolyte adjacent to the metal surface" and supported direct growth of the oxide on the metal surface. They also stated that the thickness of the Cu_2O layer does not change with potential. A number of authors have attributed film formation to a solid-state process even at pH's where dissolved species have been observed. Ord *et al.* [A20] do not explicitly state whether they believe cuprous oxide film growth proceeds via a solid-state mechanism (pH 12). But the

fact that the same ellipsometric results could be modeled as a compact film after the electrode was cycled a number of times indicates that no roughening was occurs. This results is consistent with a film that grows via a solid-state mechanism. Therefore, despite the statement by Ord *et al.* [A20] in their abstract that film transformation does not occur via a solid-state mechanism and that the anodic oxidation of copper is not a field-limited process, we believe that their data support a solid-state-film-formation mechanism. Perplexingly, in their discussion they state that a number of their results "..can be taken as evidence that the growth of the compact layer of Cu_2O is field-limited." Finally, Hampson *et al.* [A15] state "that transference of ionic species in the solid phase is the rate controlling process." This conclusion was based on the rather small value of the diffusion coefficient derived from a peak current vs root sweep rate plot.

As with the oxidation of silver in alkali, low solubility of the active ion does not necessarily exclude the role of a dissolution process in an overall oxidation process. It has been suggested that the initial thin (planar) homogeneous film on silver formed during its oxidation in alkaline solutions is formed as a concurrent "byproduct" resulting from the buildup of reacted material unable to desorb and diffuse from the surface at a rate equal to the overall anodization current [A23,A24]. Using a ring/disk apparatus, Miller [A25] has unambiguously shown that a soluble cuprous ion is detectable in solution. The solubility of the cuprous ion should increase with increasing pH. At pH 7, a value of $7x10^{-7}$ M has been reported [A19]. As indicated above, as the pH rises above 12 the solubility of cuprous ion increases to a point were dissolved species start to play an important

role in film formation. Films with thicknesses greater than 10 monolayers are formed. Ashworth and Fairhurst [A19] proposed that the dissolution reaction for the formation of cuprous ion is

$$Cu + 2\ OH^- \rightleftarrows Cu(OH)_2^- + e^- \ . \qquad 1.4$$

This species might then decompose to form solid Cu_2O:

$$2\ Cu(OH)_2^- \rightleftarrows Cu_2O + H_2O + 2\ OH^- \ . \qquad 1.5$$

They supported this proposed reaction by a favorable comparison between the observed and calculated change in the exchange current density with pH based on the above reactions. However, the calculation of the exchange current density by the procedure used by these authors may be incorrect. As discussed in more detail below, film formation occurs in the potential region of this study, and film formation will invalidate the assumptions on which the calculation was based.

Because the solubility of cuprous ion has been shown to be significant, and because Miller observed soluble cuprous ion species formed during film formation of Cu_2O in alkaline electrolyte, most authors who have studied Cu_2O oxidation at higher pH state that film formation results from precipitation from solution. After performing a series of experiments over a range of pH, Ashworth and Fairhust [A19] suggested that soluble cuprous species play an increasingly important role in film formation as pH is raised. Literature results at lower pH's (less than 12) are consistent with a solid-state formation mechanism. The anodic films formed at low pH are much thinner than those at pH 14. This makes the

physical observations of the films more inconclusive. For example, Strehblow and Titze [A12] estimate the cuprous oxide film thickness from ESCA angle-dependent data to be 14 Å at pH 9.6.

Dignam and Gibbs [A26] interpreted their galvanostatic data with a film formation model in which instantaneous nucleation followed by two-dimensional lateral growth was assumed. Following this lead, instantaneous formation of Cu_2O nuclei followed by growth of hemispherical nuclei was used to analyze the galvanostatic data of Ashworth and Fairhust [A19]. The rate-determining step was said to be the the formation of soluble copper (I) species. They correlated a "transition time" with the applied current density, which can be justified in terms of the well-known Sand equation [A27]. This equation can be used to predict the surface concentration as a function of time after an applied current step, assuming that there is no resistance to current flow at the surface. Clearly, film formation would invalidate this assumption.

In the classical dissolution/precipitation mechanism for nucleation, when the solution near the surface acquires a certain degree of supersaturation, the initiation of nucleation is assumed to occur. A given degree of supersaturation is reached when the product of the current density and the square root of time reaches a fixed value, as predicted from the Sand equation [A4]. Unfortunately, there is a large degree of uncertainty as to which feature in the galvanostatic potential/time curve is indicative of film nucleation. Ashworth and Fairhurst [A19] used the sharp increase in potential after a pseudo-steady-state plateau period to indicate the onset of Cu_2O formation. The value of the potential

during the plateau is shown to be around -230 mV vs SCE and is coincident with the potential under which cuprous oxide is formed. It could be that the transition they were studying is a result of complete coverage of the surface with Cu_2O after growing nuclei have completely covered the surface. While there may be a correlation between this transition time and the current density, it is not clear which phenomena are being correlated, and therefore the reason for the observed functional dependence is unknown. Yamashita *et al.* [A5] also proposed that cuprous oxide film forms via a classical dissolution/precipitation mechanism. They based their claim on a parabolic relationship between potential transition times in their galvanostatic transients and monochromatic ellipsometric transients. However, these authors also define their transition times arbitrarily. A slight inflection in the Δ versus time curves was used to determine a transition time from ellipsometer results. Δ undergoes a period of slow change on the order of 1° prior to a change in slope in the Δ versus time curve, which is used as an indication of nucleation. No explanation of why this observation is connected with nucleation was offered.

Section 1.6: Semiconductive Properties of Cuprous Oxide

Most studies have indicated that the film formed on copper by anodic oxidation at a pH above 10 is a p-type semiconductor [A5,A28-A31]. Unlike most semiconductors, cuprous oxide has been shown to exhibit strong exciton structure and has been used as a model compound to represent exciton electron-hole pairing [A32]. Therefore, both direct and indirect electron transfer to the conduction

band is possible. The direct band gap has been reported to have a value of 2.1 eV, and the indirect band gap a value of 1.86 eV [A28]. This helps explain the discrepancy in the literature values given for the band gap of this compound (1.8-2.3 eV). Pyun and Park [A8] have stated that the flat band potential of Cu_2O is well known to be +260 mV vs SCE. However, they give as a reference for this value a paper by Hardee and Bard [A30], which discusses the flat band of CuO and makes no reference to Cu_2O at all.

Di Quarto *et al.* [A28] have noted that pH appears to be the most influencial parameter determining the distribution of majority and minority carriers in the anodically formed films. Under certain conditions, cuprous oxide has shown evidence of n-type behavior. Bertocci [A31] found that films formed by corrosion of copper in a copper acetate solution were n-type, with the photopotential shifting to cathodic values. While these cuprous oxide films exhibited photoconductivity, based on impedence measurements, Bertocci [A31] stated that there was virtually no change in the film resistance upon illumination. Rather, he attributed the photocurrent to the charge transfer process, which appeared to be photon assisted. Bertocci also suggested that illumination of n-type cuprous oxide films can shift the potential to values cathodic of the Cu/Cu_2O reaction.

P-type oxide films have been referred to as "oxidation" semiconductors [A33], which implies that they freely allow oxidation but resist reduction. Yet despite the well known fact that copper can form a surface film of this material, there has been scant mention in the literature of the potentially important role that cuprous oxide can play on the oxidation/reduction of copper. While the

existence of a p-type semiconductor film has been established by presenting Mott-Schottky plots, there has been little discussion regarding the effect the formation of a cuprous oxide film will have on the rate of oxidation or reduction. We have not come across any literature suggesting ways in which one might change the carrier population (i.e., doping). Articles in the solar energy literature are more concerned with the feasibility of producing copper/cuprous oxide heterojuntion solar cells than in establishing any relationships between the electronic properties of the semiconducting film and the mechanism of film formation. Because of the emphasis on photovoltaic applications rather than on electrochemical energy storage or corrosion, these researchers paid little attention to the electrochemical conditions of film growth (e.g., time of anodization, potential of formation, etc.). A large number of surface preparations, solutions, and anodization techniques were studied and correlated with their corresponding photovoltaic response [A34]. It was concluded that because of the chemical complexity of electrochemically formed surface layers, there was no easy way to produce oxide layers of the necessary purity for solar cells.

Wilhelm *et al.* [A35] compared the photoelectrochemical properties of corrosion-produced, thermally oxidized, and electrochemically anodized copper oxide films. The electrochemically formed films were produced by anodization at 500 mV vs SCE for 30 min in 0.1 N NaOH. Clearly, the films so produced would be very complex and would contain $Cu(OH)_2$ or CuO as well as Cu_2O. They reported that both cupric and cuprous oxide exhibited photocurrent signals, with the signs and magnitudes of the signals dependent on potential. They suggested

that copper oxidation is inhibited by illumination. Yamashita *et al.* [A5] also reported that the growth of their Cu_2O films (formed by anodization of copper in 0.5 N KOH) were inhibited by illumination. But reported changes in current as a result of periodic illumination (photocurrents) are extremly complicated (see, for example, the data presented by Wilhelm et al [A35]), and we believe only qualitative comments can be made regarding this type of result. Both thermal and anodic oxides showed no photocurrent above 0.0 V (where CuO and $Cu(OH)_2$ would be present). All photocurrents were cathodic (i.e., an increase in the reductive component of the current).

There has been some speculation that the presence of cupric ion may affect the corrosion resistance of a cuprous oxide film. Di Quarto *et al.* [A28] reported that the addition of $5x10^{-2}$ M Cu^{+2} ion to their solutions increased the cuprous oxide film-growth rates ($3.0 < pH < 6.0$), but that the ion played only a minor role in determining the semiconductive behavior of the surface layer. Strehblow and Titze [A12] suggested that $Cu(OH)_2$ formed at potentials beyond the A1 peak disturbs the structure of the Cu_2O underlayer so that it no longer serves as a migration barrier for copper ions. No evidence was given to support this claim.

Section 1.7: Divalent Copper Oxide Formation

As noted above, the second anodic peak, A2, has a peak potential around 0 mV vs Hg/HgO in 1M KOH and is more than an order of magnitude larger than the A1 peak. Hallem [A9] reported that the peak is large at low sweep rates (<5 mV/sec), decreases at moderate sweep rates (5-25 mV/sec), and then increases

again with further increases in sweep rate, but MacDonald [A11] states only that the peak size increases with sweep rate. At the highest sweep rates this peak is resolved into what appears to be two overlapping peaks [A9] and has been attributed to competing or stepwise processes. The A2 peak becomes more anodic with increasing sweep rate [A11].

A great deal of uncertainty remains regarding the divalent species formed in caustic solutions. Much of the confusion has resulted from claims of the existence (without any strong physical evidence) of various surface species. Many have based their conclusions regarding specific surface oxides or hydroxides on the potentials where voltammetric peaks or galvanostatic plateaus occur. But even when composition-sensitive experimental techniques were employeed, other factors (e.g., the effects of pH and potential and current control) appear to play a complex role in determining the composition of the surface layer. The formation of both CuO [A9,A11,A14] and $Cu(OH)_2$ [A8,A11-A13,A17] have been associated with the A2 peak, and therefore it has been proposed that this peak may be a composite peak, with both states of oxide forming simultaneously. MacDonald [A11] has suggested that the complex peak nature arises from the dissolution of Cu(II) species prior to film formation, with film formation occuring beyond the A2 peak potential. The possible existence of a polymeric species $Cu_n(OH)_{2n-2}$ in concentrated alkali [A36] has been proposed to explain some anomalous Raman results [A14].

The location of the A2 peak potential shifts by -60 mV per unit of pH (i.e., becomes more cathodic) [A9,A12]. The peak size increases two orders of

magnitude on increasing the pH from 12 to 14 [A9]. These changes with potential and pH would be consistent with the formation of a metal hydroxide by reaction with the hydroxide in solution, but they do not rule out other processes.

There is some discrepancy between different authors regarding the charge balances for the system, though most of the differences can be attributed to the conditions under which the measurements were made and the manner of calculating the total integrated charge. Generally, at low pH (<12.5) the anodic-to-cathodic charge ratio of a complete voltammogram (including both mono- and divalent processes) is close to 1 [A9]. At higher pH, this ratio falls and becomes dependent on reversal potential, sweep rate, and pH [cf. A9,A11,A14].

$Cu(OH)_2$ is thermodynamically unstable with respect of CuO. Pyun and Park [A8] found some indirect evidence from their *in situ* reflectance measurements to indicate that $Cu(OH)_2$ is transformed to CuO in solution. Changes in the absorption spectra with time under open circuit conditions were used to justify this claim, but no optical modeling was done to support it. However, an *ex-situ* x-ray and electron diffraction [A13,A17] study found that $Cu(OH)_2$ is formed in caustic and that it is kinetically stable (with respect to CuO) at temperatures below 40 C°.

As noted above, a small reduction peak (C2) around -400 mV has been associated with the A2 peak. Unlike the C1 peak, the C2 peak has not been resolved into more than one reduction wave and is virtually pH independent [A9]. But while this peak has been associated with the A2 peak, the charge associated with this peak is generally too small to be associated with the complete reduction of

the material formed at A2. Whether the existence of more than one state of oxide, the changing properties of the film, or the contribution of dissolved species leads to this phenomenon has not been adequately discussed and clarified in the literature.

Section 1.8: Formation of Divalent Copper Surface Species

It has been clearly demonstrated by Miller [A25], using a ring disk apparatus, that there is a considerable potential range of active dissolution of Cu(II) species. As pointed out in the thermodynamic section of this chapter, cuprous oxide can react with water (or hydroxide ion) to form a cupric ion, at a potential of -317 mV vs Hg/HgO. Since cupric ion has a much larger solubility than cuprous ion, there should be a potential range where cuprous oxide or copper would react to form cupric ion at a concentration below that of the solubility of the ion. Various reaction mechanisms have been presented in the literature to account for a dissolution process occuring either directly from copper or from cuprous oxide. These include [A11,A13,A17,A37]

$$Cu + 4\ OH^- \rightleftarrows CuO_2^{-2} + 2\ H_2O + 2\ e^- \ , \qquad 1.6$$

$$Cu + nOH^- \rightleftarrows Cu(OH)_n^{2-n} + 2\ e^- \ , \qquad 1.7$$

$$Cu_2O + 6\ OH^- \rightleftarrows 2\ CuO_2^{-2} + 3\ H_2O + 2\ e^- \ , \qquad 1.8$$

$$Cu_2O + 3\ H_2O \rightleftarrows 2\ Cu(OH)_2^- + 2\ H^+ \ , \qquad 1.9$$

$$Cu(OH)_n^{2-n} \rightleftarrows Cu(OH)_2 + (n-2)OH^- \ , \qquad 1.10$$

$$Cu(OH)_n^{2-n} \rightleftarrows CuO + (n-2)OH^- + H_2O \ . \qquad 1.11$$

Based on some *ex-situ* SEM observations, Shoesmith *et al.* [A17] have stated that when the required degree of supersaturation for film formation can be avoided, nucleation of $Cu(OH)_2$ or CuO does not occur (e.g., when using a rotation disk electrode (RDE) at high rotation rates). Under conditions where film growth was found, the appearence of the crystals (long, thin needle-like structures) further supported the hypothesis that the divalent surface layer was formed via a dissolution/precipitation process. Based on the relative size of the A1 and A2 peaks, MacDonald [A11] rejected an earlier proposal that consecutive oxidation of Cu to Cu_2O and then to a divalent species was the mechanism of oxidation. These results emphasize the importance of the solution-side processes in film formation at higher pH.

Despite the relatively clear understanding that dissolved species do play an important role in the mechanism of divalent surface species formation, Becerra *et al.* [A38] have stated that their results "suggest that at least part of the anodic layer (specifically the divalent species) participates in a solid state nucleation process." CuO formation has been attributed to the oxidation of copper metal or Cu_2O. Yet most of these suggestions are based on voltammetric results, which involve assumptions that partition the oxidation and reduction waves into regions between $Cu(OH)_2$, $Cu(OH)_4^{-2}$, and Cu_2O reduction. These conclusions should therefore be considered with some scepticism.

The next logical question concerns the formation of soluble cupric species. Shoesmith *et al.* [A17] have proposed that dissolution occurs in pores of the Cu_2O layer, and that after a certain degree of local supersaturation with respect to $Cu(OH)_2$ or CuO is reached, an upper layer of $Cu(OH)_2$ or CuO is nucleated and proceeds to grow. This proposal is inconsistent with MacDonald's conclusion that the divalent oxidation is not a subsequent oxidation of a monovalent species. To justify this descrepancy, we would have to propose that monovalent oxidation occurs simultaneously with divalent soluble species formation, and that some reason exists for an increase in the rate of cuprous oxide formation at higher potentials.

The kinetics of nucleation and growth of $Cu(OH)_2$ has been reported as being more favorable than that of CuO. Indicative of a dissolution/precipitation process, potentiostatic current transients exhibited a current minimum and maximum. The derivative of the log of the peak current with potential at fixed temperature and low overpotential was reported to be 30 mV^{-1} [A21]. This result has been justified in terms of the theories of Fleischmann and Thirsk [A39], and Armstrong *et al.* [A40]. A two-electron charge-transfer process is said to be in equilibrium at the surface, and the incorporation of material into growing centers is said to be rate-controlling. However, there is no obvious reason why the peak current should be the sole indicative measure of the change in the electrochemical process with potential. Indeed, based on simple geometric models, the peak current is related to the surface concentration, number density of nuclei, and incorporation rate [A23]. These are probably functions of time as well as

potential. Also, the statement that the incorporation rate is controlling is somewhat inconsistent with the idea that $Cu(OH)_2$ is favored because its growth kinetics are fast with respect to those of CuO. At low overpotentials, the surface concentration can be essentially at equilibrium, and diffusion to a small number of growth centers might control the overall current. At low overpotentials, the degree of supersaturation at the surface is low, and therefore, the driving force for diffusion is low. The increase in current would be a measure of the change in the surface concentration from the saturation value of the hydroxideand would still increase as the crystal area increases (yielding a current maximum). Therefore, while we do not reject this hypothesis outright, we feel that the conclusion that the reaction is controlled at the crystal/electrolyte interface is not totally substantiated by these results.

At potentials above the A2 peak, or at long enough times in a potential step experiment above the A2 peak potential, the current falls off to very small values and the surface is generally considered to be passivated. Two fundamentally different reasons have been given for this phenomenon. The first is that the surface becomes completely covered with a layer of crystals (either CuO or $Cu(OH)_2$) and acts as a barrier for diffusion or as an electrically resistive film [A11]. The second reason involves the solid-state formation of a sublayer of CuO in the complex film, which acts as a barrier to the migration of electrons and chemical species. One of the most important experimental aspect of the copper-caustic system, which needs a better understanding, is the cause of the large degree of irreversibility in the reduction of surface material. Pyun [A8] has said that the

anodic surface layers can only be completely reduced after a long time at very cathodic potentials. The reported large difference in the potentials of oxidation and reduction demonstrates this point. One of the objectives of this work is to develop a working hypothesis do explain this phenomenon.

Section 1.9: Trivalent Copper Species

Some authors have suggested the existence of a Cu^{+3} oxide and soluble species. Muller [A41] was perhaps the first to propose that a trivalent copper oxide species exists on the electrode surface near the potential of oxygen evolution. He stated that the oxide is orange-yellow in color and decomposes upon washing. Potential-decay transients have indicated that a higher oxide that forms at the potential of oxygen evolution may spontaneously decompose [A16]. Miller, using a rotating ring/disk apparatus, was able to show the reduction of a higher valency oxide at around 0.5 V vs SCE [A25]. Ambrose *et al.* [A42] also stated that the voltammetric peak close to the potential of oxygen evolution was due to a trivalent copper species. This peak was found by Haleem and Ateya only above a pH of 13 [A9]. They also observed what they called a reduction wave for this reaction. Presumably the oxide would be Cu_2O_3. MacDonald [A11] found some evidence to substantiate the existence of a Cu^{+3} species from his temperature-dependent cyclic voltammetry. It has been suggested [A11] that Cu_2O_3 is the oxidation product of the soluble cuprite ion and that the bicuprite ion may assist in the production of oxygen.

$$2\,HCuO_2^- \rightleftarrows Cu_2O_3 + H_2O + 2e^- \;, \qquad 1.12$$

$$2\,CuO_2^{-2} \rightleftarrows Cu_2O_3 + \frac{1}{2}O_2 + 4e^- \;. \qquad 1.13$$

Assuming that the thermodynamic potential of the formation of Cu_2O_3 is that of the galvanostatic potential plateu, a free energy of formation of -42.42 kcal/mole has been calculated [A16].

Section 1.10: Literature Summary and Conclusions

Thermodynamic calculations indicate that at least one monovalent and two divalent soluble copper species are expected to be formed in alkaline electryolytes. The first anodic peak has been associated with a monovalent oxidation process, and the second with a divalent oxidation process. Some authors have suggeted the existence of a trivalent copper ion and oxide. Cuprous oxide film formation has been attributed to both solid-state and dissolution/precipitation mechanisms. The film is a p-type semiconductor and has been studied for its potential application in photovoltaic cells. The voltammetry peaks have been attributed to the formation of surface films and soluble species.

Despite the large number of studies on the behavior of copper in alkali, a number of fundamental questions remain. The cause of the system's large irreversiblity needs to be determined. The role of the semiconducting cuprous oxide film on the system's electrochemical behavior needs to be clarified. It is necessary to determine the surface species present at the electrode surface during the anodic oxidation process. Evidence for the existence of a trivalent oxide

needs to be examined. In general, new *in situ* data are needed to help identify and distinquish the individual chemical processes and morphological developments involved in the anodic film formation on copper.

REFERENCES FOR CHAPTER 1

A1) De Zoubov, N., C. Vanleugenhaghe, and M. Pourbaix, **Atlas of Electrochemical Equilibria in Aqueous Solutions**, Marcel Pourbaix, editor. Pergamon Press, New York, 1966.

A2) Bertocci, U., and Donald D. Wagman, **Standard Potentials in Aqueous Solutions**, Allen J. Bard, Roger Parsons, and Joseph Jordan, editors. Marcel Dekker, New York, 1985.

A3) Bertocci, U., and Dennis R. Turner, **Encylopedia of Electrochemistry of the Elements**, Vol. II, Allen J. Bard, editor. Marcel Dekker, New York, 1974.

A4) Von K. Hauffe and K. Reinhold, Ber. Bunsenges. Physik. Chem. **77,** 616 (1972).

A5) Yamashita, M., K. Omura, and D. Hirayama, Surf. Sci. **96,** 443 (1980).

A6) Droog, J. M. M., C. A. Alderliesten, P. T. Alderliesten, and Gosse A. Bootsma, J. Electroanal. Chem. **111,** 61 (1980).

A7) Gennero De Chialva, M. R., S. L. Marchiano, and A. J. Arvia, J. Appl. Electrochem. **14,** 165 (1984).

A8) Pyun, Chong-Hong, and Su-Moon Park, J. Electrochem. Soc. **133,** 2024

(1986).

A9) El Haleem, S. M., and Badr G. Ateya, J. Electroanal. Chem. **117,** 309 (1981).

A10) Droog, J. M. M., and B. Schlenter, J. Electroanal. Chem. **112,** 387 (1980).

A11) Macdonald, D. D., J. Electrochem. Soc. **122,** 651 (1974).

A12) Strehblow, H. H., and B. Titze, Electrochim. Acta **25,** 839 (1980).

A13) Shoesmith, D. W., T. E. Rummery, D. Owen, and W. Lee, J. Electrochem. Soc. **123,** 790 (1976).

A14) Hamilton, J. C., J. C. Farmer, and R. J. Anderson, J. Electrochem. Soc. **133,** 739 (1986).

A15) Hampson, N. H., J. B. Lee, and K. I. MacDonald, J. Electroanal. Chem. **32,** 165 (1971).

A16) Shams El Din, A. M., and F. M. Abd El Wahab, Electrochim. Acta **9,** 113 (1964).

A17) Shoesmith, D. W., S. Sunder, M. G. Bailey, G. J. Wallace, and F. W. Stanchell, J. Electroanal. Chem. **143,** 153 (1983).

A18) Fletcher, S., R. G. Barradas, and J. D. Porter, J. Electrochem. Soc. **125,** 1960 (1978).

A19) Ashworth, V., and D. Fairhurst, J. Electrochem. Soc. **124,** 506 (1977).

A20) Shoesmith, D. W., W. Lee, and M. G. Bailey, **Electrocrystallization**, R. Weil and R. G. Baradas, editors. Electrochemical Society Softbound Proceedings Series, Pennington, NJ, 1981.

A21) Ord, J. L., D. J. DeSmet, and Z. Q. Huang, J. Electrochem. Soc. **134** 826 (1987).

A22) Charlot, G., **Quanitative Inorganic Analysis**, John Wiley and Sons, New York, 1954, p. 206.

A23) Mayer, S. T., M. S. Thesis, University of California at Berkeley, December 1985. Lawerence Berkeley Laboratory Report LBL-15607.

A24) Mayer, S. T., and R. H. Muller, J. Electrochemical Soc. **135,** 2133 (1988).

A25) Miller, B., J. Electrochem. Soc. **116,** 1675 (1969).

A26) Dignam, M. J., and D. B. Gibbs, Can. J. Chem. **48,** 1243 (1970).

A27) Sand, H. J., Philos. Mag. **6,** 45 (1901).

A28) Di Quarto, F., S. Piazza, and C. Sunseri, Electrochim. Acta **30,** 315 (1985).

A29) Speckmann, H. D., M. M. Lohrengel, J. W. Schultze, and H. H. Strehblow, Ber. Bunsenges. Phys. Chem. **89,** 392 (1985).

A30) Hardee, K. L., and Allen J. Bard, J. Electrochem. Soc. **124,** 215 (1977).

A31) Bertocci, U., J. Electrochem. Soc. **128,** 1598 (1978).

A32) Kittel, C., in **Introduction to Solid State Physics**, 5th edition, John Wiley and Sons, New York, 1976, p. 341.

A33) Good, R. J., in **Passivity of Metals and Semiconductors**, M. Froment, editor. Elsevier Science Publishers B. V., Amsterdam, 1983, p. 43.

A34) Sears, W. M., and E. Fortin, Solar Energy Materials **10,** 93 (1984).

A35) Wilhelm, S. M., Y. Tanizawa, Chang-Yi Liu, and N. Hackerman, Corr. Sci. **22,** 791 (1982).

A36) Cotton, F. A., and G. Wilkinson, in **Advanced Inorganic Chemistry: A Comprehensive Text**, 2nd edition, Eiley Interscience, New York, 1976, pp. 895, 902.

A37) De Zoubov, N., C Vanleugenhaghe, and M. Pourbaix, in **Atlas of Electrochemical Equilibria in Aqueous Solutions**, Section 14.1, English Translation, Pergamon Press, New York, 1966.

A38) Beceraa, J. G., R. C. Salvarezza, and A. J. Arvia, Electrochim. Acta **33,** 613 (1988).

A39) Fleischmann, M., and H. R. Thirsk, in **Advances in Electrochemistry**

and Electrochemical Engineering, Vol. 3, P. Delahay and C. W. Tobias, editors, John Wiley and Sons, New York, 1963.

A40) Armstrong, R. D., M. Fleischmann, and H. R. Thirsk, J. Electroanal. Chem. **11,** 208 (1966).

A41) Muller, E., Z. Elektrochem. **13,** 133 (1907).

A42) Ambross et al., J. Electroanal. Chem., **42,** 176 (1973).

FIGURE CAPTIONS FOR CHAPTER 1

Figure 1-1. Potential/pH diagram of the copper/water system considering Cu_2O and CuO as possible solids. From reference A1.

Figure 1-2. Potential/pH diagram of the copper/water system considering Cu_2O and $Cu(OH)_2$ as possible solids. From reference A1.

Figure 1-3. Thermodynamic potential of various reactions of copper in 1M KOH versus the Hg/HgO (in 1M KOH) reference electrode.

Figure 1-4. Cyclic voltammogram of copper in 1M KOH at 10 mV/second sweep rate. Major anodic and cathodic current peaks are identified. Potential is with respect to the Hg/HgO reference electrode in the same solution.

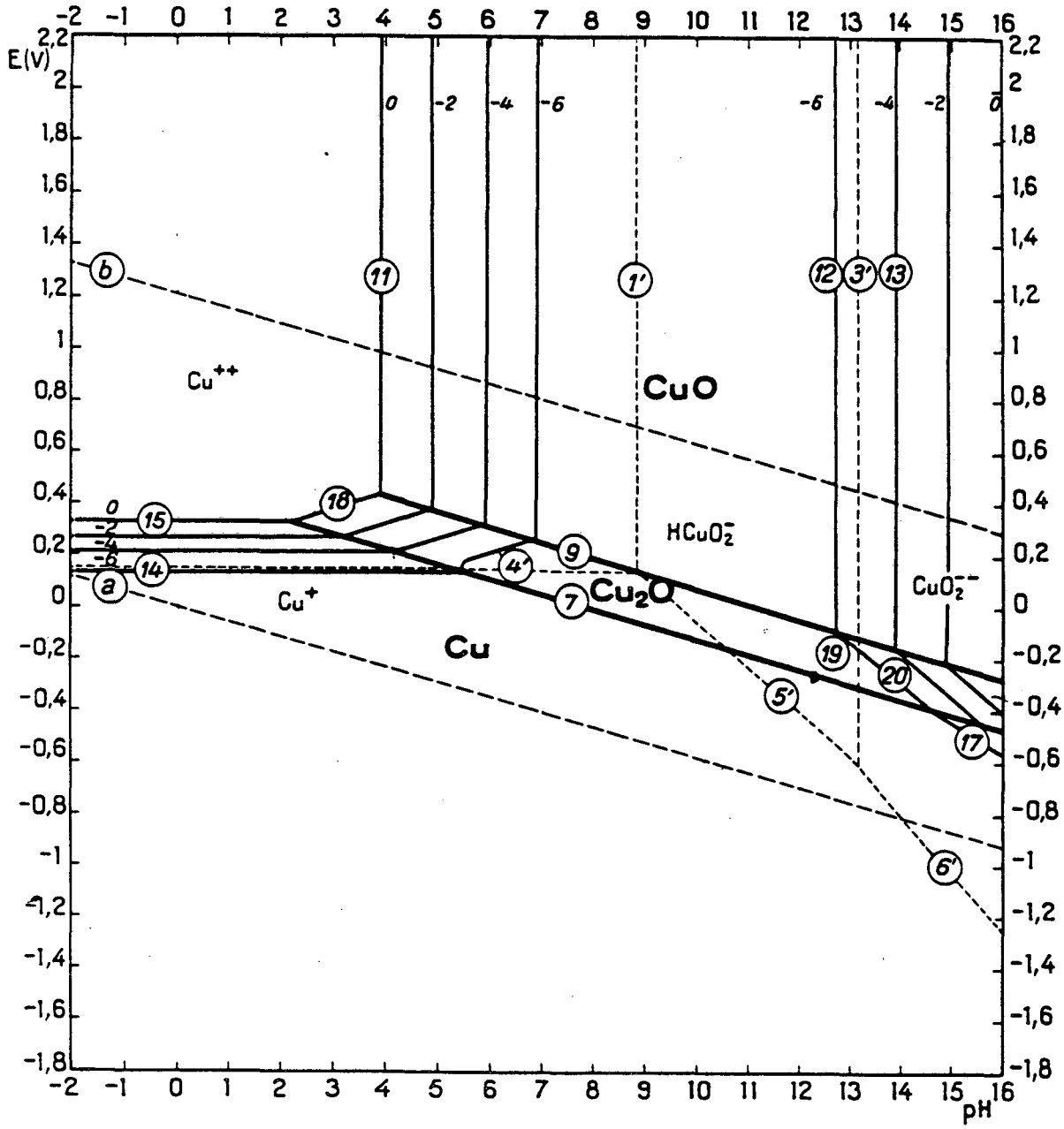
E(V)
pH
Cu++
CuO
HCuO2-
CuO2--
Cu+
Cu2O
Cu
a
b
1'
3'
4'
5'
6'
7
9
11
12
13
14
15
17
18
19
20
0
-2
-4
-6

Figure 1-1

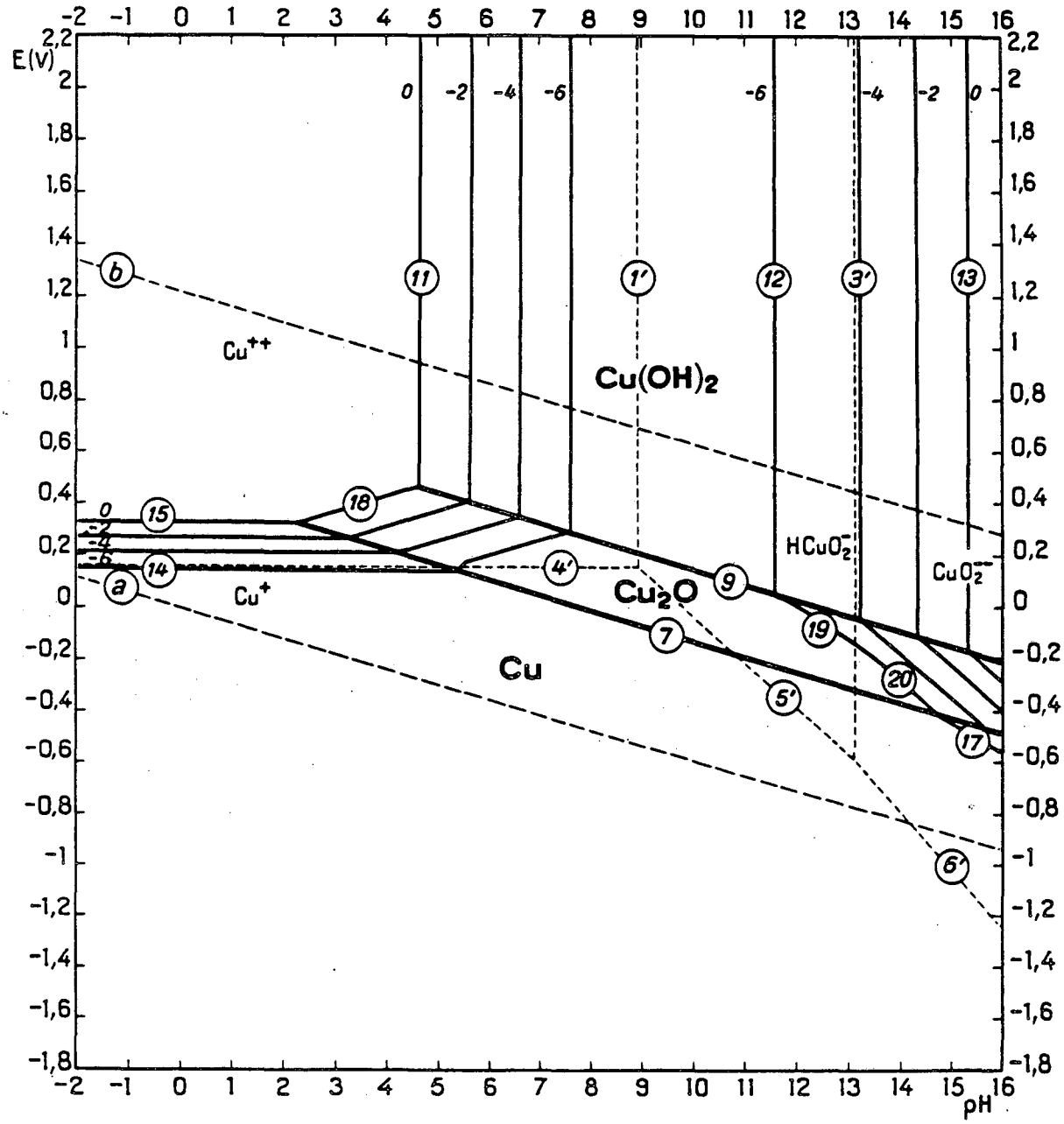

Figure 1-2

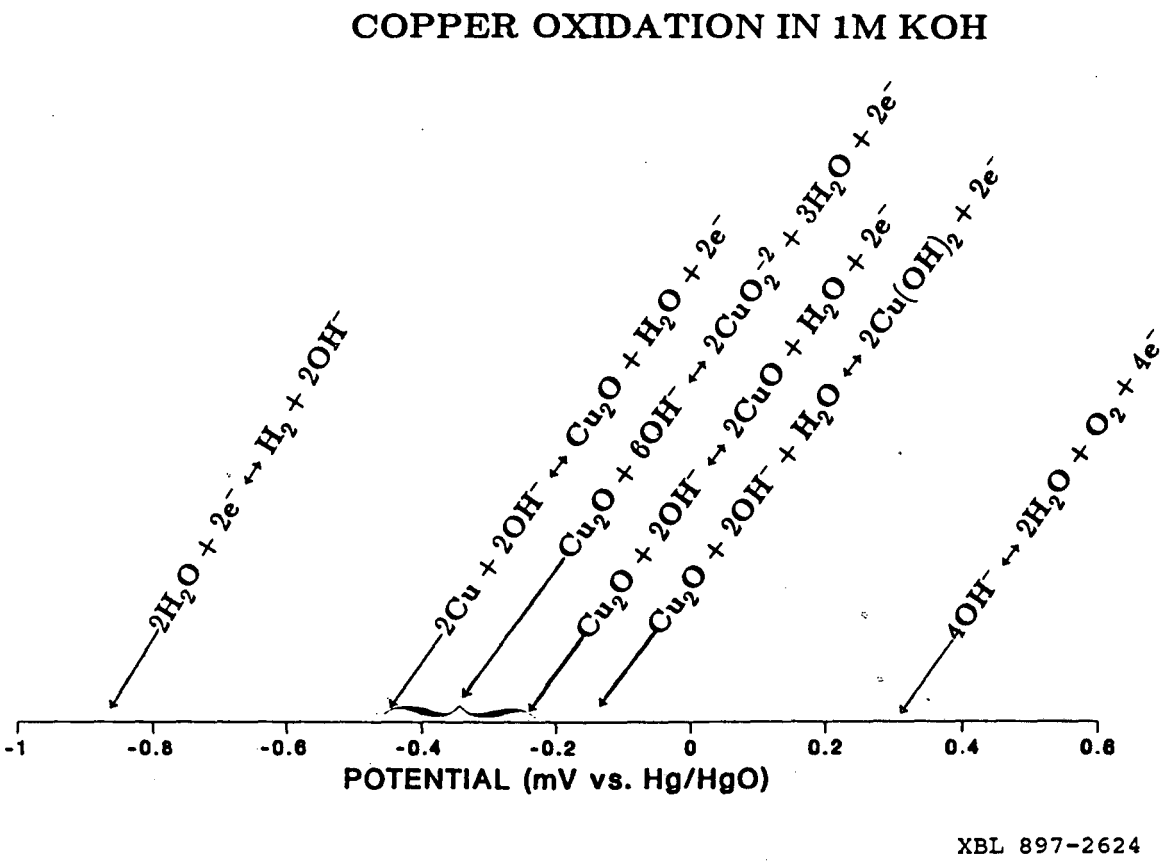

XBL 897-2624

Figure 1-3

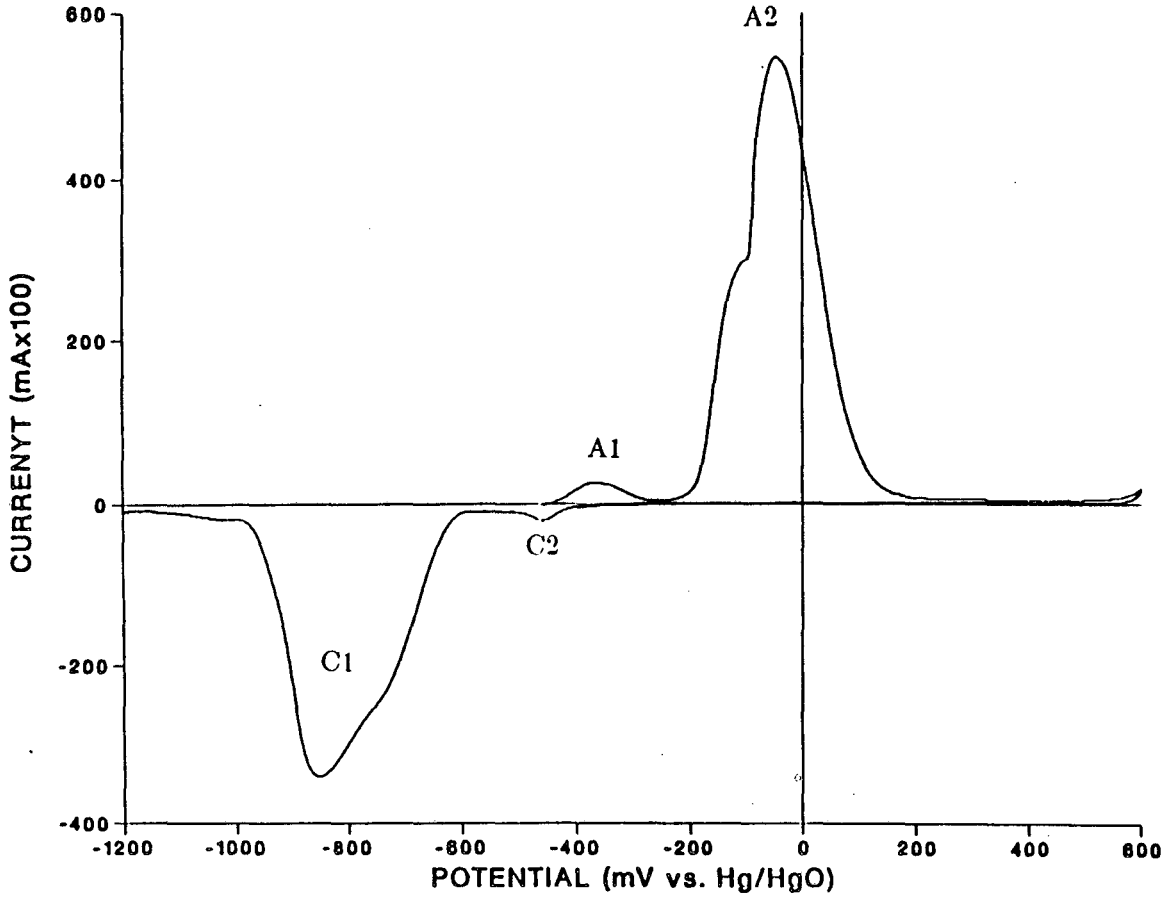

XBL 894-1412

Figure 1-4

CHAPTER 2

ANODIC SILVER FILMS IN ALKALINE SOLUTIONS: LITERATURE

Section 2.1: Introduction

The oxidation of silver in alkaline media has been studied using spectroscopic ellipsometry by this author before [B1-B5]. An in-depth analysis of the mechanism of nucleation of the monovalent Ag_2O film was undertaken using a number of new techniques to answer some outstanding questions regarding this system and to help contrast the oxidation processes of several different metals. As noted before, silver is viewed as a model system for such studies. Since the literature pertaining to this system has been discussed before [B2], only a brief review will be presented here. The formation and reduction of divalent AgO is not the subject of this investigation.

Section 2.2: Thermodynamics

Silver, being a transition metal and belonging to the second subgroup of the first period of the periodic table, is believed to exhibit three oxidation states; Ag^{+1}, Ag^{+2}, and Ag^{+3}. The corresponding oxides for these oxidation states are Ag_2O, AgO, and Ag_2O_3. The mono- and divalent species are known to exist, whereas the existence of a trivalent oxide is still a matter of controversy. Based

on some anomalous voltammetric results, the existence of a monovalent hydroxide, AgOH, has been suggested but has never been confirmed. Many now believe AgOH may exist only as a monolayer film.

Silver is a noble metal and is stable (does not corrode) in alkaline media [B6]. Face-centered cubic is the only stable crystalline form of silver metal. Silver is noted for its very low specific electrical resistance (1.59×10^{-6} ohm-cm). Ag_2O is known to be a stable compound. Its structure is a face-centered cube of silver ions merged with the oxygen cubic lattice; the oxygen atoms form the centers for tetrahedra of silver atoms [B7]. The specific electrical resistance of Ag_2O has been reported to be very high (10^8 ohm-cm) [B6,B8]. Since the source of the reported value is very old, this value is questionable. It is our opinion that this value is much too large. While the optical properties are not a sole indicator of the electrical properties of a material, the fact that the oxide is black (like carbon) might indicate a higher conductivity.

The electrochemistry of silver has been extensively studied, and the standard potentials for its reactions published in standard references are believed to be highly accurate. Silver is insoluble in alkaline media (on the order of 10^{-6}M to 10^{-4}M) [B9]. Thermodynamic data used in calculating values of the standard potentials for various silver reactions are readily available, as is the Pourbaix diagram [B6,B9-B11]. Some of the more important reactions are listed below, along with equations for the potentials of the reaction (E°) versus NHE (Hg/HgO electrode in 1M KOH is +98.6 mV vs NHE).

$$Ag_2O + 2H^+ + 2e^- \rightleftarrows 2Ag + H_2O \qquad 2.1$$

$$E^\circ = 1.173 - 0.0591\ pH$$

$$2AgO + 2H^+ + 2e^- \rightleftarrows Ag_2O + H_2O \qquad 2.2$$

$$E^\circ = 1.398 - 0.0591\ pH$$

$$2Ag_2O_3 + 2H^+ + 2e^- \rightleftarrows AgO + H_2O \qquad 2.3$$

$$E^\circ = 1.569 - 0.0591\ pH$$

$$Ag^+ + e^- \rightleftarrows Ag \qquad 2.4$$

$$E^\circ = 0.799 + 0.0591\log[Ag^+]$$

$$2Ag^+ + H_2O \rightleftarrows Ag_2O + 2H^+ \qquad 2.5$$

$$\log[Ag^+] = 6.33 - pH$$

$$Ag_2O + 2OH^- \rightleftarrows 2Ag(OH)_2^- + H_2O \qquad 2.6$$

$$\log[Ag(OH)_2^-] = -17.72 + pH$$

$$Ag(OH)_2^- + e^- \rightleftarrows Ag + 2OH^- \qquad 2.7$$

$$E^\circ = 2.220 - 0.1182\ pH + 0.0591\log\ [Ag(OH)_2^-]$$

From the linear dependence of the solubility of Ag_2O on OH^- concentration, Johnston *et al.* [B11,B12] proposed that the major soluble species is the AgO^- ion. The existence of a silver oxide ion has been supported by a chemical-stability study [B13]. The hydrated form of this ion has also been mentioned as the soluble species in a number of publications. Pound *et al.* [B10,B11] have shown that the $Ag(OH)_2^-$ ion is the most soluble ion at high pH; the silver ion Ag^+ is the most stable at lower pH.

Since our study of the oxidation of silver was performed in 1M KOH (pH 14), it may prove instructive to review the faradaic processes that occur with increasing potential in that solution. Again, as was done in the case of copper in Chapter 1, all potentials are relative to the Hg/HgO in 1M KOH reference electrode used in this study. At a potential of -898 mV (vs Hg/HgO in 1M KOH), the oxidation of molecular hydrogen begins. At more negative potentials, water is decomposed to form hydroxide and molecular hydrogen. This reaction occurs fairly rapidly because, unlike the case of zinc or even copper, silver is a fairly good catalyst for hydrogen evolution. Indeed, except for the platinum group, it exhibits one of the lowest hydrogen overpotentials of all metals.

From equation 2.6, we calculate the solubility of $Ag(OH)_2^-$ to be 1.9×10^{-4}M in 1M KOH. Using this value in equation 2.7, one finds that a saturated solution of $Ag(OH)_2^-$ exhibits an E° value of 247 mV vs Hg/HgO. This is the same potential as that of the formation of the oxide in equation 2.1. Therefore, silver can be oxidized at a potential lower than 247 mV as long as the surface concentration is lower than the saturation value. This potential value is in very good agreement with the results of Dirske *et al.* [B14], who placed silver wires in 1M KOH solutions containing various concentrations of dissolved silver from either AgO or Ag_2O. They found that under these conditions the potential of the silver wire electrode was always the same. They concluded that AgO must generate a monovalent dissolved species (since the potential of the wire was independent of the type of oxide used) and that the potential must depend on the formation of a surface layer of Ag_2O. We have previously shown that this potential is

coincident with the formation of a mono- and multiatomic layer oxide film [B2,B4].

The decomposition of hydroxide ion to water and molecular oxygen occurs at a thermodynamic potential of 301 mV, but this reaction is kinetically impeded by the formation of an oxide layer. Equation 2.5 shows that the solubility of the Ag^+ is 2.13×10^{-8}M at pH 14; using this value in equation 2.4 yields a potential of 346 mV for a saturated solution of Ag^+. Ag_2O is transformed to AgO at a thermodynamic potential of 472 mV (equation 2.2), and the divalent oxide is transformed to the the questionable trivalent oxide at 643 mV (equation 2.3). Figure 2-1 shows these processes.

Section 2.3: Film Composition and Structure

Ag is oxidized in separate stages, first to Ag_2O and then to AgO. Studies on silver oxide batteries show that a two-step (potential) reduction process occurs only at low current drains. At higher currents, a single discharge potential corresponding to the reduction of Ag_2O is observed. Several investigations have been undertaken to determine this discrepancy because of the energy loss associated with the phenomenon. However, all that can be said with certainty is that AgO is somehow irreversibly reduced to Ag_2O prior to reduction to silver.

X-ray diffraction has shown that Ag_2O precedes AgO formation, and that the oxides are crystalline. The crystals show preferential (111) orientations [B15,B16]. Briggs *et al.* [B16] described the surface films as multilayered and

crystalline. They oxidized silver galvanostatically for various times. Based on x-ray diffraction (XRD), scanning electron microscopy (SEM) and low energy electron diffraction (LEED) measurements, the structure of the film was described as consisting of an underlayer of crystals with a maximum diameter of 200 Å. This layer was said to form first. Later, larger oxide crystals of much smaller number density form on top of the underlayer. A tertiary layer of small (50-200 Å) crystals was found to form on top of the larger crystals. The size distribution and orientations of the secondary crystals were reported to depend on the manner of formation (e.g., potentiostatic, galvanostatic, potential, current density). Because the size and shape of the crystallites appeared to be independent of the applied potential, Briggs *et al.* concluded that the overall kinetics was not controlled by the kinetics at the metal-oxide interface. SEM photographs made by this author [B2,B4] are in general agreement with these ideas. However, we feel that some of the fine structure (e.g., the tertiary layer and the island crystalline underlayer) may be an artifact of the *ex-situ* treatments as well as of the method of oxidation (n.b. discussion of SEM photographs in refs. B2 and B4).

Detailed interpretation of spectroscopic ellipsometry has shown that the oxide first forms as a monolayer and continues to grow initially into a uniform multilayer. During potential-sweep measurement to low overpotentials, we have shown [B4] that a soluble anodic product diffuses from the interface into the solution and that the ellipsometer detects a very thin layer that may be an adsorbed product. We believe that it may be the slow desorption of this product that results in the formation of the uniform primary layer. The immediate nucleation

of the secondary (crystalline) layer was not found to occur after the application of a potential above the "nucleation potential." Instead, the homogeneous (primary) layer thickness increases parabolically with time until a critical thickness is reached (150-200 Å). This layer was shown to be homogeneous because the derived optical properties were thickness-independent. This finding is inconsistent with an island-film growth mechanism.

The thickness of the primary layer decreases sharply at the point of nucleation. The secondary crystals, which are rapidly formed from the material from the primary layer, have an initial size comparable to the primary layer before nucleation. If nucleation occurred directly from a supersaturated solution (as proposed by the dissolution/precipitation mechanism), no induction time should be observed under potential-controlled conditions. The surface concentration (controlled by the potential, as shown in equation 2.7) would not change with time. The induction time for nucleation does not represent the time necessary to reach a given supersaturation but results from the necessity of forming a precursor layer for the nucleation of the crystalline layer.

During the early stages of growth of the secondary crystals, the surface coverage of the crystal is observed to decrease. We believe that this is due to the fact the the secondary layer grows from the previously existing primary layer (which initially covered the entire surface). Since the nucleation process is stochastic in time, some growth centers will be larger than others at the same time. As the crystals increase in size and the diffusion regions overlap, the larger crystals, which exhibit a lower solubility (Gibbs-Thompson equation), will tend to

collect material from the smaller crystals. Ostwald ripening therefore occurs. Finally, the crystals become so large that the size effects are no longer important and the number density becomes independent of time.

Section 2.4: Kinetics

Today, electrochemical measurements are among the easiest types of measurements to perform. Modern potentiostats allow one to conveniently program a vast variety of waveforms (e.g. sinusoidal, white noise fast Fourier transform (FFT), current step, potential step, potential sweep). Largely because of the relative ease of such an experiment, a great deal of literature is devoted to the interpretation of such measurements. One of the techniques most widely used today is cyclic voltammetry (CV, also known as repetitive triangular potential-sweep voltammetry, or RTPS). Many feel that this technique is generally useful only for the qualitative interpretation of chemical and physical processes, while others have made detailed calculations and interpretations based on CV results. It is the general view of this author that CV is a very sensitive technique to both chemical and physical processes, but that the interpretation of CV results is often extremely difficult and ambiguous. Data for the CV of silver in alkali generally show four characteristic anodic peaks, referred to as A1 to A4. Only the first two are associated with the initial stages of Ag_2O formation. The A1 peak was first identified by Dirske and De Vries [B17], who reported a potential of formation of about 220 mV vs Hg/HgO. They attributed the peak to the formation of a thin AgOH film accompanied by concurrent dissolution of the electrode. This

conclusion is supported by a number of other authors, as well as our previously reported results. The suggestion that this peak is associated with carbonate impurities [B18,B19] has since been rejected [B20]. The size and appearance of the peak depends on the crystal face, with the Ag(110) face being more reactive than the Ag(111) face [B21], as well as on the open-circuit solution contact time and time of cycling [B22].

The A2 and A3 peaks (around +310 and +510 mV vs. Hg/HgO, respectively) have been associated with the formation of bulk oxide films. Some [B23] attribute the A2 peak to the "initial stages of oxidation." Other explanations include the preferential oxidation of low-coordination-number atomic planes [B4] and the formation of different hydrates of silver oxide [B25]. Our ellipsometric results indicated that the A2 peak is associated with the formation of the three-dimensional Ag_2O crystalline oxide film [B2,B4].

Because galvanostatic current sources were commercially available before the more modern potentiostats, many early experiments were performed in the constant-current mode. Typical galvanostatic polarization curves [B2,B10,B16,B26-B29] show a rising potential that peaks at around +310 mV vs Hg/HgO (see Figure 2-2). At higher current densities ($>$ 200 mA/cm^2), a shallow dip in potential appears. However, the most noticeable feature is that the potential remains relatively constant during charging. The sharpness of the potential peak and the depth of the potential dip increase with temperature and decrease with current density. The steep rise in potential that occurs at later times (greater total charge) is believed to be correlated with complete coverage of

the surface with Ag_2O. The potential rises to the AgO formation-potential range. After another plateau is reached, the potential again rises, and oxygen is observed to evolve from the electrode. Because the current flow is the controlled parameter in these experiments, the surface concentration and the double-layer charge change with time. These factors complicate the interpretation of the galvanostatic experiment.

If one assumes that current associated with double-layer charging and the potential loss due to charge-transfer irreversibility (i.e., charge-transfer overpotential) are negligable, the interpretation of potentiostatic experiments is greatly simplified. These assumptions lead to the conclusion that the potential on both sides of the electode/electrolyte interface is the same (i.e., that the activity of electrons is the same in both phases), and that the surface concentration therefore obeys the Nernst equation: the potential on the solution side of the interface is equal to that of the electrode. Therefore, to a first-order approximation, the concentration of electroactive species at the interface doesn't change with time. The boundary condition for the potential-step experiment with these assumptions is that the surface concentration undergoes a step change at the point the potential is changed (i.e., Cottrell condition). For the silver system, current transients generally follow a Cottrell inverse square-root time dependence, which indicates one-dimensional diffusion control of a soluble silver species below the nucleation potential [B2,B4,B10,B11,B19,B20,B23]. Above the nucleation potential, a transient current minimum and maximum are observed [B2,B4,B17,B31]. Many explanations have been presented to account for this observation, and while a

number of authors have attributed these current transient peaks to surface phase formation, we were the first to show conclusive physical evidence that the nucleation of crystalline Ag_2O was responsible for the phenomenon. We have previously preformed some calculations [B2] to show that the appearance of these features in the current transients is consistent with crystalline oxide nucleation and growth.

Section 2.5: Literature Summary and Conclusions

Silver is highly insoluble in alkaline solutions. The anodic formation of a monovalent Ag_2O film and the soluble ion $Ag(OH)_2^-$ have been observed. The structure of the film consists of a homogeneous compact underlayer, with three-dimensional crystals on top of the compact layer. We have shown that the growth of the compact layer is a diffusion/migration-controlled process, and that this layer provides the necessary material to form critical size nuclei and aids in the nuceation and growth of three-dimensional Ag_2O crystals. We have reported that the number of growing Ag_2O crystals decreases as a result of an Ostwald ripening phenomenon [B1,B2,B4]. In this study, we are mainly concerned with verifying our earlier findings concerning the Ag_2O film-formation mechanism.

REFERENCES FOR CHAPTER 2

B1) Mayer, Steve T., and R. H. Muller, **Nuclation of Silver (I) Oxide Studied by Spectroscopic Ellipsometery**, ext. abs. presented at Electrochemical Society Meeting, San Diego, CA, Oct. 1986. Lawerence Berkeley Laboratory Report LBL-21390 abs.

B2) Mayer, Steve T., **An Ellipsometric Spectroscopy Study of Anodically Formed Silver (I) Oxide on Silver**, M. S. Thesis, University of California at Berkeley, December 1985. Lawerence Berkeley Laboratory Report LBL-15607.

B3) Mayer, Steve T., and R. H. Muller, **Data Acquistition and Reduction Software For a Self-Nulling Ellipsometer**, March 1986. Lawerence Berkeley Laboratory Report LBL-20677.

B4) Mayer, S. T., and R. H. Muller, J. Electrochem. Soc. **135,** 2133 (1988).

B5) S. T. Mayer and R. H. Muller, **Nucleation of Silver (I) Oxide Investigated by Spectroscopic Ellipsometry**, March 1988. Lawerence Berkeley Laboratory Report LBL-23844 Rev.

B6) Shumilova, N. A., and G. V. Zhutaeva, in **Encylopedia of Electrochemistry of the Elements**, Vol. VIII, Allen J. Bard, ed., Marcel Dekker, Inc. New York, 1978.

B7) R. W. G. Wyckoff, **Crystal Structures**, Vol. 1, 2nd edition, Wiley-Interscience, New York, 1963.

B8) Le Blanc, M., and H. Sachse, Z. Physik. **32,** 887 (1931).

B9) Vanleugenhaghe, C., M. Pourbaix, and R. Van Pysselberghe, in **Atlas of Electrochemical Equilibria in Aqueous Solutions**, Section 14.2, English Translation, Pergamon Press, New York, 1966.

B10) Pound, B. G., D. D. Macdonald, and J. W. Tomlinson, Electrochim. Acta. **25,** 563 (1980).

B11) Pound, B. G., D. D. Macdonald, and J. W. Tomlinson, Electrochim. Acta. **25,** 1293 (1980).

B12) Johnston, H. L., F. Cuta, and A. B. Garrett, J. Am. Chem. Soc. **55,** 2311 (1933).

B12) Johnston, H. L., F. Cuta, and A. B. Garrett, J. Am. Chem. Soc. **56,** 1250 (1934).

B13) Antikainen, P. J., S. Heitanen, and L. Gunnar Sillen, Acta Chem. Scand. **14,** 95 (1960).

B14) Dirkse, T. P., L. A. Vander Lugt, and H. Schnyders, J. Inorg. Nucl. Chem. **25,** 859 (1963).

B15) Wales, C. P., and J. Burbank, J. Electrochem. Soc. **112,** 13 (1965).

B16) Briggs, G. W., M. Fleischmann, D. J. Lax, and H. R. Thirsk, Trans. Faraday Soc. **64,** 3120 (1968).

B17) Dirkse, T. P., and D. B. De Vries, J. Electroanal. Chem. **63,** 107 (1959).

B18) Stonehart, P., and F. P. Portante, Electrochim. Acta **13,** 1805 (1968).

B19) Tilak, B. V., R. S. Perkins, H. A. Kozlowska, and B. E. Conway, Electrochim. Acta **17,** 1447 (1972).

B20) Droog, J. M. M., P. T. Alderliesten, and Gosse A. Bootsma, J. Electroanal. Chem. **99,** 173 (1979).

B21) Droog, J. M. M., J. Electroanal. Chem. **115,** 225 (1980).

B22) Giles, R. D., and J. A. Harrison, J. Electroanal. Chem. **27,** 161 (1970).

B23) Hepel, M., and M. Tomkiewicz, J. Electrochem. Soc. **131,** 1288 (1984).

B24) Hampson, M. L., J. Electroanal. Chem. **45,** 149 (1973).

B25) Teijelo, M. L., J. R. Vilche, and A. J. Arvia, J. Electroanal. Chem. **162,** 207 (1984).

B26) Dignam, M. J., H. M. Barrett, and G. D. Nagy, Can. J. Chem. **47,** 4253 (1969).

B27) Cahan, B. D., J. B. Ockerman, R. F. Amlie, and P. Ruetschi, J. Electrochem. Soc. **107,** 725 (1960).

B28) Gibbs, D. B., B. Roa, R. A. Griffin, and M. J. Dignam, J. Electrochem. Soc. **122,** 1167 (1975).

B29) Droog, J. M. M., and F. Huisman, J. Electroanal. Chem. **115,** 221 (1980).

B30) Fleischmann, M., D. J. Lax, and H. R. Thirsk, Trans. Faraday Soc. **64,** 3128 (1968).

B31) Cotton F. A., and G. Wilkinson, in **Advanced Inorganic Chemistry, A Comprehensive Text**, 4th edition, John Wiley and Sons, Inc. 1980, p. 969.

FIGURE CAPTIONS FOR CHAPTER 2

Figure 2-1. Thermodynamic potential of various reactions of Silver in 1M KOH versus the Hg/HgO (in 1M KOH) reference electrode.

Figure 2-2. Galvanostatic oxidation of Ag (111) in 1M KOH at 50 $\mu A/cm^2$ in 1M KOH. Potential with respect to the Hg/HgO reference electrode. Total electrode area 3.12 cm^2.

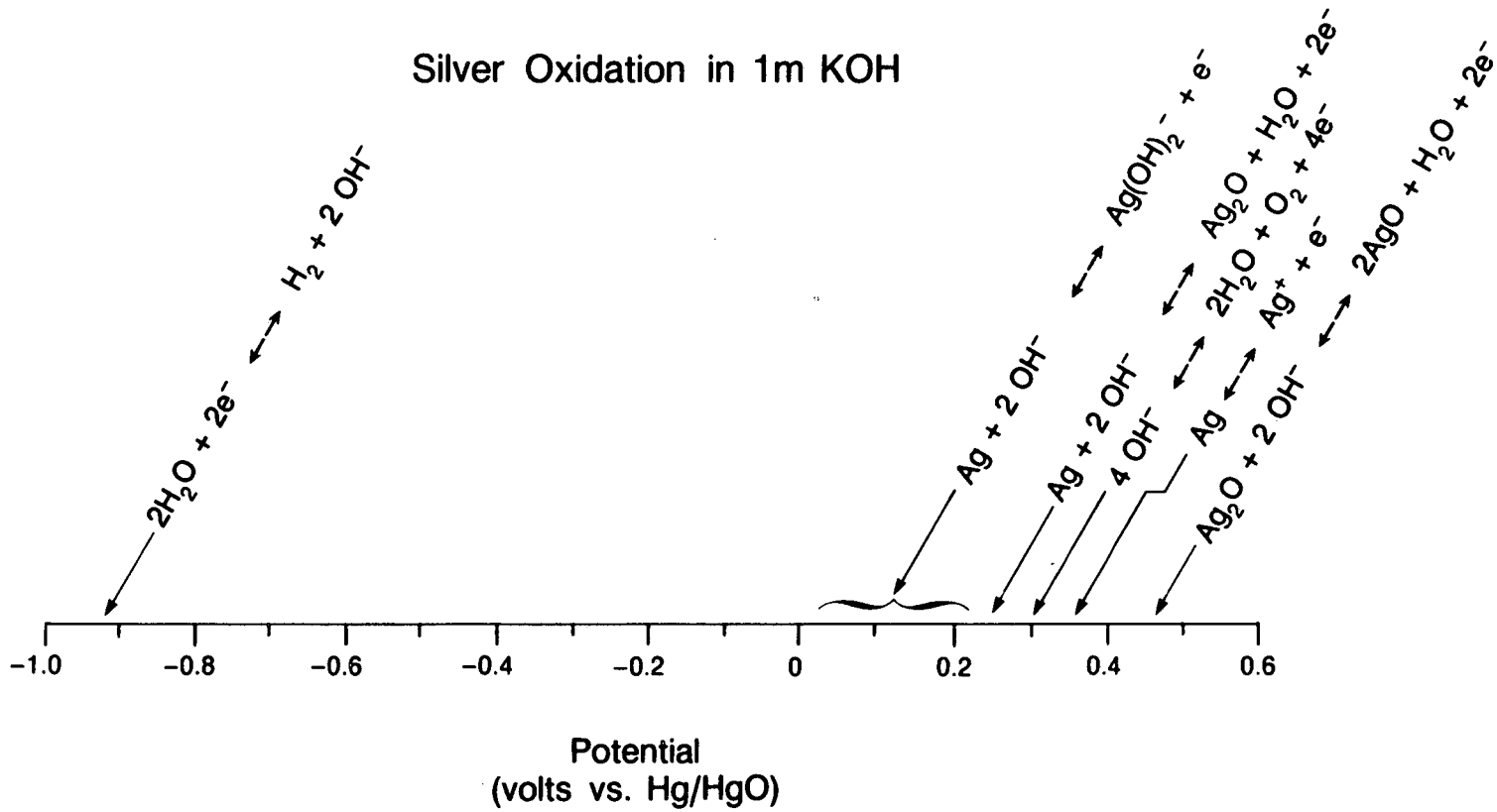

XBL 897-7210

Figure 2-1

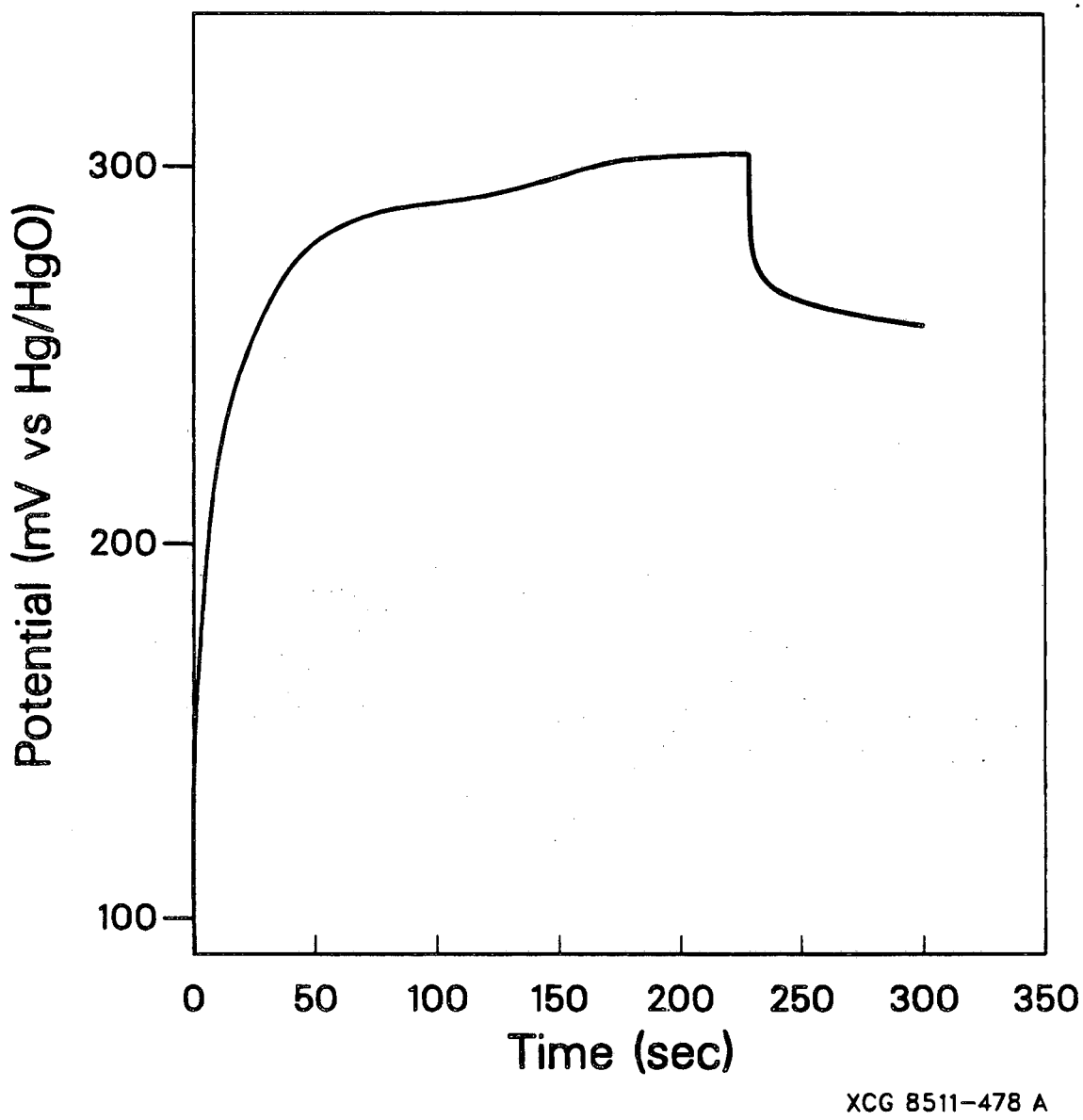
300
200
100
Potential (mV vs Hg/HgO)
0
50
100
150
200
250
300
350
Time (sec)
XCG 8511-478 A

Figure 2-2

CHAPTER 3

ZINC IN ALKALINE SOLUTIONS: LITERATURE

Section 3.1: Thermodynamics

The electrochemistry of zinc (along with hydrogen and oxygen) is one of the most extensively studied electrodes among metals. Zinc is a metal with a standard potential above (cathodic of) the hydrogen/water couple. The value of the standard potential calculated from thermodynamic data [C1] is

$$Zn^{2+} + 2e^- \rightleftarrows Zn \qquad E_{25°C} = -0.7628\,. \tag{3.1}$$

Experimental data are in close agreement with this calculated value. The effect of temperature change is small (about 0.1 mV/ C°). Potential differences of several millivolts in the standard potential of zinc reduction for the various crystal faces have been reported [C2] and are said to result from the differences in the atomic packing density of the crystal planes. The exchange current density has been reported to also depend on crystal face [C3].

Section 3.2: Dissolved Zinc in Alkaline Solutions

The outer orbital electron configuration of a zinc atom is $3d^{10}4s^2$. There is no evidence for the existence of a monovalent ion of zinc. Generally, the d orbitals do not enter into bonding (and hence, zinc is not considered a transition metal). It is the $4s^2$ electrons that are lost when a divalent ion is formed. Thus,

when a zinc bond is formed with a p bonding atom (halide or oxygen), sp^2 and sp^3 hybridized orbitals are formed. A series of soluble zinc species have been proposed, and a complex equilibrium among the various zincate species has been represented by

$$Zn^{+2} + OH^- \rightleftarrows ZnOH^+ \ , \qquad 3.2$$

$$ZnOH^+ + OH^- \rightleftarrows Zn(OH)_2 \ , \qquad 3.3$$

$$Zn(OH)_2 + OH^- \rightleftarrows Zn(OH)_3^- \ , \qquad 3.4$$

$$Zn(OH)_3^- + OH^- \rightleftarrows Zn(OH)_4^{-2} \ . \qquad 3.5$$

Increasing pH tends to drive all of these reactions to the right, and therefore, at high pH $Zn(OH)_4^{-2}$ is the most stable solution species [C1]. A calculated species distribution diagram for the zinc hydroxide system has been presented before [C1,C4]. These intermediate chemical compounds may be important because the species undergoing charge transfer may not necessarily be the most prevalent in solution. According to Gerischer [C5], the charge-transfer complex for the Zn/Zn^{+2}, OH^- couple is neutral $Zn(OH)_2$ at pH 14, despite the fact that many investigators believe $Zn(OH)_4^{-2}$ to be the predominant complex in solution. Farr and Hampson [C3] proposed the following for the reduction/oxidation reaction of zinc on solid electrodes:

$$Zn(OH)_4^{-2} \rightleftarrows Zn(OH)_2 + 2OH^- \ , \qquad 3.6$$

$$Zn(OH)_2 + e^- \rightleftarrows Zn(OH)_{ad+} OH^- \ , \qquad 3.7$$

$$Zn(OH)_{ad} + e^- \rightleftarrows Zn(OH)_{ad}^- \ , \qquad 3.8$$

$$Zn(OH)_{ad}^- \rightleftarrows Zn + OH^- \ . \qquad 3.9$$

This mechanism is among many others that have been proposed [C4]. Because of the often contradictory reports of the effects of varying OH^- concentration on the exchange current, no general agreement as to the best mechanism for the zinc reaction in alkaline media can presently be found.

Raman and NMR measurements indicate that dissolved zinc exists primarily as a tetrahedrally coordinated complex $[Zn(OH)_4^{-2}]$ in concentrated alkaline solutions [C6-C10]. The rate of dissolution of ZnO powder is slow; it may take as long as several months to reach saturation. During the discharge of zinc in alkali, supersaturated solutions may be formed. Therefore, because studies of supersaturated solutions are of importance and because electrochemically dissolved species are more easily formed, electrochemically dissolved zinc has often been used in solution studies. Concentrations corresponding to three times the equilibrium value of ZnO can be produced in this manner. Observations made in the 1930s indicated that after a long period of standing, ZnO will precipitate from a supersaturated solution (the solid hydroxides are unstable with respect to the oxide) [C11,C12], but more recent papers have not supported this observation. Dirske reported that solutions supersaturated with zincate often will not precipitate ZnO, even when shocked or seeded [C13]. The slow rate of precipitation of ZnO may result from a slow decomposition reaction step prior to the

incorporation of material into a lattice growth site. NMR and light-scattering measurements have shown that even the supersaturated solution does not contain colloidal particles [C14]. Li^+ and SiO_3^{-2} have been found to retard the precipitation process even more [C15]. Silicate has been shown to strongly influence homogeneous nucleation over a limited range of pH and concentration and to greatly increase the depth of discharge of anodic zinc [C16,C17]. However, these measurements have not been confirmed, and questions remain as to the validity of the findings at other concentrations. Despite these open questions, silicate has been added to slurry electrolytes of zinc/air battery systems [C18-C20] and appears to improve cell performance. The solubility of ZnO is generally lower than that of $Zn(OH)_2$ by a factor of two. At moderate pH (1M KOH), the solubilities are comparable. Data on the solubility of both ZnO and $Zn(OH)_2$ are available [C21,C22].

Section 3.3: The Hydrogen Overpotential of Zinc

As noted above, zinc is an electroactive metal in aqueous solutions, despite the fact that H_2 reduction occurs at a potential anodic of the standard potential of zinc. One would expect that zinc might rapidly corrode (dissolve) by reacting with water. In fact, this does happen to some extent in concentrated acid and alkaline solutions. However, the spontaneous reaction of zinc with water (or OH^-) is effectively suppressed by the large overvoltage for hydrogen evolution on zinc. Thus, the rate of hydrogen evolution is sufficiently slow that zinc can be reduced at reasonable rates. Brodd and Leger [C1] state that the large hydrogen

overpotential is a direct consequence of the weak interactions between zinc and hydrogen. They calculate values for the hydrogen-zinc bond energy (-64 kcal/mole) and the heat of hydrogen adsorption (-16 kcal/mole), and they conclude that hydride formation should not occur to any appreciable extent on zinc. We believe that the necessity of creating a weak zinc/hydrogen σ–σ bond (zinc does not act like a transition metal, and therefore does not form the more stable σ–d bonds) results in a large hydrogen overpotential. In fact, almost all non-transition metals tend to exhibit large hydrogen overpotentials.

Section 3.4: Zinc Anodic Film Formation

Zinc dissolves easily near its equilibrium potential, forming divalent zinc complexes in solution (see above). The kinetics of dissolution from solid zinc and zinc amalgam have been reported to be similar [C23]. Current efficiencies of near 100% can be expected (except in the presence of NO_3^-, ClO_3^-, and ClO_4^-, where the anions are reduced by zinc).

Galvanostatic oxidation of Zn in alkaline solutions exhibits a period of active dissolution followed by passivation of the surface. The passivation is evident by a sudden change in the potential to positive values and the evolution of oxygen. The necessary time (charge) for passivation reaches a maximum with increasing alkali concentration at around 7M KOH. Dissolved zinc in solution tends to reduce the passivation time [C1]. At sufficiently high currents, dissolution is believed to become mass-transport limited [C24], and therefore passivation has been associated with a dissolution/precipitation mechanism of film formation.

The effects of the changes in the solubility and mass-transport properties of the solution have been used to correlate the time of passivation using a relation similar to the Sand equation [25-28]:

$$(i-i_l)t^{1/2} = k \quad . \qquad 3.10$$

In equation 3.10, i is the applied current density and t the time for passivation. The adjustable parameters i_l and k depend on KOH concentration and electrolyte flow conditions. The values of the derived parameters have been a matter of controversy. Yet, as noted by McBreen and Cairns [C4], this interrelationship yields practically no information on the passivation mechanism. All that this interrelationship (equation 3.10) indicates is that diffusion and migration are the primary modes of mass transfer, as well as the amount of zinc utilization that can be expected.

The nature of the surface film has been investigated by a number of authors. A white, flocculent precipitate is found on battery electrodes during discharge [C13,C29]. SEM images of the anodized surface made by Smith and Muller [C30] show a compact, etched surface film. During potential sweep experiments, passivation is reported to be accompanied by visible film formation; the film is said to disappear on returning to more cathodic potentials. During the active phase of dissolution, a dense, shiny, bluish-black layer of ZnO is formed and is believed to contain an excess of interstitial zinc. (ZnO is known to be white.) The film tends to darken with further anodization [C31,C32]. Still, the exact nature of the film remains unknown. ZnO has been identified as a component of the passive

film by x-ray diffraction, but since $Zn(OH)_2$ readily dehydrates to ZnO [C33], and the x-ray measurements were made *ex-situ*, it is possible that a conversion of the film from $Zn(OH)_2$ to ZnO occurred. Furthermore, oxygen evolution had occurred on these electrodes, and, as noted by Dirske and Hampson [C34] "it is (therefore) not surprising that ZnO was identified." X-ray transmission and electron diffraction measurements indicated γ -$Zn(OH)_2$ to be present on the surface. Excess oxygen has been found in films formed at high current densities [C35].

Several authors have proposed structures for the anodic Zn surface layers. These include an underlayer of $Zn(OH)_2$ with an outerlayer of ZnO [C36], and a dual layer of ZnO, the inner layer formed by a solid-state mechanism and the outer layer formed via the solution [C29]. But Dirske and Hampson [C34] concluded from their electrochemical measurements that they were not able "to decide whether the initially-formed film of ZnO comes from the electrolyte or is formed *in situ* on the lattice by direct oxidation." Since direct *in situ* measurements are still very limited, the structure of the surface layers remains obscure.

Section 3.5: Literature Summary and Conclusions

Zinc is a reactive metal, with a standard potential negative (cathodic) of hydrogen evolution. Zinc can be electrodeposited because it exhibits a high overpotential for hydrogen evolution. A series of soluble zinc species has been proposed, but the highly soluble tetrahedrally coordinated zincate ion $[Zn(OH)_4^{-2}]$ is the most prevalent at pH 14. The rate of dissolution of zinc oxide to form zincate is slow, but concentrations of up to three times the saturation value can be

produced electrochemically. Silicate has been proposed to retard the precipitation process and enhance the solubility of zinc, but evidence for complexation or colloidal particle formation is needed. Also, direct *in situ* measurements are needed to clarify the mechanisms of film formation, growth, and passivation.

REFERENCES FOR CHAPTER 3

C1) Brodd, R. J., and V. E. Leger, **Encylopedia of Electrochemistry of the Elements**, Vol. V, Allen J. Bard, Editor, Marcel Dekker, Inc, New York, 1974.

C2) Straumanis, M., Z. Physik. Chem. A **147,** 161 (1930).

C3) Farr, J. P. G., and N. A. Hampson, J. Electroanal. Chem. **13,** 483 (1967).

C4) J. McBreen and E. Cairns, in **Advances in Electrochemistry and Electrochemical Engineering**, Vol. 11, H. Gerischer and C. W. Tobias, Editors, John Wiley and Sons, New York, 1978.

C5) Gerischer, H., Z. Elektrochem., **57,** 604 (1957).

C6) Fordyce, J. Stuart, and Ruth L. Baum, J. Chem. Phys. **43** 843 (1965).

C7) Newman, G. H., and G. E. Blomgren, J. Chem. Phys. **43** 2744 (1965).

C8) Briggs, A. G., N. A. Hampson, and A. Marshall, Trans. Faraday Soc. **70,** 1978 (1974).

C9) Sharma, Shiv K., and M. D. Reed, J. Inorg. Nucl. Chem. **38,** 1971 (1976).

C10) Cain, K. J., C. A. Melendres, and V. A. Maroni, J. Electrochem. Soc. **134,** 519 (1987).

C11) Fricke, R., and B. Wallhorst, Z. Anorg. Allgem. Chem. **205,** 127 (1932).

C12) Huettig, G. F., and H. Moeldner, Z. Anorg. Allgem. Chem. **211,** 368 (1933).

C13) Dirske, T. P., J. Electrochem. Soc. **102,** 497 (1955).

C14) Van Doorne, W., and T. P. Dirske, J. Electrochem. Soc. **122,** 1 (1975).

C15) Flerov, V. N., Zh. Fiz. Khim. **31,** 310 (1957).

C16) Marshal, A., and N. A. Hampson, J. Electrochem. Soc. **59,** 19 (1975).

C17) Marshal, A., N. A. Hampson, and M. P. Saunders, J. Electrochem. Soc. **78,** 307 (1977).

C18) Appleby, A., and M. Jacquier, J. Power Sources **1,** 17 (1977).

C19) Ross, P. N., Jr., **Feasibility Study of a New Zinc-Air Battery Concept Using Flowing Alkaline Electrolytes,** Lawerence Berkeley Laboratory Report LBL-21437, April 1986.

C20) Ross, P. N., Jr., **Zinc-Air Design Concept for the DOE-EHP IDSEP Van,** Lawerence Berkeley Laboratory Report LBL-24639, Janurary 1988.

C21) Dirske, T. P., Chapter 3 in **The Zinc-Silver Oxide Battery,** A. Fleischer and J. J. Lander, Editors, Wiley, Inc., New York, 1969.

C22) Schumacher, E. A., Chapter 3 in **The Primary Battery: Volume 1**, G. Heise and N. C. Cahoon, Editors, Wiley, Inc., New York, 1971.

C23) Armstrong, R. D., G. M. Bulman, and H. R. Thirsk, J. Electroanal. Chem. **22,** 55 (1969).

C24) Farmer, E. D., and A. H. Webb, J. Appl. Electrochem. **2,** 123 (1972).

C25) Eisenberg, M., H. F. Bauman, and D. M. Brettner, J. Electrochem. Soc. **108,** 909 (1961).

C26) Elder, J. P., J. Electrochem. Soc. **116,** 757 (1969).

C27) Kaesche, H., Electrochim. Acta. **9,** 383 (1964).

C28) Bartelt, H., and R. Landsber, Z. Phys. Chem. **222,** 217 (1963).

C29) Powers, R. W., and M. W. Breiter, J. Electrochem. Soc. **116,** 719, (1969).

C30) Smith, C. G., **Ellipsometry of Anodic Film Growth**, Ph. D. Thesis, University of California at Berkeley, August 1978. Lawerence Berkeley Laboratory Report LBL-8082.

C31) Euler, J., Electrochim. Acta **11,** 701 (1966).

C32) Frey, H., and M. Whitaker, J. Electrochem. Soc. **106,** 606 (1959).

C33) Schendler, P., H. Althans, and A Fertnecht, Helv. Chim. Acta **47,** 982

(1964).

C34) Dirske, T. P, and N. A. Hampson, Electrochim. Acta **17,** 387 (1972).

C35) Popeva, T. I., V. S. Bagotskii, and B. N. Kabanov, Zh. Fiz. Khim. **36,** 766 (1962).

C36) Huber, G., J. Electrochem. Soc. **100,** 376 (1953).

CHAPTER 4

THEORIES OF NUCLEATION AND GROWTH BY ELECTROCRYSTALLIZATION

Section 4.1: Introduction

The crystallization of surface films formed electrochemically is commonly referred to as electrocrystallization or "electrosolidification." Even though this topic has been discussed in some detail by this author before [D1,D2], a short review will be presented here, with emphasis on new developments and some aspects not previously presented.

Electrocrystallization differs from crystallization from the vapor phase, a melt, or solution, in part by the number of ways growth can occur on the electrode. Qualitatively, the concentration gradient of active species for a cathodic process will be opposite to that for an anodic process. Some of the growth paths have been discussed by Fleischmann and Thirsk [D3]; these paths include new phase formation (a) on an inert or similar substrate by electrodeposition of an ion from solution; (b) from the substrate by electrodissolution followed by precipitation from solution; (c) via ions that pass from the substrate through a new phase to the solution interface, with a portion of the ions reacting there to form an advancing surface layer; or (d) by a transformation of an already existing surface layer, as formed in (b) or (c). Clearly, method (a) is generally limited to metal

deposition and differs from processes (b) and (c) in that the nucleating species is found only on the metal electrode surface rather than in the solution or in a surface film. The dissolved ions in (b) or (c) can undergo further reactions in the solution phase. Since in (b) and (c) the process is not two- but rather three-dimensional, nucleation and growth will generally proceed by the latter growth mechanism.

Section 4.2: The Mechanism of Crystal Growth

The crystal growth process can be rate-limited at various stages in the overall process. These stages include diffusion to the crystal and incorporation of material into a crystal. At the turn of the century, the control of crystal growth by molecular transport was the main topic of research. Noyes and Whitney's [D4] work on the dissolution of crystals led to an early diffusion theory for growth. With the introduction of the boundary-layer film model, Nernst [D5] was able to account for the dependence of growth on agitation rate. However, shortly after these theoretical developments were presented, Marc [D6-D9] demonstrated that factors other than diffusion were often more important in crystal growth. Stranski [D10] was perhaps the first to present a theory of growth that occurs by a sequence of lattice-building steps. Growth was believed to be initiated on a complete crystal plane by the formation of a two-dimensional nucleus. Volmer [D11] presented an adsorption theory of crystal growth. Adsorbed molecules were said to be free to migrate on the 2-D surface. They can desorb, become incorporated into a growth center, or conglomerate with other

molecules to form a new nucleus. The equation for growth by a two-dimensional nucleus at completed planes takes the form [D12]

$$\frac{dL}{dt} = Z\exp[-\pi\sigma^2 a\Omega/(RT)^2\ln(\gamma+1)] \ . \qquad 4.1$$

In equation 4.1, $\frac{dL}{dt}$ is the linear growth rate (distance/time), Z is a growth constant, σ is the surface energy of the solid/electrolyte interface, a is the thickness of the monolayer, Ω is the volume of a solute molecule, and γ is the relative supersaturation, $\frac{(C-C_s)}{C_s}$. Equation 4.1 predicts significant growth only when $\gamma+1$ is much greater that 1. Since serious discrepancies between this prediction and experimental results were found (substantial growth is often observed at very low supersaturations), Frank [D13] presented a model based on screw-dislocation theory. The screw-dislocation edge spirals, and hence the formation of new growth planes is not considered necessary since a completed 2-D plane never develops. Using these ideas, and assuming that growth is limited by the migration of an adsorbed solute molecule across the crystal face to the spiral, Burton *et al.* [D14] developed a growth expression of the form

$$\frac{\frac{dL}{dt}}{A\gamma_c} = [\frac{\gamma}{\gamma_c}]^2\tanh(\frac{\gamma_c}{\gamma}) \ , \qquad 4.2$$

with

$$A = A_o\exp[-(E_d-E_s)/RT] \qquad 4.3$$

and

$$\gamma_c = \frac{A_1 \exp[-\frac{1}{2}(E_d - E_s)/RT] 4\pi\sigma\Omega}{RT} \quad . \qquad 4.4$$

In these equations, A_o and A_1 are growth constants, and E_d and E_s are the activation energies for desorption and surface diffusion of the adsorbed solute (energy/mole), respectively. The term γ_c is called the critical supersaturation. Equation 4.2 exhibits approximately second-order growth (with respect to $\frac{\gamma}{\gamma_c}$) for values of $\frac{\gamma}{\gamma_c}$ less than 0.5 and first-order growth for values greater than 5. Therefore, growth characteristics can change over a wide range of solute concentrations.

Growth data have often been correlated by equations of the form

$$\frac{dL}{dt} = k^o(C - C_s)^m \quad , \qquad 4.5$$

with m lying between 1 and 4. The shape of equation 4.2 is not radically different from that of equation 4.5. Data for the growth of the [110] surface of magnesium sulfate heptahydrate, potassium alum, itaconic acid, and citric acid have been interpreted in terms of the theory of Burton *et al.* [D14].

Section 4.3: The Nucleation Growth Site

Many authors of electrochemical nucleation theory have utilized the concept of the nucleation "site" [D3,D15-D22]. These sites are envisioned as centers on the surface where material is incorporated into a growing lattice. However,

mostly speculation has been presented as far as the nature of these sites is concerned. As discussed above, point defects or screw dislocations, as well as ledges at different crystal planes, have been suggested as centers of nucleation and growth. While a strong relationship between surface treatment (and hence surface structure) and number density of nucleation sites has been observed, defect theory at best offers only a qualitative description of this observation. Therefore, theoretical and experimental research aimed at a better understanding of the relationship between surface structure and subsequent surface activity for nucleation is of considerable interest.

Theoretical calculations [D23,D24] show that new phase growth on a substrate should result in the same crystalline structure as the underlying lattice. This is most probable when the deposition rate is slow and the deposition is thermodynamically controlled. An electrodeposited monolayer should be of the same orientation as the substrate; some *ex situ* and recent *in situ* x-ray diffraction measurements of underpotential deposite (UPD) layers support this idea [D25]. Yet epitaxial calculations, which ignore kinetic aspects of the nucleation and growth problem, lead to an oversimplified model for film growth. While epitaxy may play an important role in the embryonic stages of nucleation, Fleischmann and Thirsk [D3] have noted that epitaxial studies and the idea of small-misfit values have dominated the subject of nucleation more than is warranted by experimental facts. Instead, the focus should be on models of nucleus growth and the dynamic problems of diffusion, changes in concentration and temperature with time, and the influence of surface forces and growth inhibition.

In answering these important questions, different schools of thought have developed. The most prevalent group of researchers on nucleation in the electrochemical literature is referred to by this author as the "geometric growth" school. This group employs a special vocabulary (e.g. "overlap", "expectation number") that distinguishes them from other schools. Another distinguishing feature of this group is their consideration of nucleation centers and later interactions. Theories of diffusion-controlled growth and morphological stability have not been used previously to understand nucleation phenomena. Before we present these approaches, it is necessary to discuss the role of thermodynamics in the nucleation process.

Section 4.4: Thermodynamics of the Anodic Nucleation Process

As the potential of an electrode is made increasingly positive, a potential is eventually reached at which the formation of bulk oxide is thermodynamically possible. Some metals (e.g., aluminum and tantalum) do not undergo any appreciable dissolution of ions up to this potential [D26]. Other metals (e.g., iron and nickel) dissolve as ions only above the thermodynamic potential of bulk film formation. During the initial stages of anodization of the more active metals, the concentration of electroactive species in the vicinity of the electrode increases until nucleated crystallites form at sites on the surface. With the possible exception of a UPD oxide layer, nucleation generally will occur only at a potential above that required for the formation of the bulk solid. Once nuclei are formed, they can act as sinks for the dissolved anodic products and will reduce the

supersaturation that has developed at the interface [D1,D2]. The overall growth process can be controlled at the metal/electrolyte or electrolyte/crystal boundary, as well as by diffusion in the solution.

But how does a crystal nucleus form? Clearly, atoms and/or molecules must reach the surface and overcome any energy barriers associated with the formation of a new surface. Vermilyea [D26] has presented a calculation of the necessary change in free energy for forming a circular monomolecular oxide patch. This change is

$$\Delta G = \pi r^2(\sigma_2+\sigma_3-\sigma_1) + 2\pi r a\sigma_3 + \pi r^2 a \Delta G_\nu \ , \qquad 4.6$$

where r is the radius of the patch; σ_1, σ_2, and σ_3 are the surface free energies (surface tensions) of the electrode-solution, electrode-film, and film-solution interfaces, respectively; a is the height of the 2-D patch; and ΔG_ν is the free energy change per unit volume of film formation. The relation between ΔG_ν and overvoltage is [D26]

$$-\Delta G_\nu = \frac{4.2\text{x}10^7 nF\rho\eta}{M} \ , \qquad 4.7$$

where ρ is the density, M is the molecular weight of the oxide, and η is the overpotential of oxide formation. The value of ΔG_ν is in ergs/cc. Equation 4.6 can exhibit a maximum with increasing size (i.e., increasing r), since the last term is inherently negative for a spontaneous process and can often outweigh the first term even when this term is positive. By setting the derivative of the total free

energy of formation with respect to size to zero, the size of a "critical nucleus" is determined:

$$r^* = \frac{a\sigma_3}{-a\Delta G_v - (\sigma_2 + \sigma_3 - \sigma_1)} \quad . \qquad 4.8$$

Using this value of critical size in equation 4.6, we determine the critical free energy of nucleation, ΔG^*:

$$\Delta G^* = \frac{\pi a^2 \sigma_3^2}{-a\Delta G_v - (\sigma_2 + \sigma_3 - \sigma_1)} \quad . \qquad 4.9$$

While this classical model neglects atomistic and crystallographic effects, it can be useful in understanding many important features of the nucleation event (e.g., necessity of supersaturation, and variation from metal to metal).

Section 4.5: Geometric Nucleation and Growth Models

Geometric models for nucleation processes neglect the effects of ion transport to growth centers from the solutions. The rate of crystal growth is assumed to be controlled at the crystal/solution interface. Therefore, the changes in growth rate (and therefore current) are related to the crystal geometric surface area exposed to the solution. We represent the total current density as I_t, the current into a growth site as I_c, and the number density of growing crystals as N. The simplest model would have all crystals being formed instantaneously, growing independently, and at the same rate (i.e., all crystals will be the same size at all

times). To calculate the current response more accurately, more complicated (and therefore more realistic) models must consider the basic problem of expressing the amount of surface area for solute incorporation as a function of time since inception (i.e., nucleation of a given center) and the rate of formation of growth centers with time. Various expressions have been presented to estimate these two quantities.

Geometrical growth models often assume either an instantaneous formation or a progressive increase in the number density of nucleation sites (i.e., a number density of growth centers that is constant or increases linearly or exponentially with time). Starting with a fixed number of sites of equal activity available for nucleation, the probability of forming a nucleus would be uniform with time, and the change in the number of growing centers would be proportional to the number of unnucleated sites:

$$\frac{dN}{dt} = A(N_o - N) \quad . \qquad 4.10$$

Here, N is the number density of growing nuclei, t is the time, A is a nucleation rate constant (nuclei/area/time), and N_o is the total number of available sites. Integration of this expression leads to the progressive nucleation equation:

$$N(t) = N_o\,(1 - e^{-At}) \quad . \qquad 4.11$$

Instantaneous nucleation can be viewed as the long time scale-limit of progressive nucleation. Similarly, linear nucleation can be considered the short time scale limit of progressive nucleation. Figure 4-1 demonstrates these ideas. As noted

by Fletcher [D27], the number of active sites may depend strongly on potential, and therefore he introduced the concept of a distribution of activities toward electrochemical nucleation. Once again, it should be stressed that no theoretical understanding of the relation between surface structure and site density is offered. In this case N_o must be treated as an adjustable parameter.

To calculate the current density by geometrical models, one needs an expression for the current flowing to a growing center as a function of time in addition to an expression for the time dependence of the number density of nuclei. When we set the origin of the time scale to the time at which the nuclei of zero size first appear (i.e., the time since inception), it is relatively easy to calculate the current associated with a single growth center. This can be expressed as

$$I_c = nFKS \quad . \qquad 4.12$$

Here, S is the surface area of the growing center and K is the growth constant (rate of incorporation of material into the crystal). By assuming various geometrical forms for the growth centers and the conservation of materials, expressions have been derived for the crystal current as a function of inception time [D3]. For example, it can be shown that the current into a growing spherical nucleus is given by [D28,D29]

$$I_c(t) = \frac{2\pi nFM^2K^3t^2}{\rho^2} \quad . \qquad 4.13$$

Once one has an expression for both the current for a given nucleus as a function of inception time and the change in number density as a function of time, the total current density can be determined. The total current is just the integral of the time-adjusted current (since inception) of the individual nuclei. Mathematically, this can be expressed as [D27]

$$I_t = \int_0^t I_c(\mu)[\frac{dN(t)}{dt}]_{t=(t-\mu)}\, d\mu \quad . \qquad 4.14$$

Here, μ is a dummy variable of integration representing the time since the formation of a given nucleus. This equation simplifies in the case of a constant number density of sites (instantaneous nucleation) to

$$I_t = NI_c \quad . \qquad 4.15$$

All of these expressions assume that the number of unnucleated sites is unaffected by crystal growth and that "overlap" of crystals is not important. Overlap occurs when two or more growth centers have expanded to such a degree that the boundaries touch and they can no longer grow geometrically in a given direction. In the case of metal deposition, overlap presents no real problem to the passage of current since a new active surface is being produced all the time. For anodic film formation, overlap eventually leads to complete coverage of the surface with a more or less resistive film, which can result in surface passivation. Because a growing crystal may cover an unnucleated nucleation site, the number of available sites (referred to as the "expectation" number) will tend to decrease

with time. The assumption of both overlap-free growth and constant available site density are approximations valid only during the early growth stages. Discussion of the topics of overlap and expectation number have been presented in a number of papers [D30-D32].

Section 4.6: Models for Diffusion-Controlled Nucleation and Growth

As noted before [D1], little work has been done on the modeling of crystal growth under diffusion control. Although the mathematics of modeling this type of growth process can be more difficult than that of the geometric approach, it may still be physically realistic to have growth controlled by diffusion. When the rate of incorporation into a growing lattice and the rate of transport to the lattice are comparable, crystal growth exhibits mixed control. The following discussion of the literature is not offered as an exhaustive survey but rather presents the principal physical and chemical ideas involved.

Kappus [D33] has investigated the early stages of electrode discharge of an electrodissolution/precipitation process controlled by homogeneous nucleation and growth. Using the classical ideas of homogeneous nucleation (see section 4, "Thermodynamics of the Anodic Nucleation Process" in this chapter), he calculated the free energy of a subcritical cluster of radius r in a supersaturated solution with respect to a zero-radius cluster in saturated solution:

$$G = 4\pi\sigma r - \frac{4\pi r^3 RT\ln(C/C_s)}{3v_m} \quad . \qquad 4.16$$

In equation 4.16, v_m is the molar volume, C is the concentration (at the crystal/electrolyte boundary), and C_s is the saturation concentration of the oxide of infinitely large crystals. The maximum in G and the critical radius (i.e., the radius of the crystal of maximum free energy G^*) are given by

$$G^* = G(r^*) = \frac{16\pi\sigma^3 v_m^2}{3[RT\ln(C/C_s)]^2} \quad , \qquad 4.17$$

$$r^* = \frac{2\sigma v_m}{RT\ln(C/C_s)} \quad . \qquad 4.18$$

The Gibbs-Thompson relation relates the size of a crystal to its solubility:

$$\hat{C}(r) = C_s \exp(\frac{2\sigma v_m}{RTr}) \quad . \qquad 4.19$$

$\hat{C}(r)$ in equation 4.19 is the surface concentration of a crystal of size r. Equation 4.16 together with equations 4.18 and 4.19, demonstrates that, as the degree of supersaturation decreases due to transport to the growing crystals, the increasing critical radius will cause smaller crystals to disappear. Large crystals can in effect lower the concentration in the environment around smaller crystals to a point where the equilibrium surface concentration of small crystals is larger than that in the bulk. Hence, small crystals will dissolve. Though it was not stated, Kappus assumes independent spherical diffusion to each growth center when he writes

$$\frac{dr}{dt} = v_m D \frac{C - \hat{C}(r)}{r} \quad . \qquad 4.20$$

The characteristic boundary layer is just the radius of the growing (or shrinking) crystal.

Kappus' results have shown that the distribution of the crystallite size shifts to larger average radii and becomes sharper with time under the conditions of constant solution concentration (which might be interpreted as a zero order approximation to a potential-step process) and galvanostatic charging. He presented results for a constant-ion-source (galvanostatic charging) case. The process involved the solution of integro-differential equations. The results demonstrated that "after nucleation and growth of a certain amount of crystallites the ion sink .... exceeds the ion source .... so that the concentration as well as (the potential) begins to decrease." Eventually the potential becomes nearly constant as the source and sink terms compensate each other.

Kappus assumes a form of the radial distribution of subcritical nuclei and uses a very simple model of the diffusion process (i.e., independent radial diffusion). Also, all material dissolved from the electrode is assumed to eventually end up in the growing crystals. The relaxation of these assumptions would greatly increase the complexity of the problem, and so one can only speculate as to their effect. These calculations are interesting and instructive, but they do not address the specific problems associated with heterogeneous nucleation.

Recently, Barradas and Bosco [D34] have developed some electrocrystallization models that couple diffusion and/or dissolution to the growth process. Three

models were developed assuming different physical surface processes. All of the models assume that film growth occurs at a fixed number density of nucleation sites (i.e., instantaneous nucleation) and that a single average concentration for the diffusing species in solution near the surface can be used (i.e., a uniform effective concentration). Using Fick's diffusion equation with initial and boundary conditions, a general nonlinear integral equation for the surface concentration is obtained, valid for all the models. One model takes cognizance of the diffusion of the cations in solution to the interface and assumes that the growth rate of nuclei is proportional to the surface concentration. This model is said to be useful for cases where the active species concentration in the electrolyte is too low or the nucleation-growth rate is too high so that diffusion effects are significant (e.g., for UPD deposition). A second model couples the diffusion of an anion from the surface and the incorporation of the dissolved material into a growth center. This model should be useful for interpreting data from a dissolution/precipitation process. The current is attributed solely to the dissolution process, the surface being covered by oxide, which is insulating. The last model removes any coupling of the anodic growth and diffusion processes. Current results from both the dissolution of metal ions and the growth of the oxide are included.

Current transients predicted by these models are presented in Barradas and Bosco's paper [D34]. Though the model that deals with cation diffusion to the surface is interesting, it has little relation to the work to be presented in this thesis, and so it will not be discussed further. The potentiostatic current

transients predicted by the anodic diffusion/growth coupling model show characteristic monotonically decaying currents at small values of the adjustable parameters. The curves start to develop a hump as the parameters are increased, and they eventually exhibit a local current minimum and maximum at high parameter values. These current trends are similar to those calculated before by this author using a far simpler model, and the shape of the current transients are quite similar to those measured for the silver/silver oxide system [D1,D2]. Most notably, Barradas and Bosco's paper also presents a calculation of the surface coverage of nuclei as a function of time. These coverages are also similar in magnitude to those previously observed by *in situ* spectroscopic ellipsometry [D1,D2].

The model that decouples the dissolution and the nuclei-growth steps also shows monotonic current decays at low parameter values and a small inflection at moderate values, but at larger parameter values the dissolution current becomes masked by the much larger surface growth process. Eventually the monotonic decay of the current due to dissolution disappears altogether. A curve similar to those associated with geometric growth is observed where the current does not exhibit an initial declining period.

While the Barradas/Bosco calculations have some serious limitations because of some simplifying assumptions, their results can be useful in the qualitative interpretation of potentiostatic data. However, these calculations give no insight into the nature of the nucleation event and of the morphological stability of the surface. Some of these issues have been addressed by authors interested in the morphological stability of the surfaces during the solidification of metal from

melts and by electrodeposition.

Section 4.7: Electrocrystallization Growth Stability

The ability to form smooth electrodeposits at high rates has been a goal of electrochemists for many years. Because anodic surface products can be electrically insulating, a material that forms a porous or rough surface due to individually nucleated centers would be preferred for many battery applications. Some anodic films form as homogeneous planar films (e.g., most valve metals), while others do not (e.g., silver oxide). The interaction of solution and surface processes plays an important role in determining the type of surface film formed. Yet an understanding of the morphological stability of electrodeposition, while of great practical importance, has largely eluded scientists. A more complete review of the literature of the stability of metal electrodeposition has been presented by Barkey, Muller, and Tobias [D35]. Here we only present aspects pertinent to anodic nucleation and growth.

Wagner [D36] has found the general form (particular solution) of the solution for the primary current distribution to a low-amplitude sinusoidal surface. These solutions can also be applied to the case of diffusion-controlled deposition. For a profile defined by

$$z = A \sin(\omega x) \quad , \qquad 4.21$$

where z is the height of the surface at position x, A is the amplitude of the sine wave, and ω is the frequency of the wave. The solution to the primary current

distribution for the profile with wavelength ($\lambda = \frac{2\pi}{\omega}$) is

$$\frac{i - i_{avg}}{i} = \omega A \sin(\omega x) \ , \qquad 4.22$$

where i is the local current density and i_{avg} is the average current density over the profile. Equation 4.22 predicts that preferential growth will occur at the peaks. The current distribution given by equation 4.22 predicts that the rate of change of the aspect ratio will be inversely proportional to the square of the profiles wavelength. Sharp features (short wavelengths compared to amplitudes) are predicted to grow faster.

A number of theories of morphological stability of metal deposition have been presented in the literature. Most of these theories make use of a perturbation analysis. This involves the analysis of small (Fourier component) perturbations on the steady-state solution of the electrodeposition problem. Any arbitrary contour can be described by a series of Fourier components, and so the goal of the perturbation analysis is to determine at which wavelength the Fourier components exhibit positive (unstable) growth constants. Mullins and Sekerka treated the case of diffusion-controlled growth of a sphere from a dilute solution [D37]. To find the range of stable wavelengths in this problem, perturbations of spherical harmonics were used, taking into account the effect of radius of curvature (surface energy) on the solubility. The effect of capillarity is inversely proportional to the square of the wavelength and tends to stabilize a smooth surface. Spherical diffusion tends to favor exposed features on a surface and hence is a

destabilizing influence on growth. For wavelength (spatial periods) very much smaller than the curvature of the surface, the solution should be similar to that obtained from the perturbation on a plane. Mullins and Sekerka's results show that for perturbations greater than about seven times the critical radius (see Thermodynamic section of this chapter), the perturbations will tend to grow. Smaller radii are unstable and tend not to grow.

A more recent treatment of the diffusion-controlled stability to a planar surface has been presented by Aogaki *et al.* [D38] . These authors were concerned with the striking transition from planar to "powdered crystal" deposition. A perturbation analysis of the diffusion and surface-reaction problem was performed. Perturbations in the concentration of the cation in the electrolyte, local flux, overpotential, ohmic resistance, and shape of the surface were considered. The result of these calculations yields an equation for the magnitude and sign of the exponential growth constant:

$$k = -\frac{v_m\omega[RTJ_z^* + nFDv_m\sigma C^*\omega^2]}{\frac{D(nF)^3C^*}{\kappa} + nFRT} \quad . \qquad 4.23$$

In equation 4.23, k is the growth constant of a perturbation of frequency ω , v_m is the molar volume of the deposit, J_z^* is the z component of the steady-state current density (average current density), D is the diffusion coefficent, σ is the surface energy of the deposit/electrolyte interface, C^* is the surface concentration of the depositing material, and κ is the conductivity of the electrolyte. From this equation, the wavelength of the maximum rate of growth can be derived:

$$\lambda_{max} = 2\sqrt{3}\pi\sqrt{\frac{-nFDv_m\sigma C^*}{RTJ_z^*}} \quad . \qquad 4.24$$

Plots of equation 4.24 show that the growth rate falls off very rapidly and becomes negative for wavelengths smaller than λ_{max}. Therefore, this value can be used to determine the size of stable versus unstable perturbations. Aogaki *et al.* [D38] have said that their results point to the conclusion that all morphological developments for cathodic processes are unstable, since a positive growth constant can always be found for cathodic processes in equation 4.23. However, while equation 4.23 indicates that a positive growth constant can always be obtained for some arbitrarily large wavelength for cathodic deposition, the formation of such a long-range disturbance becomes less likely due to physical constraints. For example, the local instability in the concentration field would have to be sustained over a much larger region of space, and this becomes highly unlikely. Also, the approximation of a linear expansion of the perturbation field over large distances may become invalid. Because the two terms in the numerator of equation 4.23 can be of opposite sign for an anodic process both stable planar or hemispherical growth can occur.

Section 4.8: Literature Summary and Conclusions

There are a number of possible growth paths by which electrocrystallization can occur. Crystal growth can be controlled by a diffusion or lattice-building step. The nucleation of a new phase is envisioned to occur at a "nucleation site." Surface defects are believed to be such sites. Thermodynamic calculations show

that growth of a nucleus can occur only after a nucleation energy barrier (and its associated critical nucleus size) is surpassed. Geometrical growth models for the growth process assume that the lattice building (i.e., the rate of incorporation of material into the growing lattice) is rate-controlling. Diffusion models assume that the transport of material to the growth center is rate-controlling. The Gibbs-Thompson relation shows that small crystals are less stable than larger ones. Perturbation stability analysis shows that above a certain size and period, surface roughnesses will tend to grow. These theoretical results may in part help to explain why anodic films are formed with so many different structures.

REFERENCES FOR CHAPTER 4

D1) Mayer, Steve T., **An Ellipsometric Spectroscopy Study of Anodically Formed Silver (I) Oxide on Silver**, M. S. Thesis, University of California at Berkeley, December 1985. Lawerence Berkeley Laboratory Report LBL-15607.

D2) Mayer, S. T., and R. H. Muller, J. Electrochemical Soc. **135,** 2133 (1988).

D3) Fleischmann, M., and H. R. Thirsk, "Metal Deposition and Electrocrystalization," in **Advances in Electrochemistry and Electrochemical Engineering,** Vol. 3, P. Delahay and C. W. Tobias, Editors, John Wiley and Sons, New York, 1963.

D4) Noyes, A. A., and W. R. Whitney, Z. Phys. Chem. **23,** 689 (1897).

D5) Nernst, W., Z. Phys. Chem. **47,** 52 (1904).

D6) Marc, R., Z. Phys. Chem. **61,** 385 (1908).

D7) Marc, R., Z. Phys. Chem. **67,** 470 (1909).

D8) Marc, R., Z. Phys. Chem. **68,** 104 (1909).

D9) Marc, R., Z. Phys. Chem. **76,** 584 (1911).

D10) Stranski, I. N., Z. Phys. Chem. **136,** 259 (1928).

D11) Volmer M., and M. Marder, Z. Phys. Chem. **154A,** 97 (1931).

D12) Liu, C. Y., H. S. Tsuei, and G. R. Youngquist, Chem. Eng. Prog. Symp. Ser. **67,** 43 (1971).

D13) Frank, F. C., Discussion Faraday Soc. **5,** 48 (1949).

D14) Burton, W. K., N. Carbrera, and F. C. Frank, Philos. Trans. **A243,** 299 (1951).

D15) Armstrong, R. D., L. Pearce, and H. R. Thirsk, Electrochim. Acta **25,** 1293 (1980).

D16) Armstrong, R. D., M. Fleischmann, and H. R. Thirsk, J. Electroanal. Chem. **11,** 208 (1966).

D17) Fletcher, S., and A. Smith, Can. J. Chem. **56,** 908 (1978).

D18) Angerstien-Kozlowska, H., B. E. Conway and J. Klinger, J. Electroanal. Chem. **87,** 301 (1978).

D19) Angerstien-Kozlowska, H., B. E. Conway, and J. Klinger, J. Electroanal. Chem. **87,** 321 (1978).

D20) Bosco, E., and S. Rangarajan, J. Chem. Soc. Faraday Trans. **77,** 483 (1981).

D21) Bosco, E., and S. Rangarajan, J. Electroanal. Chem. **129,** 25 (1981).

D22) Retter, U., J. Electroanal. Chem. **179,** 25 (1984).

D23) Stranski, I. N., Naturwissenschaften **23,** 144 (1943).

D24) Pangaroff, N. A., Electrochim. Acta **7,** 139 (1962).

D25) Melroy, O. R., M. F. Toney, G. L. Borges, M. G. Samant, J. B. Kortright, P. N. Ross, and L. Blum, Phys. Rev. B. **38,** 10962 (1988).

D26) Vermilyea, D. A., "Anodic Films," in **Advances in Electrochemistry and Electrochemical Engineering,** Vol. 3, P. Delahay and C. W. Tobias, Editors, John Wiley and Sons, New York, 1963.

D27) Fletcher, S., Electrochim. Acta **28,** 237 (1983)

D28) Fleischmann, M., and H. R. Thirsk, J. Electrochem. Soc. **110,** 668 (1963).

D29) Bewick, A., M. Fleischmann, and H. R. Thirsk, Trans. Faraday Soc. **58,** 2200 (1962).

D30) Smith, A., and S. Fletcher, Can. J. Chem. **57,** 1304 (1979).

D31) Fletcher, S., and A. Smith, Electrochim. Acta **25,** 1019 (1980).

D32) Abyaneh, M. Y., Electrochim. Acta **27,** 1329 (1982).

D33) Kappus, W., Electrochim. Acta **28,** 1529 (1983).

D34) Barradas, R. G., and E. Bosco, Electrochim. Acta **31,** 949 (1986).

D35) Barkey, D., R. H. Muller, and C. Tobias, J. Electrochem. Soc. to be published.

D36) Wagner, C., J. Electrochem. Soc. **101,** 222 (1954).

D37) Mullins, W. W., and R. F. Sekerka, J. Applied Phys. **34,** 323 (1963).

D38) Aogaki, R., K. Kitazawa, Y. Kose, and K. Fueki, Electrochim. Acta **25,** 965 (1980).

FIGURE CAPTION FOR CHAPTER 4

Figure 4-1. Representative functionality of the number density of growing nuclei as a function of time for instantaneous, linear, and progressive nucleation.

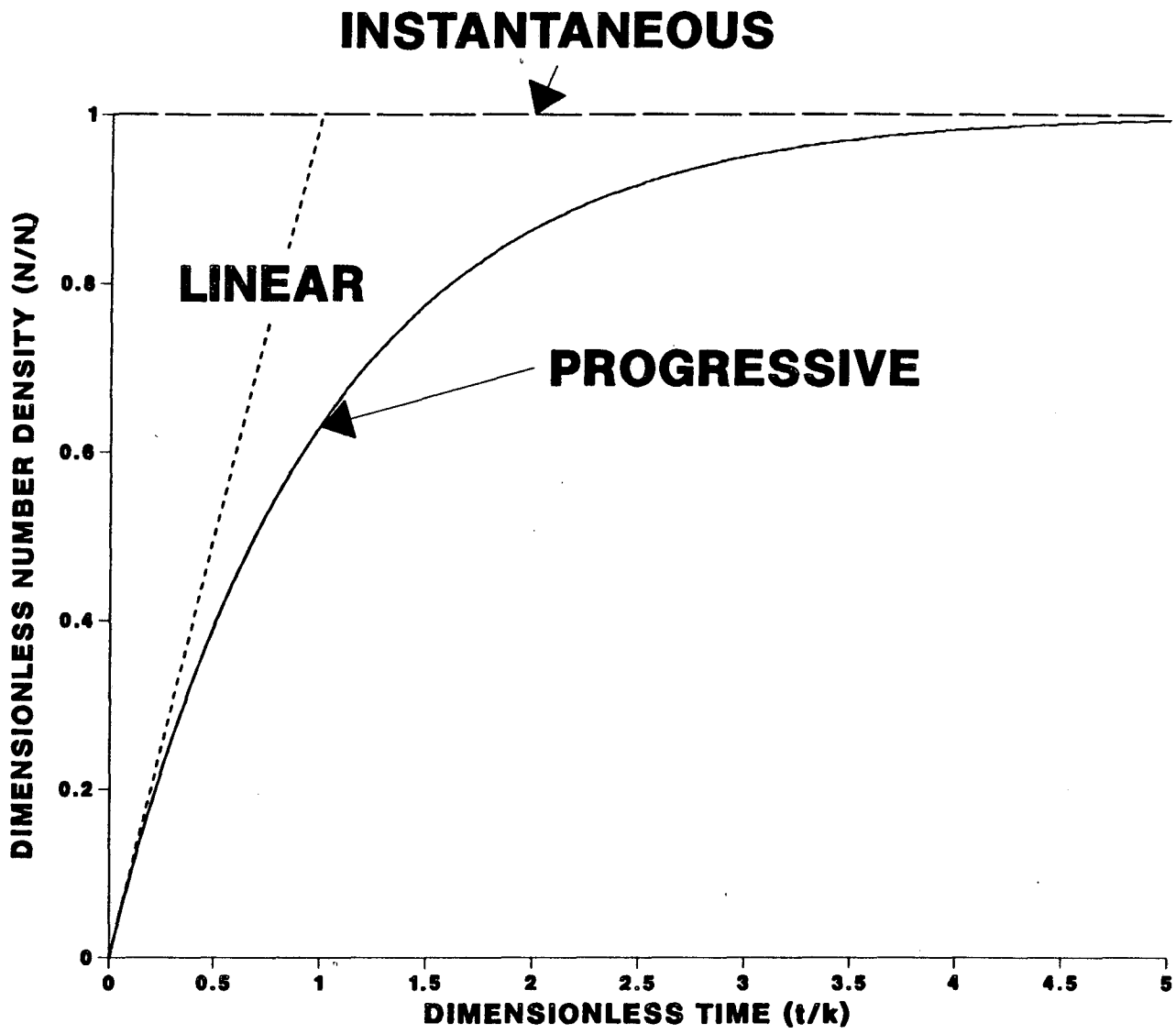

XBL 897-2668

Figure 4-1

CHAPTER 5

REVIEW OF ALKALINE BATTERY SYSTEMS USING ZINC, COPPER, AND SILVER

Section 5.1: Energy Storage in Electrochemical Systems

A study of the oxidation and reduction of metals in alkaline solutions is of practical interest since these reactions commonly occur in both primary and secondary alkaline batteries. The manner in which energy is converted by oxidation reactions varies from system to system, and it depends largely on the physical mechanism of film formation associated with the particular process. These reactions can be classified into two limiting-case mechanisms for which the storage of electrochemical energy can be discussed. The first mechanism involves a transfer of charge at the electrode/electrolyte interface, accompanied by the production of a soluble species that diffuses from the electrode. Energy conversion occurs by a change in the concentration of a reducible species in the electrolyte. I refer to this class as the soluble-material mechanism. The second mechanism involves the storage of energy at or near the metal interface as an oxide surface film or homogeneous colloidal suspension. In this case, energy is stored in the form of a solid material. I refer to this mechanism as the solid-film mechanism.

The soluble-material mechanism has a potential advantage over the surface-film mechanism in that, in principle, the total cell capacity is limited only by the total electrolyte volume. One can enhance the inherent capacity of a solubilized-

mechanism cell by choosing an anion that will result in a highly soluble metal salt or oxide and by operating the cell at a high temperature (if solubility increases with temperature). In some cases, most of the electrolyte is not stored in the reaction vessel at all but rather in a storage tank. The electrolyte is circulated though the electrochemical chamber, where the active species is either oxidized or reduced. Circulating the electrolyte through the cell and storing it in an external vessel helps in maintaining a more constant cell voltage by keeping the changes in electrolyte concentration to a minimum. An example of one such system is a porous metal flow-through zinc cell under development as a potential electrical vehicle power source [E1-E4]. The potential problem with this type of cell is that the overall reaction rate and efficiency are tied to a diffusion process that is inherently slow and irreversible (entropy-generating). For a process to occur at a reasonable rate by the solubilized-material mechanism, the concentration at the interface must be considerably higher (or lower) than the concentration in the bulk of the solution. This results in a concentration overvoltage, and the product of the concentration overvoltage and the current density is a measure of the lost work associated with the diffusion process. These ideas can be expressed by an equation that represents the entropy of diluting a solution:

$$\frac{\Delta S_{mixing}}{R} = \sum_j x_{j2}\ln(\gamma_{j2}x_{j2}) - \sum_j x_{j1}\ln(\gamma_{j1}x_{j2}) \quad . \qquad 5.1$$

In equation 5.1, ΔS_{mixing} is the entropy of mixing, R is the ideal gas constant, j is a solution component index, γ_j is the activity coefficient of the jth component, and the subscripts 1 and 2 correspond to the solute concentration at the

interface and in the bulk solution, respectively [E5,E6]. Equation 5.1 shows that any diffusion process will result in lost work. The maximum current, and therefore the maximum total power is also limited by the rate of diffusion of active ions to and from the interface. Studies in this and other laboratories have shown that very high rates of electrodissolution and electrodeposition can be obtained using extreme agitation, but that these high rates often result in adverse effects on the macro- and micromorphology of the electrodeposit [E7]. Non uniform tertiary (diffusion-controlled) current distributions tend to limit cell life [E8].

During anodic operation of an electrode, precipitation of a surface film can occur when the surface concentration exceeds the solubility limit. For a cell which that uses soluble material for energy storage, this precipitation can prove to be disastrous because film formation often leads to the passivation of the electrode. Generally, the upper limit for the rate of discharging a solublized-material cell is associated with film formation.

Despite the potential for limited capacity associated with surface-film battery cells, these types of cells do possess sufficient capacity for many applications. Many commercial cells use highly porous electrodes and pack powdered reactants into the cell chamber to increase the cell capacity. Since the reaction products are stored at or near the surface, the associated diffusion processes are much less important, and therefore the overall processes can be, in general, much more rapid and/or reversible. Furthermore, surface-film cells can maintain high currents at nearly constant potentials. Because the reaction products diffuse over relatively short distances, the surface-film battery material maintains a nearly

constant supply of reactants to the electrode surface. However, the problems associated with film passivation, reactant dissolution processes (lost capacity and short shelf life), and limited capacity need to be studied further. The solutions to these problems are tied to a better understanding of the mechanism of film formation and reduction.

Since we have focused this study on the anodic oxidation of zinc, copper, and silver in alkaline media, a brief review of the characteristics and past and present uses of these metals in various battery systems will be presented. Some of these characteristics are summarized in Table 5.1.

Section 5.2: The Zinc/Silver Oxide Alkaline Battery

The use of zinc/silver oxide batteries was first investigated by H. Andre in the late 1920s. Zinc/silver oxide storage batteries have been manufactured since the 1940s and are made throughout the industrial world. Cells have been produced for both low- and high-rate performance; with capacities ranging from 0.05 Ah (button cells) to 600 Ah (Eagle-Picher Industries Inc., USA) [E10]. As noted before (Chapter 3), high-rate drains result in lower cell voltages, which correspond to the Ag_2O (rather than AgO) discharge reaction (see also [E16]). The most favorable characteristic of these cells is the very high specific energy. This characteristic is a result of the large amount of energy stored in the silver electrode, the compact assembly of the electrodes in the cell container, and the favorable potential resulting from the zinc/silver oxide couple. Shelf-life characteristics are also reasonably favorable (80-95% of original capacity after 1 year),

as are as charge efficiencies (90%) [E9]. The overall energy efficiency is in the 70-75% range. Serious limitations for the zinc/silver oxide cell are its poor low-temperature performance and secondary-cell cycle life (only 50-100 cycles, due to separator problems), as well as its high cost [E9-E11,E14,E16]. Some of the uses of the zinc/silver oxide cell include power sources for wrist watches and hearing aids, torpedoes, mines, buoys, military communication equipment, portable radar sets, and IR night-vision equipment [E9-E11].

Section 5.3: The Cadmium/Silver Oxide Alkaline Battery

Cadmium/silver oxide batteries have much better cycle life (up to 500 deep cycles have been obtained) and better shelf-life characteristics than the zinc/silver oxide cell [E16]. This difference in behavior is largely attributed to the relatively large solubility of zinc versus cadmium in alkaline solutions (and the associate separator problems). The overall charge efficiency is comparable to that of the zinc/silver oxide cell. However, the specific energy of this cell is about one-half that of the zinc/silver oxide cell (60 Wh/kg vs 180 Wh/kg). Cells with capacities from 0.1 to 300 Ah have been manufactured [E10,E16]. Like the zinc/silver oxide battery, at high current drains the $Ag/Cd(OH)_2$ cell exhibits a single discharge voltage corresponding to the reduction of Ag_2O [E16]. A typical cell voltage of 1.1 V is observed. The very high cost of cadmium (as well as of silver) limits the use of this battery system to military applications [E14,E16].

Section 5.4: The Zinc/Nickel Oxide Alkaline Battery

Because the cost of nickel is significantly less than the cost of silver, the zinc/nickel oxide battery offers the potential combination of moderate cost and high specific energy and specific power. Present development of this battery system is centered on the zinc electrode. The separator is a crucial component in the cell design: it must prevent zinc dendrite penetration to the nickel electrode and resist swelling [E10]. Present research indicates that a specific energy of 75-90 Wh/kg can be achieved. The cell can maintain a reasonable voltage (1.6 V) during high rates of discharge over a wide range of temperatures (-40 to 50° C). Recharging problems of the secondary battery, as well as limited cycle life, appear to be the major drawback of this system [E12]. While a certain degree of overpotential is required to fully charge the nickel electrode, overcharging has a disastrous effect on the zinc electrode. Charge retention is relatively poor (only 70% of the initial charge is available after one month). Cycle life is also poor (200 cycles). However, more recently 800 to 1200 cycles have been obtain using advanced separators and a novel vibrating zinc electrode.

This battery system is presently under development as a candidate for electric vehicle propulsion. Sealed cells have been used in VCR cameras, electric shavers, tape recorders, portable tools, and calculators. Bigger vented (non-sealed) batteries have been used to propel electric vehicles. Their use in indoor fork lift trucks, electric cars, and golf carts is predicted to grow in the future [E9].

Section 5.5: The Zinc/Mercury (II) Oxide Alkaline Battery

The zinc/mercury (II) oxide cell often referred to as the Ruben cell after its inventor, Samuel Ruben, who invented this cell in the 1940s. While most surface film mechanism batteries exhibit very stable voltage during discharge, the Zn/HgO cell exemplifies this characteristic under load at significant current densities. Like the zinc/silver oxide battery, the zinc/mercury (II) oxide battery has been used as a button (e.g., watch type) cell [E19]. In the button cell, the cathode, anode, and separator are arranged in parallel planes, and they are perpendicular to the axis of symmetry of the battery. Like many other zinc alkaline cells, the zinc in this cell contains mercury to suppress the corrosion of the anode. The battery is one-third the size of conventional dry batteries of the same capacity. The reactions at the anode and cathode leave the overall cell electrolyte composition unaltered. This fact is evident by looking at the individual half reaction:

$$Zn + 2OH^- \leftrightarrow ZnO + H_2O + 2e^- \quad , \qquad 5.2$$

$$HgO + H_2O + 2e^- \leftrightarrow Hg + 2OH^- \quad , \qquad 5.3$$

which, when added, yields

$$Zn + HgO \leftrightarrow ZnO + Hg \quad , \qquad 5.4$$

which does not involve the electrolyte at all. The battery characteristics include long shelf life (90% of capacity after one year), high specific energy (surpassed

only by the Zn/Ag_2O cell), a high sustained discharge voltage under load, and a low internal resistance. However, the battery does not perform well at low temperatures, and the fact that Hg is toxic adds to the manufacturing cost (the cell must not leak) [E19]. In addition to being used in button cells (for wrist watch and hearing-aid applications), Zn/HgO cells have been used in cardiac pacemaker devices [E19] and as a secondary voltage standard [E10,E11].

Section 5.6: The Zinc/Manganese Dioxide Alkaline Battery

The earliest zinc/manganese dioxide cell, also known as the carbon-zinc battery (because of the carbon-rod current collector) or the Leclanche battery (after its French inventor, George-Lionel Leclanche, 1838-1882) used an aqueous solution of ammonium chloride as electrolyte [E17]. The first description of an alkaline MnO_2 cell appeared around 1882 in a German patent of G. Leuchs. This cell uses a gelatine filling to immobilize the alkaline electrolyte. However, the alkaline cell received little attention in the literature until after the Second World War. P.R. Mallory Company spent several years developing and marketing the alkaline Zn/MnO_2 cell and was able to establish it in the battery industry [E11]. By the late 1960s the system had established itself in the consumer battery market.

While it was originally introduced as a primary cell, rechargeable Zn/MnO_2 cells have been developed and marketed. Secondary MnO_2 cells retain their charge for longer periods of time than most rechargeable systems, but these cells have limited cycle life (about 50 cycles). The available energy decreases with

each cycle faster than with other secondary batteries, and when used as a rechargeable system, only one-third of the total capacity can be utilized to assure best cycle life. The largest disadvantage of the zinc anode is the high solubility of zinc in caustic. The migration of zinc to the cathode and the formation of zinc dentrites present major problems for further development. Despite its deficiencies, the secondary Zn/MnO_2 cell remains competitive because of its low overall cost.

The open-circuit voltage of a Zn/MnO_2 battery is about 1.5 V, but the voltage can drop to as low as 0.8 V before the cell is completely discharged [E11,E16]. Voltage-time curves typically decline significantly during discharge. This behavior is different from other alkaline systems (e.g., Zn/AgO, Zn/HgO, Zn/CuO, and Zn/air), which exhibit fairly constant cell voltages right up to cell exhaustion. Though this cell will never be able to reach the capacities of systems like the Zn/air cell, Zn/MnO_2 cells are inexpensive, have excellent shelf life (90% of original energy after 1 year), and have shown some secondary cell capabilities. Therefore, this system will continue to be a major consumer battery system into the foreseeable future [E10,E11,E16].

Section 5.7: The Zinc/Air Alkaline Battery

The zinc/air battery is perhaps the most promising electrochemical energy source because of its combination of potentially high specific energy and operating voltage, along with relatively low material costs. The cell is a device in which the oxidation reaction of zinc with air can be controlled to provide energy-

efficient electrical power. As with other zinc alkaline batteries, the zinc electrode is amalgamated to suppress the zinc corrosion reaction. The anode and cathode are separated by an aqueous KOH solution. The half reactions

$$2Zn + 8OH^- \rightarrow 2Zn(OH)_4^{-2} + 4e^- \qquad E^\circ = -1.25 \text{ NHE} , \tag{5.5}$$

$$O_2 + 2H_2O + 4e^- \rightarrow 4OH^- \qquad E^\circ = 0.401 \text{ NHE} , \tag{5.6}$$

yield an overall cell reaction tht can be written as

$$2Zn + O_2 + 2H_2O + 4OH^- \rightarrow 2Zn(OH)_4^{-2} \qquad E_c = 1.651 \text{ V} . \tag{5.7}$$

A primary zinc/air battery is presently used as a power source for hearing aids. While the original zinc/air cells could be used only as a low-drain device, recent technological advances make it foreseeable that a rechargable form could be used as a power source for electric vehicles [E13,E15]. Presently, the cells exhibit both short cycle life and low efficency.

The current collector for the oxygen-reducing cathode is generally either nickel or carbon. The zinc/air battery is not anode-limited, and therefore the effectiveness of the zinc/air cell depends largely on the efficiency of the air electrode. The reaction at the oxygen electrode occurs at the point where the three phases meet. These are the metal solid (electron conduction), gas (oxygen), and liquid (KOH solution) phases. A porous electrode is used to enhance the interfacial area, but the electrode also must allow for a stable gas-liquid boundary in the pores [E3,E13].

Three types of zinc/air cell are presently being developed. The "D" size primary cell performance against other "D" cells is impressive. At 200 mA drain, the zinc/air cell operates at a constant 1.4 V for over 100 hours. This is more than twice the time of the Zn/HgO cell (45 hours) or the alkaline Zn/MnO_2 cell (40 hours). Mechanically rechargeable zinc/air cells operate on the principle of replacing the anode and electrolyte upon exhaustion of the anode. The cathode is used for many cycles. The secondary zinc/air cell can be viewed as a rechargeable zinc/silver oxide system with the silver oxide electrode replaced with an air electrode. Zinc is converted to zinc oxide (or zincate ion) on discharge and to zinc on recharging. The air electrode can be monofunctional (two separate electrodes used for charging and discharging) or bifunctional. Rechargable cells that use porous carbon cathodes must have monofunctional electrodes because the carbon is otherwise oxidized.

Zinc is a relatively inexpensive metal. Oxygen does not contribute to the weight of the battery and can be obtained from air without cost (except in Los Angeles). The zinc/air battery therefore stores more electrical energy than any other aqueous battery presently available, and a significant development effort for this battery system is under way. A great deal of time and money is presently being spent on the development of this battery system [E10,E11,E13].

Section 5.8: The Zinc/Copper (II) Oxide Alkaline Battery

The Zn/CuO alkaline battery was first devised by LaLande and Chaperon in 1881 using granular cupric oxide, zinc anodes, and a caustic electrolyte. Edison

improved the system by using agglomerated cathodes. From its inception, the primary use of this battery system has been for low-drain applications, particularly railway signaling and telephone and telegraphic communications. Its commercial introduction largely displaced Daniell and wet Leclanche cells from these markets. Various features were added to the cell to improve its performance: copper-coated cathodes, silicate to improve electrolyte capacity, and heat- and alkali-resistant battery jars [E11].

Despite its low operating cell voltage (about 0.7 V), the Zn/CuO cell had found many applications where cost, capacity, flat discharge curves, and chemical stability are requirements. The discharge curves show no inflection due to a stepwise reduction of $CuO \rightarrow Cu_2O$ followed by $Cu_2O \rightarrow Cu$. The operating potential appears to be related to the Cu_2O/Cu couple rather than to the CuO/Cu_2O couple. The interface may become a mixture of CuO and Cu_2O during discharge, and the observed cell voltage is most likely a mixed potential. While the addition of sulfur to the CuO cathode appears to enhance the potential by as much as 200 mV, the mechanism for this phenomenon is unclear [E11].

The density of the electrolyte increases during discharge as zincate ions accumulate in it. The rapid drop in cell voltage at the end of cell capacity reflects both the buildup of zincate in the electrolyte and the formation of an anodic surface film. These films are probably crystals of $Zn(OH)_2$, but the species Na_2ZnO_2 and $Na_2Zn(OH)_4$ have also been suggested as surface products. The very high internal cell resistance appears to be attributable to the formation of a cuprous oxide layer, rather than to the effects of dissolved zincate on the

electrolyte conductivity, as previously believed [E10].

REFERENCES FOR CHAPTER 5

E1) Appleby, A., and M. Jacquier, J. Power Sources **1,** 17 (1976/1977).

E2) Iacovangelo, C., and F. Will, J. Electrochem. Soc. **132,** 851 (1985).

E3) Ross, P. N., Jr., "Feasibility Study of a New Zinc-Air Battery Concept Using Flowing Alkaline Electrolyte," April 1986. Lawrence Berkeley Laboratory Report LBL-21437.

E4) Ross, P. N., Jr., "Zinc-Air Design Concept for the DOE-EHP IDSEP Van." Janurary 1988. Lawrence Berkeley Laboratory Report LBL-24639.

E5) King, C. Judson, **Separation Processes**, McGraw-Hill, San Francisco, 1980, p. 660.

E6) Prausnitz, J. M., **Molecular Thermodynamics of Fluid-Phase Equilibria**, Prentice-Hall, Englewood Cliffs, NJ , 1969, p. 281.

E7) Barkey, D., **Studies on High Speed Electroforming**, Ph.D. Thesis, University of California at Berkeley. August 1987. Lawerence Berkeley Laboratory Report LBL-23880.

E8) McBreen, E., J. Electrochem. Soc. **119,** 1620 (1972).

E9) Fleischer, A., and J. Lander, Editors, **Zinc-Silver Oxide Batteries**, John Wiley and Sons, New York, 1971.

E10) Falk, U., in **Electrochemical Power Sources: Primary and Secondary Batteries**, M. Barak, Editor. Peter Pergrinus Ltd., 1980, p. 397.

E11) Heise, George W., and N. Corey Cahoon, **The Primary Battery**, Volume 1 and 2, McGraw Hill, 1971.

E12) Cairns, E., in **Materials for Advanced Batteries**, D. W. Murphy, J. Broadhead, and B. C. H. Steele, Editors. Plenum Press, New York, 1980, p. 3-27.

E13) Will, F., in **Power Sources For Electric Vehicles**, Elsevier Science Publishers, Amsterdam, 1982. pg. 573.

E14) Cairns, E., in **The Encylopedia of Physics**, Robert M. Besancon, Editor, Third Edition, Van Nostrand Reinhold Company, New York, 1985, pp. 396-400.

E15) Cairns, E., and E. H. Hietbrink, "Electrochemical Power for Transportation," in **Comprehensive Treatise of Electrochemistry**, Vol. 3, J. O. M. Bockris, B. E. Conway, E. Yeager, and R. E. White, Editors. Plenum Publishing Corp., 1981.

E16) Falk, S. U., and A. J. Salkind, **Alkaline Storage Batteries**, John Wiley and Sons, New York, 1969.

E17) Huber, R., K. V. Kordesch, A. Kozawa, and D. B. Wood, in **Batteries:**

Volume 1, Manganese Dioxide, Karl Kordesch, Editor, Marcel Dekker, New York, 1974.

E18) Kordesch, K. V., "The Electric Automobile" in **Batteries: Volume 2, Lead-Acid Batteries and Electric Vehicles**, Karl Kordesch, Editor, Marcel Dekker, New York, 1977. pp. 277-280.

E19) Crompton, T. R., **Small Batteries: Volume 2, Primary Cells**, John Wiley and Sons, New York, 1983.

Table 5-1

ALKALINE CELLS WHICH USE SILVER, COPPER, OR ZINC				
ANODE	CATHODE	OPEN-CIRCUIT EMF (VOLTS)	COMMON NAME	COMMENTS
PRIMARY CELLS				
Zn^*	$Mn(MnO_2)$	1.55	Zinc/Manganese Dioxide Cell	Used In Small Commercial Alkaline Cells
Zn	O_2	1.40	Air Cell	Very High Theoretical Specific Energy
Zn^*	$Cu(CuO)$	1.10	Copper Oxide cell	Used As Low Drain Primary Before 1960
SECONDARY CELLS				
$Zn^\#$	$Hg(HgO)$	1.35	Ruben Cell	Very Stable Voltage During Discharge
$Zn^\#$	$Ag(Ag_2O)$	1.60	Silver Cell	High specific energy Density And Power
Zn	$Ag(AgO)$	1.86	Silver Oxide Cell	Primarily Used For Military Applications
Zn	$Ni(NiOOH)$	1.74	Drumm Cell	Low Material Costs-Undergoing Development
Cd	$Ag(Ag_2O)$	1.30	Silver Cadmium Cell	1/2 Energy Density Of Zn cell

* Cell can be recharged, though characteristics of rechargability are poor.
\# Has been used as a primary cell

XBL 897-2669

CHAPTER 6

EXPERIMENTAL PROCEDURES FOR SURFACE PREPARATIONS AND ELECTROCHEMICAL MEASUREMENTS

Section 6.1: Introduction

The procedures for preparing working and reference electrodes, making solutions, and taking electrochemical measurements were generally the same regardless of the type of optical experiment performed. Therefore, in order to avoid repeating the description of these procedures when discussing each type of experiment, we describe them in some detail here.

Section 6.2: Crystal Preparation and Mounting

The single-crystal electrodes of Cu, Ag, and Zn used in our study were manufactured in-house using an induction furnace. The purity of the shot metals used to make the single crystals was greater than 5 nines purity. However, due to contaminations inherent in making the crystals, we feel that the final single crystals were of no better purity than 99.999%.

The crystal rods (3/4 inch in diameter) were etched to ensure that they were single crystals, and were then oriented and aligned by analyzing x-ray Laue back-reflection patterns. All crystals were oriented to within about 1° of the specified axis. The crystals were cut (by EDM) into a rectangular shape (about 1.25 cm by 2.75 cm, and of various thicknesses). Some standard mounted

crystals, along with the equipment used to mount the electrode into the cell, are shown in Figure 6-1. A screw was mounted onto the back of the electrode with silver-epoxy. The screw helped to seal and mount the electrode into the cell and acted as the electrical lead to the potentiostat working-electrode lead. After the silver-epoxy hardened, the electrodes were placed in a mold, epoxy resin was added, and the resin was allowed to harden. (For the procedure of making, removing bubbles from, and curing the epoxy resin, see Reference F1). After the epoxy had hardened, the electrode epoxy mount was machined to fit into our electrode holder and cell.

The electrode holder includes a Teflon sleeve and a brass mounting bolt (Figure 6-1). The Teflon sleeve fits into the back of all of the electrochemical cells (ellipsometry, light scattering, and Raman cells). There is a hole in the middle of the front of the Teflon sleeve where the electrode mounting screw is inserted, and in the back where a mounting bolt is inserted. The mounting bolt is inserted into the back of the Teflon sleeve, and the screw and bolt then mount the electrode in the Teflon sleeve. An o-ring is placed on the electrode screw to avoid electrolyte contact with the screw or brass mounting bolt.

Section 6.3: Electrolyte Preparation

Virtually all of the electrolytes used in this study were either 1M or 6M KOH. The electrolytes were prepared using ultrapure water (Harleco ultrapure water, a resistivity of 10 MΩ–cm, and free of organic contaminants), and analyti-

cal grade KOH pellets, low in chloride (J. T. Baker Chemical Corp.). The KOH pellets contained less than 0.5% CO_3^{-2}, and less than 1 ppm of soluble Fe. Solutions were generally made in two-liter batches and were titrated to ensure that the molarity was within 1%. Prior to injection of the electrolyte into the electrochemical cell, the solutions were pre-electrolyzed and de-oxygenated. These procedures were performed in a 1-liter Teflon separatory funnel, which contained a Teflon (PTFE or polytetrafluoroethylene) sparging tube and two Pt screen electrodes. First, the electrolyte was pre-electrolyzed by putting a 1.3 volt difference between the two Pt screens. The voltage was maintained until the current had decayed to a very small value (about 10 minutes). Next, 99.99999% pure N_2 gas was bubbled through the solution to reduce the dissolved oxygen content. Though it is known that the solubility of oxygen in alkaline solutions is small, this procedure as was preformed a precaution.

Many researchers have used HNO_3 to clean PTFE because it acts as a strong oxidizing agent for the removal of organic compounds and is known to wet TFE. Research on the underpotential deposition (UPD) of Pb on Pt has shown some anomalous effects associated with HNO_3 [F2], and later, residual HNO_3 from PTFE was found to be the cause of these effects [F3]. It appears that HNO_3 enters the pores of PTFE and may be difficult to remove (since distilled water will still be nonwetting). Therefore, rather than using HNO_3, the optical/electrochemical cell was cleaned with soap and water, a series of organic solvents (methyl ethyl ketone, acetone, and ethyl alcohol), and then distilled water. The optical/electrochemical cell was purged with N_2 gas prior to injection

of electrolyte into the cell (through TFE tubing) to remove any O_2 from the cell chamber.

Section 6.4: Electrode Surface Preparation

Electrode polishing is truly an art, and not a science. We tried a number of chemical and electrochemical polishing procedures described in the literature [F4,F5] in an attempt to create a smooth optical finish. However, we found that either these procedures did not produce a smoother surface than mechanical polishing alone or they were unreliable. For example, a HNO_3/CrO_3 chemical polish was found to etch, rather than polish, Ag (111) single-crystal surfaces. Therefore, since there is a problem associated with chemical contamination resulting from chemical polishing, and since chemical polishing does not seem to improve the surface smoothness, we decided to simply mechanically polish our electrodes.

The overall preparation technique of the various electrode surfaces (Ag, Cu, Zn) used in this study was similar. The procedure represents a continued evolution of the procedures used by this research group before [F6-F10]. After the electrodes were placed in epoxy, a series of silicon carbide papers up to 0000 grit were used to remove any large scratches. Sanding was preformed by straight, parallel motions. To minimize scratching due to particle transfer from one grit size to the next, the samples were rinsed in water and ultrasonically shaken in water between changes in grit size. Also, when going from one grit size to the next, the surface should be turned 90° so that the scratches from the previous sanding step was more uniformly removed. After the sanding steps, the

electrodes were polished with 6-, 1-, and 1/4-μm diamond paste. (This last procedure is described in detail below.)

Ag, Cu, and Zn are all soft metals, and therefore they tend to retain severe scratches when polished mechanically. Pits in silver are formed very easily during mechanical polishing. We believe that the mechanism for pit formation is the trapping of diamond particles in scratch lines, followed by the rotation of the polishing particle (hence forming a crevice). Copper tends to form a wavy surface (we call it "range peel") if care is not taken during polishing. An exact mechanism for the formation of "orange peel" is unknown, although local heating of the surface (thereby allowing the metal to flow) appears to be an important factor. Zinc scratches very easily; we have not found pitting to be a problem for zinc.

We determined that the most critical parameters in preparing mirror-like polished metal surfaces are (1) the type of cloth used for polishing, (2) the amount of pressure applied during polishing, and (3) the motion of the electrode on the polishing wheel. The procedure for mechanically polishing silver has been investigated by this author before [F10], and we now believe that we have a recipe for obtaining optically smooth surfaces of silver, copper, and zinc relatively easily.

The procedure for polishing silver is as follows. We found that the commercially available product, Imperial polishing cloth (Leco Corp., 3000 Lakeview Ave., St. Joseph, MI 49085), works excellently for polishing silver. Place the Imperial cloth on the polishing wheel and allow the wheel to rotate rapidly ($>$200 rpm). Saturate the cloth with distilled water and add water some water

as it rotates. The water aids in the removal of particles from the cloth (through the centrifugal forces generated). Next, stop the rotation of the wheel and apply a short ribbon (1-2 cm) of diamond paste to the center of the cloth. Use the electrode to spread the paste evenly around the center region of the cloth. Then turne the whell on at a slow setting (about 60-100 RPM). With the electrode held in your hand, carefully place it on the rotating wheel. Apply a minimum amount of pressure to the electrode, because excessive pressure causes pitting. Rotate the electrode in a figure eight pattern, taking special care to not apply too much pressure to the surface. After about 2-3 minutes, the polishing for that particular particle size should be complete. Make sure that the surface has not become pitted (pitting can be observed by diffuse scattering from the surface or by a quick observation under an optical microscope). To remove the pits, it is generally necessary to go back to the last silicon carbide paper sanding step. If the surface is not pitted, repeat the step above (beginning with the cleaning of the Imperial cloth) for the next smaller diamond-paste particle size.

After the electrode is polished with 1/4 μm paste, it should be polished on Imperial cloth with a commercially available colloidal silica particle suspension (Buehler "Mastermet", pH 9.8, 0.05 μm particles). The suspension tends to dry and form large agglomerates of particles, so care should be taken to ensure that no large particles of dry suspension are put onto the cloth. After this final polishing step, the electrodes should be rinsed with water, placed in a series of organic solvents of increasing polarity (methyl ethyl ketone, acetone, and ethyl alcohol), and then placed in distilled water again.

The procedures for polishing Cu and Zn are basically similar to that for Ag. However, nylon polishing cloth seems to work better at avoiding "orange peel", and therefore nylon cloth should be used at the 6-micron polishing level for copper. Nylon cloth was found to scratch zinc, and therefore only Imperial cloth or microfelt should be used. Also, Zn tends to be etched by the "Mastermet" solution (it contains some KOH), and therefore it can not be used. A water/alumina slurry of 0.05 μm particles works well and should replace "Mastermet" as an abrasive for the final polishing stage for zinc.

Generally, electrodes used in the study did not require a repeating of the silicon carbide sanding treatment after an electrochemical experiment. Instead, polishing can begin using 6-μm diamond paste. However, as noted above, when the surface became pitted, sanding with silicon carbide paper appeared to be the only way to remove the pits.

Section 6.5: Hg/HgO Reference Electrodes

The Hg/HgO half-cell reaction was chosen as the reference electrode for this study. This electrode was chosen over more readily available commercial electrodes because (1) the potential is stable and very reproducible, (2) we can use the same solution (1M or 6M KOH) in the reference electrode chamber as in the cell, thereby avoiding any liquid junction potentials, and (3) it is easily manufactured in-house. A discussion of reference-electrode theory and liquid junction potentials can be found in the references [F11,F12].

Figure 6-2 is a photograph of our Hg/HgO reference electrode. The electrode glass housing consists of a 14/20 sleeved Pyrex test tube with its bottom replaced by porous fritted glass. A capillary tube, which is connected to a 14/20 glass stopper, acts as a holder for the liquid Hg. The Hg/HgO reference couple was made by first placing some glass wool into the bottom of the capillary tube. Next, HgO powder was inserted on top of the wool and some liquid Hg was placed on top of the HgO/wool. The glass wool creates a sufficient flow barrier to hold the liquid Hg in the capillary, but it is also sufficiently porous to allow the electrolyte to reach the Hg/HgO interface. After the Hg metal is in place, a Pt wire is inserted into the liquid and acts as an inert current collector. The test tube sleeve is then filled with the solution, and the electrode can be placed into the electrochemical cell.

The electrodes made in this fashion showed remarkable consistency (generally less than 1 mV difference between electrodes) and appeared to be stable over periods of several weeks. However, the electrodes were found to give faulty readings at longer times and were particularly susceptible to Zn ion contamination. Therefore, a new Hg/HgO reference electrode (fresh chemicals) was used for each Zn experiment. Otherwise, the reference electrodes were replaced after about one month.

Section 6.6: Electrochemical Measurements

Electrochemical measurements were made using a Princeton Applied Research (PAR) Model 273 potentiostat. This instrument allows one to generate

a large variety of waveforms for electrochemical experiments. The potentiostat has a digital coulometer and IR compensator, which aids in the interpretation of results. A range setter allows increased digital or analog sensitivity. A program for the LSI 11/73 has been developed to send commands to the PAR 273 through an RS-232 serial interface board [F13]. These commands are interpreted and executed by the PAR 273 computer, and the current or potential data (depending on the type of experiment being preformed) are stored in the PAR 273 memory. After the experiment is completed the data are transfered to the LSI 11/73 computer for storage and later interpretation.

The potentiostat is turned on, and the electrode potential is set to a noble potential as soon as possible after the electrolyte is injected into the cell. For silver, the pre-experiment electrode potential was set to -200 mV vs Hg/HgO. For copper, the potential was set at -700 mV vs Hg/HgO. In the case of zinc, the potential of the electrode was set to -1.450 V vs Hg/HgO. Though this last value is more negative than the E_o value for hydrogen evolution, no hydrogen bubbles were observed. This procedure was adopted to remove any native oxides and to provide cathodic protection to the surface.

REFERENCES FOR CHAPTER 6

F1) Anderson, Paul, Ph.D. Thesis, Dept. of Chemical Engineering, University of California at Berkeley, November 1987. Lawrence Berkeley Laboratory Report LBL-24522.

F2) Omar, F. El., and R. Durand, J. Electroanal. Chem. **178**, 343 (1984).

F3) Markovic, N., M. Hanson, G. McDougale, and E Yeagar, J. Electroanal. Chem. **214**, 555 (1986).

F4) James H. Richardson, **Optical Microscopy for the Materials Sciences**, Marcel Dekker, New York, 1971.

F5) Hallmark, Vickie, **Surface Raman Spectroscopy: A New Adsorbate Vibrational Probe and its Selection Rules.** Ph.D. Thesis, University of Texas, Austin, December, 1984.

F6) Steiger, R. F., J. M. Morabito Jr., G. A. Somorjai, and R. H. Muller, Surf. Sci. **14**, 279 (1969).

F7) Smith, C. G., Ph.D. Thesis, Dept. of Chemical Engineering, University of California at Berkeley, August 1978. Lawrence Berkeley Laboratory LBL-8082.

F8) Muller, R. H., and C. G. Smith, Surf. Sci. **96**, 375 (1980).

F9) Farmer, J. C., Ph. D. Thesis, Dept. of Chemical Engineering, University of California at Berkeley, March 1983. Report Lawrence Berkeley Laboratory LBL-15607.

F10) Mayer, S. T., M.S. Thesis, Dept. of Chemical Engineering, University of California at Berkeley, December, 1985. Lawrence Berkeley Laboratory Report LBL-20503.

F11) Ives, David J. G., and George J. Janz, **Reference Electrodes: Theory and Practice**, Acedemic Press, New York, 1961.

F12) Newman, John, **Electrochemical Systems**, Prentice-Hall, Englewood Cliffs, N.J., 1973.

F13) Mayer, S. T., and R. H. Muller, to be published.

FIGURE CAPTIONS FOR CHAPTER 6

Figure 6-1. Electrodes and mounting equipment. Upper right corner: front of Ag (111) electrode in epoxy mount. Lower right corner: front of Cu (111) electrode in epoxy mount. Center: brass mounting bolt. Upper left corner: Teflon electrode holder. Electrode screw inserted from top shown. Brass mounting bolt inserted from bottom side. Lower left corner: back of Cu(111) electrode showing mounting screw.

Figure 6-2. The standard design of the Hg/HgO reference electrode used in this study.

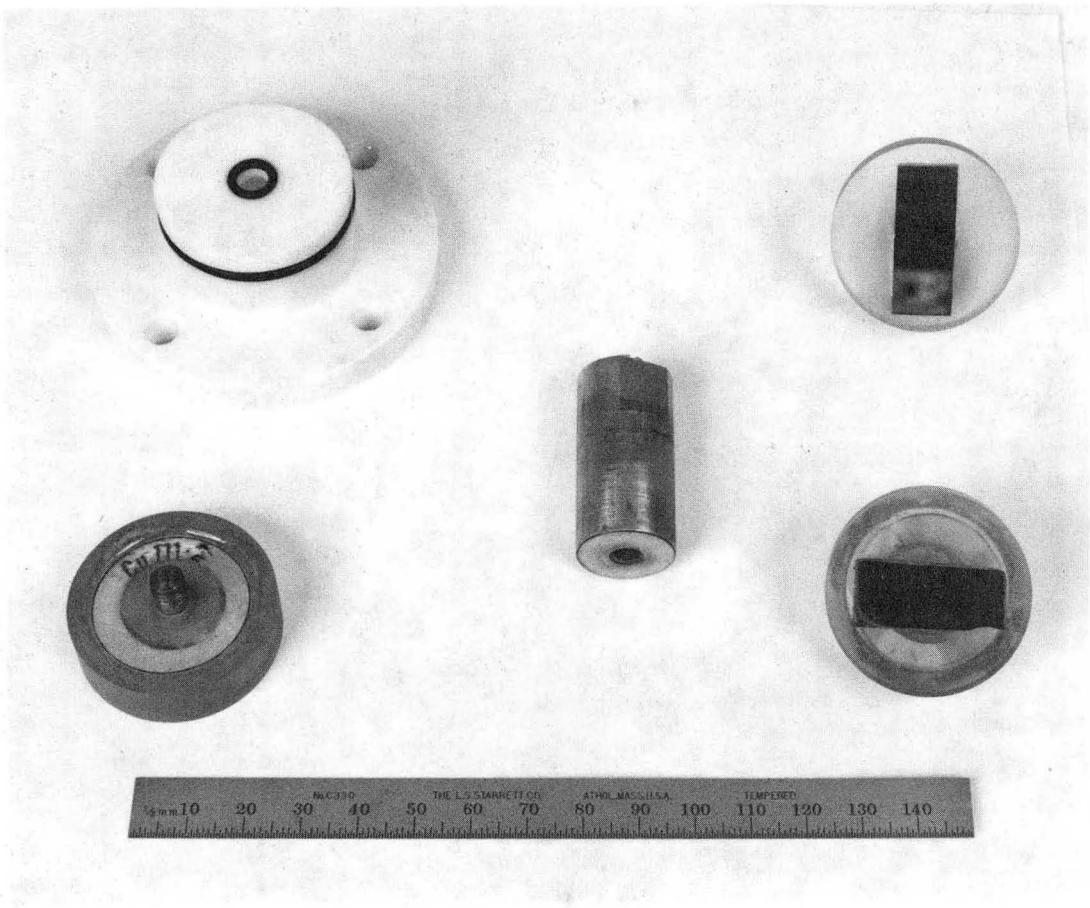

CBB 880-10607

Figure 6-1

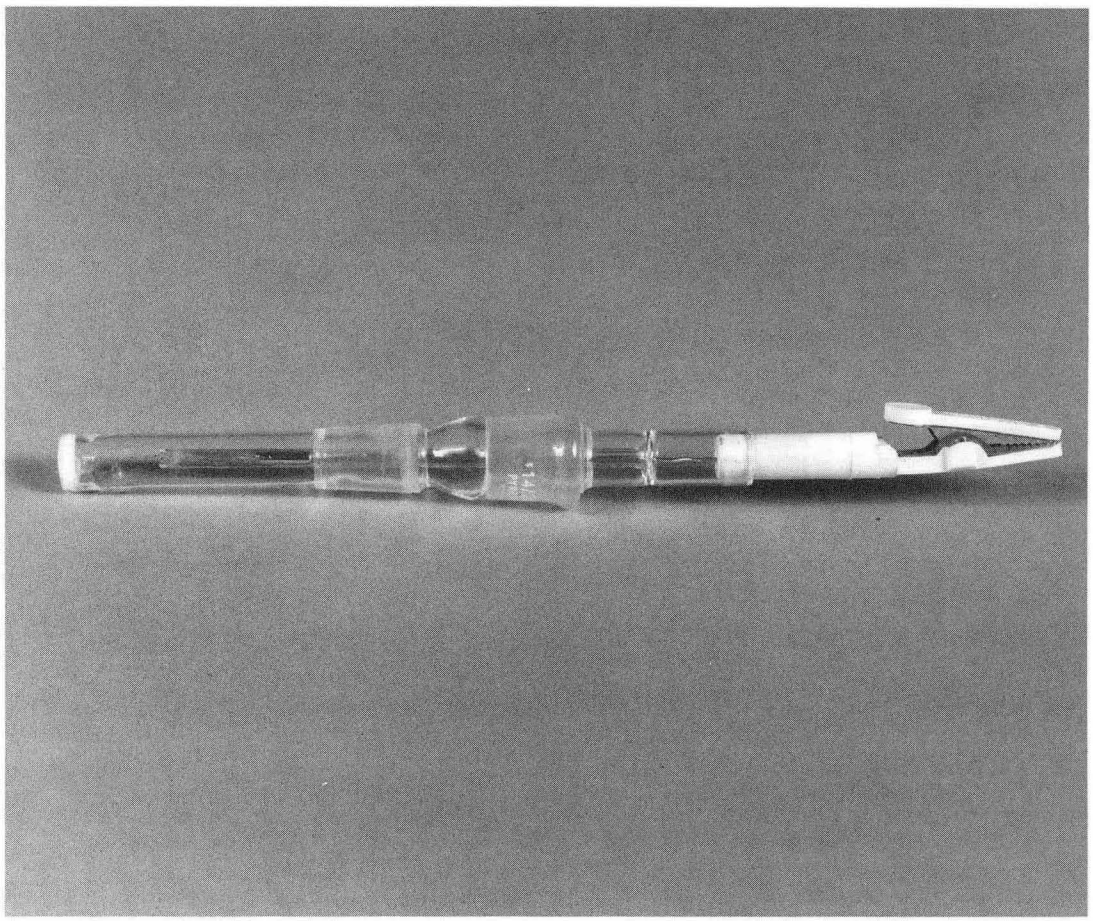

CBB 893-2067

Figure 6-2

CHAPTER 7

IN SITU ELASTIC LIGHT-SCATTERING MEASUREMENTS MADE DURING THE ANODIZATION OF METALS

Section 7.1: Introduction

The amount of light scattered from a surface is a sensitive measure of surface roughness. A surge of interest in light scattering from surfaces has been fueled by the demand for high-quality lenses, mirrors, and optical thin films. For many applications, the measurement of both the total integrated scattering (TIS) and the angular dependence of scattering are desirable. Theoretical predictions relate these measured quantities to surface roughness parameters (e.g., the RMS roughness, autocorrelation functions, spectral power density)[G1-G15]. Often, these surface parameters can be also measured by a stylus profilometer. However, light scattering has the advantage of being a nondestructive experimental technique, and it can be used for *in situ* monitoring in any transparent environment. Therefore, by making angularly resolved scattering measurements, one can in principle measure the changes in surface roughness while a chemical process is occurring.

Observations of the nucleation and growth of electrochemically formed surface layers are of great interest to electrochemists. Few unobtrusive measurements are available that are both *in situ* and sensitive to changes in topography on a submicron scale. The *in situ* angularly resolved elastic-scattering

observations made during the electrochemical oxidation of a metal shown here are the first ever to be reported. The goal of these experiments are 1) to demonstrate the utility and limitation of the technique, and 2) to futher our understanding of the mechanism of nucleation, growth, and transformation of surface layers formed on Ag and Cu in alkaline solutions.

Section 7.2: Light Scattering Principles and Theory

7.2.1 Introduction

While the optical theory for the reflection of light from surfaces with roughnesses much larger than the wavelength of light is well established (geometrical optics, interference, and diffraction theory)[G16-G19], a theory for the scattering of light from a relatively smooth surface with microrough features (i.e., roughness $<$ wavelength of light) is still undergoing refinement. Scalar and vector scattering theories, as well as some ideas relating the scattering from rough surfaces to the treatment of x-ray scattering from amorphous materials, are presented in this section.

7.2.2 Diffraction by N Identical Apertures

The mathematical treatment of the problem of diffraction from a large number of circular apertures randomly placed on a screen has been presented by Stone [G20]. Beckmann and Spizzichino [G4] have presented a similar treatment for scattering from rough surfaces. The theoretical treatment for the scattering

associated with a large number of small particles randomly positioned on a surface should be similar. We require that the particles be much smaller than the wavelength of light. Since our purpose is to discuss some ideas pertaining to scattering from small particles on a surface, the development that follows will be presented along those lines.

Refer to Figure 7-1 for the coordinate system used in the development below. The points of origin of light scattering (i.e., points O and Q) lie in a plane and are defined by coordinates (0,0) and (x_j,y_j). An arbitrary point of observation P is located at (X,Y) in a plane is parallel to the scattering plane. The optical-path difference between $\overline{OP}$ and $\overline{QP}$ can be obtained by using the Pythagorean theorem:

$$L^2 = R_1^2 - (X^2+Y^2) = R_2^2 - (X-x_j)^2 - (Y-y_j)^2 \quad . \qquad 7.1$$

The difference in the squares of the optical path can therefore be expressed as

$$R_1^2 - R_2^2 = (R_1-R_2)(R_1+R_2) = (x_j^2+y_j^2) - 2(x_jX + y_jY) \quad . \qquad 7.2$$

Since the interparticle spacing is much smaller than the distance to the observation point P (i.e., $\overline{OQ} << \overline{OP}$ and $\overline{OQ} << \overline{QP}$), $x^2+y^2<<2(xX+yY)$. Also, $R_1+R_2 \approx 2R$. Therefore, equation 7.2 can be simplified to

$$\Delta = R_1 - R_2 = \frac{x_j^2+y_j^2}{2R} - \frac{2(x_jX+y_jY)}{2R} \approx \frac{(x_jX+y_jY)}{R} \quad . \qquad 7.3$$

Since $\frac{X}{R} = \sin\theta$ and $\frac{Y}{R} = \sin\phi$, the optical-path difference Δ between $\overline{OP}$ and

$\overline{QP}$ is just

$$\Delta = x_j \sin\theta + y_j \sin\phi \ . \qquad 7.4$$

The relative phase difference between the light emanating from points O and Q as observed at P is then given by

$$\Phi_j = -k(x_j \sin\theta + y_j \sin\phi) \qquad 7.5$$

where $k = \frac{2\pi}{\lambda}$. Since we consider only the case of light that is coherent and incident normal to the plane containing O and P, the light is of the same phase at all points on the plane (surface). In this case, the scattering problem reduces to

$$E_s \approx \sum_{j=1}^{N} A_j e^{-i\Phi_j} \ , \qquad 7.6$$

where E_s is the total scattered electric field amplitude at the observation point P, A_j is the scattered field strength from the jth scatterer, and $e^{-i\Phi_j}$ is the phase factor associated with the scattered field from the jth scatterer at point P.

To simplify the problem, we consider all scatterers to be of the same size. Therefore, A_j is the same for all scattering sources. In the forward scattering direction, $\Phi_j = 0$ (since $\theta = \phi = 0$), and so the observed scattering intensity ($I = E^2$) from equation 7.5 is proportional to the square of the number of scatterers ($I \approx N^2$). In addition to this scattering intensity, the reflectance from the surface as a whole (less that from the projected area of the scatterers) is also observed in

the specular direction. Very near the forward scattering direction, the values of Φ_j are partially correlated, and so the intensity does not undergo rapid fluctuations. Away from the specular direction the values of Φ_j become random, ranging from 0 to 2π. Since even a slight movement in the observation point changes all the Φ_j vales differently, the intensity (which is a summation of these terms) will also exhibit a random behavior. These changes in Φ_j can produce large changes in I_s, and so the resulting scattering pattern shows a finely mottled appearance. A statistical analysis of the problem [G20] shows that the intensity, averaged over a large acceptance angle, is proportional to N.

Stone's treatment of this diffraction/interference problem does not include the Kirchhoff so-called *obliquity factor*, and therefore no angular dependence of the scattering pattern is predicted. However, by including the obliquity factor into the problem, equation 7.6 should be further modified to

$$I_s \approx \cos^2\theta \left[\sum_{j=1}^{N} e^{-i\Phi_j} \right]^2, \qquad 7.7$$

where θ is the scattering angle measured between the incident normal beam and the observation point. Equation 7.7 is more consistent with experimental observation than equation 7.6.

7.2.3 Scattering from Random and Semiordered Surface Particles

The theory of scattering of x-rays from ordered and semiordered materials is well developed [G21]. We will use some principles developed for the scattering of x-

rays and apply them to the scattering of visible light from small particles. The two problems should be analogous as long as the dimensionless particle size $\frac{a}{\lambda}$ (where a is the particle size and λ is the wavelength of light) is much less than 1.

The scattering of electromagnetic radiation can be represented by the induction of electric dipole moments in a material. Because of their charge, electrons are induced to oscillate with the same frequency as an incident electric field. Since the charges undergo periodic accelerations, the electrons act as secondary sources for the emission of light. From classical electrodynamics, the intensity of scattered radiation from an electron in a polarized oscillating electric field is [G21,G22]

$$I_e = I_o \left(\frac{\mu_o}{4\pi} \right)^2 \left(\frac{e^4}{m^2 R^2} \right) \sin^2 \phi_z \ . \qquad 7.8$$

In equation 7.8, I_e is the scattering intensity from the electron, I_o is the incident beam intensity, R is the distance from the scattering electron to the point of observation, and ϕ_z is the angle of observation with respect to the vector of polarization in the plane of propagation. Other symbols in equation 7.8 have their usual meanings.

Figure 7-2 shows a beam of monochromatic light of wavelength λ incident on a particle. Two points within the particle are separated by the vector $\vec{r}$. A portion of the beam will be scattered in the direction ϕ. The point O is an arbitrarily defined origin in the material. The unit vectors $\vec{k}_o$ and $\vec{k}$ are defined as the directions of the incident and scattered beam, and these vectors describe the

angle ϕ. If the distance between the two scattering points is much less than the distance to the observation point from either scatterer, then the angle ϕ is the same for both points and the optical path difference is given by $\vec{r}\cdot\vec{k} - \vec{r}\cdot\vec{k}_o$. The phase difference of the light reaching an observation point from these two points is then given by $\left(\frac{2\pi}{\lambda}\right)\vec{r}\cdot(\vec{k}-\vec{k}_o)$. By defining the vector $\vec{Q}$ as

$$\vec{Q} = \left(\frac{2\pi}{\lambda}\right)(\vec{k}-\vec{k}_o) \ , \qquad 7.9$$

$$Q = \frac{4\pi}{\lambda}\sin\frac{\phi}{2} \ , \qquad 7.10$$

the phase difference can be expressed as simply $\vec{r}\cdot\vec{Q}$.

By considering the effect of the density of electrons $\rho(\vec{r})$ in the scattering material, the following equation is obtained for the electric field scattered from the entire body:

$$E(\vec{Q}) \approx E_o\left[\frac{\sin\phi_z\mu_o e^2}{4\pi mR}\right]\int_V \rho(\vec{r})e^{-i\vec{r}\cdot\vec{Q}}d\vec{r} \ . \qquad 7.11$$

The appearance of R (the distance between the scattering particle and the point of observation) in equation 7.11 takes into account the inverse square dependence of intensity with distance. The incident field strength E_o acts as a scaling factor with respect to the incident intensity. We therefore simplify equation 7.11 to read

$$E(\vec{Q}) \approx \int_V \rho(\vec{r}) e^{-i\vec{r}\cdot\vec{Q}} d\vec{r} \ . \qquad 7.12$$

We note that the intensity of the scattered wave is determined by

$$I(\vec{Q}) = E(\vec{Q}) \cdot E^*(\vec{Q}) \ . \qquad 7.13$$

Equation 7.12 can be simplified by making assumptions regarding the symmetry properties of the scattering body. When the particle is spherically symmetric, $\rho(\vec{r})$ depends only on the magnitude of $\vec{r}$, so that equation 7.12 simplifies further to [G21]

$$E(\vec{Q}) \approx \int_0^\infty 4\pi r^2 \mathrm{sinc}(Qr) dr \ , \qquad 7.14$$

where

$$\mathrm{sinc}(x) = \frac{\sin(x)}{x} \ . \qquad 7.15$$

Integration of equation 7.14 for a spherical body of radius a of constant electron density yields [G21]

$$E(Q) = \left[\frac{4\pi a^3 \rho}{3} \right] \varsigma(Qa) \ , \qquad 7.16$$

where

$$\varsigma(x) = 3\left[\frac{\sin(x)-(x)\cos(x)}{x^3}\right] . \qquad 7.17$$

The observed scattering from the body is proportional to the volume of the body and its electron density. Figure 7-3 is a plot of the function $\varsigma(x)$, and the square of $\varsigma(x)$ (proportional to the scattering intensity). The curve in Figure 7-3 is compressed towards the origin with an increase in the size of the body. This dependence implies that scattering will occur preferentially at smaller angles for larger particles.

When there are a number of scatterers being irradiated at the same time in a region of space, the total scattered field is the vector sum of the scattering from the individual centers. In making this statement, we assume that the coherent-superposition principle is valid and that multiple scattering is of secondary importance. By considering the phase differences from a number of scattering particles arranged in a two-dimensional (2-D) plane, the scattering from an assembly of particles will be given by

$$I(Q) \approx \sum_{j}^{N} E_j^2(Q) + \sum_{j}^{N}\sum_{k\neq j}^{N} E_j(Q)E_k(Q)J_o(Qr_{jk}) . \qquad 7.18$$

The first term on the right of equation 7.18 is the scattering associated with the bodies themselves, as in equation 7.16. The second term arises from the interference of the scattered radiation between the various particles. The zero-order Bessel function of the first kind in equation 7.18 accounts for the phase difference between the various scattering particles. (The Bessel function replaces the com-

plex exponential because the problem has been posed to have 2-D symmetry.) The scattering equation, 7.18, becomes more useful if we make the further simplification that all particles are of the same size. When this is done, equation 7.18 can be expressed as

$$I(Q) \approx N\,E(Q)^2\,S(Q) \quad , \qquad 7.19$$

with

$$S(Q) = 1 + \frac{1}{N}\sum_{j}^{N}\sum_{k\neq j}^{N} J_o(Qr_{jk}) \quad . \qquad 7.20$$

S(Q) is referred to as the "interference function". If the assembly of particle interactions is considered to have a uniform "average" relationship between neighboring particles (valid for a large number of particles), then the light scattered from each of the N particles will interact with the (N-1) others. There are a total of N(N-1) identical interactions. Therefore, equation 7.20 can be further simplified, with the result that

$$S(Q) = 1 + N\sum_{k=1}^{N} J_o(Qr_k) \quad . \qquad 7.21$$

In equation 7.21, r_k is the distance from the center of an arbitrary particle to the kth particle. An arbitrary particle is therefore the center of the coordinate system, and the overall arrangement of the ensemble of particles is considered to be indistinguishable with respect to the particular particle chosen for the origin. If the number and size of the particles are known, S(Q) can in principle be derived

from the observed dependence of scattered intensity on the wavenumber Q.

The statistical relationship between the particle distribution and the interference function can be treated by the introduction of the radial distribution function g(r). The radial distribution function is a normalized function representing the probability of finding a particle at a distance r from the origin. If we invoke the radial distribution function to describe the interrelationship between particle spacings, then S(Q) and g(r) are related by [G21]

$$S(Q) = 1+n_o\int_0^\infty 2\pi r[g(r)-1]J_o(Qr)dr \quad . \qquad 7.22$$

The radial distribution function g(r) and the interference function S(Q) form a transform pair. (In the 2-D case, the relation is a Bessel-Hankel transform pair [G23]):

$$g(r)-1 = \frac{1}{n_o}\int_0^\infty 2\pi Q[S(Q)-1]J_o(Qr)dQ \quad . \qquad 7.23$$

In principle one should be able to extract the particle radial distribution function from the values of S(Q) calculated from scattering measurements. In practice, however, the range of data in wavenumber space is limited (e.g., using 633-nm light and collection angles from 5° to 85°, the range of Q is from 0.866 μm^{-1} to 13.41 μm^{-1}). Transform inversion of data of limited range can cause an effect known as aliasing [G21]. This effect can cause the transformed data to show fine structure that is not associated with the function itself.

In addition to directly transforming scattering data, one can propose a functional form for the radial distribution function to be used in equation 7.22 in an attempt to fit the observed scattering curve. For example, let us assume that the radial distribution function can be represented as

$$\begin{aligned} g(r) &= 0 \quad r<c \ , \\ g(r) &= 1 \quad r\geq c \ . \end{aligned} \qquad 7.24$$

This functional form for g(r) is similar to the "hard sphere" model used in a modified ideal gas equation. The "hard sphere" model basically implies that particles are excluded inside a certain radius but are found with uniform probability elsewhere. This excluded volume may be larger than the particle radius (e.g., crystals will be excluded from inside another crystal's diffusion boundary layer), and so we use the symbol c to represent this distance. By combining equation 7.24 with equation 7.22, the resulting expression for S(Q) becomes

$$S(Q) = 1 - \frac{2\pi n_o}{Q}\int_0^c QrJ_o(Qr)dr \ . \qquad 7.25$$

Integration of equation 7.25 yields

$$S(Q) = 1 - \frac{2\pi n_o c J_1(Qc)}{Q} \ . \qquad 7.26$$

Figure 7-4A is a plot of equation 7.26 for different values of c. By combining equations 7.16, 7.19, and 7.26, the predicted Q dependence of scattering based on the g(r) hard-sphere model is given by

$$I(Q)=N\left[\frac{4\pi c^3\rho}{3}\right]^2\left[\frac{3[\sin(Qa)-(Qa)\cos(Qa)]}{Qa^3}\right]^2\left[1-\frac{2\pi n_o a J_1(Qc)}{Q}\right]. \quad 7.27$$

Figure 7-4B shows a plot of the product of the last two terms of equation 7.27. (This is the angular dispersion of scattered light without scaling the intensity for particle size and number.)

Theories for the scattering of light from rough surfaces have been presented in the literature and are discussed in sections 7.2.5 and 7.2.6. When surface microroughness, rather than surface particles, is the major cause of light scattering, these theories should be superior to that developed above.

7.2.4 Surface Spectral Analysis

Since the discussion of optical-scattering theory invokes spectral-analysis functions (autocorrelation and spectral power density), a brief discussion of these function will be presented. The autocorrelation function has been used by this author to analyze *in situ* scanning tunnelling microscopy (STM) data [G24]. These functions are generally considered to characterize wavelength-dependent (spatial frequency) features well. Amplitude-sensitive functions, such as the amplitude density function (ADF), are also commonly used to characterize surface topography [G25].

For a one-dimensional surface profile, we can define $H(x_1)$ as the height of the surface at a position x_1 with respect to the average height determined over a long distance. The autocorrelation function of this surface, $G(x)$, is defined as

$$G(x) = \langle H(x_1)H(x_1+x)\rangle \quad , \tag{7.28}$$

where x is the variable of spatial separation (lag distance). The special case of zero lag, G(0), represents the average of the square of the height profile, or the square of the RMS value:

$$G(0) = (\mathrm{RMS})^2 \quad . \tag{7.29}$$

Equation 7.28 can also be written as

$$G(x) = \lim_{L\to\infty} \frac{1}{L}\int_0^L H(x_1)H(x_1+x)dx_1 \quad , \tag{7.30}$$

where L is the distance of the straight line measured along the surface over which the profile is taken. In principle, the autocorrelation should become representative of the surface topography as a whole for sufficiently large values of L. It can be shown that the autocorrelation function G(x), and the spectral power density function, g(k), form a Fourier transform pair [G13,G14,G20]:

$$g(k) = \int_{-\infty}^{\infty} G(x)e^{-ikx}dx \quad , \tag{7.31}$$

$$G(x) = \frac{1}{2\pi}\int_{-\infty}^{\infty} g(k)e^{ikx}dk \quad . \tag{7.32}$$

Both the autocorrelation function and the spectral-power-density function have the properties that G(x)=G(-x).

7.2.5 Scalar Scattering Theory

One of the earliest theories to address the problem of scattering from a surface was presented by Davies [G1]. Davies developed a model of light scattering from random surface irregularities from an otherwise smooth surface using scalar optical-diffraction theory based on Huygens' principle [G2]. The assumptions that Davies made regarding the properties of the surface were that:

1) the RMS roughness σ is much smaller than the wavelength of light,

2) the surface is perfectly conducting,

3) the surface height distribution is Gaussian, and

4) the autocorrelation function of the surface is also Gaussian and has a standard deviation β.

Davies' theoretical results were modified by Bennett and Porteus [G6,G7] to account for the limited conductivity of real metal surfaces. The reflected light (reflectance) can be divided into specular and diffuse reflectance. The expression for specular reflectance is given by

$$\frac{R_s}{R_o} = \exp\left[-\frac{(4\pi\sigma)^2}{\lambda^2}\right] . \qquad 7.33$$

In equation 7.33, R_s is the specular reflectance from the rough surface and R_o is that from a perfectly smooth surface. The angular distribution of the diffuse

reflectance of light from Davies' theory can be expressed as

$$r_d(\theta)d\theta = R_o 2\pi^4 \left(\frac{\beta}{\lambda}\right)^2 \left(\frac{\sigma}{\lambda}\right)^2 (\cos\theta + 1)^4 \exp\left[\frac{-(\pi\beta\sin\theta)^2}{\lambda^2}\right] d\theta \ . \qquad 7.34$$

In equation 7.34, $r_d(\theta)d\theta$ is the fraction of reflected light scattered into an angle between θ and θ+dθ at the angle θ from the surface normal. If a measurement of the reflectance is made with an instrument of acceptance angle $\Delta\theta$ at near normal incidence (θ=0), the total measured reflectance is given by [G6]

$$\frac{R_s}{R_o} = \exp\left[-\frac{(4\pi\sigma)^2}{\lambda^2}\right] + \frac{16\pi^4\beta^2}{\sigma^2}\left(\frac{\sigma}{\lambda}\right)^4 (\Delta\theta)^2 \ . \qquad 7.35$$

The first term on the right of equation 7.35 is the specular-reflectance term, and the second arises from the diffuse reflectance. Bennett and Porteus [G2,G3] compared the measured specular-reflectance data with the prediction of equation 7.35. They found that the observed wavelength dependence of scattering was in good agreement with the theory. They also calculated the error that would result in a reflectance measurement if one neglected the effects of surface roughness. These calculations show that the error in the measured reflectance from a surface with an RMS roughness as small as 100 Å is around 10% at optical frequencies (when compared to an optically flat surface). Bennett and Porteus [G2] concluded that the value of the RMS roughness σ can be obtained with good accuracy from reflectance measurements. Later work by Depew and Weir [G5] helped confirm this finding.

7.2.6 Vector Scattering Theory

More recently, classical vector scattering theory has been under development, principally by Elson and Bennett [G7-G9,G13-G15]. Elson and Bennett [G9] note that simple scalar scattering theory gives a good relation between the total integrated scattering (TIS, which is the converse of specular reflectance) and RMS roughness. However, vector scattering theory is more complete in that it includes the vector nature of the incident and scattered fields and, while not perfect, is considerably better for predicting the angular dependence of scattered light.

To use vector scattering theory in a predictive manner, one must know either the autocorrelation function (ACF) or the spectral-power-density function (SPDF) of the surface. One can either assume a form for the ACF or measure it directly. Elson and Bennett [G9] have compared calculated and measured scattering curves by measuring the ACF of a surface using a profilometer, and they showed that vector light-scattering theory can be used to determine the SPDF with fair accuracy. However, as discussed before, aliasing occurs during data transformation, and so transformation of the data back to the ACF is more difficult.

The assumptions of vector scattering theory are basically the same as those of Davies' theory [G1] described above, with the exception that the form of the roughness profile is left unspecified. The differential power dP of normally incident scattered energy per unit solid angle $d\omega = \sin\theta d\theta d\phi$ in the direction

specified by the polar angle θ measured from the surface normal, and the azimuthal angle ϕ measured from the direction of incident-beam polarization is predicted by vector theory to be [G11,G13]

$$\frac{dP}{d\Omega} = \left(\frac{2\pi}{\lambda}\right)^4 \left\{ \left[\frac{|1-\sqrt{\epsilon}|^2 \cos^2\theta}{\pi^2} \right] \left[\frac{|\nu|^2 \cos^2\phi}{|\nu - iq\epsilon|^2} + \left(\frac{2\pi}{\lambda}\right)^2 \frac{\sin^2\phi}{|\nu - iq|^2} \right] \right\} g(\mathbf{k}) \qquad 7.36$$

Here, ϵ is the complex permittivity of the surface, and ν, q, and $\vec{k}$ are defined as

$$\nu = \sqrt{\left[k^2 - \epsilon\left(\frac{2\pi}{\lambda}\right)^2\right]} \ , \qquad 7.37$$

$$q = \left(\frac{2\pi}{\lambda}\right)\cos\theta \ , \qquad 7.38$$

and

$$\vec{k} = k(\hat{x}\cos\phi + \hat{y}\sin\phi) \ . \qquad 7.39$$

Generally, $\vec{k}$ represent the overall change in the wave-vector along the surface between the incident and scattered photon. With normal incidence the incoming photon has no wavevector component parallel to the surface. In this case the vector $\vec{k}$ represents the wave-vector component of the scattered light parallel to the surface and is given by

$$k = \left(\frac{2\pi}{\lambda}\right)\sin\theta. \qquad 7.40$$

The expression inside the major brackets ({ }) in equation 7.36 is referred to as the "optical factor". The optical factor contains terms that account for the

angular dependence of scattering independent of surface features [G13] and determines the strength of the polarization currents [G4]. The optical factor depends on the optical properties of the surface through the complex dielectric constant. This term should be adjusted when the ambient is not vacuum. Equation 7.36 can be simplified when the scattered light is measured in a plane perpendicular to the plane of polarization of the incident beam and when the surface is considered to be isotropic [i.e., two-dimensional SPDF, units of (length)^4, independent of direction]. The result for this case is [G13]

$$\frac{dP}{d\Omega} = \frac{16\pi^2}{\lambda^4}\left[\frac{|1-\sqrt{\epsilon}|^2\cos^2\theta}{A + \cos^2\theta - 2\sqrt{A}\sin(\frac{\alpha}{2})\cos\theta}\right]g^2(k) \ . \qquad 7.41$$

In equation 7.41, ϕ in equation 7.36 is set to $\frac{\pi}{2}$, A and α are defined as

$$A = \sqrt{(\sin^2\theta-\epsilon_1)^2 + \epsilon_2^2} \ , \qquad 7.42$$

and

$$\tan\alpha = -\epsilon_2/(\sin^2\theta-\epsilon_1) \ , \qquad 7.43$$

with ϵ_1 and ϵ_2 being the real and imaginary components of the complex permittivity, respectively. The shape of the optical factor in equation 7.41 is largely determined by the $\cos^2\theta$ term in the numerator. The optical factor is nearly independent of scattering angle at near angles (0–40°) and optical frequencies, but drops rapidly at larger angles. Elson and Bennett [G13] have noted that the dielectric constants have only a secondary effect on the shape and magnitude of

the optical-factor curve.

The angular dependence of scattering in equation 7.32 is determined by the value of k. It is instructive to compare this fact with the grating equation [G2,G3], which can be rewritten in terms of the surface wavenumber k as

$$k = \frac{2\pi N}{d} \quad , \qquad 7.44$$

where N is the order of interference and d id the separation of surface features. Since any arbitrary wave form (randomly rough surface) can be decomposed into a Fourier sine and cosine series of different amplitudes and phases, one can view equation 7.41 as a superposition of s scattered field from a number of gratings superimposed on the same surface. If a grated surface is mathematically defined as a series of step functions of period d, then the autocorrelation of the surface is given by the periodic step function (where the amplitude is the square of the average surface height and the period is d). The transform of this autocorrelation function [to give g(k) as in equation 7.41] is a periodic delta function separated by a wavenumber of $\Delta k = \frac{2\pi}{d}$. Therefore, for a given spatial period d present on a surface, there is a corresponding scattering wavenumber k. The total amplitude of the wave scattered in the direction of the wavenumber k can be viewed as the superposition of a large number of surface structures of different amplitudes and periods.

Section 7.3: Equipment Design and Operation

7.3.1 System Specifications and Requirements

Numerous requirements determined the physical design of our scattering instrument. The present application for *in situ* electrochemical nucleation studies in caustic solutions made it necessary to construct the electrochemical cell from an inert material. Changes in surface roughness of less than 100 Å were to be detected. Since significant changes in crystal growth can occur over short periods of time, a specular scan had to be taken in no more than one second.

Analysis of some experimentally observed scattering intensities helped determine the feasibility of using fiber optics as a light-collection technique. Experimental data for scattering from quartz with RMS roughnesses on the order of 20 Å showed that, at 85° from the surface normal, the scattering intensity is around 1.0×10^{-6} of the incident irradiance [G9]. Based on the manufacturer's specification on our Hamamatsu model number R928 photomultiplier tuber (PMT), it was estimated that one analog-to-digital converter-unit count (ADCU count) would correspond to a total flux of about 1.0×10^{-10} watts. By illuminating a single optical fiber and transmitting the light to our photomultiplier operated at a voltage with reasonable gain and acceptable noise (800 V), we found that a total irradiance of about 2.4×10^{-10} watts was equivalent to 1 ADCU count. Since our collection area of the optical fiber was about 1×10^{-2} cm^2, this would correspond to an intensity of about 2.4×10^{-8} watts/cm^2. This flux density equals a fraction of 2.4×10^{-7} of the incident intensity (0.1 W/cm^2) of our 1 mW He-Ne

laser.

Teflon (polytetrafluoroethylene, or PTFE) is a polymer that is highly inert to alkaline solutions and has the added characteristic of being nonwetting. This feature generally helps to keep PTFE cells clean. Furthermore, Teflon has the forms good seals. Because of these advantages, it was chosen as the material of construction for our scattering cell. However, the material has some disadvantages that should be mentioned. Machining is difficult because the material is soft and tends to flow. Also, it is a prolific light scatterer (it is composed of very small particles). To minimize the PTFE scattering problem, we placed some ethylene propylene rubber sheets (which are black and not good scatterers) around the internal periphery of the cell. Experiments demonstrated that this material was chemically inert to caustic solutions (Viton rubber is not).

While unintensified photodiode arrays are inexpensive, they do not have the necessary sensitivity for the present application. An intensified diode array (IPDA) used with an optical multichannel analyzer would have sufficient sensitivity but typically costs around $30-40K. Also, these linear arrays are too small (generally about 1 inch long) for measuring scattered light over a large range of angles. The detector would have to be placed very close to the electrode. Optical fibers could have been used to bring the light to the detector (avoiding the proximity problem), but since a simpler method (described below) was available, the idea of using an IPDA was rejected.

7.3.2 Equipment Description

Figure 7-5 is a schematic diagram of the final design of the angular-resolving elastic-light-scattering instrument (ARELS). The working electrode is placed in the geometric center of the cell. The scattered light is collected over a quadrant in a plane that also contains the incident beam. Figure 7-6 is a close-up photograph of the cell chamber. The cell is 3.5 inches deep, and the radius of the inscribed semicircle is 2.5 inches. The maximum volume of electrolyte is 563 ml, but in practice, the cell was usually about 75% full, which corresponds to a volume of about 400 ml. The electrode is placed perpendicular to the incident laser beam (a 1 mW He-Ne laser, λ=633 nm). A photograph of the whole apparatus is shown in Figure 7-7. The laser beam is directed by two mirrors to strike the surface at a right angle. The optical fibers (a total of 80) are concentrically arranged in a cylindrical array around the cell ranging from 5° to 85° from the surface normal in 1° increments. This arrangement allows all the optical fibers to collect light at the same distance from the center of the point where the laser beam strikes the surface. The optical fibers are held in place by a housing. As part of this housing, a semicylinder (80°) of Plexiglas is placed in front of the optical fibers. Between the cell and the Plexiglas is a semicylindrical glass window. The window extends from approximately –5° to 95° from the electrode surface normal. The cell is sealed between the glass and the PTFE by applying pressure from the Plexiglas/optical-fiber-housing assembly to the glass window. The laser beam passes through the window and strikes the surface at a right

angle.

The other ends of the optical fibers are brought to another housing in front of a closed chamber, where they are arranged in a circular array. Behind the circular array of fibers is a chopper wheel consisting of a metal disk with a single opening. Beyond the opening, and aligned with each fiber, is another optical fiber which transmits the signal to the PMT. As the chopper wheel rotates, each optical fiber, is sequentially selected for transmission to the PMT. The light is focused by placing the ends of the optical fibers near the PMT (a technique known as proximity focusing). The plastic housing was removed from the optical fibers that focus the light on the detector. This was necessary so that all 80 channels could be placed in front of the PMT. Since each fiber illuminates a different portion of the detector, the amplification of the signal in the PMT is different for each channel. (See section 7.4 on calibration.)

A complication can arise (and was only recognized later) because of the large variation in the scattering intensity observed (several orders of magnitude from 5^0 to 85°). Since the resolution of the analog-to-digital converters is one part in 2048 ADCU, large variations in signal sensitivity can occur. For example, if the 5° channel is at a maximum in detected intensity (2048 counts) and the scattering at 85° is 10^{-3} of the scattering at 5°, then the ADCU reading in the 85° channel would be only 2 counts. Since the readout noise on the analog-to-digital board is about 2 ADCU, signal detection at far angles would be difficult and the resolution poor. To remedy this problem, we first attempted to vary the gain of the analog-to-digital converter using computer software. However, this technique

requires an intensity measurement to be made first to assess the required gain to achieve the greatest sensitivity (and therefore allow less time to make the actual measurement). It was found that the software switching rate was near its maximum value, and so the overall signal-to-noise ratio was not improved by this technique. The problem was corrected by placing a neutral density filter in the optical path of the first 20 optical fibers and offsetting the PMT output voltage with a -10 V bias (see below). The optical filter reduced the transmitted intensity sufficiently to make the total observed intensity at the detector more uniform for all angles.

7.3.3 Computer Data Acquisition Hardware and Software

Raw digital-intensity data were collected on a Digital Equipment Corporation LSI 11/73 microcomputer. A +/- 10 V bipolar Datal A-to-D board was used to transform the analog signal from the PMT to a digital signal at the computer. The output voltage from the PMT (which was measured across a 100 Ω resistor) was fed to a bias supply voltage box. This box offsets the voltage at the A-to D board by a value of -10 V so that the signal was in the range of -10 V to +10 V, thereby allowing the bipolar A-to-D board to be used without loss of resolution (4096 rather than 2048 ADCU). An incremental rotary encoder was attached to a constant speed motor that drove the chopper wheel. The encoder generated 400 "minor" pulses and one "major" pulse with each revolution. By illuminating only the first (5°) optical fiber, one can determine the location of the shutter opening with respect to the major pulse.

Intensity data were taken between each minor pulse by the data acquisition routine "SCATER" [G26]. The program SCATER initially requires setup information pertaining to the present location of the major pulse with respect to the first optical fiber (i.e., the number of minor pulses from the first optical fiber to the major pulse). Using a 72-rpm constant-speed motor, a single angular scan takes 0.833 seconds. SCATER allows for the averaging (over time) of a number of scans to improve the signal-to-noise ratio (when the experiment does not require a fast time resolution). Each scan (or time-averaged set of scans) was stored in an individual data file, along with the starting and ending time of the scan. Included in each data file was information supplied by the user pertaining to the particular experiment. This information included the scan rate, PMT voltage, ADCU gain, user's name, date, and an experimental description. Further details and a listing of the program can be found elsewhere [G26]. By storing intensities in an unformatted data array, SCATER can take and store data very quickly. However, the data need to be correlated (with respect to angle) and calibrated before they can be interpreted.

After the experiment was completed, the raw data stored by SCATER were converted to correlated (angular dependent) relative intensity data by using the program "TRANS". To accomplish this task, TRANS performed three major functions. It determined the average time that a particular data scan (or set of scans) took with respect to the beginning of the first scan (i.e., the beginning of the experiment). Second, the 400-minor encoder count channels were placed into 80 sets of 5 minor-encoder channels each. These 80 sets of 5 minor channels

correspond to the 80 single optical fibers that expose the PMT. An integrated intensity was determined from these five measurements for each optical fiber using a Simpson integration algorithm [G26]. The third task performed by TRANS is to place all of the correlated data into a single formatted data file. To perform a calibration of the scattering data, the program TRANS requires a calibration data file, "SCATER.DAT."

Section 7.4: Calibration

An optical fiber requires material with good optical transmittance and elastic properties. The overall transmission efficiency of a given optical fiber can depend on a number of factors: material of construction, diameter, housing, curvature, and surface preparation. The ends of the fibers used in our instrument were all placed in a holder and polished simultaneously. The fibers are 1 mm in diameter and therefore transmit light via multimode propagation.

The important factors contributing to the variations in transmission efficiency of the optical fibers were investigated using a light emitting diode connected to a housing. This housing provides a tight fit around the fiber and keeps the end from moving. The other end of the fiber was placed in front of a photomultiplier tube so that it could not be moved. The result of this investigation showed that variations in the quality of the plastic and the extent of bending (particularly near the end of the fiber) largely determined the transmission efficiency of any given fiber. We chose fibers whose transmission efficiency was the greatest.

Since bending the light pipe could change the transmission efficiency, it was necessary to calibrate the optical fibers while they were in the instrument. The optical fibers were permanently attached (by glue) at both ends to the fiber-optic housing assemblies. The present instrumental design includes a neutral density filter in front of the first 20 near-angle fibers, thereby making the collected scattering intensity more uniform for all angles.

The instrument was calibrated using a glowing Pt wire, which served as a line source. The wire was inserted into the electrochemical cell at the optical center of the apparatus. A constant-current power supply controlled the irradiance from the wire. Since a line source creates a cylindrical surface of equal intensity, the irradiance at the entrance of all the equidistant optical fibers was the same. The instrument was calibrated as follows:

1) Intensity data wre collected from the line source using SCATER.

2) A data file "SCATER.DAT" (read as input for the TRANS), was created in which the transmission efficiencies of all fibers are assumed to be equal.

3) TRANS was run, and the output data file (given an arbitrary name) contained the calibration information. This file was then given the name of the calibration file "SCATER.DAT" (for later use as input for TRANS). The data file

then accounted for the different transmission efficencies of the fibers.

The relative transmission efficiency of the various scattering instrument channels is shown in Figure 7-8. As mentioned above, a neutral density filter (ND 1.1) is in front of the first 25 optical fibers. As expected, there are significant variations in the transmission efficiency of the various channels. In addition to the causes mentioned above, variations in sensitivity among the different channels are also caused by illumination of different portions of the PMT by the different fibers.

The angularly resolved scattering intensity from a Teflon plug placed in the back of the cell and illuminated with the He-Ne laser is shown in Figure 7-9. It shows the very uniform scattering caused by the microcrystals. Figure 7-10 shows the insensitivity of the scattering from the plug as the point of laser illumination on the sample is changed. Because scattering from this plug is relatively insensitive to alignment, and since insertion and measurement of scattering from this material is considerably easier than from our line source, it served as a secondary scattering standard.

Section 7.5: Anodic Oxidation of Silver

In situ scattering measurements were taken during galvanostatic, potentiostatic, and potential-sweeping oxidation of silver in 1M KOH. In our previous ellipsometric study of the anodic oxidation of silver in alkaline media, we found

that during the nucleation and growth of Ag_2O crystals, the particles are unstable and undergo a ripening phenomenon [G27-G29]. Scattering measurements were taken in an attempt to verify these findings and to clarify the role that the compact (primary) layer plays in the nucleation process. In some of our experiments, potential control was released (i.e., the cell was set to open circuit), and corrosion of the surface layers was allowed to occur. The intent behind this type of potential/time-dependent experiment was to anodize the surface at a potential where three-dimensional nucleation is known to occur and then to observe any changes in the surface morphology under corrosion conditions.

7.5.1 Potential-Sweep Experiments

A three-dimensional plot of one of our earliest scattering measurements, Figure 7-11, shows the scattering intensity (with the initial scattering of the substrate subtracted out) as a function of time and scattering angle. The potential of the silver (111) working electrode (initially held at a potential of 0 mV) was increased at 15 mV/sec with respect to a Hg/HgO reference electrode up to a potential of 300 mV. After this potential was reached, the cell was put on open circuit. Each angular curve comprises a single angular scan (i.e., not an average of several scans). This early measurement was made without the placement of a neutral density filter in front of the near-angle optical fibers, the electrolyte was not microfiltered, and the instrumental calibration was not very good. Fluctuations in the intensity (seen in the near-angle scattering intensity), resulting from small insoluble particles in the electrolyte passing in front of the laser-beam, can

be seen in Figure 7-11. These particles could be seen moving in and out of the laser beam path. There is no change in scattering right up to a potential of 300 mV, whereupon an increase in scattering is observed.† The scattering was measured for another 325 seconds after the potential control was released. With the exception of the scattering spike in the middle of the figure (this spike is believed to be due to insoluble particles in the electrolyte), the intensity and shape of the scattering curves do not change significantly with time after potential control is released. Since our previous ellipsometric experiments [G27-G29] had indicated that nucleation of three-dimensional silver oxide crystals begin near a potential of 300 mV vs Hg/HgO, this experiment verifies that finding. In our earlier study we found that the potential of nucleation can vary by more than 20 mV, depending on the method of oxidation and preparation of the surface.

Figure 7-12 shows the relative change in intensity with respect to the maximum intensity at different angles for the experiment discussed above. The change in (relative) scattering intensity is greatest at larger scattering angles. The actual change in intensity of scattering at 9° from the surface normal (approximately 200 arbitrary units) is only about 8% of the scattering from the initial surface (approximately 2540 units). This should be compared with the change in scattering intensity at 59° (34 units). However, the background scattering from the initial substrate is also much less at 59° (also 34 units). The signal noise (equal to the square root of the background) can be calculated for

† We now believe that these particles are primarily potassium carbonate which is formed from carbon dioxide dissolved in water prior to the addition of KOH.

both of these cases, and the signal-to-noise ratio for both the near- and far-angle measurements are comparable (equal to about 5). This calculation does not include contributions to the "noise" associated with the insoluble particles.

7.5.2 Calculations of the RMS Roughness

Vector scattering theory has been shown to be inadequate to quantitatively predict the spectral-power-density function (and therefore the autocorrelation function) of a surface [G9]. Also, our scattering data do not show a great deal of correlated scattering (i.e., peaks). We have therefore primarily calculated RMS roughness from our scattering data. This calculation has been shown to be quite accurate. In this dissertation, the RMS surface roughness is derived from the scattering measurements as follows:

1) The SPDF is calculated using vector scattering theory (equation 7.41).

2) The SPDF is integrated over all collection angles. This quantity is proportional to the square of the RMS roughness. Optical properties of Ag_2O derived from ellipsometry measurements are used in equation 7.41 (see Chapter 8).

3) The square root of the integral of the SPDF is calculated.

4) The assumption is made that the initial RMS roughness of the surface is about 100 Å. Then, all subsequent changes in roughness are measured with respect to the initial surface roughness.

The assumption that the initial surface roughness is about 100 Å is based on RMS roughness measurements of similarly prepared surfaces using STM. Figure 7-13A is a plot of RMS roughness as a function of time derived from the measurements shown in Figure 7-11. It shows an increase in roughness as the potential reaches 300 mV (20 seconds), and continues to increase slightly after potential control is released. An estimated total increase in roughness of 20 Å is calculated. Later, the roughness of the surface does not change with time. Because of the problems inherent in using vector scattering theory, along with the fact that we are not making absolute intensity measurements (thereby making it necessary to estimate the initial surface roughness), we feel that these interpretations should be considered to be semiquantitative. However, this experiment demonstrates the inherent sensitivity of the instrument.

7.5.3 Calculation of the Near-to-Far Angle SPDF Ratio

In Figure 7-13B, the ratio of the integral of the spectral power density function over near angles to that over large scattering angles is shown for the same data shown in Figure 7-11. The integral is split at the middle of our wavevector specular range (5.377 μm^{-1}, or about 33°). Large values of this parameter (i.e., significantly greater than 1) indicate preferential scattering into small wavevector space (near angles). Small values of this parameter (close to 1) indicate approximately $\cos^2\theta$ scattering (as would be expected for scattering from features much smaller than the wavelength of light). Figure 7-14 is a plot of the scattering from the initial substrate (i.e., absolute scattering without any background removed).

The largest fraction of the light is scattered in the first 15° from the surface normal. The initial near-to-far-angle spectral-power density-function ratio (NFSPDF) is greater than one (about 2.7). This large value indicates preferential scattering into near angles and is associated with a long-range surface waviness introduce by the polishing procedure. Some of this "scattering" may not be scattering at all but rather geometrical reflections from a wavy surface whose period is greater than the wavelength of light. As the potential reaches 300 mV (20 seconds), Figure 7-13B shows that the NFSPDF ratio decreases rapidly, indicating the formation of small surface features. The NFSPDF value appears to increase rapidly (within one scan) to a slightly larger value but does not change thereafter.

Another potential-sweep experiment is shown in Figure 7-15. Starting at 200 mV vs Hg/HgO, the potential was increased at only 0.5 mV/sec until a value of 300 mV was reached, whereupon potential control was released. The scattering data were averaged over 10 scans (8.33 sec/curve). As with the data in Figures 7-11 through 7-13, these data were taken without removing insoluble particles from the electrolyte and without the use of the neutral density filter in front of the near-angle optical fibers. Figure 7-15A is a three-dimensional plot of the change in scattering during the anodic potential-sweep portion of the experiment. Noise in the near-angle scattering intensity can be seen as particles move into the region of laser illumination. Up to a potential of about 275 mV (140 seconds), no change in scattering is observed. Beyond this potential, scattering increases, uniformly at first, but later showing two peaks, at 20° and 45°. Near the end of the

anodization process, the rate of increase of scattering intensity diminishes. Figure 7-15B shows the scattering measurement under open circuit conditions. The time/potential axis is inverted from that of Figure 7-15A to improve its readability. Soon after the potential control was released, the general scattering level decreased three fold, reaching an unchanging value (with time) within 20 seconds. The peaks in the scattering curves disappear.

The calculated RMS roughness and NFSPDF plots for this potential-sweep measurement are shown in Figure 7-16. The surface begins to roughen at a potential of 275 mV (140 seconds) and reaches an estimated RMS roughness of 250 Å before the cell is set to open circuit. The initial rate of increase in roughness is about 4 Å/sec, but the rate begins to diminish later (at higher potentials). When potential control is released, the RMS roughness continues to increase for a short time, but then (within 16 seconds) decreases to a constant value of 150 Å. The NFSPDF plot (Figure 7-16B) starts at a value significantly greater than 1 (again associated with long-range waviness of the surface due to polishing). Beginning near a potential of 265 mV, the NFSPDF parameter decreases to approximately 1. When potential control is released, the NFSPDF parameter increases to about 1.4 and remains approximately constant beyond this point. Qualitatively, the results from the potential-sweep measurement show that:

1) The potential of three-dimensional nucleation of Ag_2O depends slightly on sweep rate. Nucleation occurs at around 280 mV for an 0.5 mV/sec sweep rate, and at approximately 300 mV at 15 mV/sec.

2) Ag_2O nuclei are formed as very small crystals, which grow later.

3) After the cell is set to open circuit, there is a significant change in the surface scattering, indicating a rearrangement and/or dissolution of oxide material.

7.5.4 Potential-Step Measurements

Figure 7-17 is a three-dimensional plot of the change in scattering after a step change in potential from -100 mV to 290 mV vs Hg/HgO at time zero. The latter value was chosen because our previous ellipsometric results [G27-G29] indicated that three-dimensional nucleation would occur at 290 mV in a potential-step experiment. The potential was held at 290 mV for 60 seconds, after which the cell was set to open circuit. A peak at about 20° in the scattering curve appears after about 12 seconds of anodization, and the level of scattering generally increases for the first 16 seconds after the potential-step change. After this point the intensity decreases, rapidly at first, but later more slowly (16-60 seconds). Just before the release of the potential control, the scattering intensity is observed to start to increase again. When the control is released, the intensity increases, and a peak (again near 20°) is observed. Within a few seconds after going to open circuit, the scattering intensity becomes time-independent. Figure 7-18 shows the current transient data taken during this potential-step experiment. This current response, showing a local minimum (7 seconds) and maximum (13 seconds), is typical of Ag on which Ag_2O has undergone three-

dimensional nucleation (see Reference [G27]). The minimum and particularly the maximum occur at a much earlier time than that observed in one of our previous measurements at a similar potential. Also, the maximum is more shallow (see Figure C27 in reference [G27]). This finding would indicate that, in this experiment, the number density of nuclei initially formed was greater and/or the crystal growth rate was smaller than in our previous measurement (n.b. Reference [G27], pp. 148-154). Variations in anodization potential, surface preparation, and changes in potential due to variations in liquid junction potentials between the Ag/AgCl reference electrode and the working electrode used in the previous study could be the cause of this discrepancy.

Figure 7-19A is a plot of the calculated RMS roughness for the potential-step experiment shown in Figure 7-17. The RMS roughness initially increases to about 80 Å, reaches a local maximum after about 20 seconds, and then decreases to 25 Å until the potential control is released. After the potential control is released, the RMS roughness **increases** to about 180 Å. During a short transition time after the potential control is released (10 seconds), the RMS roughness increases to 180 Å.

In Figure 7-19B, the NFSPDF parameter is plotted with respect to time for the experiment discussed above. The NFSPDF value rapidly decreases from a relatively large value, reaching 0.95 within 10 seconds. After this point the parameter increases slightly (reaching 1.02), and then decreases slightly (down to 0.98). When potential control is released, the NFSPDF decreases to about 0.94. It is difficult to know whether these small changes are statistically significant,

and if so, how to interpret them. At this point we conclude that the value of the NFSPDF is approximately constant, with a value of around 0.97 for this experiment, consistent with the formation of very small surface crystals.

We performed a similar potential-step experiment (to 290 mV) in which the anodization was continued for a longer period of time (about 160 seconds, Figure 7-20). Here we observe that the scattering initially increases fairly uniformly but then reaches a local maximum. Beyond this point the scattering intensity decreases for a short time before increasing again. The light is progressively scattered into near angles as the anodization continues. The current measurement associated with these scattering measurements is shown in Figure 7-21. Again, as in Figure 7-18, the typical minimum and maximum in the current transient are evident, but they occur very early (<15 seconds). The current density is larger than that shown in Figure 7-18.

Calculated RMS roughness values are shown in Figure 7-22A. There is a local maximum in surface roughness after about 22.5 seconds, and a shallow minimum after 50 seconds of anodization. Later, the roughness appears to increase linearly with time. The NFSPDF ratio shown in Figure 7-22B initially decreases as the scattering from the initial waviness of the surface is overwhelmed by the scattering associated with the formation of a large number of small surface crystals. A minimum in the parameter is reached after 20 seconds, whereupon the NFSPDF starts to increase. The rate of increase is fast initially, then decreases, and later increases again. The local maximum in roughness shown in Figure 7-22A corresponds to a minimum in the NFSPDF ratio in Figure 7-22B.

The period of minimum rate of change of the NFSPDF corresponds to the minimum in the RMS roughness. The similarities in the results for the two potential-step experiments discussed above (Figures 7-19 and 7-22) are a good indication of the reproducibility for these measurements. Both experiments show the local maxima and minima in RMS roughness of similar magnitudes and at comparable times. The first experiment differs from the second only after the cell was set to open circuit.

7.5.5 Current-Step Measurements

Scattering data taken during the galvanostatic oxidation of silver at 50 $\mu A/cm^2$ are shown in Figure 7-23. The general characteristics of the data are similar to those discussed above. A local maximum and minimum in the surface roughness are evident. In this experiment, the shift of scattering toward near angles at later times does not occur as rapidly as in Figure 7-20, and may not occur at all. The RMS roughness (Figure 7-24A) does follow a similar trend as in Figure 7-22, but the maximum and minimum are less distinct. The NFSPDF ratio initially decreases but then changes little with time (Figure 7-24B). Our previous ellipsometric observation made during a 50 $\mu A/cm^2$ galvanostatic experiment showed an induction time of about 120 seconds prior to 3 dimensional nucleation of surface crystals. Prior to three-dimensional nucleation of oxide, a compact layer of oxide has been shown to form [G27]. In the scattering RMS measurement shown in Figure 7-24A, there is an induction time of only about 40 seconds before substantial increases in roughness are observed. The magnitude of

the change in surface roughness is quite small (on the order of 35 Å) and could be complicated by surface roughening due to local dissolution (etching) of the surface. However, if this were the case, no induction time would be expected at all. The derived optical properties of the initial thin film (primary layer) from ellipsometery are consistent with the formation of a thin oxide layer rather than a metal roughness layer (see Chapter 9 and references [G27-G28]). We therefore believe that the discrepancy in the time for nucleation may be due in part to experimental error.

We have attempted to curve-fit our observed scattering data of Figure 7-23 to a model of scattering from randomly positioned surface particles [equations 7-16 and 7-19, with S(Q) set to unity]. It is clear (Figure 7-25A) that good fits are obtained for the inital scattering data (prior to the local maximum in RMS roughness). However, later curve fits become progressively worse (Figure 7-25B). The structures of the later scattering curves are almost bimodal. It is possible that the effects of a distribution of particle sizes become significant (i.e., some large and some small crystals, with few of intermediate size), thereby giving rise to this bimodal phenomenon. The physical parameters derived from the measurements using this model are believed to be unrealistic (the particle sizes are too large). These results make it clear that interpretation of our data using an optical model to derive physical parameters of particle size (and spacing) is difficult. Because of this limitation, we have analyzed our data only in terms of the RMS roughness and the NFSPDF ratio parameters.

Section 7.6: Effects of Size and Number Density on RMS Roughness

How would changes in the size and number density of crystals affect the RMS roughness of a surface? The RMS roughness of a surface can be expressed as

$$[\mathrm{RMS}]^2 = \frac{1}{L}\int_0^L [z(x)-z_{avg}]^2 \ ,dx \qquad 7.45$$

where the average height is simply

$$z_{avg} = \frac{1}{L}\int_0^L z(x)dx \ . \qquad 7.46$$

In these expressions, L is an arbitrary (large) length over which height samples z(x) are taken. Let us make the assumption that all surface particles are of the same width and height (i.e., all particles are cubical). To accomplish this integration, we can rearrange the particles on the surface to form a contiguous film (Figure 7-26). This procedure will not alter our result but will make the mathematics easier. It is clear that z_{avg} is simply

$$z_{avg} = \frac{1}{L}\int_0^L z(x)dx = \int_0^\theta hdx = \theta h \ , \qquad 7.47$$

where θ is the fractional surface coverage and h is the height of the islands. The

surface coverage and average height can be expressed as

$$\theta = Nh^2 \ , \tag{7.48}$$

$$z_{avg} = \theta h = Nh^3 \ , \tag{7.49}$$

where N is the number density of cubical islands. If we use these expressions in equation 7.45 and rearrange the islands as shown in Figure 7-26, the RMS roughness can be expressed as

$$[RMS]^2 = \int_0^{\theta} (h-Nh^3)^2 dx + \int_{\theta}^{1} (Nh^3)^2 dx \ . \tag{7.50}$$

Integration yields

$$[RMS]^2 = \theta(h-Nh^3)^2 + (1-\theta)(Nh^3)^2 \ , \tag{7.51}$$

which can be rearranged to

$$[RMS] = \sqrt{Nh^4-N^2h^6} = h\sqrt{(\theta-\theta^2)} \ . \tag{7.52}$$

Since coverages greater than unity are physically impossible,

$$h_{max} = \sqrt{\frac{1}{N}} \ . \tag{7.53}$$

For a fixed particle size, the surface roughness is zero for both zero and full coverage and reaches a maximum at 50% coverage. For a fixed coverage, the roughness increases linearly with size (equation 7.52). The rates of change with

respect to coverage and particle size are given by

$$\frac{\partial[\mathrm{RMS}]}{\partial\theta} = \frac{\mathrm{h}(1-2\theta)}{2\sqrt{\theta-\theta^2}} \ , \qquad 7.54$$

$$\frac{\partial[\mathrm{RMS}]}{\partial\mathrm{h}} = \sqrt{\theta-\theta^2} \ . \qquad 7.55$$

From the last expressions it is clear that, for a fixed coverage, the RMS roughness always increases with increasing size. This is equivalent to saying fewer but larger particles covering the same fraction of surface will give a rougher topography. On the other hand, equation 7.54 shows that for coverages greater than 50%, the roughness will decrease with either increasing size or increasing coverage.

What effect would growth and/or redistribution of material have on the observed RMS roughness? A calculation of how the RMS roughness changes when we redistribute a fixed amount of material on the surface is instructive in addressing this question. A schematic of such a process is shown in Figure 7-27A. Conservation of matter yields the restriction that

$$\mathrm{N}_1\mathrm{h}_1^3 = \mathrm{N}_2\mathrm{h}_2^3 \ , \qquad 7.56$$

which is equivalent to saying that z_{avg} is unchanged (n.b. equation 7.49). By using equation 7.48 for θ, equation 7.56 can be rewritten as

$$\theta_1\mathrm{h}_1 = \theta_2\mathrm{h}_2 = \beta \ , \qquad 7.57$$

where β is a constant equivalent film thickness. By using the restriction of

Equation 7.57 in equation 7.52, equation 7.52 can be written as

$$[\mathrm{RMS}] = \sqrt{\mathrm{h}\beta - \beta^2} \qquad 7.58$$

for a fixed equivalent film thickness.

Figure 7-28 is a plot of RMS roughness for a number of equivalent film thicknesses as a function of particle size, as predicted by equation 7.58. This equation shows that, by redistributing a fixed amount of surface material into larger particles, the RMS roughness increases. Therefore, a ripening phenomenon at open circuit (a condition of fixed surface material) would tend to increase the surface roughness. However, the roughness of the surface can decrease as the amount of surface material is increased. Figure 7-29 shows the calculated RMS roughness versus size for a fixed particle number density (the process is shown schematically in Figure 7-27B). A maximum in the roughness occurs at 50% coverage, and roughness decreases at larger coverages. These results demonstrate that increases in size at fixed number density as well as decrease in number density at fixed size can yield a decrease in surface roughness.

For comparative purposes, a calculation of the RMS roughness changes during the anodic oxidation of silver from our previous ellipsometry data (i.e., Figures D38 and D39 from Reference [G27]) is shown in Figure 7-30. The figure shows the "elbow" in the RMS roughness versus time results characteristic of a number of the scattering experiments described above. The second increase in roughness occurs at the end of the crystal-ripening process (where the decrease in number density stops and the crystals grow).

Section 7.7: Anodic Oxidation of Copper

Scattering measurements were made during anodic potential-sweep and potential-step experiments with copper. These measurements were taken to aid in the examination of the structure of the cuprous and cupric oxide/hydroxide surface species and to aid in the interpretation of other optical measurements (ellipsometery, Raman spectroscopy).

7.7.1 Potential-Sweep Measurements

A plot of current versus potential taken during a 0.5 mV/sec potential-sweep experiment beginning at -500 mV and ending at -360 mV is shown in Figure 7-31. As can be seen, the experiment was ended when the current had reached a maximum (the A1 peak). The negative (cathodic) current at potentials below -440 mV is associated with the reduction of residual oxygen.

The change in surface scattering during a potential-sweep experiment up to a potential of -360 mV is negligible. The calculated RMS roughness during the potential sweep described above is shown in Figure 7-32A. The roughness does not change with time (it may actually decrease slightly). Figure 7-32B shows the NFSPDF ratio for this potential-sweep experiment. This parameter decreases slightly, and inspection of the data showsthat the near-angle scattering actually decreases from the initial scattering level, whereas the far-angle scattering increases slightly. This phenomenon may be due to preferential dissolution of metal at the large-spatial-period waviness generated by the polishing process.

If one increases the potential beyond the first anodic peak, the current decreases by a factor of about 3, and remains relatively constant up to a potential of 200 mV (see Figure 7-33). Beyond this potential, the current increases five fold over a range of 50 mV. This current increase is associated with the rising portion of the A2 current peak.

Figure 7-34 is a three-dimensional plot of scattering intensity versus time and scattering angle for the experiment whose current transient is shown in Figure 7-33. Each curve is an average of 15 individual angular scans. The calculated RMS roughness and NFSPDF curves are shown in Figure 7-35. Roughening of the surface occurs at -375 mV, which coincides with the maximum current of the A1 wave in this experiment. Beyond the current-peak maximum, the roughness of the surface has doubled with respect to the polished substrate. Beyond a potential of 200 mV, the scattering and RMS roughness increase rapidly. The initial roughening of the surface occurs after a small amount of anodic current has been passed (i.e., anodic current begins at -475 mV, whereas surface roughening begins at -375 mV). This finding is consistent with the results shown in Figures 7-31 and 7-32, though the point of initial increase in roughening is slightly different. The surface begins to roughen at -375 mV in Figure 7-31, but hasn't begun to roughen until to a potential of -360 mV is reached (Figure 7-35). This descrepancy may be due to slight differences in surface preparation and reference potentials.

It is suggested here (and substantiated later) that cuprous oxide film growth begins at a potential below the first anodic current-peak maximum and

coincident with the onset of current. Our ellipsometry data have shown that the efficiency for film growth is low. As noted in Chapter 1, the formation of a monovalent copper species can occur at potentials near (and below) the A1 peak maximum. Ring/disk measurements made by Miller [G30] have shown the presence of the soluble cuprous ion in solution. This ion must leave the surface and become hydrated before it can enter the solution. How is the dissolved ion formed? Here I suggest two possible models.

1) As the potential increases, a positive charge is distributed uniformly near the surface. The positively charged surface will attract negatively charged hydroxide ions from the solution, which can become physically and chemically bonded to the surface, resulting in the formation of either a film of Cu_2O or a soluble cuprous species. Solid state film nucleation would begin in many different locations, yielding a polycrystalline oxide film from a single-crystal metal (cf. Raman and x-ray data in this dissertation).

2) A positively charged ion is formed at the surface for each electron that leaves the surface. These cations are formed preferentially from kink and end-plane atoms, and are first ejected from their lattice position to form a cation free to move in two-dimensions along the surface. The removal of the cation from the surface (i.e., its desorption) requires some energy (it is still weakly bonded to the surface). Whereas there is a driving force (coulombic repulsion) for the cation to leave the surface, the surface

charge can also be balanced by the arrival of an adsorbed hydroxide ion. If the desorption step for the cation is slow, the adsorbed species will have time to diffuse along the surface and react with adsorbed hydroxide. Two absorbed Cu(OH) species could then combine to form Cu_2O and water, and film growth would proceed via a two-dimensional reaction mechanism.

A cuprous oxide film formed by either of the above mechanisms would be expected to have the following characteristics: (1) current efficiencies for film growth would be significantly less than 100%, and (2) the film would be polycrystalline, even when the substrate is a single crystal. These mechanisms are favored over the classical solid-state film-growth mechanism because a significant fraction of the oxide does dissolved into the electrolyte (cf. Chapter 8) and our x-ray data show the film to be polycrystalline (cf. Chapter 10). However, at present it is difficult to know which of these mechanisms (or any other mechanism consistent with the data) is best. At sufficently anodic potentials, the formation of the divalent cuprite ion from cuprous oxide will become thermodynamically possible (see equations 1.8 and 1.9). This reaction should begin to occur at a potential near the A1 peak potential. If the film is polycrystalline, the reaction would occur preferentially at grain boundaries. We believe that the initial increase in surface roughness shown in Figure 7-35A is associated with the preferential electrochemical oxidation of the cuprous oxide film to form the soluble cuprite ion (equations 1.8 and 1.9) at grain boundaries. Further increase in potential eventually results in the precipitation of the cuprite ion from solution to form $Cu(OH)_2$

(near -150 mV), resulting in a large increase in scattering.

The NFSPDF ratio for the scattering data of Figures 7-33 and 7-34 are plotted in Figure 7-35B. The initial large NFSPDF ratio decreases, beginning at a potential of -400 mV. The parameter quickly reaches a value near unity and continues to decrease slowly. This finding is consistent with the very local etching of the cuprous oxide film at grain boundaries. The size of the boundaries must be much less than the wavelength of light, since the scattering follows an approximately $\cos^2\theta$ dependence. Even after the nucleation of the $Cu(OH)_2$ film at a potential of near 200 mV, the NFSPDF ratio does not changes significantly. This latter finding is consistent with the formation of very small $Cu(OH)_2$ particles. SEM photographs (Chapter 10) show that the $Cu(OH)_2$ film is composed of needle-like crystals of very small diameter (600 Å). These particles form a porous, matted surface structure. The structure of this film indicates that it is formed by a dissolution/precipitation mechanism.

7.7.2 Potential-Step Measurements

The change in scattering following a step change in potential from -600 mV to -300 mV is shown in Figure 7-36. This anodic potential value was chosen because it lies between the A1 and A2 current-peak maxima. Initially, the scattering intensity increases rapidly. Later, the rate of increase of scattering decreases significantly. As with the potential-sweep experiment of copper, the angular distribution of scattering shows little structure. The associated current for this experiment initally rises rapidly, then decreases. It is not altogether clear

why the current rises over a relatively long time (3-4 seconds). We know that reduction of residual oxygen is occurring prior to the potential step. This reaction may continue (at a smaller rate) after the application of the anodic potential step. However, the initial current density for the oxygen reduction (at -600 mV) is smaller than the copper oxidation current and therefore should not be a factor. The current transient may indicate the necessity for generating an intermediate before the reaction can proceed (i.e., a consecutive elementary reaction whose intermediate step is higher than first order in surface concentration).

The calculated RMS roughness and NFSPDF ratio for the potential-step change shown in Figure 7-36 are shown in Figures 7-37A and 7-37B. The surface roughness increases rapidly but later reaches a plateau. The total roughness increase with respect to the initial surface roughness is only about 25%. This level of roughness is significantly smaller than that which develops during a potential sweep to the same potential (cf. Figure 7-35A). The NFSPDF ratio undergoes the typical initial decrease and rapidly reaches a value near unity. The roughness becomes invariant after 30-40 seconds. Again, a value of unity for the NFSPDF ratio indicates the formation of very small surface features (much smaller than the wavelength of light). We note here the constrast between the transient current data (where anodic current continues at a reasonable rate) and the surface roughness (which does not change signifantly at later times). The transient current does not decay as rapidly as is typical for a dissolution process (e.g., as given by the Cottrell equation, which predicts a parabolic decrease in current with time) and appears to approach a steady-state value. The roughness

of the surface reaches a constant value although the current continues to flow. Therefore, we must assume that the surface topography of the film formed by a potential step is more stable than that formed via a potential sweep. Ellipsometry results (see Chapter 9) show that at lower overpotentials, cuprous oxide film growth is generally homogeneous under potential-step conditions and follows a parabolic growth law (with time). The growth rate of new film may compensate for the dissolution rate of the film, thereby achieving a steady state between a leveling and a roughening mechanism.

Section 7.8: Conclusions

Optical theory from the literature (along with some new developments) has been presented to aid in the interpretation of elastic light-scattering measurements. Scattering from a random array of particles is expected to show large variations in intensity with angle, thereby exhibiting a finely mottled appearance. Semiordered arrays of particles can exhibit detailed structure in the scattering pattern, as revealed by the interference function (equation 7.19). Vector scattering theory (equation 7.47.36) allows one to derive the spectral-power-density function from the angular scattering data. The Fourier transform of the spectral-power density is the autocorrelation function. In the absence of any clear structure (i.e., peaks) in the scattering data, it is unclear as to what would be accomplished by performing such a transformation. While one should be able in principle to derive some parameters associated with assumed trial functions, this is difficult to do in practice. Errors introduced by transform inversions

(aliasing, associated with a finite wavenumber data set) are not small. Also, theoretical predictions do not always match observed scattering results. However, RMS roughnesses derived from vector scattering theory are in excellent agreement with RMS roughness measurements from a stylus (see [G9]). Therefore, we have presented our data in terms of RMS roughness and the near-to-far spectral-power density-function parameter (NFSPDF). This latter parameter measures the deviation from ideal $\cos^2\theta$ scattering, as predicted for the scattering from small particles. The parameter gives a qualitative measure of particle size.

We have built an angular-resolving scattering instrument consisting of a He-Ne laser, PTFE electrochemical cell, 80 light-collecting optical fibers, and apparatus to selectively sample the intensity as a function of angle at a PMT. Computer-data acquisition software and procedures used in the acquisition of data, instrumental calibration, and data-intensity conversion are discussed.

Scattering measurements made during the anodic oxidation of silver show that the onset of three-dimensional crystal nucleation is easily observed. Changes in RMS roughness as small as 20 Å have been observed. However, it is important that small insoluble particles contained even in analytical KOH be removed from the electrolyte by microfilters to obtain the greatest instrumental sensitivity.

During the earliest stages of anodic oxidation of silver, the surface forms a compact film [G27,G28]. Some preferential corrosion (etching) of either the film or the metal may occur (as indicated by Figures 7-13A and 7-13B). The increase in roughness associated with the nucleation process is accompanied by the decrease in the NFSPDF, indicating that light is predominantly scattered by very

small particles. In agreement with earlier ellipsometry measurements, an induction time (of scattering) for the formation of the primary layer prior to nucleation has been observed (e.g., Figure 7-24), but most of our experiments were performed at rates where this process is not visible.

The effects of changes in number density and particle size on the observed RMS values have been presented. The redistribution of material during an Ostwald ripening phase has been shown to occur as the RMS roughness goes though a maximum and minimum as a function of time. Later particle growth is indicated by an increase in the NFSPDF ratio.

The oxidation of copper also begins as a compact film. However, this film does not undergo three-dimensional nucleation. Rather, the cuprous oxide is further oxidized to form a cuprite ion preferentially at grain boundaries. If the potential is maintained at a fixed value, this roughening mechanism is offset by a leveling mechanism associated with the formation of new film. However, at sufficently high anodic potentials, the solution becomes supersaturated in cuprite ion near the interface, and $Cu(OH)_2$ precipitates as a porous film.

REFERENCES FOR CHAPTER 7

G1) Davies, H., Proc. IEEE. **101,** 209 (1954).

G2) Bennett, H. E., and J. O. Porteus, J. Opt. Soc. Am. **51,** 123 (1961).

G3) Bennett, H. E., J. Opt. Soc. Am. **53,** 1389 (1963).

G4) P. Beckmann and A. Spizzichino, **The Scattering of Electromagnetic Waves from Rough Surfaces**, Pergamon, Oxford, 1963.

G5) Depew, C. A., and R. D. Weir, Appl. Opt. **10,** 969 (1971).

G6) Marvin, A., F. Toigo, and V. Celli, Phys. Rev. B. **11,** 2777 (1975).

G7) Elson, J. M., and R. H. Ritchie, Phys. Status Solidi B **62,** 461 (1974).

G8) Elson, J. M., Phys. Rev. B **12,** 2541 (1975).

G9) Elson, J. M., and J. M. Bennett, J. Opt. Soc. Am. **69,** 31 (1979).

G10) Rasigni, G., F. Varnier, M. Rasigni, and J. P. Palmari, J. Opt. Soc. Am **73,** 1235 (1983).

G11) Wang, Y., and W. L. Wolfe, J. Opt. Soc. Am. **73,** 1596 (1983).

G12) Roche, P., and E. Pelletier, Appl. Opt. **23,** 3561 (1984).

G13) Guenther, K. H., P. G. Wierer, and J. M. Bennett, Appl. Opt. **23,** 3820

(1984).

G14) Bennett, J. M., Thin Solid Films **123,** 27 (1985).

G15) Bennett, J. M., H. H. Hurt, J. P. Rahn, J. M. Elson, K. H. Guenther, M. Rasigni, and F. Varnier, Appl. Opt. **24,** 2701 (1985).

G16) Born, M., and E. Wolf, **Principles of Optics**, Pergamon, New York, 1964.

G17) Jenkins, F. A., and H. E. White, **Fundamentals of Optics**, McGraw-Hill, New York, 1957.

G18) Hecht, E., and A. Zajac, **Optics**, Addison-Wesley, Menlo Park, Ca. 4th edition, 1979.

G19) Jackson, J. D., **Classical Electrodynamics**, 2nd edition, Wiley, New York, 1975.

G20) Stone, J. M., **Radiation and Optics**, McGraw-Hill, San Francisco, 1963.

G21) Hukins, D. W., **X-ray Diffraction by Disordered and Ordered Systems**, Pergamon, New York, 1981.

G22) Reitz, J. R., F. J. Milford, and R. W. Christy, **Foundations of Electromagnetic Theory**, 3rd edition, Addison Wesley, Menlo Park, CA, 1980.

G23) Hildebrand, Francis B., **Advanced Calculus for Applications**, 2nd edition, Prentice-Hall, Englewood Cliffs, NJ, 1976.

G24) Mayer, S. T., R. H. Muller, and P. N. Ross, ***In Situ* Scanning Tunneling Microscopy of Multilayer Pb Electrodeposits on Ag**, Lawerence Berkeley Laboratory Report LBL-26454, December 1988.

G25) Young, R. D., and E. C. Teague, "The Measurement and Characterization of Surface Finish", in **Properties of Electrodeposits: Their Measurement and Significance**, R. Sard, H. Leidheiser and F. Ogburn, Editors, The Electrochemical Society Inc., Princeton NJ, 1975.

G26) Mayer, S. T., and R. H. Muller, to be published.

G27) Mayer, S. T., **An Ellipsometric Spectroscopy Study of Anodically Formed Silver (I) Oxide on Silver**, M. S. Thesis, University of California at Berkeley, December 1985. Lawerence Berkeley Laboratory Report LBL-15607.

G28) Mayer, S. T., and R. H. Muller, J. Electrochem. Soc. **135,** 2133 (1988).

G29) Mayer, S. T., and R. H. Muller, **Nucleation of Silver (I) Oxide Investigated by Spectroscopic Ellipsometry**, Lawerence Berkeley Laboratory Report LBL-23844 Rev. March 1988.

G30) Miller, B., J. Electrochem. Soc. **116,** 1675 (1969).

FIGURE CAPTIONS FOR CHAPTER 7

Figure 7-1. Coordinate system used for the development of scattering theory of random particles (equations 7.1 through 7.7). Points of origin of scattering (O and Q) located in a plane on the left at (x_j, y_j). Arbitrary point of observation P located in plane on the right at (X,Y). Polar angles θ and ϕ correspond to angles from O to P in the X and Y directions respectively.

Figure 7-2. Schematic of a monochromatic beam of light incident on a particle defining incident $(\vec{k}_o)$ and scattered $(\vec{k})$ wavevectors, scattering angle ϕ, and intraparticle separation vector $\vec{r}_{ij}$.

Figure 7-3. Functions $\varsigma(x)$ and $[\varsigma(x)]^2$ (equation 7.17). In general, x is equal to the product of Q (equation 7.10) and a (the particle size).

Figure 7-4. A) Interference function S(Q) for hard-sphere excluded-volume model (equation 7-26) forcylindrical excluded volumes of 2500 Å (dashed line) and 5000 Å (solid line). Number density (N_o) set to $10^8/cm^2$. B) Product of the last two terms in equation 7-28. This plot shows the Q (equation 7-10) dependence of scattered light on some assumed parameters. Solid line: particle size a = 250 Å, excluded volume c = 500 Å. Dashed line: particle size a = 1000 Å, excluded volume c = 2000 Å. Number density $N_o = 10^8$ for both curves.

Figure 7-5. Schematic diagram of the angular-resolving elastic-scattering instrument. Top: cross section. Bottom: side view. 1) Electrochemical cell. 2) Glass and Plexiglas windows. 3) Optical-fiber housing assembly. 4) Optical fibers. 5) Constant-speed motor. 6) Digital encoder. 7) Optical-fiber selector. 8) Optical-fiber focusing assembly. 9) Photomultiplier tube.

Figure 7-6. Photograph of PTFE electrochemical cell for angular-resolving elastic-scattering instrument. Black interior is ethylene propylene rubber. Electrode can be seen in interior of cell.

Figure 7-7. Photograph of angular-resolving elastic-scattering instrument.

Figure 7-8. Relative transmission efficiency versus scattering angle of elastic-scattering instrument. First 25 fibers have a neutral density filter (ND 1.1) in front of them. Variations in transmission due to 1) different transmittance of fibers, 2) alignment of fibers (at cell and in selector chamber), and 3) location of fiber-channel terminations at the detector.

Figure 7-9. Angular dependence of scattering from a PTFE plug inserted in the back of the electrochemical cell. This plug was used as a secondary calibration standard.

Figure 7-10. Angular dependence of scattering from a PTFE plug inserted in the

back of the electrochemical cell at two different positions.

Figure 7-11. Background-subtracted scattering intensity versus time and scattering angle during a 15 mV/sec potential-sweep anodization of Ag(111) in 1M KOH from 0 to 300 mV vs Hg/HgO. After 20 seconds, the cell was set to open circuit. Each scan required 0.833 second to acquire.

Figure 7-12. Relative change in scattering intensity (with respect to the maximum of the particular channels for the experiment) versus time during the potential program experiment described in Figure 7-12. Background not subtracted (i.e., scattering from initial substrate included).

Figure 7-13. A) NFSPDF parameter versus time during a potential-sweep anodization of Ag(111) in 1M KOH from 0 to 300 mV vs Hg/HgO. After 20 seconds, the cell was set to open circuit. B) RMS roughness versus time during a 15 mV/sec potential sweep anodization of Ag(111) in 1M KOH from 0 to 300 mV vs Hg/HgO. After 20 seconds, the cell was set to open circuit.

Figure 7-14. Angle dependence of the scattering intensity from the Ag(111) substrate for the experiment described in Figure 7-11.

Figure 7-15. A) Background-subtracted scattering intensity versus time and scattering angle during a 0.5 mV/sec potential-sweep anodization of Ag(111) in 1M KOH from 200 to 300 mV vs Hg/HgO. B)

Background-subtracted scattering intensity versus time and scattering angle after potential control was released following the anodization described in A). Each scan required 8.33 seconds to acquire, and is an average of 10 individual scans.

Figure 7-16. A) RMS roughness versus time during a 0.5 mV/sec potential sweep anodization of Ag(111) in 1M KOH from 200 to 300 mV vs. Hg/HgO. After the potential reached 300 mV (200 seconds), the cell was set to open circuit (Figure 7-15). B) NFSPDF parameter versus time during a 0.5 mV/sec potential-sweep anodization of Ag(111) in 1M KOH from 200 to 300 mV vs Hg/HgO. After the potential reached 300 mV (200 seconds), the cell was set to open circuit.

Figure 7-17. Background-subtracted scattering intensity versus time and scattering angle after potential step from -100 to 290 mV vs Hg/HgO at time zero. After 60 seconds, the cell was set to open circuit. Each scan required 4.17 seconds to acquire and is an average of 5 individual scans.

Figure 7-18. Current transient for a Ag(111) electrode after a potential to 290 mV is applied at time zero (cf. Figure 7-17). Electrode area is 3.12 cm^2.

Figure 7-19. A) RMS roughness derived from scattering measurements as a function of time for a 290 mV potential-step experiment. B) NFSPDF

parameter as a function of time for a 290 mV potential step experiment. Cell set to open circuit after 60 seconds.

Figure 7-20. Background-subtracted scattering intensity versus time and scattering angle after potential step from -100 to 290 mV vs Hg/HgO at time zero. Potential held at 290 mV for 160 seconds. Each scan required 3.92 seconds to acquire and is an average of 4 individual scans.

Figure 7-21. Current transient for a Ag(111) electrode after a potential step from -100 mV to 290 mV at time zero. Electrode area is 3.24 cm^2.

Figure 7-22. A) RMS roughness derived from scattering measurements shown in Figure 7-19. B) NFSPDF parameter derived from measurements shown in Figure 7-19.

Figure 7-23. Background-subtracted scattering intensity versus time and scattering angle after a current step from 0 to 50 $\mu A/cm^2$ at time zero. Each scan required 5.8 seconds to acquire and is an average of 7 individual scans.

Figure 7-24. A) RMS roughness derived from scattering measurements shown in Figure 7-23. B) NFSPDF parameter derived from the measurements shown in Figure 7-23.

Figure 7-25. A) Experimental scattering data from galvanostatic anodization shown in Figure 7-31 and fits of matching theoretical random-particle

model curves (equations 7-16 and 7-19, with S(Q) set to unity). Δ: Experimental scattering data after 40.5 seconds of anodization. X: Matching theoretical model fit: particle size=1523 Å, relative-number density parameter=4.39. ● : Experimental scattering data after 81 seconds of anodization. ○ : Matching theoretical model fit: particle size = 2012 Å, relative number density parameter = 2.5. □- Experimental scattering data after 121 seconds of anodization. □- Matching theoretical model fit: particle size 2250 Å, relative number density parameter=2.12. B) □ : Experimental scattering data after 162 seconds of anodization. □ : Matching theoretical model fit: particle size 2123 Å, relative number density parameter=2.46. ● : Experimental scattering data after 202.5 seconds of anodization. ○ - Matching theoretical model fit: particle size 2253 Å, relative number density parameter=1.91. Δ: Experimental scattering data after 243 seconds of anodization. X: Matching theoretical model fit: particle size=2431 Å, relative number density parameter=1.41.

Figure 7-26. Artist's rendition of analogous mathematical process useful in performing the integration of equation 7-45 for the monodispersed cubical particle model.

Figure 7-27. A) Artist's rendition of the mathematical process of a surface roughened by the redistribution of material contained in a thin film. B) Artist's rendition of fixed number density cubical island film

growth.

Figure 7-28. Theoretical predictions of surface roughness versus particle size for the redistribution of fixed amounts of surface film material from a compact film to a monodispersed cubical island film (see equation 7.53). □ : 100 Å equivalent film thickness. □ : 125 Å equivalent film thickness. ●: 150 Å equivalent film thickness. ○ : 175Å equivalent film thickness. Δ: 200 Å equivalent film thickness.

Figure 7-29. RMS roughness versus particle size (axis is incorrect) for growth of a fixed number density of cubical islands (as depicted in Figure 7-27B). □ : Number density = $1x10^{10}$ cm^{-2}. □ : Number density = $5x10^{9}$ cm^{-2}. ●: Number density = $2.5x10^{9}$ cm^{-2}. ○ Number density = $1x10^{9}$ cm^{-2}.

Figure 7-30. RMS roughness during the potentiostatic oxidation of silver at 290 mV vs Hg/HgO calculated from ellipsometric data (Figures D38 and D39 from Reference [G27].

Figure 7-31. Current versus potential during a 0.5 mV/second potential sweep of Cu(111) in 1M KOH. Potential with respect to Hg/HgO in 1M KOH. Electrode area is 3.2 cm^2.

Figure 7-32. A) RMS roughness derived from scattering measurement taken during a 0.5 mV/sec potential sweep of Cu(111) in 1M KOH. B)

NFSPDF parameter derived from scattering measurements as in A).

Figure 7-33. 0.5 mV/sec potential sweep of Cu(111) in 1M KOH from -500 to -150 mV vs Hg/HgO in 1M KOH.

Figure 7-34. Background-subtracted scattering intensity versus time and scattering angle obtained during a 0.5 mV/sec potential-sweep experiment of Cu(111) in 1M KOH. Potentials with reference to the Hg/HgO in 1M KOH reference electrode. Each scan required approximately 25 seconds to acquire and is an average of 30 individual scans.

Figure 7-35. RMS roughness versus potential derived from the scattering data shown in Figure 7-34. B) NFSPDF parameter versus potential derived from the scattering data shown in Figure 7-34.

Figure 7-36. Background-subtracted scattering intensity versus time and scattering angle obtained during a potential-step experiment of Cu(111) in 1M KOH from -600 to -300 mV vs Hg/HgO in 1M KOH. Each scan required approximately 8.3 seconds to acquire and is an average of 10 individual scans.

Figure 7-37. A) RMS roughness versus time derived from the scattering data shown in Figure 7-36. B) NFSPDF parameter derived from the scattering data shown in Figure 7-36.

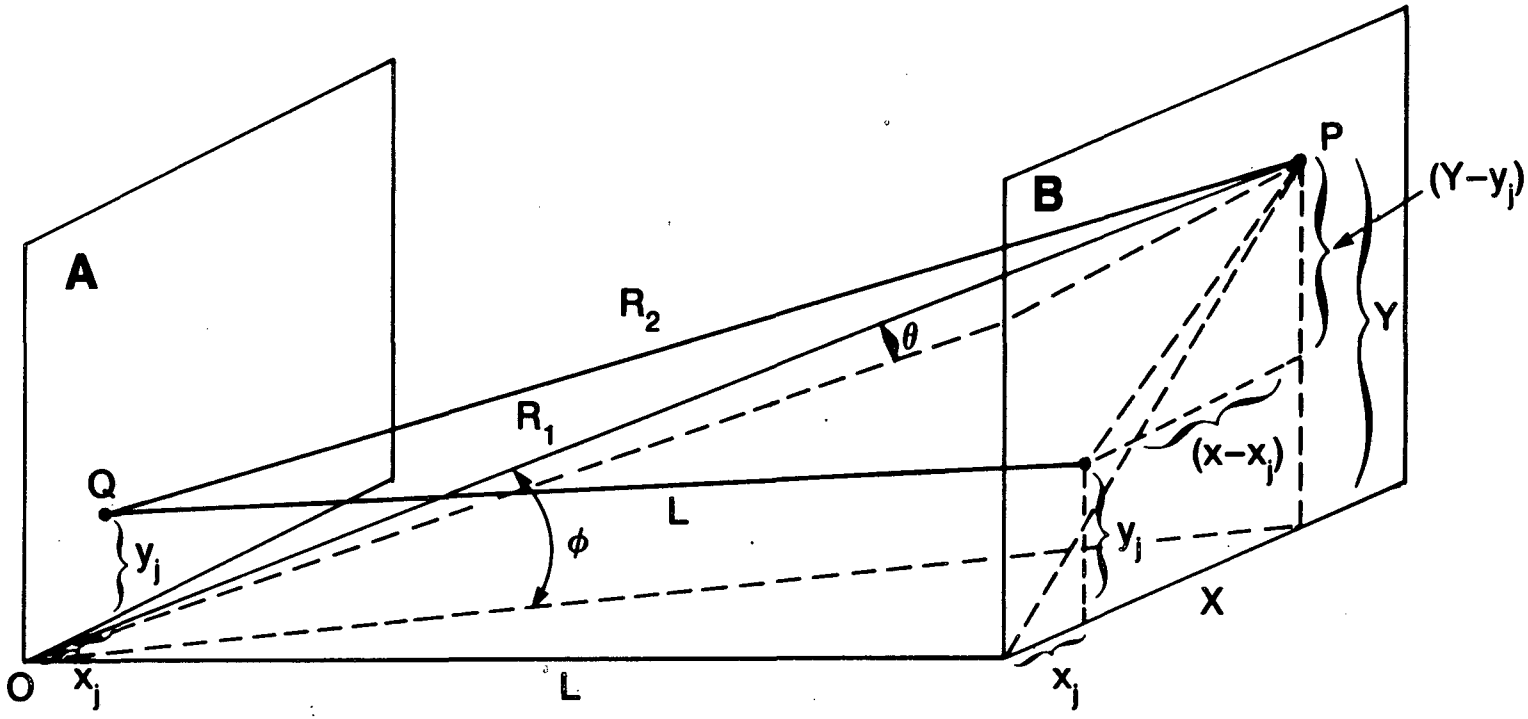

XBL 897-7208

Figure 7-1

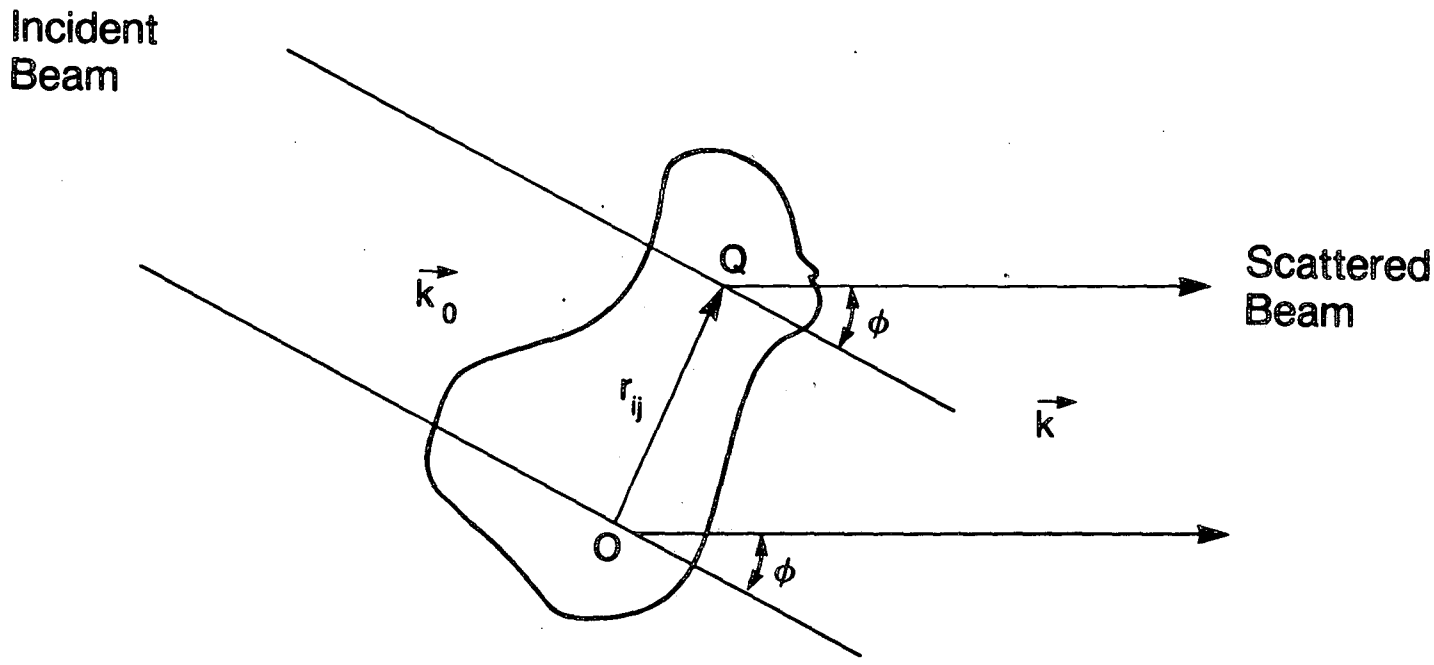

XBL 897-7207

Figure 7-2

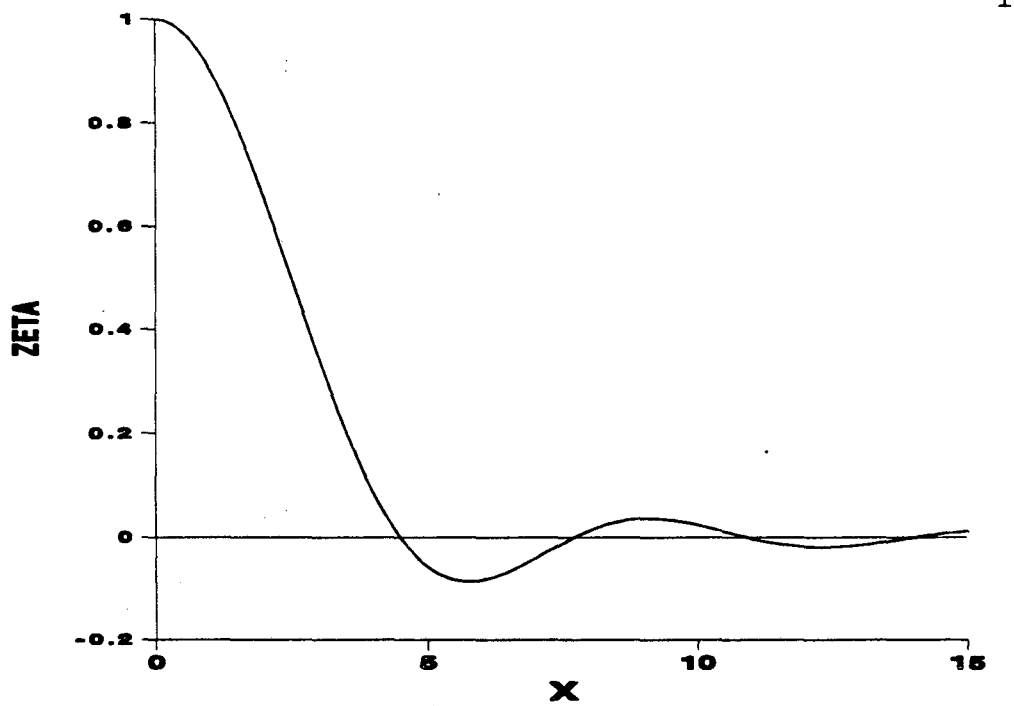

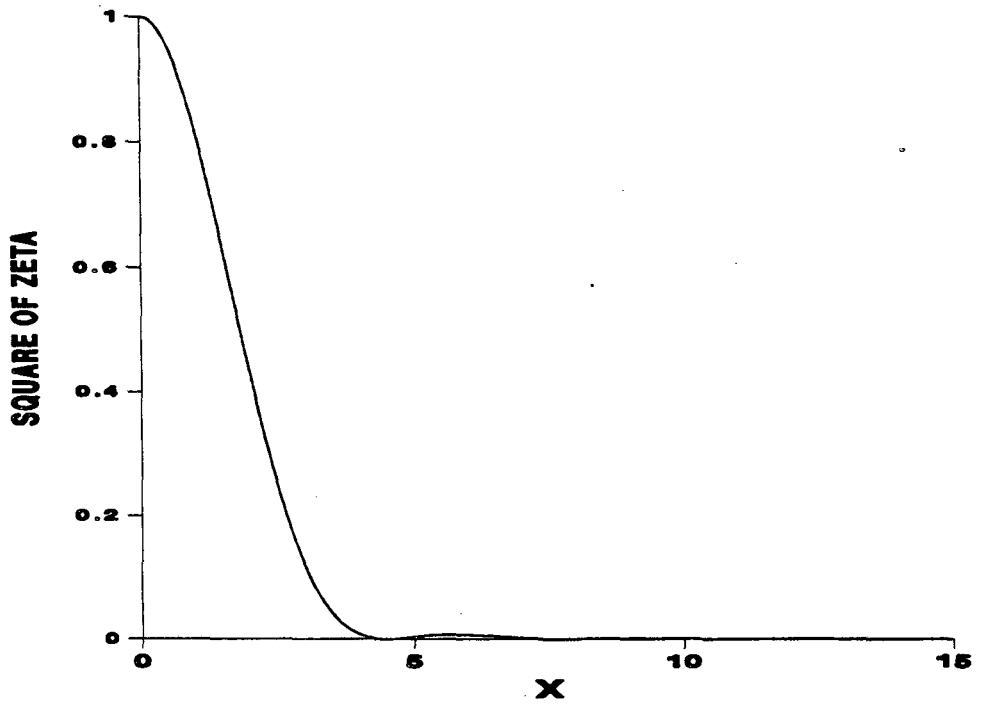

XBL 897-2661

Figure 7-3

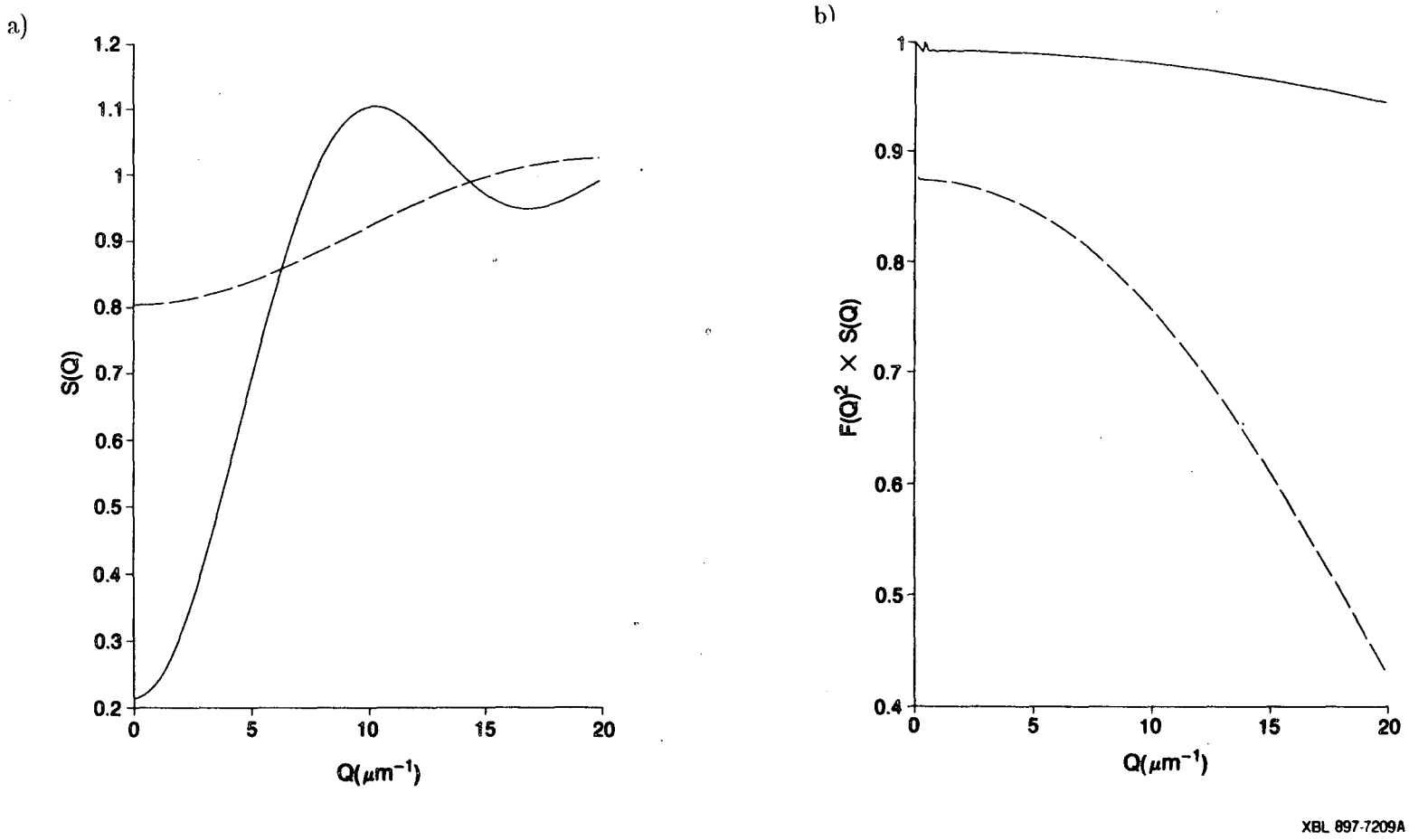
a)
S(Q)
1.2
1.1
1
0.9
0.8
0.7
0.6
0.5
0.4
0.3
0.2
0
5
10
15
20
Q(μm⁻¹)
b)
F(Q)² × S(Q)
1
0.9
0.8
0.7
0.6
0.5
0.4
0
5
10
15
20
Q(μm⁻¹)
XBL 897-7209A

Figure 7-4

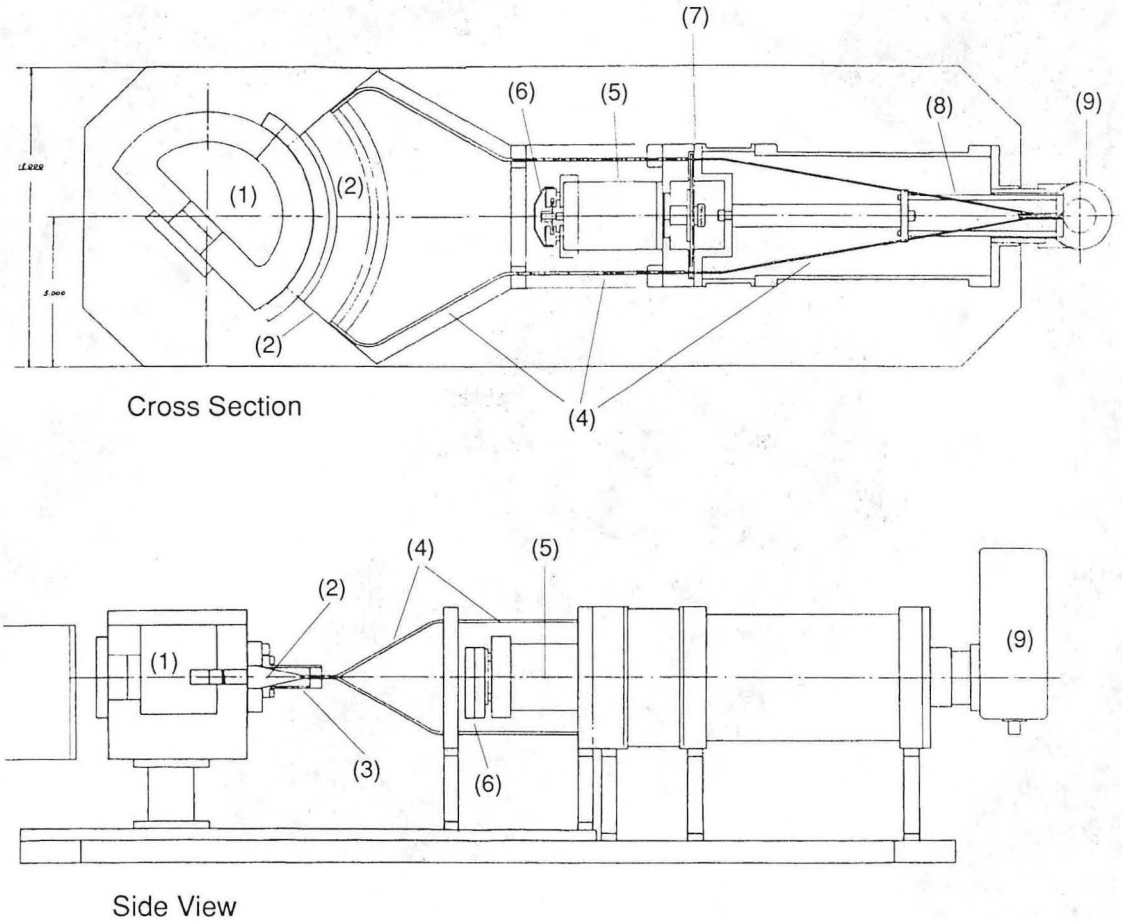

Figure 7-5

XBL 897-2858

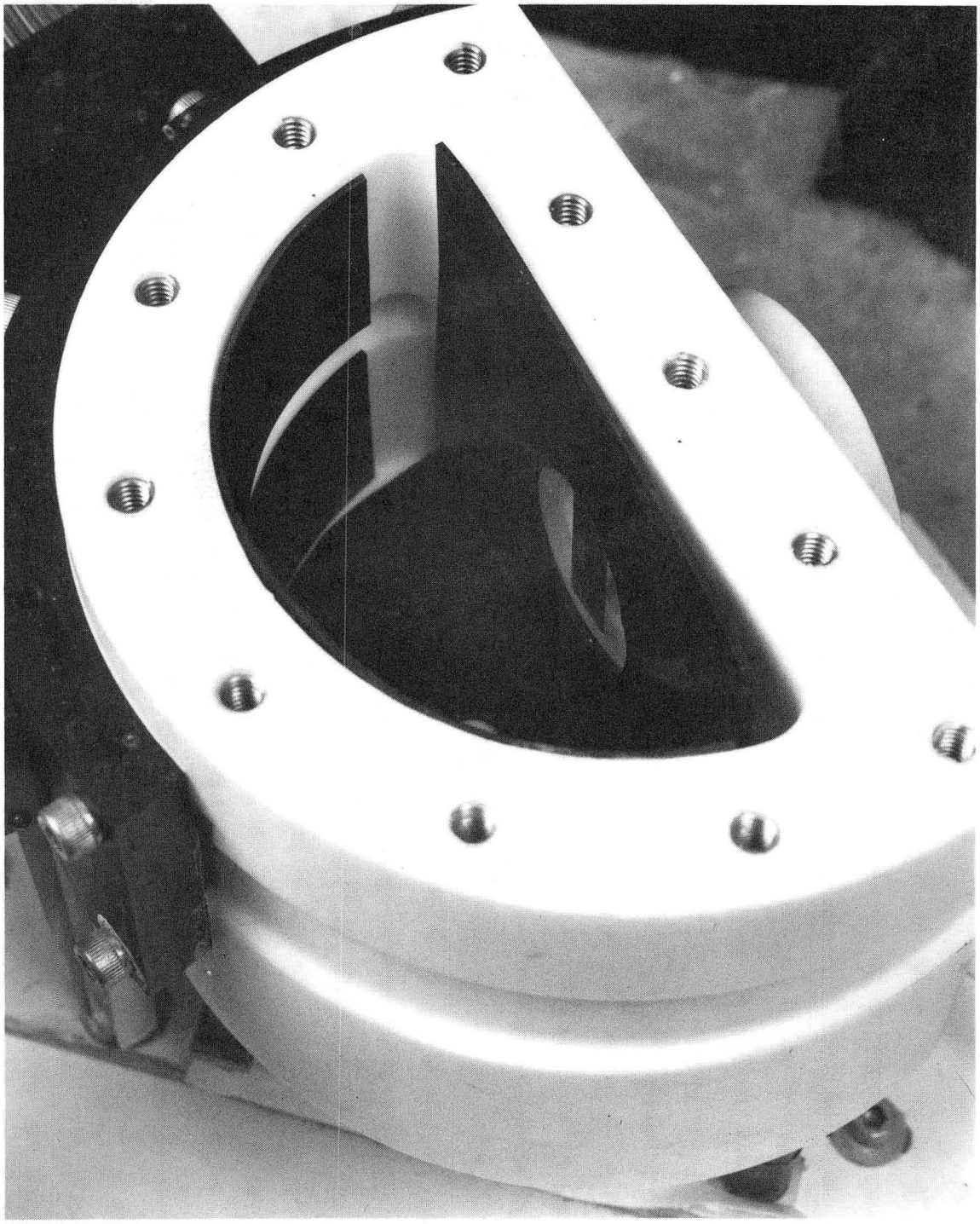

CBB 880-10621

Figure 7-6

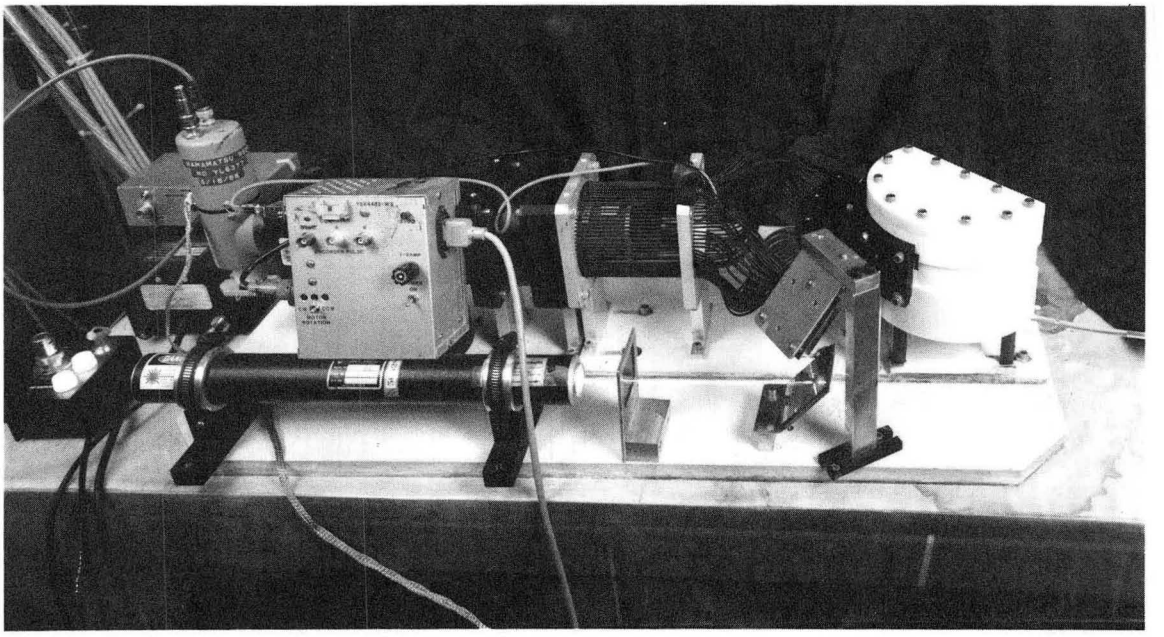

CBB 880-10615

Figure 7-7

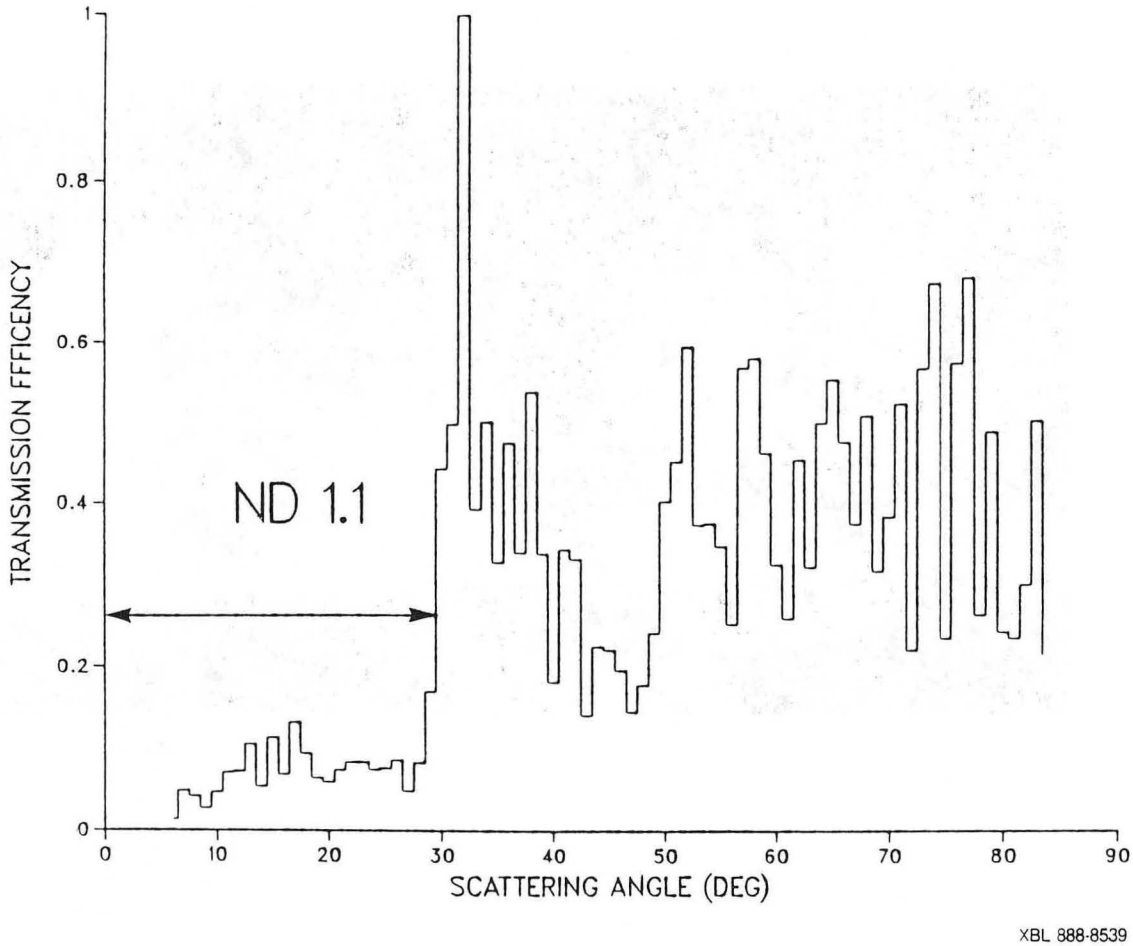
TRANSMISSION FFFICENCY
1
0.8
0.6
0.4
0.2
0
ND 1.1
0
10
20
30
40
50
60
70
80
90
SCATTERING ANGLE (DEG)
XBL 888-8539

Figure 7-8

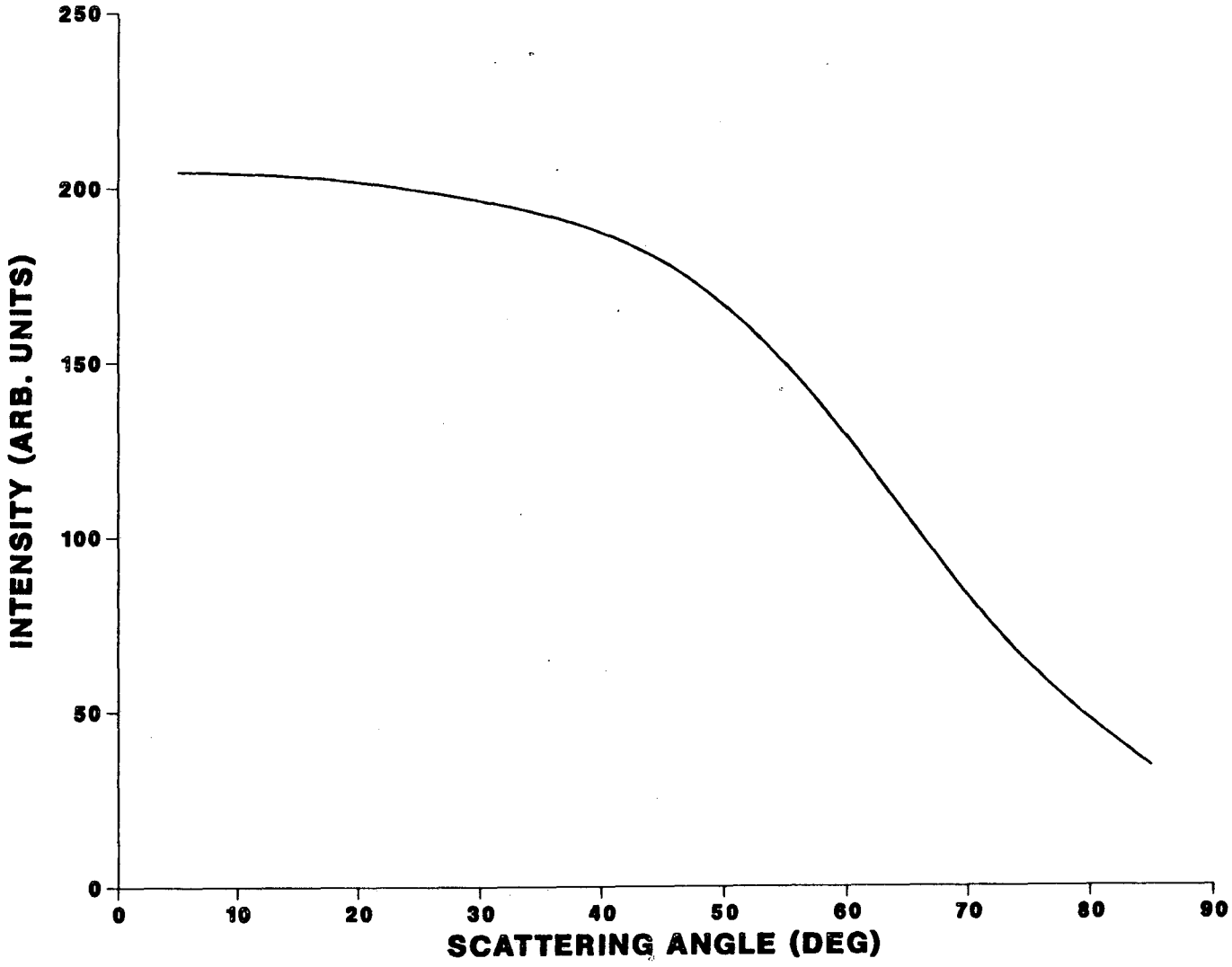

Figure 7-9

XBL 897-2662

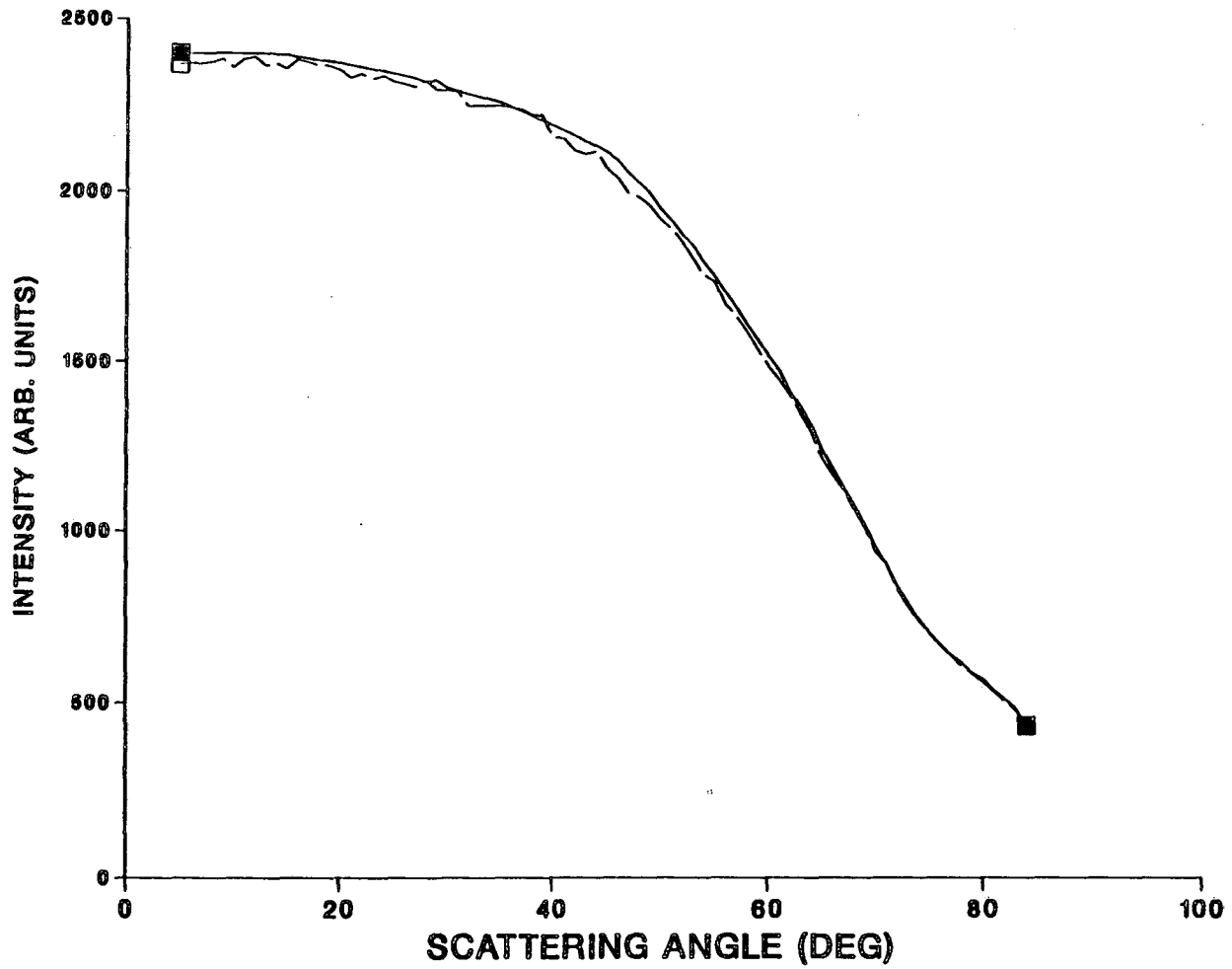

XBL 897-2667

Figure 7-10

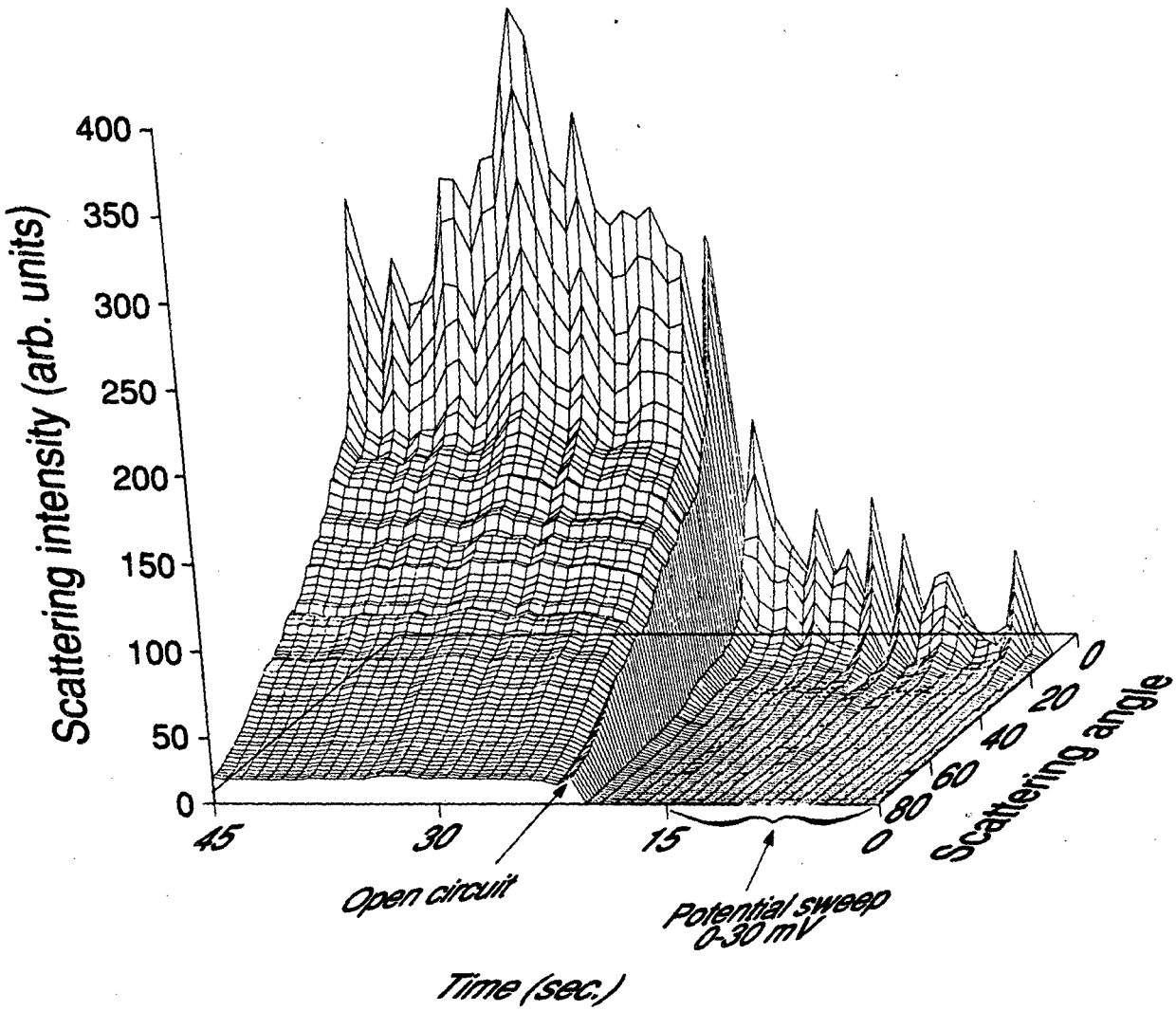

XBL 898-7225

Figure 7-11

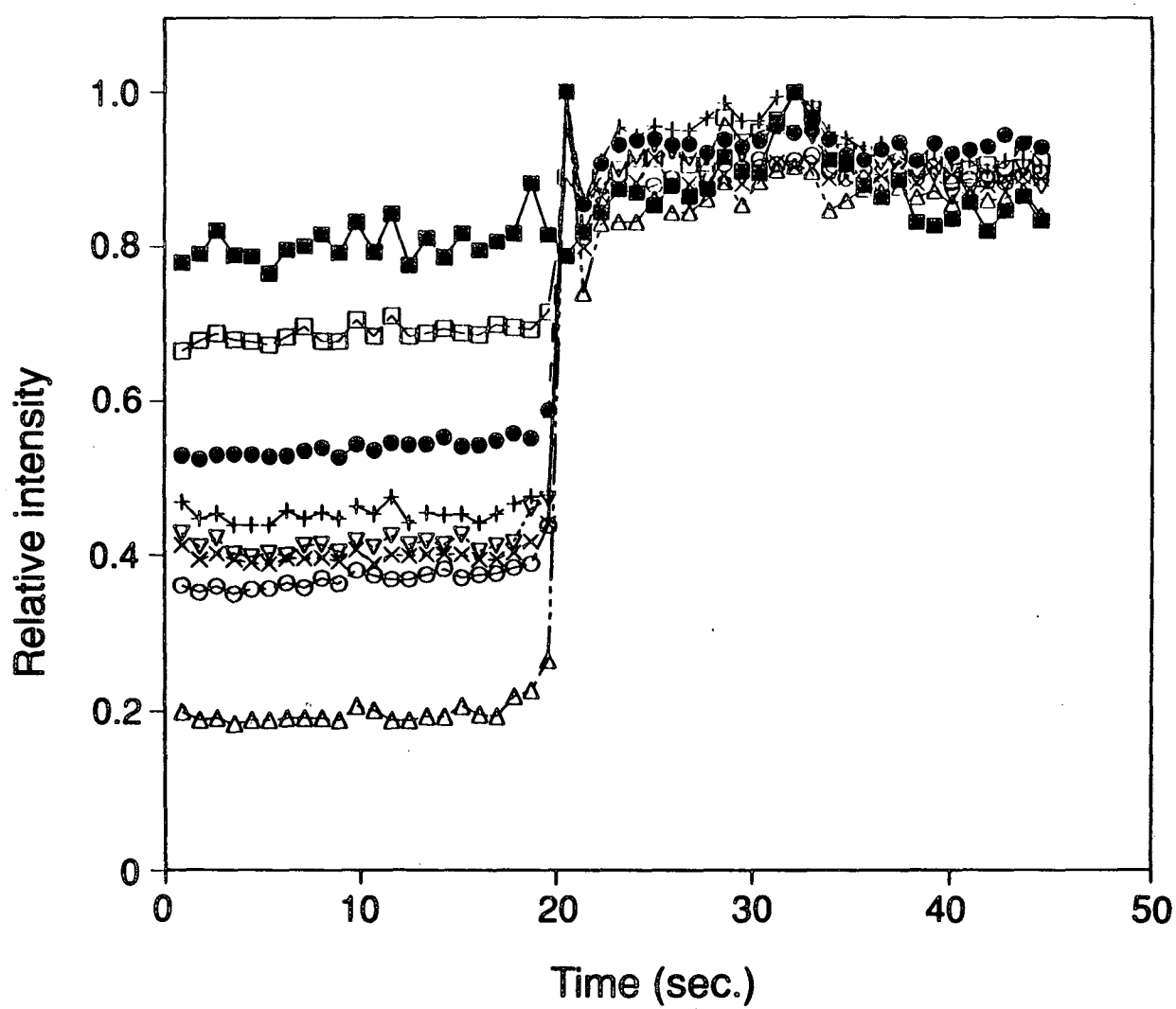

XBL 899-7291

Figure 7-12

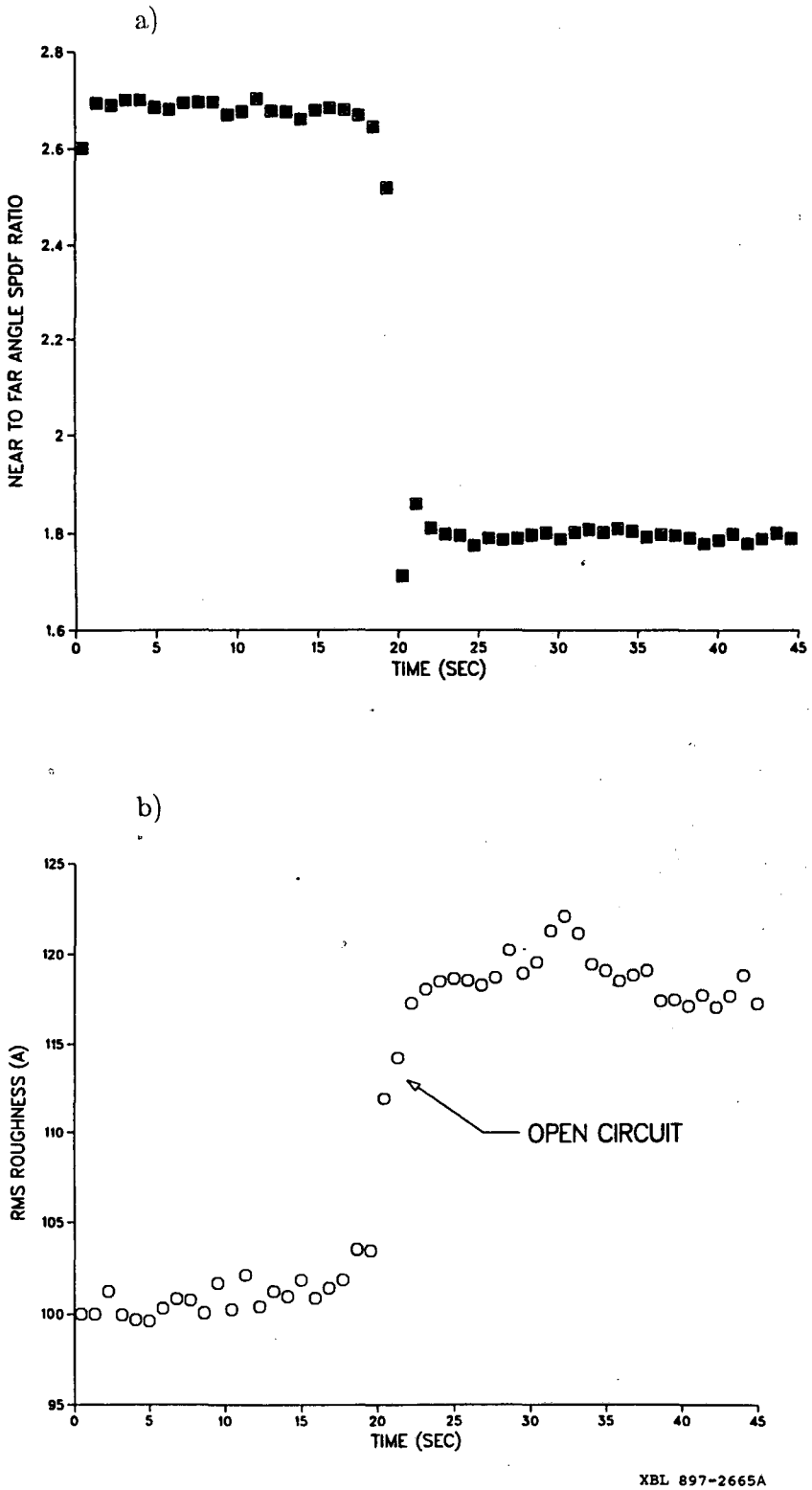
a)
NEAR TO FAR ANGLE SPDF RATIO
2.8
2.6
2.4
2.2
2
1.8
1.6
0
5
10
15
20
25
30
35
40
45
TIME (SEC)
b)
RMS ROUGHNESS (A)
125
120
115
110
105
100
95
OPEN CIRCUIT
TIME (SEC)
XBL 897-2665A

Figure 7-13

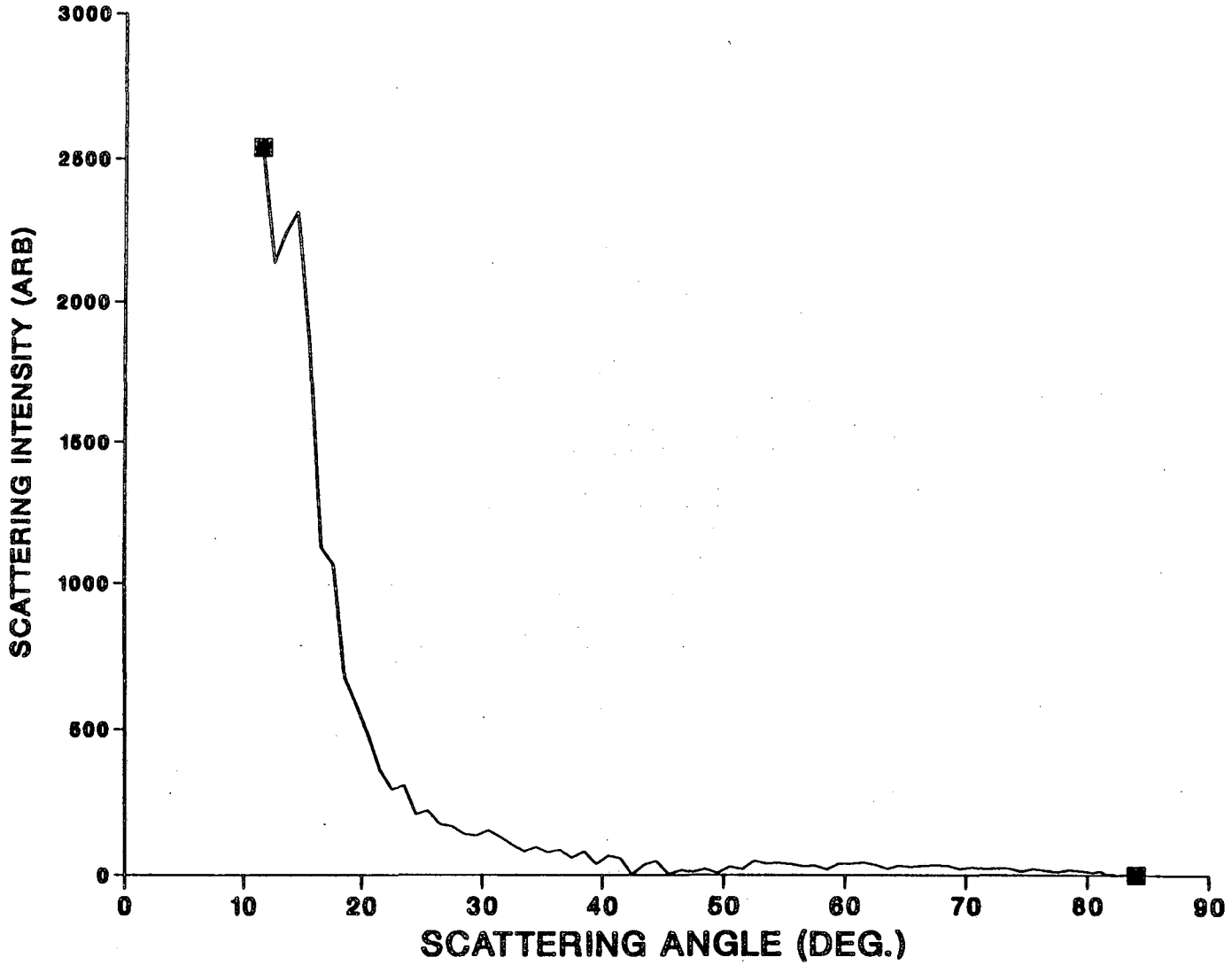

Figure 7-14

XBL 897-2663

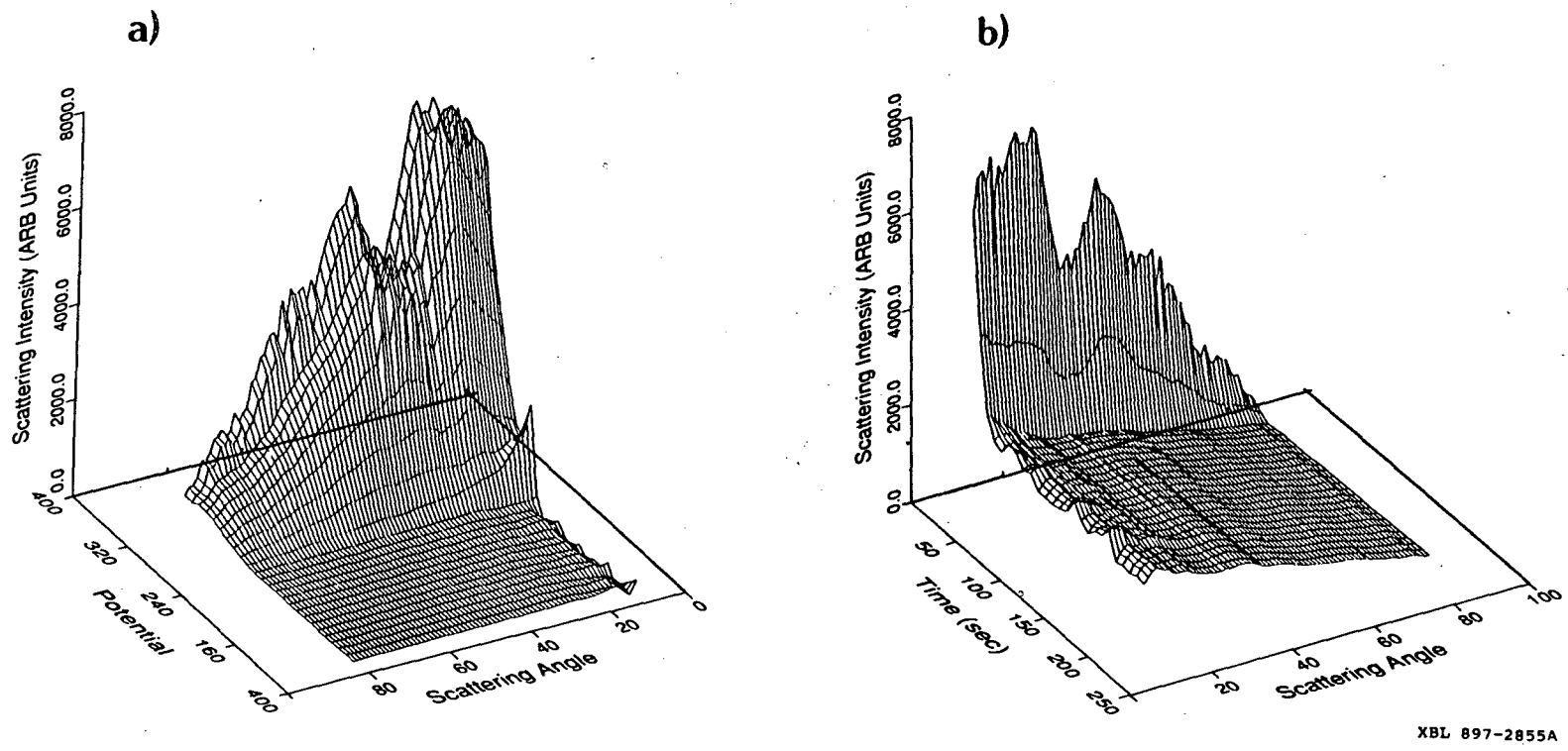
a)
Scattering Intensity (ARB Units)
0.0
2000.0
4000.0
6000.0
8000.0
400
320
240
160
400
Potential
80
60
40
20
0
Scattering Angle
b)
Scattering Intensity (ARB Units)
0.0
2000.0
4000.0
6000.0
8000.0
50
100
150
200
250
Time (sec)
20
40
60
80
100
Scattering Angle
XBL 897-2855A

Figure 7-15

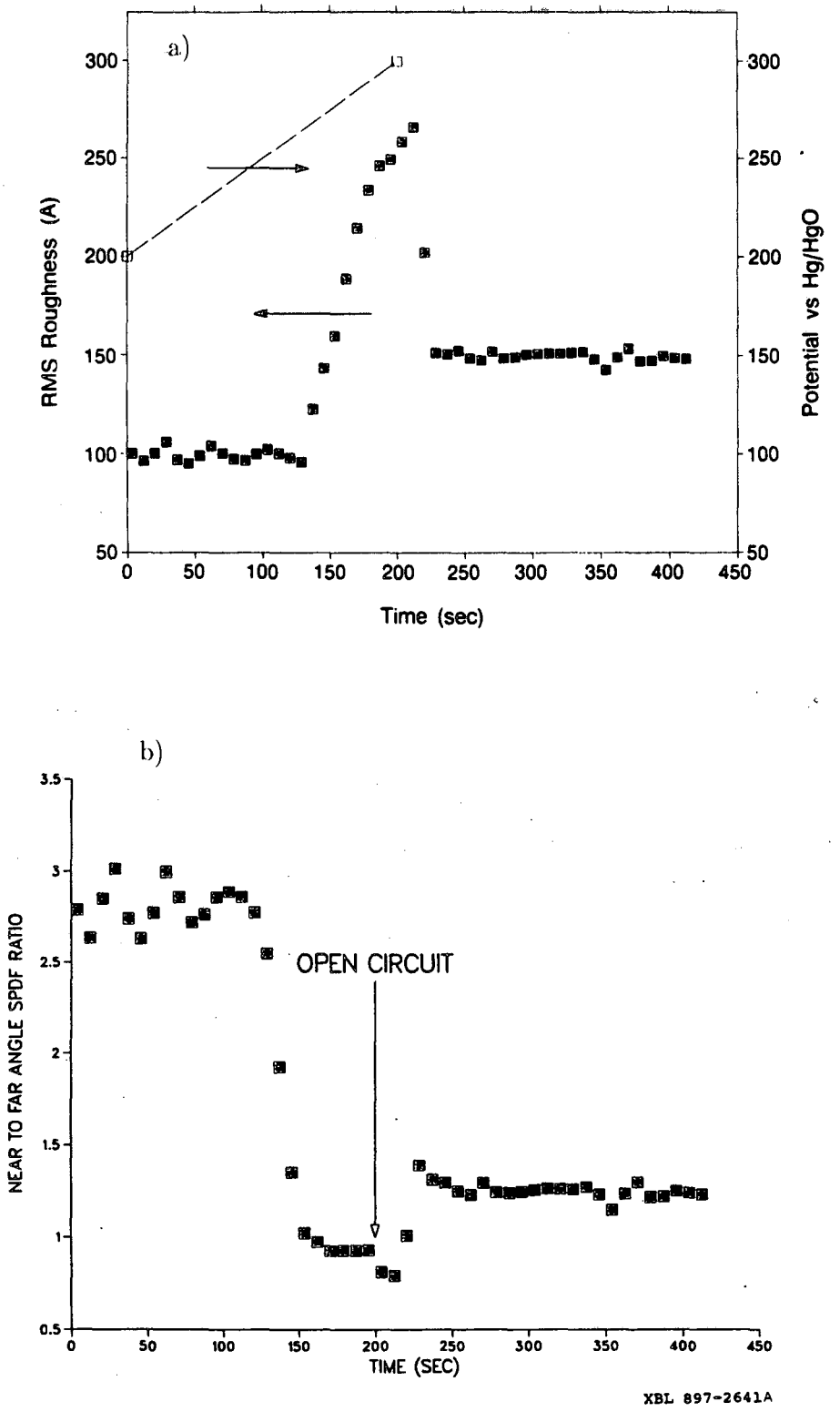
a)
RMS Roughness (A)
Potential vs Hg/HgO
Time (sec)
b)
NEAR TO FAR ANGLE SPDF RATIO
OPEN CIRCUIT
TIME (SEC)
XBL 897-2641A

Figure 7-16

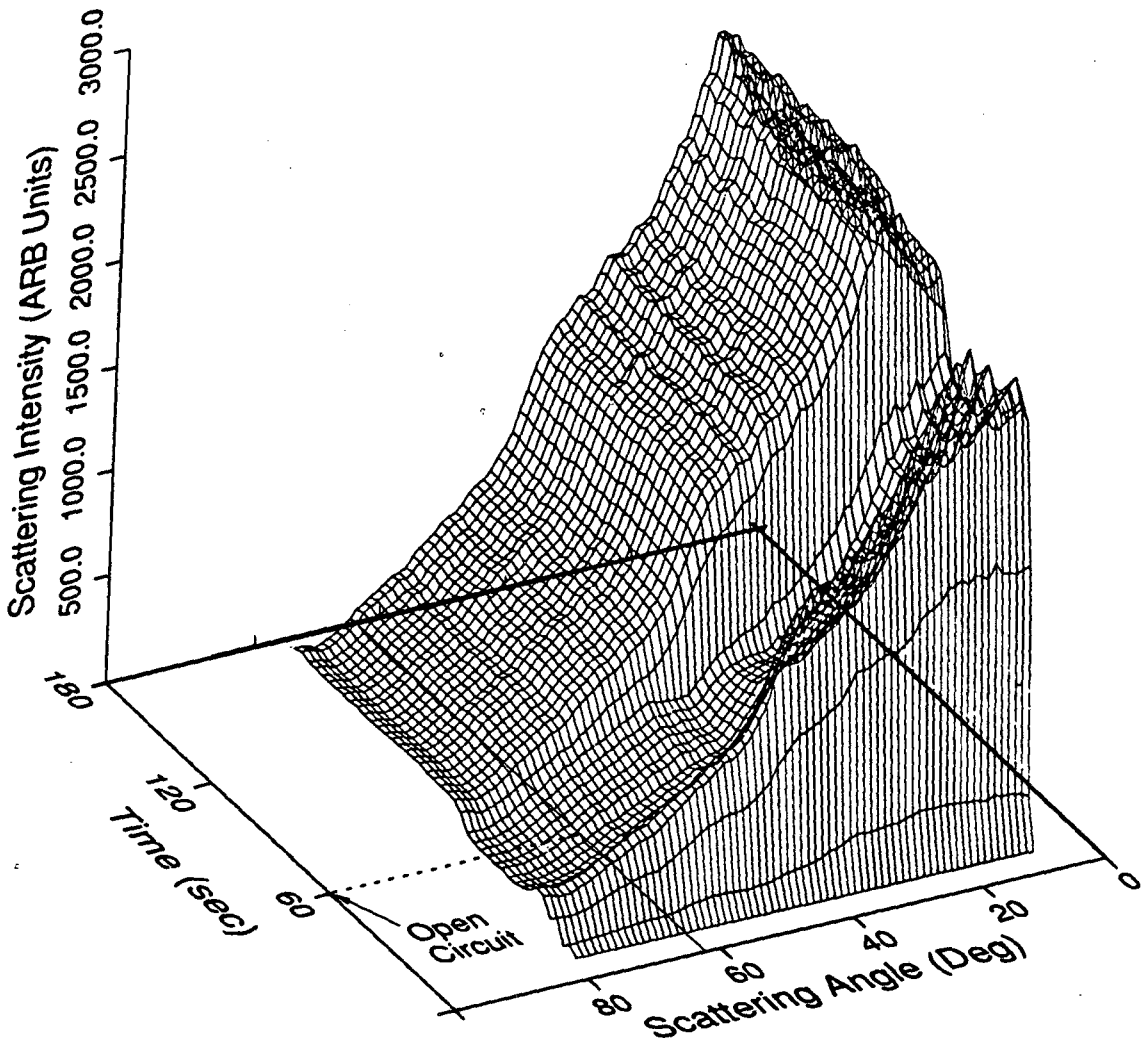

XBL 897-2854

Figure 7-17

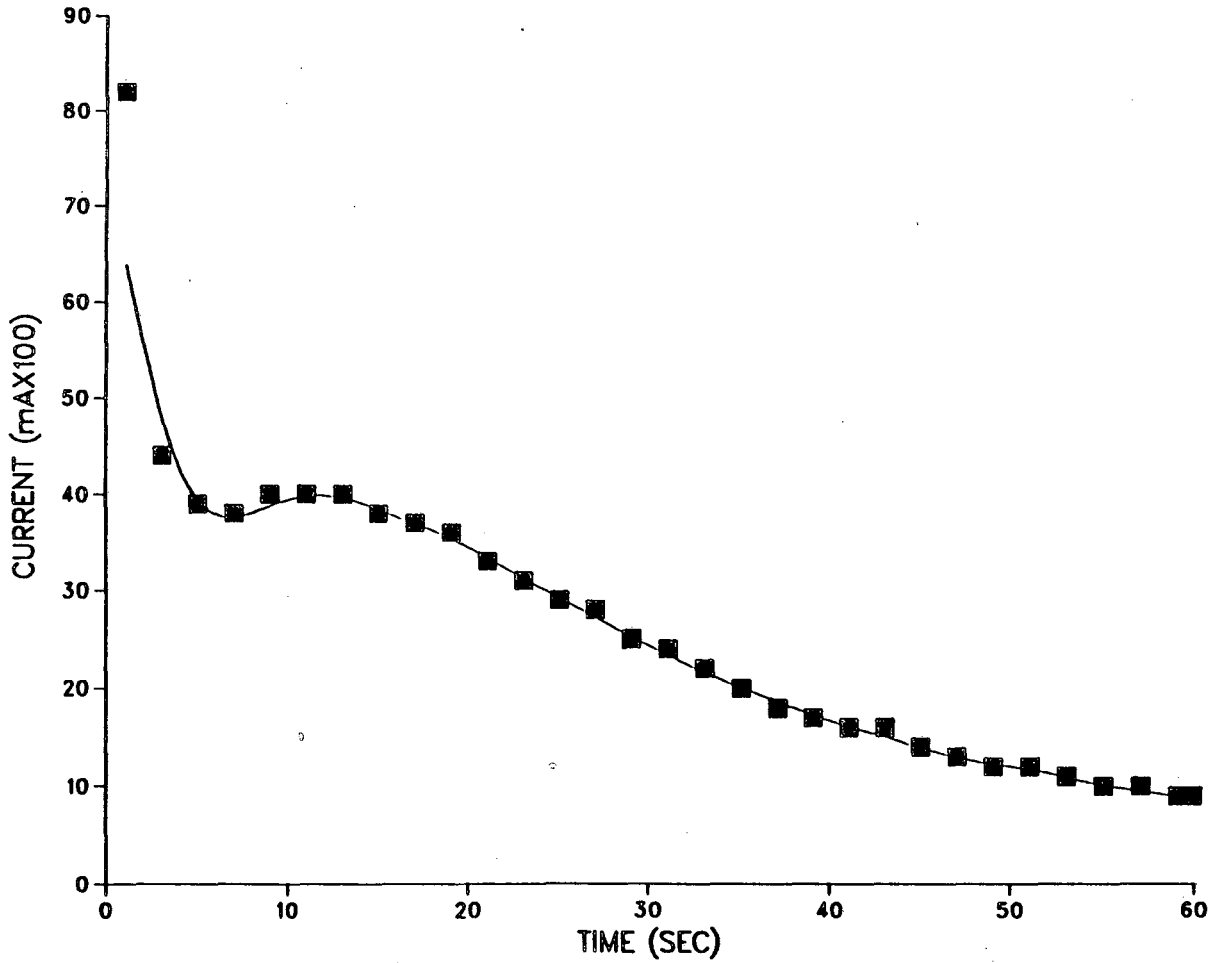

XBL 897-2658

Figure 7-18

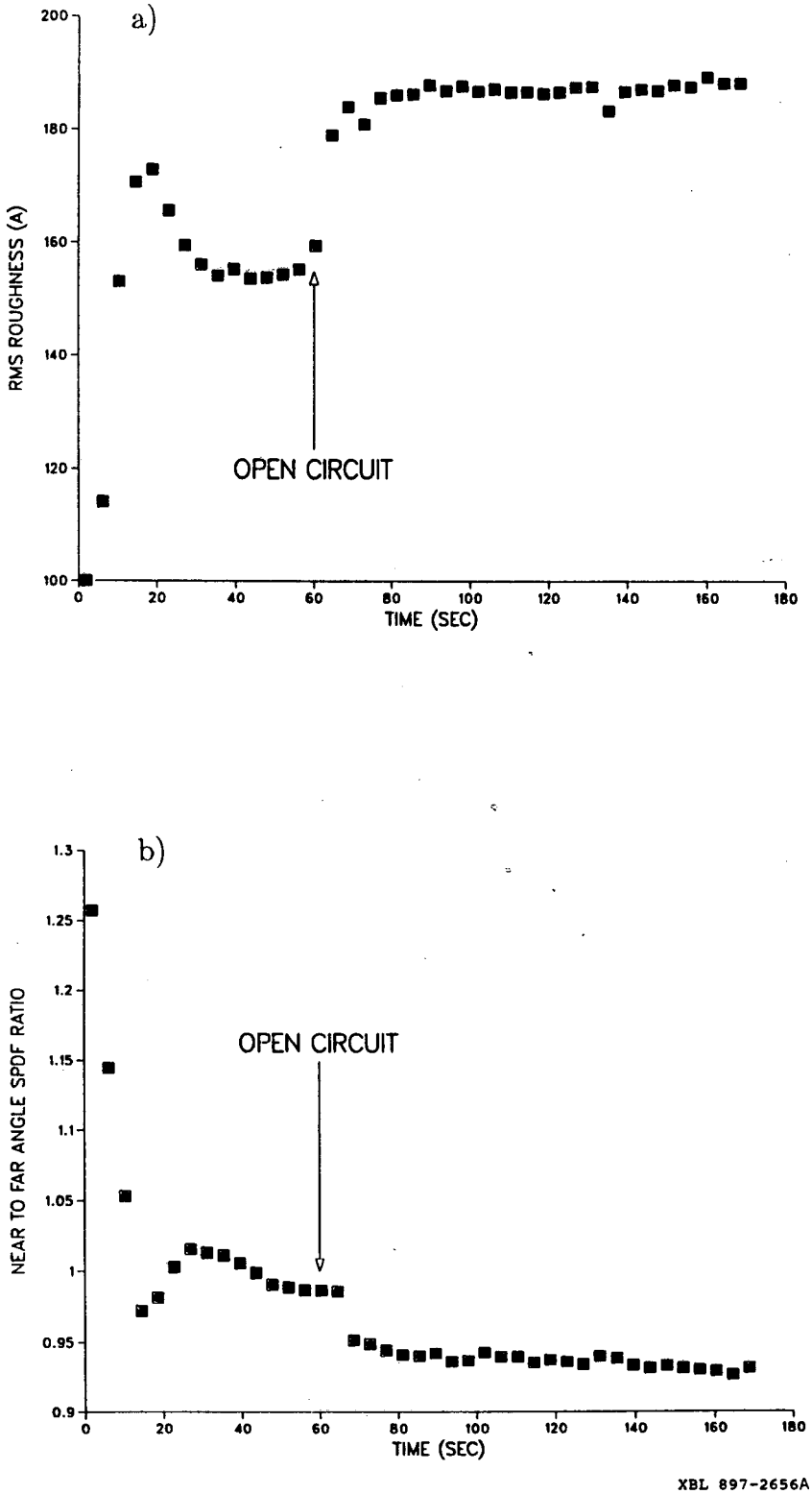
a)
RMS ROUGHNESS (A)
200
180
160
140
120
100
OPEN CIRCUIT
0
20
40
60
80
100
120
140
160
180
TIME (SEC)
b)
NEAR TO FAR ANGLE SPDF RATIO
1.3
1.25
1.2
1.15
1.1
1.05
1
0.95
0.9
OPEN CIRCUIT
TIME (SEC)
XBL 897-2656A

Figure 7-19

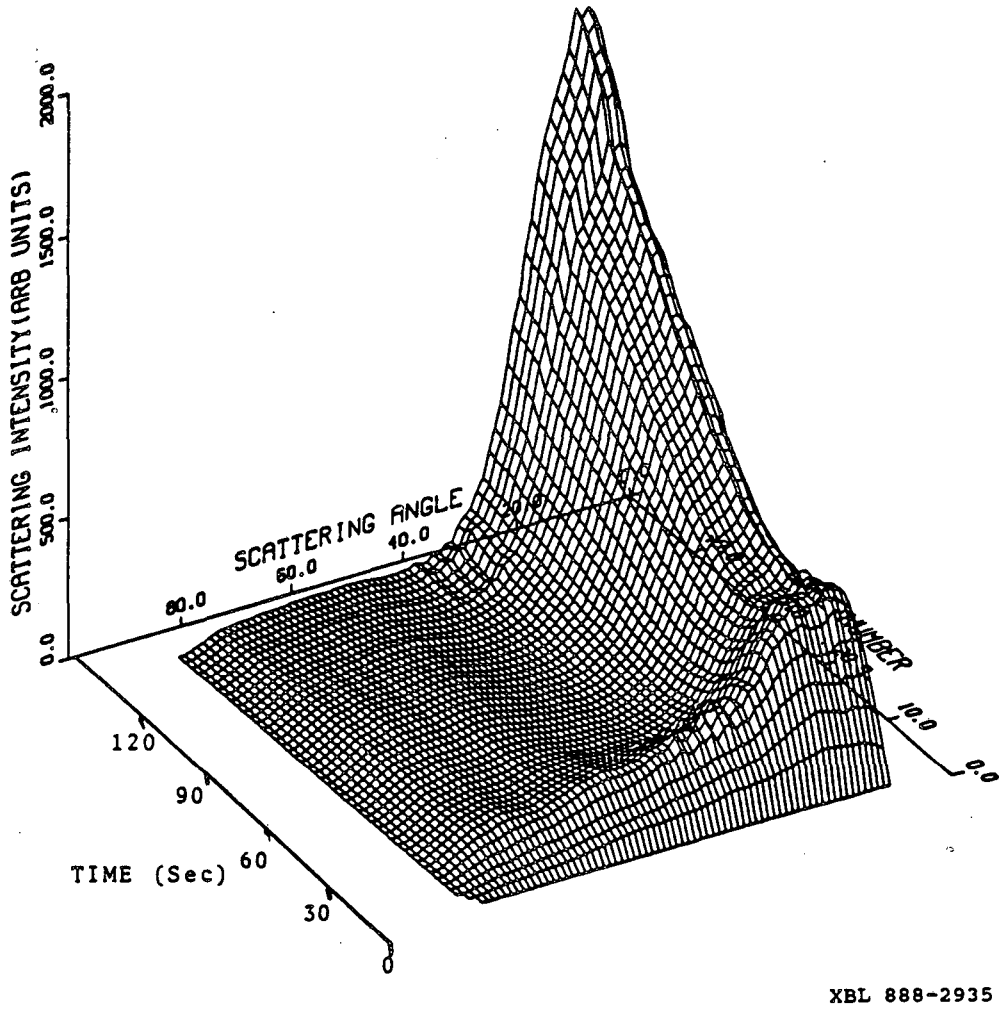
SCATTERING INTENSITY(ARB UNITS)
0.0
500.0
1000.0
1500.0
2000.0
SCATTERING ANGLE
80.0
60.0
40.0
20.0
0.0
TIME (Sec)
120
90
60
30
0
10.0
0.0
XBL 888-2935

Figure 7-20

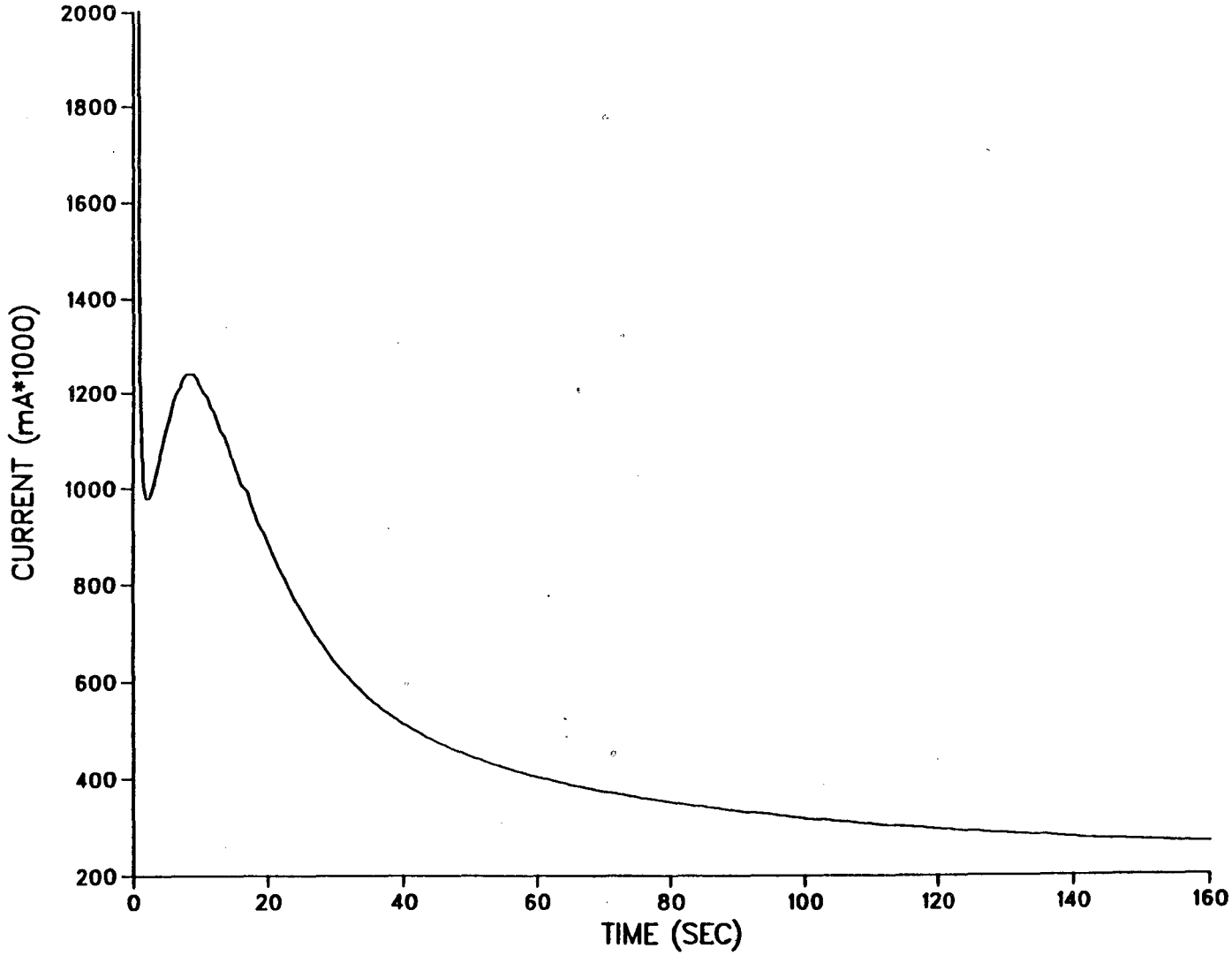

XBL 897-2655

Figure 7-21

a)

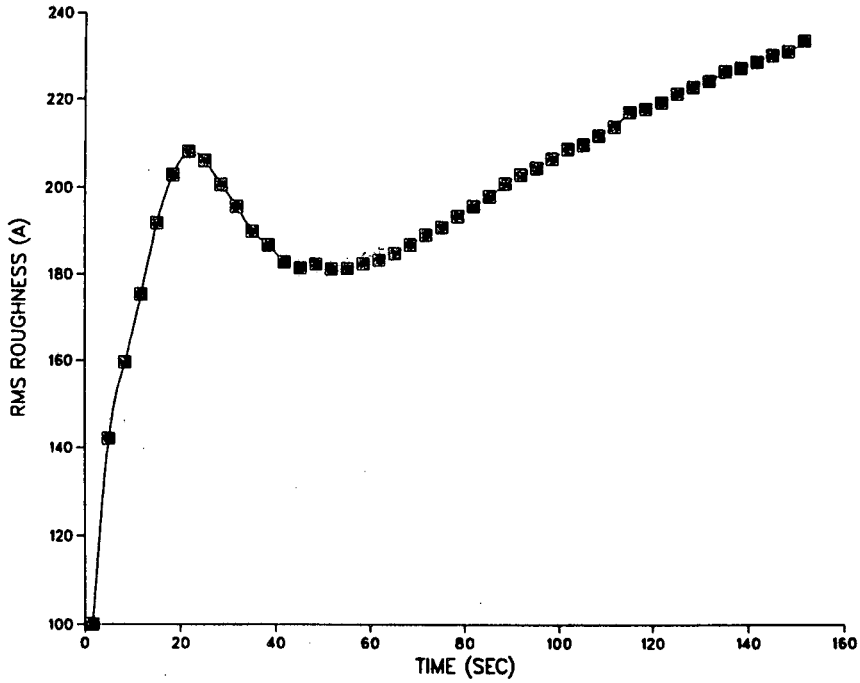

b)

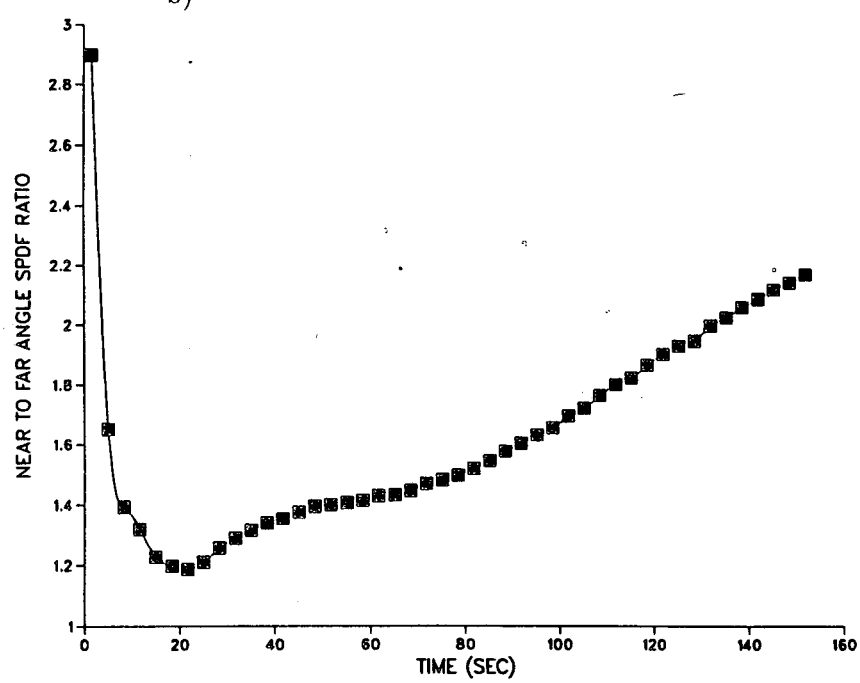

XBL 897-2653A

Figure 7-22

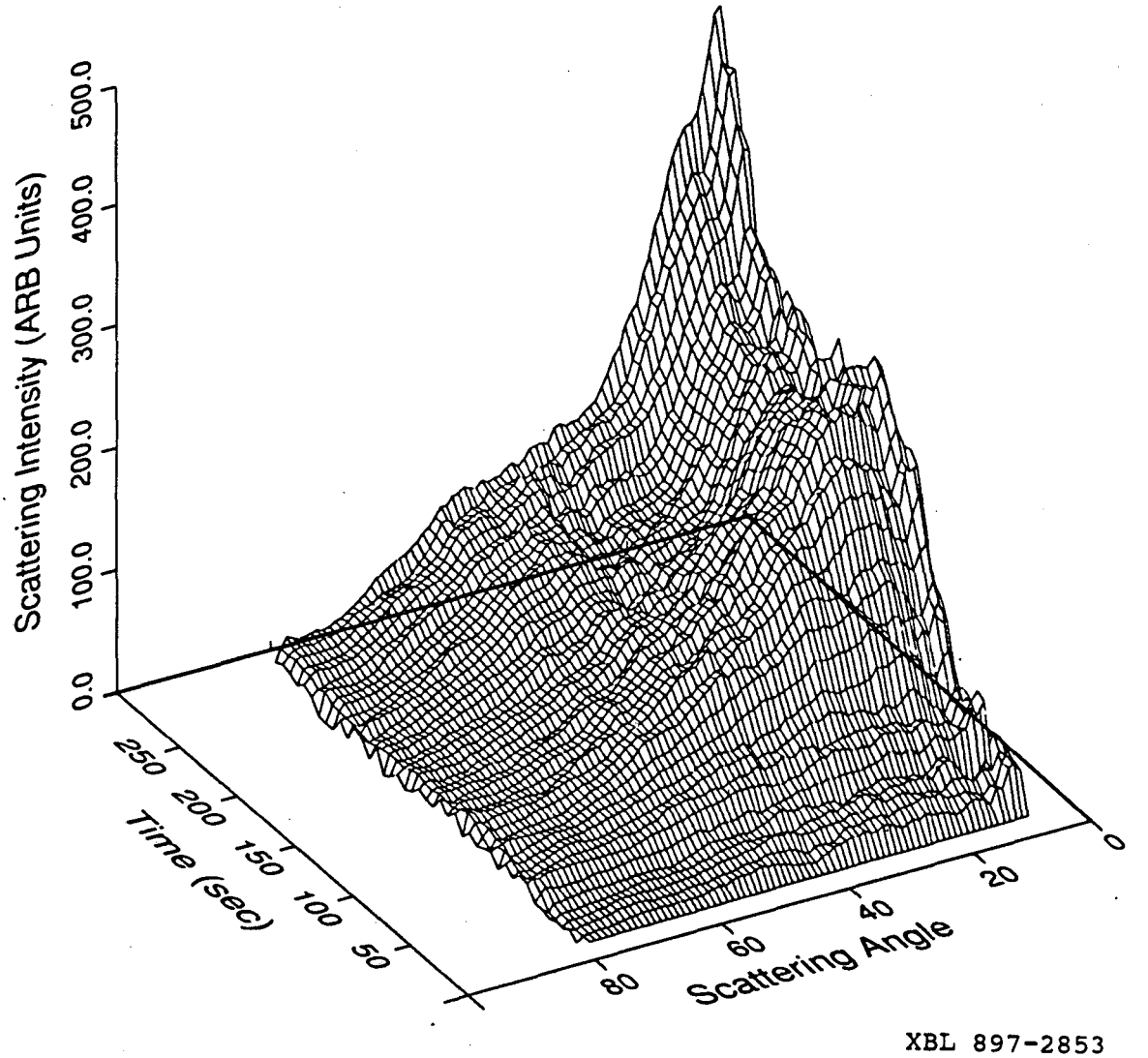
Scattering Intensity (ARB Units)
0.0
100.0
200.0
300.0
400.0
500.0
Time (sec)
250
200
150
100
50
Scattering Angle
80
60
40
20
0
XBL 897-2853

Figure 7-23

a)

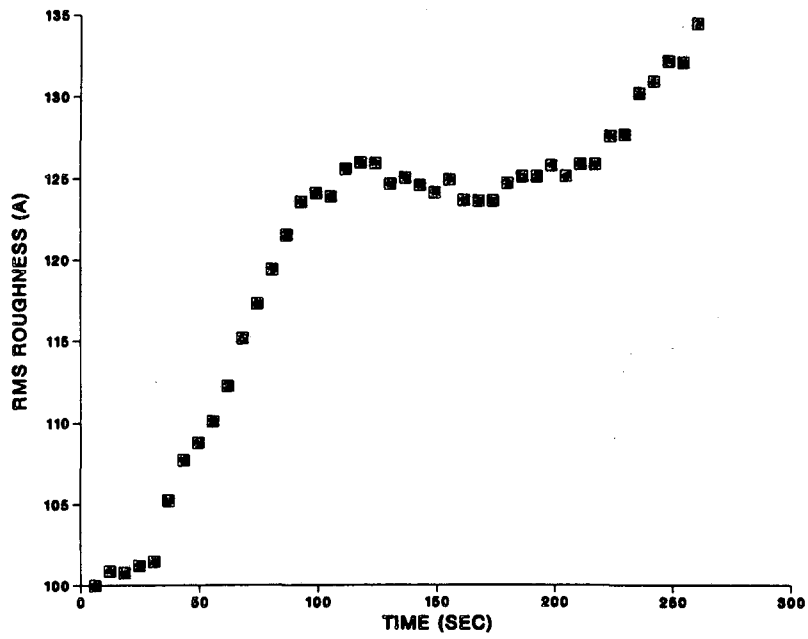

b)

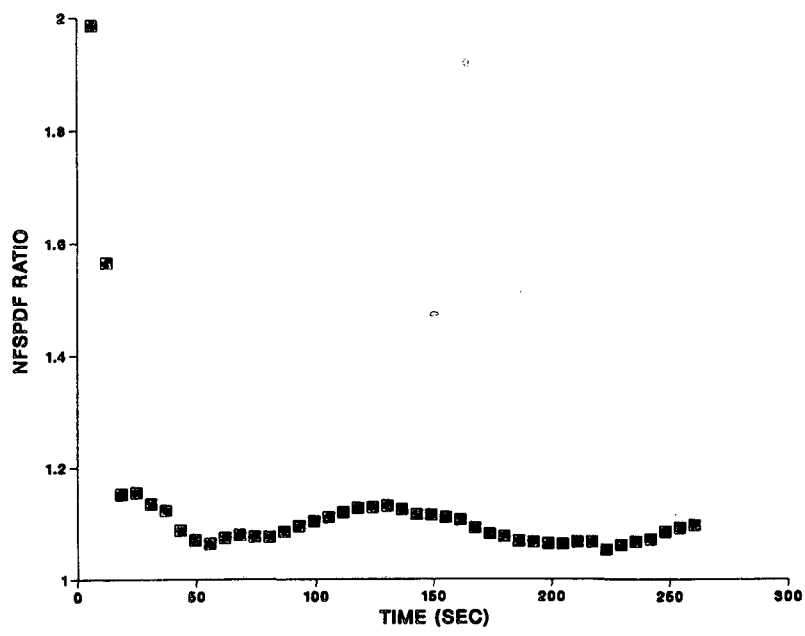

XBL 897-2650A

Figure 7-24

a)

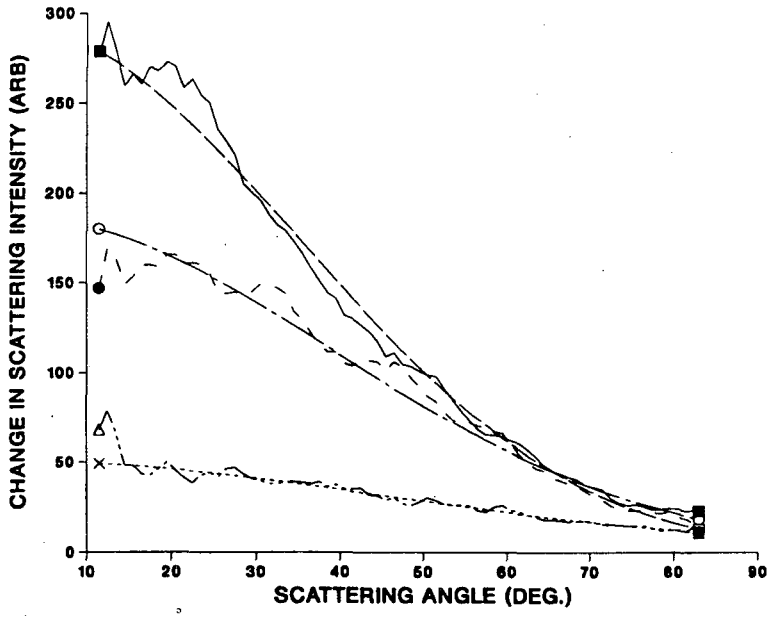

b)

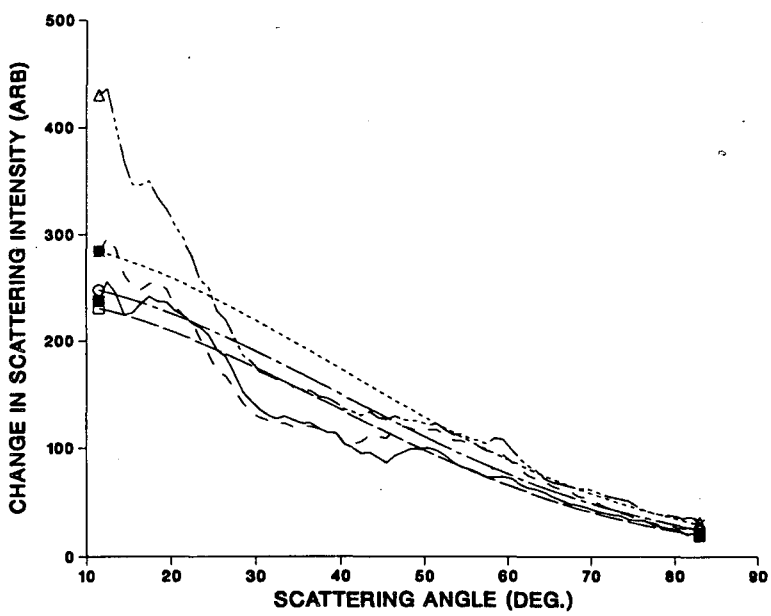

XBL 897-2652A

Figure 7-25

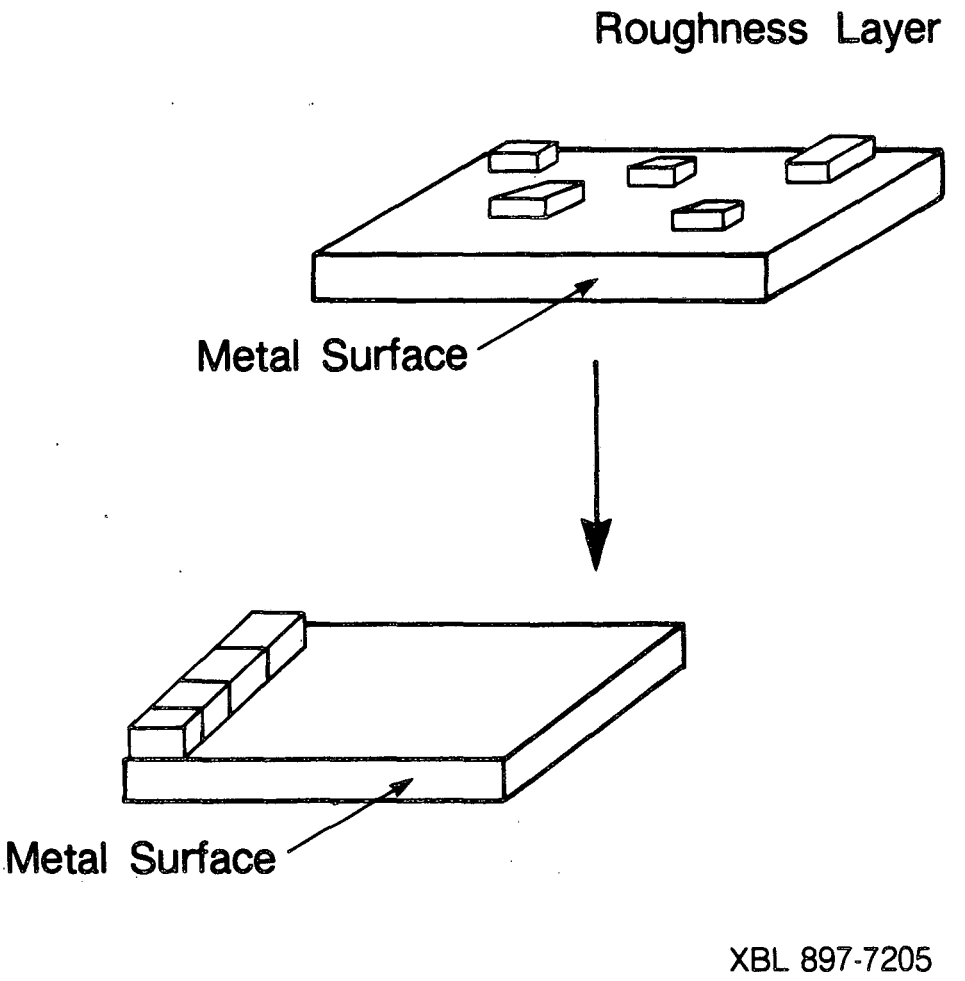

Figure 7-26

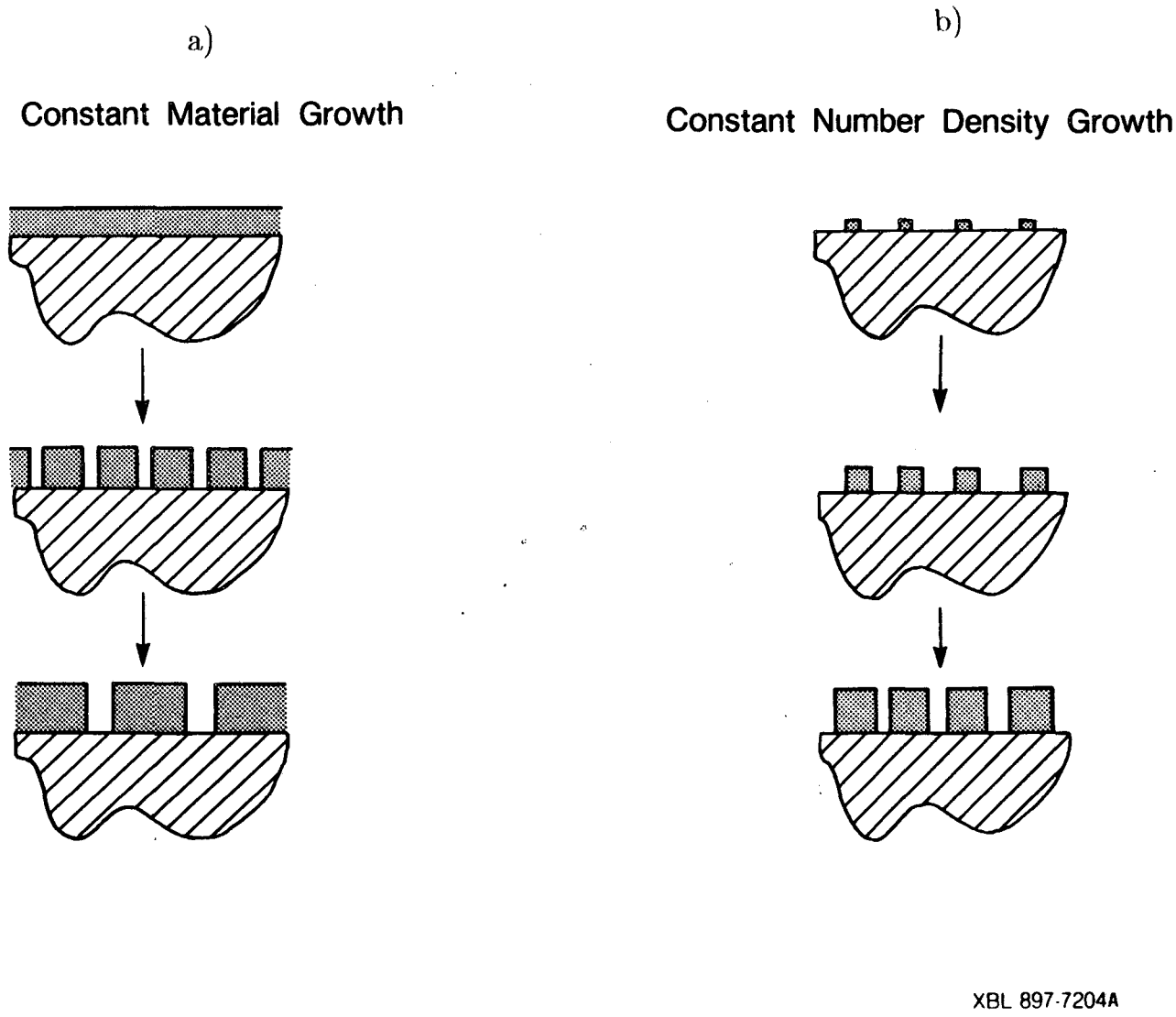
a)
Constant Material Growth
b)
Constant Number Density Growth
XBL 897-7204A

Figure 7-27

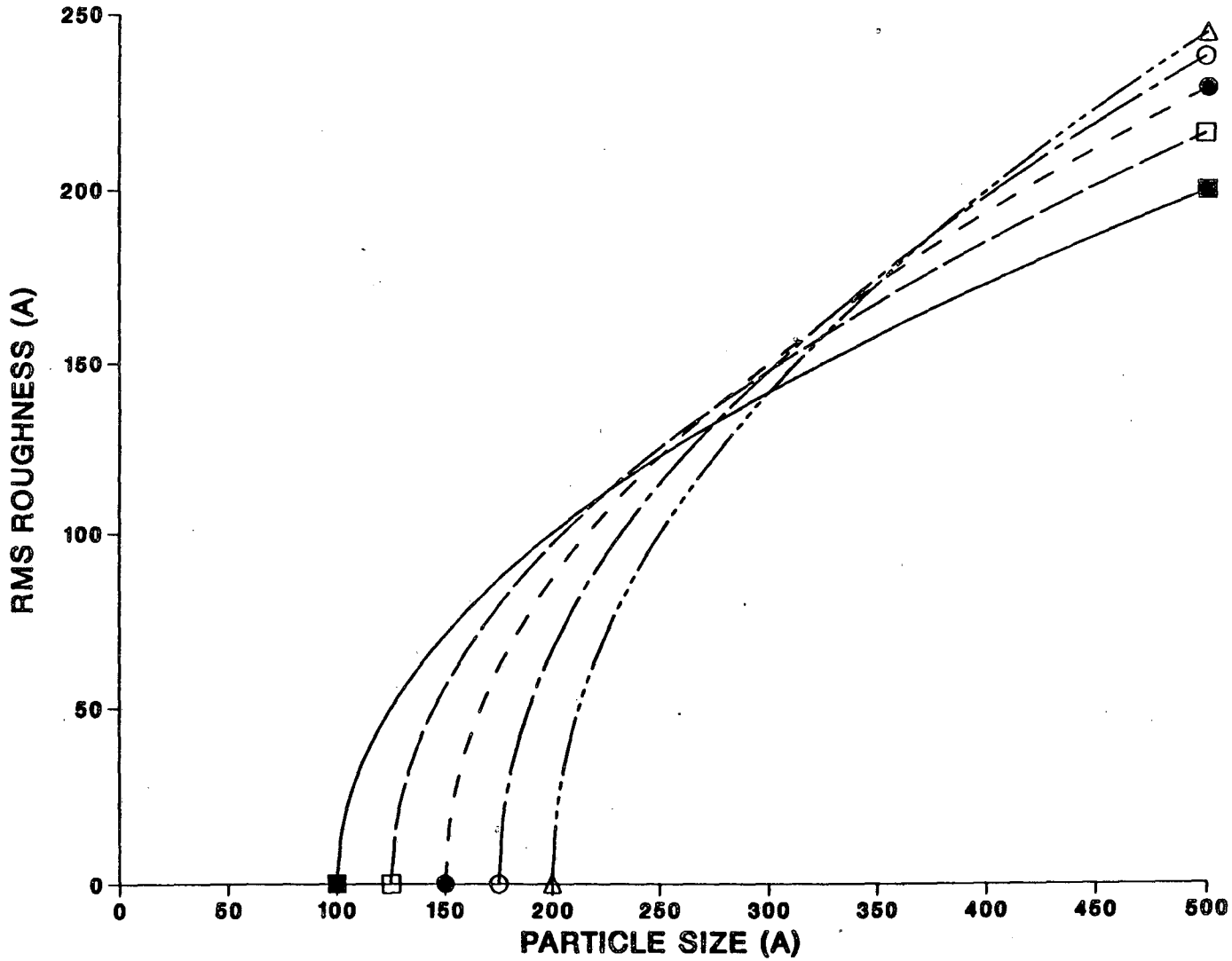

XBL 897-2647

Figure 7-28

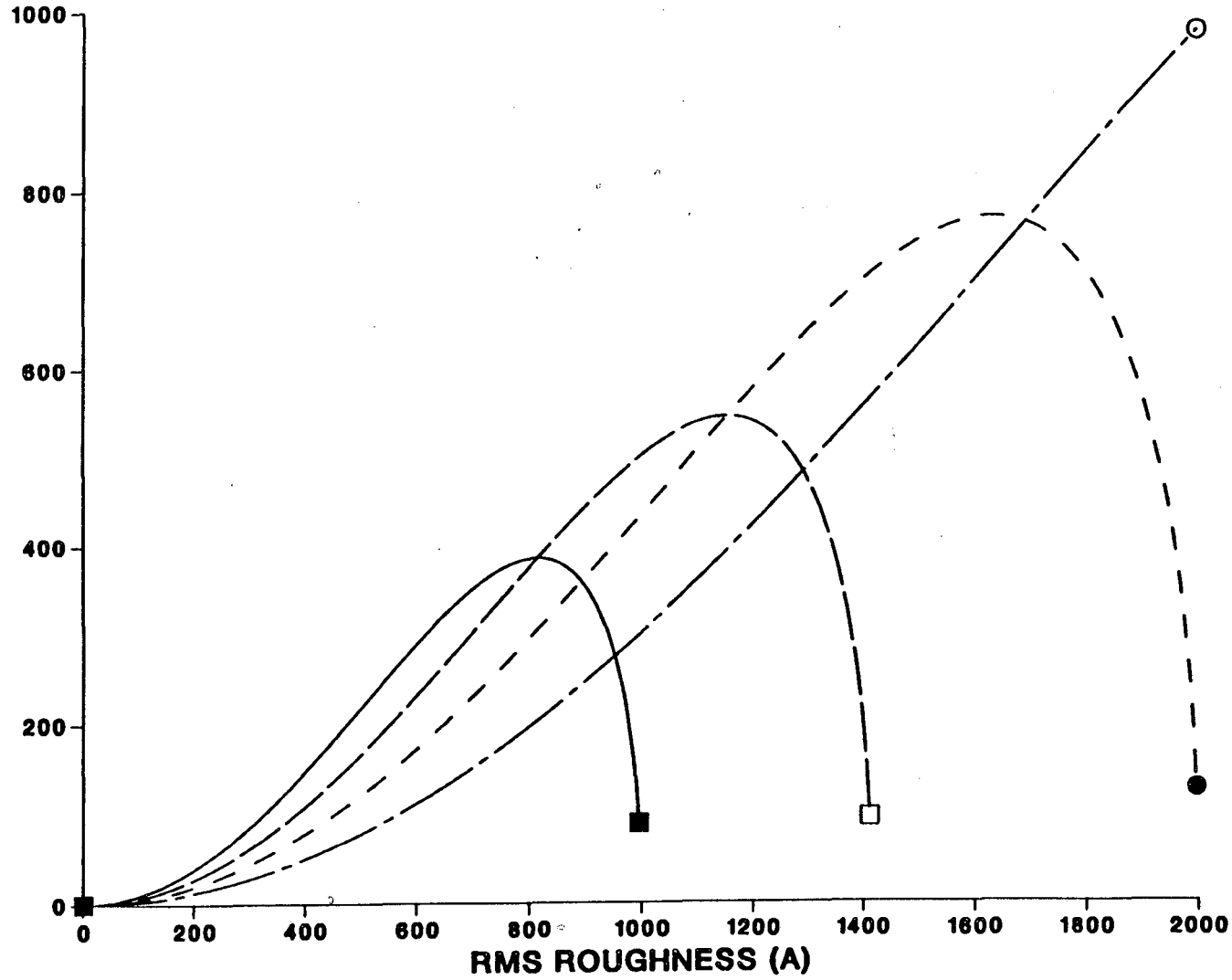

XBL 897-2646

Figure 7-29

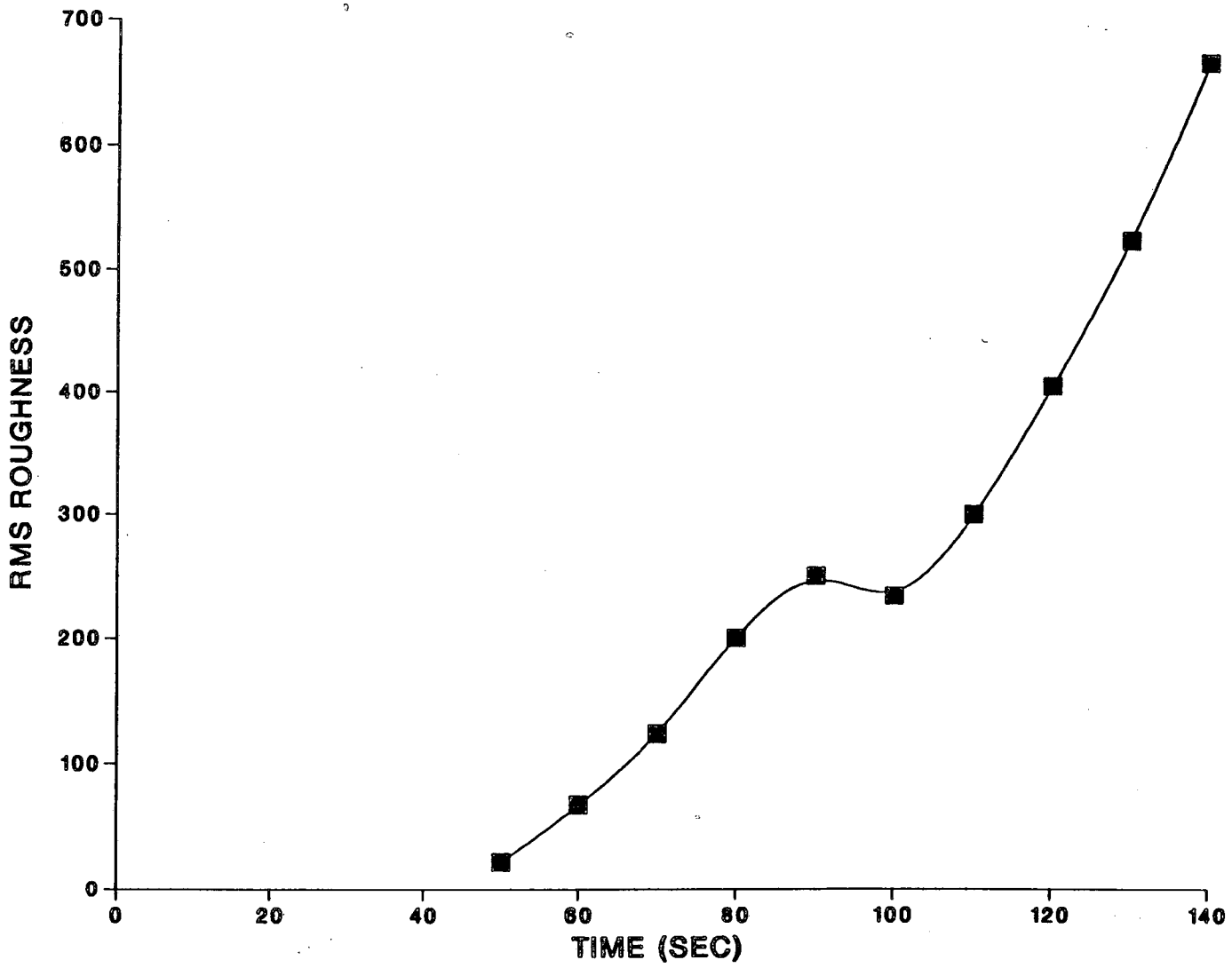

XBL 897-2645

Figure 7-30

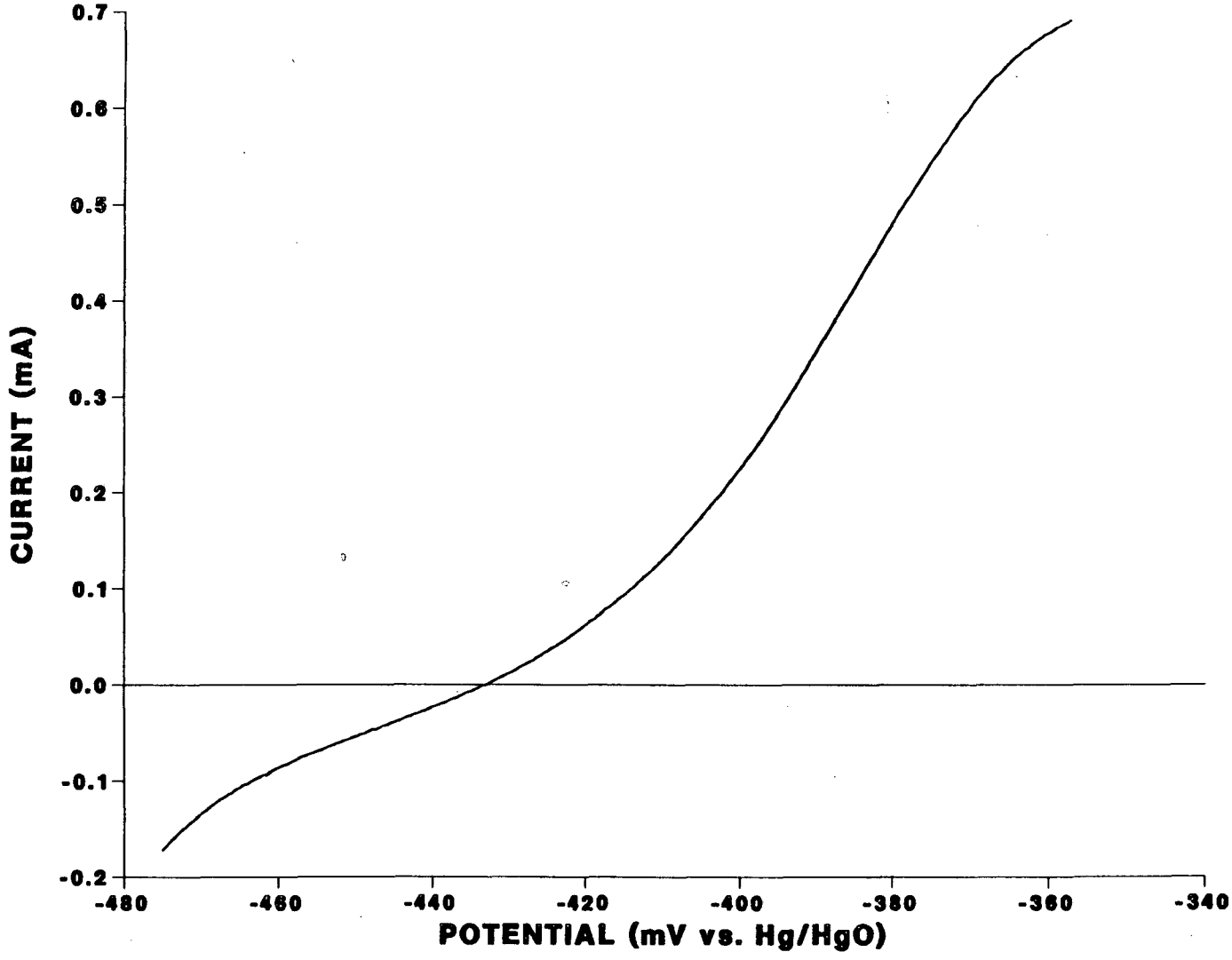

XBL 897-2639

Figure 7-31

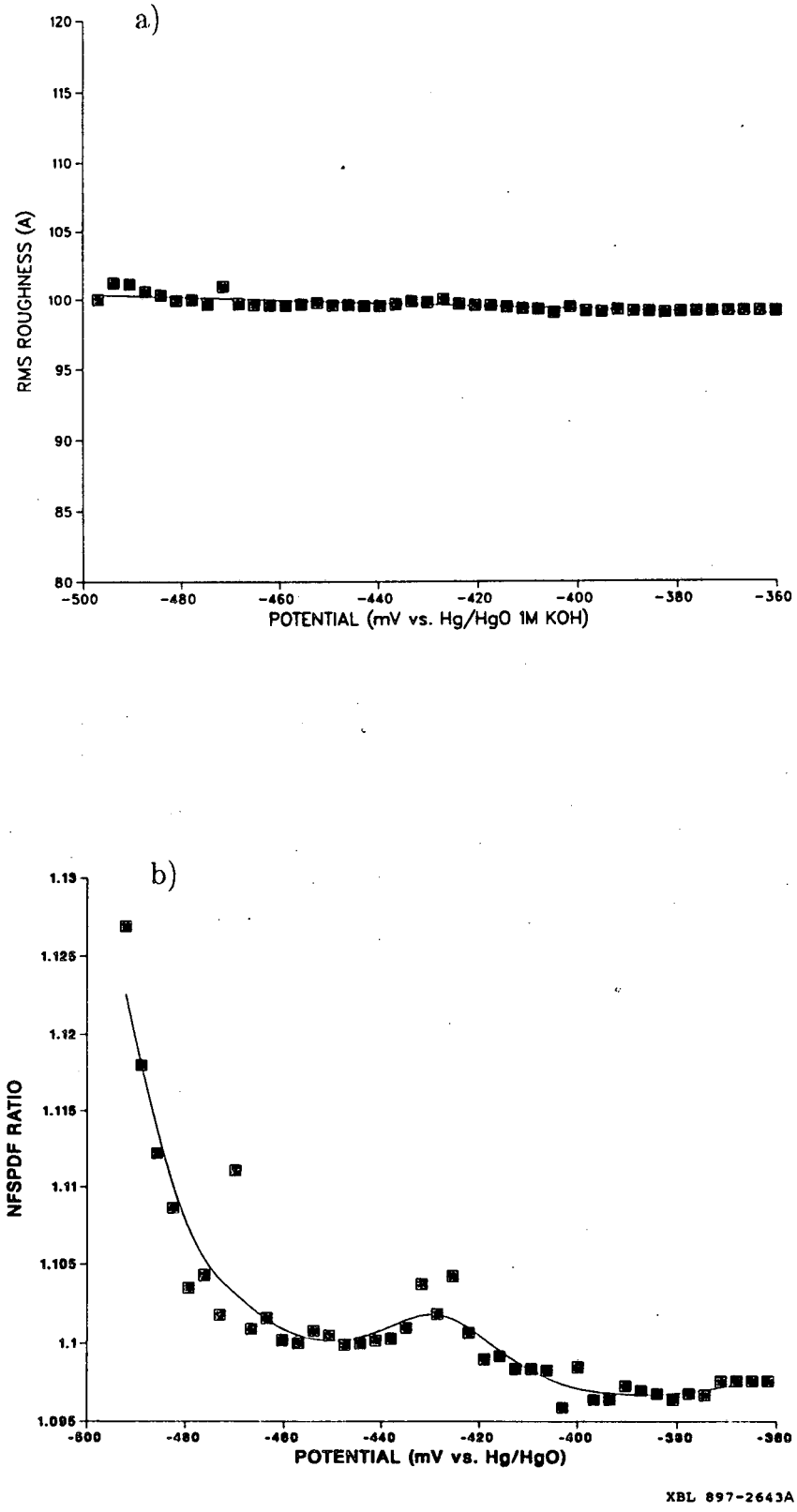
a)
RMS ROUGHNESS (A)
120
115
110
105
100
95
90
85
80
-500
-480
-460
-440
-420
-400
-380
-360
POTENTIAL (mV vs. Hg/HgO 1M KOH)
b)
NFSPDF RATIO
1.13
1.125
1.12
1.115
1.11
1.105
1.1
1.095
-500
-480
-460
-440
-420
-400
-380
-360
POTENTIAL (mV vs. Hg/HgO)
XBL 897-2643A

Figure 7-32

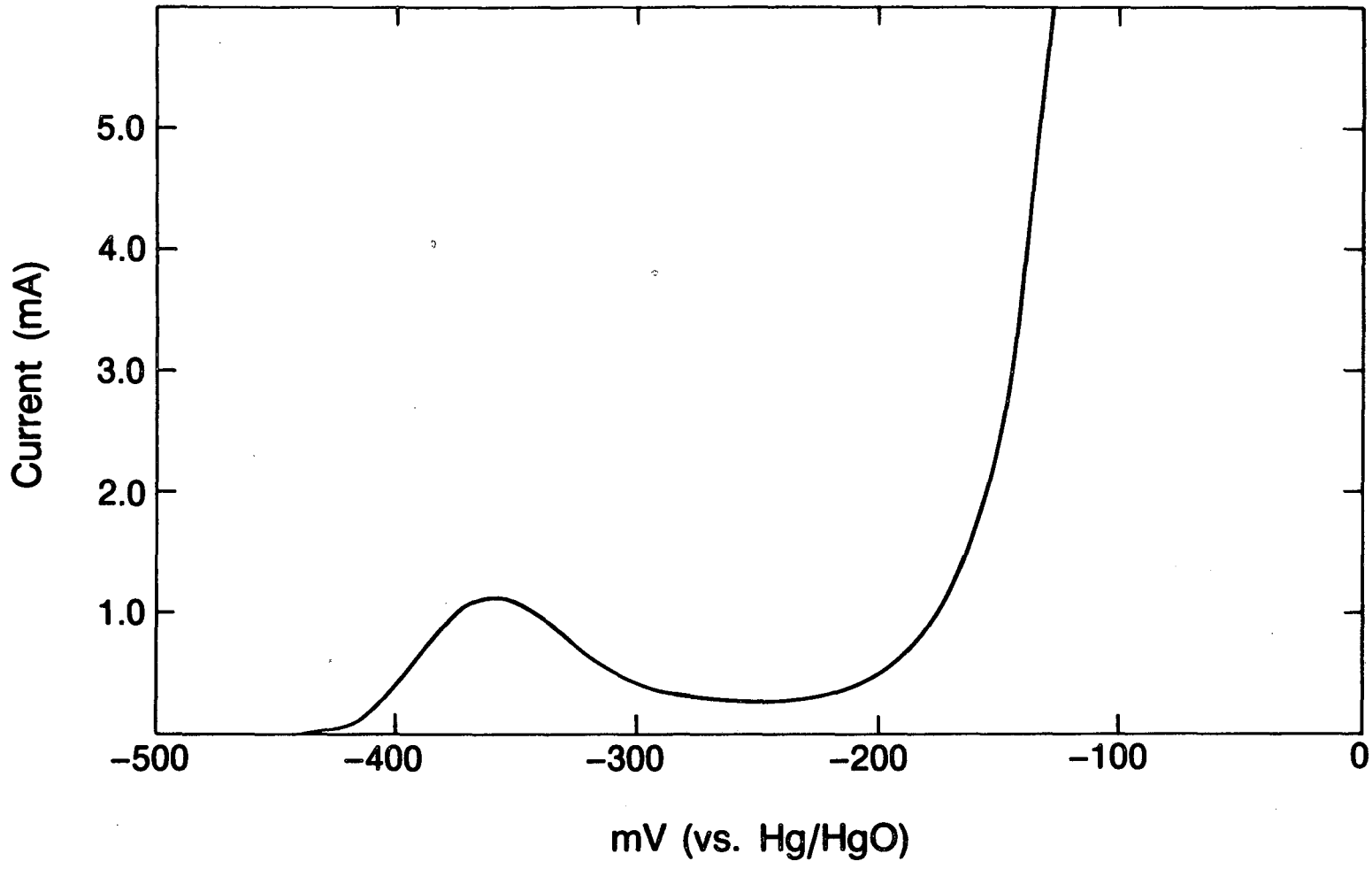

Figure 7-33

XBL 897-7206

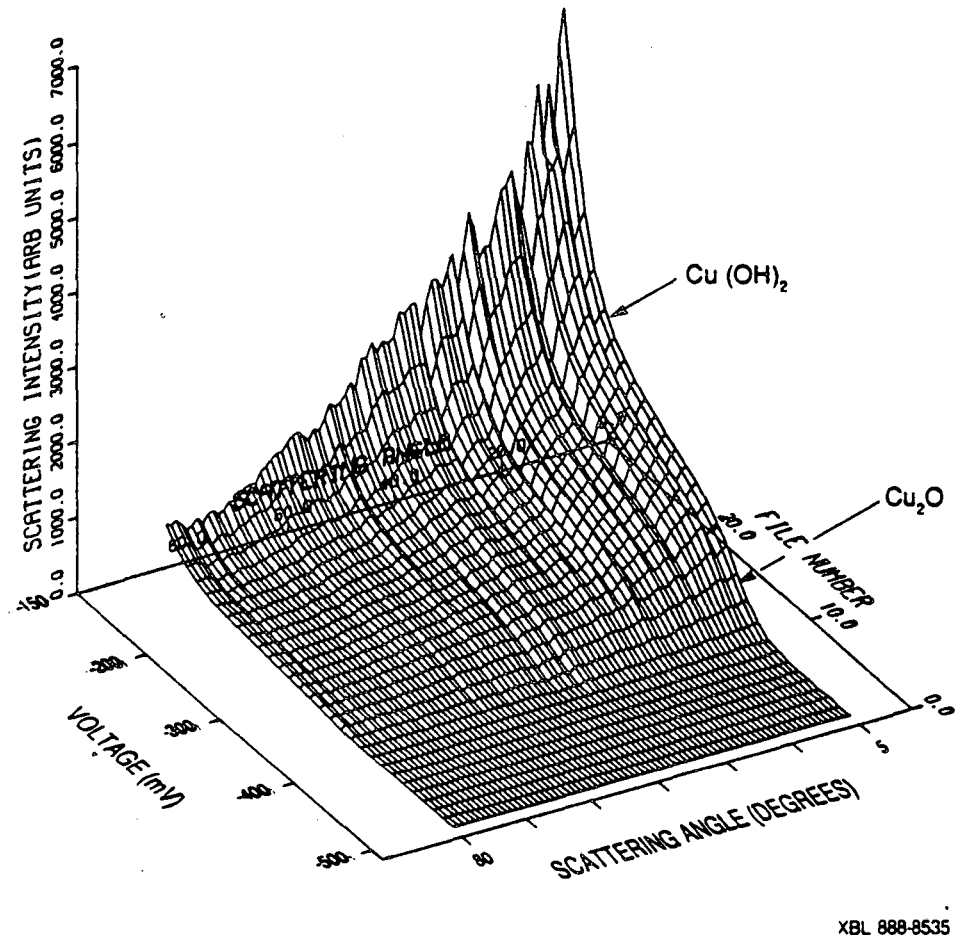
SCATTERING INTENSITY(ARB UNITS)
0.0
1000.0
2000.0
3000.0
4000.0
5000.0
6000.0
7000.0
Cu (OH)$_2$
Cu$_2$O
FILE NUMBER
0.0
10.0
20.0
VOLTAGE (mV)
-500
SCATTERING ANGLE (DEGREES)
80
XBL 888-8535

Figure 7-34

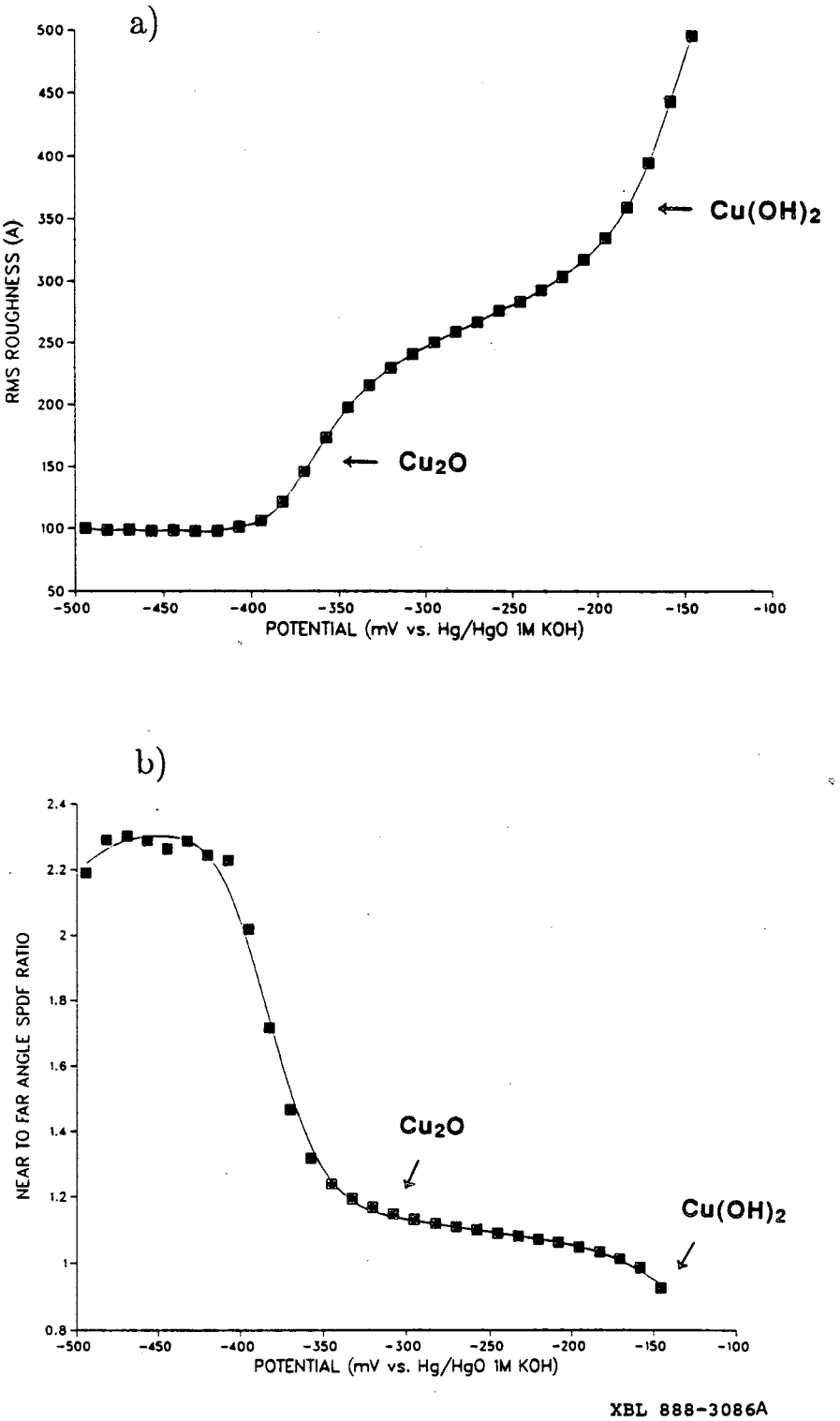
a)
RMS ROUGHNESS (A)
500
450
400
350
300
250
200
150
100
50
-500
-450
-400
-350
-300
-250
-200
-150
-100
POTENTIAL (mV vs. Hg/HgO 1M KOH)
Cu(OH)2
Cu2O
b)
NEAR TO FAR ANGLE SPDF RATIO
2.4
2.2
2
1.8
1.6
1.4
1.2
1
0.8
-500
-450
-400
-350
-300
-250
-200
-150
-100
POTENTIAL (mV vs. Hg/HgO 1M KOH)
Cu2O
Cu(OH)2
XBL 888-3086A

Figure 7-35

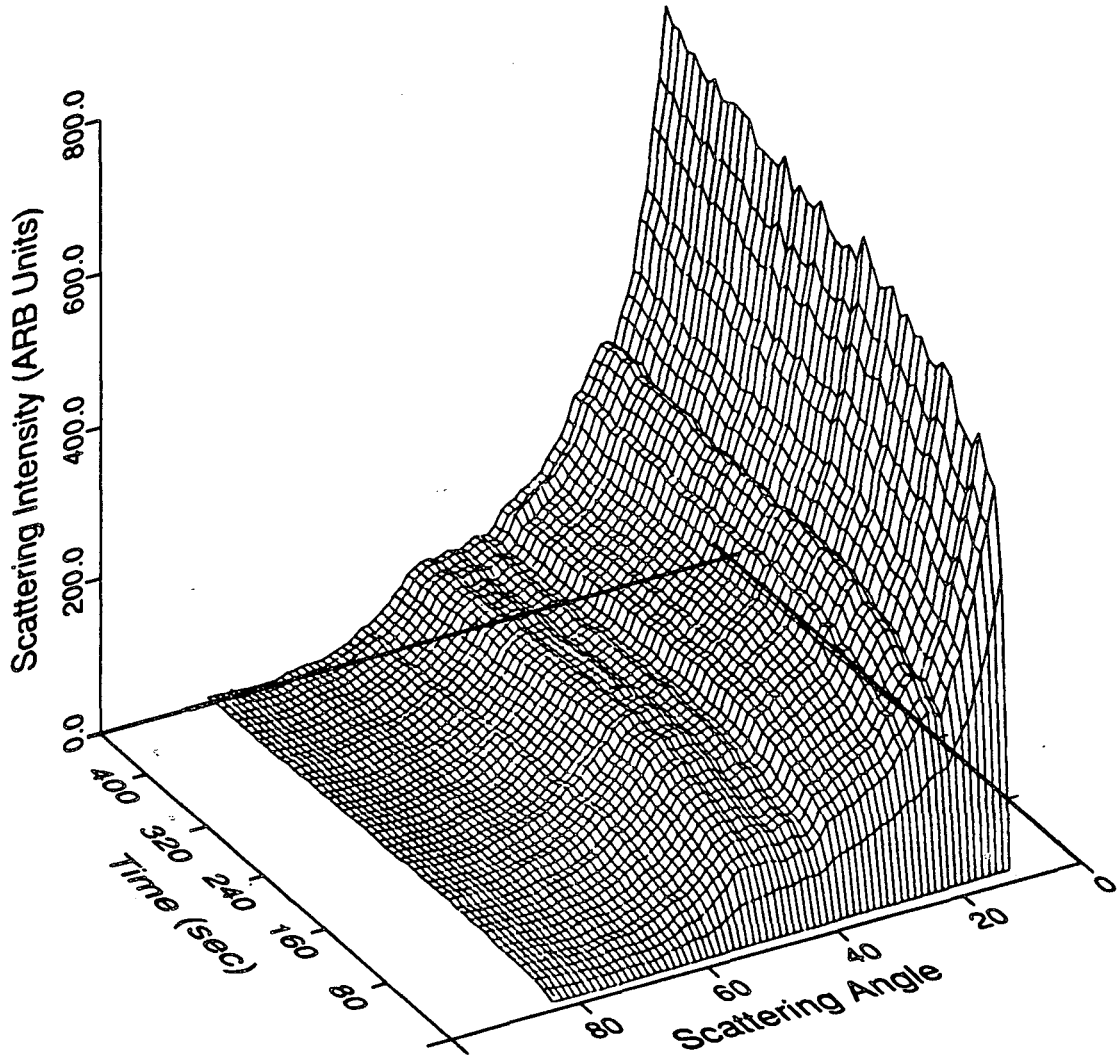

XBL 897-2856

Figure 7-36

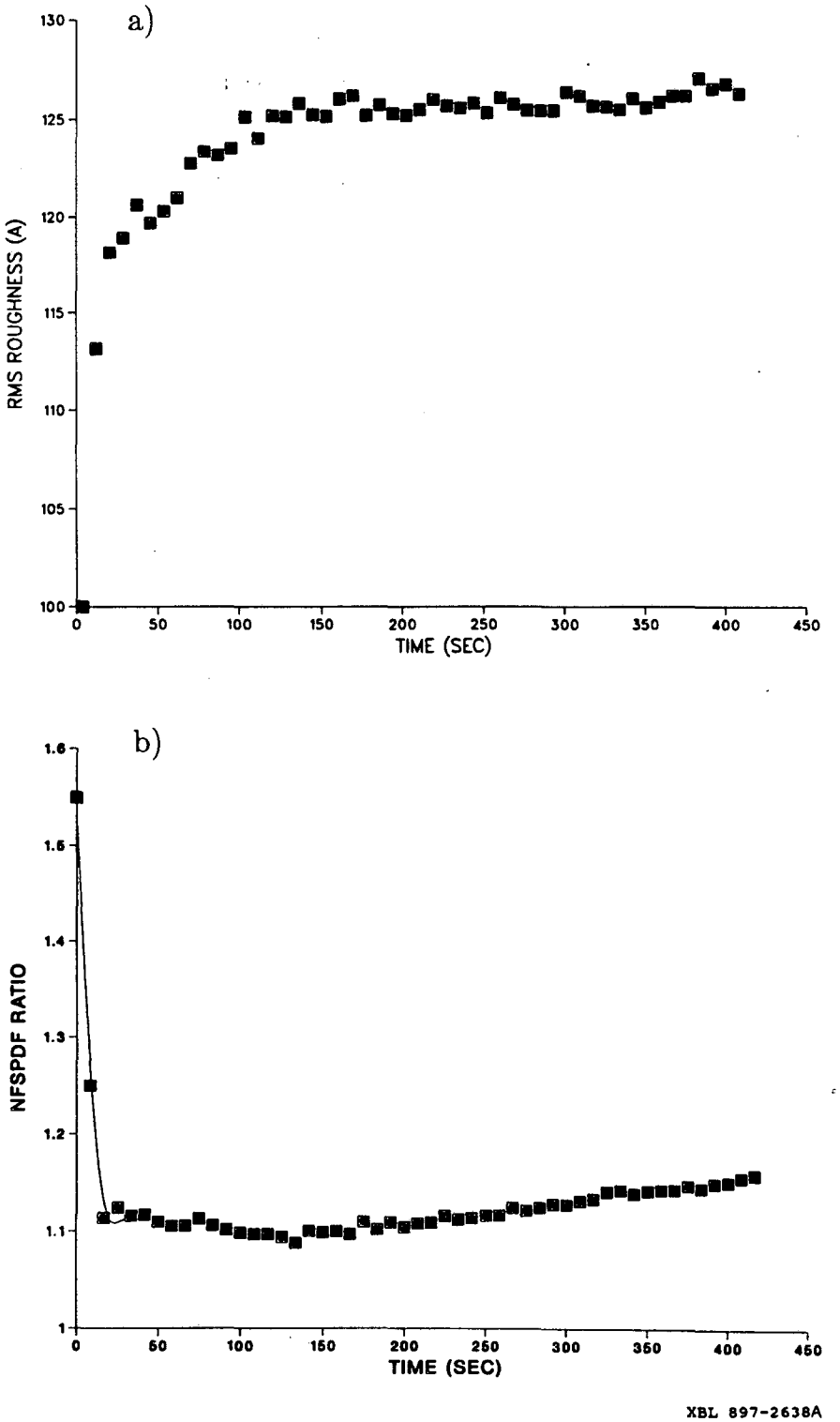
a)
RMS ROUGHNESS (A)
130
125
120
115
110
105
100
0
50
100
150
200
250
300
350
400
450
TIME (SEC)
b)
NFSPDF RATIO
1.6
1.5
1.4
1.3
1.2
1.1
1
0
50
100
150
200
250
300
350
400
450
TIME (SEC)
XBL 897-2638A

Figure 7-37

CHAPTER 8

OBSERVATIONS OF THE ANODIZATION OF METALS USING *IN SITU* LASER RAMAN SPECTROSCOPY

Section 8.1: Introduction

The scattering of light with a change in wavenumber by the addition or subtraction of vibrational or rotational energy is called Raman scattering, after C. V. Raman, who first observed this phenomenon in 1928 [H1]. This type of radiation scattering is one of the many examples of the quantum interaction of matter and energy. Like Raman spectroscopy, infrared spectroscopy (IR) is also a vibrational/rotational spectroscopy (i.e., it involves quantum vibrational transitions in molecules). Many electron spectroscopies (e.g., Auger, XPS, EELS) require the use of an ultrahigh-vacuum chamber and therefore are not useful for *in situ* electrochemical studies. Raman spectroscopy, which is a nonlinear optical technique, produces small signals. This fact becomes important in the study of thin films.

The process of elastic light scattering was observed many years prior to the discovery of Raman scattering. Rayleigh scattering (named after Lord Rayleigh, who successfully explained the phenomena using classical electrodynamics, equation 7.8 [H2]) is a process wherein light interacts with particles whose sizes are much smaller than the wavelength of light. Rayleigh scattering always accompanies Raman scattering [H3]. However, elastic scattering of radiation can also

occur as a result of the interaction of light with larger centers (i.e., by geometrical scattering). This type of scattering can be quite intense. For particles of intermediate size, the scattering mechanism is not well understood. We encountered the problem in Chapter 7. For *in situ* electrochemical surface Raman spectroscopy, the level of elastic light scattering is largely determined by the roughness of the surface and the presence of insoluble particles in the electrolyte. Rayleigh scattering intensities are on the order of 10^{-3} of the incident radiation, and Raman scattering intensities are about 10^{-6} of the Rayleigh scattering intensities.

Other forms of light scattering exist. Scattering with a change in energy associated with interatomic Doppler effects was predicted by Brillouin in 1922 [H4] and observed by Gross in 1930 [H5]. Brillouin scattering (as the effect is now called) gives rise to very small energy changes (on the order of 0.1 cm^{-1} at ambient conditions). Brillouin scattering can only be detected using an extremely high-resolution instrument.

The discovery of "surface enhanced" Raman scattering in 1974 by Fleischmann *et al.* [H6] made it possible to perform *in situ* studies of monolayer films on silver. By roughening the surface of silver in alkaline media by a series of oxidation and reduction cycles, Raman scattering from the first few monolayers of an adsorbed material on the surface is greatly enhanced (scattering cross sections are reported to increase as much as 10^6). A large number of papers using the enhancement effect have been published concerning the electrochemical behavior of various chemical adsorbates on silver, though the phenomenon itself is not well understood. This fact makes the interpretation of the Raman spectra difficult.

More recently, reports of Raman enhancement on copper [H8,H9,H11,H15], gold [H10-H12], and platinum [H13,H14] have been presented, though the level of enhancement is significantly less than that of Ag [H7]. Raman scattering from thin films (more than a few monolayers in thickness) do not exhibit enhancement, and therefore the issue of small signal again becomes important. Recently, the unenhanced detection of monolayers of N_2 on Ag in UHV has been reported [H16] using a very sensitive instrument [H17].

In this chapter we first present some basic principles of Raman scattering. Next, we discuss the design of our Raman instrument for the *in situ* detection of thin oxide films. We then present and interpret our Raman data taken during the anodic film formation of Ag, Cu, and Zn. A more in-depth discussion of the optical theory for Raman scattering [e.g., H3,H18] or laboratory techniques for collecting Raman spectra [H19,H20] can be found elsewhere.

Section 8.2: Principles of Raman Spectroscopy

8.2.1 Electromagnetic Waves

The magnitude of an electric field E_x traveling in free space in the z direction and polarized in the x direction is given by

$$E_x = E_{xo} \cos[\omega(\frac{z}{c}+t)+\theta_x] \ , \qquad 8.1$$

where E_{xo} is the amplitude of E_x, ω is the angular frequency, t is the time, z is the displacement along the z-axis, c is the velocity of light, and θ_x is the phase

angle. This equation can be simplified when spatial (z) and phase (θ_x) information are not important.

A complex exponential notation is often used as an alternative to equation 8.1. At a fixed position in space, equation 8.1 can be expressed as

$$E_x = \text{Re}\, E_{xo} e^{i(\omega t + \theta_x)} \quad , \qquad 8.2$$

where the symbol Re indicates that we are interested only in the real part of the expression that follows. The choice of i rather than -i is arbitrary and differs from the convention of whether movement in the positive z direction corresponds to moving forward or backward in time. The symbol Re is often omitted when it is obvious that only the real component of the expression is of interest. Some important operations are considerably easier to perform when using the complex notation. A phase shift of 90° is equivalent to multiplying the expression by -i. Also, differentiation of the equation in exponential form is considerably easier than in the trigonometric form. By defining the useful "k" wavevector as

$$\vec{k} = \frac{\omega}{c} \quad , \qquad 8.3$$

where it is understood that the vector points in the direction of propagation, equation 8.1 becomes, in complex notation,

$$E_x = E_{xo} e^{i(kz + \omega t)} \quad . \qquad 8.4$$

States other than linear polarization exist. By superimposing two orthogonal

states of linear polarization, all states of elliptical polarization can be obtained. These two linear states can be represented as

$$E_x = E_{xo}e^{i(kz+\omega t)} \qquad 8.5$$

and

$$E_y = E_{yo}e^{i(kz+\omega t+\theta_y)} \ . \qquad 8.6$$

In the expression above, θ_x is arbitrarily set to zero. These equations can be combined so that the electric field can be given in a single expression as

$$\vec{E} = \vec{E}_o e^{i(kz+\omega t)} \ . \qquad 8.7$$

with

$$\vec{E}_o = E_{xo}\vec{x}+E_{yo}e^{i\theta}\vec{y}. \qquad 8.8$$

$\vec{E}_o$ is a complex vector that contains the relative phase angle of the two orthogonal components of the wave. The complete state of polarization can be characterized by using the Stokes parameters [H3,H22,H23].

The time-averaged energy density ρ_{total} of a polarized electromagnetic wave is given by [H3,H22]

$$\rho_{total} = \frac{1}{2}\epsilon_o E_{xo}^2 = \frac{1}{2}\mu_o H_{yo}^2 \ , \qquad 8.9$$

$$\rho_{total}/J{\cdot}m^{-3} = 4.427x10^{-12}(E_{xo}/V{\cdot}m^{-1})^2 \ , \qquad 8.10$$

where ϵ_o is the permittivity of free space. The total amount of energy passing through a unit surface area perpendicular to the propagation direction in one second (irradiance) can be found by multiplying the energy density by the velocity of light (i.e., speed of propagation). The irradiance is a flux density of energy and, for example, has units of W/m^2:

$$I = \frac{1}{2} c\epsilon_o E_{xo}^2 \ , \qquad 8.11$$

$$I(W/m^2) = 1.327 \times 10^{-3} (E_{xo}/V \cdot m^{-1})^2 \ . \qquad 8.12$$

The total irradiance of the sun on the earth's surface is about 1.4×10^3 W/m^2. A medium-power CW gas laser emits 1 W of power in a nondiverging monochromatic beam with a cross section of about 10^{-5} m^2. This corresponds to an irradiance of 10^5 W/m^2. By focusing the beam, powers of 10^8 to 10^9 W/m^2 can be obtained. Focused pulsed lasers can achieve irradiance of 10^{17} W/m^2, and at these fluxes, atoms can be ionized. Other important relationships include

$$\omega = 2\pi\nu \ , \qquad 8.13$$

where ν is the frequency (units of sec^{-1}), and

$$\lambda\nu = c \ , \qquad 8.14$$

where λ is the wavelength. The wavenumber $\hat{\nu}$ associated with a wave is defined as

$$\hat{\nu} = \lambda^{-1} \quad . \tag{8.15}$$

The magnetic field associated with the electric field is perpendicular to the electric field vector, and when the E field is polarized in the x direction, is given by

$$H_y = H_{yo}\cos[\omega(t+\frac{z}{c})+\theta_y] \quad . \tag{8.16}$$

The ratio of the electric field strength to the magnetic field strength in vacuum is a constant and is referred to as the impedance of free space:

$$\frac{E_x}{H_y} = \mu_o c = 377 \text{ ohm} \quad . \tag{8.17}$$

In equation 8.17, μ_o is the permeability of free space.

8.2.2 Sources of Electromagnetic Radiation

Electromagnetic radiation emanates from oscillating electric dipoles, quadrupoles, and magnetic multipoles. The scattered intensity from an oscillating dipole is generally much greater than from other sources and is of primary interest when discussing Raman and Rayleigh scattering. Consider a polarized wave traveling though some material in the z direction. The oscillating electric field can induce dipoles in the material. In the simplest case, where the material is isotropic and is struck by a monochromatic linearly polarized beam, the molecule will be polarized only in the direction of the incident beam's polarization (see Figure 8-1). The polarization will then be given by

$$\vec{P} = \alpha\vec{E} \ , \qquad 8.18$$

where $\vec{P}$ is the polarization and α is the scalar polarizability. The far-field solution for the intensity of the scattered light due to the induced field is

$$I_s = \frac{\alpha^2 E_o^2 \sin^2\theta}{2\epsilon_o^2 \lambda^4 r^2} \ , \qquad 8.19$$

where θ is the angle between the observation point and the plane of polarization (Figure 8-1). There is no scattering in the direction of the beam's polarization, $\theta = 0$. A maximum in scattered light is observed at $\theta = 90°$. The intensity falls off with the square of the distance from the source (r), and depends on the fourth power of the incident beam's wavelength. The wavelength of the scattered radiation is unchanged.

8.2.3 A Classical Theory of Raman Scattering

Some aspects of Raman scattering can be understood using a purely classical model, while others can not (e.g., rotational Raman spectra). Despite its limitation, the classical model is useful because (1) the mathematics are considerably easier and (2) it can led to a more intuitive understanding of the phenomenon than a quantum-mechanical treatment. Generally, even when the classical treatment is not quantitatively correct, the fundamental parametrical dependencies are correct [H4].

The polarization of a material can be represented by

$$\vec{P} = \alpha \cdot \vec{E} + \text{higher-order terms} \quad . \qquad 8.20$$

Since the directions of the incident electric field and the induced dipole are not always the same, in general α is a second-rank tensor. Raman frequencies generated by the interaction of light with higher-order terms (nonlinear hyperpolarizability terms) give rise to hyper-Raman scattering. When higher-order terms are not important (typically for electric fields smaller than 10^{10} V·m^{-1}) [H4], equation 8.20 can be written as

$$\begin{pmatrix} P_x \\ P_y \\ P_z \end{pmatrix} = \begin{pmatrix} \alpha_{xx} & \alpha_{xy} & \alpha_{xz} \\ \alpha_{yx} & \alpha_{yy} & \alpha_{yz} \\ \alpha_{zx} & \alpha_{zy} & \alpha_{zz} \end{pmatrix} \begin{pmatrix} E_x \\ E_y \\ E_z \end{pmatrix} = \mathbf{a}_k \begin{pmatrix} E_x \\ E_y \\ E_z \end{pmatrix} \quad . \qquad 8.21$$

The polarizability tensor for materials that absorb light can be both complex and nonsymmetrical. Near an absorption band (generally due to the presence of a fundamental electron oscillation frequency), the phenomenon of resonance Raman enhancement can occur.

The polarizability of a molecule is a function of intramolecular position (i.e., nuclear coordinates), and therefore is a function of the phase (time) for a particular vibrational mode. A schematic of this principle is shown in Figure 8-2. We can express each component of the polarizability tensor α_{ij} as

$$\alpha_{ij} = (\alpha_{ij})_o + \sum_k \left(\frac{\partial \alpha_{ij}}{\partial Q_k} \right)_o Q_k + \dots \quad , \qquad 8.22$$

where $(\alpha_{ij})_o$ is the polarizability in the equilibrium (pure kinetic energy) configuration, and Q_k is a "coordinate" within the cycle for the normal

vibrational mode of the molecules associated with the vibrational frequency ω_k. The time-dependent polarizability can be expressed as

$$(\alpha_{ij})_k = (\alpha_{ij})_o + (\alpha_{ij}')_k Q_k \ , \qquad 8.23$$

where

$$(\alpha_{ij}')_k = \left(\frac{\partial \alpha_{ij}}{\partial Q_k}\right)_o \ . \qquad 8.24$$

Equation 8.24 is actually a set of equations representing the polarizability tensor $\mathbf{a}_k$, which we write as

$$\mathbf{a}_k = \begin{pmatrix} (\alpha_{xx})_o & (\alpha_{xy})_o & (\alpha_{xz})_o \\ (\alpha_{yx})_o & (\alpha_{yy})_o & (\alpha_{yz})_o \\ (\alpha_{zx}) & (\alpha_{zy})_o & (\alpha_{zz})_o \end{pmatrix} + \begin{pmatrix} (\alpha_{xx}')_o & (\alpha_{xy}')_o & (\alpha_{xz}')_o \\ (\alpha_{yx}')_o & (\alpha_{yy}')_o & (\alpha_{yz}')_o \\ (\alpha_{zx}') & (\alpha_{zy}')_o & (\alpha_{zz}')_o \end{pmatrix} \left(Q_k\right) \ . \qquad 8.25$$

To simplify our notation, we give the name $\mathbf{a}_k'$ to the second matrix on the right. If we assume that the molecular (or symmetry group) oscillation of the kth normal mode is harmonic, the time dependence of Q_k is given by

$$Q_k = Q_{ko}\cos(\omega_k t + \delta_k) \ , \qquad 8.26$$

where Q_{ko} is the normal coordinate vibrational amplitude, ω_k is the frequency of the molecular oscillation, and δ_k is a phase factor. If a molecular system interacts with an oscillating electric field of angular frequency ω_o, the time-dependent linear induced dipole vector $\vec{P}_1$ is

$$\vec{P}_1 = \mathbf{a}_k \cdot \vec{E}_o \cos\omega_o t \ . \qquad 8.27$$

By combining equations 8.25 through 8.27 we arrive at an equation for the time dependent polarization vector:

$$\vec{P}_1 = \mathbf{a}_o \cdot \vec{E}_o \cos(\omega_o t) + \mathbf{a}_k' \cdot \vec{E}_o Q_{ko} \cos(\omega_o t) \cos(w_k t + \delta_k) \ . \qquad 8.28$$

Using a trigonometric identity

$$\cos\alpha \cos\beta = \frac{1}{2}\Big(\cos(\alpha+\beta) + \cos(\alpha-\beta)\Big) \ , \qquad 8.29$$

Equation 8.28 becomes

$$\vec{P}_1 = \mathbf{a}_o \cdot \vec{E}_o \cos(\omega_o t) + \frac{1}{2} Q_{ko} \mathbf{a}_k' \cdot \vec{E}_o \cos(\omega_o - \omega_k) + \frac{1}{2} Q_{ko} \mathbf{a}_k' \cdot \vec{E}_o \cos(\omega_o + \omega_k) \ . \qquad 8.30$$

This expression makes it clear that, for a material to be Raman active, at least one component of the derivative polarizability tensor must be nonzero (for IR activity, a component of the derivative dipole-moment tensor must be nonzero). An example of the determination of Raman and IR activity for a triatomic CO_2-type molecule is shown in Figure 8-3.

One problem with the classical treatment can be seen at this point: it does not predict the significant difference between Stokes and anti-Stokes scattering intensities. This is because the relative density of atoms in the "normal" modes is not uniform but depends on the energy of the given state from which the transition is occurring. The intensity dependence of Raman bands can be predicted by introducing a Boltzmann distribution factor.

If we assume that $\mathbf{a}_k'$ is a scalar (denoted by α'), then the intensity of Raman scattered light will be given by

$$I_{Stokes,k} = \frac{(Q_{ko}\alpha' \; E_o(\omega_o-\omega_k)^2 \sin\theta)^2}{64\pi^4 c^4 \epsilon^2 \lambda r^2} \qquad 8.31$$

and

$$I_{anti-Stokes,k} = \frac{(Q_{ko}\alpha' \; E_o(\omega_o+\omega_k)^2 \sin\theta)^2}{64\pi^4 c^4 \epsilon^2 \lambda r^2} \; , \qquad 8.32$$

where $I_{Stokes,k}$ and $I_{anti-Stokes,k}$ are the Raman Stokes and anti-Stokes scattering intensities from the kth vibrational frequency. In this case the scattered beam will be polarized in the x direction (direction of incident polarization, see Figure 8-4). However, when cross-polarization terms are nonzero, the scattered beam will be depolarized: the ratio of the intensities of the scattered light parallel to and perpendicular to the direction of incident polarization is called the depolarization ratio. This quantity is important in assigning vibration frequencies to their respective modes of vibration.

As mentioned before, one can determine only average polarization properties for molecules that are free to rotate (e.g., in gases and liquids). For solids, the assembly of molecules is essentially fixed in space. By making a series of depolarization measurements along different crystalline axes, one can determine the relative magnitude of all components of the derivative polarizability tensor and therefore assign vibrational modes. An example of this process is given by Long [H4]. The quantum mechanical treatment of Raman scattering from crystals has

been presented by Cowley [H21].

Section 8.3: Raman Equipment Design and Operation

There are five basic components essential to a laser Raman spectrometer suited for *in situ* electrochemical studies:

1) a laser light source,
2) a laser focusing system,
3) an optical electrochemical cell,
4) a monochromator, and
5) a signal detector and processing system.

When one is putting a Raman spectrometer together, a large number of design choices that need to be made. In what follows, the various components of the instrument and the constraints that led us to our particular design are discussed. A photograph of the instrument is shown in Figure 8-5.

8.3.1 Argon-Ion Laser

C. V. Raman discovered the Raman effect using the sun as a light source [H1]. Later, Hg arc lamps were used as monochromatic light sources to illuminate a sample. However, the discovery and commercial introduction of lasers have made collecting Raman spectra considerably easier. Lasers emit intense, monochromatic beams. Since first-order Raman scattering is proportional to the incident-light intensity, signal strengths can be greatly increased by

using a laser. Multiphoton-phonon interactions are even more sensitive to incident intensity.

A Lexel model 75.2 argon-ion laser used previously in our laboratory was used in this study. Argon-ion lasers have a number of lines (ranging in wavelength from 457.9 to 528.7 nm); the most intense of these are the 488.0 and 514.5 nm lines. The output power from our laser, as determined by a Coherent model 2000 power meter, has decreased approximately 36% since its first use (e.g., the 488 nm line intensity has decreased from 150 mW to 96 mW over six years). In order to maintain or improve our signal-to-noise ratio, this unit will need to be repaired or replaced soon.

Other types of visible-frequency lasers include the He-Ne laser (single line at 632.8 nm) and the Kr-ion laser (647.1 and 676.4 nm). At present it is necessary to use a dye laser to obtain laser light in the 530 to 630 nm wavelength range. Equation 8.31 shows that Raman scattering is proportional to the inverse fourth order of the incident-beam wavelength. Based on this consideration, irradiation with an equally powerful Ar-ion 488 nm line rather than the 514.5 nm line will result in almost a 20% increase in scattering intensity. On the other hand, when enhancement is important, the simple fourth-order wavelength dependency is no longer valid. Resonance enhancement can occur when the energy of the incident radiation is close to a fundamental transition in a material (absorption band). The cross section for scattering greatly increases in the vicinity of the absorption band. To make use of this type of enhancement, one would need to "tune" the laser to the frequency of the absorption.

Though a complete understanding of the mechanism of surface-enhanced Raman scattering (SERS) is not yet available, an experimental determination of the wavelength dependence of SERS for silver [H24] and copper [H25] has been reported. The SERS scattering from a monolayer of pyridine on silver is five times greater at 647 nm than at 488 nm. SERS is generally seen on roughened surfaces at wavelengths for which the imaginary component of the dielectric constant is small [H26]. For copper, the imaginary component of the dielectric constant is small only for wavelengths larger than about 580 nm. It is therefore necessary to use laser sources with a longer wavelengths to obtain SERS on copper (e.g., Kr-ion laser).

8.3.2 Laser Focusing System

In order for the Raman scattered light to be dispersed in the monochromator, the light must be focused at the entrance slit (100 μm in size). The f-number of our ISA HR 320 single monochromator is 5. To maximize our collection efficiency, a 3x magnification f/1.4 35-mm camera lens was used.

When using this lens, the laser-focused spot size had to be 33.3 μm (i.e., 1/3 of 100 μm) so that all the scattered light collected by the lens would be focused at the monochromator slit. Though geometrical optics treats the focus as a point, electromagnetic theory shows that focusing a Gaussian light beam is limited by diffraction. Therefore, this "point" actually has a finite size. In the focal region the beam is constricted to a cone called the "beam waist." The diameter of the beam waist (d_o) is given by

$$d_o = \frac{2f\lambda}{d} \quad , \qquad 8.33$$

where f is the focal length and d is the diameter of the lens [H27]. The length of the beam waist is generally at least three times the focal diameter. Since f/d is the f number of the lens, one can see that a small f-number lens will yield a small spot size. Using the above equation, we find that a lens with an f number of 26.3 can focus a beam to a spot size of 33.3 μm. A lens with this or a smaller f number will meet the criterion.

By using a smaller f-number lens, one can create a much finer beam waist, thereby increasing the power density unnecessarily. This high power density can led to difficulties if the material under investigation is photoactive. Small f-number lenses have a short focal length. Since locations near the surface are not accessible (we are restricted by the electrochemical cell, thereby making it necessary to place the lens outside the cell), a compromise was made. We chose to use an f/10 focusing lens (1 inch diameter, 10-inch focal length). The measured beam waist using this lens was 45 μm. We believe that this larger-than-theoretical value is due largely to lens aberrations.

In the above calculation, we have assumed that light completely fills the focusing lens. Since the beam exiting the laser is only about 2 mm in diameter, an f/2, 2-inch-diameter lens was used to expand the beam over a distance of 1.4 m.

It is possible to focus the laser beam using a cylindrical lens. When this is done, a focused line rather than a point is produced. This line can then be

imaged on the monochromator slit. By using a cylindrical lens, the power at the electrode surface can be greatly reduced (by a factor of about 1000), but the alignment of the optics is considerably more difficult.

Lasers are known to emit light at frequencies other than their fundamental lasing frequencies by the depopulation of the excited ions to lower electronic states (i.e., via nonstimulated emission). A list of wavelengths for the plasma lines for various lasers is given by Strommen and Nakamoto [H19]. Table 8-1 shows the wavelength, relative power, and difference in wavenumber from the Ar-ion 488 and 514.5 nm lines (i.e., apparent Raman shifts). Though the intensities of the plasma lines are many orders of magnitude smaller than the intensity of the laser lines, they can be as bright as typical Raman lines. It is therefore necessary to remove plasma lines from the illuminating light so that (1) they are not confused with Raman lines and (2) the signal-to-noise ratio of the results is not diminished. The plasma lines are removed by using a band-pass filter for the 488 or 514.5 nm lines (band width 10 nm, 10^{-6} rejection outside of band, 55% transmission), which is placed behind the laser focusing lens. Since plasma-line frequencies are fundamental, they can be used for the calibration of the instrument (see monochromator calibration below).

8.3.3 Electrochemical Cell

The optimal angles of incidence and collection of Raman scattered light for monolayer films have been investigated both theoretically [H28] and experimentally [H29]. For thicker films, interference phenomena can become important.

Intensity calculations have been presented for the effects of thickness, angle of incidence, angle of collection, and polarization [H30]; a clear and concise presentation of this information will be published [H31]. The results of these calculations show that the optimal angle of incidence is around 70° from the surface normal and that the optimal collection angle is about 60° from the surface normal in the plane perpendicular to the plane of incidence. Our cell was designed accordingly.

A photograph of the Raman electrochemical cell is shown in Figure 8-6. The cell is made of Teflon, which, as noted before, is chemically inert and seals well. The laser beam enters the bottom of the cell through a small (0.5 inch diameter) window and strikes the surface at about 70°. Geometrically reflected light exits the cell through a similar window symmetrically located at the top of the cell. Two larger (2 inch diameter) windows are located on the sides of the cell. One of these windows is used to optically align the cell, and the other allows the camera lens to collect the scattered light at 60° from the surface normal.

The standard-sized electrodes (see Chapter 6) are mounted in their holders and inserted though an opening in the back of the cell. Also, a fitting for the injection of the electrolyte is located in the back of the cell. The PTFE top for the cell holds the Pt screen counter electrode and Hg/HgO reference electrode in place and minimizes the uptake of O_2 into the purged electrolyte.

For Raman studies of liquids, a rectangular cuvette with a mounting holder was used (Figure 8-7). For maximum collection efficiency when studying gases or liquids, the plane determined by the laser-beam path and polarization should be normal to the direction of scattered light collection (cf. discussion of polarization

of Raman scattering and Figure 8-1).

8.3.4 The Monochromator and Optical Filters

An ISA HR-320 single monochromator was used in this study. The aperture of the instrument is f/5.0, which we matched with our scattered light focusing lens. Usually, a 100 μm slit and a 1200 groove/mm holographic grating were used, which yield a manufacturer's specified resolution of 0.4 Å (approximately equal to 1.7 cm^{-1}). The dispersion of light using this setup is 25 Å/mm, which is equivalent to about 2.6 cm^{-1} between neighboring channels on the intensified photodiode array. (Each channel is separated by 25 μm.) Therefore, the resolution of the instrument is limited by the resolution of the diode array and not by the dispersion of the monochromator. By changing the diffraction grating, the resolution and spectral range of the instrument can be altered, as shown in Table 8-2.

As mentioned above, Raman scattering intensities are about 6 orders of magnitude smaller than the Rayleigh scattered intensity (referred to as the "Rayleigh line"). Although the Rayleigh line is not imaged on the detector, the scattering of light inside the monochromator can overpower the Raman signal. In the past investigators have used a series of monochromators (e.g., double and triple monochromators), which have apertures between each dispersion stage. These instruments are able to removed the scattering from the Rayleigh line from the rest of the spectrum, but operate at a lower overall transmission efficiency. In this investigation, we remove the Rayleigh scattered light before it entered the mono-

chromator using various multilayer optical filters (Omega Corporation). All of these filters have a transmittance of less than 10^{-6} at the Rayleigh line (either 488 or 514.5 nm) and a maximum transmittance of about 70% inside their transmission band.

The spectral dependence of the filters' transmittance was determined using a Optronic Laboratory model 245A 45-Watt quartz-halogen tungsten coiled-coil filament standard lamp powered by a HP model 6023A DC power supply. The lamp was placed at the focal point of the collection lens and turned on. A spectrum was taken with and without the filter in front of the monochromator. (A convenient slide-in filter holder was made.) A background spectrum was also taken. Figure 8-8 is a plot of the transmittance of some filters we used with 488 nm sample illumination. The shapes of the curves are complex as a result of the interference between the various layers in the filter. Table 8.3 gives some data pertaining to the filter presently used in our laboratory. A correction to the observed Raman spectrum was made by dividing the background-corrected spectrum by the filter fractional transmittance.

8.3.5 Intensified Photodiode Array Detector

A 1024-channel PAR model 1420 intensified photodiode array (IPDA) was used as a detector for this system. This device was controlled by a PAR model 1463 detector controller board, which is part of our PAR optical multichannel analyzer (OMA III) unit. The optically active area is divided into 1024 individual channels separated by about 25 μm (total detector length is therefore

approximately 2.5 cm) and are each 2.5 mm in width. The IPDA consists of a photocathode, a microchannel plate intensifier, a phosphor screen, and a silicon photodiode array. Photons that strike the photocathode (the quantum efficiency of this process is about 11%) can eject an electron, which is then accelerated through the microchannel plate. The excited (accelerated) electrons strike the phosphor screen, causing light to be emitted near the photodiode array. The microchannel plate intensifier coupled with the phosphor screen results in an amplification of around 5000. The absorption of light by the silicon photodiode array (PDA) creates an electron/hole pair that discharges the capacitor in the diode array, thereby draining the device. The quantum efficiency of the absorption of light in the PDA is about 70%. After a variable time period, the diodes are "read" by measuring the charge necessary to fully recharge the capacitor. This charge measurement is amplified, converted to a voltage, digitized, and fed to the computer.

The resolution of an IPDA is determined by the "blooming" on the phosphor screen as well as by the width of the individual diodes (see discussion on monochromator resolution). The frequency width at half-maximum reading (FWHM) for the device is about three diodes (75 μm), which is equivalent to 7.8 cm^{-1} when using the 1200 g/mm grating.

A number of factors contribute to the "background" noise associated with this detector; these factors tend to reduce the signal-to-noise ratio of the data. They are (1) readout noise, (2) dark current noise, and (3) background noise. Readout noise (N_{ro}) is associated with the amplifying and transferring of a small

electronic signal. This type of noise is not statistical, since it adds a single contribution every time the detector channels are read. An exact value is difficult to determine, but 1-2 counts per reading can be reasonably assumed. Dark-current noise (N_{dc}) is associated with the leakage current across the charged capacitor. This type of noise is statistical and can be expressed as

$$N_{dc} = \frac{\sqrt{I_{dc}t/q}}{\Theta} \quad , \qquad 8.34$$

where I_{dc} is the discharge dark current (typically $3x10^{-13}$ A at -20 C), t is the integration time, q is the charge of an electron, and Θ is the number of electrons per count (which depends on the readout electronics: typically 1000). Using these values for I_{dc} and Θ, N_{dc} is approximately given by

$$N_{dc} = \sqrt{2t} \quad . \qquad 8.35$$

What we call "background noise" includes thermal emissions and high-energy particle noise. Thermal-emission noise can be reduced by cooling the detector. High-energy particle noise depends only on the time of integration. We can therefore express the background noise (N_{bg}) as

$$N_{bg} = \sqrt{(A_t+A_{hep})t} \quad , \qquad 8.36$$

with A_t as the (temperature dependent) thermal-emission noise and A_{hep} the high energy particle noise. The effect of temperature on the number total background counts for a one second integration on our detector is shown in Figure 8-9A.

There is a large decrease in thermal-dependent background with temperature down to about -20° C, after which changes in temperature appear to have a minimal effect. The detector readout counts appear to approach 180 counts at zero time. By subtracting two -30° C background scans, we find that the noise is not 13 counts (i.e., the square root of 180) but about 1-2 counts. This indicates that the limiting value of 180 counts at these low temperatures is not a statistical noise but rather a readout offset. This is made clear in Figure 8-9B, where the total dark counts are plotted as a function of time for a number of temperatures. While the background increases linearly with time, all of the curves intercept the y axis at about 180 counts. This value should therefore be subtracted from the total background signal when assessing the thermal contribution to the noise (see Figure 8-10). The total signal s (in counts per second) is proportional to the time of exposure, so the signal-to-noise ratio (SNR) for this type of device is given by

$$\mathrm{SNR} = \frac{s\,t}{2+\sqrt{(A_t+A_{hep})t+\frac{I_{dc}t/q}{\Theta^2}}} \quad . \qquad 8.37$$

At -30° C, the total time-dependent background noise of our detector is about 28 counts/sec. This yields a time-dependent SNR of

$$\mathrm{SNR} = \frac{s\,t}{2+\sqrt{28t}} \quad . \qquad 8.38$$

A plot of the SNR versus integration time, assuming 1 count/sec of signal at various temperatures, is shown in Figure 8-11. Actual SNR can be obtained from

this plot by multiplying the SNR for 1 count/sec by the actual signal. We have estimated the SNR values for the detector at –40° C based on an extrapolation of the data from Figure 8-10. It should be noted that actual single-reading integration time is limited by the maximum A/D converted count limit (16,000 counts for our instrument). The maximum integration time increases rapidly as the dark current decreases (see Table 8.4).

The relatively new photon-counting image-acquisition system (PIAS) produced by Hamamastsu Corporation has some characteristics that make it superior for collecting very weak Raman signals. The PIAS consists of a photocathode, three microchannel plate intensifiers that work in tandem, and a silicon position-sensitive detector (PSD). Photons that strike the photocathode can eject an electron (QE = 11%) that is accelerated to the microchannel plates with a 10^7 amplification. The electrons strike the PSD, where an additional 100x amplification takes place. The PSD is a square silicon surface with electrodes at its four sides. The magnitude of the current at each of the four electrodes depends on the incident position of the electron. The total magnitude of the currents from the four electrodes depends on the source of the current (whether it originated from the microchannel plates or from a photoelectron) and can be used to discriminate and reject spurious signals. This allows the discrimination of high-energy particles (e.g., x-rays or gamma rays). When this device is compared with the IPDA, it can be seen that the PIAS system is superior when background noise is a problem.

Section 8.4: Calibration

The monochromator was calibrated using Ar-ion plasma lines as reference frequencies. Table 8-1 shows the wavelength, relative power, and difference in wavenumber from the Ar-ion 488 and 514.5 nm lines (i.e., the apparent Raman shifts from these lines). The procedure we used for calibration is as follows:

1) Remove the plasma-line filter from the Raman focusing optical system.

2) Turn the manual monochromator knob to the desired value. The reading on the dial gives an approximate setting in nanometers. When using the 1200 g/mm grating, the reading is given directly in nanometers. When using the 600 or 2400 g/mm gratings, the reading is either 2x or 1/2x the actual setting, respectively.

3) Align the instrument using a rough sample (i.e., one that scatters well).

4) De-tune the laser (thereby removing the laser frequency).

It is not necessary to have the Rayleigh line filters in place when calibrating the instrument since the intensity of the plasma lines is small. The description of the software-driven calibration program for the OMA can be found elsewhere [H32]. The program fits the standard-line data to a best-fit linear or cubic curve. An Ar-ion plasma-line spectrum calibrated for shift with respect to the 488 nm line is shown in Figure 8-12.

The first test of the integrated instrument was an attempt to gather the Raman spectrum of oxygen in air. The instrument was calibrated using the 2400 g/mm grating. Figure 8-13 shows the rotation-vibration spectrum of oxygen we obtained with a 15-minute exposure time and about 90 mW of power. These data were used in an evaluation of the relative sensitivity of the PIAS vs IPDA systems [H17]. The figure shows the ν_1 purely vibrational transition of O_2 at 1558 cm^{-1}. Stokes and anti-Stokes ν_1 rotational transitions can be seen in more detail in Figure 8-13B. Vibrational and rotational constants derived from the data are consistent with those in the literature ($\omega_e = 1580.36$, $\omega_e\chi_e = 12.07$, $B_e = 1.446$ [H18]). The selection rules for rotational Raman spectra allow only $\Delta J = +/- 2$ transitions. This makes the observed spacing between rotational lines equal to $4B_e$. However, for homonuclear diatomic molecules (e.g., O_2, Cl_2, H_2) symmetric to antisymmetric transitions are forbidden (see Reference H18, p. 130 and discussion of nuclear spin), and therefore every second rotational Raman line is missing. Therefore, the spacing of rotational lines in the Raman spectrum of homonuclear diatomic molecules is equal to $8B_e$, which we observed for oxygen.

Section 8.5: Anodic Oxidation of Silver

8.5.1 Introduction

Raman spectroscopy studies of the anodic oxidation of silver in 0.1M KOH [H26] and in 1M NaOH [H33] have shown that the monovalent oxidation product (Ag_2O) is transformed to AgO under illumination. Ag_2O has been reported to be

a weak Raman scatterer. Kotz and Yeager [H33] suggested that Ag_2O may decompose to silver metal under strong illumination. Since Ag_2O has a cubic structure (oxygen atoms are at sites of inversion in the lattice), first-order Raman scattering from Ag_2O should be forbidden. Hamilton et al. [H26] suggested that the rate of AgO photochemical generation is greater than the rate of reduction of the species and that reduction of AgO is hindered by illumination. They found that reduction of the photoelectrochemically formed AgO occurs at a potential more than 300 mV cathodic of the reduction of bulk Ag_2O.

The objective of our Raman study of Ag oxidation in 1M KOH was to (1) confirm the results of Kotz and Yeager, (2) investigate the effects of illumination on the rate of oxidation and reduction of the oxide layer, and (3) test the suggestion of Hamilton *et al.* that there is a competitive oxidation/reduction processes involved in the photochemical generation of AgO (hereafter referred to as the Hamilton hypothesis).

8.5.2 Potential Sweep Experiments

Silver (111) crystals were placed in our Raman cell and subjected to a series of anodic and cathodic linear potential sweeps. The cycling was then halted, and the potential was held at -200 mV vs Hg/HgO. Inspection of the electrode showed that the surface was quite rough, making the alignment of the electrode in our Raman apparatus simple. During the experiment, the potential was increased at 10 mV/sec to a potential of 700 mV (anodic sweep). This peak potential is anodic of the Ag_2O-to-AgO dark-transformation reaction. After the

anodic peak potential was reached, the direction of the potential sweep was reversed (cathodic sweep), and once the electrode potential reached -200 mV, the cell was set to open circuit. The voltammogram for this experiment is shown in Figure 8-14A. It is well known that the oxidation of silver in 1M KOH is highly reversible, and so we expect the surface to be oxide-free at -200 mV. However, the Raman spectrum of the surface at potentials cathodic of the formation of Ag_2O ($<$ 275 mV) show a large level of "white" background scattering. The level of this background scattering is about 10 times greater than that observed from film-free copper and zinc surfaces. We believe that this observation results from the surface-enhanced Raman scattering (SERS) of water and KOH (i.e., SERS scattering of water and OH^- located near the surface of the roughened silver electrode). This finding is consistent with the conclusion of Iwasaki *et al.* [H34], whose Raman results also showed a large background SERS signal in this potential regime.

Figure 8-15 shows Raman spectra from silver in 1M KOH at several potentials during the potential-sweep experiment. The exposure time for each spectrum in the figures is 10 seconds, and therefore there is a 100 mV span in potential per scan. Near the onset of Ag_2O formation ($>$250 mV), the level of background scattering decreases and a peak is observed at around 430 cm^{-1} (not shown). This peak has been associated with the presence of AgO [H26,H33,H34,H36]. The broad band centered at 275 cm^{-1} evident in the spectra of Figure 8-15 may be an aberration introduced by the division of the observed spectra by the filter transmission efficiency. The broad band at 635 cm^{-1} is

definitely due to this effect. As the potential is increased further (up to 350 mV), the background scattering intensity continues to decrease and the 430 cm^{-1} peak grows. For potentials anodic of 350 mV, there is a slight increase in background scattering without a change in the size of the 430 cm^{-1} peak. During the cathodic sweep, the 430 cm^{-1} peak disappears at around 50 mV, accompanied by an increase in background scattering. The disappearance of the 430 cm^{-1} peak at this potential coincides with the Ag_2O voltammetric reduction wave. This finding is contrary to the finding of Hamilton *et al.* [H26] (who saw AgO reduction 300 mV cathodic of the Ag_2O reduction wave) and may be attributed to the lower solution pH used in their study. The large increase in background scattering after the reduction of the surface oxides can be attributed to the re-established conditions necessary for SERS (i.e., a bare, microrough silver surface).

The integrated intensity of the 430 cm^{-1} peak as a function of potential is shown in Figure 8-14B. Negative values are arbitrarily used for the intensity of the cathodic potential sweep to make the figure more readable. During the anodic sweep, the size of the 430 cm^{-1} peak does not change above 300 mV, despite the fact that current continues to flow. Also, the size of the peak is invariant during the cathodic sweep down to a potential of 50 mV. Both Kotz and Yeager [H33] and Iwasaki *et al.* [H36] have reported that the 430 cm^{-1} scattering intensity reaches a maximum with increasing thickness at around 20 monolayers. Since their films were too thin to exhibit interference effects in the Raman spectra (the first maximum should occur at a thickness of around 1/4 the wavelength of light [H31]), this maximum is most certainly due to the competing

effects of a diminishing SERS signal and a nonenhanced signal that increases with film thickness. When the film is thicker than the penetration depth of the light (about 400 nm), there should be little change in the peak size with thickness. In our experiment, the film rapidly reaches such a thickness. At higher potentials, increases in thickness had no effect on the intensity of the scattered radiation because scattering occurred only from the top layer of the film.

By varying the voltammetric sweep rate and turnaround potential, we hoped to determine if the reduction potential of photoelectrochemically formed AgO is linked to the reduction of Ag_2O, as indicated above. Only one experiment is discussed here; it is representative of the conclusions that can be drawn from several experiments of this type. Starting at a potential of -200 mV, the potential was swept at 1 mV/sec to 400 mV and then swept in the reverse direction to -200 mV. (The voltammogram is shown in Figure 8-16.) Note that 400 mV is cathodic of the Ag_2O-to-AgO transformation and is near the maximum in the Ag_2O A3 oxidation wave. The C2 peak (reduction of Ag_2O to Ag metal) in Figure 8-16 is located at 200 mV (cf. Figure 8-14A, where the C2 peak is located at 75 mV). The exposure time for each spectrum was 25 seconds (i.e., a 25 mV span per spectrum). At potentials below the formation of Ag_2O, a large SERS background is present. Near the A2 potential (300 mV), a slight change can be observed around 430 cm^{-1}. A band at 430 cm^{-1} appears in the spectrum at 312.5 mV along with a sharp decrease in SERS scattering. Further increases in potential result in further decreases in the SERS background intensity and the continued presence of the AgO 430 cm^{-1} band (Figure 8-17). The signal-to-noise ratio in

these spectra are better than those taken in the 10 mV/sec experiment, and therefore a broad band at 485 cm^{-1}, also associated with AgO, is observed. Reference spectra of Hamilton *et al.*[H26] at 469 and 493 cm^{-1}. Results of other authors are of lower resolution and show this band simply as a shoulder of the 430 cm^{-1} peak. Comparison of the spectra with the voltammogram demonstrates that the appearance and disappearance of the 430 cm^{-1} peak corresponds to the onset of Ag_2O oxidation and its complete reduction. Again, this result is contrary to the data reported by Hamilton *et al.* [H26]. As with the 10 mV/sec experiment, the Raman-peak size does not change during the anodic sweep despite the fact that current continues to flow.

Iwasaki et al. [H34] reported SERS bands at 330, 470, and 860 cm^{-1}, and by correlating these bands with data reported for EELS, SERS from UHV evaporated films, and IR spectroscopy, assigned them to various vibrations of adsorbed oxygen species on silver. They concluded that oxygen and OH^- were being adsorbed on a roughened silver surface during the early stages of oxidation. This conclusion is consistent with our previous ellipsometric results [H35]. However, inspection of their data shows that the spectral features that the authors designate as peaks are questionable. In addition, the correlation of the energy of these bands with those derived using other techniques is quite poor. Inspection of our spectra taken as the potential was decreased after the surface oxide was reduced shows little change with potential. A comparison of SERS spectra over a wide potential range (-800 to +200 mV) is shown in Figure 8-18. There is no difference in these spectra. Therefore, while we believe that oxygen may be

adsorbed at potentials below that of bulk oxidation, the SERS data presented to date do not give any clear evidence of this.

8.5.3 Silver Photochemical Transformations

Experiments were preformed to investigate the rate of the photoelectrochemical transformation of AgO to Ag_2O and vice versa. We believed that we might test the Hamilton hypothesis [H26] by searching for a critical illumination below which the rate of AgO electrochemical reduction exceeds the rate of photoelectrochemical production. AgO was first formed by sweeping the potential at 10 mV/sec to a potential of 500 mV, after which the potential was held at this value. The surface was then illuminated with the laser at time zero, and a sequence of Raman spectra was taken. Figure 8-19 shows spectra taken at various times using a laser power of 60 mW. The data have been digitally smoothed and have not been corrected for the transmission efficiency of the Rayleigh line filters so as to minimize the noise. An increase in the size of the 430 cm^{-1} band with time later levels off and reaches a constant value. The time dependence of the integrated AgO band intensity for both a 60 and a 90 mW experiment can be found in Figure 8-20. This result demonstrates that the transformation reaction of Ag_2O to AgO occurs rapidly (within 15 seconds) and is not a strong function of laser power.

For weak illumination (less than 30 mW), the AgO Raman signal was too small to be detected despite an increase in exposure time. This result may indicate that there is a threshold power density for the Ag_2O/AgO transformation as

discussed above, but the result could also be due to a diminishing signal to noise ratio. Therefore, we suggest that these results neither support nor reject the Hamilton hypothesis.

In an attempt to further test the Hamilton hypothesis and get around the possible signal-to-noise problem discussed above, another type of experiment was performed. A surface was oxidized while under illumination by sweeping the potential at 10 mV/sec to 500 mV, and then reversing the sweep direction. When the potential reached 250 mV, it was held at this value. This potential is about 150 mV cathodic of the AgO voltammetry reduction peak but is still 50 mV anodic of Ag_2O reduction. As expected, Raman spectra taken at this potential showed a time-invariant AgO 430 cm^{-1} peak. The laser was then shut off for various lengths of time, after which it was turned on again, and a sequence of Raman spectra was collected to determine whether AgO is reformed (from electrochemically reduced photoelectrochemically formed AgO). All our results showed that there was very little reduction of the layer during the off period. Figure 8-21B shows a sequence of spectra taken after the laser was turned off for over one hour, and the time dependence of the integrated 430 cm^{-1} peak is shown in Figure 8-21A. Unlike the oxidation of virgin Ag_2O, where we observed the change in spectra associated with a photo-oxidation process (Figure 8-20), there is no change in the Raman spectra when the illumination is halted. This result shows that AgO produced under illumination is more difficult to reduce than AgO electrochemically formed in the dark, and therefore there is a chemical or structural difference between the compound, formed in the two manners. We

propose that the chemical pathway for reduction is changed due to this chemical or structural alteration, making the reduction occur preferentially via a soluble monovalent intermediate, thereby linking the reduction to the Ag_2O/Ag reaction potential.

Section 8.6: Anodic Oxidation of Copper

8.6.1 Introduction

An *in situ* Raman spectroscopy study of the electrochemical oxidation of Cu in 0.1M NaOH has previously been reported [H26]. The investigators used cyclic and potentiostatic voltammetry. The major findings of that work were as follows:

1) During a voltammetric sweep (1 mV/sec) Cu_2O was detected at potentials higher than the A2 (divalent oxidation) peak.

2) A Cu_2O Raman band was observed at potentials as high as 1 V anodic of the A1 (monovalent oxidation) voltammetry peak.

3) At a potential slightly below oxygen evolution, scattering from Cu_2O diminishes and a broad (300 cm^{-1}) band centered at 500 cm^{-1} is seen. This band was tentatively assigned to a hydrated or polymeric form of $Cu(OH)_2$.

4) During a voltammetric cathodic sweep, this broad band disappears and the Cu_2O band reappears (with a small intensity) at a potential just cathodic of

oxygen evolution. The size of the Cu_2O band increases greatly at around 0 mV vs SCE.

5) Complete reduction of the Cu_2O layer occurs at -700 mV vs SCE.

6) Based on the parabolic dependence of the integrated charge with time following a potential step, film growth was proposed to be diffusion-controlled.

7) Detection of Cu_2O by Raman spectroscopy was suggested to be resonance-enhanced.

8) Discrepancies between voltammetric and spectroscopic observations were attributed to nucleation and kinetic effects.

We felt that Raman spectroscopy could be useful in addressing some of the many unanswered questions concerning the copper system in alkaline media. The objectives of this portion of our study were to investigate (1) the formation and transformation of the anodic copper film in 1M KOH, (2) illumination effects on these processes, and (3) the reason for the differences between the voltammetric and spectroscopic results presented above.

8.6.2 Copper Oxide Reference Spectra

The Raman spectra of reagent grade Cu_2O, CuO, and $Cu(OH)_2$ powders were obtained in air and in 1M KOH. The powders were compressed in a die, and the resulting pellets were imbedded in an epoxy mold. Figures 8-22, 8-23, and 8-24 show the Raman spectra of compressed Cu_2O, CuO and $Cu(OH)_2$

powders, respectively, taken in air, and are similar to those reported by Hamilton et al. [H26]. Whereas the large cross section for scattering from Cu_2O and $Cu(OH)_2$ makes their detection relatively easy, Raman scattering from CuO, which is a weak scatterer, was difficult to observe. As noted in the Chapter 1 of this dissertation, Cu_2O exhibits an interband transition near 2.1 eV [H37], as well as some fine structure in the absorption spectrum due to the presence of exciton electron-hole pairing. The proximity of an interband transition to the excitation wavelength, as well as the relative stability of excitons, can result in a large resonance enhancement. $Cu(OH)_2$ has an absorption edge in the visible region, and this may cause it to exhibit resonance Raman enhancement. The location of the major scattering peaks observed from the powdered samples is given in Table 8-5.

Theoretically, Cu_2O should have three acoustic and 15 optical branches. Data compiled in Reference H33 gives nine Raman active modes, despite the fact that only the Γ_{25^-} modes should be optically active in a perfect crystal. It has been suggested for Cu_2O that the observation of these other modes arises from crystal defects [H37]. The location of these peaks at ambient conditions, along with a comparison of their location with those observed in the powder, is shown in Table 8-6. With the exception of the 297 and 634 cm^{-1} bands, all the others are not fundamental frequencies and are most likely due to multiple phonon/photon combinations. In Table 8-6 some suggestion for possible multiple phonon/photon scattering combinations that may account for the other peaks in the Cu_2O powder standard spectrum have been given.

8.6.3 Effect of Illumination on Raman Standards

Hamilton *et al.* [H26] reported that it was necessary to reduce the laser power to below 60 mW in order to obtain a $Cu(OH)_2$ spectrum. They believed that at higher powers, laser-induced thermal conversion of the sample to CuO and water occurred (due to the low thermal conductivity of the powder sample). Figure 8-25 shows the time dependence of the 488 cm^{-1} $Cu(OH)_2$ peak of a compressed powder in air (90 mW total power). The intensity decreases to one-half of its initial value within 100 seconds. The agreement of these results with those of Hamilton *et al.* demonstrates the potential of the conversion process to hamper the interpretation of our *in situ* spectra. However, it seems possible that the local heating would be reduced by the higher thermal conductivity in water. The time-dependent spectrum from the $Cu(OH)_2$ compressed-powder pellet in a 1M KOH solution is shown in Figure 8-26A. When immersed in the aqueous solution, the rate of change of the peak intensity was considerably smaller (only about 2% per 100 seconds). This result supports the proposition that decomposition of the hydroxide is caused by thermal decomposition.

Integration times of 100 seconds or more were necessary in our experiments and, therefore, a decrease in peak intensity of even 2% might be significant. Since electrochemically formed $Cu(OH)_2$ has a metal electrode acting as a heat sink, the rate of thermal decomposition might be reduced further. To test this idea, the Raman spectrum of a copper sample oxidized for 100 seconds at 200 mV vs Hg/HgO was observed in air. The 488 cm^{-1} $Cu(OH)_2$ peak intensity as a function of time is shown in Figure 8-26B. The intensity does not change at all with

time, and therefore the presence of the metal electrode alone should be sufficient to diminish the photothermal dehydration of the hydroxide.

8.6.4 Potential-Sweep Experiments

Cyclic voltammetry experiments were performed at 0.5, 1, and 10 mV/sec. In each case the sweep was begun at a potential cathodic of all the copper oxidation reactions. Unless otherwise stated, the data have been corrected for background scattering (in which we include scattering from the electrolyte) by subtracting the spectrum taken at a film-free potential from all subsequent spectra.

8.6.4.1 Cyclic Voltammetry:

A 10 mV/sec cyclic voltammogram of Cu in 1M KOH shows the first anodic current peak (A1) located at -400 mV (Figure 8-27). The second peak (A2), around -25 mV, may actually be two separate overlapping peaks, since it has a shoulder near -150 mV. Very little current passes at potentials beyond the A2 peak (out to 600 mV). On the reverse sweep, the small C2 cathodic peak is seen at -500 mV. The complex C1 peak has a shoulder at -800 mV, and a maximum at -1000 mV.

In our 10 mV/sec experiments, each scan was averaged from data taken from twenty-five 10 second exposures, each at the same potential. The time averaging yielded a good signal-to-noise ratio but made it impossible to determine spectral changes between cycles (since any hysteresis effects were being averaged). At the time that the Raman data corresponding to the above voltammetry were taken, we did not have an optical filter with an operative "window" allowing

both the Cu_2O 633 cm^{-1} and the $Cu(OH)_2$ 488 cm^{-1} peaks to be observed simultaneously. Therefore, the experiment was conducted twice, using two different filters, and the two spectra were connected at 600 cm^{-1}.

At potentials cathodic of the A1 peak, the observed spectra are similar to that of a 1M KOH solution (see section 8.7.2) and change very little up to -250 mV. In Figure 8-27B the integrated intensity of both the 633 cm^{-1} and 488 cm^{-1} peaks as a function of potential are given. At -250 mV, a band at 633 cm^{-1} associated with the formation of Cu_2O is observed. All the peaks observed in the reference spectra can be seen at this potential (297, 411, 492, 633 and 786 cm^{-1}), though there is a high level of background scattering accompanying the data. The identification of cuprous oxide at a potential only 150 mV anodic of the A1 peak is in sharp contrast to the results obtained at a lower pH [H26] (see section 8.1). Up to 150 mV, the major Cu_2O peak continues to grow and is accompanied by an increasing level of background scattering. A 488 cm^{-1} $Cu(OH)_2$ peak begins to form around -150 mV, as well as a minor band centered near 300 cm^{-1} (Figure 8-28A). Increasing the potential further to 600 mV results in a decrease in the background scattering level and Cu_2O peak intensity (Figure 8-28B). The changes in the background scattering are most likely due to scattering from the small crystals formed during the early stages of $Cu(OH)_2$ formation. Long-range translational symmetry is not present in smaller crystals, and many normally inactive Raman modes can be observed due to the breakdown of selection rules [H38]. Because of the large surface-to-volume ratio, surface vibrational modes will be more prevalent. Both of these phenomena will tend to increase the overall

level of background scattering.

When the potential is decreased during the cathodic sweep from 600 to 250 mV, the size of the 633 cm^{-1} band remains constant (Figure 8-29A). Below this value its size increases, a finding is qualitatively consistent with the data of Hamilton *et al.* [H26], who also reported an increase at a potential anodic of any significant voltammetric reduction current. The Cu_2O band increases up to a potential of 0 mV and then remains constant to a potential of around -650 mV. $Cu(OH)_2$ is reduced at around -850 mV, and Cu_2O near -1000 mV. (The spectra are shown in Figure 8-29B.) $Cu(OH)_2$ is reduced at the shoulder in the C1 wave and Cu_2O at the C1 peak potential.

No appearent film reduction/transformation processes appears to be connected with the C2 peak. Since the peak is too small and accounts for only a fraction of the total charge stored in the film, it may be difficult to detect changes associated with the process. A photoelectrochemical effect may also shift the potential(s) of the associated reaction(s).

Since both Cu_2O and $Cu(OH)_2$ show a minor band around 300 cm^{-1} in the reference spectra, the appearence of this peak in the *in situ* spectra could arise from the presence of either (or both) of these compounds. A plot of the integrated intensity of this peak with respect to potential shows that the band is correlated more strongly with cupric hydroxide than cuprous oxide (Figure 8-30). The band appears and grows at a potential coincident with the 488 cm^{-1} hydroxide band, and, unlike the band of cuprous oxide, its size does not decrease beyond

the A2 peak. During the cathodic sweep the peak dissappears at a potential between the reduction of the two compounds indicated above (-850 mV). Since the 300 cm^{-1} peak is significantly smaller than either the 488 or 633 cm^{-1} peak, the noise level in the integrated intensity is large and makes further interpretation unwarranted.

One of the interesting aspects of these observations is the change in the relative monovalent-to-divalent peak intensities at potentials where little current is observed. For example, during the anodic sweep, the cuprous oxide peak intensity diminishes beyond the A2 potential. If a photoelectrochemical process does occur, it is unlikely that we would observe the associated photocurrent because the fraction of the electrode that is illuminated is small (10^{-5}), and therefore the total current observed is overwhelmingly dark current. If a photochemical process either causes a new reaction to occur or shifts the potential of an existing reaction, we don't expect to observe the associated current for such a process.

To differentiate between the time versus potential dependence of the monovalent/divalent transformation process, an experiment similar to the one discussed above was run with the potential held for 100 seconds at the maximum anodic value (600 mV) before reversing the direction of the sweep. The potential and integrated peak intensities as a function of time are shown in Figure 8-31. These results are consistent with those discussed above up to the point where the experiments are no longer similar (i.e., potentiostatic phase), indicating good reproducibility of the results. As before, anodic of the A2 peak potential the cuprous oxide band diminishes without a corresponding increase in the cupric

hydroxide band. When the potential is held at 600 mV, the cuprous oxide peak continues to decrease in size and eventually disappears completely (see Figure 8-32A). During the cathodic sweep (after the potential arrest), the size of this peak increases with decreasing potential (Figure 8-32B). The peak size increases rapidly around +100 mV and reaches a maximum at -150 mV. Cathodic of this value, the size of the band begins to decrease and completely vanishes around -950 mV.

8.6.4.2 Interpretation of Integrated Peak Height

How do we interpret the changes in spectral peak size with potential? One should always practice caution when interpreting the size of a Raman band: it is not generally proportional to the amount of material present at a surface. There are two major reasons for this. First, planar films can exhibit interference effects, causing the Raman-scattered intensity to go through a series of maxima and minima with increasing thickness [H31]. Since our SEM data show that the hydroxide is composed of fine needle-like crystals that tend to scatter light (as shown by our elastic scattering measurements), this film will not give rise to interference effects. Though the initial Cu_2O layer exists as a homogeneous planar film, the thickness of the layer is too thin to cause major deviations from a linear approximation (cf. section 9.3, ellipsometry of copper and Reference H31). The second reason for a deviation from linearity harder to ignore: when the thickness of the film exceeds the penetration depth of the light, further increases in film thickness will not cause a corresponding change in peak intensity. The

hydroxide film could possibly reach such a thickness.

Our data show that at potentials near the A2 peak, both Cu_2O and $Cu(OH)_2$ are present at the electrode surface, but the distribution of the compounds (within the film) is unknown. If the materials are dispersed evenly, a linear relation between the amount of material and the band intensity should be valid. On the other hand, if the film has a laminated structure (one film on top of the other), the penetration of light into and from the underlayer will be diminished by the presence of the overlayer. Since cuprous oxide is the sole reaction product at lower potentials, we might suppose that it is still present at the metal/film interface at higher potentials. Our elastic scattering measurements have shown that the cuprous oxide film begins to roughen due to a local reaction of the film at potentials slightly cathodic of the A2 peak. The buildup of divalent soluble species will eventually supersaturate the interfacial region, resulting in hydroxide precipitation. The growth of this film could lead to a diminished level of scattering from the underlayer of cuprous oxide due to the limited depth of light penetration. However, for this hypothesis to be true, the hydroxide peak should increase in size at the same time that the cuprous oxide peak decreases, a result that was not observed. Futhermore, since no charge is passed at potentials anodic of the A2 voltammetry peak (where the cuprous oxide band is seen to decrease in size), we suggest that Cu_2O may be transformed to CuO via a photoassisted process. This idea is supported by our x-ray diffraction measurement (see Chapter 10).

The transformation of Cu_2O to CuO and vice versa is likely to be a solid-state process (due to the compact structure of cuprous oxide layer), and therefore it should occur more slowly than the dissolution/precipitation formation of the hydroxide. This could account for the fairly high potential at which the proposed transformation occurs. However, the reappearance of the Cu_2O band at a potential anodic of the thermodynamic potential of the Cu_2O/CuO redox couple suggests that the reaction is shifted anodically by several hundred millivolts under illumination. This hypothesis would explain why Cu_2O is reformed at potentials anodic of both dark divalent redox reactions. The potential shift may arise from the absorption of light in the CuO layer (CuO is black), increasing the local temperature at the surface. Furthermore, the fact that the Cu_2O band can be greater on the cathodic sweep than the anodic sweep may result from the chemical decomposition of cupric hydroxide to the more stable oxide, which can then be reduced to Cu_2O.

8.6.4.3 Cyclic Voltammetry: 6M KOH, 10 mV/sec

The contrast of our pH 14 Raman/voltammetry data with those of others obtained in pH 13 solutions is intriguing. The overall oxidation reactions presented in Chapter 1 are second order in OH^- for all the Cu oxide products (see Figure 1-3), and therefore the thermodynamic potential differences between these species are unaltered by changes in pH. Therefore, the spectral differences with pH must be attributed largely to kinetic phenomena. The appearance of the 488 cm^{-1} $Cu(OH)_2$ peak in our spectra (and its absence at lower pH) shows that

the kinetics of hydroxide formation becomes increasingly favored with increasing alkalinity. The fact that the Cu_2O band disappears from the spectra at lower potentials (and at a greater rate at a higher pH) could be due to an increased rate of the solid-state reaction of a cuprous oxide underlayer to form CuO (as discussed above). If the hydroxide ion is a reactant of an elementary rate-determining step for any of the oxide products, the rate of product formation should increase about ten fold with an increase in pH from 13 to 14 (assuming the reaction is first order in $[OH^-]$). A dissolution/precipitation reaction path will become increasingly favored as a result of the increasing solubility of $Cu(OH)_2$ with pH.

To test these fundamental ideas, we performed a few cyclic voltammetry experiments in 6 M KOH solution (pH 14.8), similar to the one discussed above. Figure 8-33A shows the voltammetry at this higher pH. Note that the A2 peak is three times as large and the A1 peak five times as large as was observed at pH 14. The shoulder in the A2 peak, observed at pH 14, is no longer evident. There is no change in anodic peak positions. The small cathodic C2 peak position is unaltered, and its size has increased five fold. The C1 peak has shifted cathodically about 200 mV, and the structure of the peak is now made up of two distinct current waves. Another peak, at -1100 mV, is observed, which was not seen at the lower hydroxide concentration.

The integrated Cu_2O and $Cu(OH)_2$ Raman peak intensities as a function of potential are shown in Figure 8-33B. Spectra at selected potentials are shown in Figures 8-34 through 8-36. The signal-to-noise ratio in these data is much better

than at pH 14. Since the total integrated anodic charge in the 6M KOH voltammogram is larger than that at 1M KOH, this would indicate that the films may be considerably thicker. The integrated cuprous oxide peak intensity versus potential follows a trend similar to that observed in 1M KOH, but there are some subtle differences. During the anodic sweep, the appearance of the 633 cm^{-1} peak occurs close to the A1 voltammetry peak, a shift of about 100 mV cathodic of its 1M KOH values to -350 mV (see Figure 8-34). Around 250 mV the cuprous oxide band reaches a local maximum intensity (cf. 150 mV at pH 14); above this potential the peak size appears to fall more rapidly than at pH 14 (Figure 8-35A). Note that the relative Cu_2O-to-$Cu(OH)_2$ integrated intensity is significantly greater in this experiment, which could be due to either a greater dissolution of the divalent product or an increased rate of Cu_2O growth at higher pH. During the cathodic sweep, the Cu_2O peak intensity starts growing at -250 mV (100 mV anodic of the result in 1M KOH), continues increasing down to -550 mV (Figure 8-35B), and then falls as the oxide is reduced (Figure 8-36). The separate reduction of the two compounds is clearly seen in this last figure.

The 488 cm^{-1} peak intensity also shows some significant differences from the lower pH results. In addition to the smaller $Cu_2O/Cu(OH)_2$ peak size, a shift in the potential of formation (-250 mV) and reduction (-550 mV) is observed. The relative difference between these two values (300 mV) is considerably less than in 1M KOH (600 mV), showing an increase in the reversibility of the reactions with increasing pH.

The last result is intriguing. Since the voltammetry results don't indicate any dependence of the potentials of reduction with pH, this suggests that a photoassisted reduction occurs whose effect increases with pH. The structure or defect concentration of the cuprous oxide underlayer may be altered significantly to allow for such a difference. The shift in the potential of formation of both compounds at higher pH is in agreement with our suggestion that increases in hydroxide, which is a primary reactant, will increase the rate of film formation and transformation. The lower relative $Cu(OH)_2$ signal could result from the diminished fraction of divalent species present as a $Cu(OH)_2$ film due to the higher solubility of the material at higher pH, or an increased solid-state growth of the Cu_2O underlayer.

8.6.4.4 Cyclic Voltammetry: 1M KOH, 1 mV/sec

The Raman spectra discussed above highlight some of the interesting features about the chemistry of the Cu system in alkaline media. While an understanding of the photoelectrochemical behavior is interesting in and of itself, the effects of illumination on the oxidation and reduction processes can also be used to probe the films' transport properties. The broad band reported by Hamilton *et al.* [H26] (at around 500 cm^{-1}) was not observed in our spectra. Also, the potentials that the Raman bands appear do not coincide with voltammetry peaks. In order to determine the reason for these findings, cyclic voltammetry experiments in 1M KOH at 1 mV/sec were performed (an experiment analogous to the Hamilton experiment but differing in pH). We thought that the potential

lag between the voltammetry peak and the appearence of Raman bands might be due to a slow film nucleation-and-growth process cocurrent with or following an anodic dissolution step. Since the dissolution current would affect the location of the peaks, a slower sweep rate might shift the potential at which Raman bands first appear.

A voltammogram of Cu in 1M KOH using a 1 mV/sec sweep rate is shown in Figure 8-37A. The anodic A1 and A2 peaks are shifted only slightly (to -350 mV and -50 mV, respectively) from the location in the same solution and at 10 mV/sec. In contrast, the C1 peak has moved anodically 325 mV to -675 mV and shows no complex structure. The C2 peak is difficult to see in the figure.

Raman peak intensities versus potential are shown for a 1 mV/sec experiment in Figure 8-37B. As predicted, the 633 cm^{-1} peak of Cu_2O is observed coincident with the A1 peak at slower sweep rates (spectra are shown in Figure 8-38). At -375 mV, where the Raman peak is first observed, the film is only about 50 Å thick. (This value is derived from a comparable ellipsometry experiment discussed in the next chapter.) Further increases in potential cause an increases in the cuprous oxide peak intensity. Eventually, the appearance of the 488 cm^{-1} hydroxide band occurs near the voltammetry A2 peak (around -50 mV; see Figure 8-39A).

As with all our previous results, during the anodic sweep the Cu_2O Raman intensity decreases at potentials anodic of the A2 voltammetry peak. In this case the Raman signal completely disappears from the spectra at potentials anodic of 550 mV. In the 10 mV/sec experiment, this band decreased to only half its

maximum value at this potential (see Figure 8-27B). This comparison can be misleading: when the time for the process to occur is considered, we discover that the average **rate** of film transformation is seven times smaller at the lower sweep rate. Since the peak doesn't disappear at potentials significantly cathodic of that observed at the faster sweep rate, the rate of anodic layer transformation is more strongly dependent on the potential than on time.

This conclusion can also be drawn for the cathodic transformation of the layers (spectra are shown in Figure 8-39B). In the 10 mV/sec experiment, the peak increases about 40% over a range of 200 mV (20 seconds); in the 1 mV/sec experiment, the peak increases from zero to its maximum intensity over a range of 500 mV (500 seconds). The rate of transformation is therefore 10 times larger for the higher sweep rate, indicating potential control of the process.

Whereas the potential controls the rate of the Cu_2O/CuO tranformation reaction, Cu_2O reduction is limited by a time-dependent process (at least when it is illuminated). In Figure 8-39B, the reduction of the cuprous oxide layer is seen to begin around -300 mV (a value actually anodic of the reversible potential for the reaction) and is fully reduced at -750 mV. At 10 mV/sec significant reduction begins at -650 mV and is complete at -1000 mV. Though the rate of reduction is 10 times greater at this higher sweep rate, the driving force for reduction is also larger. It is feasible that the reduction begins to occur at -350 mV (as in the 1 mV/sec results), but that the amount of reduction (due to a much smaller rate at this potential) is too small to be detected in the integrated results. Using the film reduction rate derived from the decrease in Raman peak intensity at 1

mV/sec, we calculated that the peak intensity would decrease only about 5% over the same potential 350 mV range in the 10 mV/sec experiment. Since our noise level is at least 10%, we don't expect to observe this reduction. These arguments lead us to the hypothesis that the reduction of Cu_2O is dependent on both an electron transfer process (potential dependence) and a diffusion processes (time dependence) for time scales of around 1 second.

Based on the proximity of the broad band found in their Raman spectra to that of the 488 cm^{-1} cupric hydroxide peak, Hamilton *et al.* [H26] concluded that a polymeric or hydrated cupric hydroxide compound is formed near the oxygen evolution potential in 0.1 M NaOH. Since we observed the actual hydroxide Raman peak in our spectra at a much lower potential, we wondered if this broad band might also be observed near oxygen evolution at pH 14. Figure 8-40 shows spectra taken at 450 and 650 mV vs Hg/HgO. Oxygen evolution is believed to occur at the latter potential. (A rising current is observed but not the formation of bubbles.) The hydroxide 488 cm^{-1} peak is seen in both spectra, but a broad band, similar to that observed by Hamilton *et al.*, accompanies this peak at the higher potential. Also, the small Cu_2O peak in the spectrum at 450 mV is no longer present at 650 mV. During the cathodic sweep, the broad band completely disappears at 450 mV.

The broad band observed at 550 cm^{-1} and found at potentials far above that of the divalent copper oxidation may not be a divalent oxidation product at all. Our results clearly show that at potentials near the second anodic voltammetric peak, a sharp 488 cm^{-1} $Cu(OH)_2$ band is observed. Miller's ring/disk experiments

demonstrated the existence of a trivalent soluble species in this potential range [H39] (see Chapter 1, Section 9), and therefore we suggest that the appearance of the broad 550 cm^{-1} band may be due to the formation of a trivalent copper surface species. Since the cuprous oxide band has disappeared at this potential (presumably due to the transformation of the layer to CuO by the solid-state process discussed above), we further propose that at the potential where the broad band is observed, the CuO compact layer may be transformed to Cu_2O_3

8.6.4.5 Effect of Illumination on Cu_2O Reduction

The Cu_2O reduction potential under illumination is anodic of any voltammetry reduction peak and becomes increasingly more so as the sweep rate is decreased. In fact, at 1 mV/sec, the oxide reaction appears to occur at a potential anodic of the dark reversible redox potential. To check this finding, a 1 mV/sec potential-sweep experiment was performed in which an anodic reversal potential of -200 mV was used. It was felt that by using this value (which is cathodic of the A2 peak), only cuprous oxide would be formed, thereby freeing the interpretation from the effects of divalent species. The spectra for this experiment are shown in Figure 8-41, which clearly show the formation of cuprous oxide without the presence of hydroxide. The intensity of the Cu_2O band decreases immediately after the change in sweep direction (Figure 8-42) and at a potential comparable to that in the 1 mV/sec sweep-rate experiment discussed above. When the anodic peak potential is below -200 mV, only one reduction wave is observed (at around -575 mV). These Raman results show that, under

illumination, the reduction occurs at potentials close to the anodic reaction potential.

Does the dark reduction wave correspond to the reduction of the Cu_2O film? To answer this question, two experiments were performed in which a Cu_2O film was first formed by sweeping the potential at 1 mV/sec out to -300 mV. The sweep direction was then reversed, and the potential was held constant for 600 seconds once a certain potential was reached (either -500 or -600 mV). Raman spectra were taken continuously during the experiment (100-second exposures). To check if cuprous oxide is present "in the dark" at either of these values, the electrode was displaced vertically upwards (thereby not radically altering the alignment), exposing a previously unilluminated portion of the surface. At the end of the 600-second potential arrest, the cathodic sweep was continued. The electrode was moved halfway (300 seconds) into the potential-arrest phase of the experiment.

Plots of the current, potential, and 633 cm^{-1} Raman peak intensity versus time for each experiment are shown in Figures 8-43A and 8-43B. In both figures, there is a small amount of offsetting cathodic current that we attribute to the reduction of residual dissolved oxygen. Consistent with the result discussed above, the integrated cuprous oxide peak intensity increases at the onset of anodic current and begins to diminish as the sweep direction is reversed. When the potential is held at -500 mV (a value cathodic of the voltammetry reduction wave), the peak intensity continues its decreasing trend during the constant-potential stage (Figure 8-43A). However, when the electrode is moved, the

cuprous oxide peak size increases markedly; later, the signal decreases again. This result clearly shows that, while illuminated cuprous oxide can be reduced at potentials anodic of the voltammetry reduction peak, the film is still present over the unilluminated portion of the electrode. This finding should be contrasted with the results of Figure 8-43B, which shows that when the potential is held at -600 mV (cathodic of the voltammetery reduction wave), the Cu_2O peak size is unchanged after moving the electrode.

8.6.5 Potential-Step Oxidation of Copper in 1M KOH

The intensity of the Raman 633 cm^{-1} cuprous oxide band versus the square root of time following the application of a potential step from -600 to -300 mV is shown in Figure 8-44. The parabolic time dependence is typical for potential-step experiments in the range of -350 to -250 mV vs Hg/HgO. Assuming that the integrated intensity is proportional to the film thickness, this parabolic dependence indicates a diffusion-controlled growth of the oxide layer [H40,H41] and is consistent with our ellipsometry results discussed in the next chapter.

More complicated behavior is observed when the potential is stepped to a value where divalent species are formed. The current transient following the application of a potential step from -600 to -150 mV is shown in Figure 8-45A. The very large initiall current density (upwards of 25 mA/cm^2) decreases rapidly to values on the order of 0.2 mA/cm^2 within 200 seconds. Afterwards, the current decreases slowly.

The associated Raman spectra as a function of time for this experiment are shown in Figure 8-45B. After only 50 seconds (i.e., in the first spectrum shown), the cupric hydroxide peak is clearly seen. The background scattering is large in this first spectrum, and is attributed to the formation of the small crystals (cf. discussion in Section 8.6.4.1). The apparent decrease in the hydroxide-peak intensity in the subsequent spectra is actually only a decrease in the background scattering level. The hydroxide integrated peak intensity as a function of time is given in Figure 8-46A. After what must be a very rapid initial growth period (at less than 50 seconds), the peak intensity grows more slowly (increasing only about 50% in 30 minutes).

The integrated 633 cm^{-1} cuprous oxide peak intensity also shows an approximately linear time dependence. However, it doesn't initially increase as rapidly as the hydroxide does in Figure 8-46A but rather begins at a value near zero (Figure 8-46B). The growth rate of the cuprous oxide intensity is much greater than that of the hydroxide, but it does decrease slightly at much greater times. Since cuprous oxide is not initally present, the large initial current is associated with formation of the hydroxide and soluble divalent copper on an almost cuprous-oxide-free surface. The linear growth of the cuprous oxide layer at higher potentials is consistent with our elastic scattering measurements, which showed that the oxide was dissolving (mostly likely at grain boundaries) to form the soluble divalent species. The growth rate of this now porous layer is controlled by the rate of hydroxide reaction with the metal (kinetic/linear growth) and not the diffusion of hydroxide or metal in a compact layer (parabolic/diffusion growth).

The hydroxide growth is probably subject to the supply of soluble divalent species formed at the surface, which in turn is controlled by the competing rate of cuprous oxide formation and dissolution.

8.6.6 Soluble Copper Species

After about 50 oxidation and reduction cycles, the electrolyte is seen to change color, becoming blue. The fact that the color is much deeper in the 6M than in the 1M electrolyte is consistent with the trend of solubility of cupric hydroxide. In an attempt to identify the soluble species and its properties both voltammetry and Raman spectroscopy were performed on the spent solution.

After the solution was thoughly deoxygenated, it was placed in a cell containing two Pt electrode plates. The potential was then swept cathodically at 10 mV/sec from its initial open-circuit potential (50 mV vs Hg/HgO). The voltammogram shows a broad shoulder at -450 mV and a peak at -625 mV (Figure 8-47). After the potential reached -850 mV, the cell was set to open circuit. After about three minutes, a steady open-circuit potential of about -480 mV was observed. If the solution was saturated with a species originating from cupric hydroxide, it should be reduced 60 mV cathodic of the equalibrium value (E_o=-364 mV). Though the current shoulder occurs at around this potential, the peak current is much closer to that for cuprous oxide reduction.

The Raman spectrum of the spent solution shows a single Raman band at about 1125 cm^{-1} (Figure 8-48). This relatively large vibrational energy indicates that the soluble complex ligand bonding is strong. If there is only one Raman

active vibrational mode, then the molecule is most likely structurally simple. If the soluble species is CuO_2^{-2}, as some have suggested (see Chapter 1), then this molecule may have a linear structure similar to CO_2. Molecules of this symmetry group have only one Raman active mode (and two IR active modes). For comparison, the vibrational frequency of the CO_2 Raman active symetric streching mode is 1340 cm^{-1}

At present we have no definitive evidence as to the structure or valency of the soluble species observed in alkaline solutions. Though it is possible that a stepwise reduction of the soluble species is occuring and cuprous oxide is formed as an intermediate product, more experiments on the soluble species are needed.

Section 8.7: Anodic Oxidation of Zinc

8.7.1 Introduction

Raman spectroscopy measurements of the soluble zinc species have been conflicting, and whereas it is generally agreed that $Zn(OH)_4^{-2}$ is the only species present at pH $>$ 13, the structure of the compound has been a matter of controversy. Based on the observation of what was believed to be four Raman bands (a polarized 484 cm^{-1} band, and three depolarized bands at 430, 322, and 285 cm^{-1}), the molecule was said to be tetrahedral [H42,H43]. Later investigators found all four bands to be polarized [H44-H46], and stated that the two lower-energy bands may be associated with KOH and not zincate. Sharma [H44,H45] concluded that the soluble species was the linear ZnO_2^{-2} molecule, but Briggs [H46] still main-

tained that it was tetrahedral $Zn(OH)_4^{-2}$.

When we began the zinc-solution portion of our Raman study, the work of Cain *et al.* [H47] had not been published. Their NMR and Raman results clearly show that only the symmetrical tetrahedral $Zn(OH)_2^{-2}$ complex exists in highly alkaline solutions. Though it had been suggested that the complex might polymerize into hydroxy-bridged aggregates in near-saturated and supersaturated solutions [H48,H49], Cain *et al.* [H47] conclude that no truly definitive evidence exists to support this idea. After reviewing the paper of Cain *et al.* and noting that they had performed many of the same measurements we did and that their data agreed with ours, we decided to shift the emphasis of our work to the more subtle issues of (1) the nature of the supersaturated solution and (2) the effects of silicate on the chemistry of the soluble product.

It is generally believed that ZnO forms on zinc anodes at high pH. However, it is still a matter of discussion whether $Zn(OH)_2$ or ZnO constitutes the passive film. Since the solubility of $Zn(OH)_2$ and ZnO are similar in 1M KOH, it is unclear which compound's formation should be favored. Most authors support a dual-layer film model for the structure of the anodic film. This idea (originally proposed by Powers and Breiter [H50]) suggests that a flocculent $Zn(OH)_2$ film (called the type I film) forms on the electrode during active dissolution, followed by a more compact ZnO layer upon passivation. McKubre and MacDonald [H51] have stated that the type I film may be a precursor to the type II layer. Raman/potential-sweep experiments were undertaken to (1) identify the species present in the surface film, (2) determine if chemical transformation of the film

occurs, and (3) determine the processes that accompany the active/passive transition.

8.7.2 Raman Spectra of Zinc Dissolved in Alkali

Raman spectra of distilled water, 30% KOH, and 48% KOH are shown in Figure 8-49. A comparison of these spectra demonstrates that the broad band at low wavenumbers (peak at around 275 cm^{-1}) is associated with the presence of KOH in solution (also see Figure 8-53). This "background" KOH spectrum was either subtracted out improperly in earlier work or not subtracted at all. Background subtraction is considerably easier now that digital data storage is available. When the background scattering is properly removed from a spectrum of saturated zincate solution in 30% KOH, only Raman bands at 425 and 470 cm^{-1} are observed (Figure 8-50). The 470 cm^{-1} band is polarized, and the 425 cm^{-1} band is depolarized, in agreement with Cain *et al.* [H47].

NMR results indicate that the excess zinc present in supersaturated solutions exists as a soluble species rather than in a colloidal form [H49,H50,H53]. To test this idea, a ZnO-saturated 30% KOH solution was prepared. The solution containing solid ZnO was shaken for 10 days to ensure that is was saturated. The solution was then either diluted with 30% KOH or placed in an electrochemical cell where zinc was added by anodic dissolution of the metal. The electrochemical cell consisted of an anode and cathode compartment (50 ml) separated by a glass frit and initially contained a saturated zincate solution. Zinc dissolved from the anode increased the concentration beyond saturation in the anodic chamber while

the cathode chamber was depleted of zinc.

The Raman spectra of zinc solutions of various concentrations are shown in Figure 8-51. The 470 cm^{-1} peak is observed in solutions that are both sub- and supersaturated. The integrated intensity of both the 470 (zincate) and 275 cm^{-1} (hydroxide) bands versus zinc concentration are displayed in Figure 8-52. In making this figure, we used the literature value for the solubility of zinc oxide in 30% KOH (about 4% by weight)[H54], and assumed that the rate of diffusion through the separator was negligible so that the total increase in zincate concentration could be calculated based on the charge passed. Since Figure 8-52 shows the size of the 275 cm^{-1} band to be invariant with concentration, we can conclusively report that this peak is solely attributable to KOH in the solution. The zincate band intensity increases linearly with concentration, even in the supersaturated region. No new Raman bands appear in the spectra in the range from 200 to 1600 cm^{-1} for the supersaturated solutions. These two facts demonstrate that the zincate solution does not form a polymeric ion in supersaturated solutions, as previously suggested.

Since we know that the rate of ZnO growth from a zincate solution is slow and that the zincate ion and its hydration do not change in the supersaturated state, the kinetics of zinc oxide nucleation from zincate ion must be slow. This is not surprising, since the ion is quite complex and (more importantly) in a stable tetrahedral configuration. This rigid methane-like structure tends to limit intramolecular rearrangement because of the spatial separation of the atoms. The overall reaction is complex, since the molecule must be broken into the

several solid and dissolved species:

$$Zn(OH)_4^{-2} \rightarrow ZnO + H_2O + 2OH^- \ . \qquad 8.39$$

The chemical reaction to form ZnO from zincate must certainly involve a number of elementary steps, any one of which could be slow (e.g., reaction of the ion with hydroxide to form water and an energetic trivalent complex). Together, the high solubility and slow precipitation kinetics inhibit film formation from zincate ion and therefore permit large anodic currents.

The effects of silicate as a solubility extender are not well understood. Its presence can retard the precipitation of ZnO from a supersaturated solution and has been used as a solubility extender in pilot alkaline zinc cells [H55-H57]. Raman spectra of distilled water, 30% KOH solution, 2% potassium silicate-30% KOH solution, and a zincate-saturated 30% KOH 2%-potassium silicate solution are shown in Figure 8-53. An increasing level of scattering at wavenumbers less than 250 is present in all the spectra and is associated with the scattering from water. As mentioned above, the broad 275 cm^{-1} band apparent in all KOH-containing spectra is associated with the presence of the hydroxide ion. No new Raman bands appear with the addition of silicate to the electrolyte in the spectral region investigated. The dissolution of ZnO in the electrolyte gives rise to the appearance of the 425 and 470 cm^{-1} bands similar to the non-silicate-containing solutions. This result shows that the tetrahedral zincate ion is still the major species present and that there is no change in its aqueous environment. We conclude that silicate suppresses the precipitation of zincate by an inhibition

of the (already slow) nucleation kinetics rather than by changing the thermodynamics (i.e., structure) of the soluble species.

8.7.3 Zinc Oxide and Hydroxide Reference Spectra

Raman spectra of reagent-grade ZnO powder show a number of bands in the 200-800 cm^{-1} range (see Figure 8-54). Zinc oxide has a hexagonal structure, with C_{6_v} point group symmetry for the unit cell. Members of this symmetry group have six optically active Raman modes [H58]. The location of the powder peak and their vibrational assignments are given in Table 8-7. (Multiphonon assignments were made by this author using first-order phonons reported in reference H55.) The strongest vibration in the powder (by an order of magnitude) is the E_2^2, located at 430 wavenumbers. Using 90 mW of laser power, we observed 3691 counts/sec from this band. Assuming that the region from which scattered light is collected is limited by the collection optics and not limited by the penetration depth of the laser (we assumed a scattering depth of 33μ), we calculated that we should be able to detect a 60 Å-thick film of ZnO with a signal-to-noise ratio of 2 ($T_{detector} = -20°$ C).

Attempts to observe the Raman spectra of reagent-grade ϵ–$Zn(OH)_2$ (Alpha Products) proved unsuccessful. The compound inelastically scatters light primarily by fluorescence. As expected for fluorescence from a colorless compound, the spectrum shows no structure [H59]. The x-ray diffraction pattern of the powder matches that of the JCPDS standards for ϵ–$Zn(OH)_2$ and is presented in Chapter 10. Hugot-Le Goff *et al.* [H60] produced a material that they stated was

$Zn(OH)_2$ (no allotrope given) by the reaction

$$ZnCl_2(aq) + 2\ NaOH(aq) \rightleftarrows Zn(OH)_{2(solid)} + NaCl(aq)\ . \qquad 8.40$$

The Raman spectrum of the compound displayed peaks at 385 and 3450 cm^{-1}. The 385 wavenumber band was assigned to a Zn-O vibration, and the 3450 wavenumber peak is undoubtedly an O-H stretch. Feitnecht [H61] reported that zinc hydroxide can form two stable allotropes in alkaline media. This fact could explain the difference between our results and those of Hugot-Le Goff.

We made a compound by the above reaction. The precipitate is white and exhibits phonons at 385 and 3450 cm^{-1}. However, the x-ray diffraction pattern of the material is not characteristic of the ϵ, γ, or β allotrope of $Zn(OH)_2$ (see Chapter 10). The O-H stretch phonon should be observed in any incompletely dried or hydrated compound. It is therefore probable that the compound produced by the above reaction is not $Zn(OH)_2$.

8.7.4 Potential-Sweep Oxidation of Zinc

Initially, the Raman scattering results from the films that formed during active dissolution of zinc were confusing. Only "white" scattering [which we now attribute to the presence of ϵ–$Zn(OH)_2$] was observed. The recent Raman study of Hugot-Le Goff et al. [H60] does not include results from anodically active surfaces. Spectra taken in air also exhibited fluorescence. However, after we rinsed the surface with distilled water, Raman bands wereobserved at 330(?), 430, 560, and 1080 wavenumbers (see Figure 8-55). While these same peaks are observed

in the powder spectra, the relative size of the 430 to 560 cm^{-1} bands have changed dramatically (by a factor of about 20). Corrosion films made by placing zinc (1100) and (1000) crystals in an oxygen- and zinc-saturated solution followed by rinsing display similar spectra to that shown in Figure 8-54.

Despite the band-size discrepancy, x-ray diffraction data clearly show that the surface layer present after rinsing is composed primarily of ZnO (see Chapter 10, X-Ray Results). X-ray diffraction is sensitive to long-range order while Raman spectra depend strongly on the local order of the molecular point group. Small changes in molecular bonding and/or doping can be observed in a Raman spectrum. Changes in intensity and location of the IR bands in ZnO (including both the E_2^2 430 cm^{-1} and the A_1(LO) 575 cm^{-1} modes) with particle size have been attributed to surface phonons [H62,H63]. A theory to predict these changes has been presented in the literature [H64].

To determine whether the apparent change in the 430/560 peak size ratio could be attributed to crystal-size effects, we separated ZnO powder based on the particle-settling velocity in a column of water. The spectra of all the separation fractions were similar, and therefore we reject crystal-size effects and surface phonons as an explanation for the band-size discrepancy.

Powers and Breiter [H50] stated that passive ZnO is black and attributed its color to an excess of zinc. Hugot-Le Goff *et al.* [H60] have shown that Raman spectra of a zinc metal surface thermally oxidized in air at 380° C exhibits only a broad 560 cm^{-1} band after two days, but that after 18 days a strong 430 cm^{-1} peak is observed. These authors have attributed the 560 cm^{-1} band to

multiphonon scattering and claim that evolution of the spectrum with increased oxidation time is due to improved "crystallinity and the diminution of ZnO structural defects." We believe that more information concerning the relation between ZnO structure and its corresponding Raman spectrum are needed before any further conclusions can be drawn about the chemical makeup of the ZnO layer. We conclude that the fluorescence of the surface in the active dissolution region indicates that the film is mostly ϵ–$Zn(OH)_2$, which may either dehydrate or be dissolved when rinsed, leaving an underlayer of exposed ZnO.

The active-to-passive transition is unmistakable in the voltammetry of the system (Figure 8-56). During an anodic potential sweep at 1 mV/sec, the current initially increases slowly at potentials slightly positive of the reversible values (E_o= -1.38 V vs Hg/HgO). From -1.3 to -1.15 V, the current increases linearly with potential. Beyond this value, the rate of increase in the current decreases. At around -1.02 V the current reaches a maximum value (28 mA/cm^2), beyond which the current falls abruptly to almost zero. Further increases in potential from -1.0 to -0.95 V cause a significant increase in current (to about 6 mA/cm^2), but even at voltages as high as -0.4 V the current never exceeds 6.5 mA/cm^2.

Raman spectra were taken that correspond to the voltammetry shown in Figure 8-55. The exposure time for each spectrum was 100 seconds and therefore represent and average over a 100 mV range. The fluorescence discussed above is observed at potentials from -1.4 to -0.95 V and increases with increasing potential (Figure 8-57). Since the amount of white background scattering levels off at higher potentials (-1.2 to -1.0 V), it appears that its intensity is more closely

related to current than to total charge passed (cf. Figure 8-56). If the film is ϵ–$Zn(OH)_2$, as we have proposed, then this result would suggest that the current in the active region is controlled by the rate of dissolution of the zinc hydroxide film and the diffusion of hydroxide through the film to the metal surface, rather than by the rate of film growth. Also, most of the charge ends up as products in the electrolyte and not in the film. In a pseudo-steady state of the slow potential sweep, the rate of removal of the flocculent $Zn(OH)_2$ layer balances its rate of growth. Increases in potential cause higher IR loss in the film (with a slightly increased oxidation rate).

At potentials above the active/passive transition, the level of background scattering decreases and is accompanied by the appearance of a Raman band centered at 560 cm^{-1} (Figures 8-58A and 8-58B). The decreased background scattering occurs over a fairly large potential range (-1.05 to -0.85 V). This finding indicates that beyond the transition potential, the rate of hydroxide formation is diminished and the layer is slowly dissolved. At even higher potentials (E > -0.85 V), the 560 cm^{-1} band increases in size. McKubre and MacDonald [H51] consider type I (hydroxide) film formation to be a prerequisite for passivation by the type II (ZnO) film. We suggest that the ZnO layer forms at the metal/film interface and grows outward towards the electrolyte. The active/passive transition is induced when the supply of hydroxide to the surface becomes limited so that the less-favored product, ZnO, is formed. Once a ZnO layer is produced (most likely formed by a solid-state mechanism), the surface becomes electrically insulated, and current is effectively shut off.

If potential control is released from a passivated surface, the ZnO band disappears rapidly (Figure 8-58). This demonstrates that, like the zinc hydroxide film, the rate of ZnO growth is matched by its rate of dissolution. Within 10 seconds the potential assumes its equilibrium value. The time for the ZnO film to dissolve is slightly longer (about 50 seconds, Figure 8-59).

To further test some of these ideas, a slower potential-sweep/Raman experiment was performed (0.25 mV/sec, 400 sec/scan exposure). Once the potential reached its peak anodic value (-0.7 V), it was held there (for 4000 seconds) before a cathodic sweep was begun. The Raman results (shown in Figure 8-60) are similar to the 1 mV/sec results, with a rising background-scattering level with increasing potential in the active regime. Near the active/passive transition Raman peaks appear at 560 cm^{-1}, and later at 430 cm^{-1}. The spectra do not change noticeably during the constant-potential phase of the experiment. These results are different from those of Hugot-Le Goff *et al.* [H60], whose potential-step/Raman measurement showed a decrease in the 430 cm^{-1} peak size with increasing potential. It remains unclear whether the potential or the oxidation time more strongly influences the appearance of this peak, since Hugot-Le Goff *et al.* said that the 430 cm^{-1} band slowly evolves at high anodic potentials and at long times.

During the cathodic sweep the spectra are unchanged down to -1.25 V (Figure 8-61), whereupon the intensity of both peaks and the overall background-scattering level decrease. At -1.35 V, no Raman scattering is observed (when corrections for scattering from the electrolyte are made). This finding is also

contrary to earlier reports [H60], in which a noisy spectrum at potentials slightly cathodic of the equilibrium value was said to show the 560 cm^{-1} peak.

Section 8.8: Conclusions

Raman spectroscopy is useful for interfacial studies in aqueous media and is a valuable *in situ* technique for the study of the formation and transformation of anodic silver, copper, and zinc films formed in alkaline media. In IR spectroscopy the vast majority of the incident and reflected energy is absorbed by the electrolyte. The small shift in wavelength associated with the interaction of light with a vibrational phonon allows Raman spectroscopy to be performed totally at visible frequencies and therefore without losses due to absorption. A review of the optical principles of Raman spectroscopy has been used to guide our design of the Raman/electrochemical instrument and to understand our measurements. Details of instrument design, calibration, and performance have been discussed.

Silver surfaces roughened by repetitive oxidation/reduction cycles exhibit surface-enhanced Raman scattering (SERS). Large levels of SERS from water on a silver surface at noble potentials (i.e., free of oxide) is observed. This "background" scattering is greatly diminished when a AgO film is formed. However, we found no SERS evidence to support the idea that oxygen and OH^- are initially adsorbed on a roughened silver surface during the early stages of oxidation.

Strong illumination causes the photoelectrochemical transformation of Ag_2O to AgO at potentials where the monovalent oxide is known to form. Time-dependent photoinduced experiments demonstrate that the Ag_2O/AgO

transformation occurs over 15 seconds and is not a strong function of illumination at the power density we used. We were unable to observe a threshold illumination energy for the process, due to the small signal-to-noise ratio of the data. We have shown that, at potentials well below the equilibrium value for the dark reaction, photoelectrochemically produced AgO is not reduced to Ag_2O when illumination is terminated. This photochemically produced film is chemically or structurally different from electrochemically produced AgO in that its reduction occurs preferentially via a soluble monovalent intermediate.

Reference spectra of CuO, Cu_2O, and $Cu(OH)_2$ have been presented. We have demonstrated that these materials are either stable under laser illumination (CuO and Cu_2O), or that the thermal decomposition of the film is negligible in the presence of an aqueous solution and a metal electrode [$Cu(OH)_2$]. However, the transformation of oxidic layers on copper is influenced by illumination. The process is electrochemical rather than thermal in nature.

At sufficiently slow sweep rates, the formation of cuprous oxide is observed at potentials coincident with the monovalent voltammetric oxidation peak. At higher sweep rates the appearance of the Cu_2O Raman signal is slightly delayed. These results demonstrate a concurrent dissolution process that contributes to the voltammetric current and occurs along with Cu_2O film formation (see also Chapter 9). Potential-step/Raman measurements show that the film growth is parabolic, indicative of a diffusion-controlled process. For higher potential steps, the film growth is linear. Under these conditions, $Cu(OH)_2$ initially forms very rapidly on a cuprous-oxide-free surface, and is correlated with the initial high

current density. Later, the rate of $Cu(OH)_2$ growth is greatly diminished as the cuprous oxide layer forms. The appearance of the Cu_2O film decreases the rate of generation of divalent copper despite the fact that the film is porous.

$Cu(OH)_2$, rather than the more thermodynamically preferred CuO, forms at potentials coincident with the voltammetric divalent oxidation peak (A2). This finding should be contrasted with the results of Hamilton *et al* [H26], who did not observe the formation of the hydroxide in pH 13 solutions. The kinetics of hydroxide formation is favored at higher pH. A large level of white background scattering accompanies the appearance of the hydroxide peak indicating that the film is initially composed of a large number of very small particles. The intensity of the hydroxide band is constant at potentials anodic of the A2 peak and demonstrates that the film does not decompose to CuO over the periods of time of our experiments. The reduction of $Cu(OH)_2$ occurs at increasingly anodic potentials with decreasing sweep rate. In all cases the film is reduced at potentials anodic of the major cathodic reduction peak. The differences between the reduction potential indicated by the Raman results (i.e., under illumination) and that by voltammetry are attributed to a photoenhanced conductivity of the cuprous oxide base layer.

At potentials above the A2 peak, the compact underlayer of cuprous oxide is transformed to CuO. The thermodynamic potential for this reaction is shifted anodically under illumination, since CuO is reduced to Cu_2O at potentials 300 mV anodic of the dark divalent formation reaction. The rate of transformation depends more strongly on the driving potential than on the time for the process

to occur.

Reduction of Cu_2O to copper metal is influenced by illumination. Under strong illumination the oxide is reduced at potentials anodic of the thermodynamic potential. In the dark, the reduction of the film occurs at large overpotentials. The p-type semiconductive oxide acts as a Schottky barrier (i.e., like a diode). Illumination generates charge carriers which minimize the resistance of the layer and allow for its reduction at a more reversible potential. We have shown that the effectiveness of the barrier layer decreases with increasing pH. The rate of Cu_2O reduction is not a strong function of potential and is controlled by both an electron transfer and diffusion process. The presence of the cuprous oxide film is responsible for the large irreversibility of the system.

A broad band observed at 550 cm^{-1} and found near oxygen evolution was previously interpreted as being due to the presence of a hydrated or polymeric form of $Cu(OH)_2$. Our results clearly show the formation of $Cu(OH)_2$ near its thermodynamic potential. Miller's ring/disk experiments demonstrated the existence of a trivalent soluble species in this potential range [H39]. We believe that the appearance of this band is due to the formation of a trivalent copper surface species (possibly Cu_2O_3) via the solid-state transformation of CuO.

Electrochemically generated soluble copper compounds are blue and establish (depending on concentration) an open-circuit potential near 50 mV vs Hg/HgO in 1M KOH. Identification of the soluble species valancy and reduction potential is inconclusive. We were unable to correlate the voltammetry of the solution to that

of bulk metal because both reduction waves are complicated. The Raman spectrum of the solution shows a single vibrational band at 1125 cm^{-1}. This could indicate that the soluble species is a linear CuO_2^{-2} molecule, but more information is needed.

The Raman spectra of sub- and supersaturated zinc solutions in alkaline media exhibit vibrational peaks at 425 cm^{-1} (depolarized) and 470 cm^{-1} (polarized). The intensities of these bands increase linearly with concentration. The broad peak near 275 cm^{-1} is associated with the presence of hydroxide. A careful subtraction of a spectrum of a zinc-free KOH solution from the spectrum of a zincate solution shows that, contrary to earlier reports, no zinc vibrational bands are observed in this spectral range. The major soluble zinc species at all concentrations is the tetrahedral $Zn(OH)_4^{-2}$ ion. The ion does not polymerize or form polynuclear aggregates at higher concentrations. Solutions containing silicate show no new Raman bands, and therefore the $Zn(OH)_4^{-2}$ environment is not radically altered by the presence of silicate. Both of these facts suggest that the relative stability of the supersaturated solution is due to the slow kinetics of ZnO nucleation, with silicate further hindering the process.

A reference spectrum of ZnO powder has been presented along with the assignment of the peaks observed. Attempts to observe the Raman spectrum of ϵ–$Zn(OH)_2$ were unsuccessful because of a large amount of fluorescence. The reaction of $ZnCl_2$ and KOH does not yield $Zn(OH)_2$, as previously suggested [H60]. The conclusions of these authors, that $Zn(OH)_2$ is not present in the anodic films, disagree with the present findings.

The spectrum of anodically polarized active zinc is featureless, displaying a large amount of fluorescence. We attribute this observation to the formation of a flocculent ϵ–$Zn(OH)_2$ film. The level of scattering does not increase with the total charge passed and appears to be proportional to the current. This finding suggests that the current of an active electrode is controlled by the rate of dissolution of the $Zn(OH)_2$ layer and the diffusion of hydroxide through the film. Most of the charge ends up as products in the electrolyte and not in the film.

When an active surface is removed from the electrolyte and rinsed with distilled water, a surface layer of ZnO is formed. The relative peak sizes of the Raman spectrum of this ZnO film are different from those fof the powder. Some authors have said that the passive ZnO film is black due to the presence of excess zinc [H50, H60]. Whereas we have excluded the possibility that the differences in the relative peak size are associated with a crystal-size effect (i.e., surface phonons), more information concerning the relation between ZnO structure and its corresponding Raman spectrum is needed before a definitive explanation can be found.

Above the active/passive transition potential, the level of fluorescence decreases, and a Raman spectrum of ZnO is observed. The spectrum also exhibits peak sizes different from the powder standard. The ZnO layer forms at the metal/film interface and grows outward towards the electrolyte. The active/passive transition is induced by the limited supply of hydroxide to the surface. Once formed, the electrically insulating ZnO film effectively shuts off the current. The smaller passive current does not generate enough zincate to

compensate for the rate of dissolution of $Zn(OH)_2$. The hydroxide layer is therefore removed. As was the case of the $Zn(OH)_2$ layer, the rate of ZnO film growth is matched by its rate of dissolution. The removal of potential control from a passive film causes the rapid dissolution of the ZnO layer. During a cathodic sweep, the film is observed down to -1.35 V and is not present at potentials where cathodic current is passed.

REFERENCES FOR CHAPTER 8

H1) Raman, C. V., and K. S. Krishnan, Nature **121,** 501 (1928).

H2) Rayleigh, J. W. S (Lord), Philos. Mag. **XLI,** 274 (1871).

H3) Long, D. A., **Raman Spectroscopy**, McGraw Hill, New York, 1977.

H4) Brillouin, L., Ann. Phys. (Paris) **88,** 17 (1922).

H5) Gross, E., Z. Physik. **63,** 685 (1930).

H6) Fleischmann, M., P. J. Hendra, and A. J. McQuillan, Chem. Phys. Lett. **26,** 123 (1974).

H7) Creighton, J. A., C. G. Blachford, and M. G. Albrecht, J. Chem. Soc. Faraday Trans. **275,** 790 (1979).

H8) Paul, R. L., A. J. McQuillan, A. J. Hendra, and M. Fleischmann, J. Electroanal. Chem. **66,** 248 (1975).

H9) Fleischmann, M., P. J. Hendra, A. J. McQuillan, R. L. Paul, and E. S. Reid, J. Raman Spectrosc. **4,** 269 (1976).

H10) Wenning, U., B. Pettinger, and H. Wetzel, Chem. Phys. Lett. **70,** 49 (1980).

H11) Pettinger, B., and H. Wetzel, Ber. Bunsenges. Phys. Chem. **85,** 499 (1981).

H12) Loo, B. H., J. Electroanal. Chem. **131,** 381 (1982).

H13) Loo, B. H., Solid State Commun. **42,** 349 (1982).

H14) Loo, B. H., and Y. G. Lee, J. Electroanal. Chem. **163,** 401 (1984).

H15) Irish, D. E., L. Stolberg, and D. W. Shoesmith, Surf. Sci. **158,** 238 (1985).

H16) Veirs, D. K., V. K. F. Chia, and G. M. Rosenblatt, Langmuir **5,** 633 (1989). Lawerence Berkeley LAboratory Report LBL-25758.

H17) Veirs, D. K., V. K. F. Chia, and G. M. Rosenblatt, Appl. Opt. **26,** 3530 (1987).

H18) Herzberg, G., **Spectra of Diatomic Molecules,** 2nd edition, Litton Educational Publishing, New York, 1950.

H19) Strommen, Dennis P., and Kazuo Nakamoto, **Laboratory Raman Spectroscopy**, John Wiley and Sons, New York, 1984.

H20) Grasselli, Jeanette G.. Marcia K. Snavely, and Bernard J. Bulkin, **Chemical Applications of Raman Spectroscopy**, Wiley, New York, 1982.

H21) Cowley, R. A., The Theory of Raman Scattering from Crystals, in **The Raman Effect**, J. Anderson edito, Marcel Dekker, New York, 1971.

H22) Reitz, J. R., R. J. Milford and R. W Christy, **Foundations of Electromagnetic Theory**, 3rd edition, Adisson-Wesley, Menlo Park, CA, 1980.

H23) Jackson, J. D., **Classical Electrodynamics**, 2nd edition, John Wiley, New York, 1975.

H24) Creighton, J. A., M. G. Albrecht, R. E. Hester, and J. A. Mathew, Chem. Phys. Lett. **55,** 55 (1978).

H25) Benner, R. E., J. U. Von Raben, R. Dornhaus, R. K. Chang, B. L. Laube, and F. A. Otter, Surf. Sci. **102,** 7 (1981).

H26) Hamilton, J. C., J.C. Farmer, and R. J. Anderson, J. Electrochem. Soc. **133,** 739 (1986).

H27) Siegman, A. E., **An Introduction to Lasers and Masers**, McGraw-Hill, New York, 1971.

H28) Greenler, Robert G., and T. L. Slaner, Spectrochim. Acta **29A,** 193 (1973).

H29) Mullins, David R., and Alan Campion, J. Phy. Chem. **88,** 8 (1984)

H30) Dilella, D. P., A. Gohin, R. H. Lipson, P. McBreen, and M Moskovits, J. Chem. Phys. **73,** 4282 (1980).

H31) Veirs, D. K., J. Agler, and G. M. Rosenblatt, J. Chem Phys., to be published.

H32) Model 1460 Optical Multichannel Analyzer Preliminary Operating Manual, Revision D. Princeton Applied Research Corp., 1986.

H33) Kotz, R., and E. Yeager, J. Electroanal. Chem. **111,** 105 (1980).

H34) Iwasaki, N., Y. Sasaki, and Y. Nishina, Surf. Sci. **198,** 524 (1988).

H35) Mayer, S. T., and R. H. Muller, J. Electrochem. Soc. **135,** 2133 (1988).

H36) Iwasaki, N., Y. Sasaki, and Y. Nishina, J. Electrochem. Soc. **135,** 2531 (1988).

H37) Landolt and Bornstein, **Numerical Data and Functional Relationships in Science and Technology**, New Series, Group III: Crystals and Solid State Physics. Volume 17, Semiconductors, Subvolume 4. Physics of Non Tetrahedrally Bonded Elements and Binary Compounds I. O Madelung, Editor. Berlin, 1983.

H38) Tuinstra, F., and J. L. Koenig, J. Chem. Phys. **53,** 1126 (1970).

H39) Miller, B., J. Electrochem. Soc. **116,** 1675 (1974).

H40) Fromhold, A. T., Jr., **Theory of Metal Oxidation: Volume 1 and 2.** Elsevier North-Holland, New York, 1976.

H41) DiBenedetto, A. T., **The Structure and Properties of Materials,** McGraw-Hill, 1967.

H42) Lippincott, E. R., J. A. Psellos, and M. C. Tobin, J. Chem. Phys. **20,** 536 (1952).

H43) Fordyce, J. S., and R. L. Baum, J. Chem. Phys. **43,** 843 (1965).

H44) Sharma, S. K., J. Chem. Phys. **58,** 1626 (1973).

H45) Sharma, S. K., and S. C. Kashyap, J. Inorg. Nucl. Chem. **34,** 3623 (1972).

H46) Briggs, A. G., N. A. Hampson and A. Marshall, J. Chem. Soc. Faraday Trans. II **201** 1978 (1974).

H47) Cain, K. J., C. A. Melendres, and V. A. Maroni, J. Electrochem. Soc. **134,** 519 (1987).

H48) Dirkse, T. P., J. Electrochem. Soc. **128,** 1412 (1981).

H49) Van Doorne, W., and T. P. Dirske, J. Electrochem. Soc. **122,** 1 (1975).

H50) Powers, R. W., and M. W. Breiter, J. Electrochem. Soc. **116,** 719 (1969).

H51) McKubre, M. C. H., and D. D. MacDonAld, J. Electrochem. Soc. **128,** 525 (1981).

H52) Briggs, A. G., N. A. Hampson, and A. Marshall, Trans. Faraday Soc. **70,** 1978 (1974).

H53) Newman, G. H., and G. E. Blomgren, J. Chem. Phys. **43,** 2744 (1965).

H54) McBreen, J., and E. J. Cairns. The Zinc Electrode, in **Advances in Electrochemistry and Electrochemial Engineering**, Vol. 11, H. Gerischer

and C. W. Tobias, Editors., Wiley, 1978.

H55) Appleby, A., and M. Jacquier, J. Power Sources **1,** 17 (1977).

H56) P. N. Ross Jr., **Feasibility Study of a New Zinc-Air Battery Concept Using Flowing Alkaline Electrolytes**, Lawerence Berkeley Laboratory Report LBL-21437, April 1986.

H57) P. N. Ross Jr., **Zinc-Air Design Concept for the DOE-EHP IDSEP Van**, Lawerence Berkeley Laboratory Report LBL-24639, Janurary 1988.

H58) Vinogradov, E. A., N. N. Mel'nik, A. E. Tsurkan, and L. V. Kicherman, Zhurnal Prikladnoi Spektroskopii (English translation), **26,** 764 (1977).

H59) Alberty, R., and F. Daniels, **Physical Chemistry**, 5th edition, Wiley, New York, 1979.

H60) Hugot-Le Goff, A., S. Joiret, B. Saidani, and R. Wiart, J. Electroanal. Chem. **263,** 127 (1989).

H61) Feitnecht, W., Metaux et Corrosion **23,** 192 (1947).

H62) Yamamoto, K., K. Ueda, M. Yamada and K. Abe, J. Phys Soc. Japan **46,** 1792 (1979).

H63) Hayashi, S., N. Nakamori, H. Kanamori, and Y. Yodogawa, Surf. Sci. **86,** 665, (1979).

H64) Genzel, L., and T. P. Martin, Phys. Stat. Sol. (B) **51**, 91 (1972).

FIGURE CAPTIONS FOR CHAPTER 8

Figure 8-1. Schematic of the geometry for Raman scattering. Dipole (polarized in x direction) located at center of coordinate system. Incident beam propagates in z direction.

Figure 8-2. Schematic of the polarization of a molecule as a function of intramolecular position and its corresponding Q coordinate dependence.

Figure 8-3. Determination of IR and Raman activity of a CO_2-type molecule by variation in the polarization and dipole-moment derivative at equilibrium.

Figure 8-4. Schematic showing induced polarization (in the x direction) of a non-depolarizing molecule producing Raman scattered light polarized in the x direction.

Figure 8-5. Photograph of Raman spectroscopy instrument used in this study.

Figure 8-6. Photograph of Raman spectroscopy electrochemical cell.

Figure 8-7. Photograph of apparatus used to study Raman spectroscopy of liquids.

Figure 8-8. Transmittance of optical filters used with the 488 nm Ar-ion laser line.

Figure 8-9. A) Background "dark" detector counts of the optical multichannel anaylzer (OMA) as a function of temperature for 1 sec exposures. B) Background "dark" counts as a function of exposure time for several different temperatures. Zero second intercept of all curves is 180 counts.

Figure 8-10. Log-linear plot of "dark" detector counts vs detector temperature, corrected for 180 readout counts.

Figure 8-11. Calculated signal-to-noise ratio vs integration time for several detector temperatures.

Figure 8-12. Plasma line spectrum of the Ar-ion laser vs apparent wavenumber shift with respect to 488 nm.

Figure 8-13. A) Rotation-vibration spectrum of oxygen; 15 min exposure, 90 mW power. B) Detail of the stokes and anti-Stokes rotational transitions.

Figure 8-14. A) Voltammetry of Ag in 1M KOH at 10 mV/sec. B) Integrated intensity of the 430 cm^{-1} peak vs potential corresponding to the voltammetry in A).

Figure 8-15. Raman spectra of silver in 1M KOH during a 10 mV/sec potential-sweep experiment at selected potentials during the anodic sweep. a) 350 mV, b) 450 mV, c) 550 mV , d) 650 mV.

Figure 8-16. 1 mV/sec voltammetry of silver in 1M KOH. Maximum potential during anodic sweep is 400 mV (i.e., prior to divalent oxide formation in dark).

Figure 8-17 Raman spectra of silver in 1M KOH at several potentials during the anodic portion of a 1 mV/sec potential-sweep experiment. Both the 430 and 485 cm^{-1} bands are evident. a) 312.5 mV, b) 337.5 mV, c) 367.5 mV, d) 387.5 mV, e) 387.5 mV (cathodic sweep).

Figure 8-18. Comparison of SERS spectra of silver in 1M KOH at several different potentials. Curves are offset to allow readability. a) -0.8 V, b) -0.2 V, c) 0.2 V.

Figure 8-19. Spectra of silver in 1M KOH at various times after laser is turned on at time zero. Laser power 60 mW. Surface oxidized in dark at 10 mV/sec and held at 500 mV prior to illumination. a) 24 sec, b) 20 sec, c) 16 sec, d) 12 sec, e) 8 sec, f) 4 sec.

Figure 8-20. Integrated 430 cm^{-1} wavenumber peak vs time for surface oxidized as in Figure 8-19. A) 60 mW, B) 90 mW.

Figure 8-21. A) Integrated 430 cm^{-1} peak vs time, as described in B). B) Raman spectra of Ag for various times after illumination in 1M KOH. Film was formed by oxidizing the surface under illumination by first increasing potential at 10 mV/sec to 500 mV and then reversing the

sweep direction to 250 mV. The potential was held at this value. Total laser power 90 mW. a) 4 sec, b) 8 sec, c) 12 sec.

Figure 8-22. Raman spectrum of Cu_2O powder. Laser power 40 mW. Exposure time 5 min.

Figure 8-23. Raman spectrum of CuO powder. Laser power 90 mW. Exposure time 45 min.

Figure 8-24. Raman spectrum of $Cu(OH)_2$ powder. Laser power 40 mW. Exposure time 5 min.

Figure 8-25. Integrated intensity of the 488 cm^{-1} peak of $Cu(OH)_2$ powder in air as a function of time. Laser power 90 mW.

Figure 8-26. A) Integrated intensity of the 488 cm^{-1} peak of $Cu(OH)_2$ powder in 1M KOH as a function of time. Laser power 90 mW. B) Integrated intensity of the 488 cm^{-1} peak of a Cu surface with a $Cu(OH)_2$ surface film in 1M KOH. Laser power 90 mW.

Figure 8-27 A) 10 mV/sec cyclic voltammogram of Cu in 1M KOH. B) Integrated Raman peak intensities corresponding to voltammetry shown in A). ●: Cu_2O 633^{-1} peak intensity during anodic sweep. □: $Cu(OH)_2$ 488 cm^{-1} peak intensity during anodic sweep. ○ : Cu_2O 633^{-1} peak intensity during cathodic sweep. □ : $Cu(OH)_2$ 488 cm^{-1} peak intensity during cathodic sweep.

Figure 8-28. Raman spectra of Cu during the anodic sweep of a 10 mV/sec potential-sweep experiment. Spectra shown are an average of five 10-sec exposures taken at the average potential shown during repeated cycles.

Figure 8-29. Raman spectra of Cu during the cathodic sweep of a 10 mV/sec potential-sweep experiment. Spectra shown are an average of five 10-sec exposures taken at the average potential shown during repeated cycles.

Figure 8-30. Integrated intensity of 300 cm^{-1} peak versus potential during a 10 mV/sec experiment on Cu in 1M KOH. □ : anodic sweep. □ : cathodic sweep.

Figure 8-31. Integrated intensity of Cu_2O (□) and $Cu(OH)_2$ (□) during a potential-sweep/potentiostatic experiment.

Figure 8-32. Raman spectra of Cu in 1M KOH at selected potentials using the potential program shown in Figure 8-31. A) Constant potential (0.6 V) held for a) 0 sec, b) 50 sec, c) 100 sec. B) Cathodic sweep a) 350 mV, b) 150 mV, c) -50 mV.

Figure 8-33. A) Cyclic voltammetry of Cu in 6M KOH at 1mV/sec. B) Integrated peak intensities corresponding to voltammetry in A). ● : Cu_2O 633 cm^{-1} peak, anodic sweep. □ : $Cu(OH)_2$ 488 cm^{-1} peak,

anodic sweep. ○ : Cu_2O 633 cm^{-1} peak, cathodic sweep. □ : $Cu(OH)_2$ 488 cm^{-1} peak, cathodic sweep.

Figure 8-34. Raman spectrum of Cu in 1M KOH at -350 mV during a 1 mV/sec potential-sweep experiment in 6M KOH.

Figure 8-35. Raman spectrum of Cu in 1M KOH at selected potentials during a 1 mV/sec potential-sweep experiment in 6M KOH. A) Anodic sweep: a) -50 mV, b) 150 mV, c) 350 mV, d) 550 mV. B) Cathodic sweep: a) -450 mV, b) -250 mV, c) -50 mV, d) 150 mV, e) 350 mV.

Figure 8-36. Raman spectrum of Cu in 1M KOH at selected potentials during the cathodic sweep of a 1 mV/sec potential-sweep experiment in 6M KOH. a) -450 mV , b) -550 mV, c) -650 mV, d) -750 mV, e) -850 mV.

Figure 8-37. A) Cyclic voltammogram of Cu in 1M KOH during a 1 mV/sec potential sweep. B) Integrated peak intensities vs potential corresponding to voltammetry shown in A). ●: anodic sweep, Cu_2O peak; □ : anodic sweep, $Cu(OH)_2$ peak; □ : cathodic sweep, Cu_2O peak; ○ : cathodic sweep, $Cu(OH)_2$ peak.

Figure 8-38. Raman spectra of Cu in 1M KOH at selected potentials during a 0.5 mV/sec anodic sweep.

Figure 8-39. Raman spectra of Cu in 1M KOH during a 0.5 mV/sec potential-sweep experiment at selected potentials. A) anodic sweep, B) cathodic

sweep.

Figure 8-40. Raman spectra of Cu in 1M KOH during a 0.5 mV/sec potential-sweep experiment at 450 and 650 mV.

Figure 8-41. Raman spectra of Cu in 1M KOH during a 1mV/sec potential-sweep experiment. Maximum anodic potential -200 mV.

Figure 8-42. Integrated Cu_2O 633 cm^{-1} peak of data shown in Figure 8-41.

Figure 8-43. Current, potential, and 633 cm^{-1} Raman peak intensity versus time in 1M KOH. Area of illumination was moved during the potentostatic portion of the experiment in both A) and B).

Figure 8-44. Integrated 633 cm^{-1} Cu_2O peak intensity vs square root time after a potential step from -600 to -300 mV vs Hg/HgO in 1M KOH.

Figure 8-45. A) Current vs time after a potential-step change from -600 to -150 mV of Cu in 1M KOH. B) Corresponding Raman spectra vs time.

Figure 8-46. Integrated Raman peak intensity for experiment shown in Figure 8-45. A) $Cu(OH)_2$, B) Cu_2O.

Figure 8-47. Potential-sweep voltammetry of dissolved copper species on Pt formed during cyclic voltammetry in 6M KOH.

Figure 8-48. Raman spectra of dissolved copper species formed during cyclic vol-

tammetry in 6M KOH. 90 mW power, 15 min exposure.

Figure 8-49. Raman spectra of a) distilled water, b) 30% KOH, and c) 48% KOH solutions.

Figure 8-50. Raman spectra of a saturated zincate solution in 30% KOH. Spectra shown have been corrected for the Raman scattering associated with a 30% KOH solution. 425 and 470 cm^{-1} band envelopes are shown.

Figure 8-51. Raman spectra of zincate solution at several concentrations in 30% KOH. a) 8%, b) 6%, c) 4%, d) 2%, e) 1%, f) 0.5%.

Figure 8-52. Integrated Raman peak intensities of zincate solutions vs concentration.

Figure 8-53. Raman spectra of distilled water and various KOH, silicate, and ZnO-containing solutions. Curves are offset to improve their readability.

Figure 8-54. Raman spectrum of ZnO powder. 90 mW, 5 min exposure.

Figure 8-55. Raman spectra of zinc surface oxidized in 1M KOH at -0.8 V for 100 seconds. Surface was rinsed with distilled water and spectra were taken in air.

Figure 8-56. Voltammetry of Zn in 1M KOH during a 1 mV/sec potential sweep.

Figure 8-57. Raman spectra of Zn in 1M KOH at selected potentials corresponding to voltammetry data shown in Figure 8-56.

Figure 8-58. Raman spectra of Zn in 1M KOH at selected potentials corresponding to voltammetry data shown in Figure 8-56. Exposure time 100 sec/scan, 90 mW. Spectra are offset to allow readability.

Figure 8-59. Raman spectra of Zn anodized as in Figure 8-56 and then set to open circuit. Exposure time 100 sec/scan, 90 mW. a) E= -0.4 V, b) open circuit for 100 seconds, c) open circuit for 200 seconds.

Figure 8-60. Raman spectra of Zn in 1M KOH vs potential/time. Exposure time 400 sec/scan, 90 mW.

Figure 8-61. Raman spectra of Zn in 1M KOH at selected potentials during cathodic potential sweep: a) -1.05 V, b) -1.15 V, c) -1.25 V.

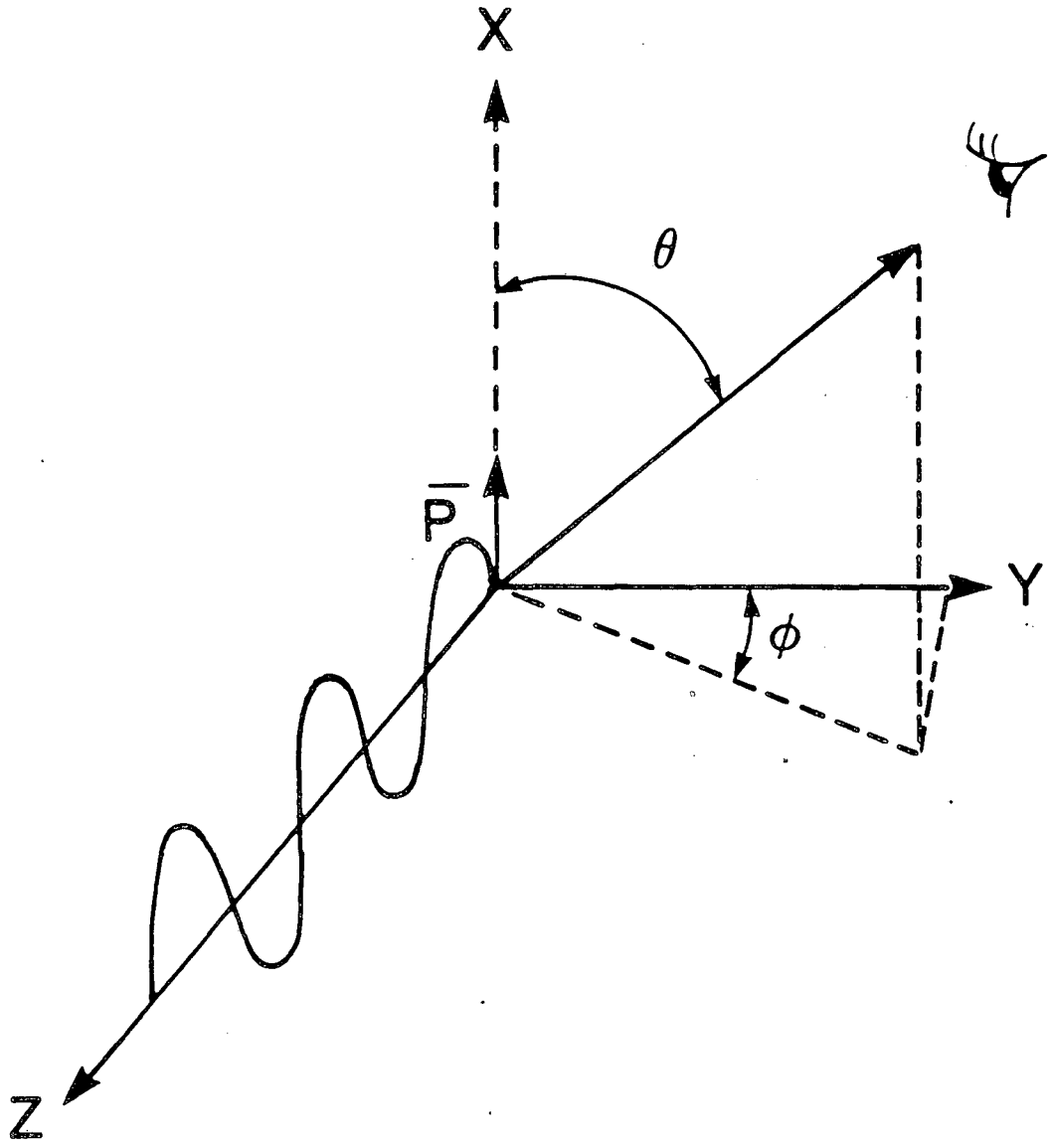

XBL 898-7217

Figure 8-1

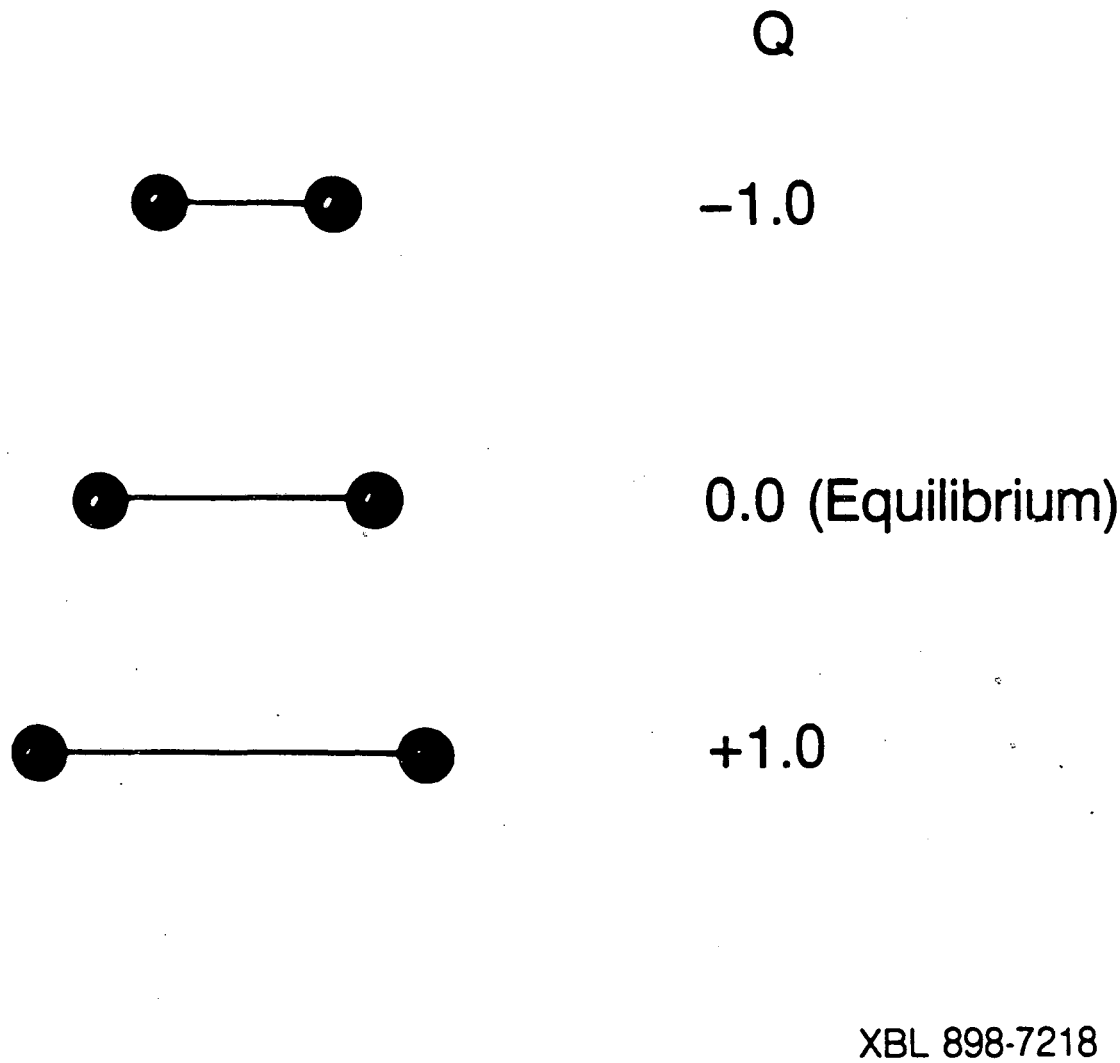

Figure 8-2

Vibration Mode	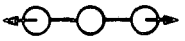	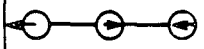	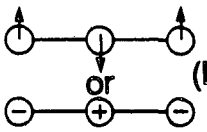 (Degenerate)
Polarizability Curve	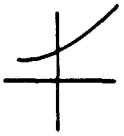	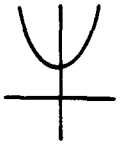	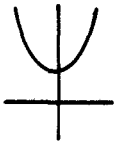
Polarizability Derivative at Equilibrium Position	$\neq 0$	$= 0$	$= 0$
Raman Activity	Yes	No	No
Dipole Moment Curve		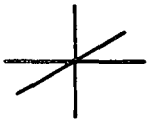	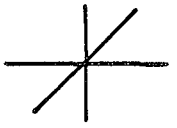
Dipole Moment Derivative	$= 0$	$\neq 0$	$\neq 0$
I.R. Activity	No	Yes	Yes

XBL 898-7215

Figure 8-3

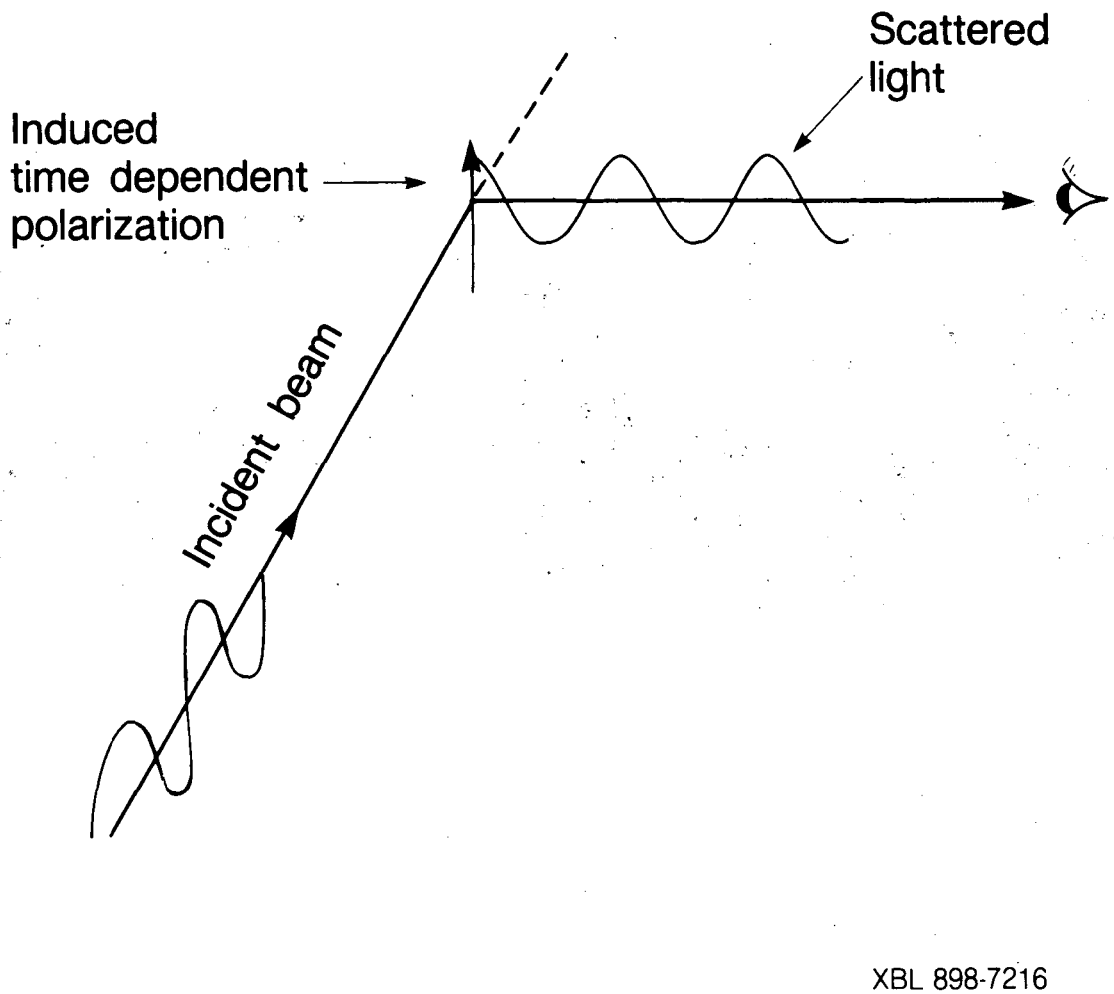
Scattered
light
Induced
time dependent
polarization
Incident beam
XBL 898-7216

Figure 8-4

XBB 898-6478

Figure 8-5

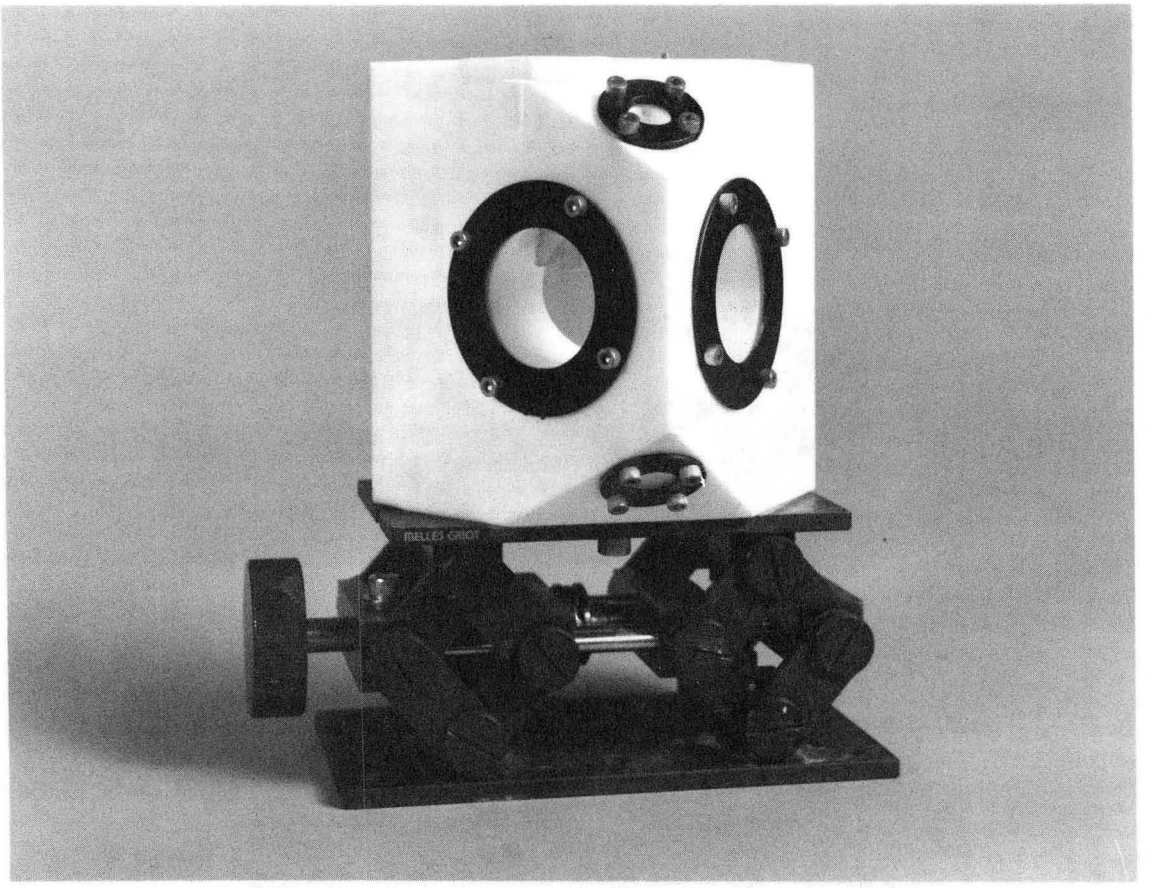

CBB 893-2065

Figure 8-6

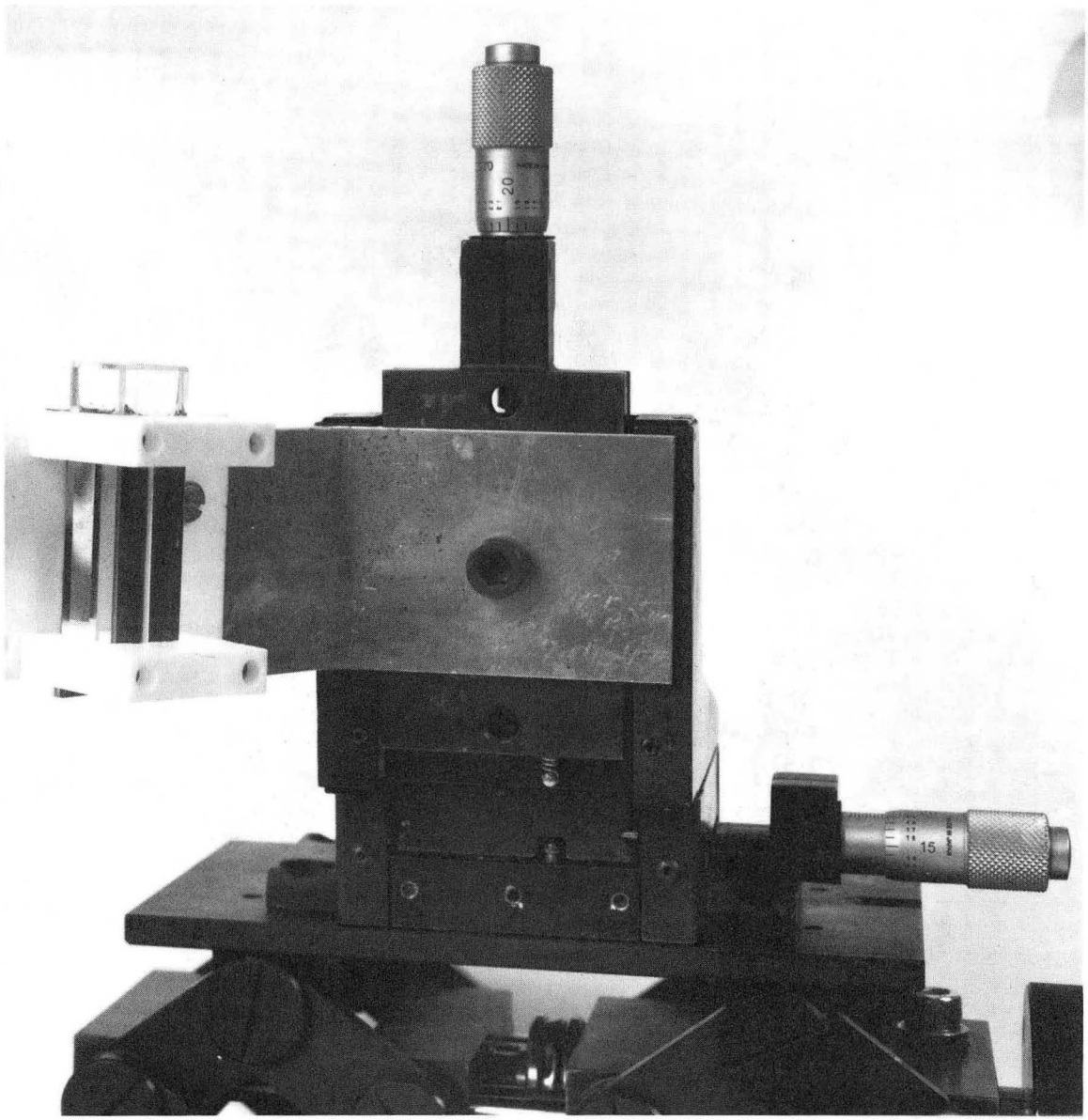

XBB 898-6480

Figure 8-7

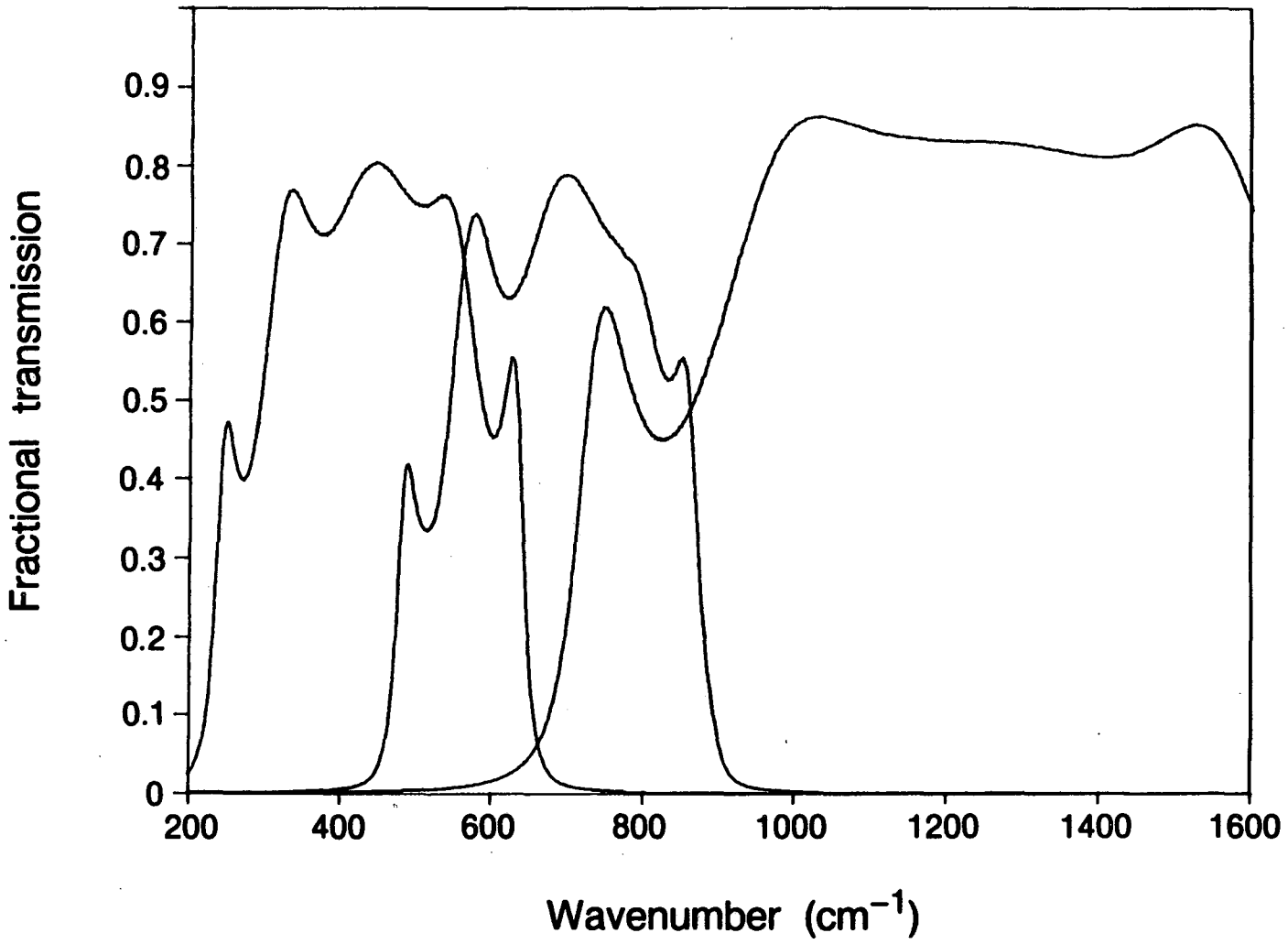

Figure 8-8

XBL 898-7220

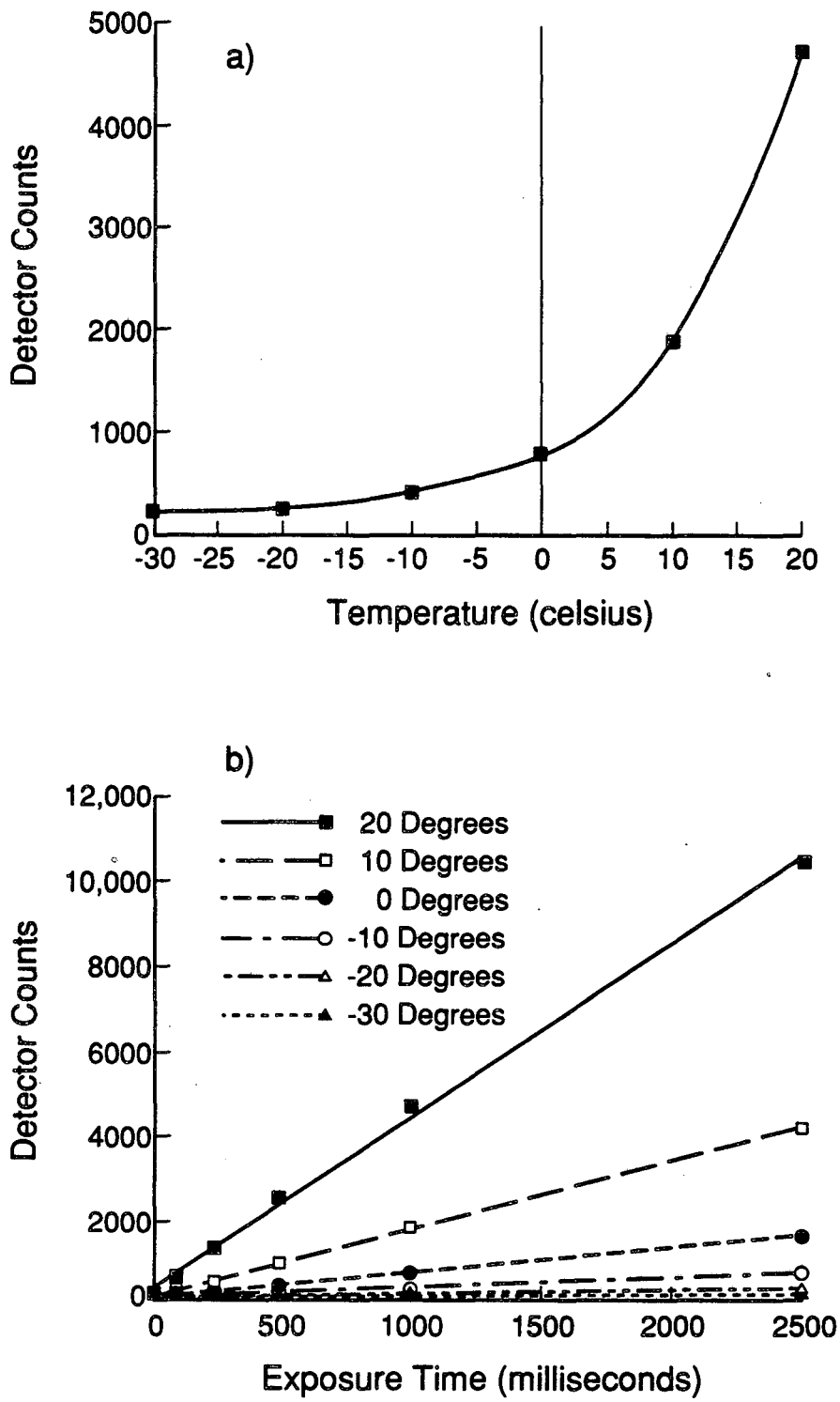

XBL 899-7799

Figure 8-9

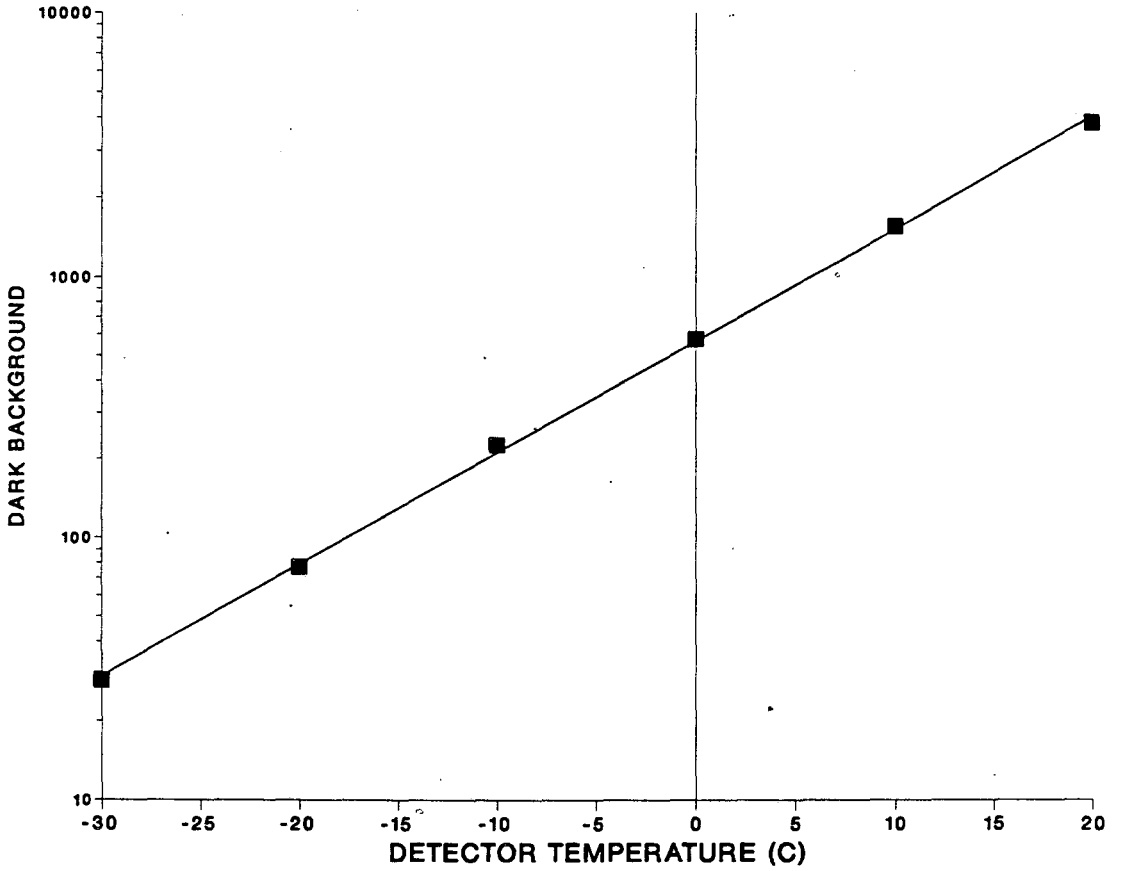

XBL 897-2630

Figure 8-10

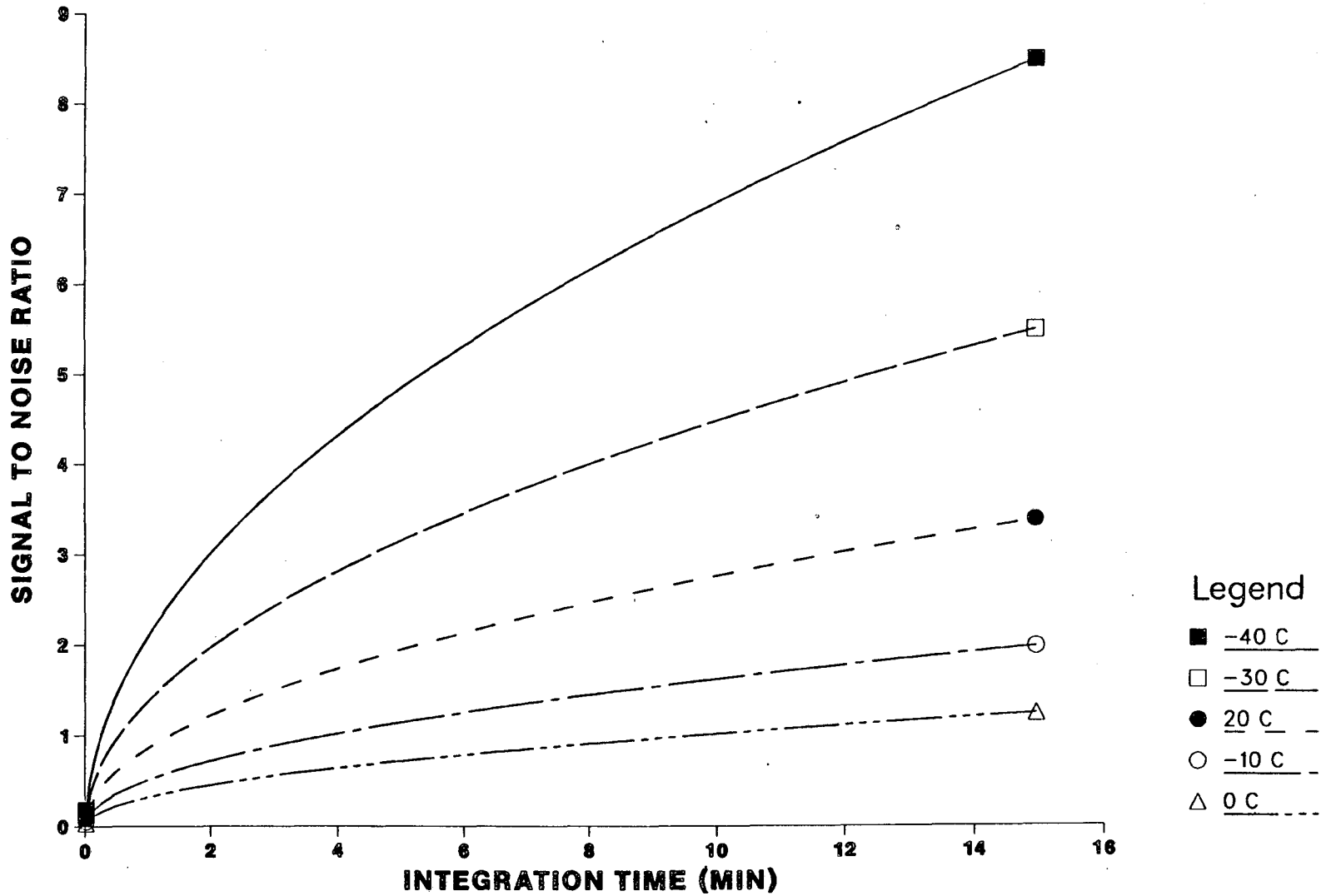

Figure 8-11

XBL 897-2629

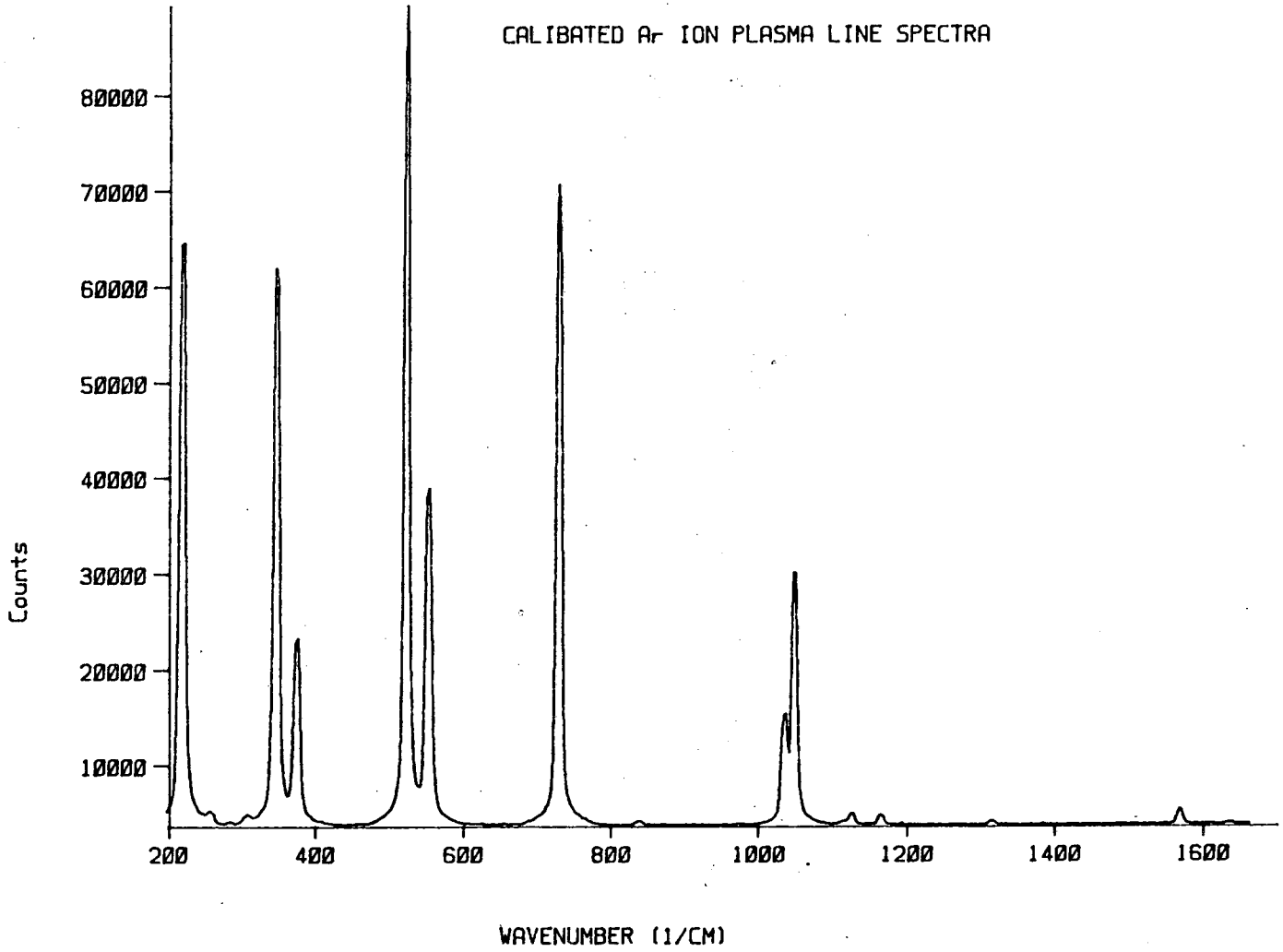

Figure 8-12

XBL 897-2631

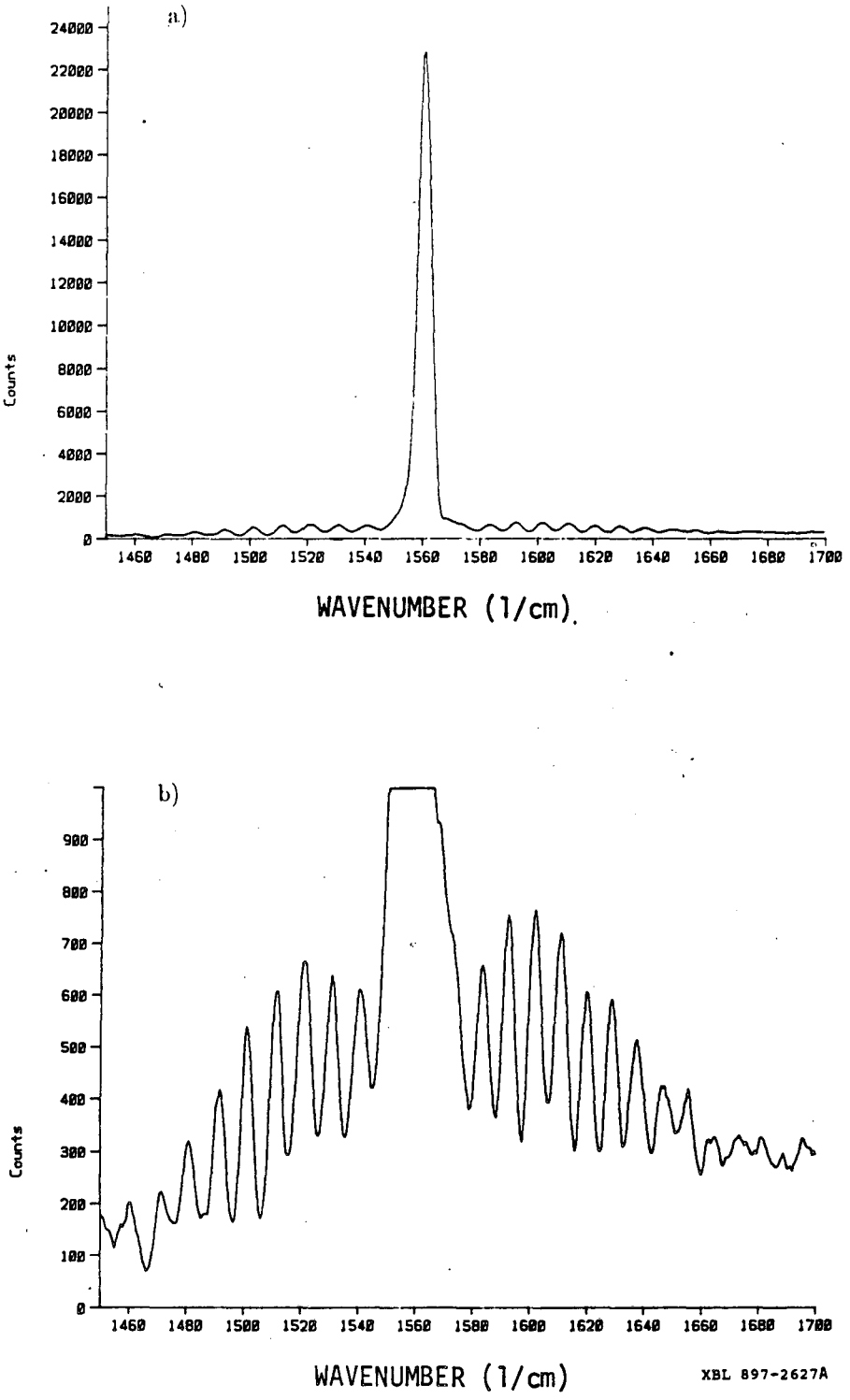
a)
24000
22000
20000
18000
16000
14000
12000
10000
8000
6000
4000
2000
0
Counts
1460 1480 1500 1520 1540 1560 1580 1600 1620 1640 1660 1680 1700
WAVENUMBER (1/cm)
b)
900
800
700
600
500
400
300
200
100
0
Counts
1460 1480 1500 1520 1540 1560 1580 1600 1620 1640 1660 1680 1700
WAVENUMBER (1/cm)
XBL 897-2627A

Figure 8-13

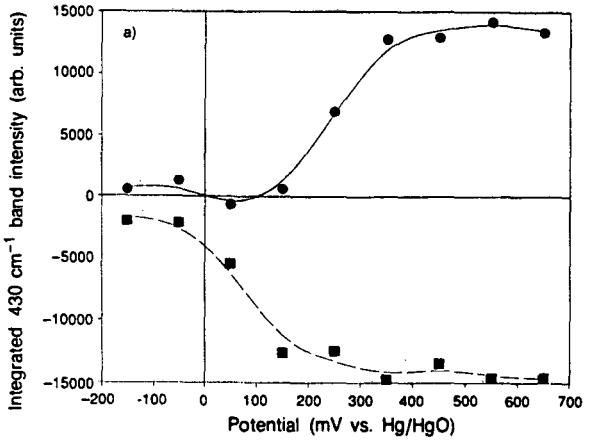

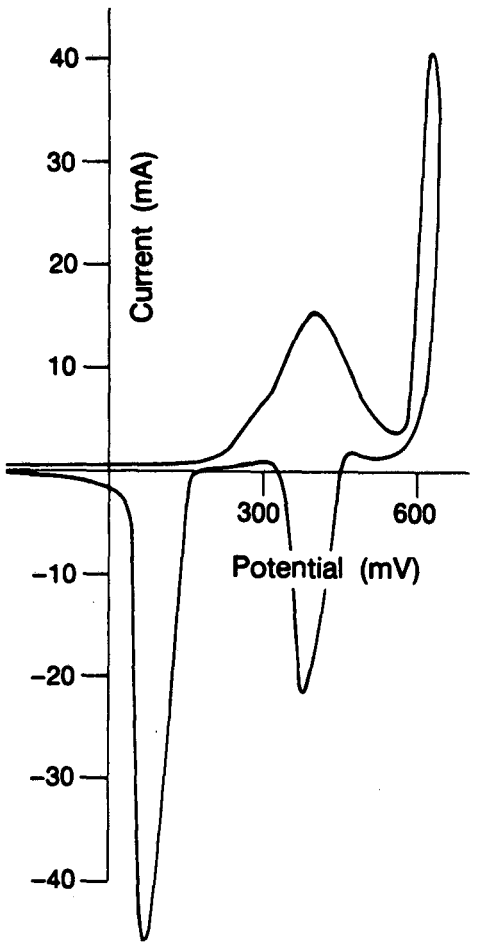

XBL 898-7219

Figure 8-14

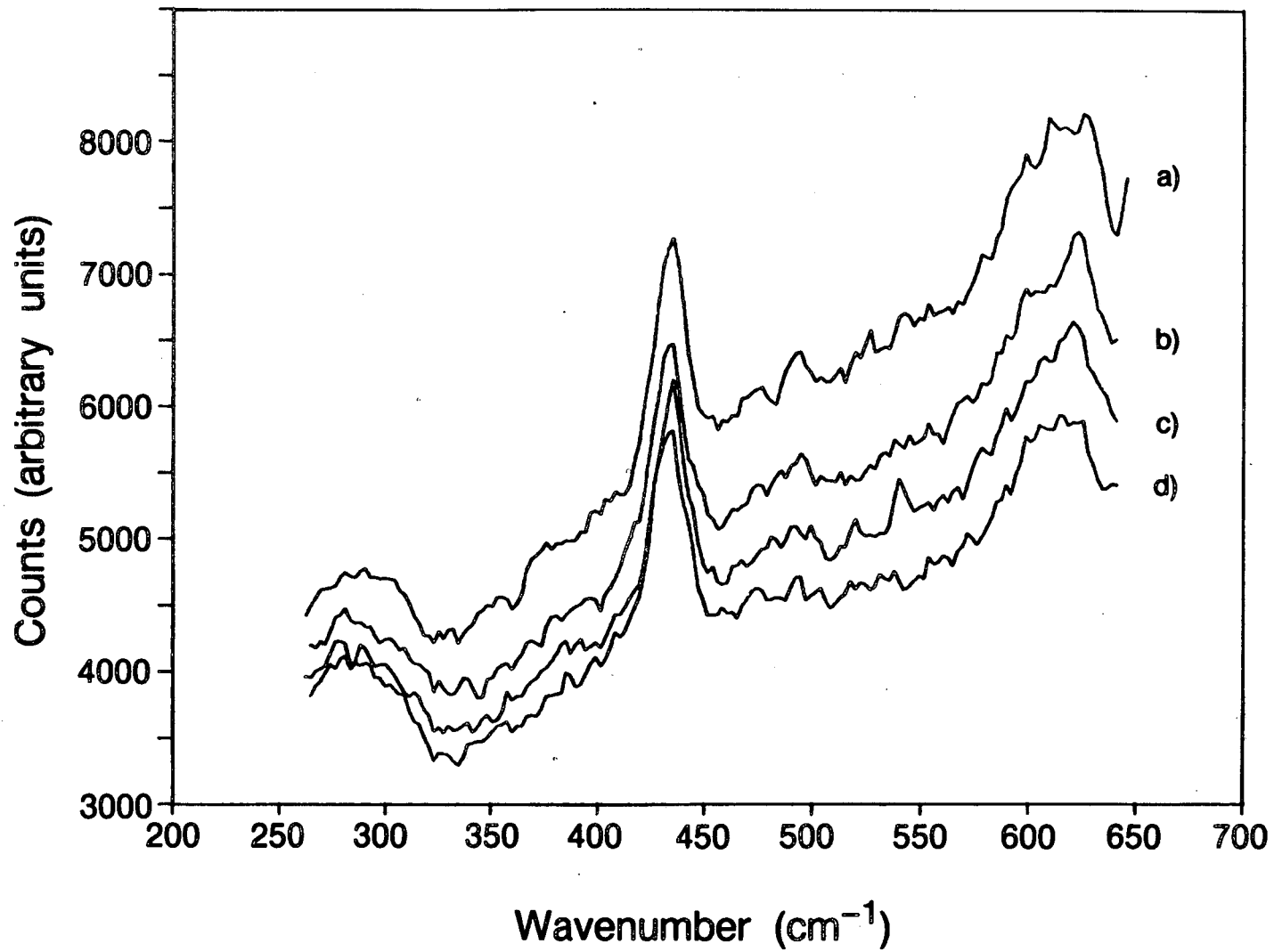

Figure 8-15

XBL 898-7223

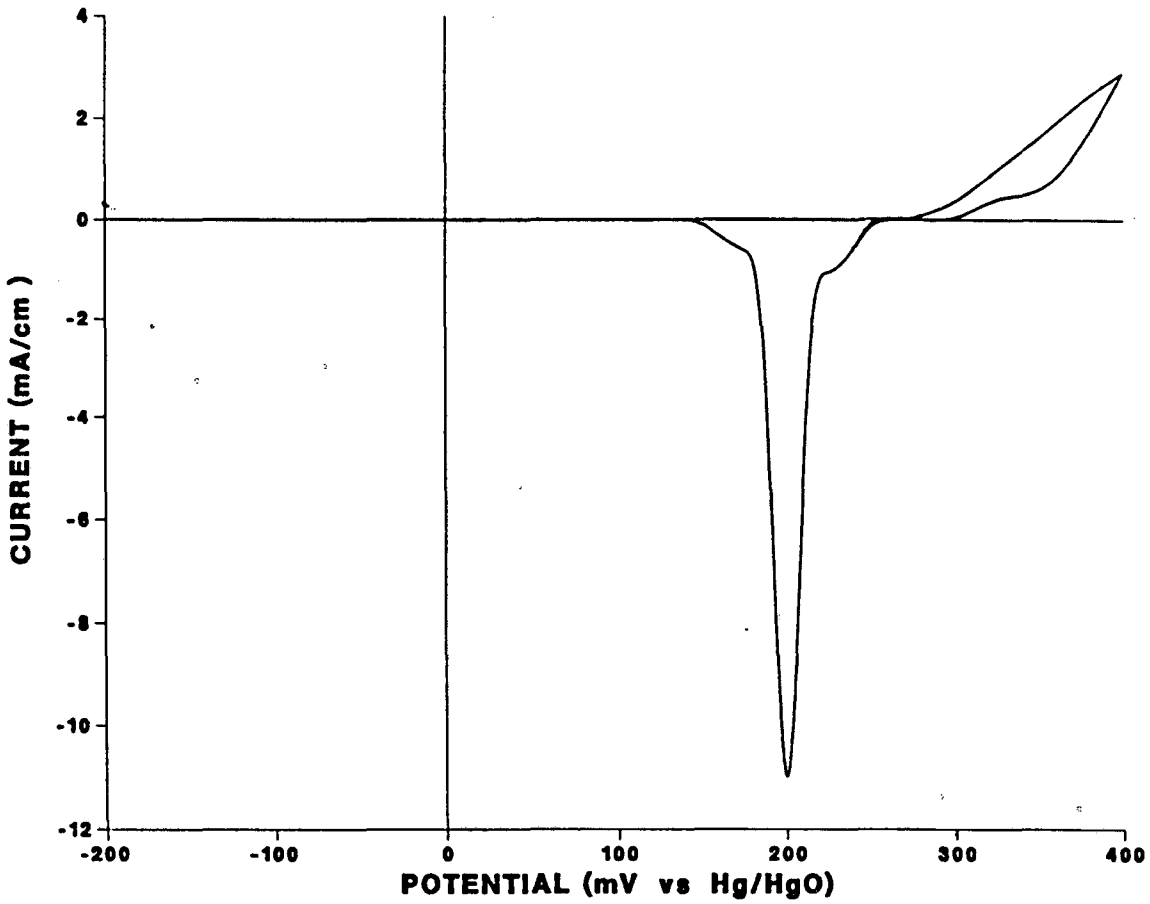

XBL 899-3396

Figure 8-16

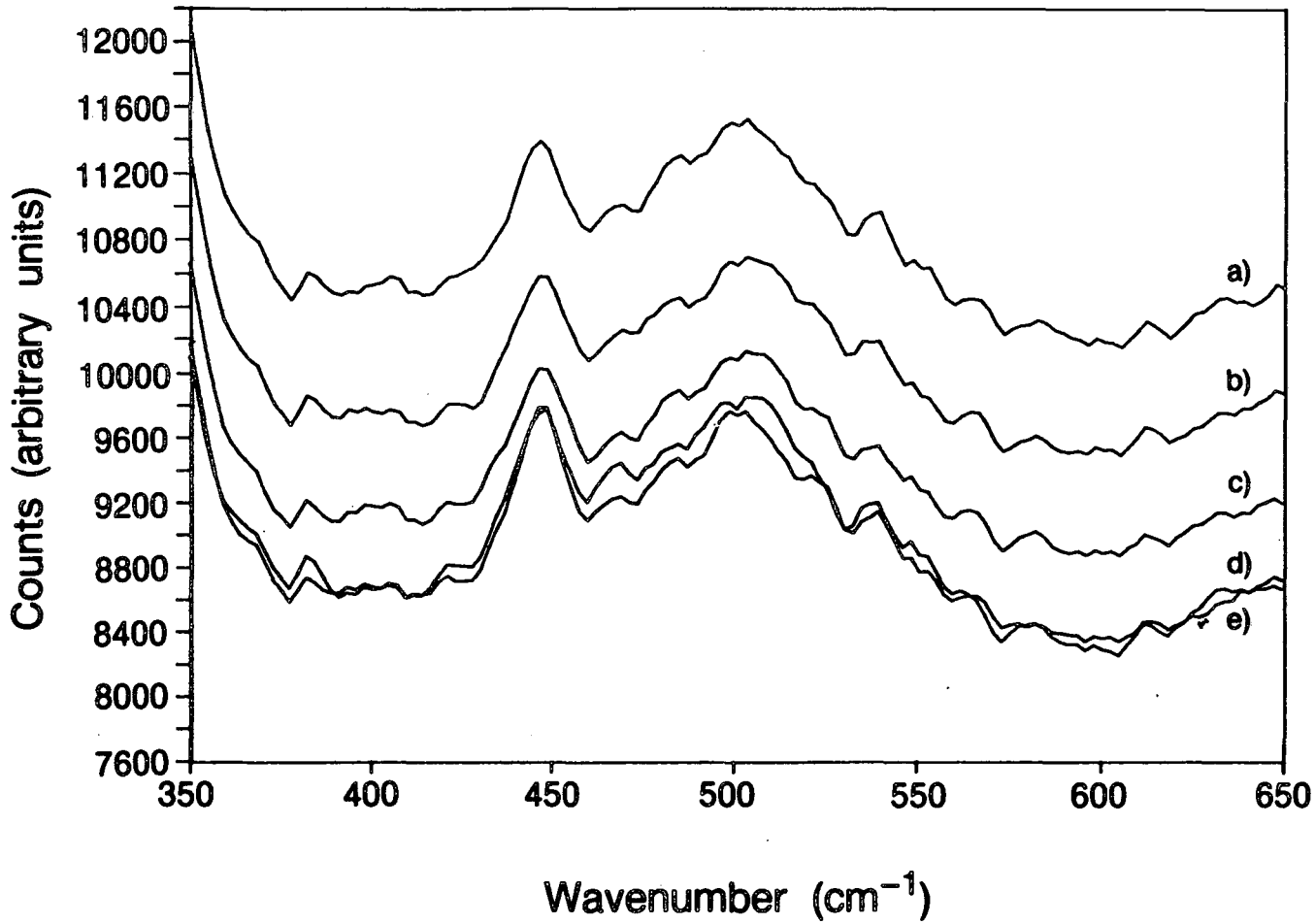

Figure 8-17

XBL 898-7228

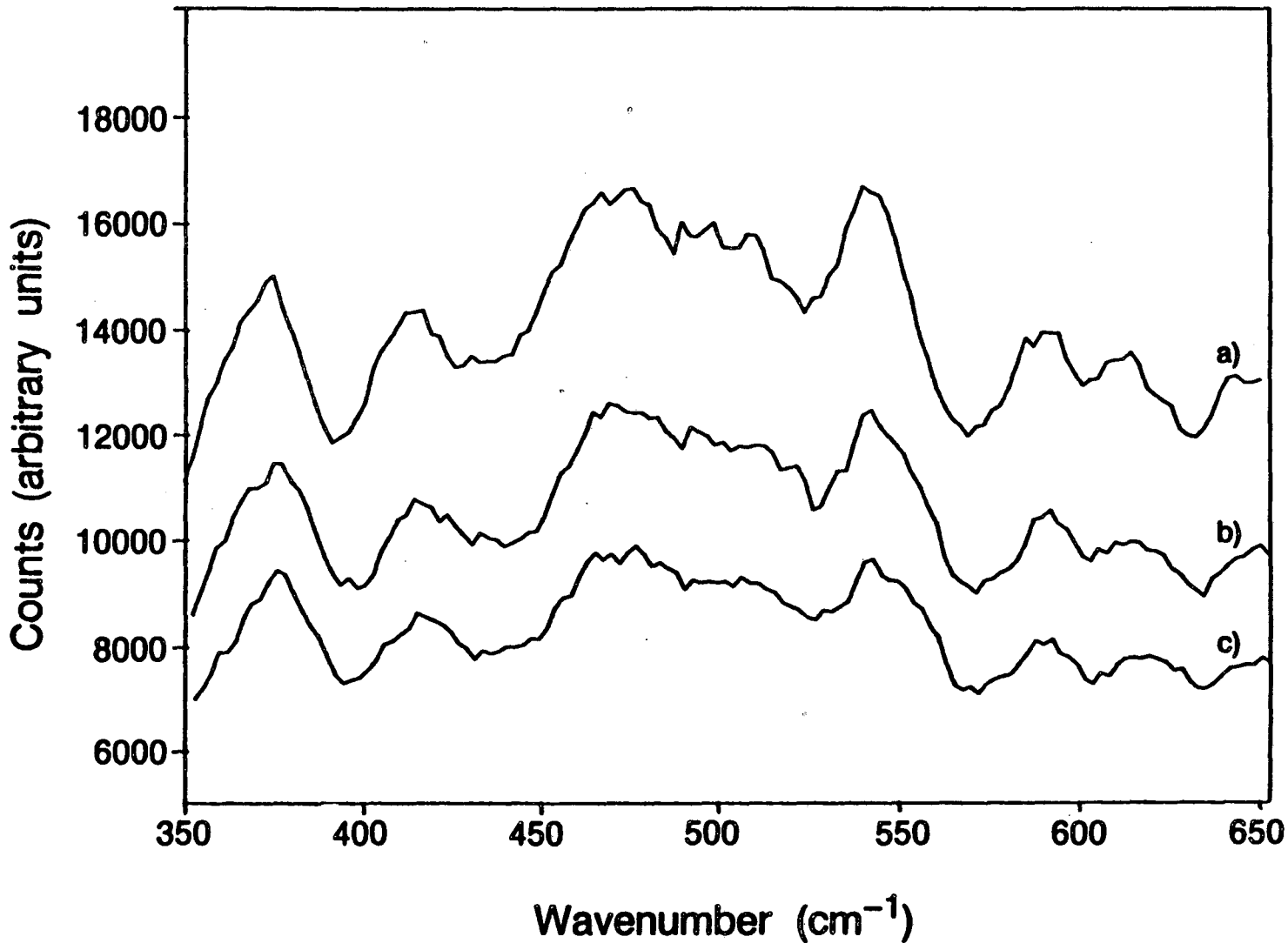

XBL 898-7230

Figure 8-18

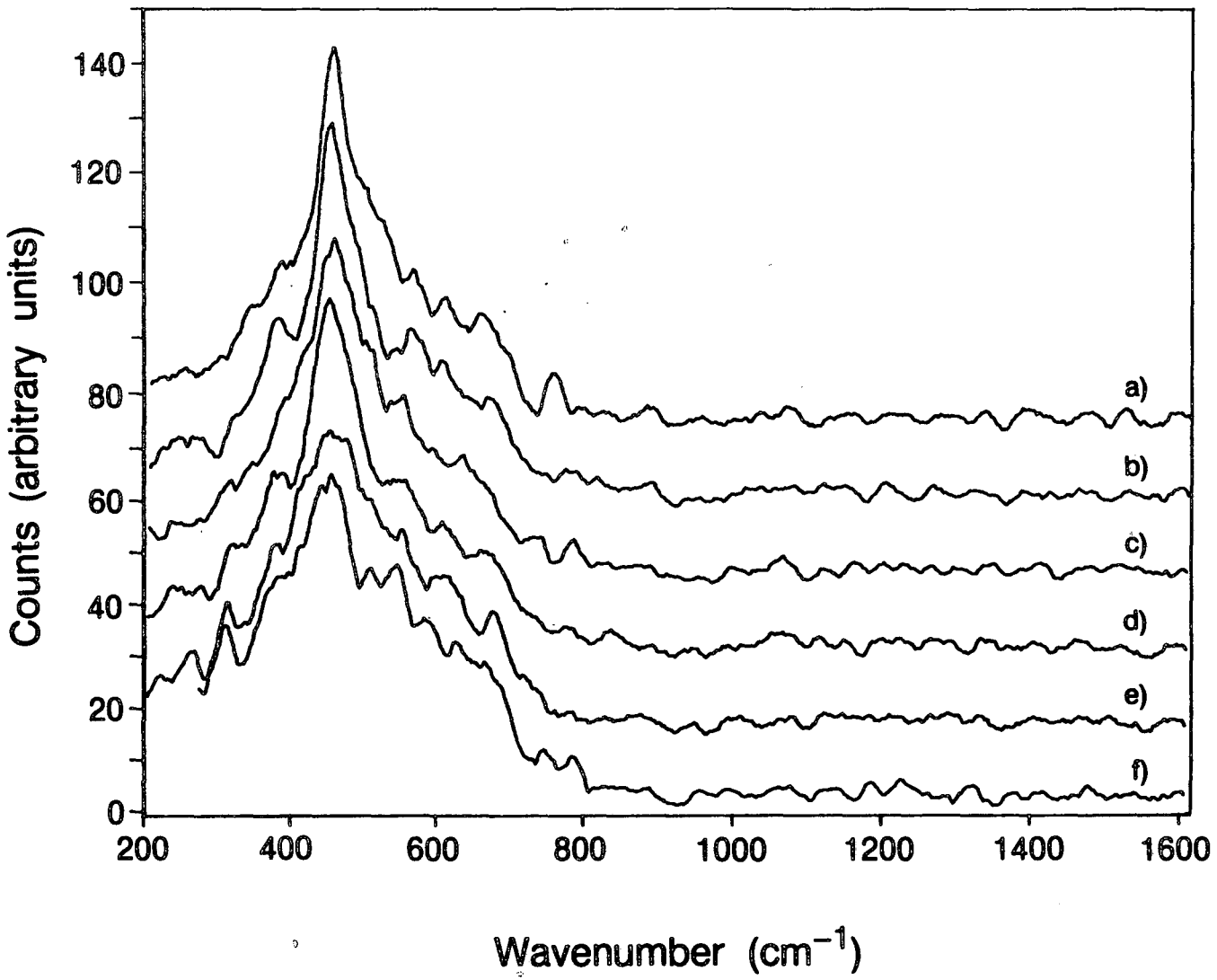

Figure 8-19

XBL 898-7231

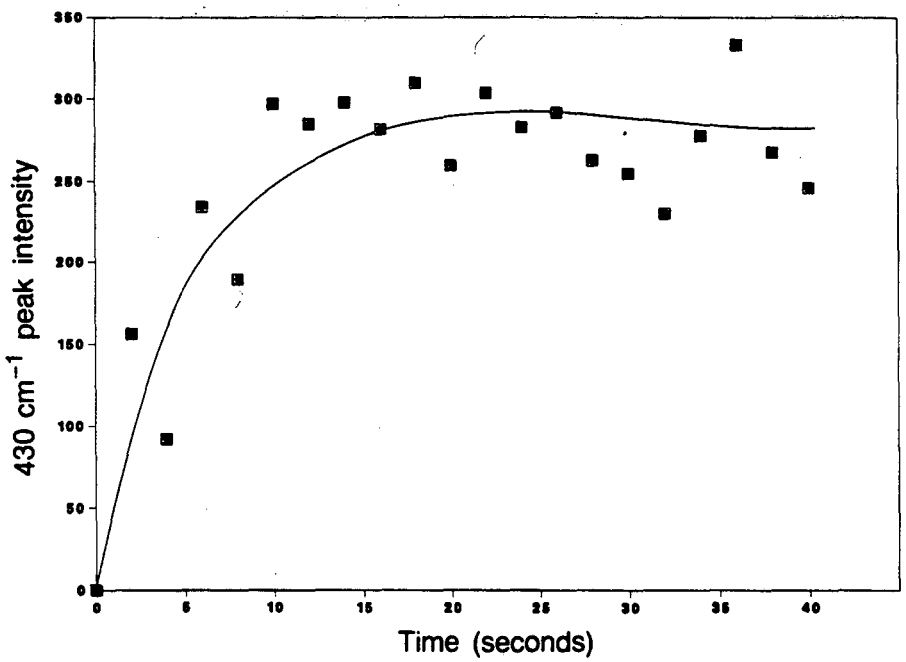

XBL 898-7248

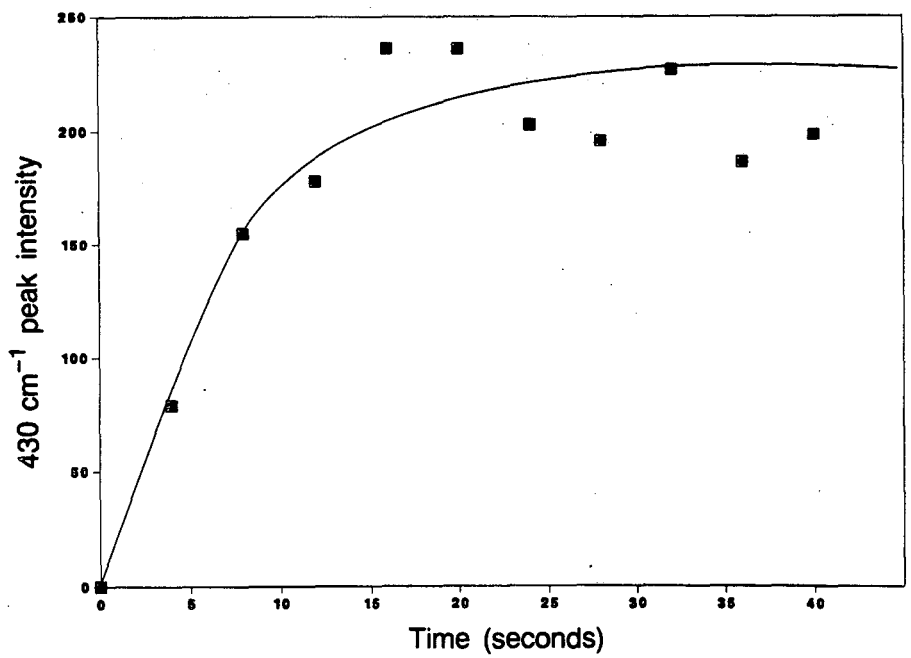

XBL 898-7247A

Figure 8-20

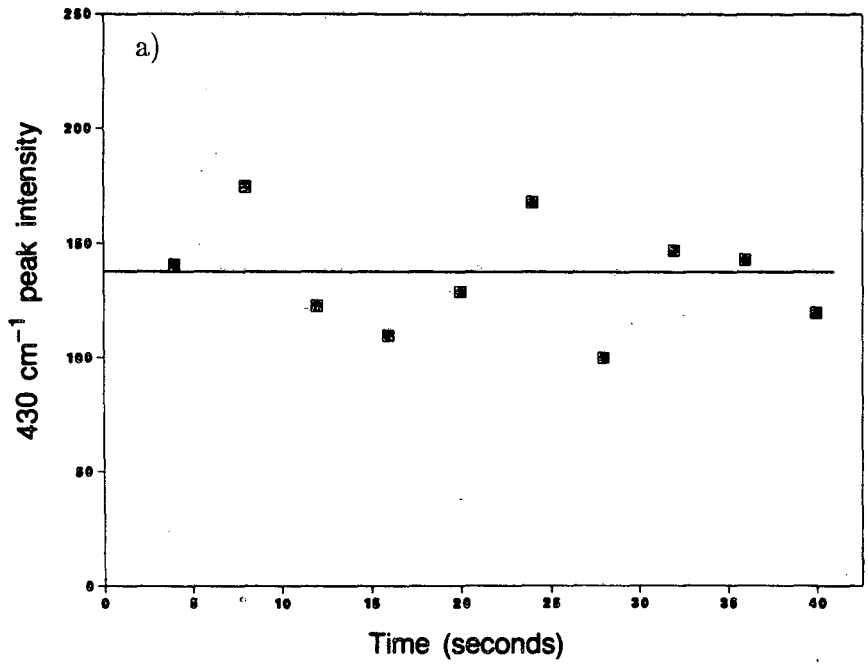

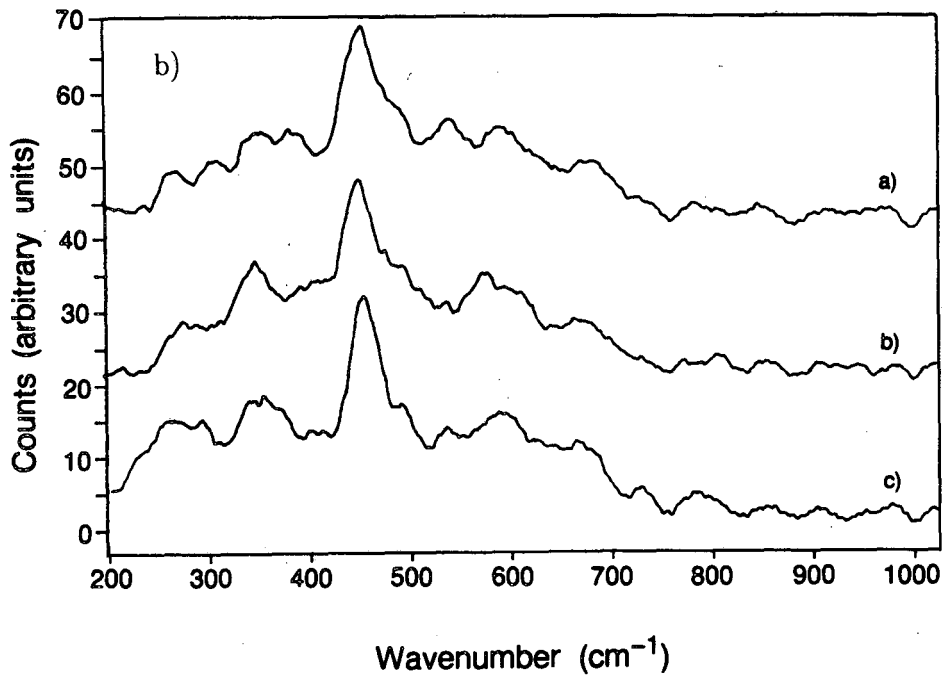

XBL 898-7243A

Figure 8-21

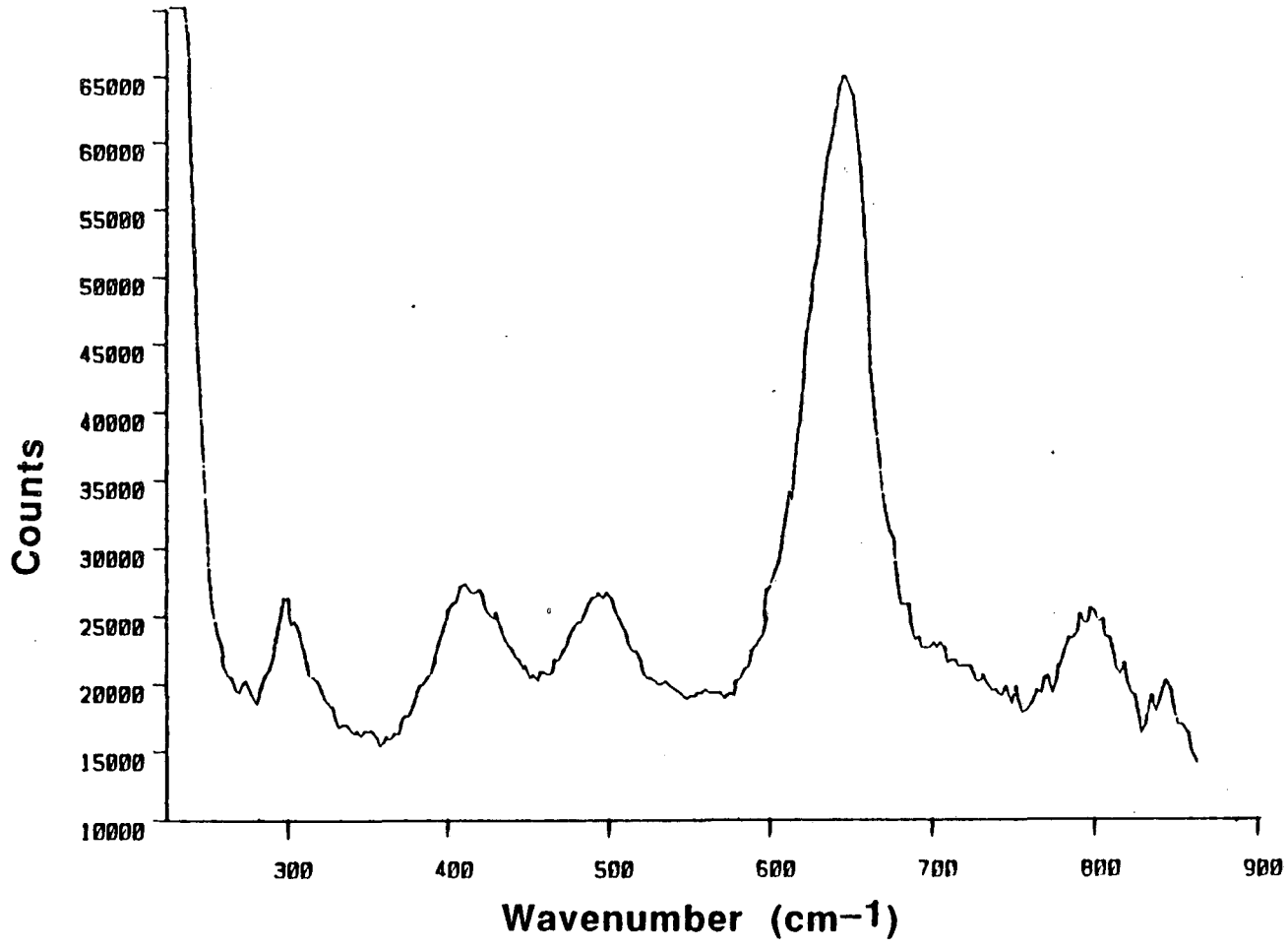

Figure 8-22

XBL 888-3089

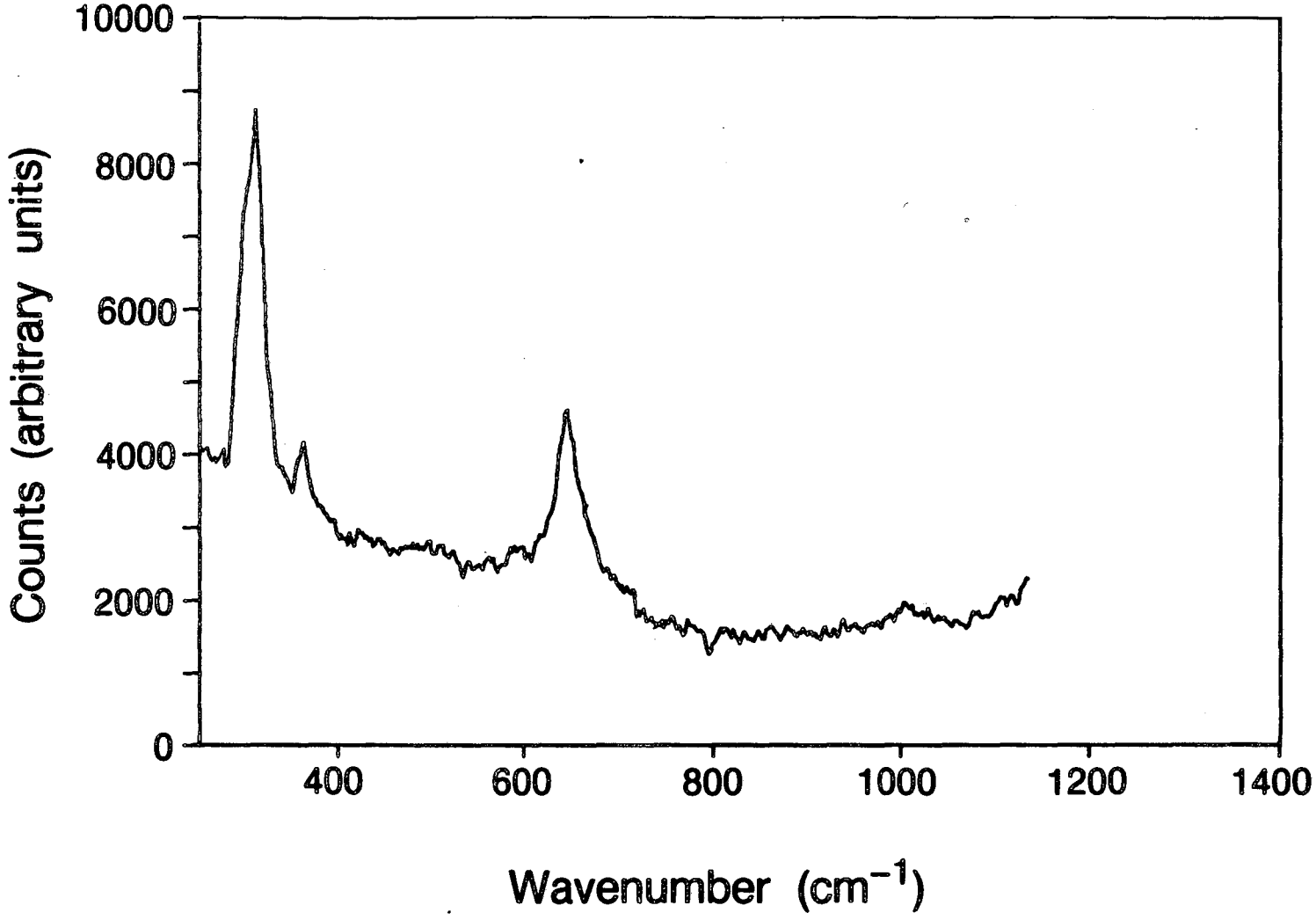

Figure 8-23

XBL 898-7233

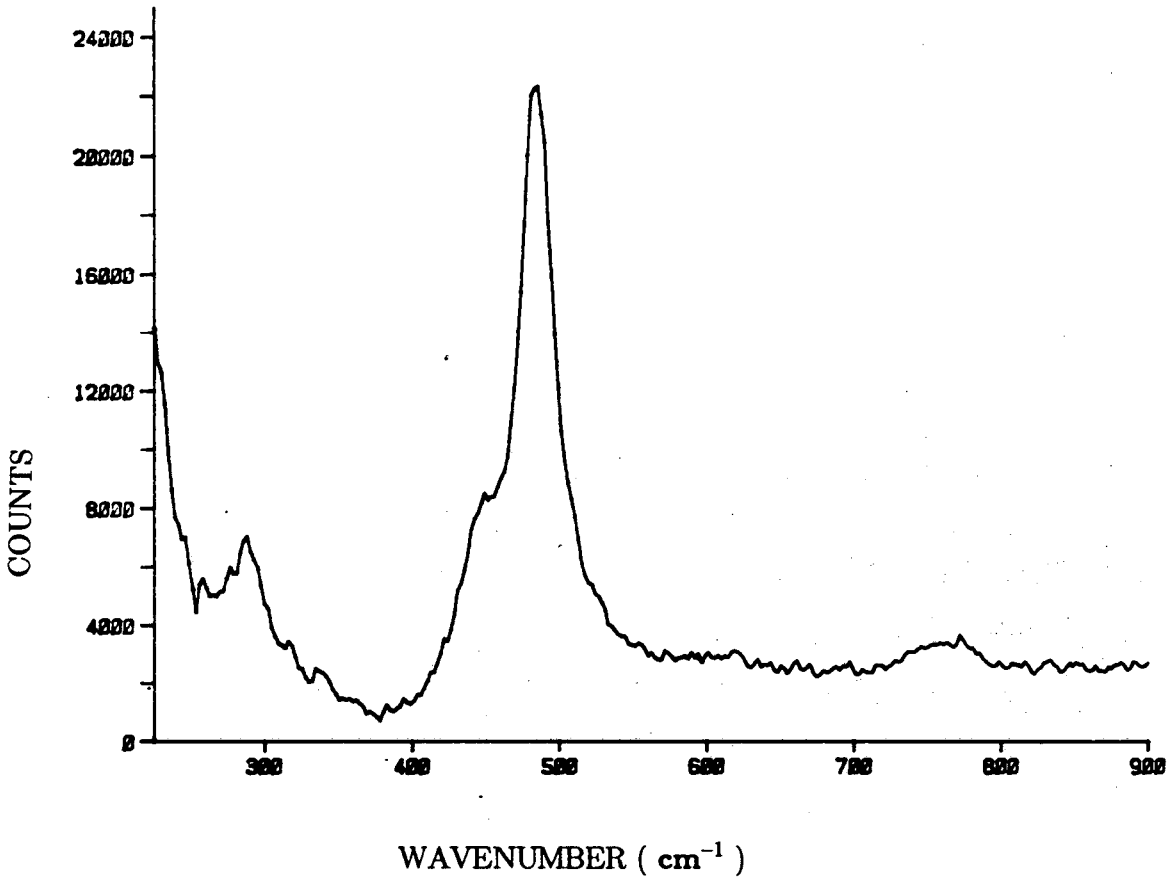

Cu(OH)$_2$ RAMAN SPECTRA OF POWDER

XBL 895-1691

Figure 8-24

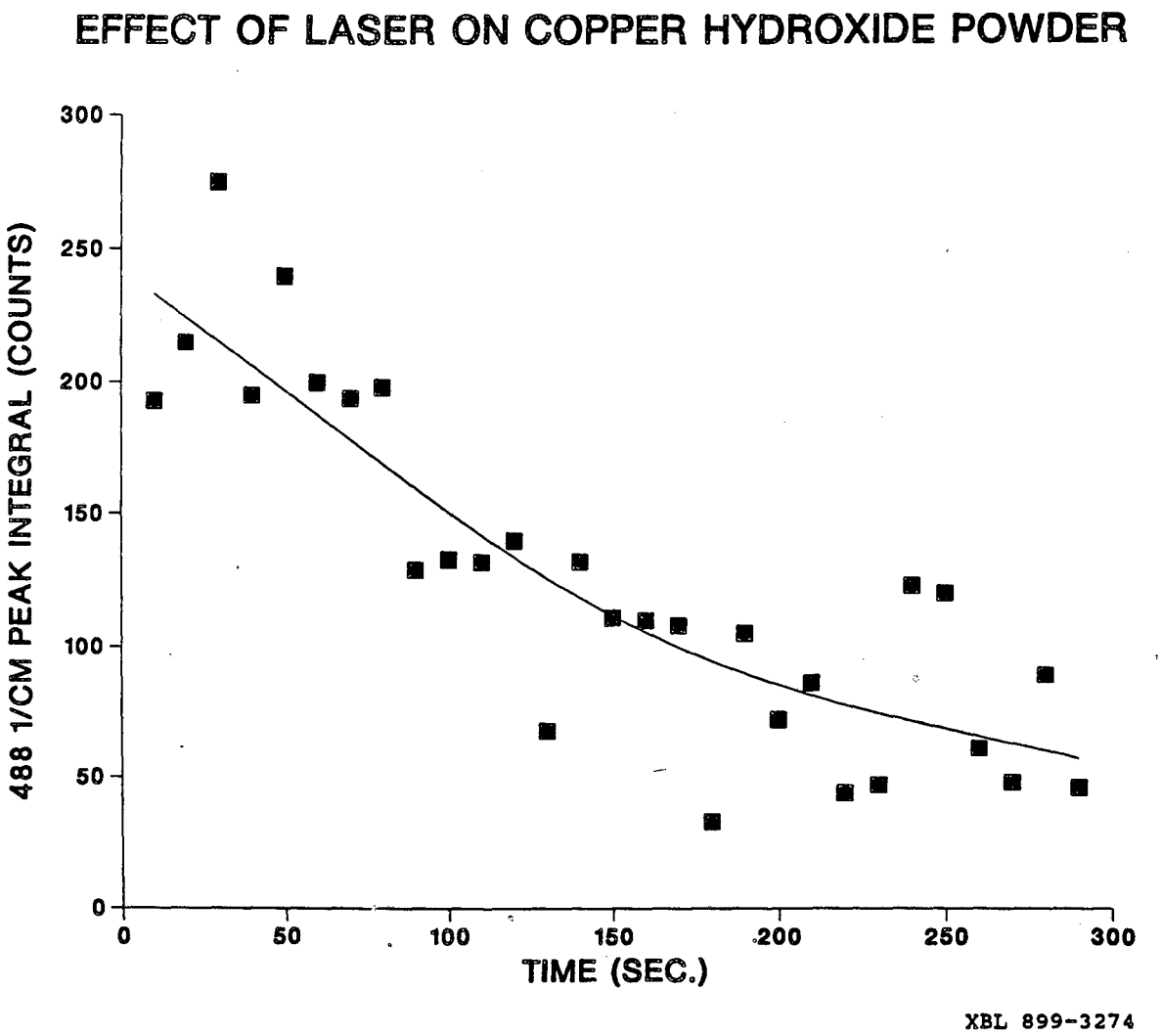
EFFECT OF LASER ON COPPER HYDROXIDE POWDER
488 1/CM PEAK INTEGRAL (COUNTS)
300
250
200
150
100
50
0
0
50
100
150
200
250
300
TIME (SEC.)
XBL 899-3274

Figure 8-25

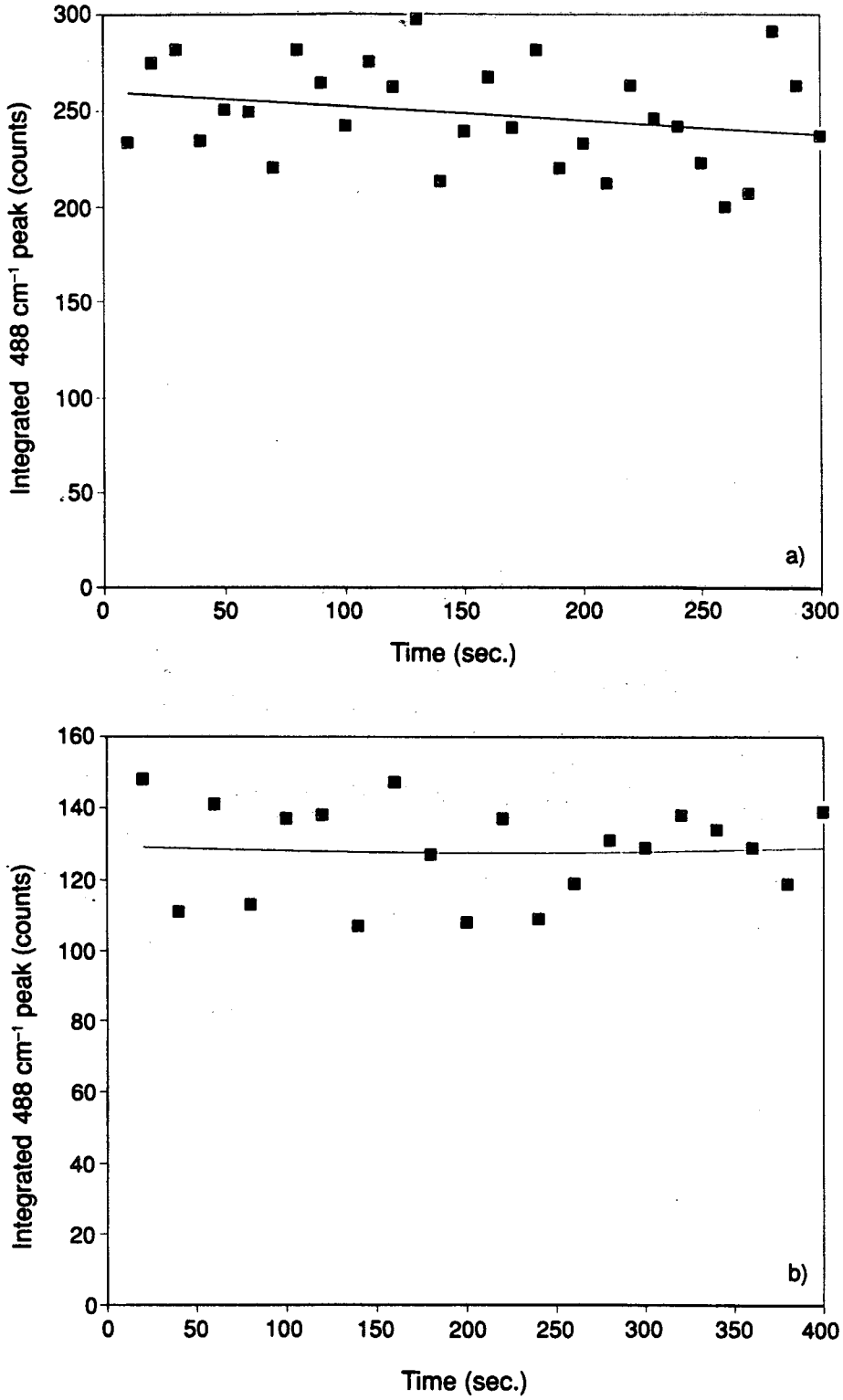

XBL 899-7293

Figure 8-26

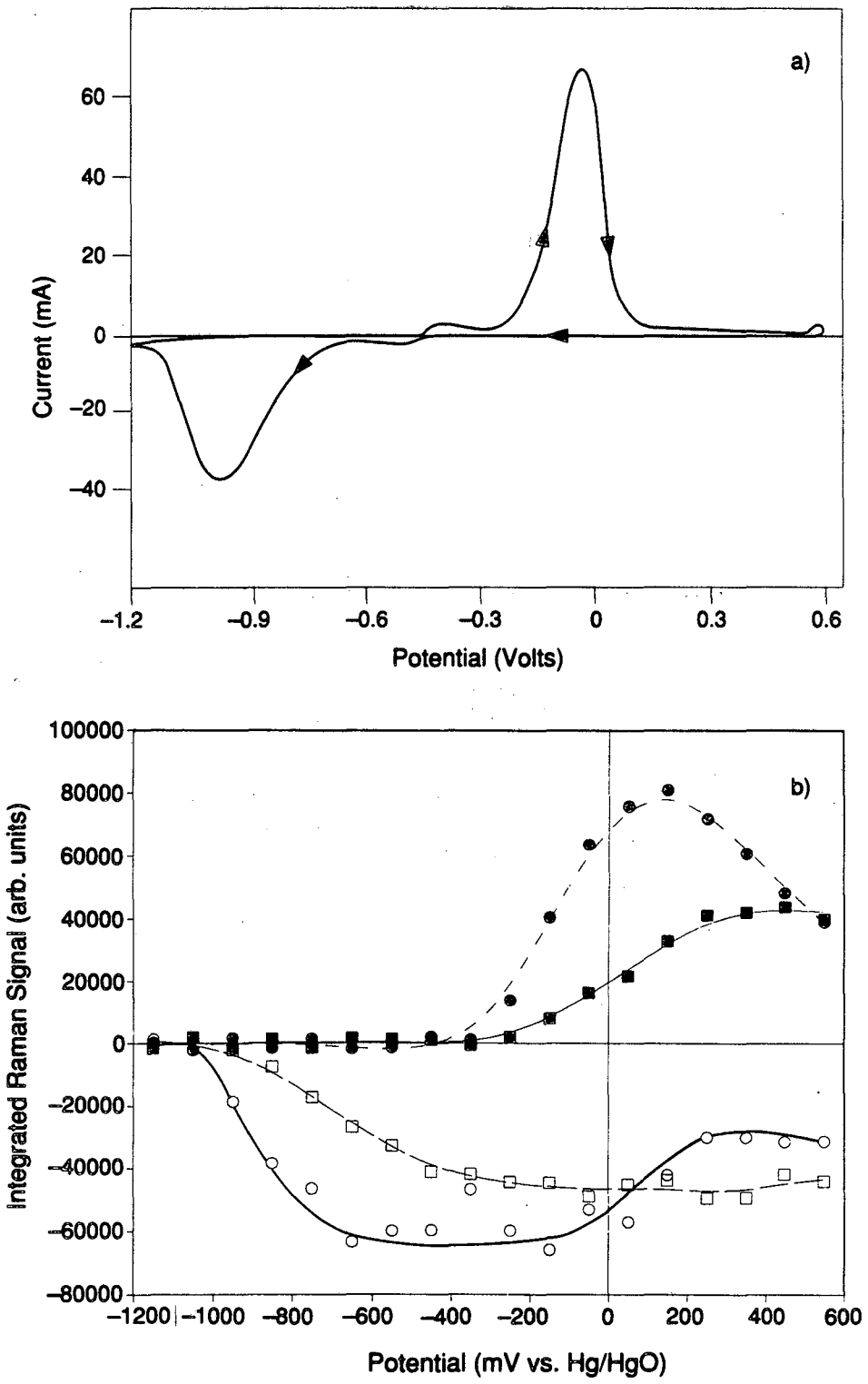

XBL 898-7249

Figure 8-27

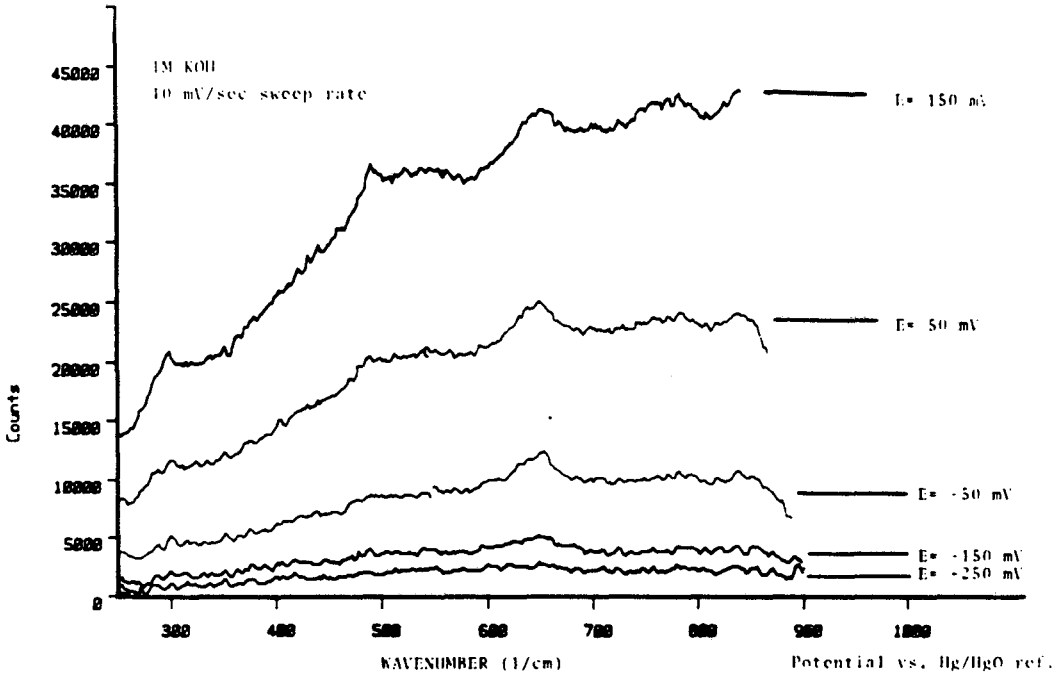

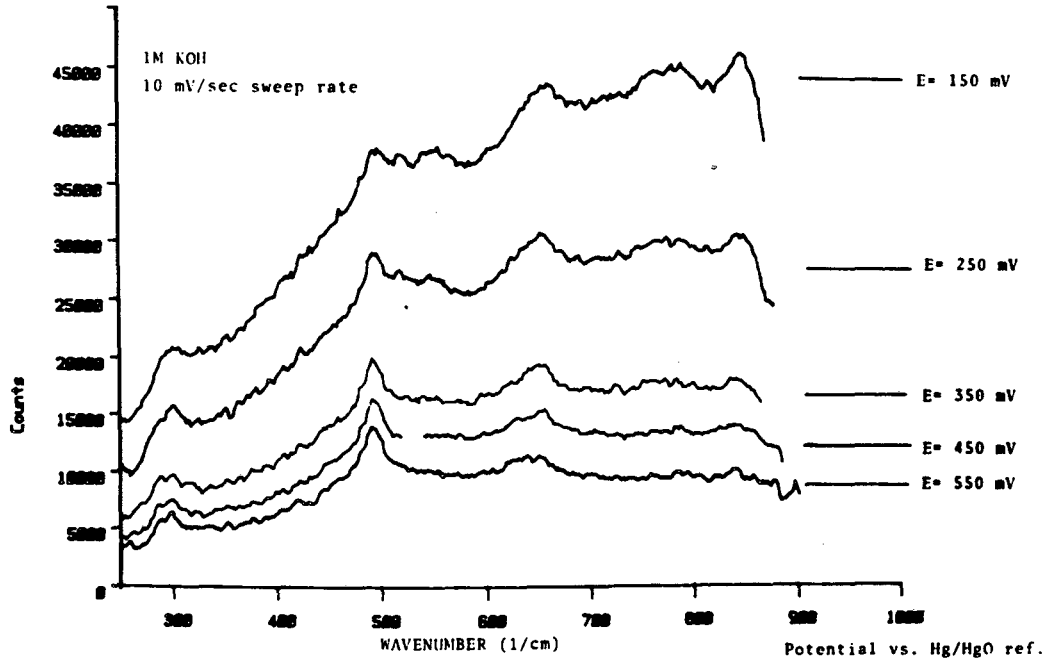

XBL 899-3378

Figure 8-28

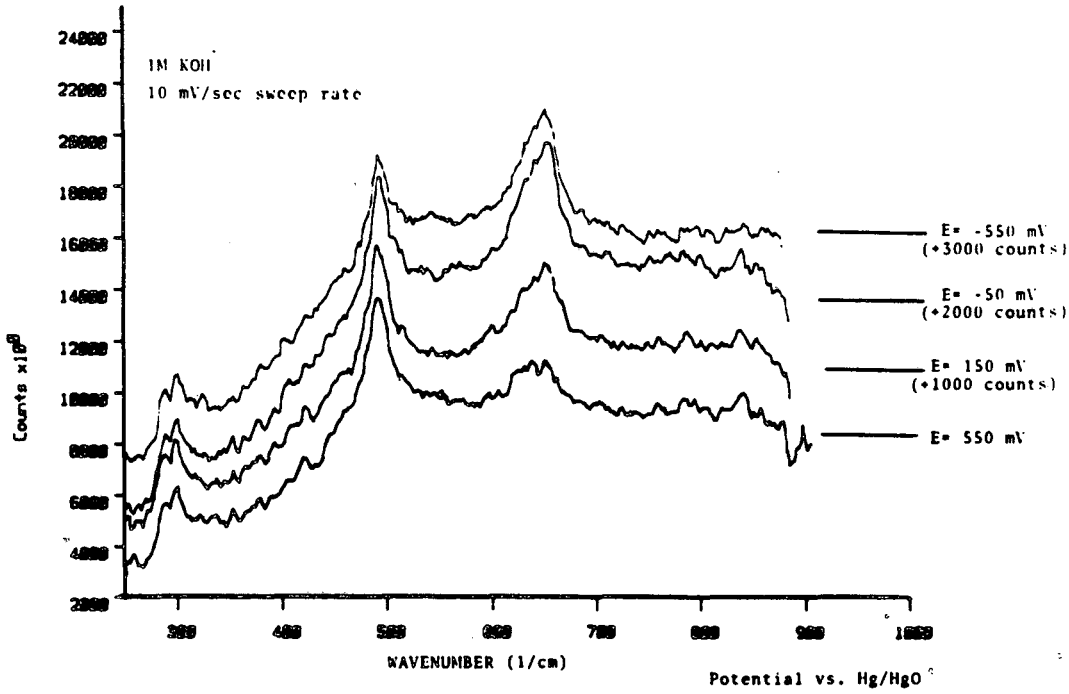

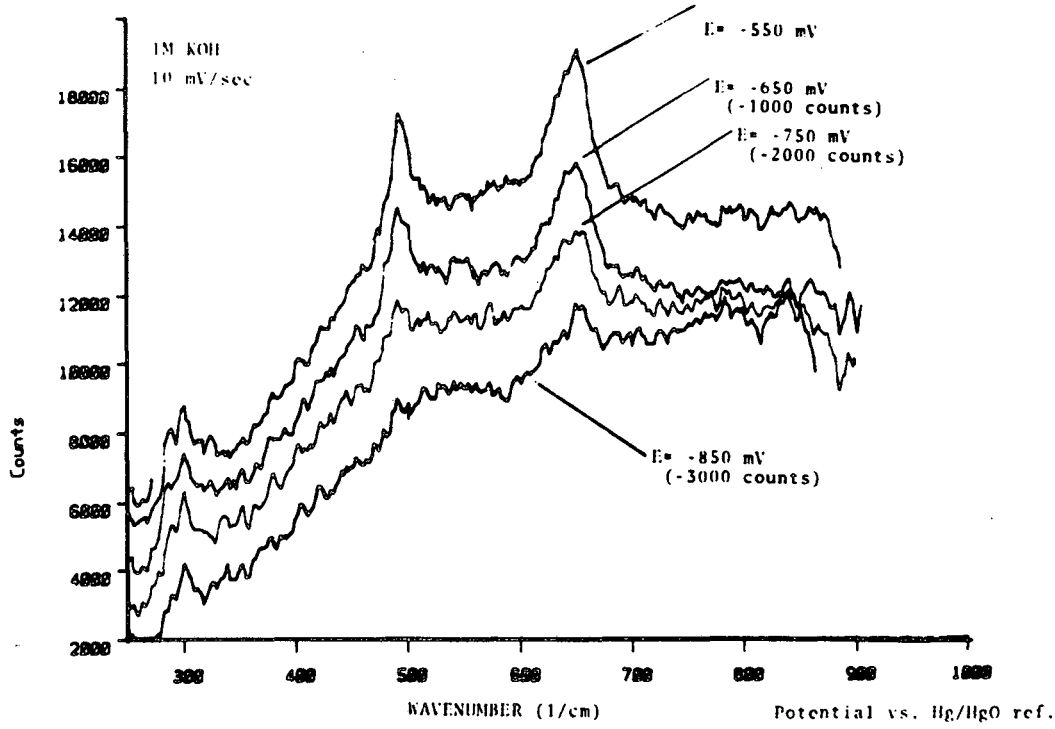

XBL 899-3379

Figure 8-29

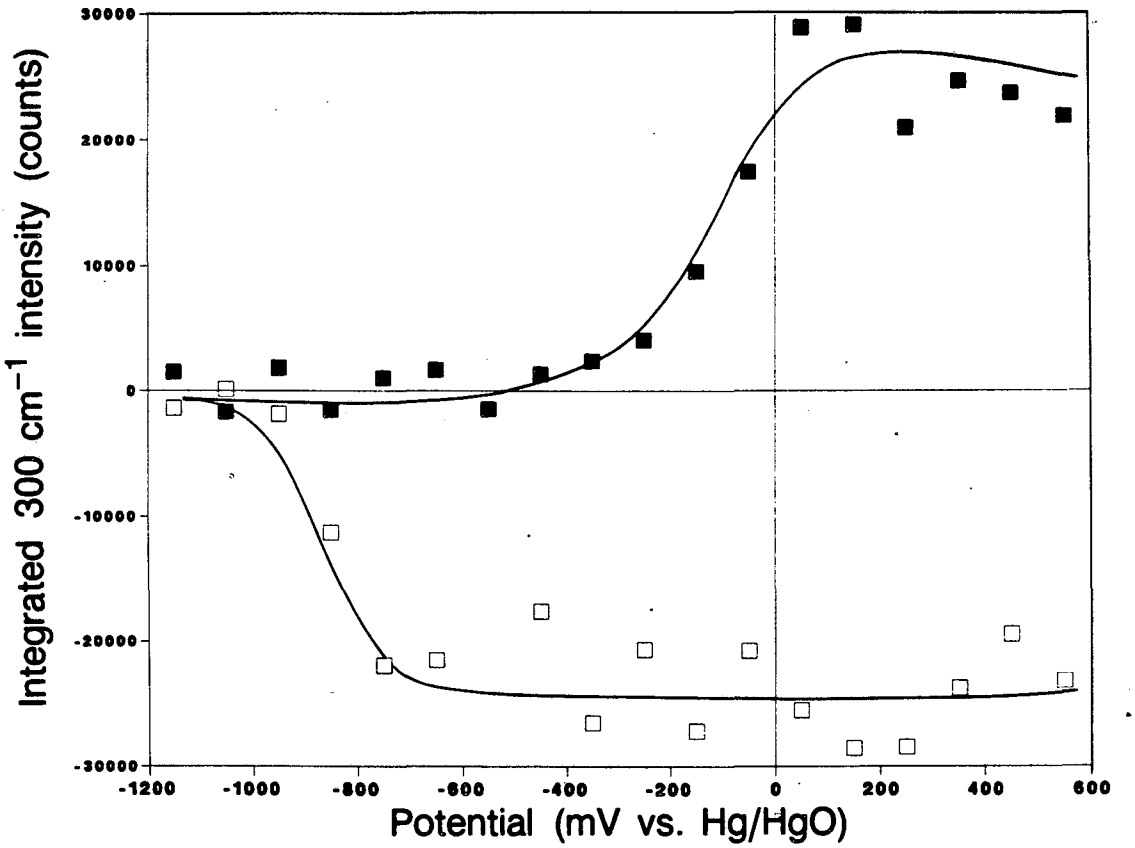

XBL 898-7250

Figure 8-30

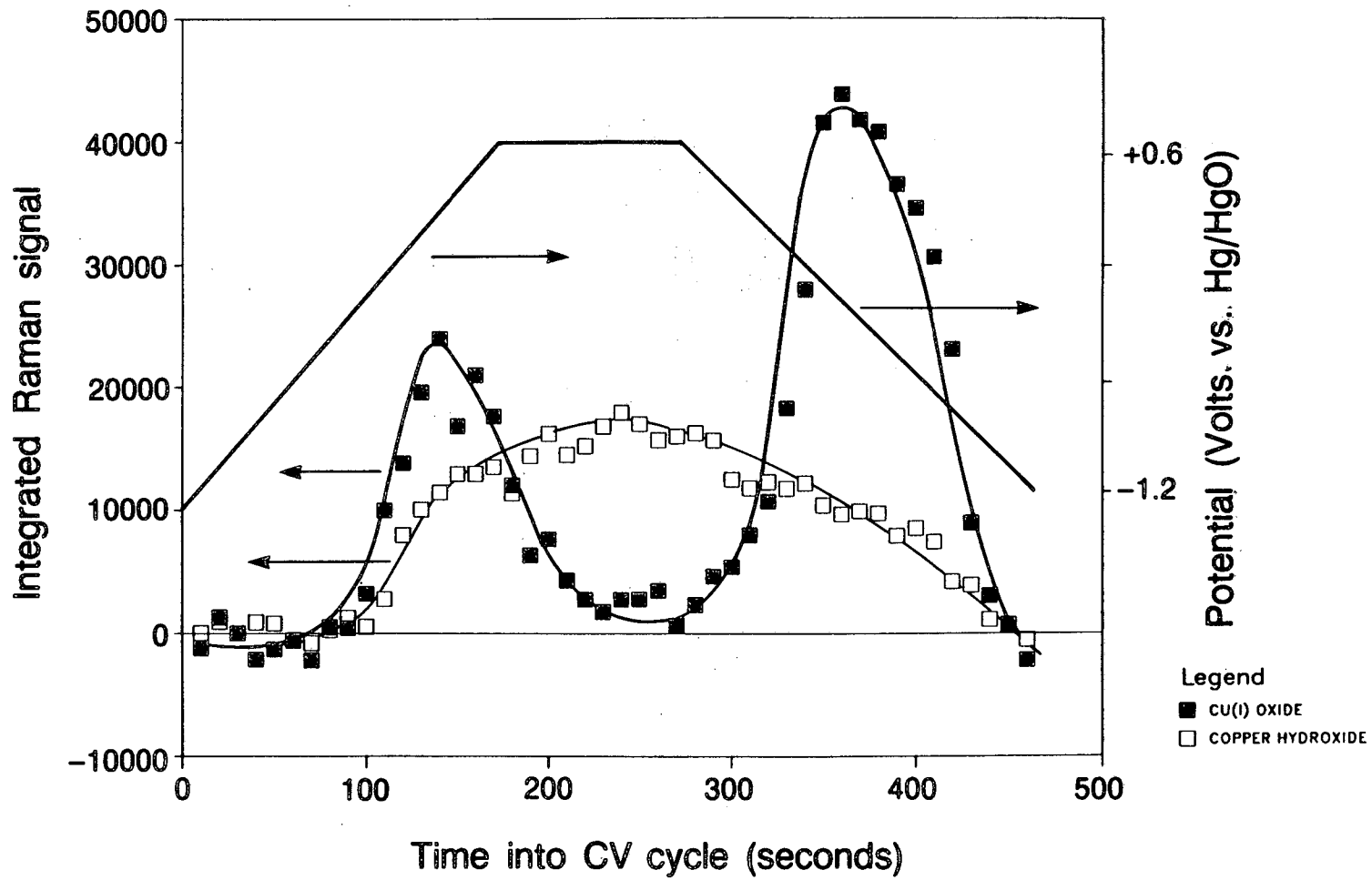

XBL 898-7252

Figure 8-31

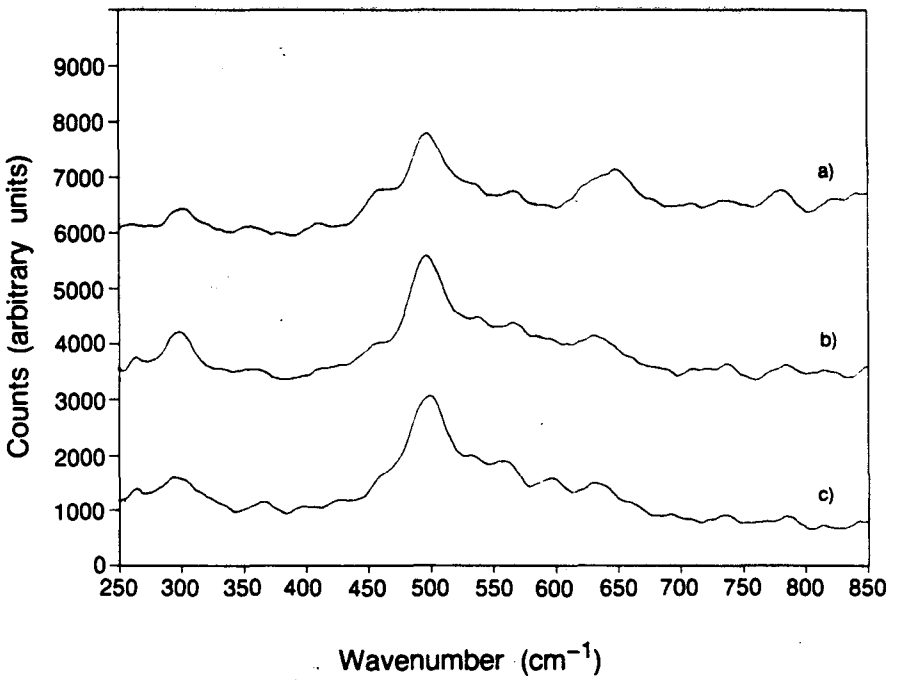

XBL 898-7239

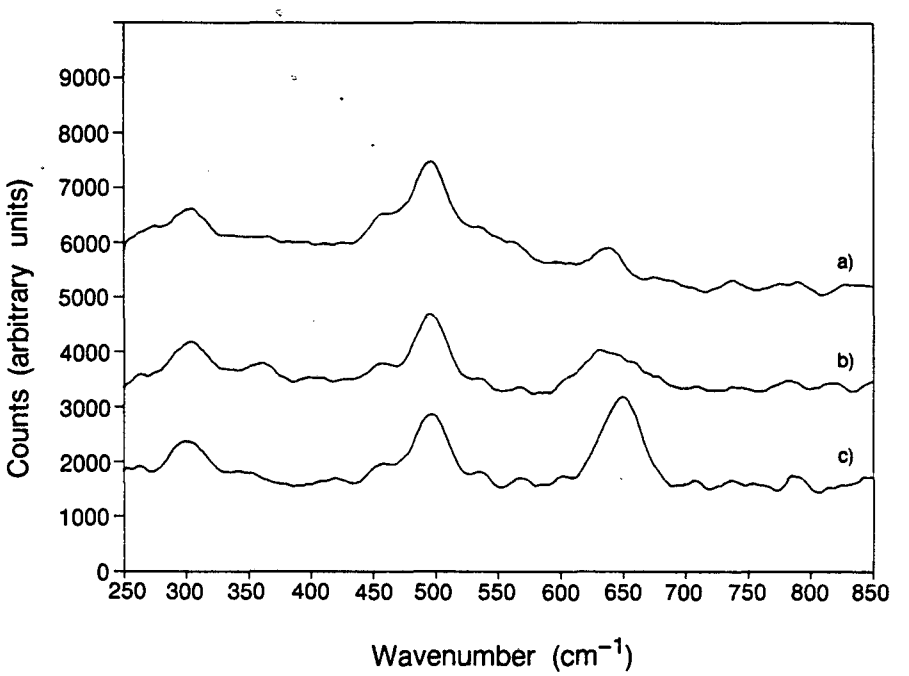

XBL 898-7240A

Figure 8-32

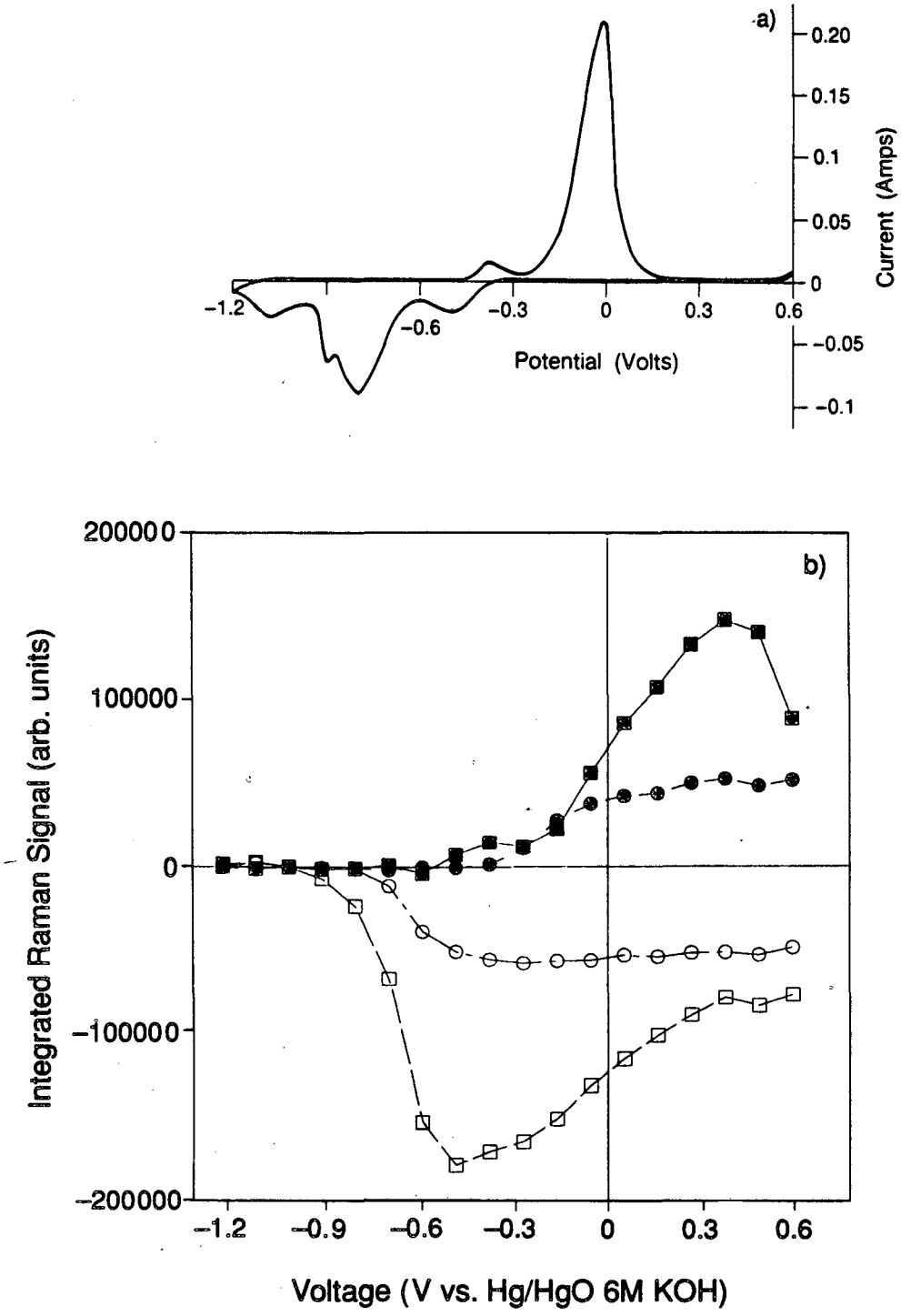

XBL 899-7299

Figure 8-33

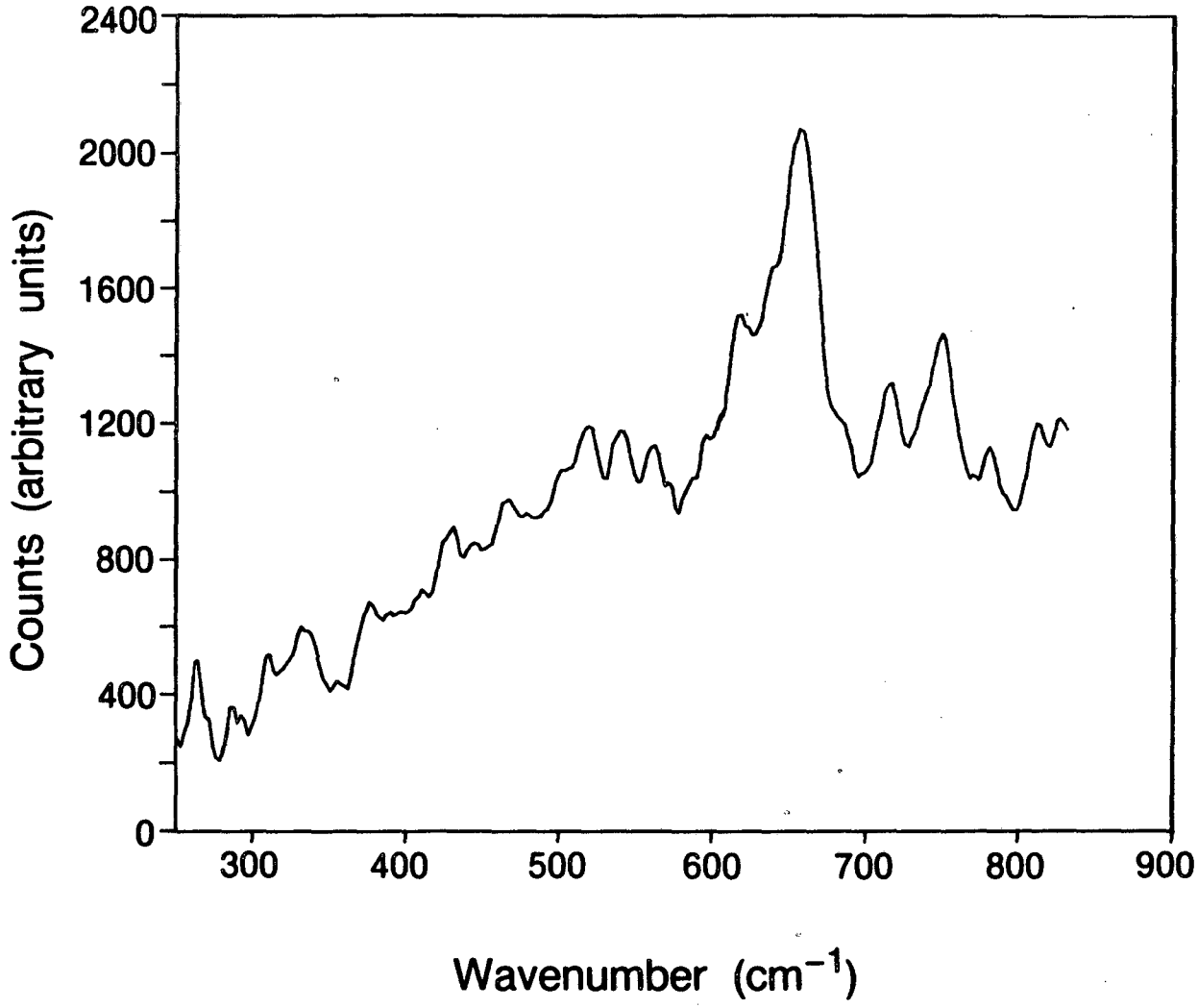

Figure 8-34

XBL 898-7254

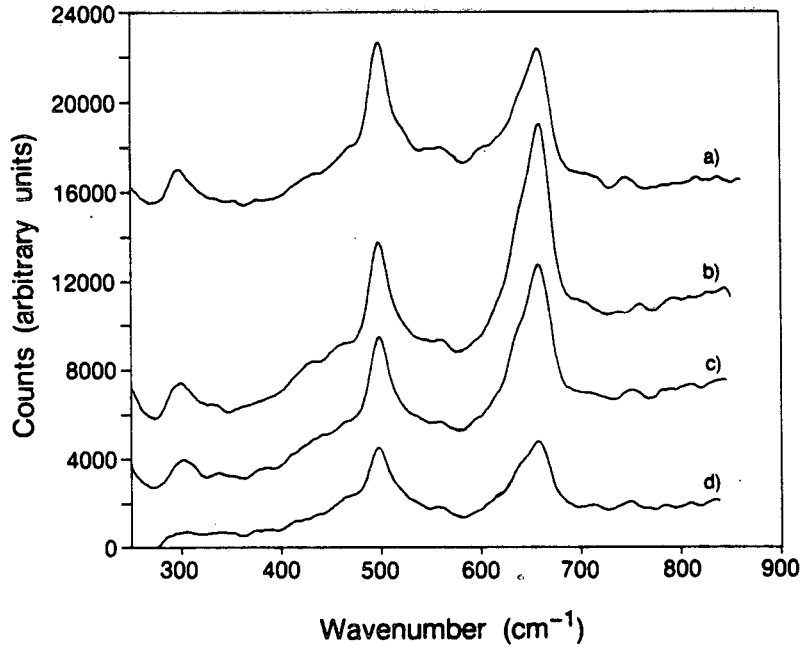

XBL 898-7258

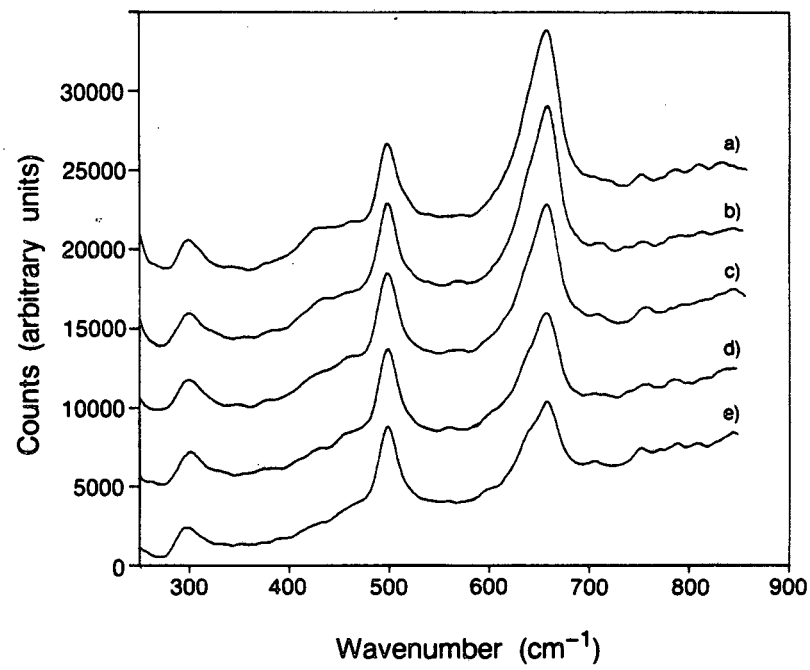

XBL 898-7257A

Figure 8-35

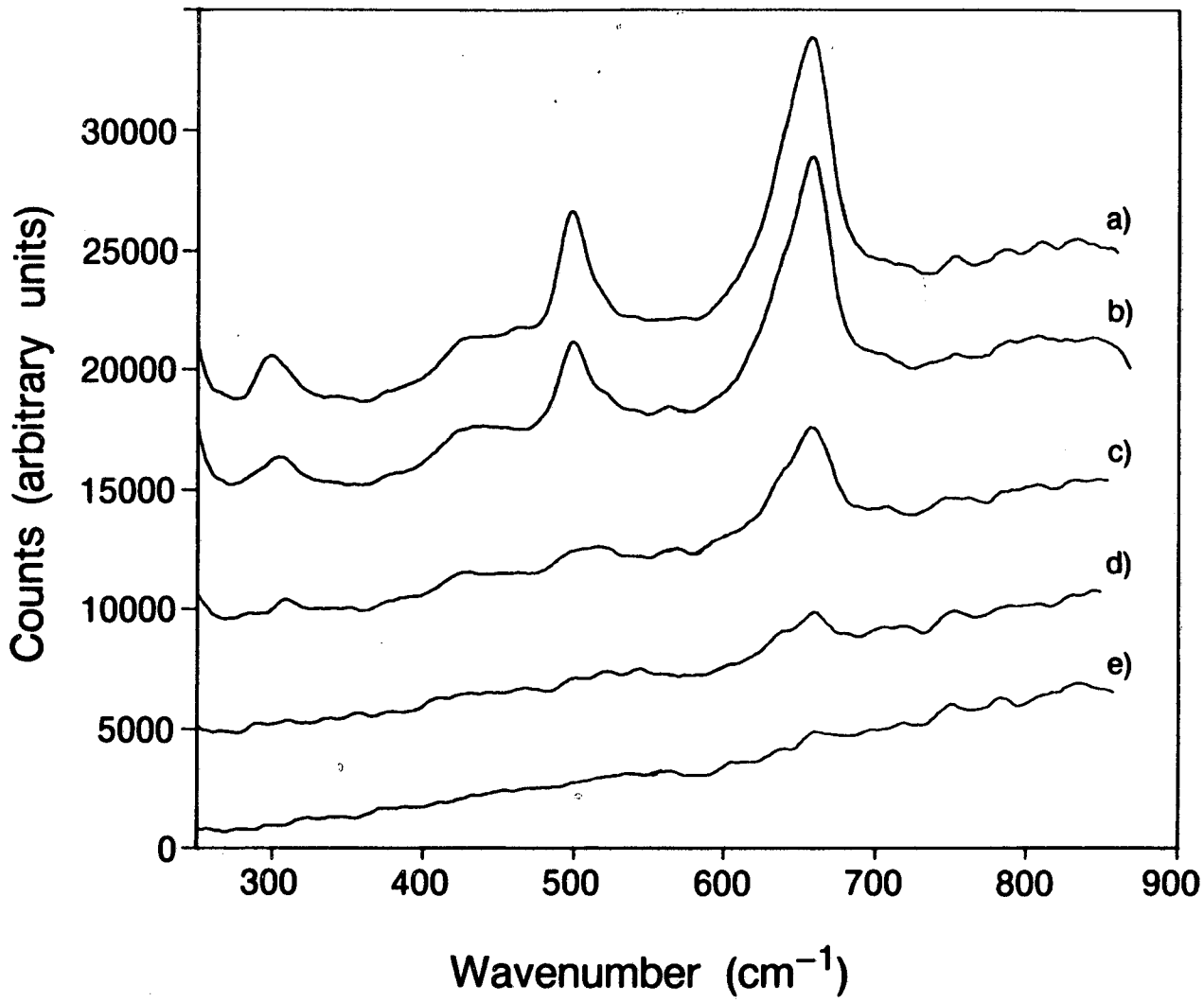

Figure 8-36

XBL 898-7256

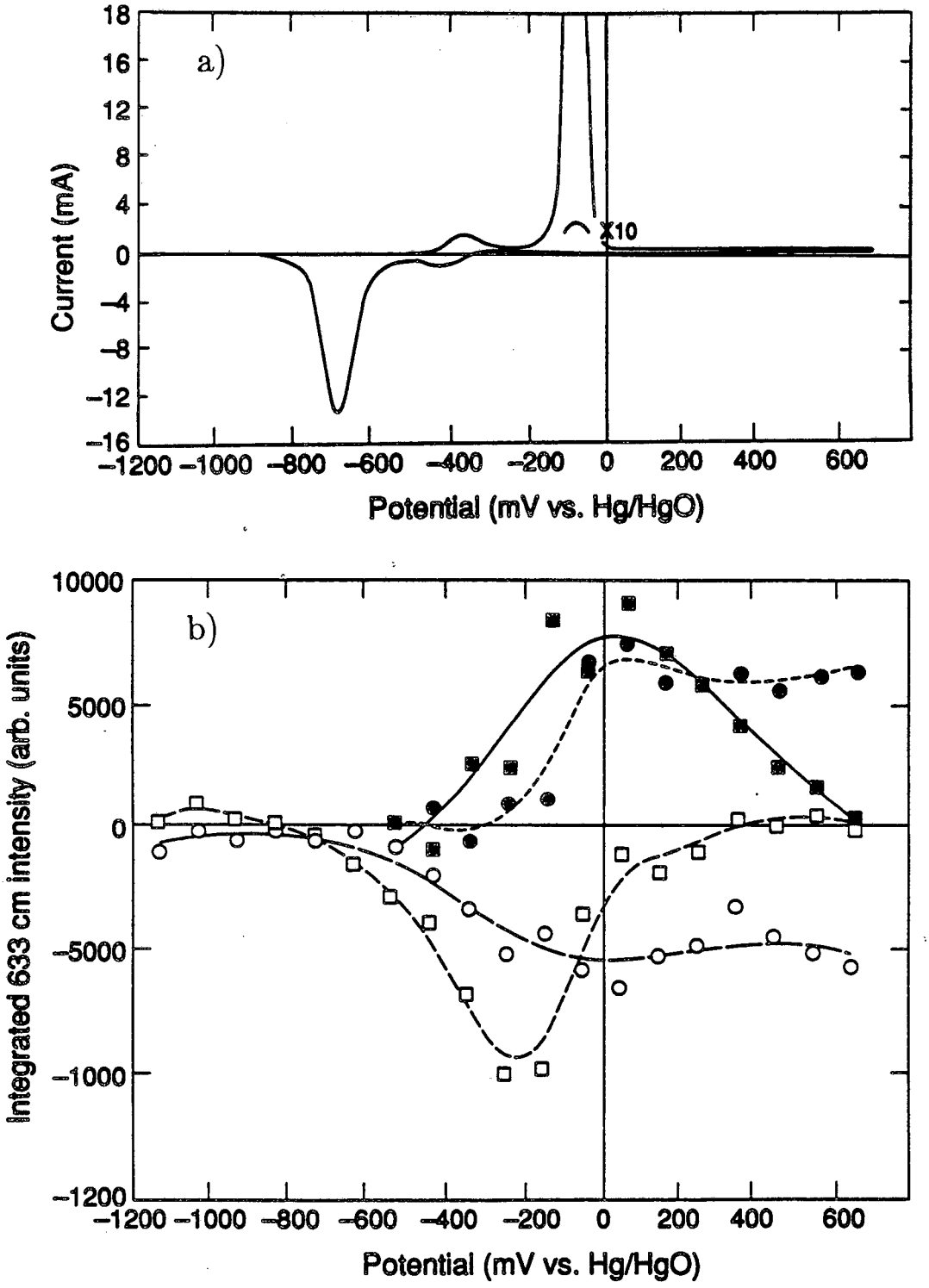
a)
Current (mA)
18
16
12
8
4
0
−4
−8
−12
−16
X10
−1200 −1000 −800 −600 −400 −200 0 200 400 600
Potential (mV vs. Hg/HgO)
b)
Integrated 633 cm intensity (arb. units)
10000
5000
0
−5000
−1000
−1200
−1200 −1000 −800 −600 −400 −200 0 200 400 600
Potential (mV vs. Hg/HgO)
XBL 899-7298

Figure 8-37

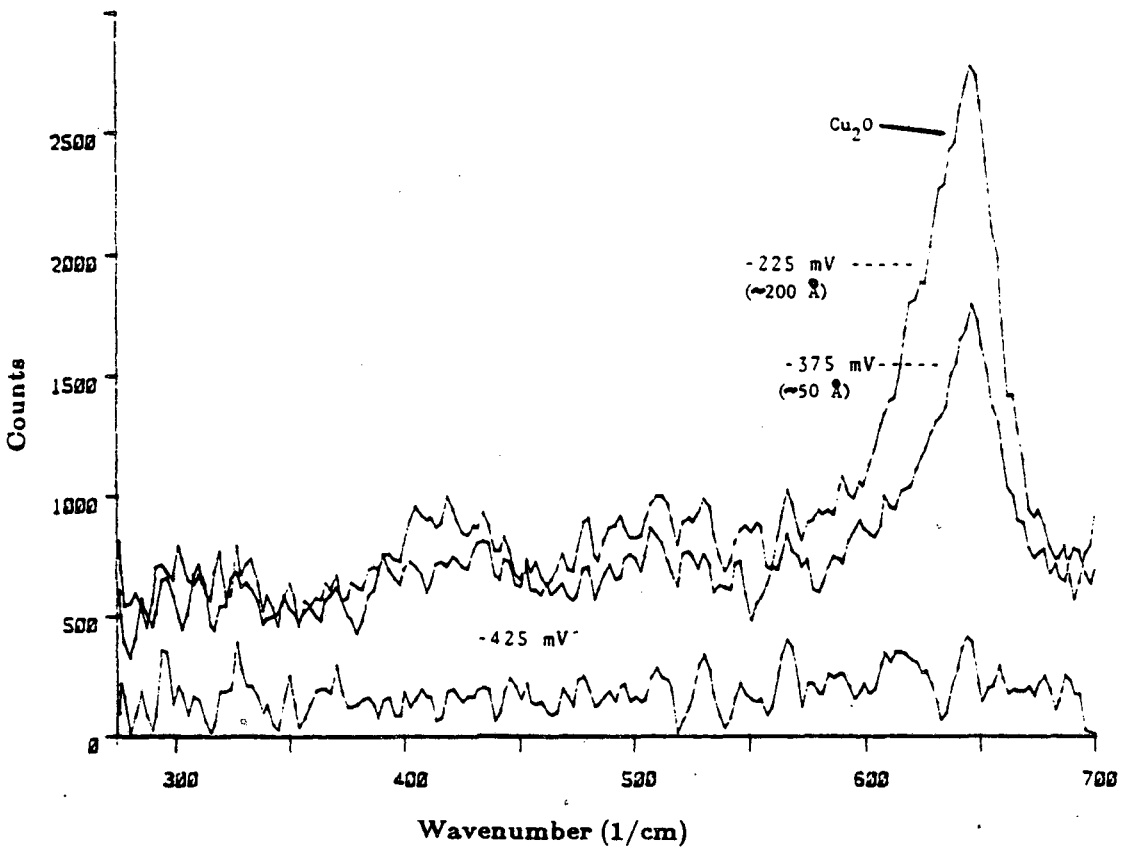

Figure 8-38

XBL 888-3090

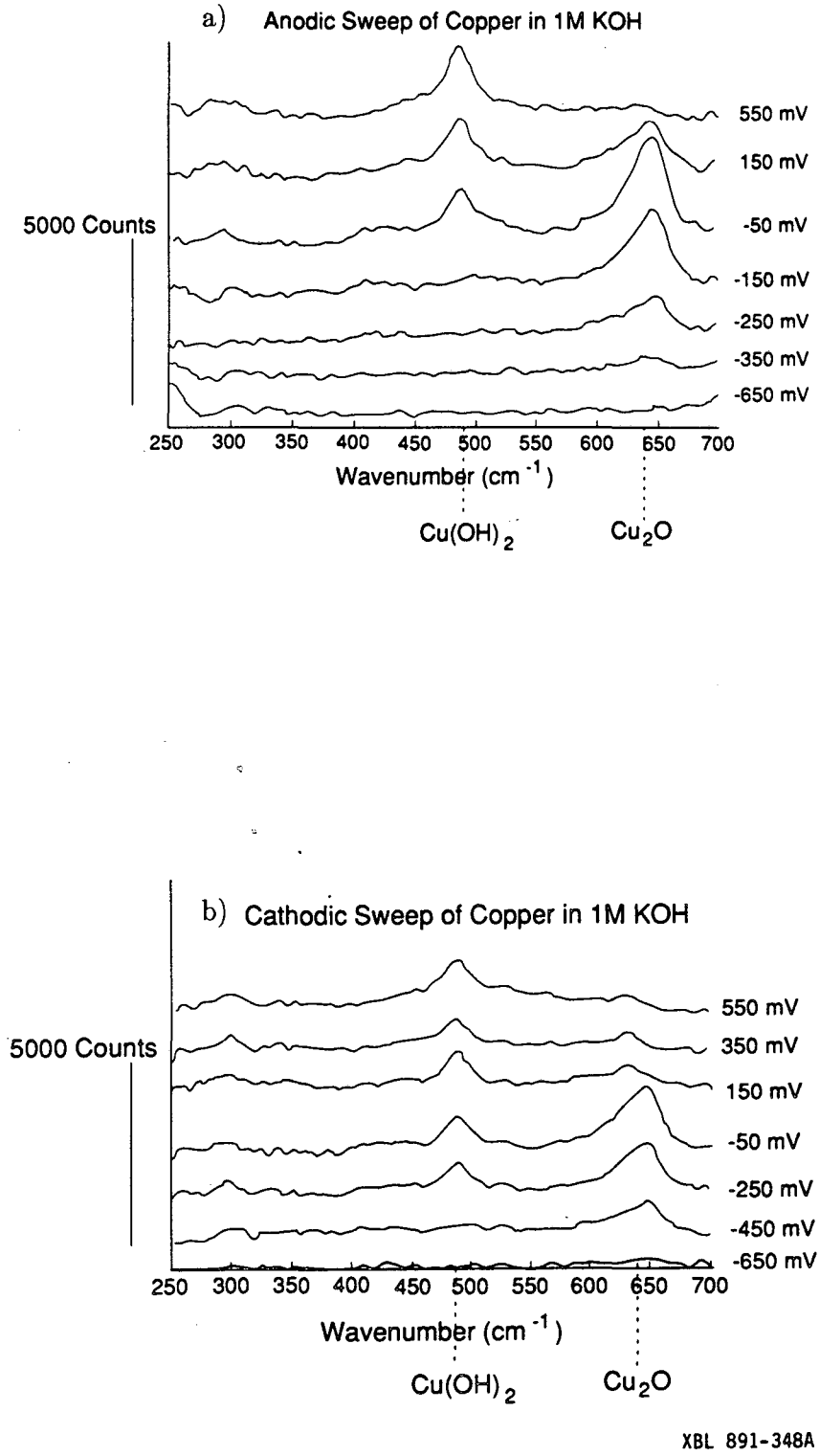
a) Anodic Sweep of Copper in 1M KOH
5000 Counts
550 mV
150 mV
-50 mV
-150 mV
-250 mV
-350 mV
-650 mV
250 300 350 400 450 500 550 600 650 700
Wavenumber (cm -1)
Cu(OH) 2
Cu2O
b) Cathodic Sweep of Copper in 1M KOH
5000 Counts
550 mV
350 mV
150 mV
-50 mV
-250 mV
-450 mV
-650 mV
250 300 350 400 450 500 550 600 650 700
Wavenumber (cm -1)
Cu(OH) 2
Cu2O
XBL 891-348A

Figure 8-39

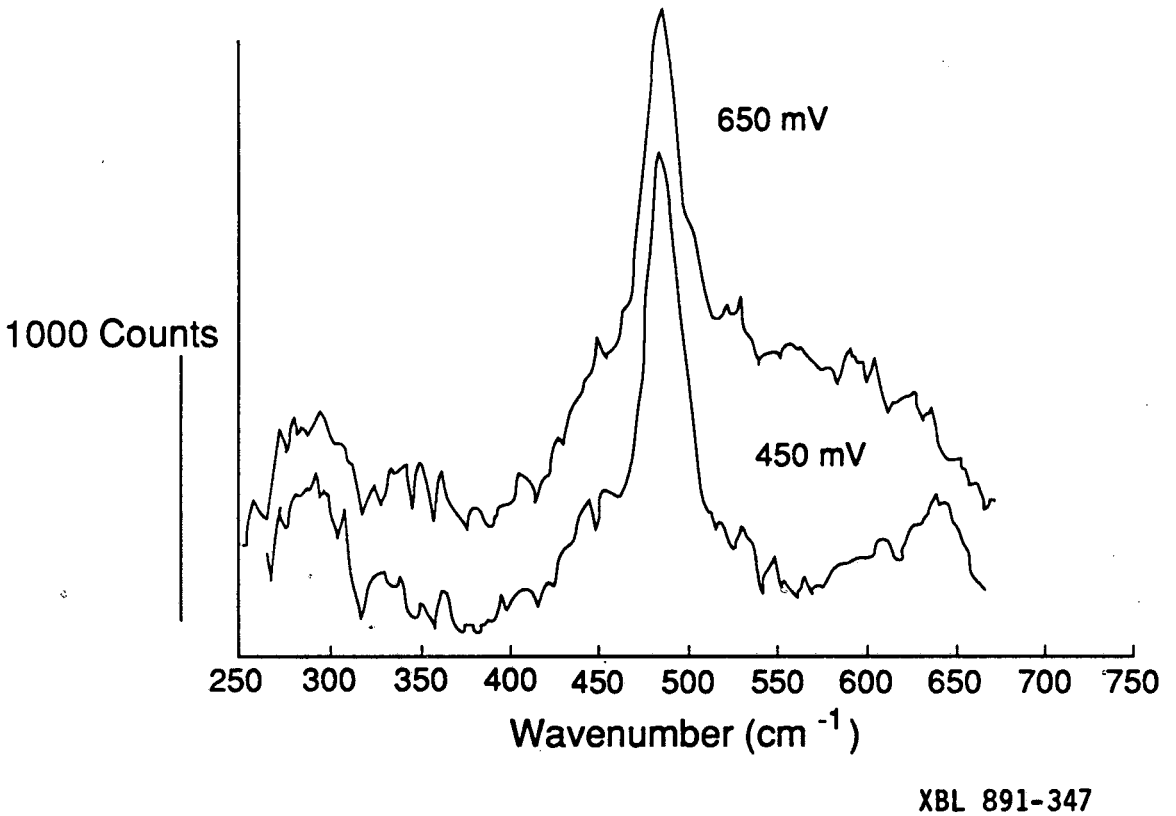
650 mV
450 mV
1000 Counts
250
300
350
400
450
500
550
600
650
700
750
Wavenumber (cm -1)
XBL 891-347

Figure 8-40

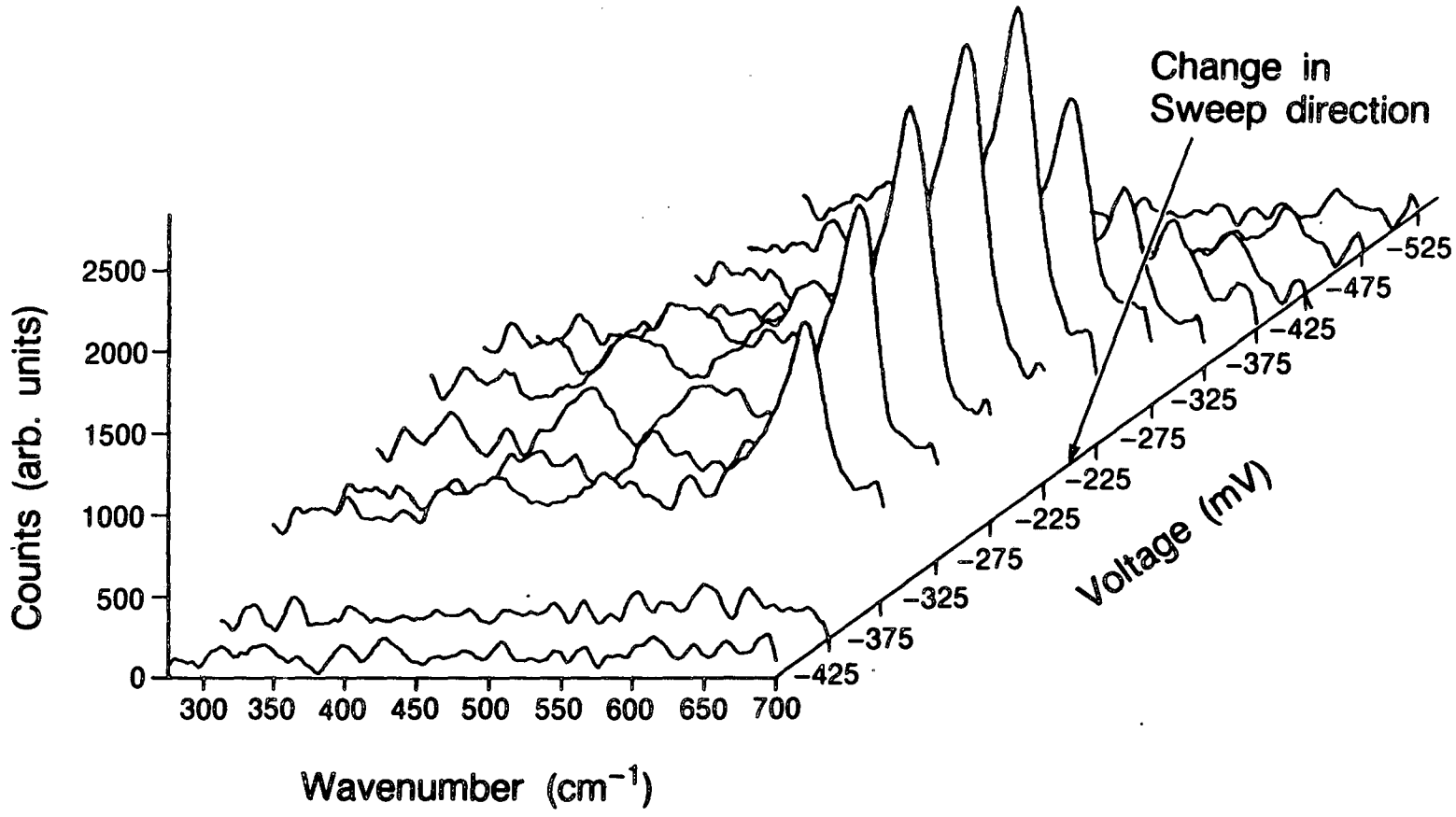

Figure 8-41

XBL 898-7253

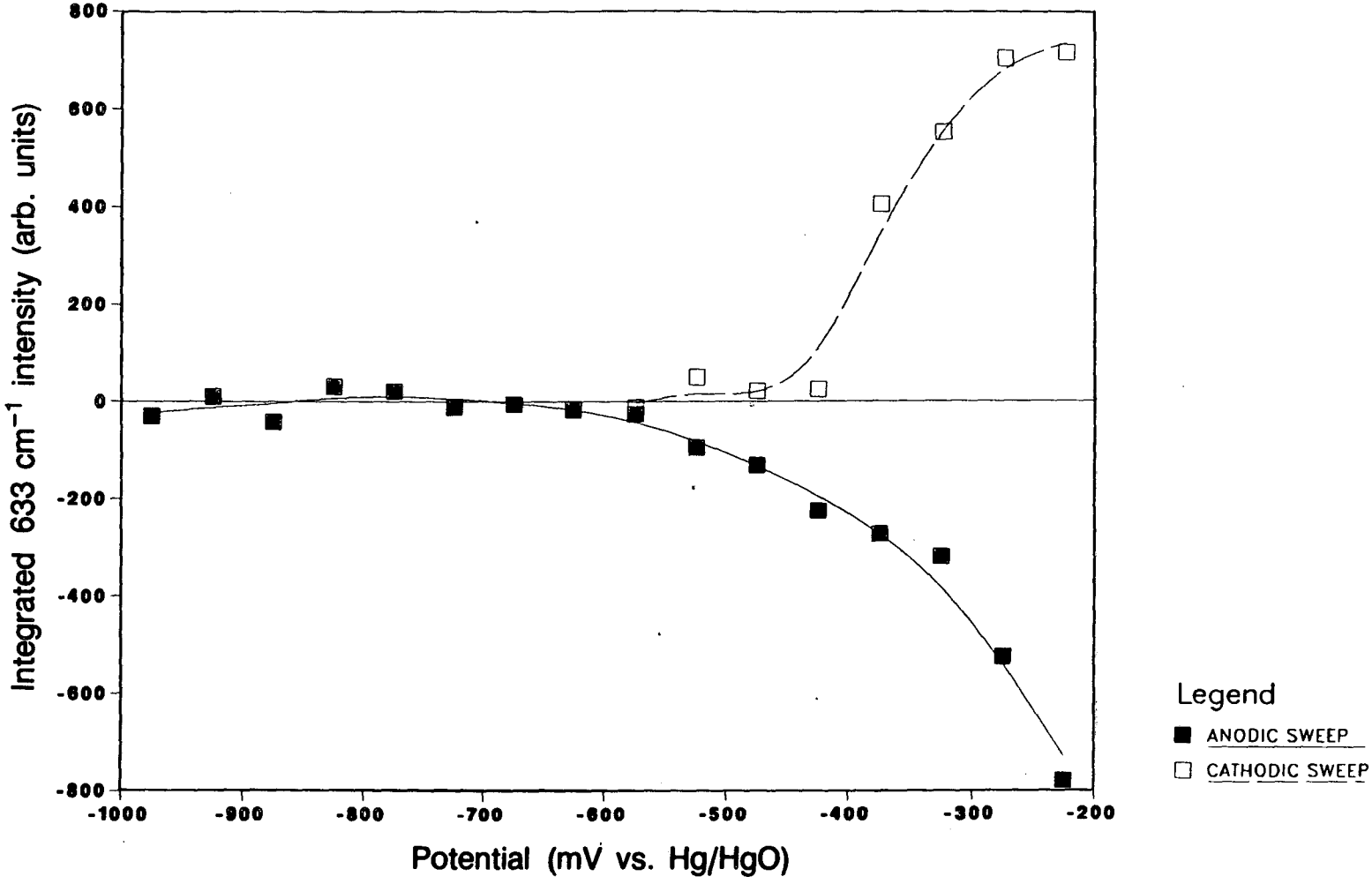

Figure 8-42

XBL 898-7245

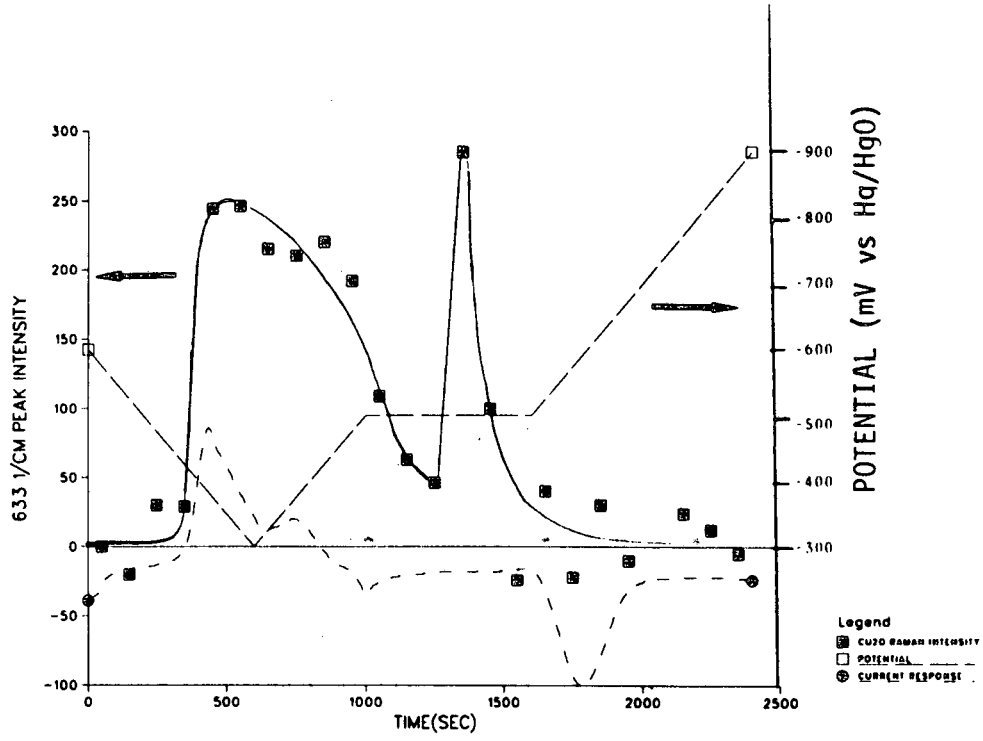

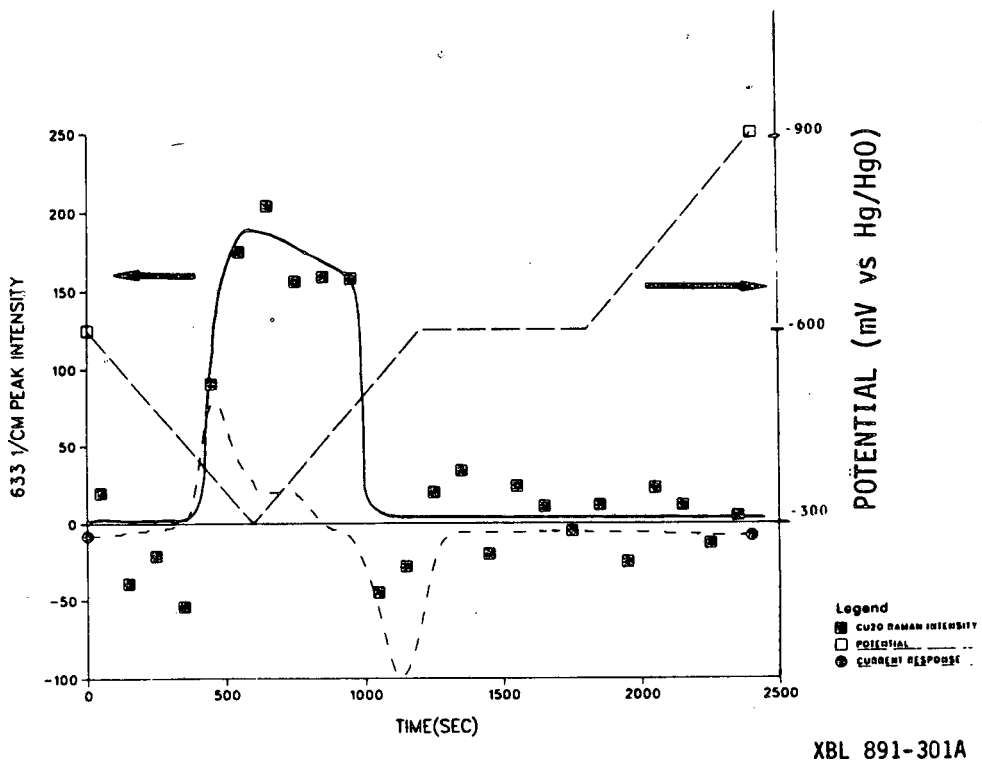

XBL 891-301A

Figure 8-43

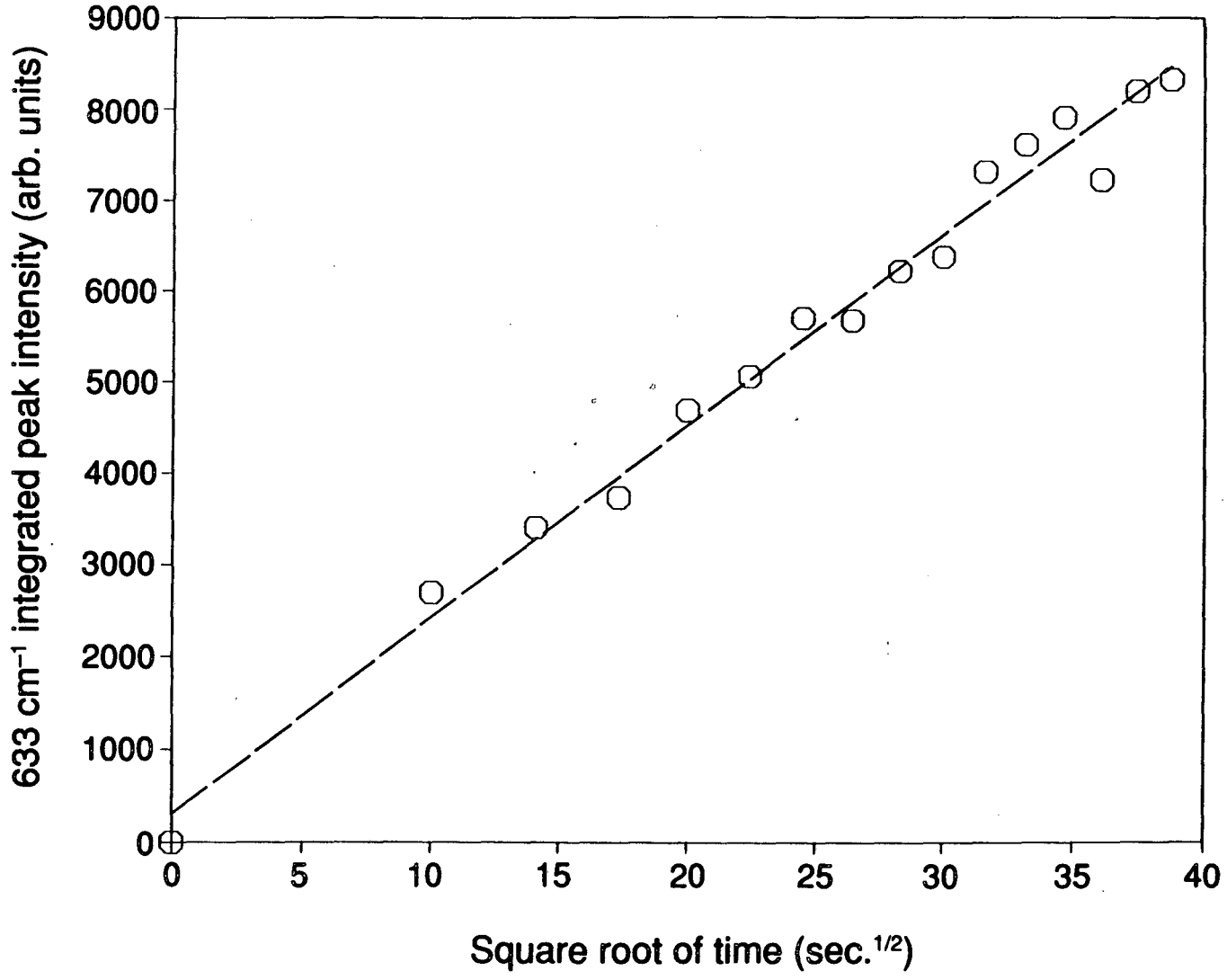

Figure 8-44

XBL 899-7288

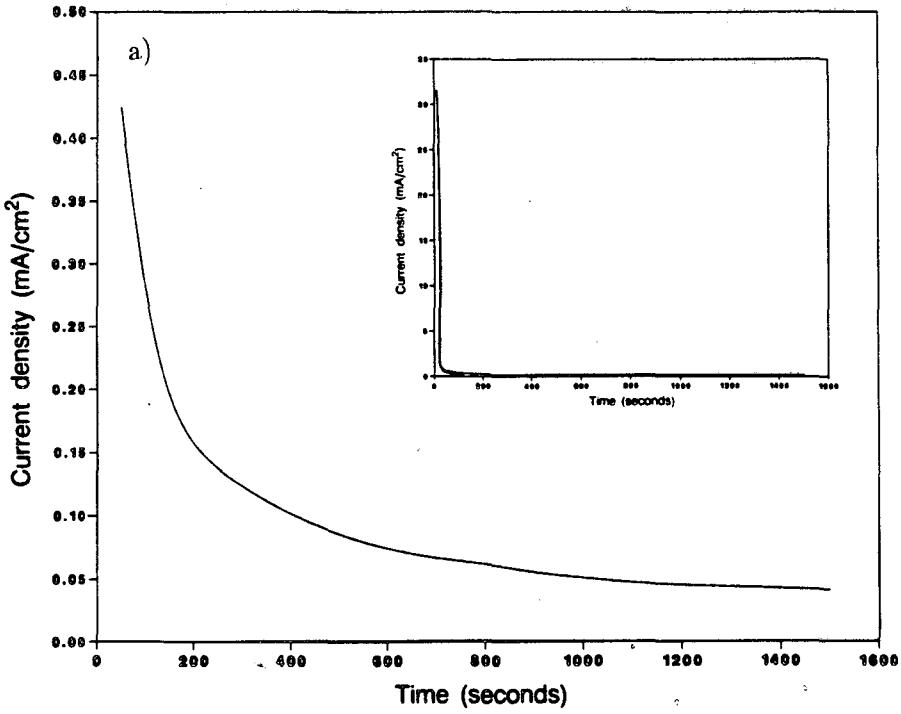

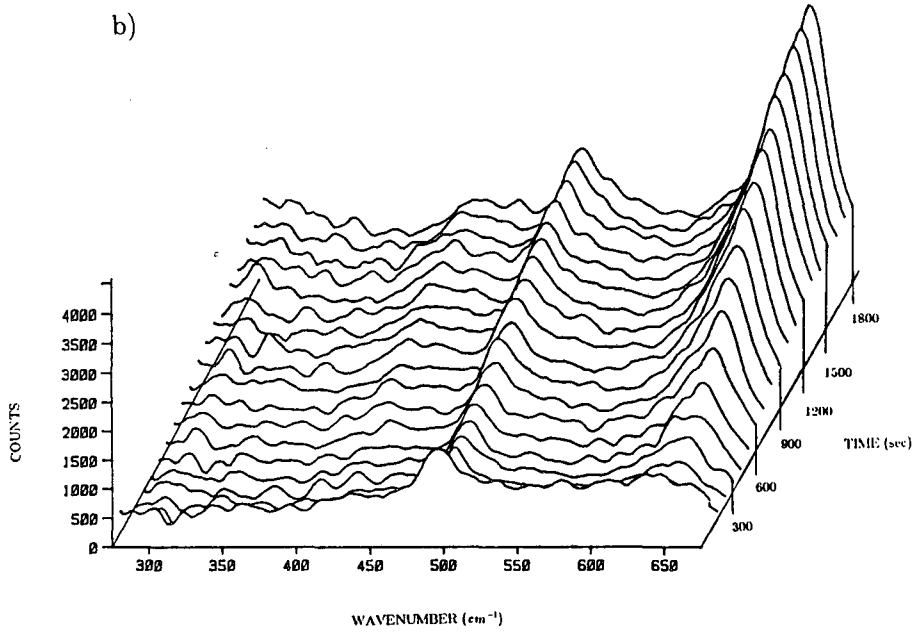

XBL 891-303A

Figure 8-45

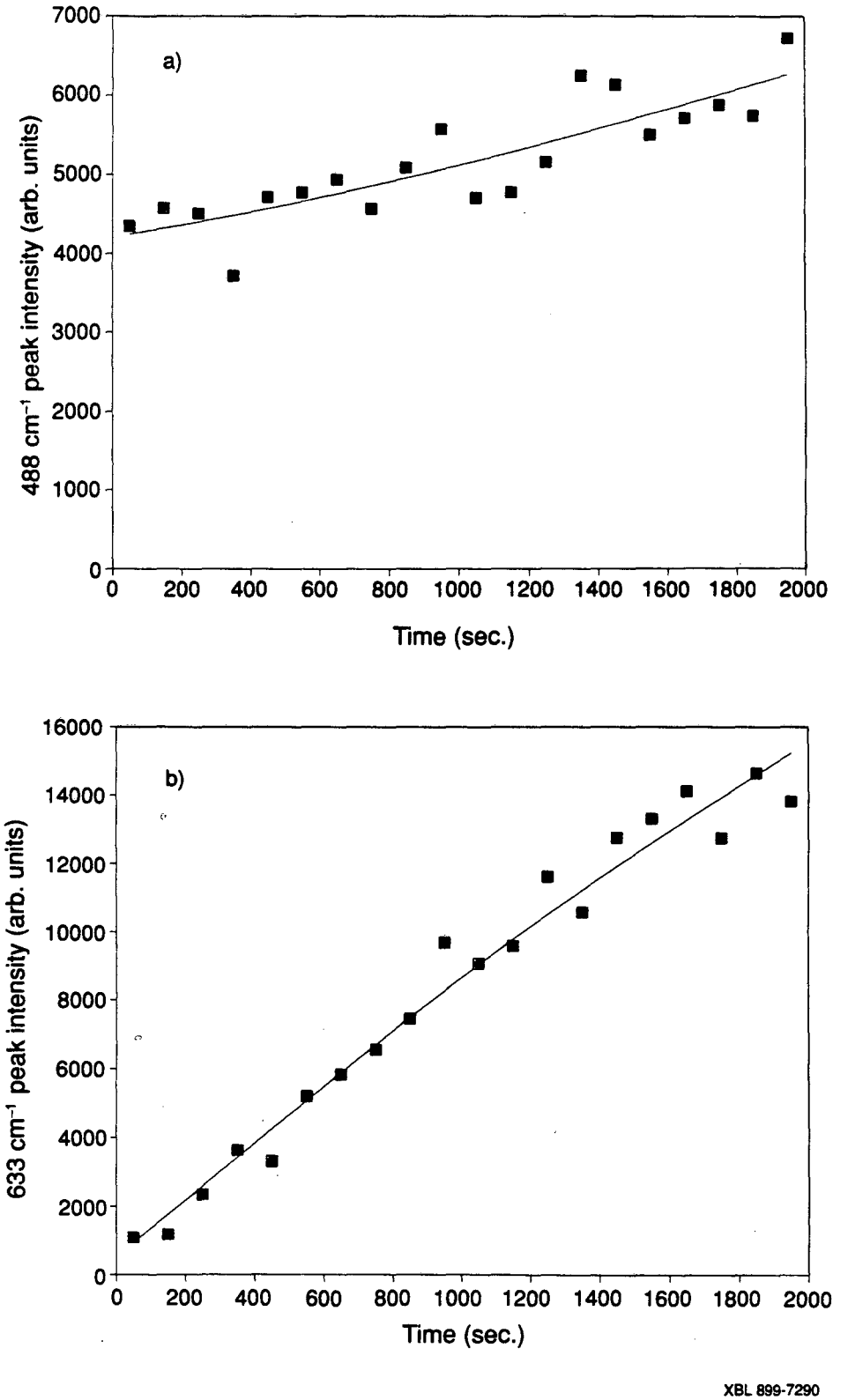
a)
488 cm⁻¹ peak intensity (arb. units)
Time (sec.)
b)
633 cm⁻¹ peak intensity (arb. units)
Time (sec.)
XBL 899-7290

Figure 8-46

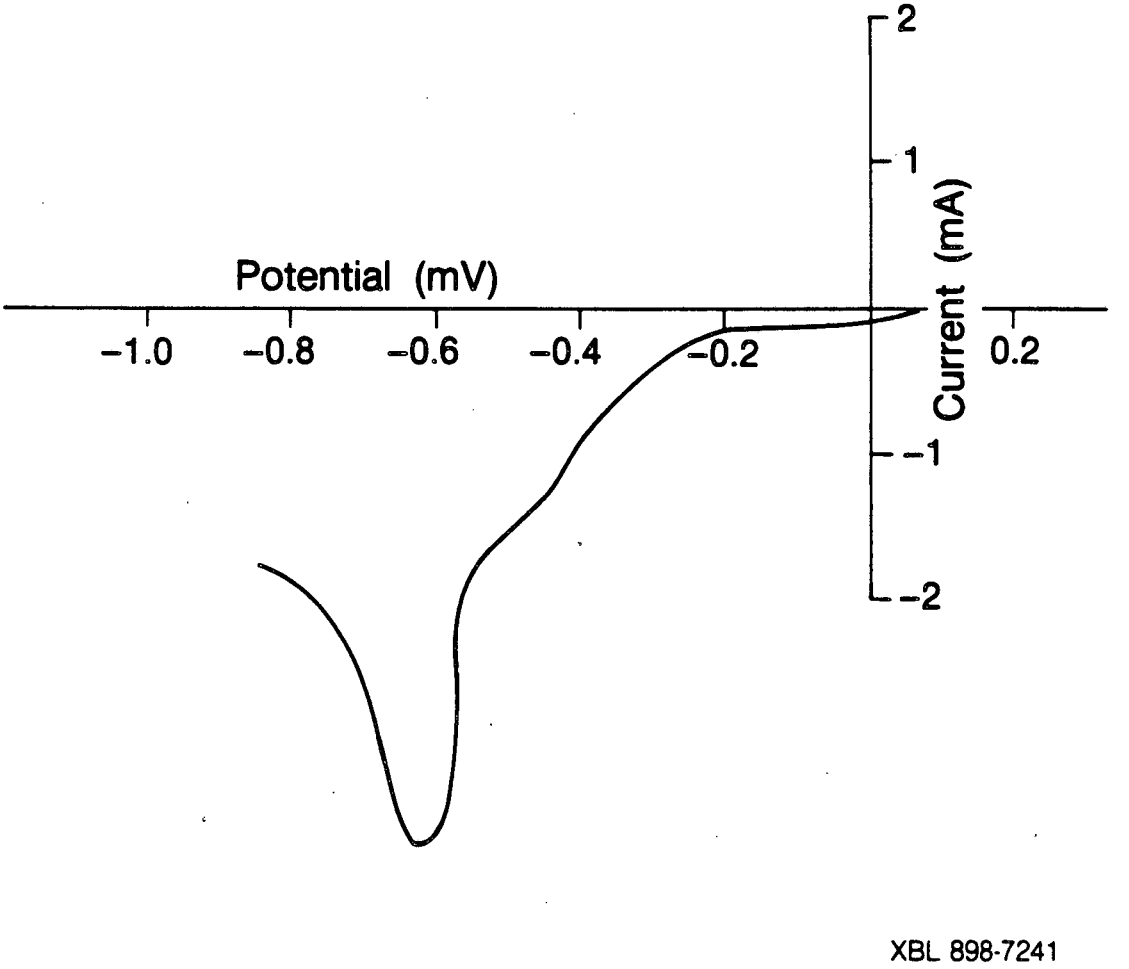

Figure 8-47

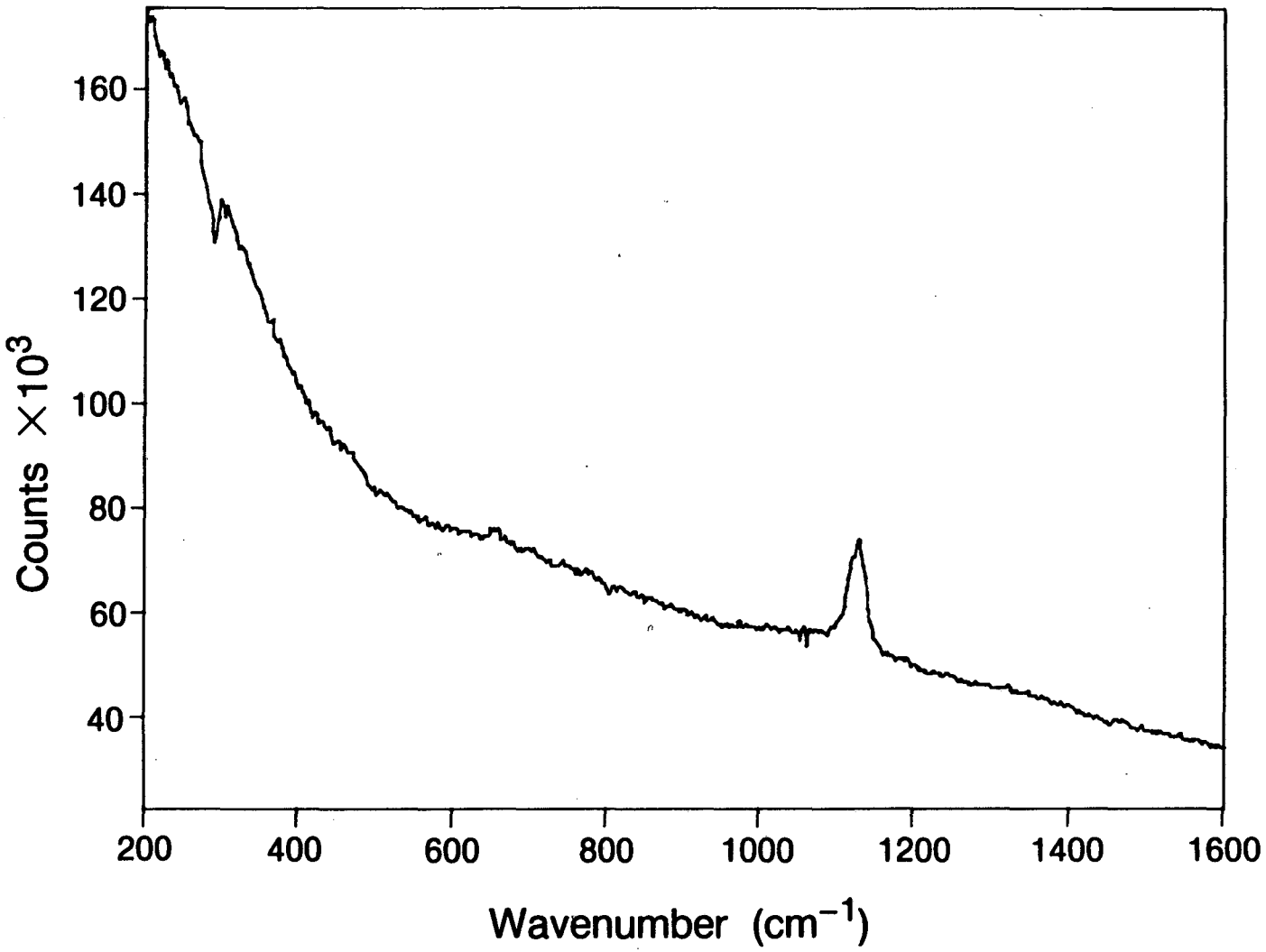

Figure 8-48

XBL 898-7255

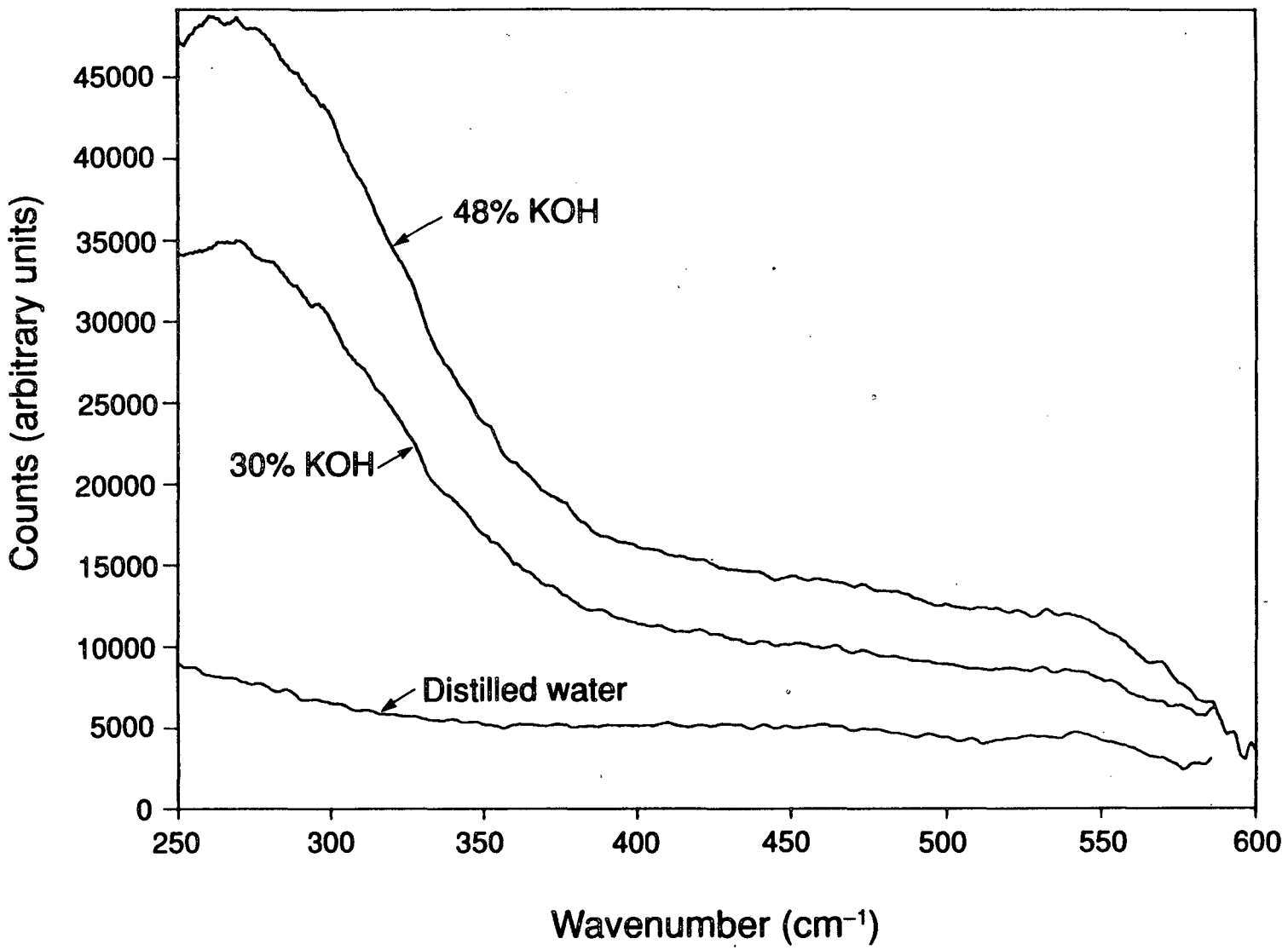

XBL 898-7280

Figure 8-49

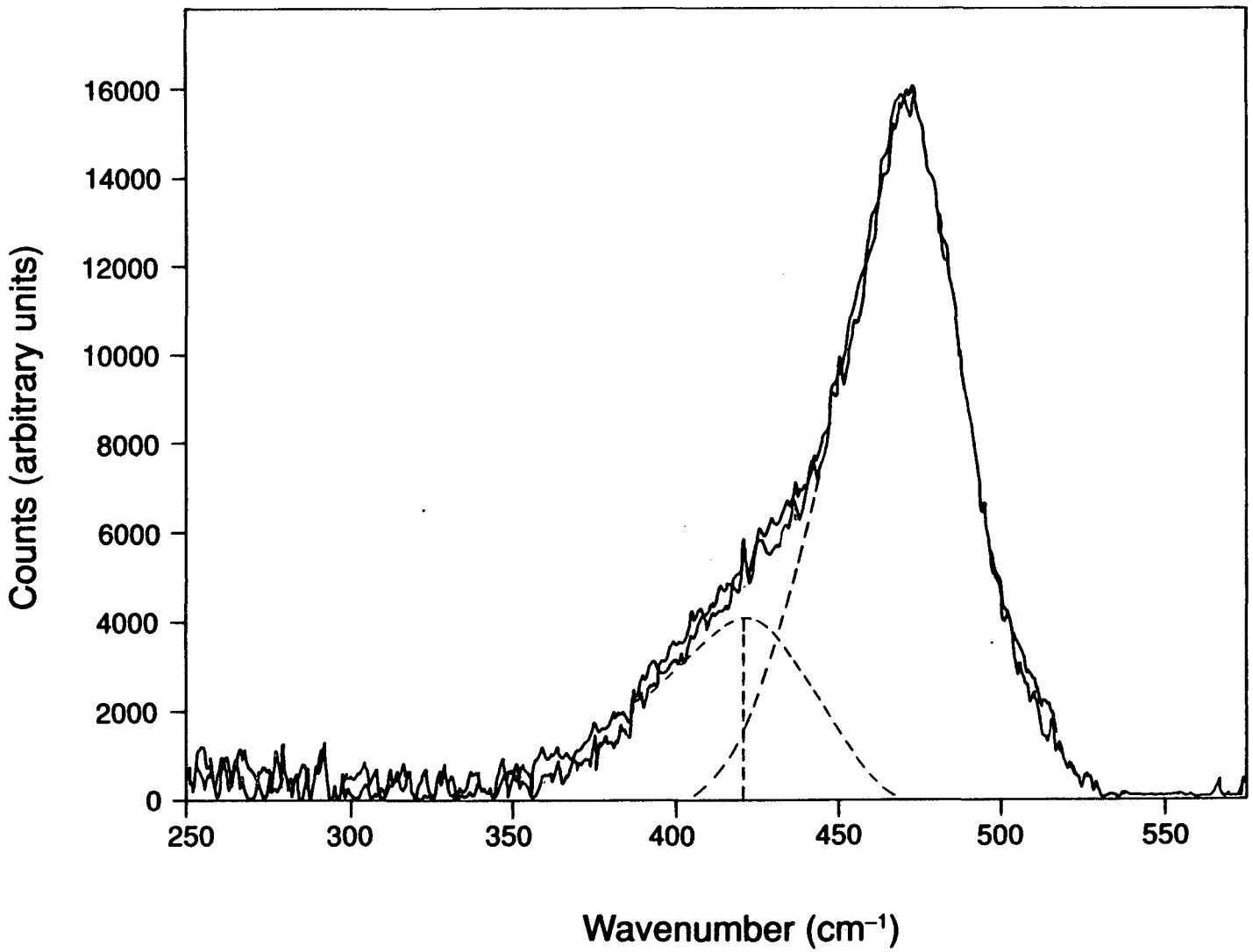

Figure 8-50

XBL 898-7269

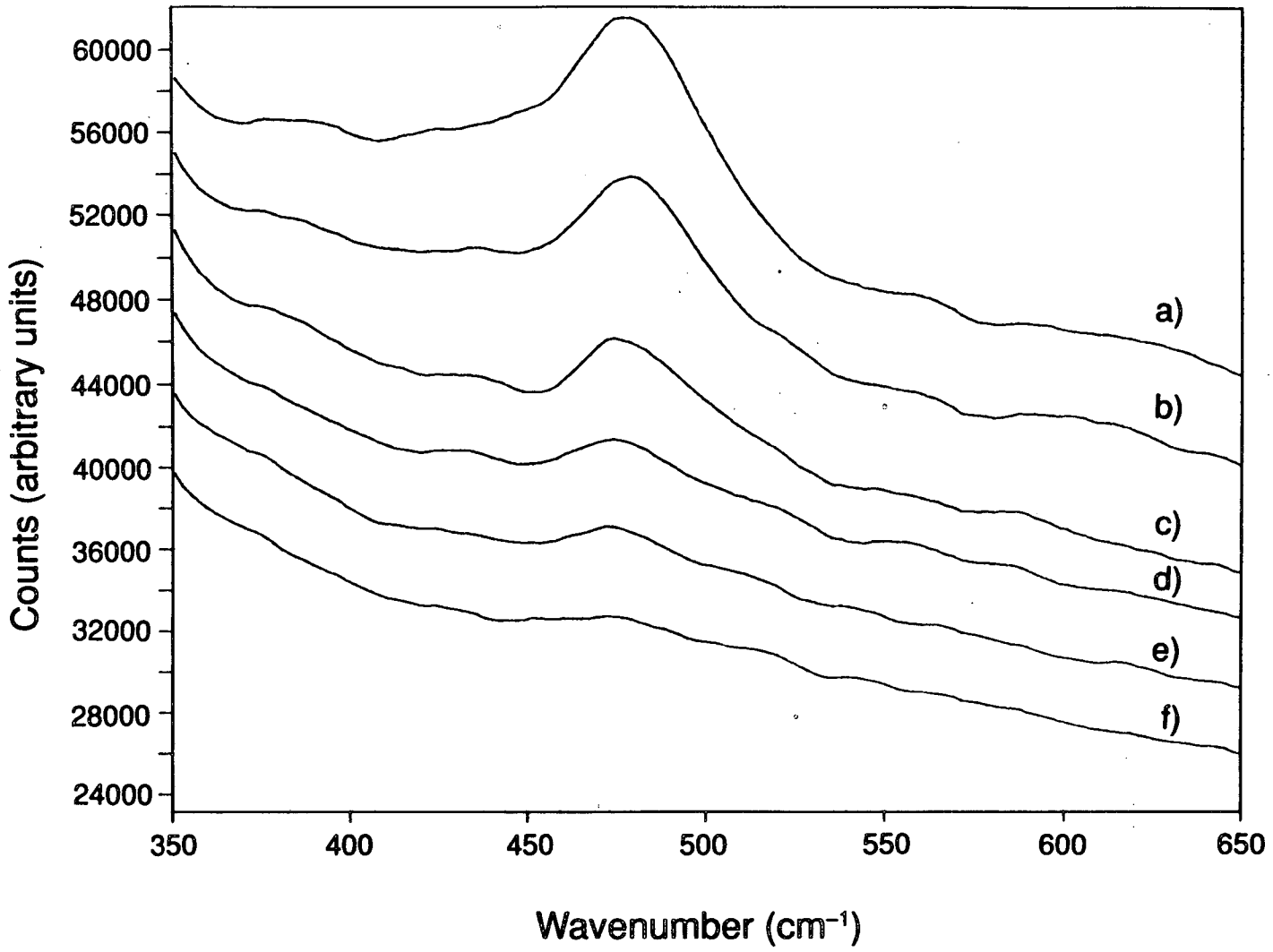

Figure 8-51

XBL 898-7276

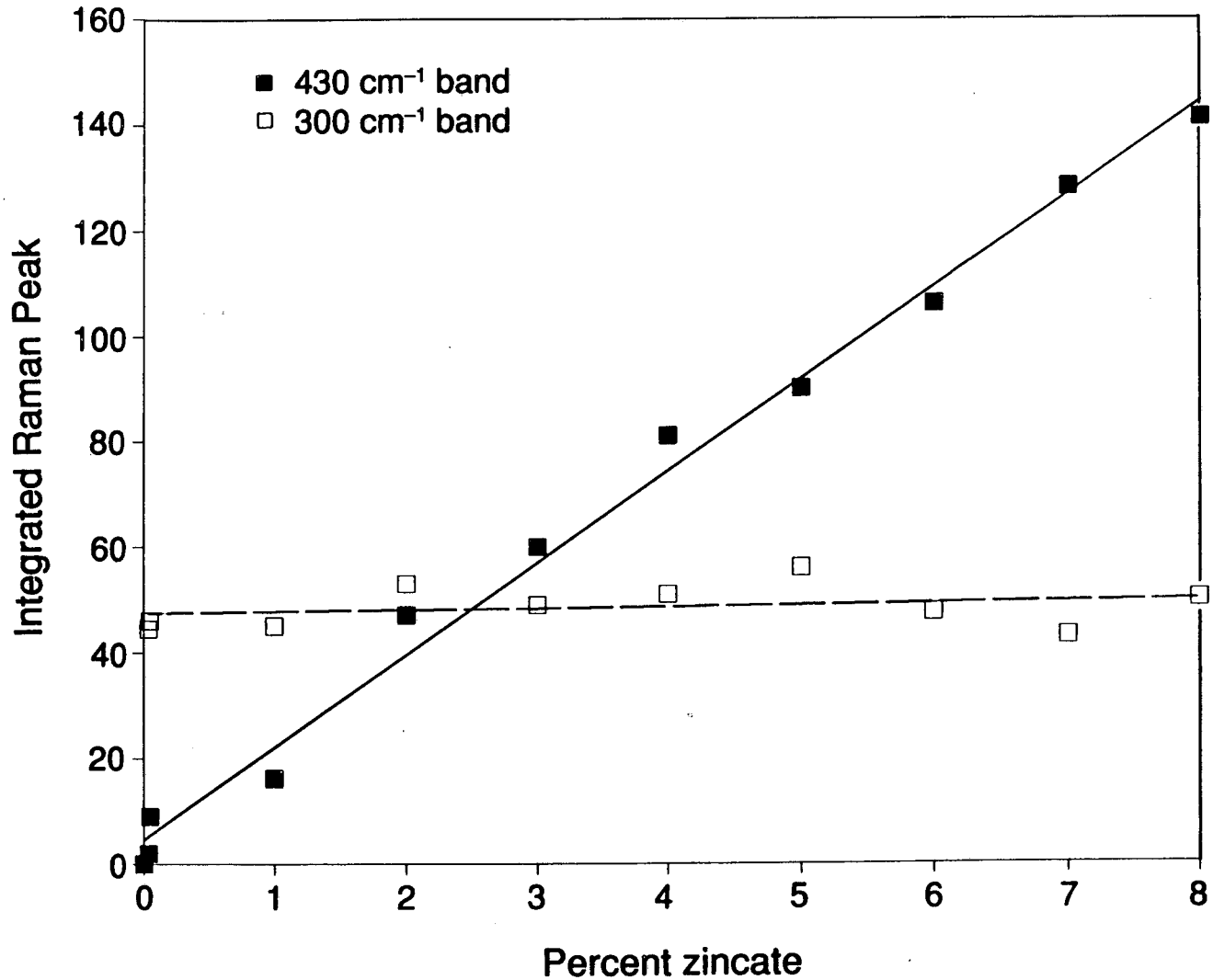

Figure 8-52

XBL 899-7289

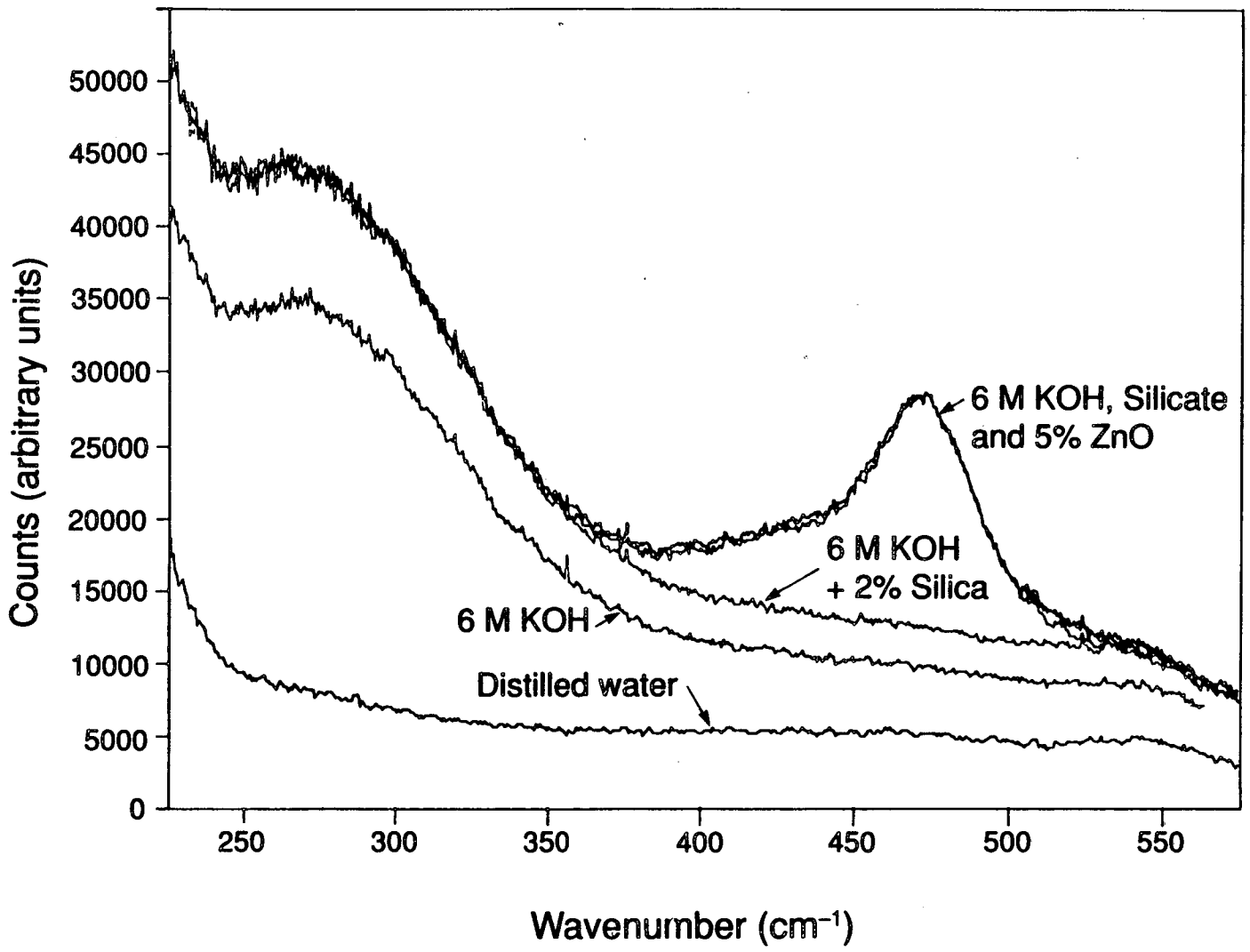

Figure 8-53

XBL 898-7277

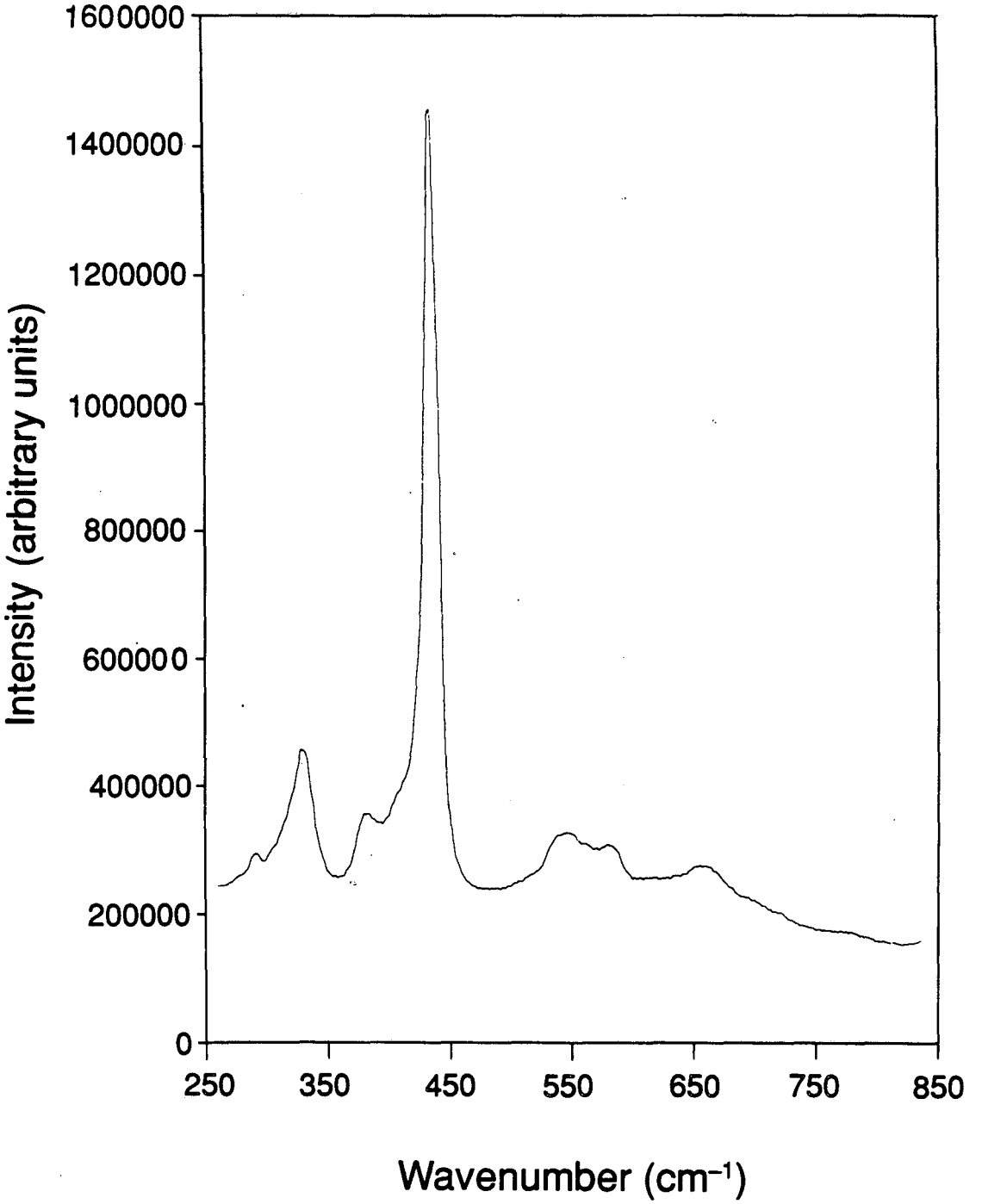

XBL 898-7278

Figure 8-54

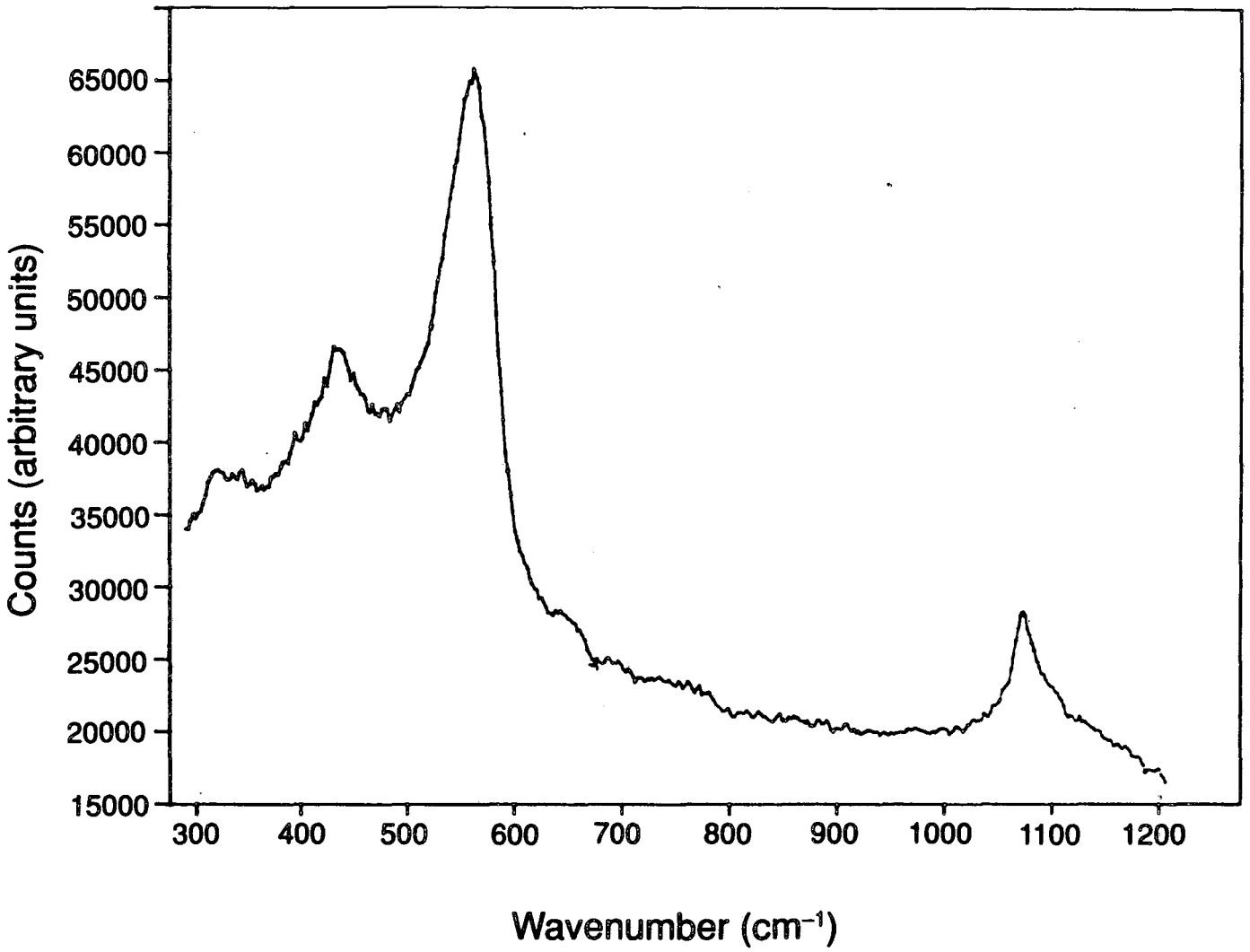

Figure 8-55

XBL 898-7274

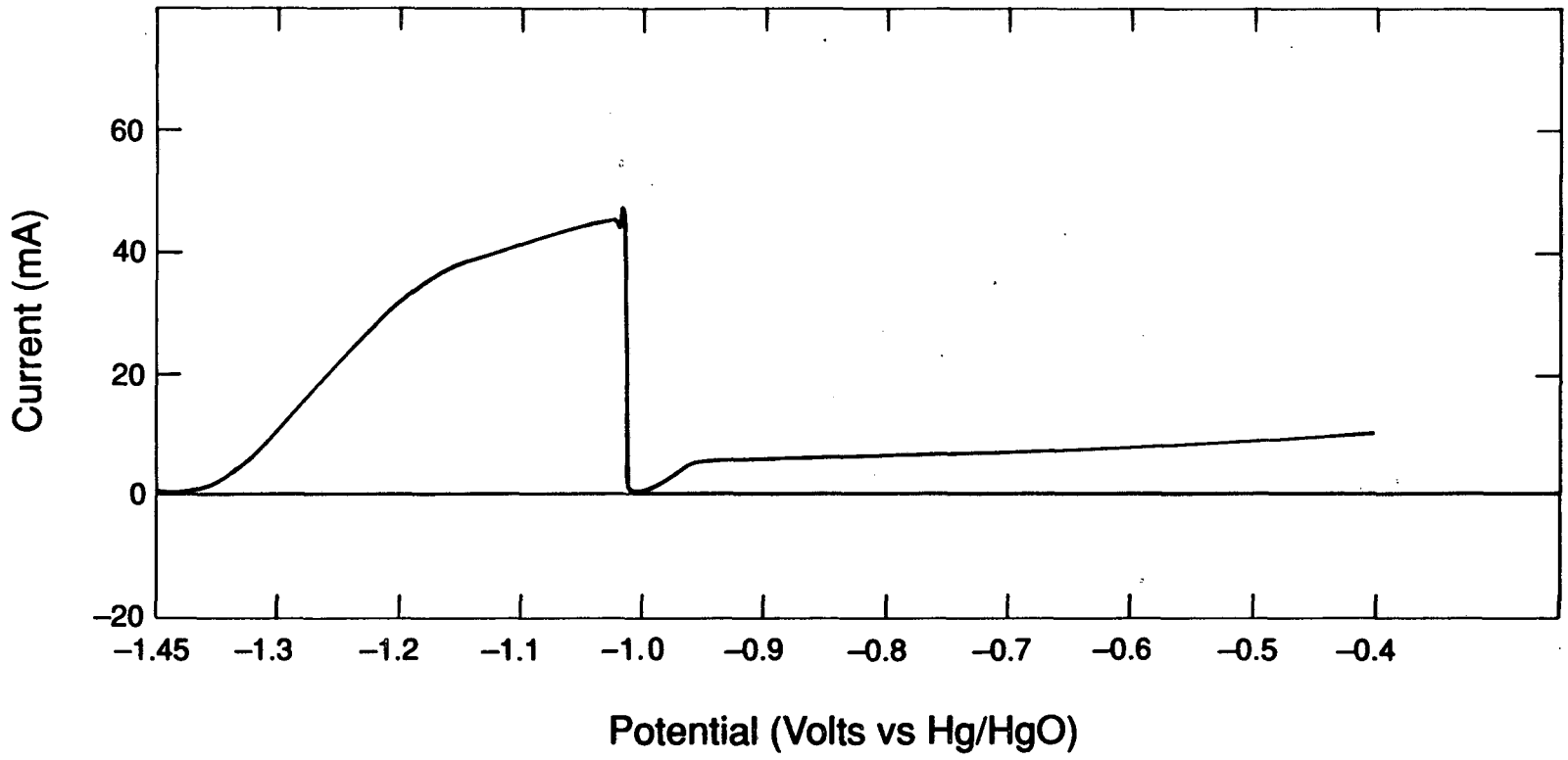

XBL 898-7281

Figure 8-56

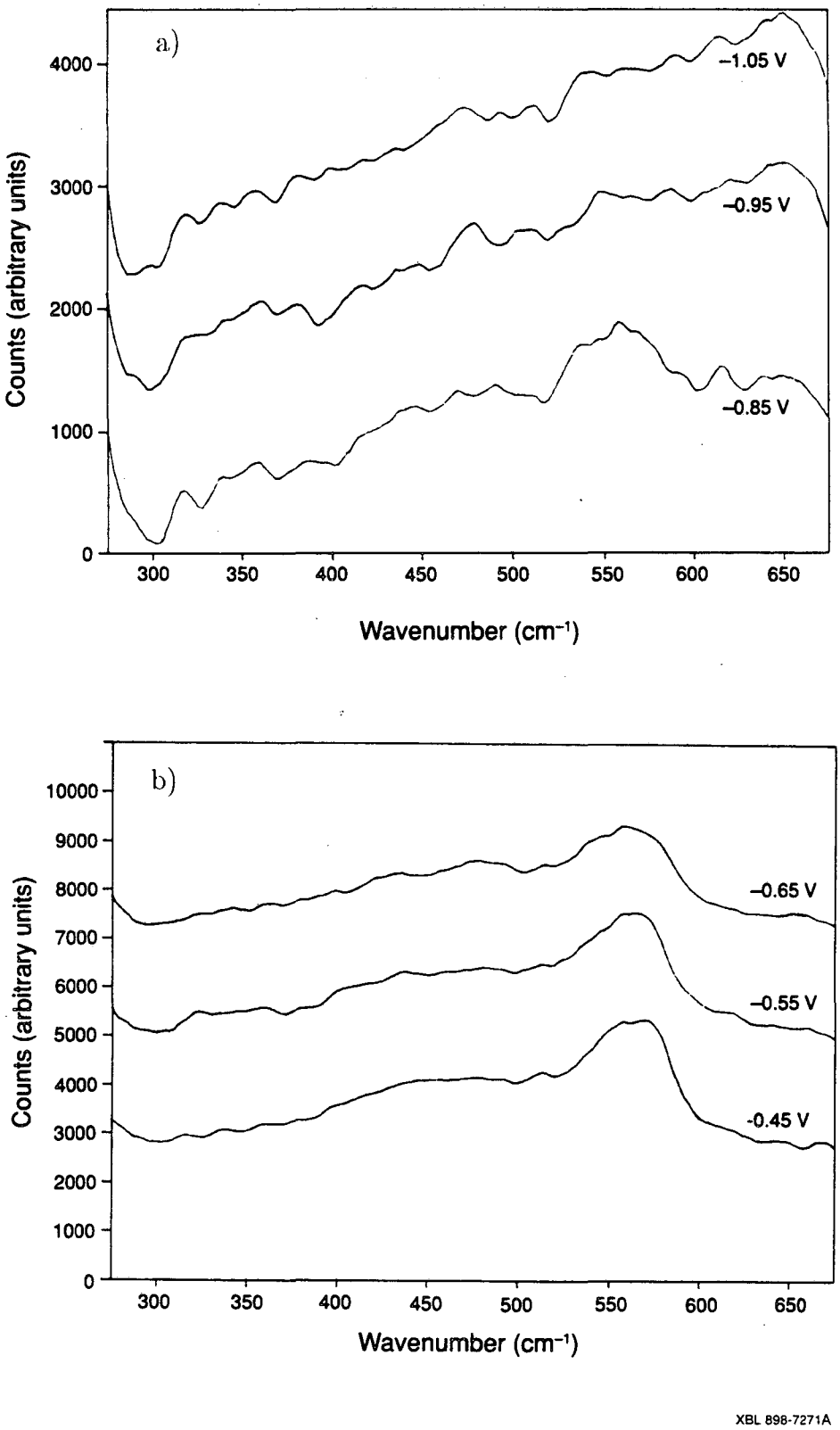
a)
Counts (arbitrary units)
4000
3000
2000
1000
0
300
350
400
450
500
550
600
650
Wavenumber (cm⁻¹)
−1.05 V
−0.95 V
−0.85 V
b)
Counts (arbitrary units)
10000
9000
8000
7000
6000
5000
4000
3000
2000
1000
0
300
350
400
450
500
550
600
650
Wavenumber (cm⁻¹)
−0.65 V
−0.55 V
-0.45 V
XBL 898-7271A

Figure 8-57

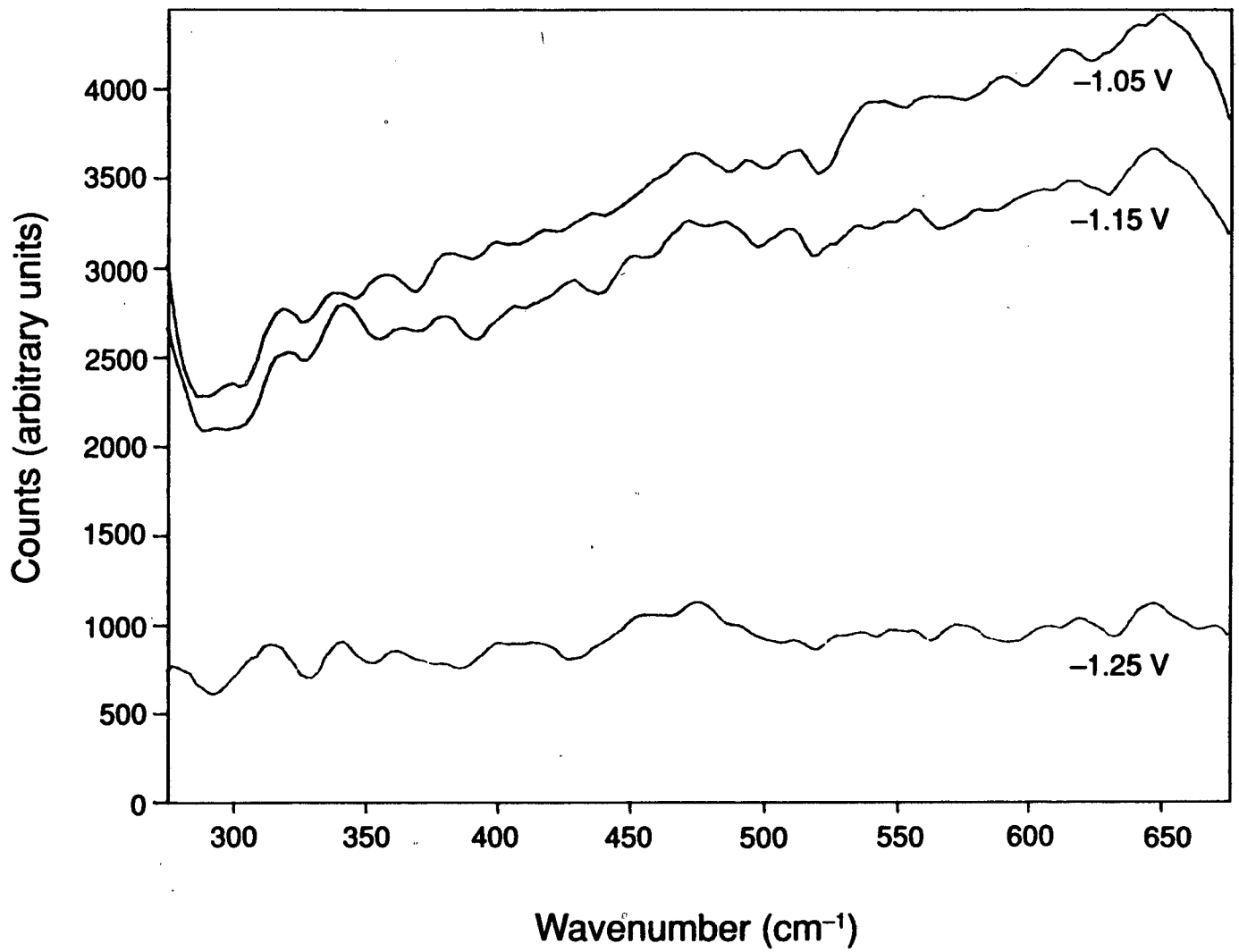

Figure 8-58

XBL 898-7273

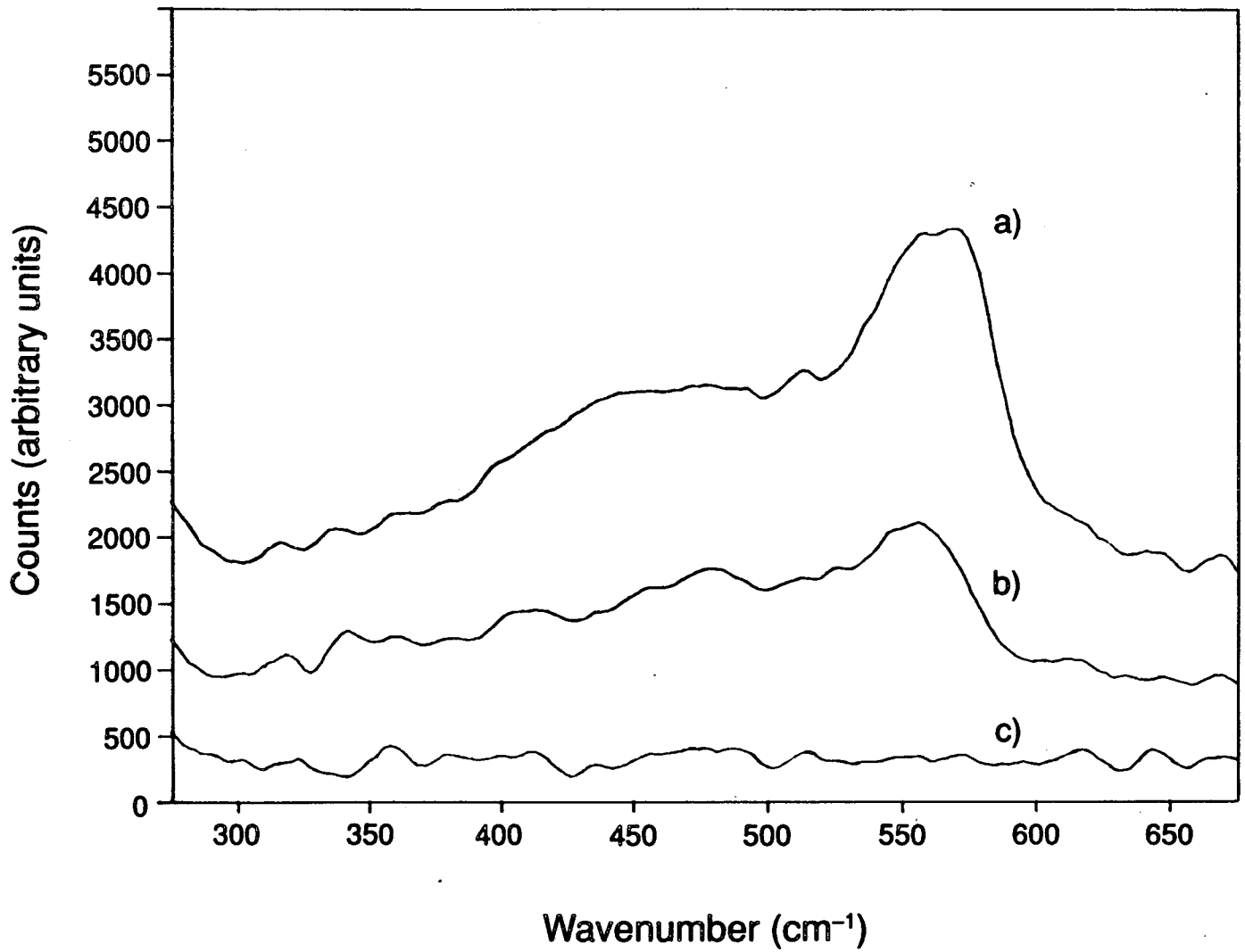

Figure 8-59

XBL 898-7270

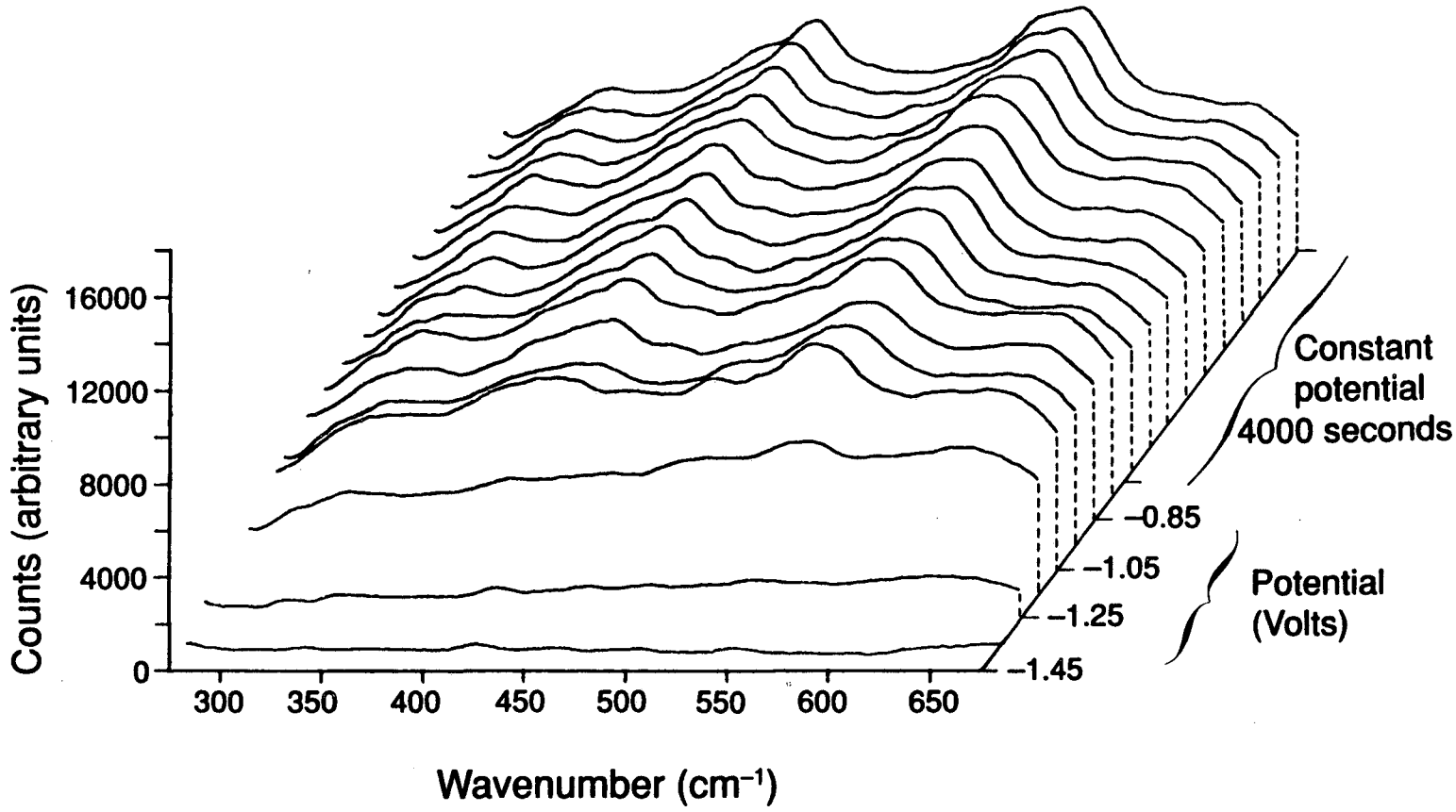

XBL 898-7268

Figure 8-60

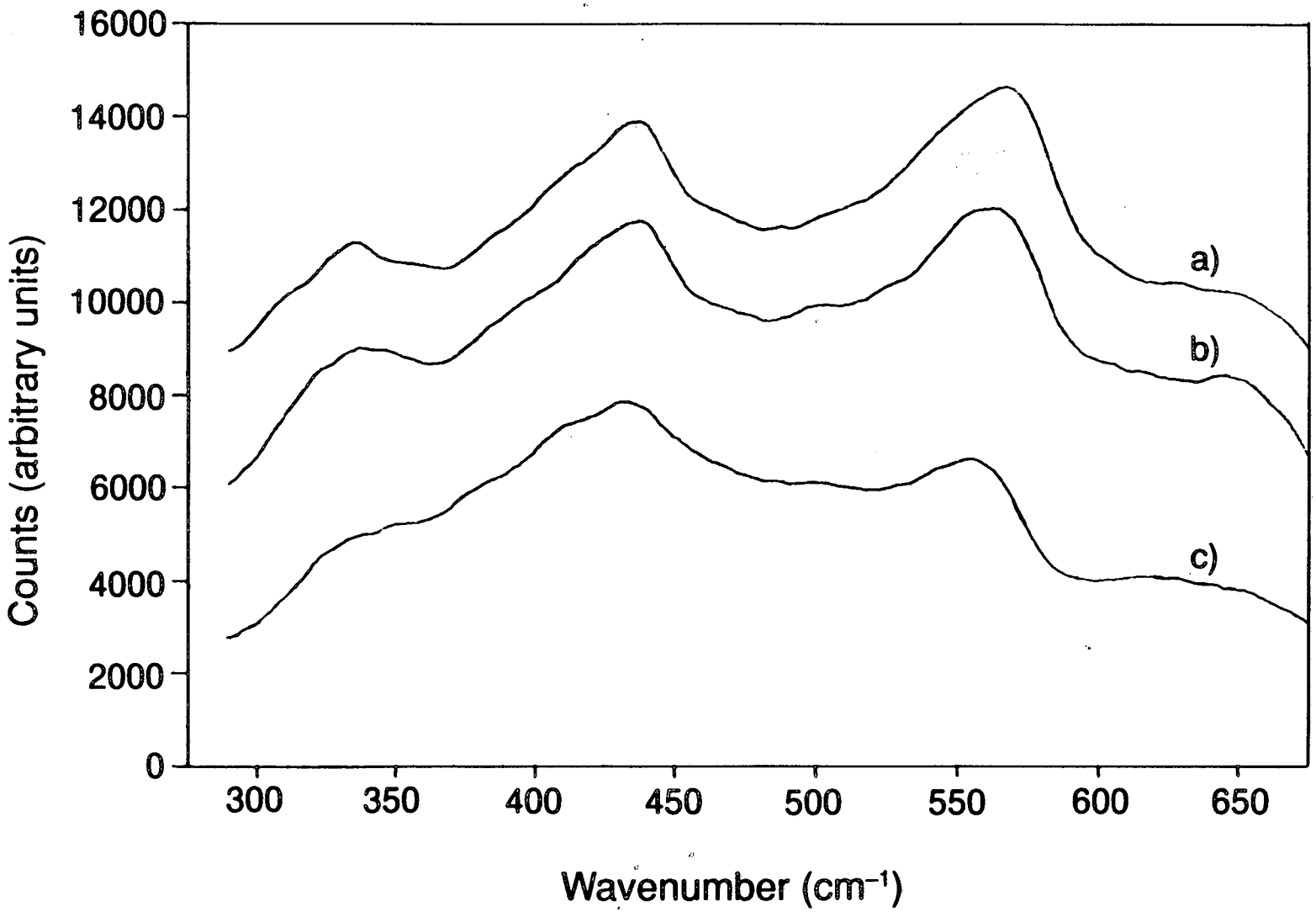

Figure 8-61

XBL 898-7279

TABLE 8.1

APPARENT DISPLACEMENT OF PLASMA LINES OF THE ARGON ION LASER			
WAVELENGTH IN AIR (nm)	DISPLACEMENT vs. 488 (cm^{-1})	DISPLACEMENT vs. 514.5 (cm^{-1})	RELATIVE INTENSITY
488.86	37	- 1019	0.108
490.44	103	- 954	0.073
493.28	220	-836	0.554
494.28	261	-795	0.012
496.51	352	-704	0.639
497.20	380	-676	0.325
500.89	528	-528	1.000
501.72	561	-495	0.400
506.19	737	-319	0.952
514.15	1043	-13.2	0.033
514.52	1057	0	0.114
516.57	1134	77	0.025
517.64	1174	117	0.031
521.69	1324	267	0.010
528.70	1578	521	0.090
555.90	2503	1446	0.012
560.70	2657	1600	0.014
565.07	2795	1738	0.010
588.87	3510	2453	0.013
591.24	3578	2521	0.023

XBL 897-2625

TABLE 8.2

CHARACTERISTICS OF THE HR-320 MONOCHROMETER			
HOLOGRAPHIC GRATING	SPECTRAL RANGE	DISPERSION	RESOLUTION
600 grove/mm	0-2.4μm	50 Å /mm	0.8 Å (3.36 cm^{-1})
1200 grove/mm	0-1.2μm	25 Å /mm	0.4 Å (1.67 cm^{-1})
2400 grove/mm	0-0.6μm	12.5 Å /mm	0.2 Å (0.84 cm^{-1})

XBL 897-2632

TABLE 8.3

TRANSMISSION CHARACTERISTICS OF OMEGA OPTICAL FILTERS		
FILTER	λ BAND (nm)	ν band (cm^{-1})
488 LINE FILTERS		
498/10	493-504	207-650
501/12	495-507	290-767
504/15	496.5-511.5	351-941
505/10	500-510	491-884
512/20	502-522	572-1335
522/30	507-537	767-1870
514.5 LINE FILTERS		
525/10	520-530	206-568
530/15	522.5-537.5	298-831
544/30	529-559	533-1547
575/50	550-600	1255-2770
575/60	545-605	1087-2907
605/90	560-650	1579-4051

XBL 897-2633

TABLE 8.4

TEMPERATURE DEPENDENT BACKGROUND OF THE PAR 1463 DETECTOR		
DETECTOR TEMPERATURE (C)	BACKGROUND COUNTS (sec^{-1})	MAXIMUM INTEGRATION TIME
20	3796	4.16 SEC
10	1550	10.21 SEC
0	576	27.4 SEC
-10	226	1.17 MIN
-20	77.3	3.41 MIN
-30	28.6	9.21 MIN
-40	12†	22.0 MIN†

† estimate

XBL 897-2626

TABLE 8.5

RAMAN PEAKS OF COMPRESSED POWDER STANDARDS	
COMPOUND	RAMAN PEAK (cm^{-1})
Cu_2O	297,411,492,633†,786
$Cu(OH)_2$	292,450,488†
CuO	250,300,347,635

† indicated the strongest Raman peak for the compound

XBL 899-3271

TABLE 8.6

SINGLE CRYSTAL PHONONS OF Cu_2O AND ASSIGNMENT OF POWDER RAMAN PEAKS		
SINGLE CRYSTAL WAVENUMBER (cm^{-1})	ASSOCIATED PHONON(S)	POWDER WAVENUMBER (cm^{-1})
100	Γ_{25}^{-}	-
110	Γ_{12}^{-}	-
146	$\Gamma_{15}^{(1)}$(TO)	-
150	$\Gamma_{15}^{(1)}$(LO)	-
176 (T=15 K)	$\Gamma_{15}^{(1)}$(LO,TO)	-
307	Γ_{2}^{-}	297
407	$\Gamma_{25}^{-} + \Gamma_{2}^{-}$	411
483	$\Gamma_{15}^{(1)}$(LO,TO) + Γ_{2}^{-}	492
514	Γ_{25}^{+}	-
634	$\Gamma_{15}^{(2)}$(TO)	633
665	$\Gamma_{15}^{(2)}$(LO)	
779	$\Gamma_{15}^{(1)}$(TO) + $\Gamma_{15}^{(2)}$(TO)	786

XBL 899-3272

TABLE 8.7

SINGLE CRYSTAL PHONONS OF ZnO AND ASSIGNMENT OF POWDER RAMAN PEAKS		
SINGLE CRYSTAL WAVENUMBER (cm^{-1})	ASSOCIATED PHONON(S)	POWDER WAVENUMBER (cm^{-1})
99	E_2^1	-
281	$A_1(TO)-E_2^1$	280
330	$E_2^2-E_2^1$	330
380	$A_1(TO)$	380
405	$E_1(TO)$	405
430	E_2^2	430
530	$E_2^2+E_2^1$	530
575	$A_1(LO)$	560
592	$E_1(LO)$	-

XBL 899-3273

CHAPTER 9

OBSERVATIONS OF THE ANODIZATION OF METALS USING SPECTROSCOPIC ELLIPSOMETRY

Section 9.1: Introduction

Ellipsometry is a technique for the the measurement of the change in state of polarization of light upon reflection from an interface. Two parameters are measured: the relative phase change (Δ) and amplitude change ($\tan[\Psi]$) of the s- and p-components upon reflection. These measured quantities are related to the (complex) refractive index of the substrate, and to the optical properties, thickness, and structure of any film on the surface. Small differences in phase can easily be measured by ellipsometry, and therefore this technique can be extremely sensitive (e.g., fractional monolayer changes in coverage can be observed). Additional information about the interface can be obtained by varying the wavelength or the angle of incidence (i.e., by varying the optical path length in the film). Because most aqueous solutions are transparent to visible light, ellipsometry, like Raman spectroscopy and elastic light scattering, is a useful *in situ* technique for electrochemical interfaces.

One of the advantages of spectroscopic ellipsometry over monochromatic measurements is that characteristic spectral features (such as absorption peaks) can be detected. Furthermore, a single scan ideally represents many measurements of the same surface morphology whose physical characteristics are indepen-

dent of the light probe's wavelength. Since the dimensionless optical-path length is inversely proportional to wavelength, measurements of the dimensions of the surface layer relative to the incident wavelength are made. One scan is equivalent to many simultaneous independent measurements, allowing a greater certainty in the data interpretation and a larger number of unknown parameters to be determined.

Theoretical aspects of ellipsometry have been covered by several authors (see, for example, References I1-I3), as have derivations of electromagnetic theory on which the classical theory of ellipsometery is based [I4-I7].

The instrument used in this study has been described in detail before [I8-I10] and will be discussed only briefly. The polarizer-compensator-analyzer configuration of optical components was used. White light from a 75-watt xenon lamp is passed through a continuously variable interference filter positioned between a Glan-Thompson polarizer and the light source. Monochromatic light with a bandwidth of 10 nm is obtained in the 370 to 730 nm range. After being linearly polarized, the light enters a Faraday cell, where the plane of polarization can be rotated rapidly while the linear polarization state is maintained. Calibration of the rotation with current allows the instrument to be operated in a self-nulling spectral-scanning mode. A quarter-wave Fresnel-Rhomb achromatic compensator is used, which, along with the polarizer/Faraday-cell components, produces all possible states of elliptical polarization. If light strikes the surface with the proper degree of elliptical polarization, the reflected light will be linearly polarized. Another polarizer and Faraday cell-combination (referred to as the

analyzer) extinguishes the beam by having the resultant transmission azimuth orthogonal to that of the reflected beam. The intensity of the beam is detected by a photomultiplier tube. The polarizer and analyzer Faraday cells are modulated in quadrature, generating two error signals used to obtain the "null setting." Measurements of Δ and Ψ are derived from the mechanical azimuth settings of the polarizers and the level of current in the Faraday cells. The self-nulling feature allows rapid changes in the surface optical properties to be followed. (One spectral scan requires only about 3.5 seconds to complete.) Typically, measurements of Δ, Ψ, time, current, and potential are collected during an experiment.

Since one is generally more interested in the structure of a film (e.g., film thickness and coverage) than its effect on light reflected from the surface, ellipsometric observations of physical parameters are inherently indirect. Quantitative analysis is possible by using a suitable model to interpret the results. Multiple-layer film models have been used before to interpret ellipsometric spectra [I10-I12] and were employed in this study as well. To derive physical parameters, the model must be fitted to the observed spectrum. To do this, an error function σ is used that specifies the quality of the fit for a given set of parameters:

$$\sigma(a_1,a_2,\ldots) = \frac{1}{N}\sqrt{\sum_{n=0}^{N}(\Delta_m-\Delta_p)^2-2(\Psi_m-\Psi_p)^2} \quad . \qquad 9.1$$

In equation 9.1, σ is the error (in degrees) between the observed and measured spectra, a_1, a_2, ... are the values of the model parameters of the trial fit, N is the

number of data points in the spectrum being fit by the model, Δ_m and Δ_p are the measured and model-predicted Δ values, and Ψ_m and Ψ_p are the measured and model-predicted Ψ values. The factor of two accounts for the greater sensitivity in the measurements of Ψ (due to its definition and relation to the measured analyzer azimuth).

All models were fitted to the observed spectra using a Simplex optimization algorithm. This technique determines the value of the error function σ at several different combinations of parametric values. These sets of test-parameter combinations (refered to as points of the Simplex) are ranked in order of decreasing corresponding error function. The location of the average of the "Simplex" parameter values (called the "centrex") is then determined. Next, the value of the error function is found at a point location by projecting a multidimensional line an equal distance from the best Simplex point and through the centrex point. If this new point has a corresponding error function less than that of the worst Simplex point, it replaces the worst Simplex point. However, if this is not the case, the Simplex undergoes a contraction; all parametric values are contracted towards the center point. Clearly, this type of routine is inherently stable and therefore useful when one is interested in optimizing highly nonlinear equations. The commonly used Newton-Raphson technique determines the (multidimensional) slope and (in our case) the derivative of the slope of the error function at a point and then attempts to determine the location of the minimum error by projecting the tangent to the error-function derivative curve to its zero value. While this technique can be fast, it works poorly for highly nonlinear equations

where the curvature changes rapidly over the multidimensional surface. On the other hand, a Simplex algorithm can become slow as the solution is approached. Therefore, the combined use of the Simplex technique with a faster linear optimization method may be helpful in reducing computation times.

All of our theoretical models use the results obtained by Drude [I13] for the reflection from a flat layer of material placed between two semi-infinite media. The (complex) reflection coefficient of the surface $\hat{r}_\nu$ (where ν signifies either s- or p-polarization) is given by

$$\hat{r}_\nu = \frac{\hat{r}_{01,\nu} + \hat{r}_{12,\nu}e^{-iD}}{1 + \hat{r}_{01,\nu}\hat{r}_{12,\nu}e^{-iD}} \quad . \qquad 9.2$$

In equation 9.2, $r_{01,\nu}$ is the reflection coefficient of the solution/film interface, and $r_{12,\nu}$ is the reflection coefficient of the metal/film interface (0 refers to the solution, 1 to the film, and 2 to the substrate). The (complex) phase delay is given by

$$\hat{D} = 4\pi(\frac{T}{\lambda})\hat{n}_f\cos(\hat{\phi}_f) \quad . \qquad 9.3$$

In equation 9.3, T is the film thickness and λ is the wavelength of light in vacuum. With o, f, and s referring to the ambient, film, and substrate, the Fresnel reflection coefficients are calculated by [I4-I7]

$$\hat{r}_{01,p} = \frac{\tan(\phi_o - \hat{\phi}_f)}{\tan(\phi_o + \hat{\phi}_f)} \quad , \qquad 9.4$$

$$\hat{r}_{01,s} = -\frac{\sin(\phi_o - \hat{\phi}_f)}{\sin(\phi_o + \hat{\phi}_f)} \quad , \qquad 9.5$$

$$\hat{r}_{12,p} = \frac{\tan(\hat{\phi}_f - \hat{\phi}_s)}{\tan(\hat{\phi}_f + \hat{\phi}_s)} \quad , \qquad 9.6$$

$$\hat{r}_{12,s} = -\frac{\sin(\hat{\phi}_f - \hat{\phi}_s)}{\sin(\hat{\phi}_f + \hat{\phi}_s)} \quad . \qquad 9.7$$

The propagation directions $\hat{\phi}_i$ used in the Drude equation are calculated from a complex form of Snell's law:

$$n_o \sin(\phi_o) = \hat{n}_f \sin(\hat{\phi}_f) = \hat{n}_s \sin(\hat{\phi}_s) \quad , \qquad 9.8$$

where n_o, $\hat{n}_f$, and $\hat{n}_s$ are the refractive indices of the solution, film, and substrate, respectively. The substrate and solution refractive indices are determined experimentally, leaving only the optical properties and thickness of the surface layer as unknowns.

When one uses the "homogeneous-film" model, the optical properties of the layer are assumed to be uniform. Despite this limitation, the equations can be used in a modified form for films whose properties vary both normal and parallel to the surface.

Simulations of a refractive index varying with position normal to the surface are performed by artificially dividing the inhomogeneous film into many thinner homogeneous layers. A functional form of the variation of film composition with position normal to the surface is often assumed and is used to predict the variation in optical properties.

Approximations of a composite material's optical properties are made using effective-media approximations (EMA). These include the Lorentz-Lorenz, Maxwell-Garnett [I14], and Bruggeman [I15] models. These approximations are used to calculate the dielectric constants of the mixture from the volume fraction of its components θ_i and can be expressed in a single form [I16,I17]:

$$\frac{\hat{\epsilon}-\hat{\epsilon}_k}{\hat{\epsilon}+2\hat{\epsilon}_k} = \sum_{i=1}^{N} \theta_i \frac{\hat{\epsilon}_i-\hat{\epsilon}_k}{\hat{\epsilon}_i+2\hat{\epsilon}_k} \quad . \qquad 9.9$$

In equation 9.9, $\hat{\epsilon}$, $\hat{\epsilon}_k$, and $\hat{\epsilon}_i$ are the (complex) dielectric functions of the effective, host, and inclusion media, respectively.

These models all assume that the inclusions are spherical and that only dipole interactions occur. They differ in what is considered the "host" medium. The Lorentz-Lorenz EMA assumes that the host is a vacuum. The Maxwell-Garnett EMA chooses one of the components of the mixture (generally the one with the largest volume fraction). The Bruggeman model avoids the ambiguity in choosing a host medium by replacing the host medium with the effective medium (i.e., $\hat{\epsilon}_k$ is replaced by $\hat{\epsilon}$ in equation 9.9). Predicted dependencies of the refractive index on volume fraction have been presented by this author before [I10]; they show that significant differences in the calculated extinction coefficient are obtained depending on which effective-medium approximation is chosen.

Films that are discontinuous in the plane parallel to the surface ("island films") can be represented by the principle of coherent superposition of light. The general equation used for the coherent superposition of light in ellipsometry

is

$$\hat{r}_\nu = \Omega\hat{r}_{1\nu} + (1-\Omega)\hat{r}_{2\nu} \ , \qquad 9.10$$

where $\hat{r}_{1\nu}$ and $\hat{r}_{2\nu}$ are the (s- and p-component) reflection coefficients of the island/electrolyte and substrate/electrolyte interfaces, respectively, and Ω is the fractional coverage of the surface with islands.

Combinations of the principal equations above (9.2, 9.9, and 9.10) allow one to predict the optical response from a large number of surface film structures. These include roughness layers, diffusion boundary layers, and homogeneous, porous, island, and multilayered films. Various optical models were used in an attempt to reproduce the observed time-dependent spectroscopic ellipsometry measurements. Many of these have been described before [I10,I16]. However, only two optical models were found that reproduced our silver and copper oxide results. These were a single-film and a two-layer island-film model.

In fitting the data to the single-film model, the refractive index was assumed to be independent of the film thickness, allowing the problem to be solved. The importance of the assumption can be understood if one calculates the number of uncorrelated parameters and the number of independent observations made. If N is the number of "independent" spectral observations made, there are 2N independent measurements per scan (one each for the Δ and Ψ values). Let S be the number of spectra taken, each with a different film thickness, thereby generating a total of 2NS independent measurements. This value should be compared with the number of parameters used to fit the spectra. Without the

independent-thickness assumption, there are two optical constants at each wavelength for each scan and one (wavelength-independent) film thickness for each spectrum, for a total of 2NS+S parameters. Since this value will always be greater than the number of independent measurement (2NS), the problem is indeterminate. However, if we assume that the optical properties are independent of thickness, then there are only 2N+S parameters. Since the number of measurements must always be greater than the number of unknowns, the problem will be determinate if

$$S > \frac{2N}{2N-1} \quad . \qquad 9.11$$

Assuming that the measurements are independent at twice the bandwidth of the monochromator (20 nm), there will be 18 such measurements over the spectral range of our instrument. Using this value in equation 9.11, only two measurements of different film thicknesses are required for the problem to be solvable (and there will be almost twice as many measurements as parameters). Typically, we measure 25 spectra of differing thicknesses. The ratio of the number of measurements to the number of parameters for such an experiment would be almost 15.

When three-dimensional crystals form, the simple homogeneous-film model no longer accurately predicts the measured spectra. When this is the case, a two-layer island-film model, consisting of a homogeneous underlayer and a hydrated island overlayer, is used. The optical properties of the film are determined from the optical properties of the underlayer prior to the formation of the

island overlayer and are therefore not parameters. The island film represents the optical effects of isolated crystals by the coherent superposition of polarization states resulting from the reflection on the islands and between them. The free parameters of the model are the thickness of the underlayer (T_1); and the thickness (T_2), coverage (Ω), and hydration (θ) of the crystal overlayer. The Bruggeman EMA is used to calculate the effective optical constants of the hydrated crystals since it is self-consistent (i.e., optical constants at 0% and 100% void fractions are correct). Theoretical predictions of the effects of an island-film size distribution on the ellipsometer parameters have been discussed previously [I10]. While this model more accurately represents the true film morphology and predicts the observed spectra, the calculation is extremely time consuming because of the complex integration required inside the optimization routine. Since increased uncertainties are introduced when the statistical parameter is added, and because the average island-layer thickness is not greatly affected by the introduction of the complication, the simpler duplex-film (nonstatistical) model was chosen.

Section 9.2: Anodic Oxidation of Silver

9.2.1 Introduction

We have previously reported results on the anodic oxidation of silver in 1M KOH using spectroscopic ellipsometry [I10,I16]. The formation of an initial monolayer occurs rapidly, followed by the much slower growth of a compact multilayer

(referred to as the primary layer). Concurrent with the film-formation process is the diffusion of a soluble oxidized species into the electrolyte. The dissolved material accounts for most of the oxidized product generated at low overpotentials. After the application of a potential step, the film obeys a parabolic growth law, indicative of a solid-state diffusion-controlled process. When the multilayer reaches a critical-thickness which occurs at a potential of about 290 mV vs Hg/HgO, a large number of small seed crystals are formed in the primary layer. During the initial stages of growth, the crystals (referred to as secondary crystals) grow by the transfer of oxide material from the primary layer. Crystals that form earlier will tend to be larger. Because the solubility of crystals increases with decreasing size, (Gibbs-Thompson equation), large crystals tend to act as sinks near smaller crystals, causing the total number of crystals to decrease. Eventually, the crystals reach a size where size effects are no longer important.

It is a general observation that the size of crystals formed via a dissolution/precipitation mechanism decreases with increasing potential. The grain size of electrodeposited metals shows a similar tend. Classical nucleation theory tells us that the size of a critical nucleus will decrease with increasing overpotential (see Chapter 4, Section 4). Once the size of the nucleus is larger than the critical size and surpasses the nucleation energy barrier, the center will grow as long as the driving force remains. These ideas suggest that one could form a large number of small growth sites by the application of a high overpotential and then allow growth at the sites at a lower potential. When potential control is released, the crystals will dissolve. The rate of dissolution should increase

with decreasing size because small crystals exhibit a surface concentration higher than the saturation concentration for "infinitely large" particles.

Our modified dissolution/precipitation nucleation theory involves different steps for film growth following "nucleation pulses" than that of the classical model. The formation of a compact layer is required first. The primary layer may be too thin to undergo three-dimensional nucleation if the pulse duration is too short. Assuming that the properties of the Ag_2O primary layer are not affected by the presence of the underlying silver substrate, its rate of dissolution should be smaller than that of any nucleated crystals since its radius of curvature is large. For these purposes, the surface can be viewed as an infinitely large Ag_2O crystal. Under corrosion conditions, the primary layer should be relatively stable. The relaxation of the voltage to a "growth" potential will cause crystal growth only if (1) critical nuclei have been formed and (2) the potential corresponds (e.g., though the Nernst equation) to a value greater than the crystal's surface concentration (via the Gibbs-Thompson equation 4.19).

The objectives of the silver ellipsometry work reported here were to (1) derive the wavelength-dependent optical properties of the primary layer, (2) examine the potential at which this layer can lead to nucleation, and the layer's role in three-dimensional nucleation, and (3) examine the growth stability of small secondary crystals. To do this, we performed a number of single and double potential-step and/or sweep experiments that we felt would test some of the underlying ideas of our proposed growth mechanism and that of the classical dissolution/precipitation mechanism.

9.2.2 Slow Potential-Sweep Measurements

In an attempt to accurately derive the wavelength-dependent optical constants of a silver (I) oxide film, a thin compact layer (primary layer) of the material was grown by stepping the potential to 250 mV vs Hg/HgO and then ramping the voltage anodically at 0.04 mV/sec. Four-zone averaged ellipsometry spectra were collected over a range of about 2.4 mV. The derived film thickness versus potential is shown in Figure 9-1. The model fits to the observed spectra are within experimental error (0.05° in Δ and 0.025° in Ψ). Because the potential was first stepped to 250 mV, the potential at which film growth began is not evident from the results shown in Figure 9-1. However, as previously shown [I10], primary film growth will occur at potentials anodic of about 245 mV vs Hg/HgO, a value coincident with the equilibrium potential of the Ag_2O electrode reported by Pourbaix [I17] (see equation 2.1). The rate of film growth decreases with increasing voltage (Figure 9.1).

The wavelength-dependent optical constants derived from all the spectra of the experiment are shown in Figure 9-2. The values are nearly independent of wavelength, consistent with an uncolored material. Optical constants derived from model fits using fewer spectra over a more limited potential range show that (1) the optical constants are nearly independent of film thickness (to within 0.01 in n and 0.04 in k), and (2) the film is not nucleating at the higher potentials.

9.2.3 Single Potential-Step Measurements

Potential-step measurements of Ag_2O film formation have been reported before [I10,I16]. In this study, only step changes above the "nucleation" potential were used. The duration of the E-step was varied, after which the potential control was removed. The corrosion of the surface layers after the cell was set to open circuit was observed using spectroscopic ellipsometry.

If the period of anodization is short (e.g., $t < 30$ sec at 290 mV), on open circuit, a slow change occurs in the surface optical properties. The direction of change is such that the optical parameters approach the values of the substrate over a period of many minutes. For slightly longer anodization (e.g., step duration of about 30 to 60 sec at 290 mV), the changes in optical parameters also reverse direction on open circuit and approach the optical properties of the substrate, but the process occurs more rapidly (Figure 9-3A). Finally, when the duration of the potential step is relatively long ($t > 90$ sec), no change at all is observed on removing the potential control (Figure 9-3B). These last films are stable for several hours.

These qualitative results demonstrate the three regimes of crystal growth. At short anodization times, a primary layer forms that is too thin to lead to three-dimensional nucleation. Further anodization causes the nucleation of many small growth centers that quickly dissolve into the electrolyte when the supply of reaction products is removed (at open circuit). The rate of corrosion (dissolution) of the crystals is greater than that of the primary layer because their solubility is larger (as discussed above). As the crystals are allowed to grow, their rate of

dissolution decreases because (1) the surface-to-volume ratio decreases, (2) their solubility (which can be viewed as a concentration boundary condition at the surface) decreases, and (3) more silver has been dissolved into the electrolyte, thereby increasing the bulk electrolyte silver concentration. These factors cause the corrosion rate of the surface films to eventually decrease with increasing oxidation time.

9.2.4 Double Potential-Step Experiments

Double potential-step experiments were performed in an attempt to determine whether the formation of the primary layer is necessary for three-dimensional nucleation. These experiments involve the application of an initial short-duration (1-10 sec) large potential step (320 to 350 mV), followed by a step change to a lower "growth" value (270 mV). The first pulse is anodic relative to the nucleation potential for the system. At the second potential-step value, primary-layer growth occurs without nucleation as in a single E-step experiment.

The typical current transient of a double E-step experiment displays an initially large value after the first pulse, which later decreases in an approximately parabolic manner. Following the second potential-step change, the current is cathodic for a short time (about 1.5 sec), after which it becomes anodic, reaches a maximum, and then falls (see Figure 9-4). Though both capacitive and faradaic processes are occurring, time constants of capacitive currents are generally only a small fraction of a second. After the second potential step, the surface concentration is reduced from its previous value. This causes a momentary reversal in the

sign of the surface-concentration gradient, yielding a cathodic current. If nucleation occurs, the higher solubility (and therefore higher equilibrium potential) of the small crystals should cause a partial reduction of the film. However, comparison of spectra before and after the second potential step shows only a slight film reduction. Therefore, the cathodic portion of the second transient is largely associated with a faradaic reduction of dissolved oxide material.

Though the changes in Δ and Ψ with time are affected by both the size and length of the first potential step, when the potential is decreased the rate of change in the ellipsometer parameters almost always diminishes (and sometimes stops altogether). If the cell is set to open circuit after the second E-step, the optical parameters change slowly toward substrate values (see Figure 9-5), similar to the single potential-step results for unnucleated films discussed above. Therefore, all of our results indicate that a compact primary layer forms prior to three-dimensional nucleation.

To help determine the potential at which nucleated film **growth** occurs, we performed some multiple-step and/or sweep experiments. Film nucleation was first accomplished by the application of a potential step to 295 mV vs Hg/HgO for 60 sec. Next, the potential was stepped to 250 mV vs Hg/HgO and held for 300 sec. Finally, the voltage was increased again using a 0.5 mV/sec sweep. The results (Figures 9-6 and 9-7) show that an initially large rate of change in optical parameters stops, coincident with the reduction in voltage. The Δ and Ψ values are almost constant during the second potentiostatic phase; they start to change slightly after the sweep begins (a change too small to be observed in Figures 9-6

and 9-7), and they change rapidly as the voltage reaches about 290 mV.

Model interpretations of the data shown in Figures 9-6 and 9-7 are presented in Figures 9-8 and 9-9. Some measured and calculated spectra are given in Figures 9-10 and 9-11. As with our previous results (see references I10 and I16), the general shape of the Ψ spectrum is accurate. However, the location of the spectral maximum is off by 50 nm, and, when compared with the level of change in the parameters, shows that it is not a close fit. As discussed before, allowances for a distribution of crystal size can improve the fit.

In the experiment discussed above, the growth of the primary layer stops when the potential is reduced to 250 mV after reaching a thickness of about 25 Å (Figure 9-8). The film growth begins again as the voltage is increased during the anodic potential sweep.[†] Secondary-layer growth also stops with potential reduction but then shows a slow decrease in thickness and coverage during the 250-mV potentiostatic phase (Figure 9-9). Most importantly, the growth of this layer does not start until the potential reaches about 290 mV.

To summarize, the results presented have demonstrated that (1) the optical constants of silver oxide are approximately constant in the spectral range studied (3.0-0.9i) and are different from those used initially in our previous study (I10); (2) thin nucleated films tend to dissolve into the electrolyte at a rapid rate, while thin unnucleated films and thicker nucleated ones are relatively more stable; (3)

[†] Note that the thicknesses in Figure 9-8 are about four times smaller than those shown in References I10 and I16. Some of the difference can be explained by the different (but more accurate) optical constants used here (3.0-0.9i vs. 2.18-0.28i).

the formation of a compact "primary layer" always occurs prior to film nucleation; and (4) three-dimensional film **growth** does not occur at potentials below a nucleation potential (near 290 mV vs Hg/HgO). These findings are in agreement with our primary layer/nucleation/Ostwald-ripening hypothesis and demonstrate that anodic film formation is much more complicated than the simple dissolution/precipitation model would indicate.

Section 9.3: Anodic Oxidation of Copper

9.3.1 Introduction

Only two ellipsometric studies of the anodic oxidation of copper in alkaline media have been reported in the literature, both of which were fixed-wavelength measurements [I18,I19]. Ord *et al.* [I18] investigated the oxidation and reduction of a film formed in a pH 12 sodium carbonate solution. They claimed that the film consists of an inner compact monovalent oxide covered by a outer divalent oxide, and that reduction takes place in three separate stages. The divalent oxide is first reduced to monovalent oxide via a soluble intermediate, which is followed by the reduction of the underlayer of monovalent oxide. Finally, the monovalent oxide produced by the reduction of the divalent layer is reduced. During this final reduction stage, the oxide was said to be reduced to copper metal at the film/electrolyte interface, thereby producing a duplex film whose interface moves inwards toward the metal/film interface. The voltammetry and optical model used to interpret their monochromatic ellipsometry results appears to be overly

complicated.

Yamashita et al. [I19] used fixed-wavelength ellipsometry to investigate the anodic film formation of copper in 0.5N KOH. They reported values for the optical properties of Cu_2O as (1.9 to 2.0) - (0.3 to 0.5)i at what we believe was 546.1 nm. (It was not explicitly stated.) In many cases, the oxidation potential was well within the range where we have shown that divalent oxide forms. Unfortunately, Yamashita et al. consistently used a simple single Cu_2O film optical model to interpret their results. They concluded that the passive film forms via a dissolution/precipitation mechanism, the oxide film has two layers, and that light inhibits the oxidation of the Cu_2O cation-deficient semiconductor.

In our study of the oxidation of copper in 1M KOH, no attempt was made to model the spectra of films formed at potentials above -200 mV (ie. where divalent oxide begins to form). We modeled the Cu_2O film as a single homogeneous film with wavelength-dependent optical properties. The objectives of this portion of our ellipsometery work were to (1) derive the optical properties of the Cu_2O film *in situ*, (2) determine any correlation between the A1 voltammetry peak and film formation (ie. film growth and efficency), and (3) determine the controlling mechanism for film formation. Galvanostatic, potentiostatic, and potential-sweep voltammetry experiments were performed in tandem with spectroscopic ellipsometry measurements to help answer these questions.

9.3.2 Potential-Sweep Experiments

Typical potential-sweep experiments at slow sweep rates show film formation to begin coincident with the onset of anodic current. Here we discuss only one such experiment in which the potential, intially held at -600 mV, was increased at 0.5 mV/sec to a maximum value of -300 mV. The potential was then swept at the same rate in the reverse direction until it reached -900 mV. The corresponding changes in Δ and Ψ are quite large (see Figure 9-12 and 9-13). The wavelength-dependent Δ values are observed to start a general decreasing trend when the potential reaches -380 mV. Anodic current continues to flow and accompanies continued changes in optical parameters after the sweep direction is changed. The reduction of the film is evident by the reversal of these changes during the cathodic sweep starting at around -525 mV. There is a slight offset in the optical properties that is not recovered, even at the lowest potential.

A comparison of some measured and best-fit model-predicted spectral ellipsometry data of Figure 9-12 and 9-13 is presented in Figure 9-14. The results demonstrate that the simple single-film model with wavelength-dependent but thickness-independent optical properties reproduces the observed data remarkably well. Large peaks and troughs in the measurements are predicted accurately by the model. The film thickness is greater at one of the more negative potentials in Figure 9-14 because anodic current flows during a portion of the cathodic potential sweep.

The current corresponding to the ellipsometry discussed above is shown in Figure 9-15A. The current density starts to increase at around -425 mV, reaches

a maximum of 0.18 mA/cm^{-2} at -375 mV (the A1 peak), and then falls. Upon changing sweep direction, the current actually increases slightly with **decreasing** potential, achieving another maximum at around -375 mV. It is interesting to note that at potentials lower than -450 mV, the anodic current is actually greater on the cathodic sweep than on the anodic sweep. This phenomenon could be associated with a general roughening of the surface at potentials anodic to the A1 peak (as discussed in Chapter 7), leading to a greater rate of monovalent oxide dissolution and/or film formation. Cathodic current is observed at voltages more negative than -475 mV, only 50 mV cathodic of the onset of anodic current during the anodic potential sweep. The maximum cathodic current occurs at -600 mV.

The Cu_2O film thickness as a function of potential derived from the optical model is presented in Figure 9-15B. When compared with the current results of Figure 9-15A, it is evident that film formation begins with the onset of anodic current. The film continues to grow during the early portion of the cathodic sweep where anodic current is still observed. The film reaches a maximum thickness of 138 Å. Reduction of the film starts at about -490 mV, coincident with the onset of cathodic current. The film is completely reduced at -700 mV, where the tail end of the reduction peak is found. The negative film thicknesses, derived from the optical model, are not physically real and are caused by a forced interpretation of a roughened copper surface as a film of Cu_2O on a copper substrate. The fact that the optical parameters and the interpreted film thicknesses do not change at potentials cathodic of -700 mV leads to the conclusion that the

residual cathodic current (0.015 mA/cm^{-1}) at these potentials is due to the reduction of a small amount of residual oxygen.

Integration of the digital current data of Figure 9-15A to determine the charge passed is shown in Figure 9-16. The shape of the curve is similar to that of the thickness-versus-potential data (Figure 9-15B). The linearly decreasing total charge at more negative potentials is associated with the reduction of residual dissolved oxygen. A comparison of the thickness derived from our ellipsometry measurements with that based on the charge balance of Figure 9-16 indicates that the current efficiency for film formation is only about 50%. This finding is consistent with that of Miller [I20], whose ring/disk measurements also demonstrated that only a fraction of the total charge was used to form the Cu_2O film. The balance of the oxidation products dissolve into the electrolyte. One might be surprised by this finding, since the monovalent oxide is highly insoluble in the electrolyte and therefore shouldn't contribute significantly to the overall charge balance. However, only a small amount of material (equivalent to about 140 Å of a compact layer of oxide) is dissolved into 400 ml of electrolyte (equivalent to a $5x10^{-7}$M solution). This concentration of cuprous ion is three orders of magnitude lower than that of the arganate ion, which is known to be very "insoluble."

In another experiment, rather than change the direction of the sweep at -300 mV, we continued to increase the potential 0.5 mV/sec up to -150 mV. This experiment is analogous to the scattering experiment whose results are shown in Figures 7-33 through 7-35. At potentials above the A1 peak (located at -360 mV

in Figure 9-17), the current falls. Between -300 and -200 mV a small anodic current continues to flow. Above -200 mV, a sharp rise in the current density is observed that is associated with the rising portion of the A2 process and $Cu(OH)_2$ formation (Figure 9-17). The spectroscopic ellipsometry results obtained during the experiment are shown in Figure 9-18. Significant changes in optical properties are found at potentials between -300 and -400 mV, and above -200 mV.

The corresponding spectroscopic-ellipsometry-interpreted film thicknesses as a function of potential are shown in Figure 9-19A. As with the ellipsometry results discussed above, film growth begins at a potential where anodic current is first observed. The integrated current (i.e., charge) vs potential corresponding to the data given in Figure 9-17 is shown in Figure 9-19B. As the potential is increased beyond the A1 peak-potential maximum, film growth stops despite the fact that current continues to flow. The current efficiency for film growth at -350 mV is only about 44% and decreases to about 25% at -200 mV. This finding indicates that, in the potential regime between -350 and -200 mV, the rate of film growth is equal to the rate of film dissolution and/or electrochemical reaction (to form CuO_2^{-2}). While our scattering measurements showed that the film becomes microscopically rough due to this dissolution (cf. Figure 7-35), the ellipsometer is sensitive only to light collected in the forward propagating direction. Therefore, ellipsometry is less sensitive to film breakup than are elastic-scattering measurements. Further significant film growth does not begin until the potential reaches -200 mV, where the onset of divalent film formation begins. The increase in film thickness at potentials slightly anodic of this value could be due to an increase in

Cu_2O film thickness prior to $Cu(OH)_2$ film formation. This conclusion is consistent with that of our Raman results, which showed an increase in the cuprous oxide peak intensity accompanying cupric hydroxide formation.

Errors in the theoretical fits of the observed spectra using the single homogeneous-film model become large at potentials anodic of -175 mV, and indicate that the model no longer represents the surface morphology. This is not surprising since, as indicated by our scattering and SEM results, a "porous" film of small $Cu(OH)_2$ needle-like crystals forms at this potential by the precipitation of soluble divalent copper from the solution.

9.3.3 Constant Current Experiments

An understanding of film growth under galvanostatic (constant-current) conditions is often more complicated than that under potentiostatic conditions. In general, both the potential and surface concentration vary with time. Typical constant-current charging curves show a potential that rises to -400 to -325 mV (depending on the current density), and then remains relatively constant. Later, the potential increases to a second plateau near -50 mV as the divalent oxidic film is formed. At sufficiently long anodization times, the potential increases again as oxygen evolution occurs.

Δ and Ψ spectra taken during the galvanostatic anodic oxidation of copper in 1M KOH at 22 $\mu A/cm^2$ are shown in Figure 9-20. This small current density was chosen to study slow film growth and to allow four-zone averaged data to be taken over an extended time. The charge passed in a 0.5 mV/sec potential-sweep

experiment up to the A1 peak maximum potential is about 35 mC/cm^2. We stopped the galvanostatic anodization at a significantly smaller total charge than this value (11 mC/cm^2, 500 sec). During the anodization, a plateau potential of -385 mV was observed. The Δ values followed a general decreasing trend during anodization. The total change in Δ after 500 sec is about 25°. Changes in Ψ occur primarily at shorter wavelengths (<550 nm), where the extinction coefficient of Cu_2O is larger (see Figure 9-24). As the film thickens, a hump in the Ψ spectrum is observed.

After 500 seconds of anodization, the film was reduced at the same current density (22 $\mu A/cm^2$) for 400 sec. The Δ and Ψ spectra reverse the changes that occured during the anodization (Figure 9-21). For example, the hump in the Ψ spectrum is removed first, followed by continued spectral changes that approach that of the substrate.

The change in the film thickness as a function of time for this experiment as interpreted by the ellipsometric model is shown in Figure 9-22. The film thickness increases and decreases linearly with time during anodization and reduction, respectively. The film growth and reduction rates are approximately the same (about 0.27 Å/sec). This value is equal to the calculated growth rate, assuming that all the charge passed goes to film formation (0.28 Å/sec). This finding shows that at very low current densities, the current efficiency for film formation is large because (at the correspondingly low potential) little soluble divalent product is formed. Likewise, at higher potentials (or currents), the current efficiency decreases.

9.3.4 Potential-Step Experiments

Following the application of a potential-step change from a noble values to where Cu_2O film formation occurs, both the current density and the rate of change in ellipsometer parameters decrease monotonically with time. The film thickness, derived from our ellipsometry optical model, is plotted as both a function of time and the square root of time in Figure 9-23 for a potential step experiment from -600 to -350 mV. The parabolic dependence of film thickness with time demonstrates that film growth is controlled by a diffusion and/or migration process [I21]. The cuprous oxide film growth could be limited by the migration of the Cu^+ ion to the surface. The cuprous ion has a smaller ionic radius than oxygen (0.96 vs 1.32 Å [I22]). However the species whose diffusion/migration is rate-controlling cannot be determined based on our results alone.

9.3.5 Cuprous Oxide Optical Properties

In addition to film thickness, the optical properties of the Cu_2O film were derived from ellipsometry measurements. The real and imaginary components of Cu_2O films formed by anodic oxidation in 1M KOH are shown in Figure 9-24 and are the average of all our copper ellipsometry measurements. An average value of the refractive index over the spectral range studied is about 3.2. It exhibits a general increasing trend from 2.8 at 3700 Å to 3.6 at 7200 Å, with a trough at around 5500 Å. The extinction coefficient initially decreases linearly with increasing wavelength from 1.0 at 3700 Å to about 0.5 at around 5500 Å. An absorption band between 5500 and 6000 Å is evident, as the extinction coefficient

increases 50% in this range. At wavelengths above 6000 Å, the extinction coefficient decreases in an approximately linear manner.

The real and imaginary components of the dielectric constants are related to the real and imaginary components of the refractive index by [I5-I7]

$$\epsilon_1 = n^2 + k^2 \qquad 9.12$$

and

$$\epsilon_2 = 2nk \ , \qquad 9.13$$

where ϵ_1 is the real component and ϵ_2 is the imaginary component of the dielectric constants. The dielectric constants of Cu_2O are shown in Figure 9-25. The increase in the imaginary component of the dielectric constant from 5500 to 6000 Å is associated with the excitation of electrons from the valance to the conduction band across the band gap. As discussed before (Chapter 1, Section 6), the absorption peak is not sharp because exciton-hole pairing allows indirect interband transitions to occur. However, the local maximum in the absorption spectrum occurs at 6000 Å, which corresponds well with the reported direct transition bandgap of Cu_2O of 2.1 eV. The results shown in Figures 9-24 and 9-25 demonstrate that a material's wavelength-dependent optical properties can be determined by spectroscopic ellipsometry using an appropriate calculation procedure and that these properties can be useful in identifying the composition of the film.

Section 9.4: Anodic Oxidation of Zinc

Because zinc is a metal with a standard potential cathodic of the hydrogen/water couple, the metal corrodes spontaneously when placed in an alkaline solution (see Chapter 3, Section 1). Furthermore, the interpretation of ellipsometric observations of anodic film-formation on zinc is difficult because of the complicated film structure as well as the optical effect due to the diffusion boundary layer.

A previous ellipsometry study concluded that only qualitative aspects of anodic film formation process on zinc could be determined [I23]. In this work, we made spectroscopic ellipsometry measurements of film growth only under corrosion conditions, thereby eliminating the complications described above.

A Zn (1000) single crystal was placed in a deoxygenated, ZnO-saturated solution of 1M KOH. Prior to the experiment, distilled water was placed in the ellipsometry cell. (This procedure allowed the electrode to be aligned and the manual azimuths to be set without corrosion of the electrode.) The water was then removed from the chamber, and the cell was purged with nitrogen. As soon as the KOH solution was introduced into the chamber (through the fitting in the bottom of the cell) and reached the level of the electrode, the ellipsometer was turned on, and four-zone measurements were taken.

Since ZnO is white and ϵ–$Zn(OH)_2$ is colorless, the model used to interpret the data assumed that the optical properties of the (homogeneous) film were wavelength-independent. The real component of the refractive index of the film

derived from our measurements was determined to be 2.1-0.02i, nearly identical to that of ZnO (2.0-0.0i) [I22]. Figure 9-26 shows the thickness of the layer as a function of time after the introduction of the electrolyte. Following a period of approximately linear growth (0 to 200 sec), the film thickness approaches a limiting thickness asymptotically. Therefore, film growth obeys a limiting-thickness growth law. However, the exact form of the law is uncertain. Figure 9-26 shows two best-fit exponential equations to the data:

$$T(t) = T_{\infty}(1-e^{-\alpha t}) \qquad 9.14$$

and

$$T(t)^2 = T_{\infty}^2(1-e^{-\alpha t}) \ . \qquad 9.15$$

The simple exponential equation (9.14) (best-fit parameters T_{∞}=128, α=172 sec^{-1}) represents the data better than equation 9.15 (best fit parameters T_{∞}=138, α=377 sec^{-1}). However, equation 9.14 has a theoretical basis, whereas to the best of our knowledge, the simple exponential relationship does not. Limited film-thickness growth indicates a process controlled by the internal electric field generated in a space-charge region [I21].

If the transport of a single species is rate-controlling, the overall rate of film growth can be obtained by solving the linear diffusion/migration equation:

$$\overline{m}\frac{dT}{dt} = D\frac{dC}{dx} + \mu_o E(x)C \ . \qquad 9.16$$

In equation 9.16, $\overline{m}$ is the molar volume of the oxide, T is the film thickness, t is

the time, D is the diffusion coefficient (in the solid), C is the concentration of diffusing/migrating species, x is the position within the film, μ is the ionic mobility, and E(x) is the electric field-strength. In general, the solution of this equation requires the simultaneous solution of the Poisson equation. If the transport of more than one species is rate-limiting, an equation similar to equation 9.16 must be solved simultaneously for each species.

To decouple the problem, one often approximates the distribution of charge in the space-charge region so that the field can be calculated directly and then inserted into equation 9.16. Perturbation techniques are often used to solve this problem in the limit of low space-charge fields. Field-averaging techniques (introduced by Fromhold [I21]) allow one to obtain approximate (and often closed-form) solutions to film-growth problems by decoupling the two partial differential equations. An example of this procedure follows.

If one assumes that, during film growth, charged defects are trapped in the film in a uniform concentration C_o (in moles/cm^3), the corresponding electric field E(x) can be obtained from Poisson's equation. The result is

$$E(x) = (\frac{4\pi}{\epsilon})q_o C_o x \quad , \qquad 9.17$$

where q_o is the amount of charge (eZ) on the diffusing/migrating species. In obtaining equation 9.17, we have assumed that the field at the metal/film interface is zero (an assumption that doesn't affect the form of our results). The average electric field in the film is then

$$<E(x)> = (\frac{2\pi}{\epsilon})q_oC_oL \ . \qquad 9.18$$

Let us further assume that the oxidation occurs under pseudo-steady-state conditions, so that the concentration profile is linear with position in the film. (This type of profile would be found in the absence of any field effect.) Therefore, we can write

$$C(x) = C(0) - \frac{[C(0)-C(L)]x}{L(t)} \qquad 9.19$$

and

$$\frac{dC}{dx} = -\frac{C(0)-C(L)}{L(t)} \ , \qquad 9.20$$

so that the average concentration in the film is simply

$$<C> = \frac{C(0)+C(L)}{2} \ . \qquad 9.21$$

Finally, we assume that the concentrations at the two interfaces do not vary with time. Using equations 9.18, 9.20, and 9.21 in equation 9.16 yields

$$\bar{m}\frac{dL}{dt} = \frac{\beta}{L(t)} + \gamma L(t) \ , \qquad 9.22$$

with

$$\beta = -D\ [C(0)-C(L)] \qquad 9.23$$

and

$$\gamma = \frac{\mu_o \pi q_o C_o [C(0)-C(L)]}{\epsilon} \quad . \qquad 9.24$$

Integration of equation 9.22 yields

$$L(t)^2 = -(\frac{\beta}{\gamma})[1-e^{(2\gamma t)}] \quad . \qquad 9.25$$

Fromhold has referred to this result as the "first order" limiting-film growth equation [I21].

The assumptions made to derive equation 9.25 don't warrent the calculation of film-growth parameters from the model. However, the development is useful in understanding the effect that space-charge layers have on surface-layer formation. The migration of species in the film due to the field established by the space-charge layer eventually balances the diffusion of these species in the opposite direction. A comparision of the theoretical results of rigorous numerical solutions to the space-charge problem by Fromhold [I21] shows that the exact solutions would not fit the data shown in Figure 9-26 better than the approximate solution. (The "exact" result rises more rapidly to the limiting thickness.) Furthermore, the intial Zn oxide film growth occurs more slowly than that predicted by either the "first order" or simple exponential model. The "first order" best fit limiting thickness is about 10 Å greater than that observed, and therefore the optimization forces both the time constant α and the limiting thickness T_∞ to be artificially large.

The most likely explanation for these discrepancies is associated with the simultaneous dissolution of the film into the electrolyte as it forms. This

suggestion could also explain why there is a slight decrease in film thickness after the maximum is reached. (This decrease could be attributed to the local etching of the film, thereby roughening it and making the optical-model fit less accurate.) Such a process would increase the time for the balance between migration and diffusion (in the film) to be established. If we assume that the dissolution of the film into the semi-infinite electrolyte can be expressed using the Cottrell equation [I24],† the equation to be solved for film growth would be modified to

$$\overline{m}\frac{dL}{dt} = \frac{\beta}{L(t)} + \gamma L(t) - C_{sat}\sqrt{D_o/\pi t} \ , \qquad 9.26$$

where D_o is the diffusion coefficient of dissolved ZnO in the electrolyte. The first term on the right-hand side of the equation is associated with the transport of material though the film by diffusion. The second term corresponds to the migration of the ion in the film due to the space charge set up in the film. The last term represents the rate of dissolution of the film in the electrolyte. No attempt was made to curve-fit our data using this equation because of the large number of simplifying assumptions used to obtain it.

Section 9.5: Conclusion

In this chapter we have discussed the instrument used in this study, some principles of ellipsometry, and the application of these principles to optical modeling. The Fresnel reflection coefficients and the results obtained by Drude

† Note that this assumption implies that there is a step change in the (dissolved) ZnO surface concentration at time zero from 0 the saturation concentration.

[I13] for the reflection from a flat layer of material placed between two semi-infinite media are used in all our optical models. The optical properties of composite materials are derived using an effective-media approximation (EMA). The reflection coefficients from "island films" are determined using the coherent superposition principle. Combinations of the equation corresponding to these principles allow the prediction of a large number of surface film structures, including roughness layers, diffusion-boundary layers, and homogeneous, porous, island, and multilayered films.

Physical parameters are derived from the optical model using a Simplex algorithm. This optimization method is inherently stable and robust but is slower than linear optimization techniques near the solution (e.g., Newton-Raphson). For future work, we suggest the use of a techniques that combines these two methods.

We have shown that the wavelength-dependent anisotropic optical properties of a film and the film thickness can be derived simultaneously from ellipsometric measurements if (1) the optical properties of the film are thickness-independent and (2) spectra are gathered at more than one film thickness. This model was used for films that did not undergo three-dimensional nucleation. A two-layer island-film model, consisting of a homogeneous underlayer and a hydrated island overlayer, was used to model the observed spectra of nucleated films.

We have previously reported spectroscopic ellipsometry results on the anodic oxidation of silver in 1M KOH [I10,I16]. The present findings are consistent and complementary to our earlier work. There are three distinct periods of film

growth. During the first phase, a compact underlayer (also refered to as the primary layer) forms whose growth is controlled by a diffusion process. The wavelength-dependent optical properties of this layer have been derived. At a sufficiently large potential (above about 290 mV vs Hg/HgO in 1M KOH) and time (which depends on the potential), three-dimensional crystals form out of and on top of the underlayer. Even at large overpotential, nucleation does not occur until the primary layer has reached a critical thickness. We have shown that both the nucleation and growth of these crystals require a potential greater than about 290 mV vs Hg/HgO in 1M KOH. Thin nucleated films tend to dissolve into the electrolyte rapidly, while thin unnucleated films and thicker nucleated ones are relatively more stable. These findings are in agreement with our primary layer/nucleation/Ostwald-ripening hypothesis and show that the formation of anodic films on silver is more complicated than the simple dissolution/precipitation model would indicate.

The rate of oxidation and reduction of copper in 1M KOH to form Cu_2O run parallel to the overall charge passed. Film formation begins with the onset of anodic current. Cuprous oxide film growth follows a parabolic growth law, indicating that the process is controlled by the diffusion of the Cu^+ ion in the layer. During a potential-sweep experiment, the thickness of the film is about 140 Å at the A1 peak potential.

The efficiency for cuprous oxide film formation is generally low. At potentials between the A1 and A2 peaks, the film does not grow despite the fact that current continues to pass. This finding is associated with the reaction of the

Cu_2O film to form the divalent CuO_2^{-2} ion. The rate of film formation is equal to the rate of film dissolution in this potential range. At very low current densities (or overpotentials), where this reaction does not occur at an appreciable rate, current efficiencies for film formation approach 100%.

The optical properties of Cu_2O films formed by anodic oxidation in 1M KOH have been derived from our spectroscopic ellipsometry results. An observed adsorption band, located at 6000 Å (2.1 eV), is consistent with the compounds reported direct interband transition band gap. The absorption peak is broad because of the presence of exciton-hole indirect transition.

A study of anodic film formation of Zn using ellipsometry is difficult because of the optical effects of a complicated film structure and the diffusion boundary layer. Therefore, spectroscopic ellipsometry measurements were made of Zn only under corrosion conditions in a deoxygenated, zincate-saturated 1M KOH solution.

A single-film model with wavelength- and thickness-independent optical properties was used to model our observed Zn corrosion data. The derived optical constants (2.0-0.02i) are consistent with those reported for ZnO [I22]. Film growth follows a limiting-thickness growth law whose exact form is unknown. We suggest that film formation is controlled by simultaneous diffusion and migration in the film and the dissolution of the film into the electrolyte. An electric field set up by a space charge within the film causes the migration of ions in the film to be in the direction opposite to that of the diffusion process, thereby balancing the growth rate. The dissolution process increases the time for this

equilibrium to be achieved.

REFERENCES FOR CHAPTER 9

I1) Bashara, N. M., and R. M. A. Azzam, eds., **Proceedings of the Third International Conference on Ellipsometery**, North-Holland Publishing Co., New York, 1976.

I2) Azzam, R. M. A., and N. M. Bashara, **Ellipsometery and Polarized Light**, North-Holland Publishing Co., New York, 1977.

I3) Muller, Rolf. H., "Principles of Ellipsometry", In **Advances in Electrochemistry and Electrochemical Engineering.** Vol. 9, P. Delahay and C. W. Tobias, editors, Wiley, New York, 1973.

I4) Stone, J., **Radiation and Optics**, McGraw-Hill, New York, 1963.

I5) Reitz, J. R., R. J. Milford, and R. W Christy, **Foundations of Electromagnetic Theory**, 3rd edition, Addison-Wesley, Menlo Park, CA, 1980.

I6) Hecht, E., and A. Zajac, **Optics**, 4th edition, Addison-Wesley, Menlo Park, CA, 1979.

I7) Jackson, J. D., **Classical Electrodynamics**, 2nd edition, John Wiley, New York, 1975.

I8) Mathieu, H. J., D. E. McClure, and R. H. Muller, Rev. Sci. Instrum. **45**, 798 (1974).

I9) Muller, R. H., and Joseph C. Farmer, Rev. Sci. Instrum. **55,** 371 (1984).

I10) Mayer, Steve T., M. S. Thesis, Dept. of Chemical Engineering, University of California at Berkeley, December 1985. Lawrence Berkeley Laboratory Report LBL-20502.

I11) Farmer, Joseph C., Ph. D. Thesis, Dept. of Chemical Engineering, University of California at Berkeley, March 1983. Lawrence Berkeley Laboratory Report LBL-15607.

I12) Armstrong, M. J., M.S. Thesis, Dept. of Chemical Engineering, University of California at Berkeley, December 1984. Lawrence Berkeley Laboratory Report LBL-18599.

I13) Drude, P., Ann. Phys. Chem., N. F. **36,** 865 (1889).

I14) Maxwell-Garnett, J. C., Philos. Trans. R. Soc. London **203,** 385 (1904).

I15) Bruggeman, D. A. G., Ann. Phys. (Leipzig) **24,** 636 (1935).

I16) Mayer, S. T., and R. H. Muller, J. Electrochem. Soc. **135,** 2133 (1988).

I17) Vanleugenhaghe, C., M. Pourbaix, and R. Van Pysselberghe, in **Atlas of Electrochemical Equilibria in Aqueous Solutions**, Section 14.2, English Translation, Pergamon Press, New York, 1966.

I18) Ord, J. L., D. J. DeSmet, and Z. Q. Huang, J. Electrochem. Soc. **134** 826

(1987).

I19) Yamashita, M., K. Omura, and D. Hirayama, Surf. Sci. **96,** 443 (1980).

I20) Miller, B., J. Electrochem. Soc. **116,** 1675 (1969).

I21) Fromhold, A. T., Jr., **Theory of Metal Oxidation**, Volume I and II, North-Holland, New York, 1976, 1980.

I22) Weast, Robert C., and Melvin J. Astle, editors, **CRC Handbook of Chemistry and Physics**, 62nd edition, CRC Press, Boca Raton, FL, 1981-1982, p. F-175.

I23) Smith, C. G., Ph. D. Thesis, Dept. of Chemical Engineering, University of California at Berkeley, August 1978. Lawrence Berkeley Laboratory Report LBL-8082.

I24) Macdonald, D. D., **Transient Techniques in Electrochemistry**, Plenum Press, New York, 1977, p. 72.

FIGURE CAPTIONS FOR CHAPTER 9

Figure 9-1. Ellipsometer derived primary layer film thickness versus potential for a 0.04 mV/sec potential sweep of silver anodized in 1M KOH. The potential was initially step from -50 mV to 250 mV vs Hg/HgO in 1M KOH prior to the potential sweep. Optical model used is a homogeneous compact film with thickness independent and wavelength dependent optical properties (c.f., Figure 9-2).

Figure 9-2. Optical constants of a thin Ag_2O film formed and derived from ellipsometry measurements as described above.

Figure 9-3. A) Change in Ψ for Ag in 1M KOH at various times after going to open circuit following a 60 sec potential step to 290 mV. B) Change in Ψ for Ag in 1M KOH immediately after and 3 minutes after open circuit following a 120 sec potential step to 290 mV.

Figure 9-4. Current versus time for a double potential step experiment for Ag in 1M KOH. The first potential step (from -50 to 320 mV) was applied for 10 sec, followed by a decrease in potential to 270 mV.

Figure 9-5. Change in Ψ after going to open circuit following a double E-step experiment. First potential step- -320 mV, 10 sec. Second potential step-270 mV, 60 sec.

Figure 9-6. 3-dimensional plots of Δ vs time for the anodization of Ag in 1M

KOH. Potential stepped from -50 to 295 mV at time zero. Potential held at 295 mV from 0 to 60 sec. From 60 to 360 sec, potential held at 250 mV. After 360 sec, potential increased at 0.5 mV/sec.

Figure 9-7. 3-dimensional plots of Ψ vs time corresponding to Δ results shown in Figure 9-6.

Figure 9-8. Primary layer film thickness vs time corresponding to experiment described in Figure 9-6. Dual layer optical model includes a homogeneous compact layer (primary layer) adjacent to the substrate with a porous island film (secondary layer) on top.

Figure 9-9. Optical model derived secondary layer film coverage vs time derived from ellipsometer measurements for the experiment described in Figure 9-6.

Figure 9-10. Measured and dual layer optical model predictions of Ψ for a Ag_2O film formed after 60 seconds of anodization as described in Figure 9-6. □ - Substrate spectrum.

Figure 9-11. Measured and dual layer optical model predictions of Δ for a Ag_2O film formed after 60 seconds of anodization as described in Figure 9-6. □ - Substrate spectrum.

Figure 9-12. Measured changes in Δ during a 0.5 mV/sec potential sweep of copper in 1M KOH. Initial potential -600 mV. Peak anodic potential

-300 mV. Peak cathodic potential -600 mV.

Figure 9-13. Measured changes in Ψ during a 0.5 mV/sec potential sweep of copper in 1M KOH. Initial potential -600 mV. Peak anodic potential -300 mV. Peak cathodic potential -600 mV.

Figure 9-14. Comparison of measured and best-fit model-predicted ellipsometry data corresponding to data shown in Figure 9-12 and 9-13. Optical model consists of a single film with thickness independent and wavelength dependent optical properties.

Figure 9-15. A) Current vs potential during a 0.5 mV/sec potential sweep experiment corresponding to ellipsometry measurements presented in Figure 9-12 and 9-13. B) Optical model interpreted film thickness vs potential using model described above.

Figure 9-16. Total integrated charge vs potential during experiment described above (Figure 9-12).

Figure 9-17. Current vs potential during a 0.5 mV/sec anodic potential sweep of Cu in 1M KOH.

Figure 9-18. Spectroscopic ellipsometry measurement vs potential during a 0.5 mV/sec potential sweep experiment.

Figure 9-19. A) Single-film optical-model interpreted Cu_2O film thickness vs

potential for 0.5 mV/sec anodic potential sweep experiment. B) Integrated charge vs potential.

Figure 9-20. Four-zone averaged Δ and Ψ spectra taken during galvanostatic oxidation of copper in 1M KOH. Current density 22 $\mu A/cm^2$.

Figure 9-20. Four-zone averaged Δ and Ψ spectra taken during galvanostatic oxidation of copper in 1M KOH. Current density 22 $\mu A/cm^2$.

Figure 9-21. Four-zone averaged Δ and Ψ spectra taken during galvanostatic reduction of a Cu_2O film formed on copper in 1M KOH as discussed above. Current density 22 $\mu A/cm^2$.

Figure 9-22. Film thickness vs time derived from ellipsometry measurement from a galvanostatic oxidation and reduction of copper using a single film model with optical properties which are thickness independent and wavelength dependent (selected spectra are shown in Figure 9-20 and 9-21).

Figure 9-23. Thickness vs time of Cu_2O film formed by potentiostatic oxidation of copper in 1M KOH at -350 mV vs Hg/HgO in 1M KOH. (Optical model discussed above and in text).

Figure 9-24. Real and imaginary components of the refractive index of Cu_2O film formed by potentiostatic oxidation of copper in 1M KOH at -350 mV.

(Optical model discussed above and in text).

Figure 9-25. Real and imaginary components of the dielectic constants of a Cu_2O film formed by potentiostatic oxidation of copper in 1M KOH at -350 mV. (Optical model discussed above and in text).

Figure 9-26. Single-film model (with wavelength independent optical constants) interpreted ZnO layer film thickness vs time formed by corrosion of Zn in an oxygenated ZnO saturated 1M KOH solution.

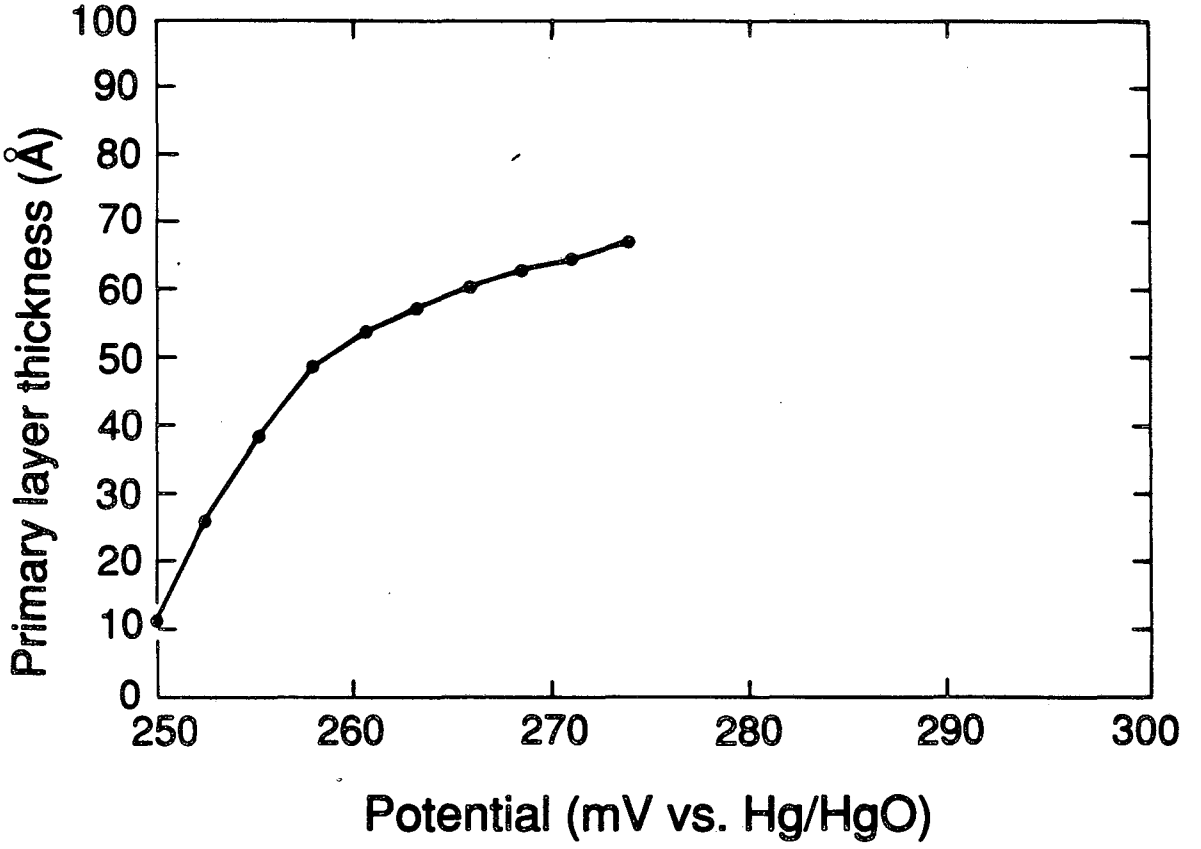

XBL 899-7283

Figure 9-1

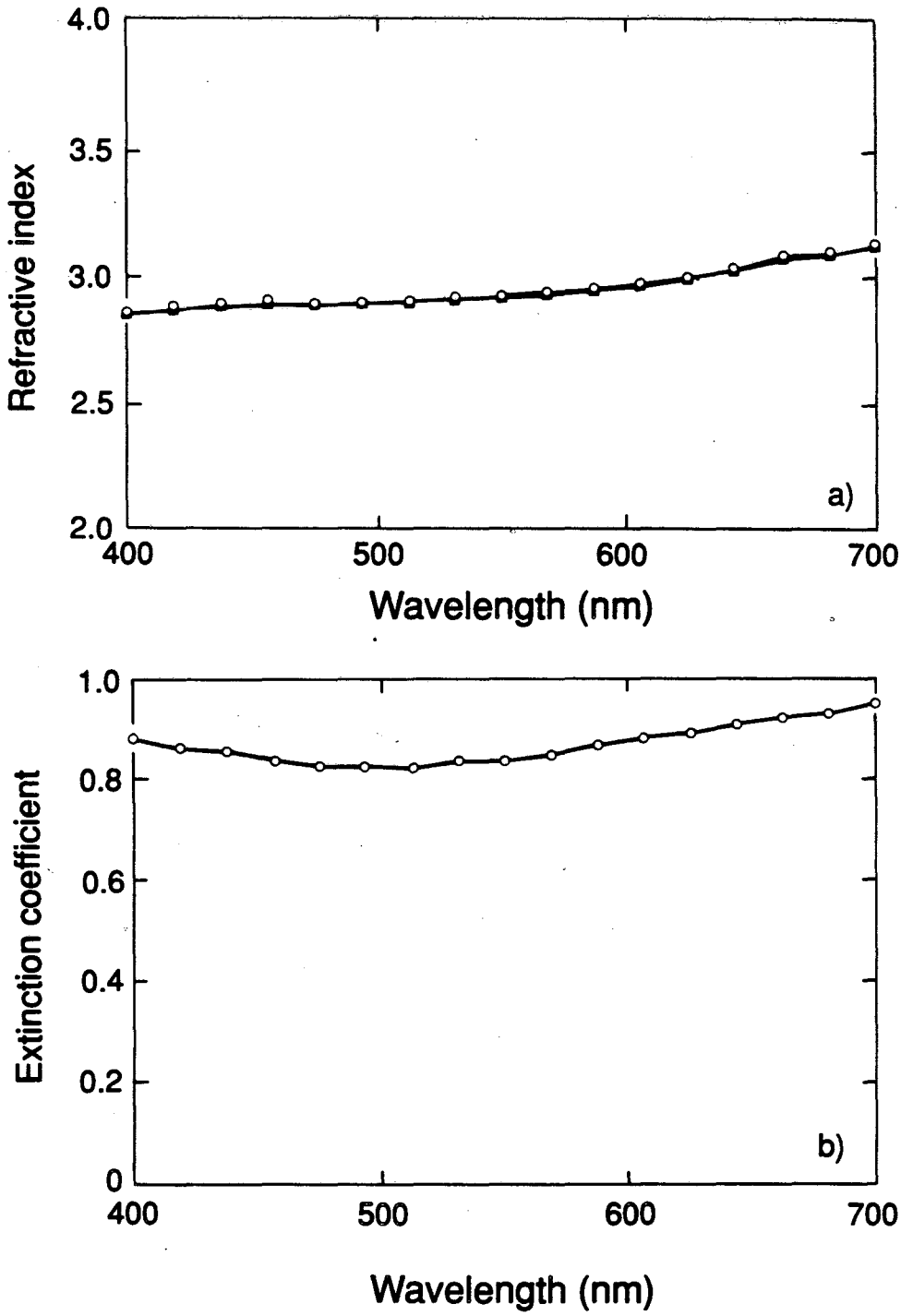

XBL 899-7282

Figure 9-2

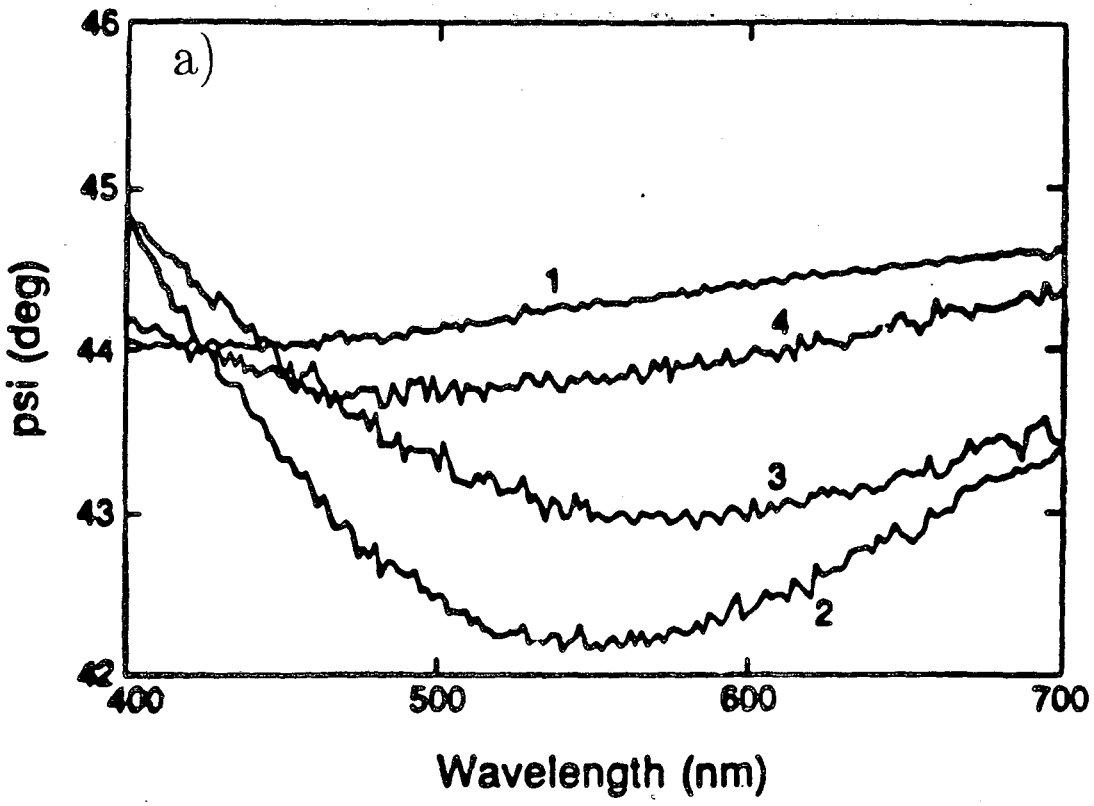

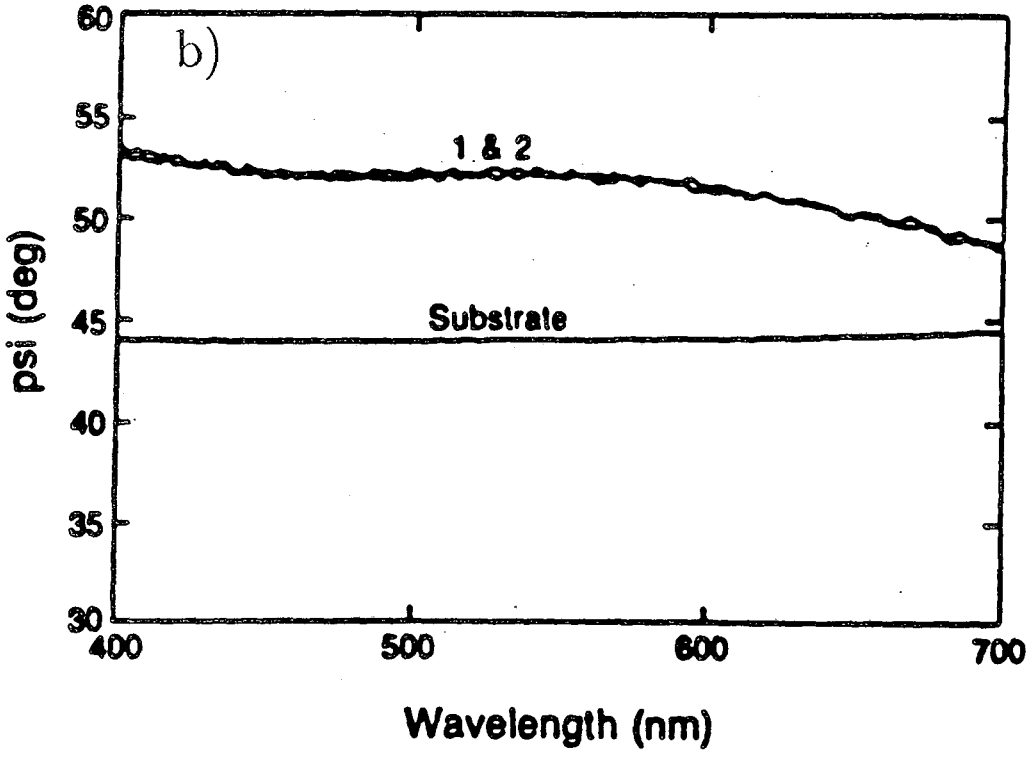

XBL 899-3315

Figure 9-3

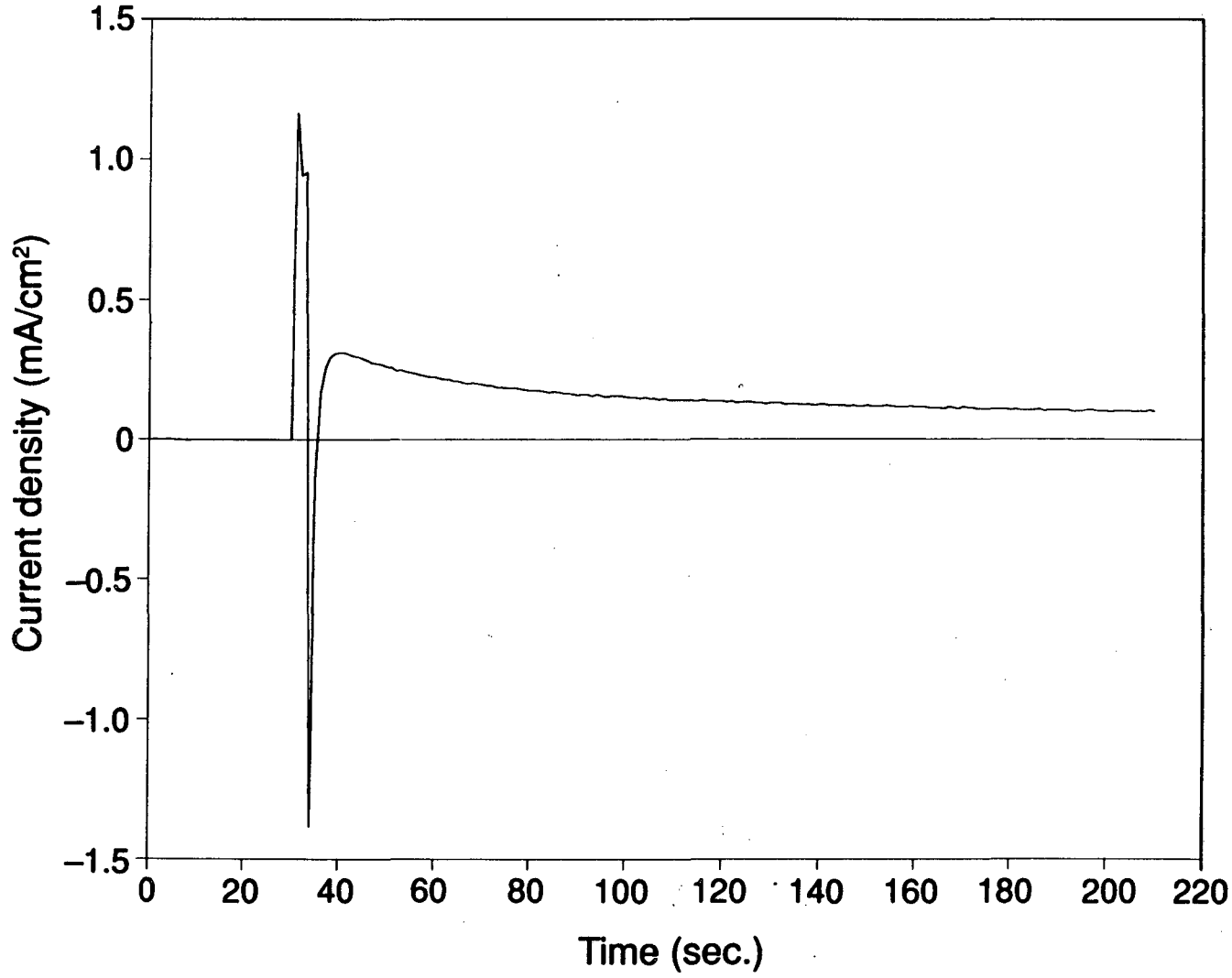

Figure 9-4

XBL 899-7286

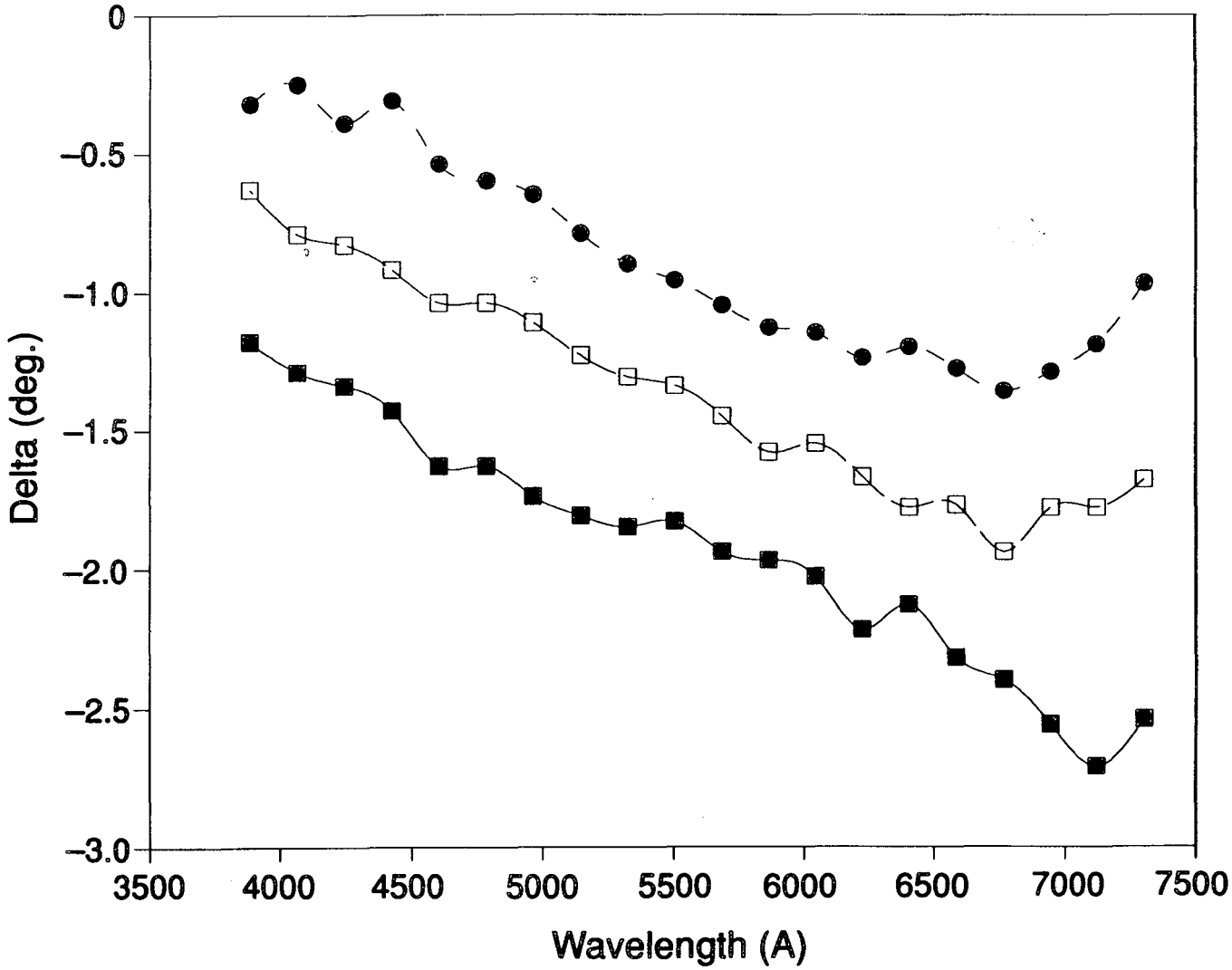

Figure 9-5

XBL 899-7292

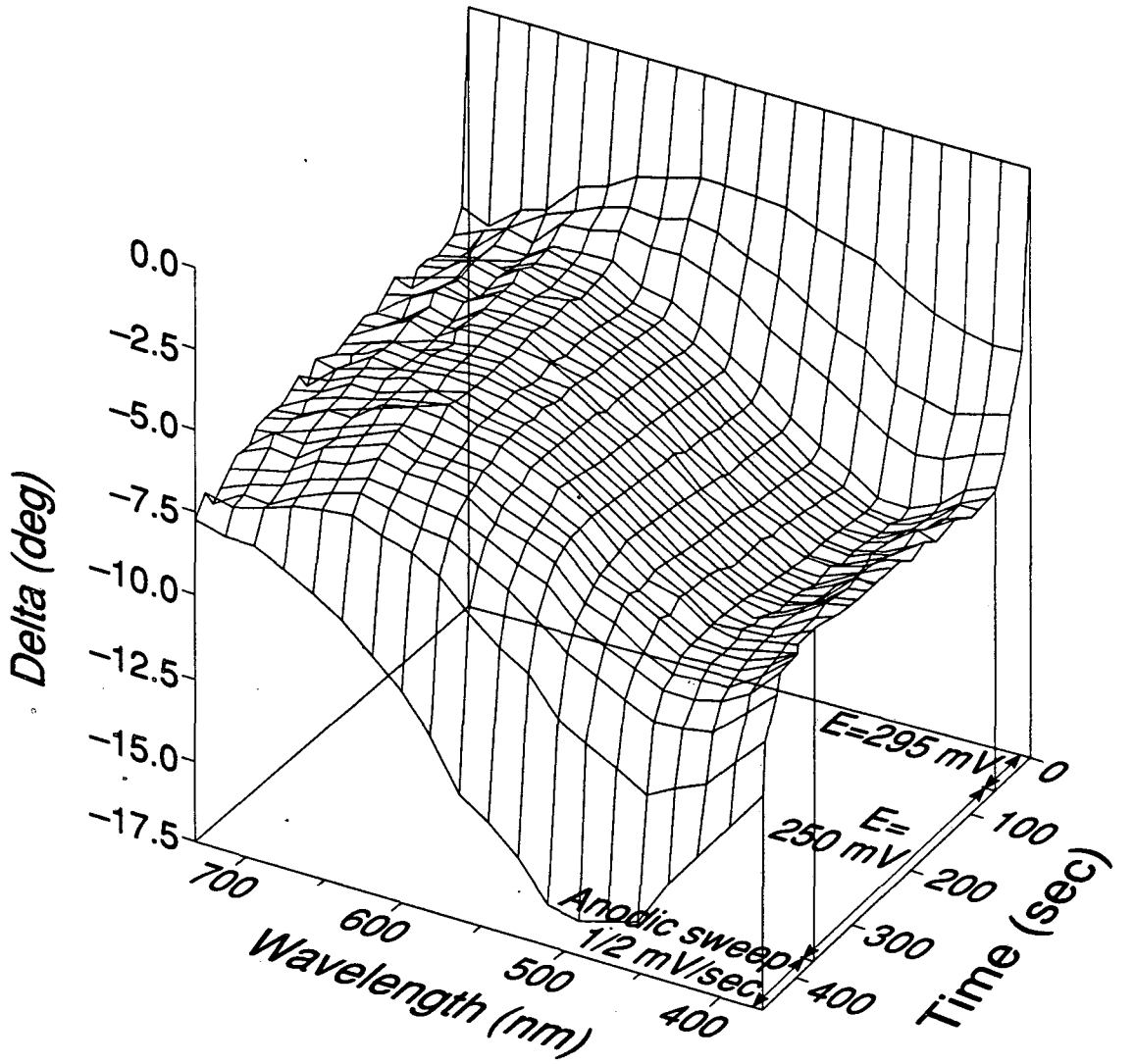

XBL 899-7297

Figure 9-6

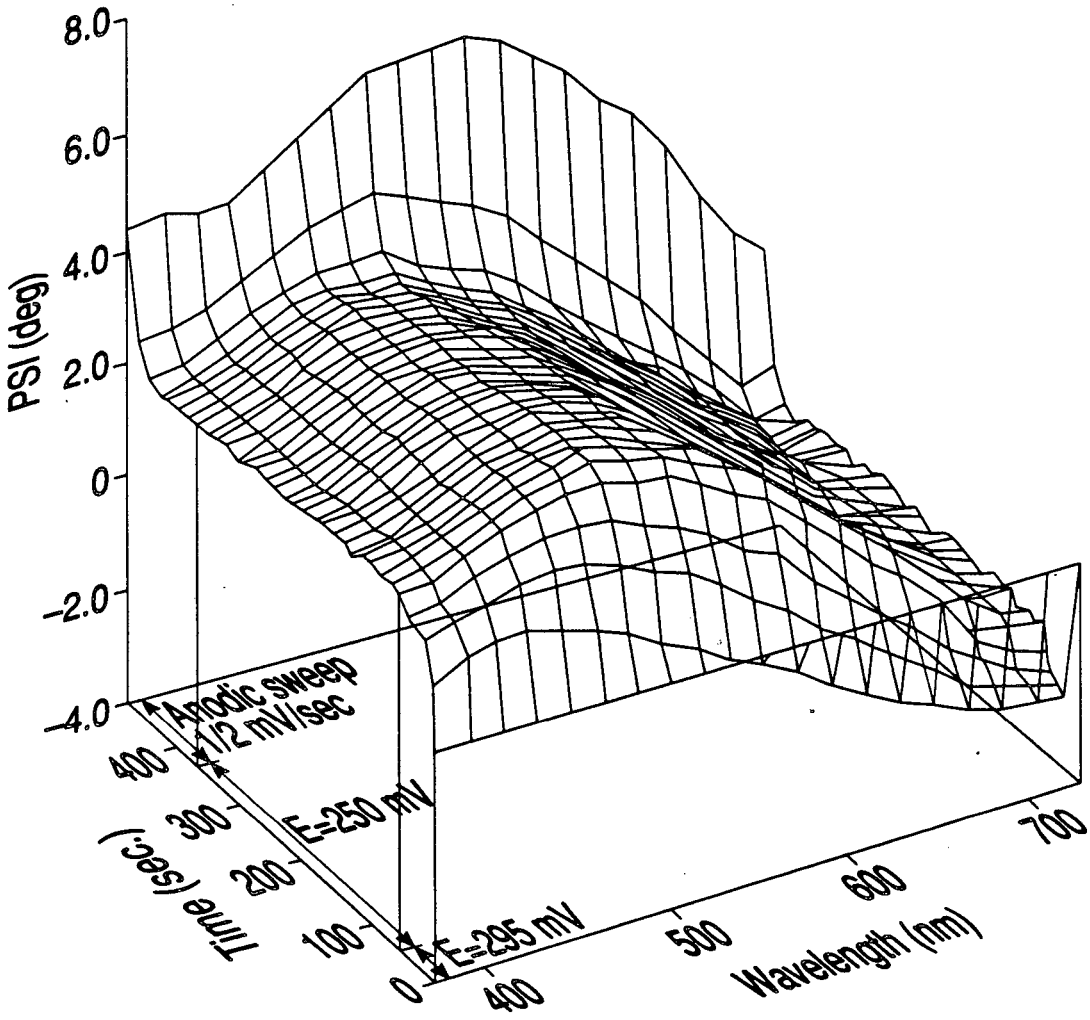

XBL 899-7294

Figure 9-7

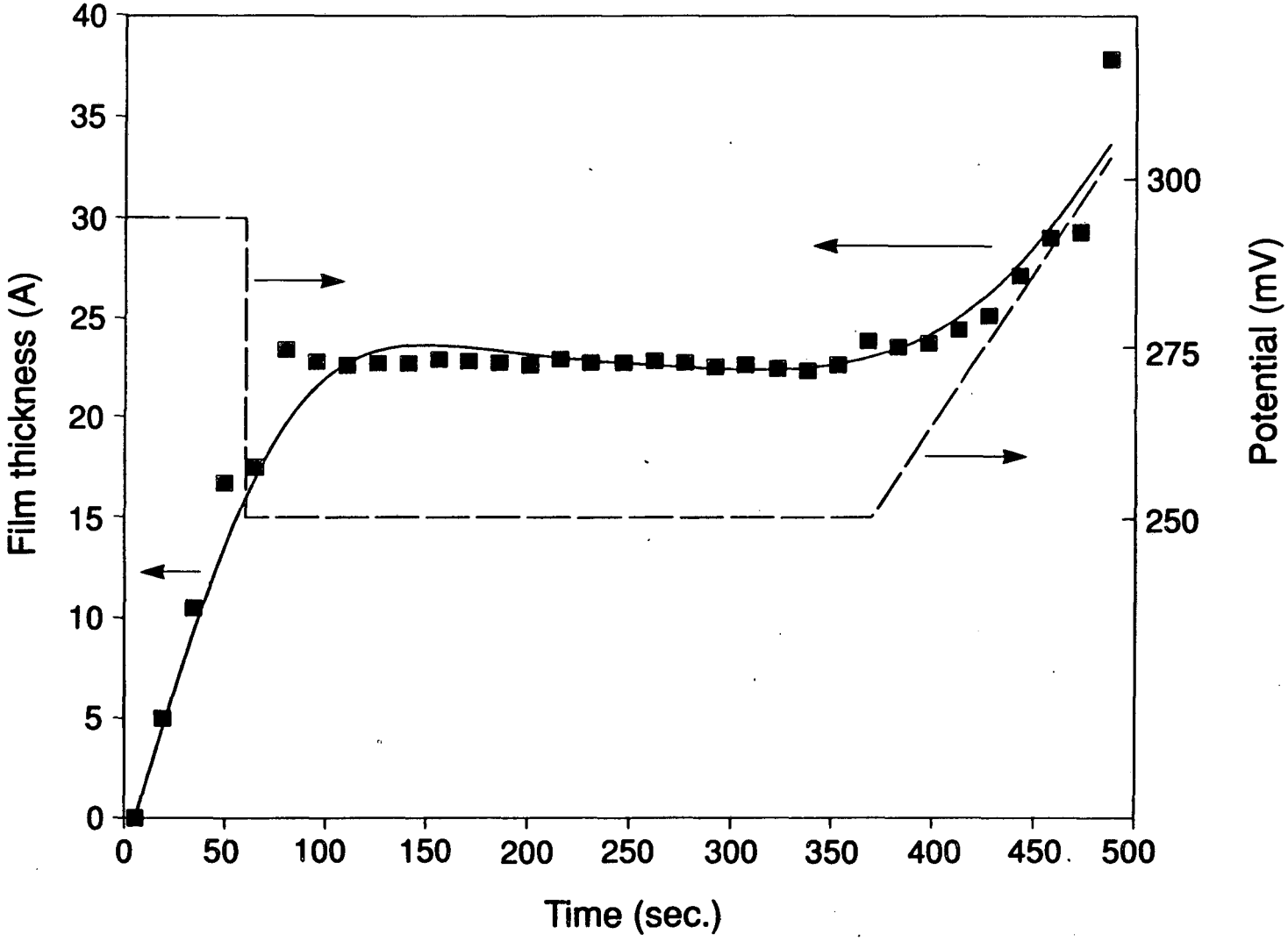

Figure 9-8

XBL 899-7285

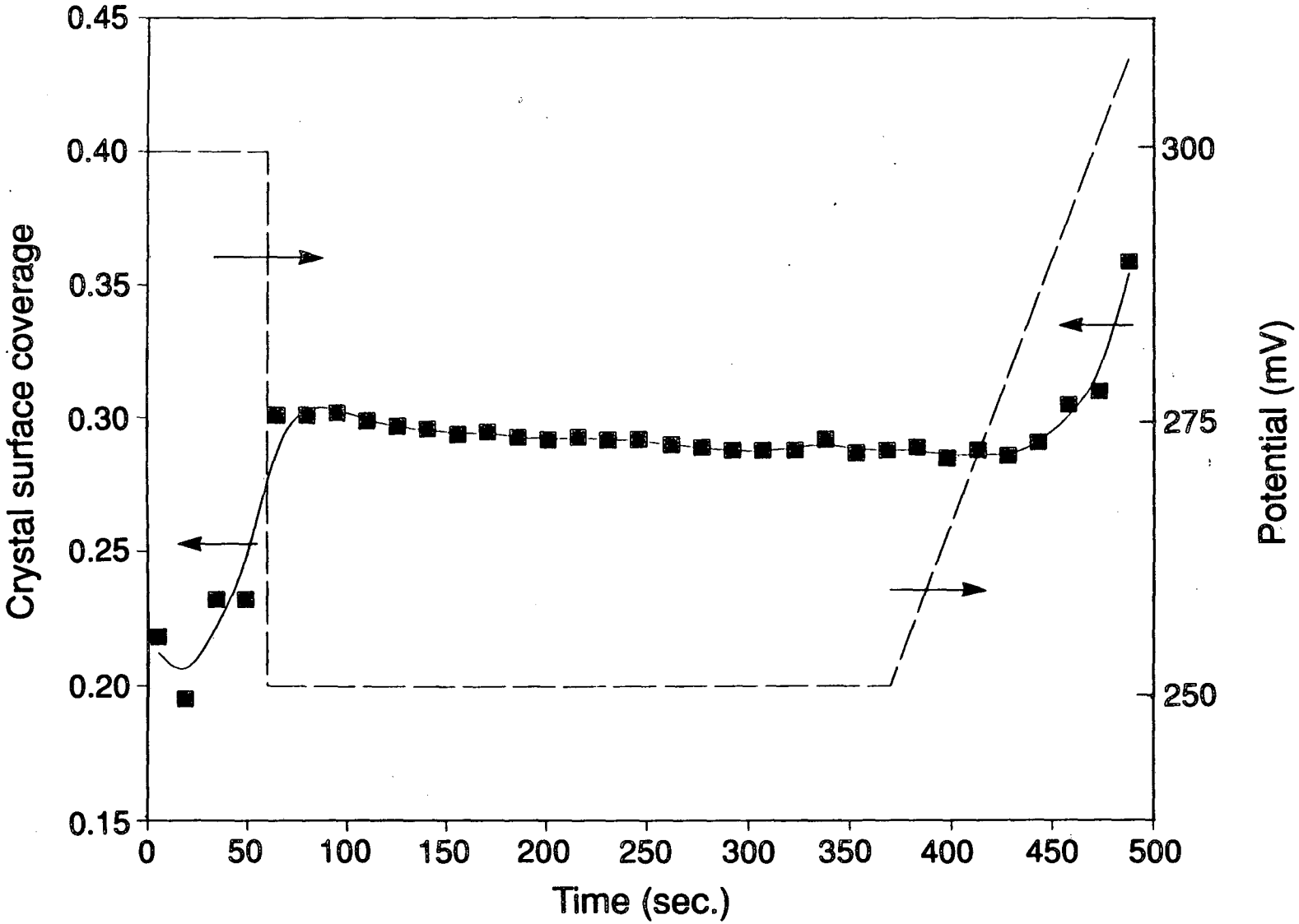

Figure 9-9

XBL 899-7284

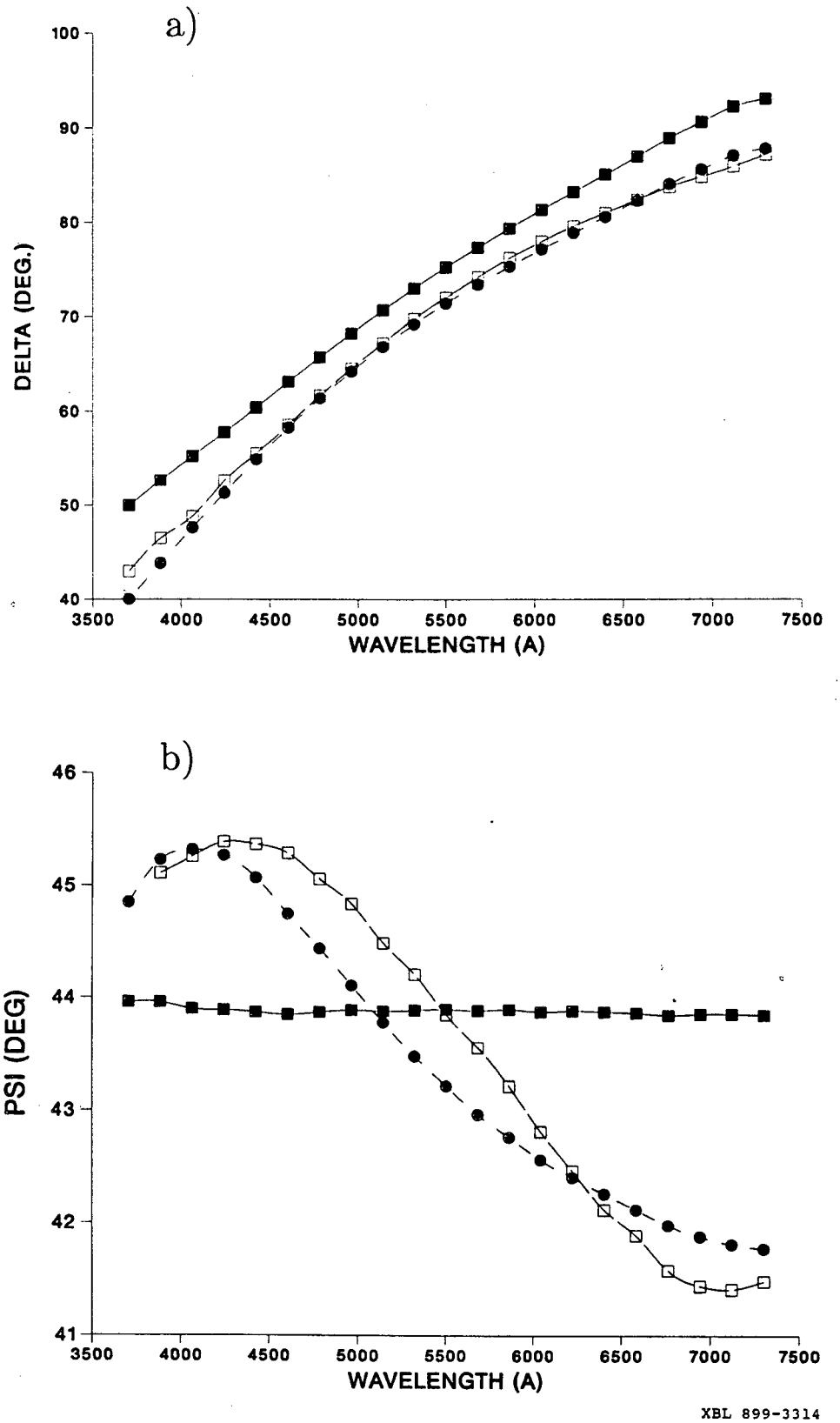
a)
DELTA (DEG.)
100
90
80
70
60
50
40
3500
4000
4500
5000
5500
6000
6500
7000
7500
WAVELENGTH (A)
b)
PSI (DEG)
46
45
44
43
42
41
3500
4000
4500
5000
5500
6000
6500
7000
7500
WAVELENGTH (A)
XBL 899-3314

Figure 9-10

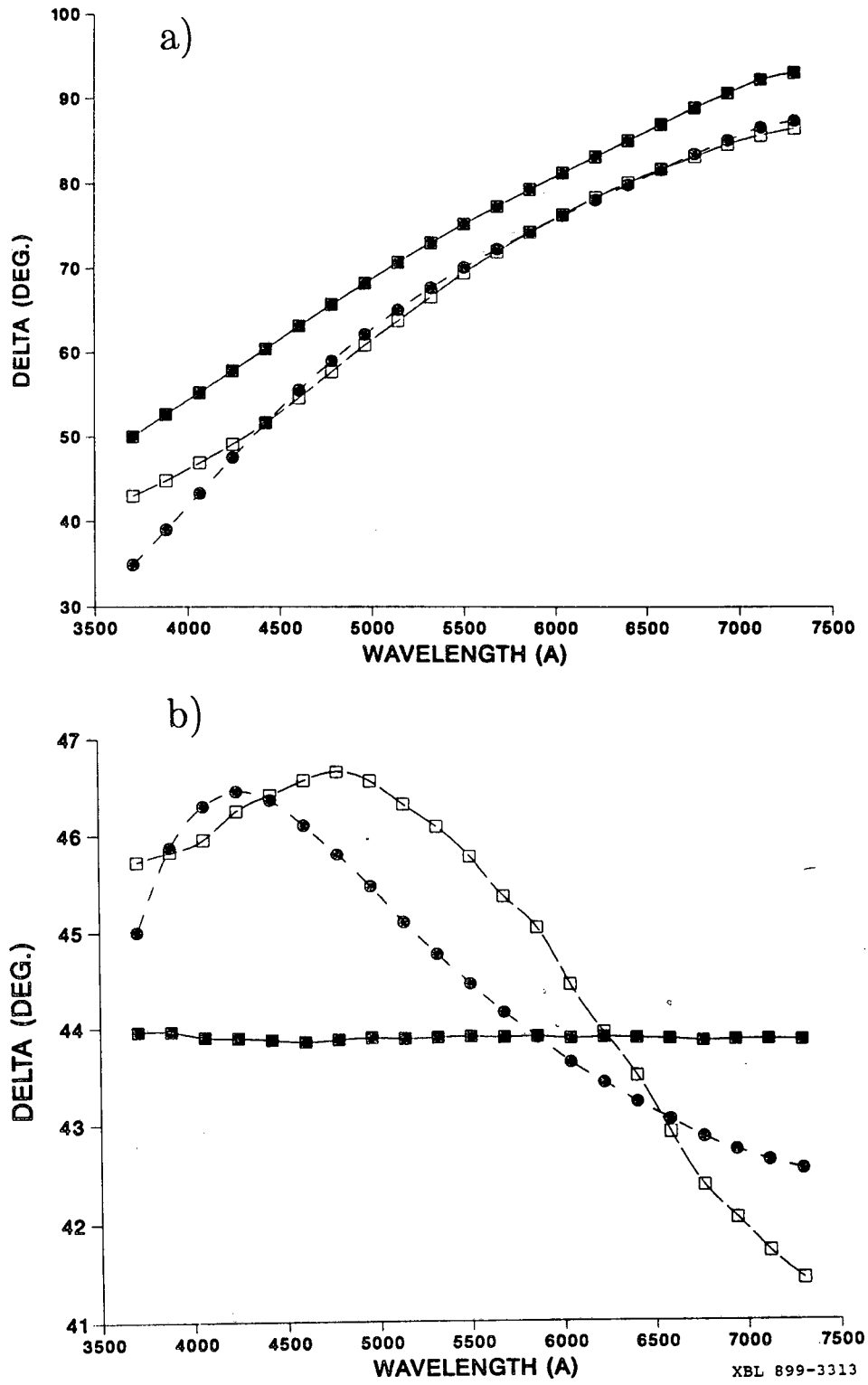
a)
DELTA (DEG.)
100
90
80
70
60
50
40
30
3500
4000
4500
5000
5500
6000
6500
7000
7500
WAVELENGTH (A)
b)
DELTA (DEG.)
47
46
45
44
43
42
41
3500
4000
4500
5000
5500
6000
6500
7000
7500
WAVELENGTH (A)
XBL 899-3313

Figure 9-11

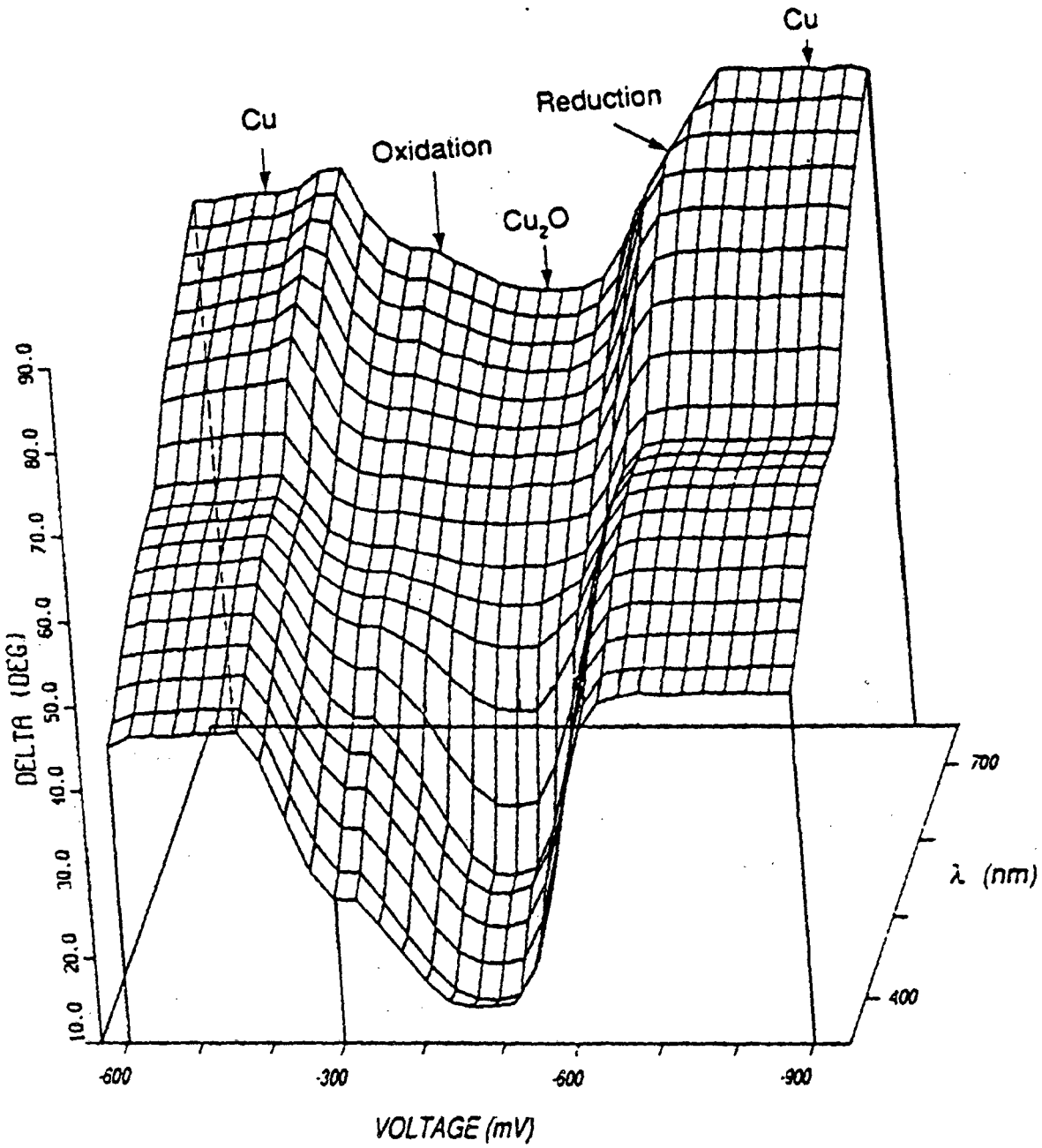

XBL 888-8536

Figure 9-12

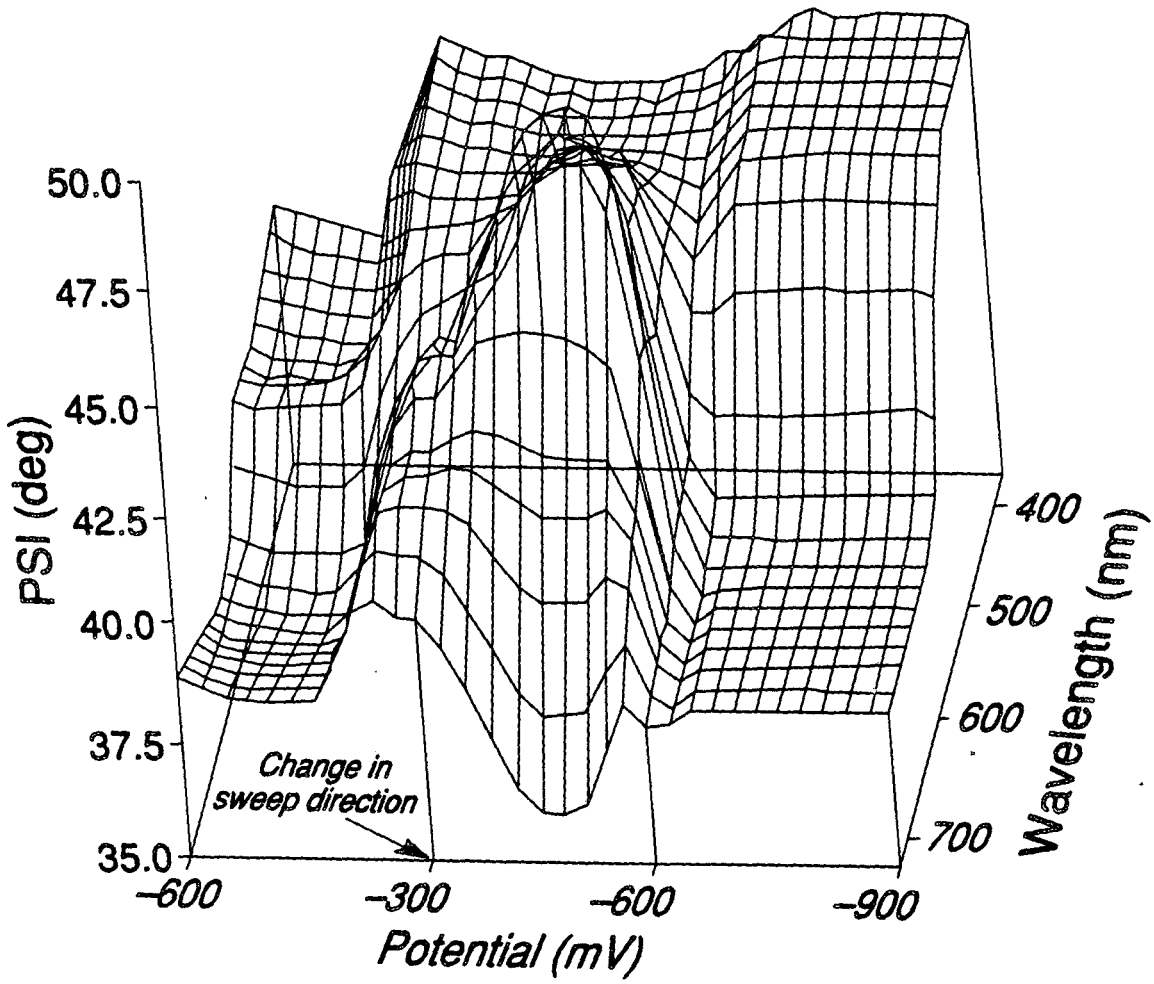

XBL 899-7295

Figure 9-13

POTENTIAL SWEEP ANODIC OXIDATION OF Cu(111)

Measured and Predicted Ellipsometer Parameters

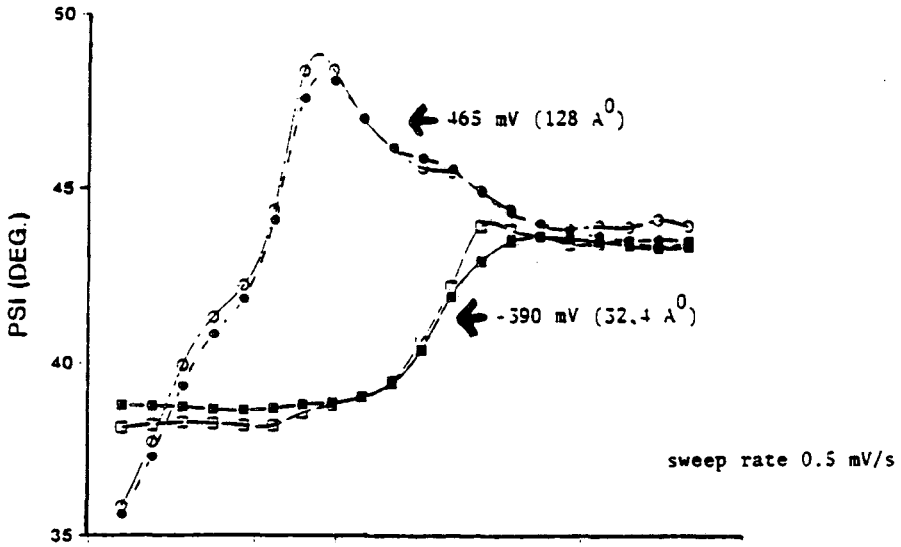

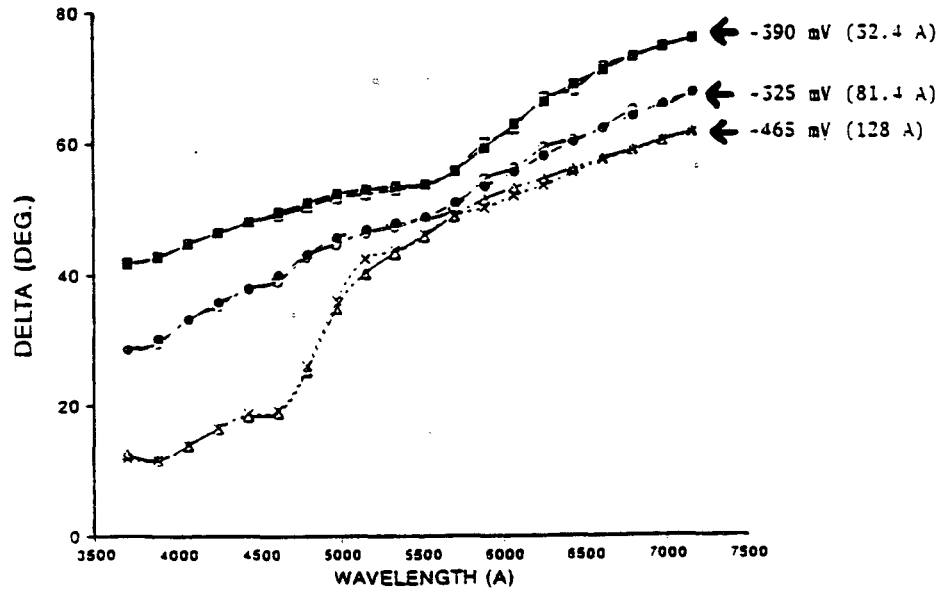

Film thicknesses and optical constants derived by a multi-dimensional optimization of a single-film optical model

XBL 888-3085

Figure 9-14

a)

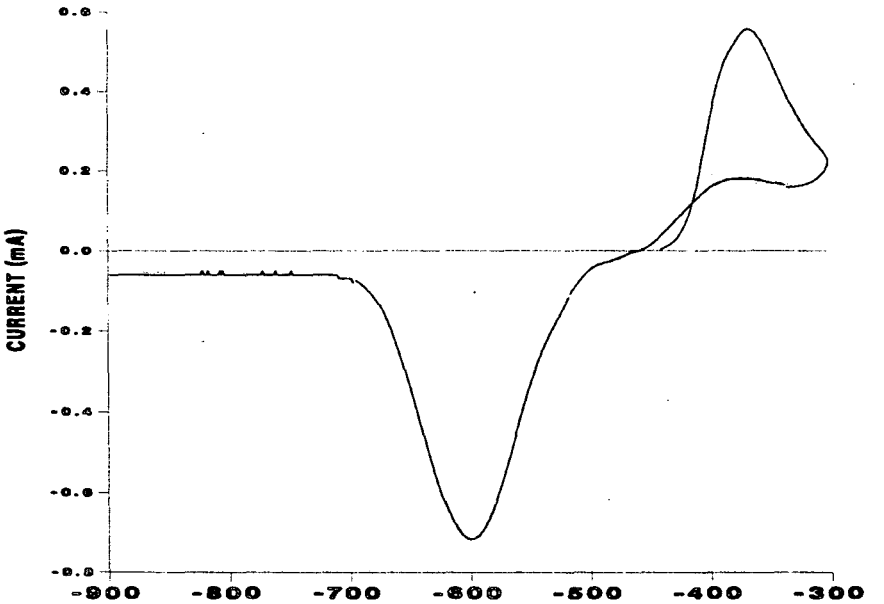

b)

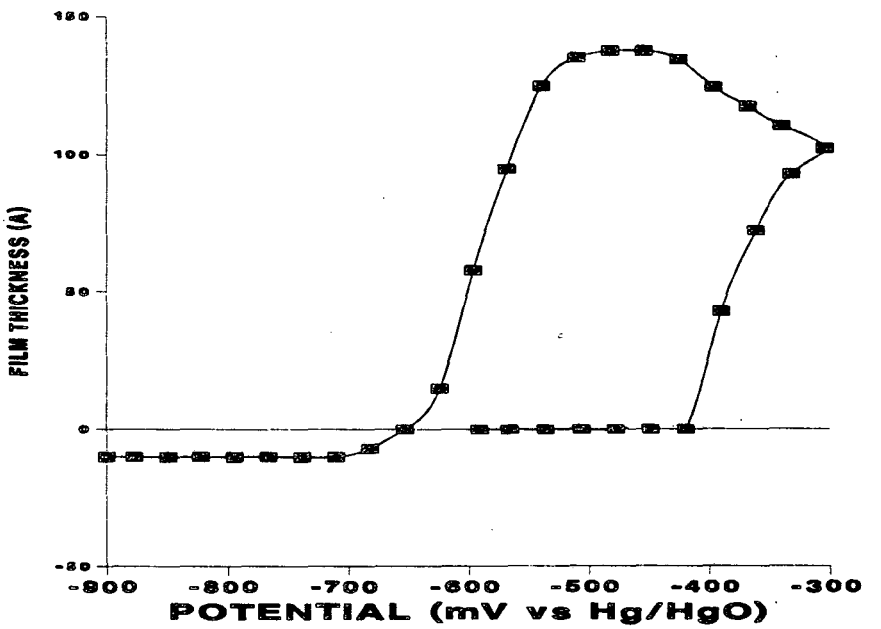

XBL 899-3374

Figure 9-15

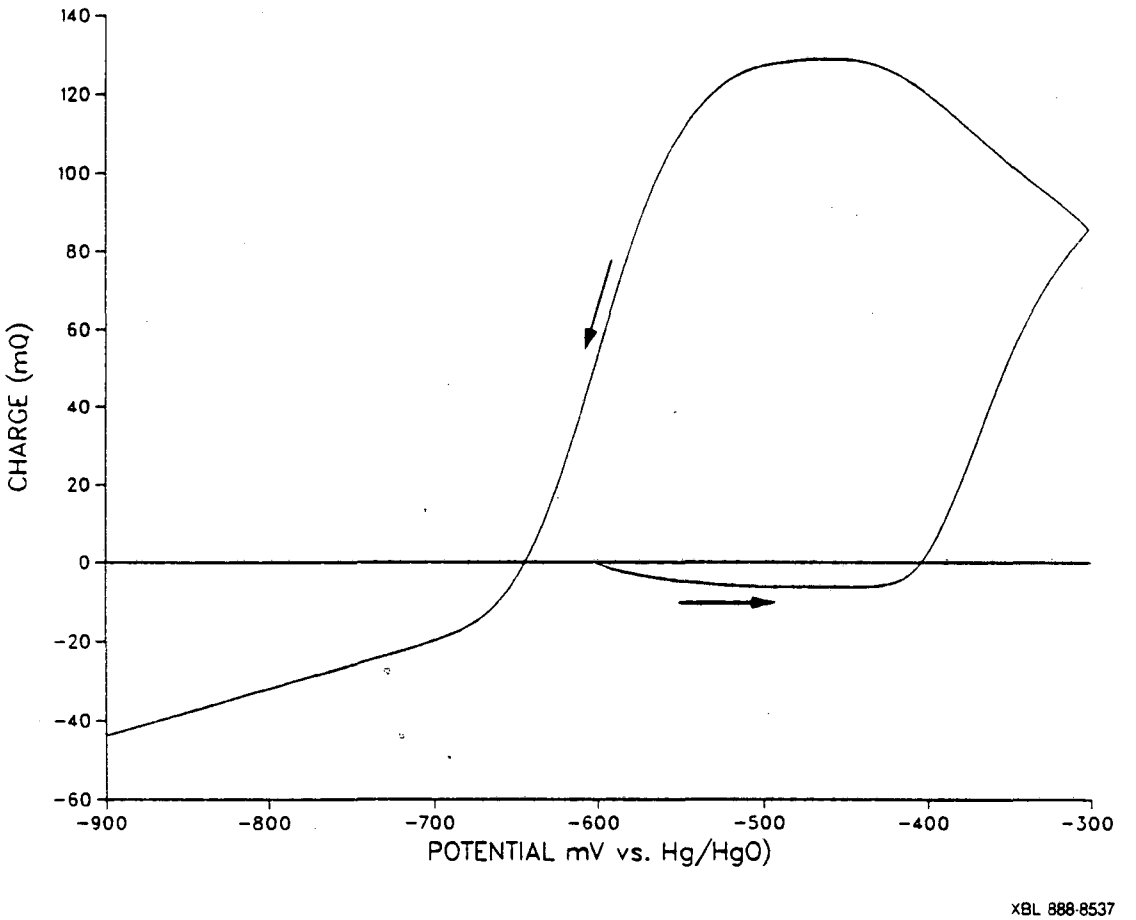
140
120
100
80
60
40
20
0
-20
-40
-60
CHARGE (mQ)
-900
-800
-700
-600
-500
-400
-300
POTENTIAL mV vs. Hg/HgO)
XBL 888-8537

Figure 9-16

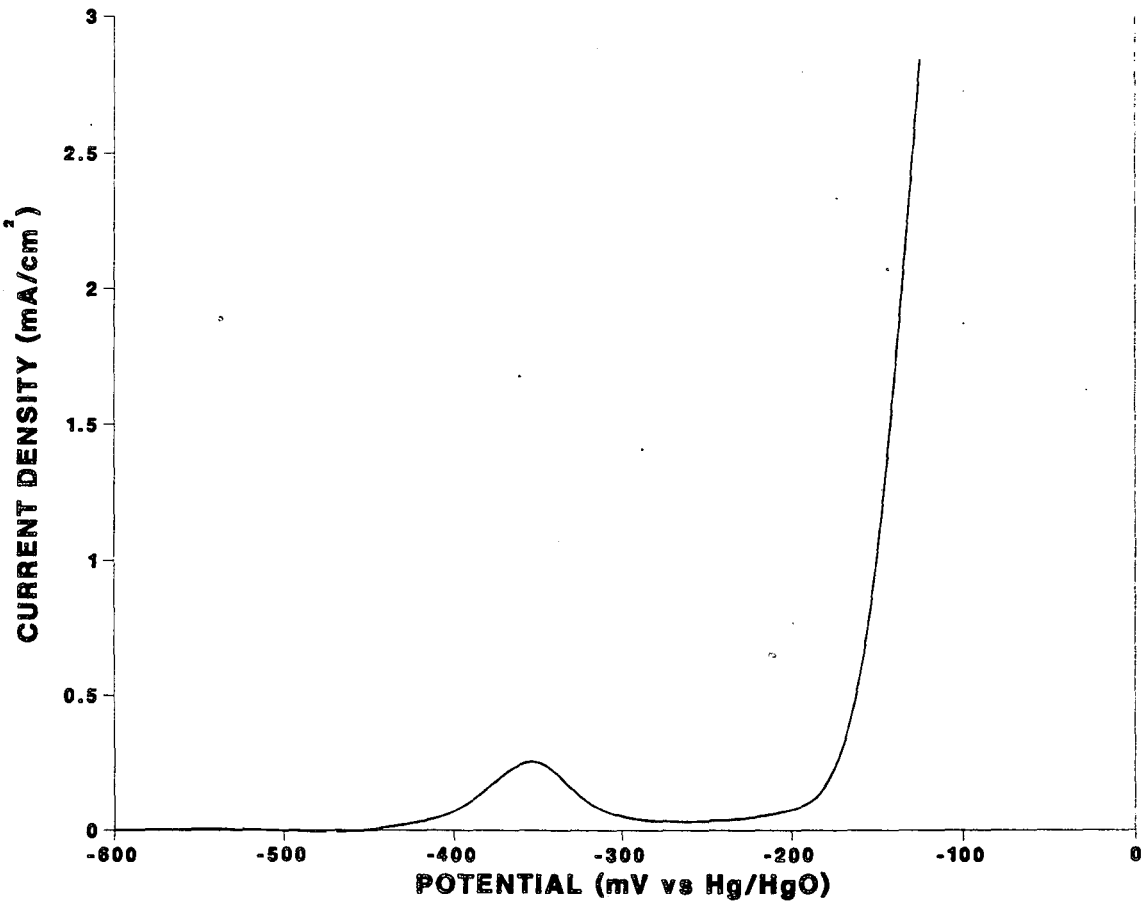

XBL 899-3317

Figure 9-17

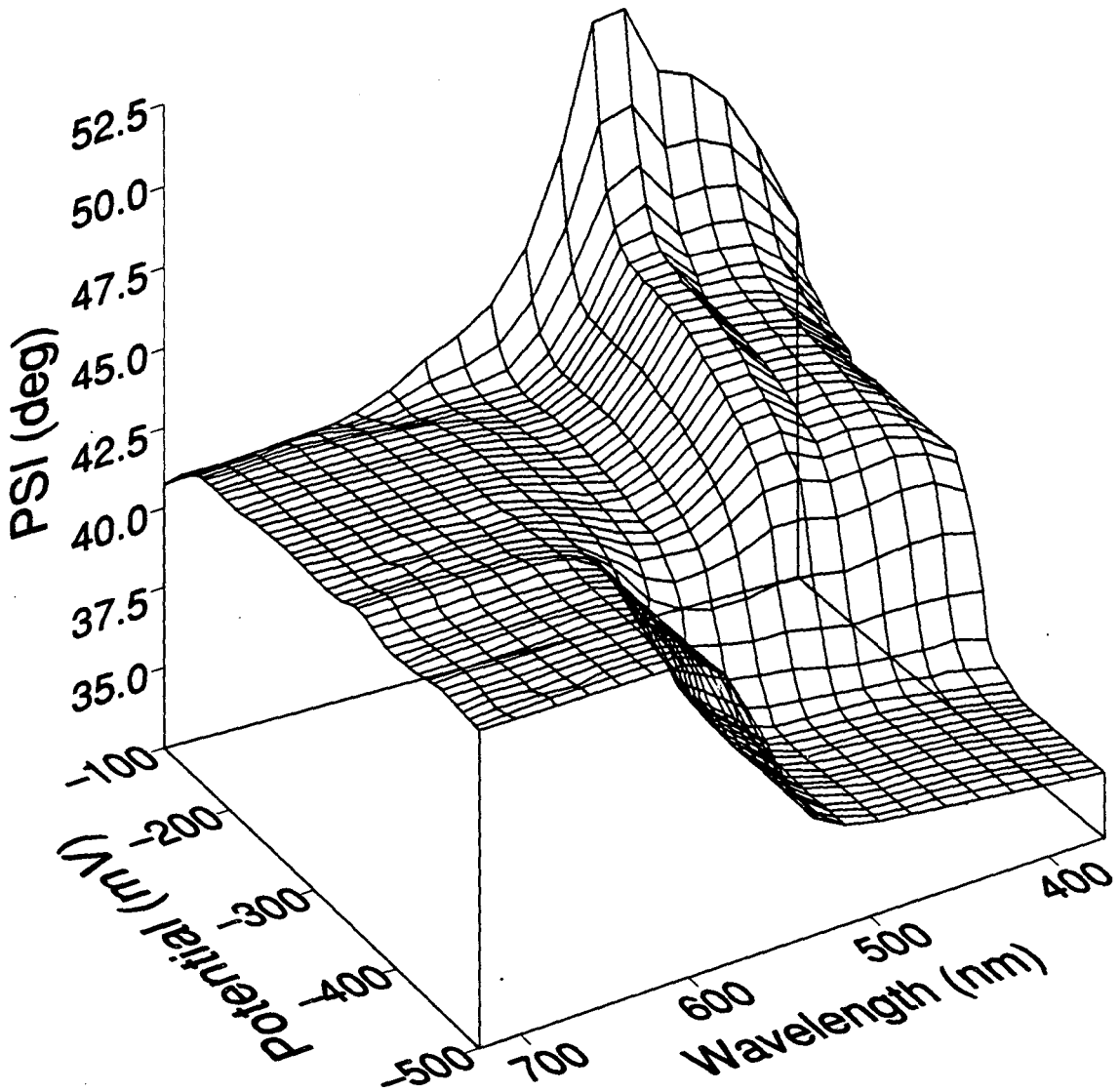

XBL 899-7296

Figure 9-18

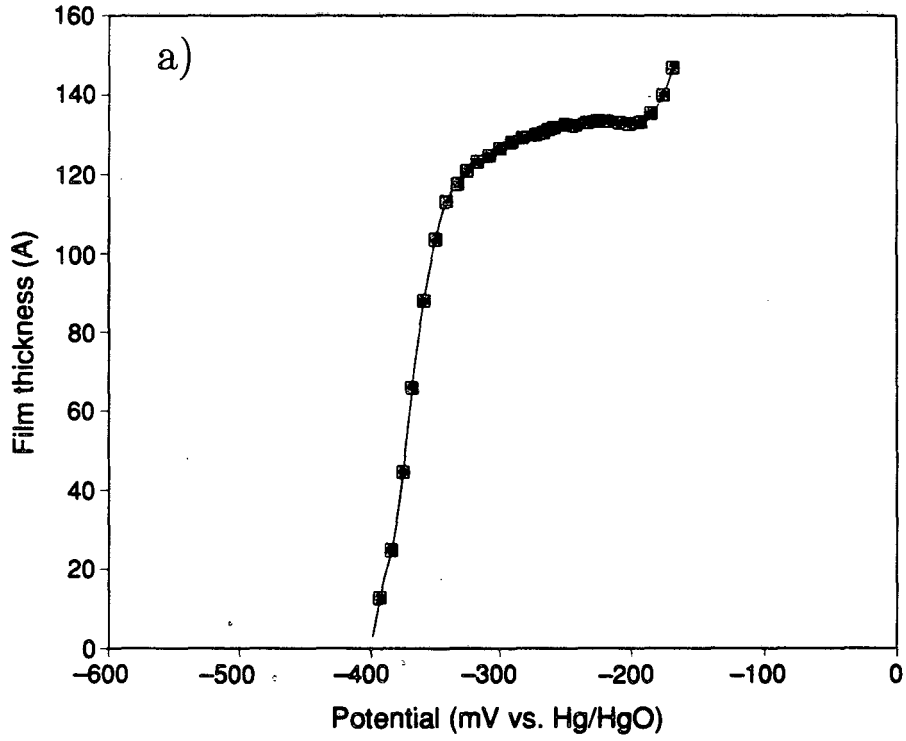

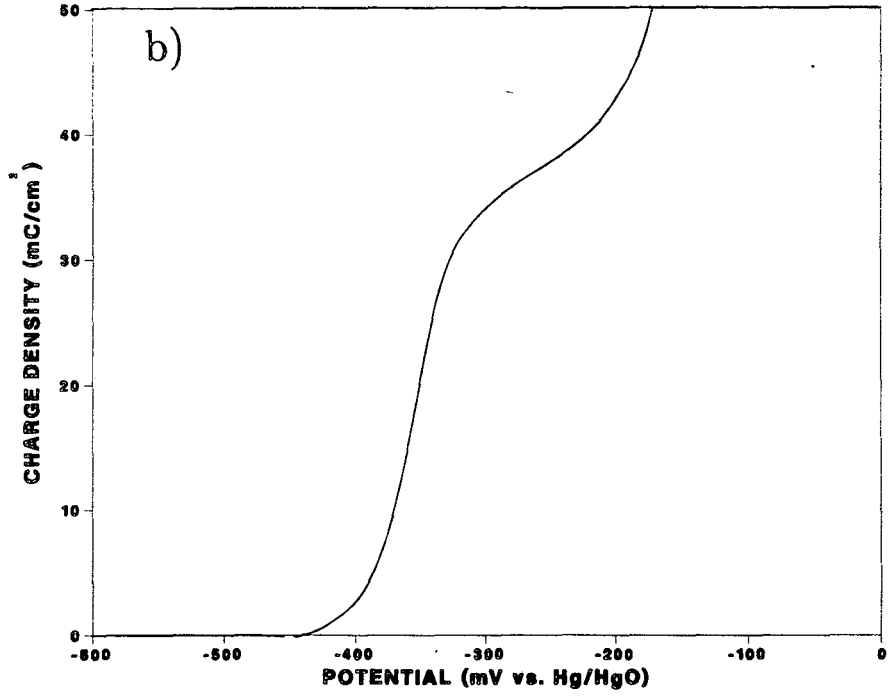

XBL 899-7287

Figure 9-19

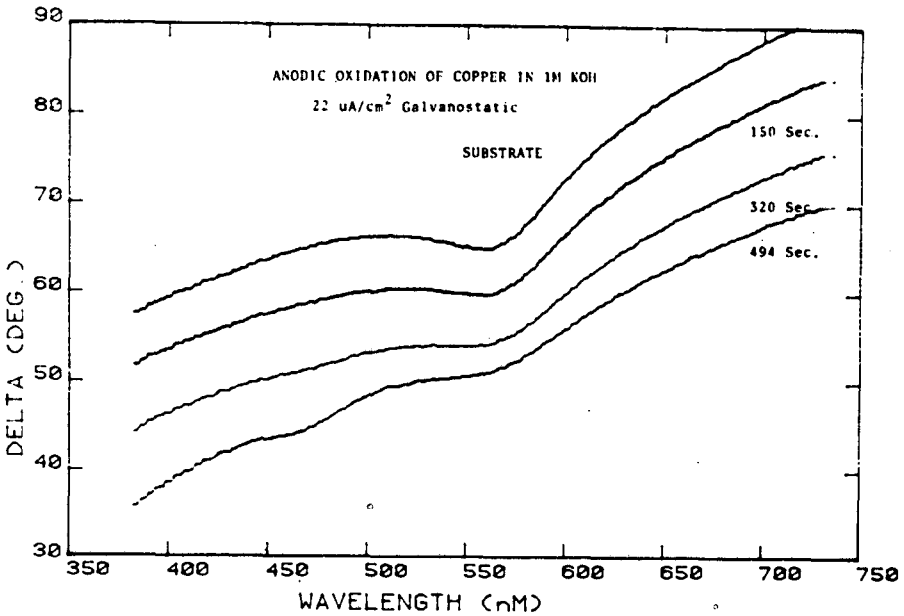

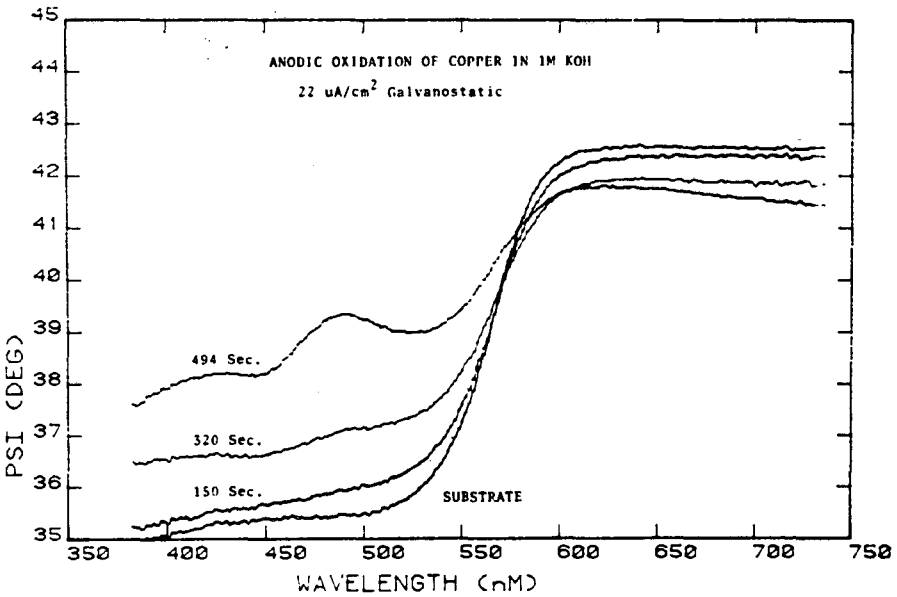

XBL-899-3399

Figure 9-20

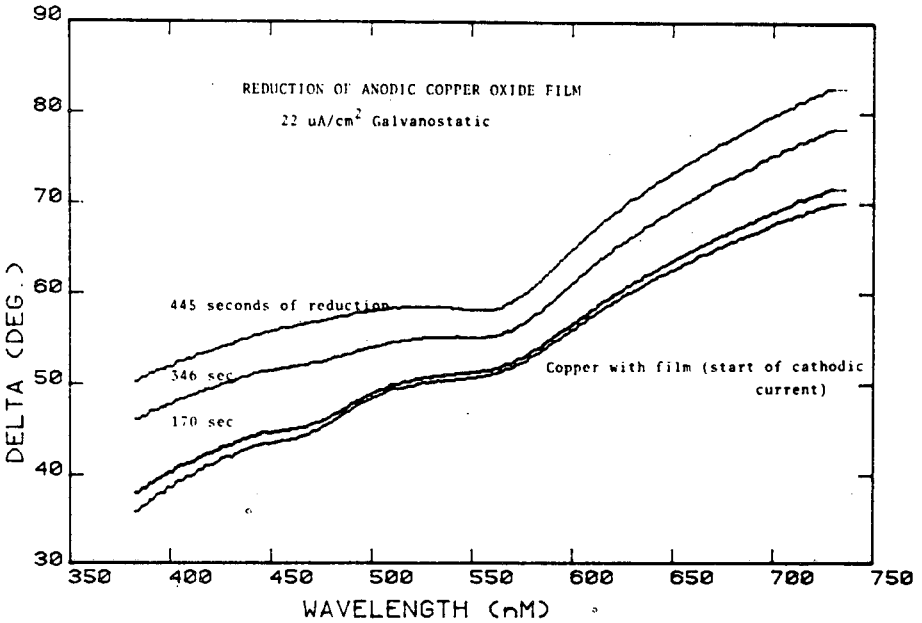

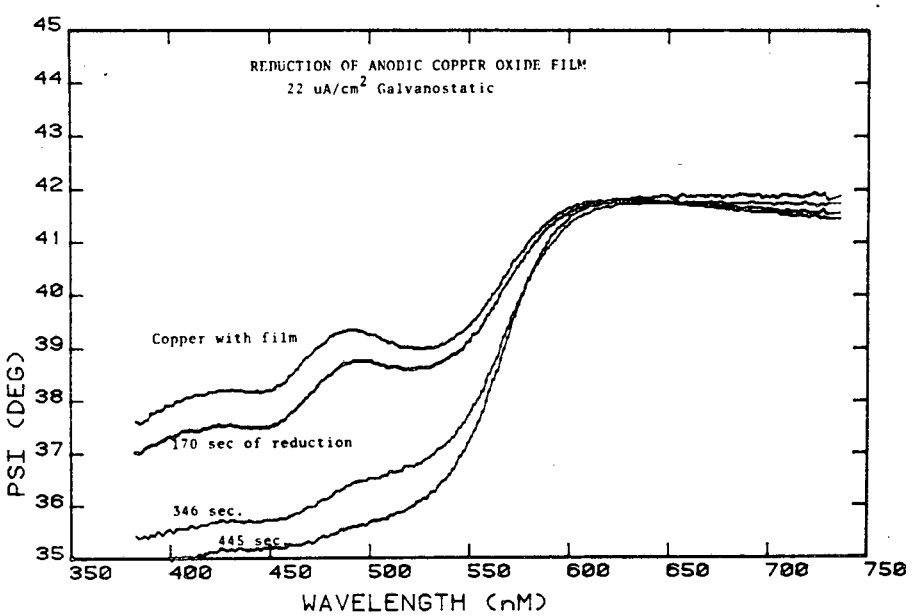

XBL 899-3397

Figure 9-21

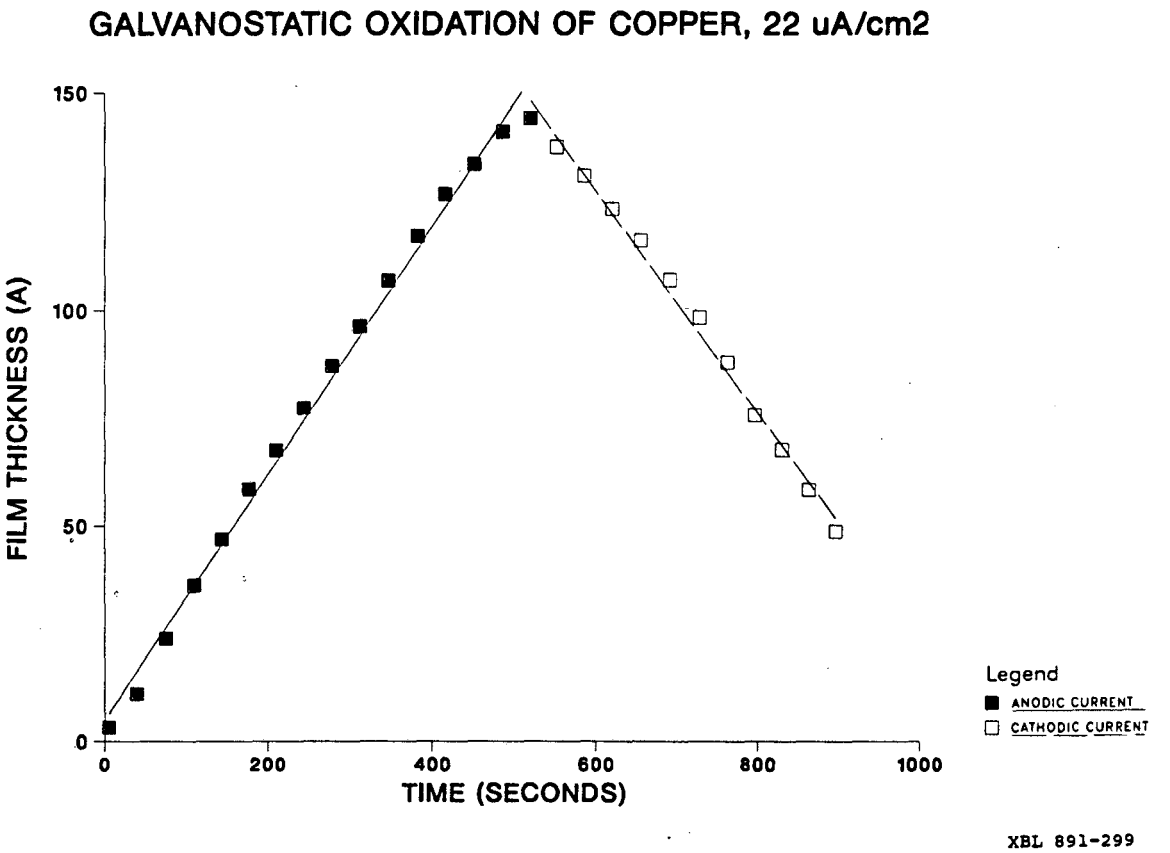
GALVANOSTATIC OXIDATION OF COPPER, 22 uA/cm2
FILM THICKNESS (A)
150
100
50
0
0
200
400
600
800
1000
TIME (SECONDS)
Legend
ANODIC CURRENT
CATHODIC CURRENT
XBL 891-299

Figure 9-22

CUPROUS OXIDE FILM THICKNESS AFTER POTENTIAL STEP

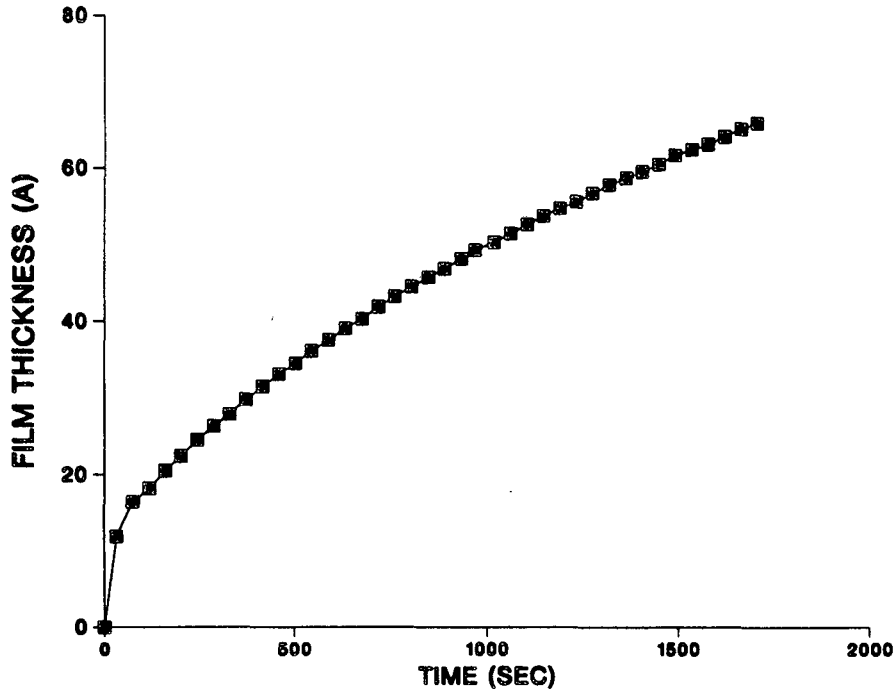

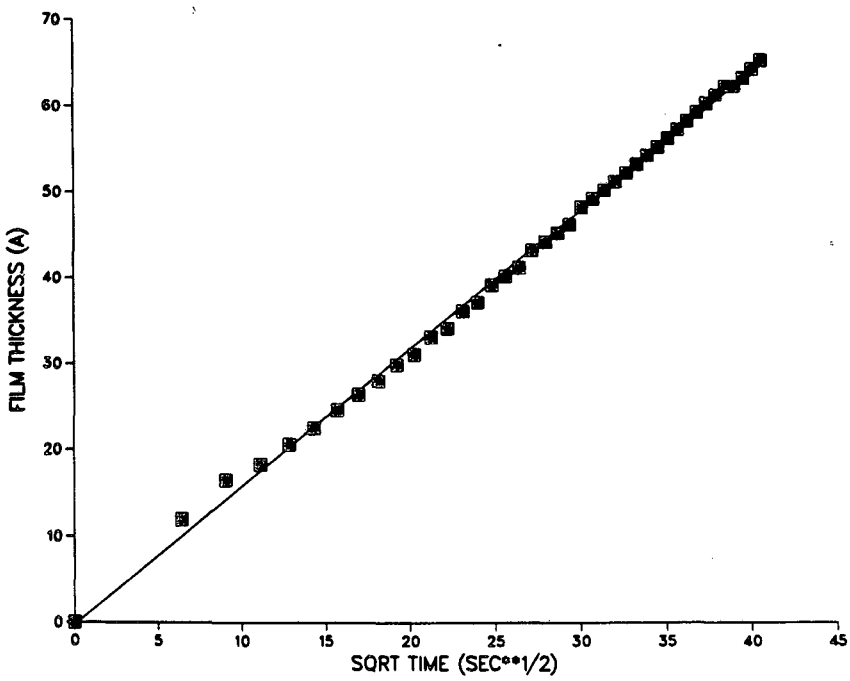

XBL 891-300

Figure 9-23

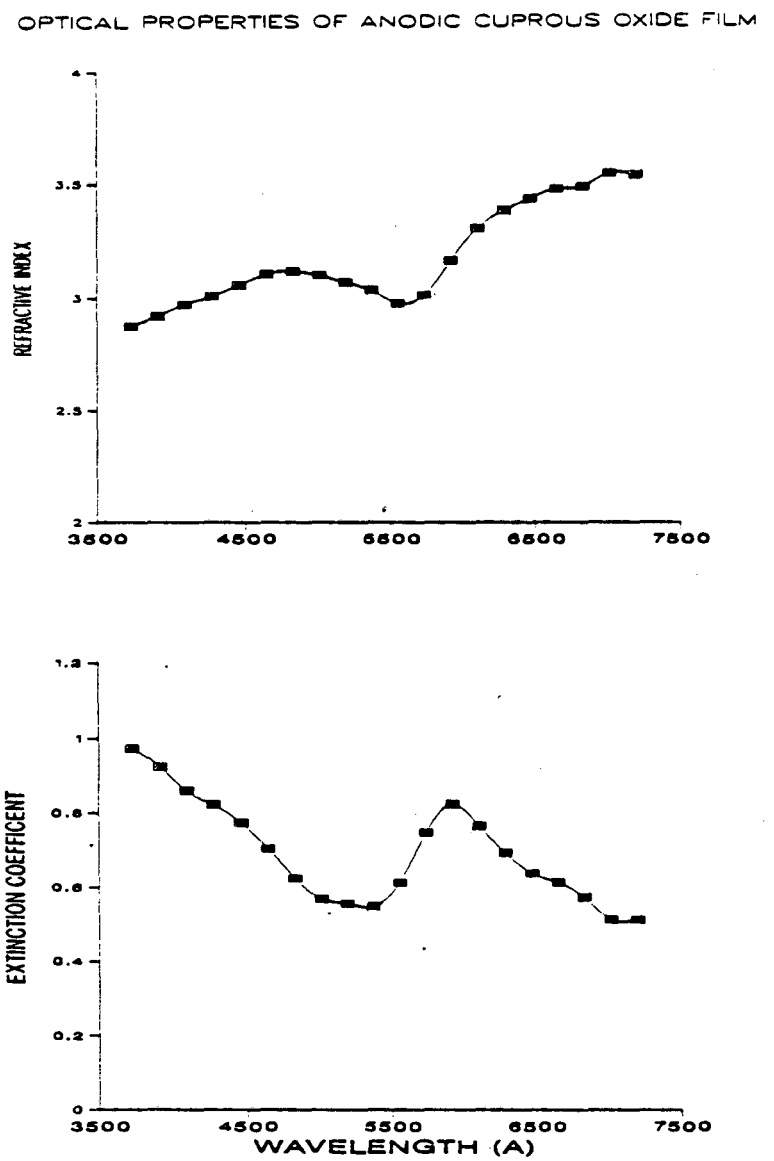

Figure 9-24

XBL 888-3091

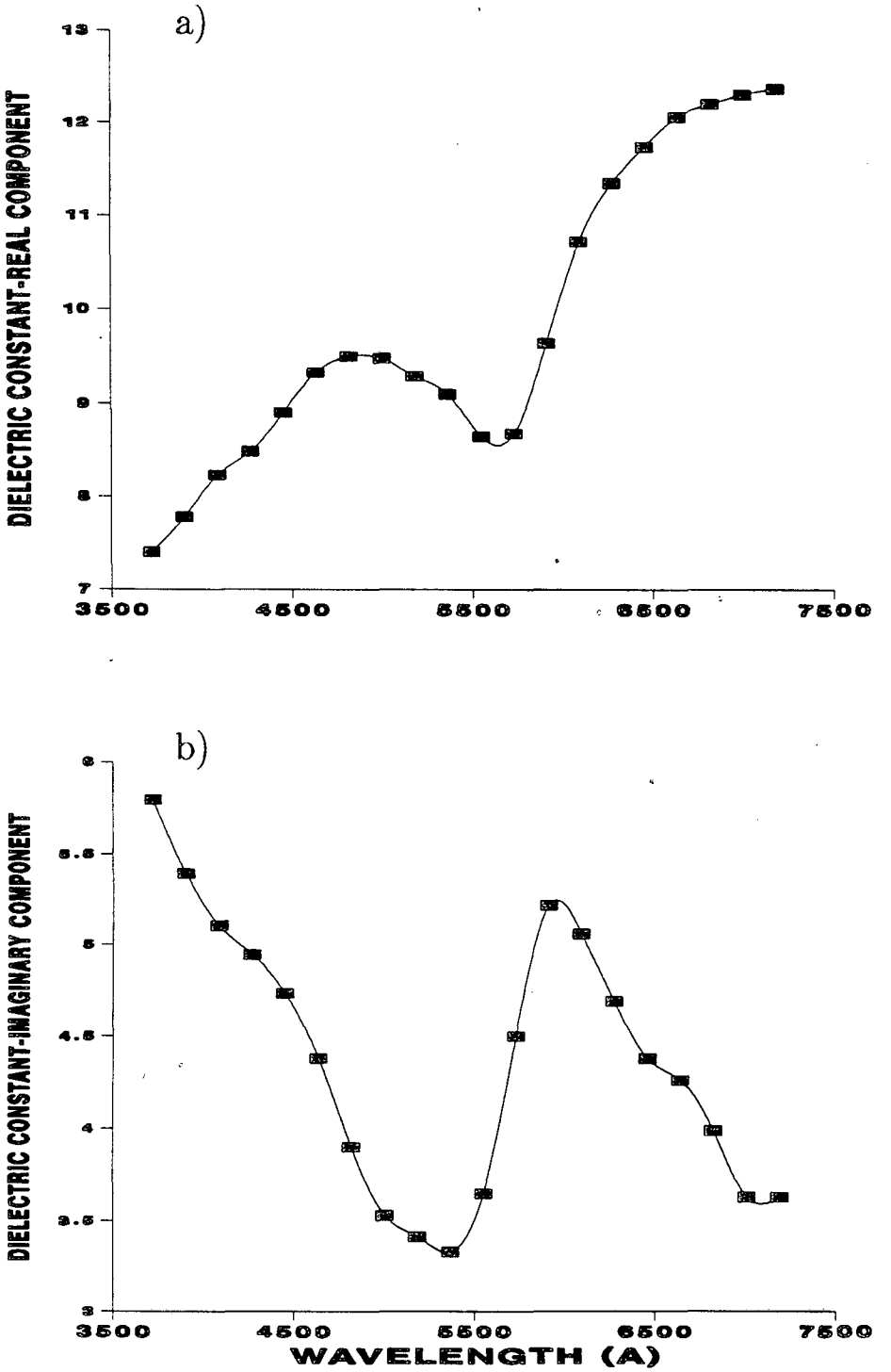

XBL 899-3316

Figure 9-25

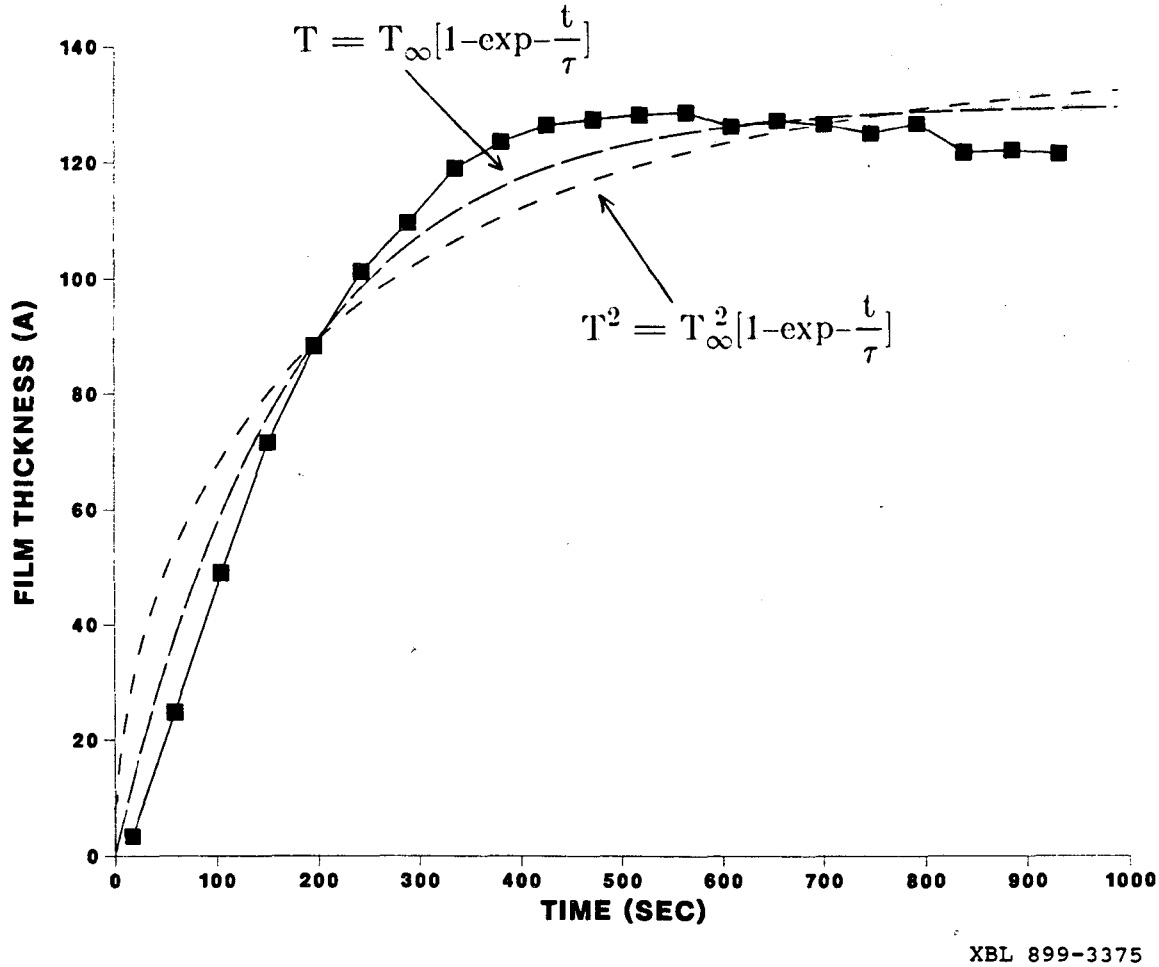
$T = T_\infty[1-\exp-\frac{t}{\tau}]$
$T^2 = T_\infty^2[1-\exp-\frac{t}{\tau}]$
FILM THICKNESS (A)
TIME (SEC)
0
20
40
60
80
100
120
140
0
100
200
300
400
500
600
700
800
900
1000
XBL 899-3375

Figure 9-26

CHAPTER 10

EX SITU MEASURMENTS OF ANODIC FILMS FORMED IN ALKALINE MEDIA

Section 10.1: Introduction

Several *ex situ* measurements of the films formed by anodic oxidation of Ag, Cu, and Zn were performed to complement our *in situ* measurements. These include x-ray diffraction (XRD), scanning electron microscopy (SEM), and scanning tunneling microscopy (STM). For both the x-ray and SEM measurements, the electrode was rinsed in distilled water and placed in a desiccator after having undergone an electrochemical treatment. Preparation of the surfaces for STM study is discussed later.

Section 10.2: Scanning Electron Microscopy of Anodic Films

10.2.1 Introduction

An ISI DS-130 scanning electron microscope was used to examine the morphology of anodic films formed in alkaline media. Because of the relatively large size of our electrodes, we were limited to observations using only the second stage of the instrument. The maximum image magnification that we could obtain using this stage was about 50,000x, though generally we made measurements at a lower magnification.

Microscopists often sputter a thin metal film on surfaces to improve the SEM image. All the surfaces shown are of native metal and/or oxide only. We did not want to introduce any changes in morphology caused by the heating of the surface or the irregular deposition of the metal from the sputterer.

10.2.2 SEM of Silver

Scanning electron micrographs of silver anodized in 1M KOH have been reported before [J1-J4]. We interrupted the anodization process at various times during potential-step experiments to observe changes in the surface-film properties with time.

At low overpotentials or short anodization times, no changes in surface morphology can be observed. At the minimum in the potentiostatic current transient, a large number of small crystals appear to form, but the poor quality of these images makes their interpretation difficult. STM images are more sensitive to surface morphology on this small scale than SEM images (see Section 10.4).

As the oxidation proceeds, the crystals undergo the processes of redistribution and growth, as discussed in earlier chapters. Figure 10-1 shows a surface anodized at 290 mV vs Hg/HgO in 1M KOHfor 285 seconds. Crystals of various sizes are distributed unevenly over the surface. Continued oxidation results in an increase in the coverage of the surface with crystals without a significant change in number density (cf. Figure 10-2, 375 sec at 290 mV). Single-crystal (111) faces of the oxide are also observed. (Note the crystal planes that form at 60° angles.) Crystal coverages are moderate (<20%). The average "secondary" crystal diam-

eter is about 2500 Å, although some smaller crystals (300 Å) can also be seen in regions away from the larger ones. Figures 10-3 and 10-4 are SEM images of a Ag surface anodized by a series of three small potential steps. A very small number of large (secondary) crystals are observed, though many smaller crystals (200 Å) are seen between these larger crystals. Since these crystal appear to form from the primary layer, we refer to them as primary crystals. The surface coverage by small crystals is high.

10.2.3 SEM of Copper

Copper electrodes were removed from the electrolyte at various times and potentials during the oxidation/reduction voltammetry in 1M KOH, and then observed using SEM. During an anodic potential sweep, no discernible surface features can be observed at potentials cathodic of the A2 voltammetry peak. This finding is consistent with our ellipsometry and light-scattering results, which show that the Cu_2O layer is very thin and dissolves at grain boundaries above -350 mV. If the electrode is repeatedly cycled between -1.2 V and 0.6 V, and the potential sweep is then halted around -0.7 to -0.8 V during the cathodic sweep, an *ex situ* Raman spectrum shows the presence of Cu_2O, and SEM photographs indicate that the electrode is rough (RMS roughness about 5000 Å) but that the film is compact (Figure 10-5). Figure 10-6 shows a surface of Cu anodized to -50 mV vs Hg/HgO in 1M KOH using a 1 mV/sec potential sweep. This value coincides with the A2 peak current maximum. A large number of needle-like $Cu(OH)_2$ crystals covers the entire surface. The crystals are perhaps 5 μm in

length but only 600-800 Å in diameter. The finely-matted porous structure of the film makes it particularly well suited for energy storage, as was discussed in Chapter 5. With increasing potential (and charge passed), the voids between the crystals are filled due to crystal growth. This growth is primarily by an increase in the width of the crystals, though some limited continued nucleation does occur.

10.2.4 SEM of Zinc

As was discussed in Section 8.7, the anodic films formed on zinc during active dissolution are primarily ϵ–$Zn(OH)_2$. At higher potentials, only ZnO is observed. Both of these materials are soluble in the electrolyte. Therefore, the solution was rapidly drained from the cell while the surface was held at the anodic potential. We believe that this procedure diminished the rate of film dissolution, thereby enabling us to observe its structure. The solutions used were deoxygenated and saturated with ZnO.

An SEM photograph of zinc anodized at -1.1 V for 50 seconds is shown in Figure 10-7. Is is difficult to know what fraction remains of the total amount of hydroxide originally present on the surface. The $Zn(OH)_2$ film structure is similar to that of $Cu(OH)_2$ formed on Cu electrodes, although the film's surface coverage is significantly lower than that shown in Figure 10-6. Fine needle-like crystals, whose average diameter is about 800 Å and average length is about 8000 Å, are formed. Unlike the $Cu(OH)_2$ layer, the ϵ–$Zn(OH)_2$ crystals branch more often. Futhermore, these crystals tend to be found in bunches rather than in a uniform

distribution.

SEM photographs of passive films on zinc show that the needle-like $Zn(OH)_2$ crystals are no longer present. Rather, a layer of nonporous ZnO is observed (Figures 10-8 and 10-9). Regions of the surface are clearly etched. The etched pits form both in a direction normal to the (1110) surface and at another indeterminate direction.

Section 10.3: X-Ray Diffraction Measurements of Anodic Films

10.3.1 Introduction

The Siemens D500 x-ray diffractometer used in this study has a maximum resolution of greater than 0.01°. However, the major factor limiting the use of x-ray diffraction to study thin films is the small signal involved. By using a beam that strikes the surface at a grazing angle, the diffracted intensity from a thin film can be increased greatly [J5]. Unfortunately, the Siemens D500 instrument does not have grazing-angle measurement capabilities. Therefore, simple θ-2θ measurements were made using large integration times (usually 20 sec/point). Typically, scans were made over a range of about 30° and at a resolution of 0.1°. (Total time for the measurement was 1 hr 40 min.).

10.3.2 XRD of Copper

X-ray diffraction measurements of copper films were undertaken to help verify the results obtained by Raman spectroscopy and ellipsometry. At potentials between -450 and -200 mV, XRD data show a small peak at 29.54° and a much

larger one at 36.45° (Figure 10-10). These values should be compared to the XRD spectrum of Cu_2O powder (Figure 10-11), and they indicate that only Cu_2O is present on the surface in this potential range.

At potentials near and above the A2 voltammetry peak, the XRD spectrum shows peaks at 16.74°, 23.80°, 34.04°, and 39.81°, in addition to those due to the presence of Cu_2O (Figure 10-12). These peaks are associated with a $Cu(OH)_2$ film [n.b., powder diffraction pattern of $Cu(OH)_2$, Figure 10-11]. The XRD hydroxide peaks are much smaller than those from the cuprous oxide layer, but we attribute this difference largely to the inherently lower scattering intensity of the hydroxide (see Figure 10-11). The peak at around 21–22° in Figure 10-12 is associated with the copper substrate. In all of our other copper XRD spectra, XRD scattering from the substrate was removed by subtracting out a pattern obtained from the polished metal.

We have suggested that, at long times and at potentials anodic of the A2 peak, the Cu_2O film might react to form CuO (see Section 8.6.4.2). To confirm this hypothesis an XRD spectrum of a surface held at 0.6 V for 1 hr was taken (Figure 10-13). Though the signal is weak, several peaks can be identified. In agreement with our Raman results, Cu_2O is not present, and peaks associated with both $Cu(OH)_2$ and CuO (32.60°, 35.52°, and 38.17°) are observed. The rise in intensity at the far end of the spectrum is associated with the leading edge of the copper metal peak located at 43.30°.

10.3.3 XRD of Zinc

Raman spectra of the film formed on zinc indicate that, while bands associated with the presence of ZnO are present, the relative sizes of these bands are different from those of powdered ZnO (see Section 8.7.1). A Zn electrode was anodized via a 1 mV/sec potential sweep out to -0.4 V and held at this potential while the electrolyte was removed from the cell (to minimize the dissolution of the layer). Afterwards, the electrode was rinsed in distilled water. The XRD spectrum of the electrode shows all the characteristic peaks associated with both Zn metal and ZnO (Figure 10-14A). The XRD spectrum of ZnO powder is shown for comparison (Figure 10-14B). We therefore conclude that, while the relative intensities of the ZnO-film Raman peaks are different from those of the ZnO powder, on a global scale the film is ZnO. The effect of an oxygen deficiency in the ZnO crystal on Raman-band peak sizes needs to be examined in more detail. This information could lead to a better understanding of the nature of the ZnO layer and the associated changes that occur in the film during the anodic process.

Section 10.4: Scanning Tunneling Microscopy of Ag_2O Nucleation

A Digital Instruments, Inc., Nanoscope 1 scanning tunneling microscope has been used to study the deposition of Pb on Ag by this author before [J6]. Here we discuss STM observations of the anodic film formation on Ag in 1M KOH. The objective of this work was to examine the nucleation and growth of Ag_2O at sizes (early times) that are not accessible to SEM.

Attempts to use STM as an *in situ* technique for this system turn out to be difficult. The bias of the scanning tunneling microscope tip was set to -100 mV with respect to the surface. During anodization at potentials where the primary layer forms, the surface features observed at a lower potential are lost, and the surface profile becomes very flat. It is uncertain whether this observation is associated with (1) the growth of the primary layer, (2) an effect of dissolved silver species on the tunneling probe, (3) the limited conductivity of the layer while it is in an electrolytic solution, or (4) a combination of these factors. Further work is needed to discriminate the processes occuring before any *in situ* results can be reported for this system.

The scanning tunneling microscope with a 6.0-μm scanner was interfaced with an AST personal computer (IBM PC clone). Both digital-to-analog (x/y position control) and analog-to-digital (z height data) converter were employed. A 320x200-point array was used to store the data. Details of the hardware and software will be published in the near future [J7].

Smooth silver surfaces were prepared by sputtering silver (VCR Group, Inc., Model 705/TM170s) onto a freshly cleaved mica substrate. Approximately 3000 Å of metal was sputtered onto the mica surface. The film layer was totally reflecting, and the resistivity of the layer was small. Several samples were made from a single mica sheet by cutting it into many smaller sections. (Each sample was approximately 1 cm x 3 cm.) This procedure minimized the differences in metal film thickness and in the level of contamination between sputtered samples. The samples were then placed in 1M KOH and anodized at 290 mV vs

Hg/HgO in 1M KOH for different times. After the anodization was completed, the sample was quickly removed from the solution and carefully rinsed with distilled water before being examined by the scanning tunneling microscope

Figure 10-15 shows the current transient of the silver/mica sample anodized for 120 seconds. Points corresponding to times at which other samples were removed from the solution are indicated in the figure (and should be compared with the STM line drawing shown in Figure 10-14). The current transient is similar to that reported before and shows a typical current minimum and maximum associated with the nucleation and growth of the crystalline Ag_2O layer (see Section 9.2 and References J3 and J4). The change in shape of the curve beyond the current maximum (i.e., at times greater than 80 sec) may be due to the limited supply of silver in the sputtered metal film. The oxide crystals are approximately equivalent in size to the initial metal film thickness at these times (cf. Figure 10-16F).

The initial substrate is flat to within 100 Å over a distance of one micron (Figure 10-16A). A change in the height of the film on the right of the image is most likely due to the termination of a plane in the underlying mica substrate.

At early anodization times (Figures 10-16B and 10-16C), the film remains fairly flat, although a large number of small "ripples" appear on the surface. Further oxidation results in the formation of a large number of small crystals (Figure 10-16D) whose size increases but whose number density decreases with time (Figures 10-16E and 10-16F). We estimate the number density at 75 sec to be 5.7×10^9 cm^{-2} and at 120 sec to be 2.8×10^8 cm^{-2}. These values compare very

favorably with those previously derived from ellipsometric and SEM measurements [J3,J4].

The amplitude-density function (ADF)† of the images shown in Figures 10-16A through 10-16F are given in Figures 10-17A through 10-17F. The initial very sharp peak of the ADF widens slightly as the primary layer is formed. This is not surprising, since small variations in the local growth rate of the layer should be expected. Coincident with secondary-layer film nucleation, the ADF becomes bimodal. A small, very broad peak is observed under a sharper, larger peak (Figures 10-17E and 10-17F). The small, broad component of the ADF is most likely due to the large variations in height introduced by the secondary crystals, which cover only a fraction of the total surface. The sharp peak is associated with the still relatively smooth regions between the crystals.

Calculations of the autocorrelation functions (ACF, see section 7.6) from the STM data are shown in Figure 10-18. The value of the ACF at zero shift lag distance (i.e., at x origin) is equal to the square of the RMS roughness. For random surfaces like those studied here, the correlation length is a useful parameter to quantify the distance over which surface features (eg. crystal formation) are related though processes that occured during their formation.

The correlation length is generally defined as the lag distance at which the ACF falls to e^{-1} of its zero shifted value. The initial substrate has an RMS roughness of around 35 Å and a correlation length of about 4000 Å. These values

† The amplitude density function is defined as the relative frequency that a particular height value is found in a given profile.

are characteristic of a surface which is extremly smooth. The average change in surface height varies by only a few monolayers in thickness over a distance of approximatley the wavelength of light. Another way of describing the extreme smoothness of the surface is to note that the magnitude of the height variations is only one percent of the correlation length.

Initially, as the surface is anodized, the RMS roughness increases slightly and the correlation length decreases (0 to 30 seconds). Further oxidation leads to an increase in the roughness with little change in the correlation length (30 to 45 sec). At the time where 3-dimensional nucleation has been reported to occur before [J3, J4], the correlation length decreases dramatically (n.b. 60 sec). Beyond the time for nucleation the correlation length does not change significantly, but the RMS roughness does decreases after 75 seconds.

This interesting behavior can be understood in terms of our primary layer/nucleation/Ostwald ripening hypothesis and the discussion of the relation between RMS roughness, particle size, and number density (see Section 7.6). As the primary layer forms, small lateral variations in the film growth rate cause the surface to roughen slightly. This causes the correlation length to decrease and the roughness to increases. Not surprisingly, the correlation length of primary layer film growth is shorter than that of the Ag sputtering process.

Further primary layer growth (30 to 60 seconds) causes an increase in RMS roughness with little change in the correlation length. The formation of small nuclei from the primary "seed" layer may occur as the layer becomes unstable to further planar growth. If we assume that the primary layer's roughness is of the

same order of magnitude as its thickness, the film should start to nucleate (i.e., exhibit 3-dimensional growth via diffusion from the solution) sometime after the average thickness is about 7 times the critical nucletion radius (see Section 4.6 and 4.7). After nucleation occurs the diffusion fields for crystal growth can overlap. During this phase of crystal growth, the roughness and correlation length should increase due to Ostwald ripening (e.g. after 60 seconds). As the remaining crystals grow they eventually will tend to decrease the surface roughness (c.f. Figures 7-28 and 7-29). This may account for the smaller roughness of image 10-16F vs 10-16E.

Section 10.5: Conclusions

Several *ex situ* measurements of the films formed by anodic oxidation of Ag, Cu, and Zn have been discussed. SEM photographs of anodized silver support our primary layer/nucleation/Ostwald rippening hypothesis for this system. The crystals formed under the conditions of this study preferentially show (111) index planes. A large number of small crystals appear to form from the primary layer ("primary crystals"). Our SEM data shows that anodically formed cuprous oxide exists as a compact film but that $Cu(OH)_2$ is formed as a highly porous film consisting of needle-like crystals. $Zn(OH)_2$, which is formed at active potential on Zn in alkaline media, also exhibits a needle-like crystaline structure. The passive ZnO layer is compact. Regions where the Zn single crystal electrode is etched are clearly observed.

Ex situ X-ray diffraction measurements have confirmed our *in situ* Raman finding that cuprous oxide film formation is followed by the formation of a thermodynamically less stable $Cu(OH)_2$ layer. Some evidence has been presented which suggests that the compact Cu_2O film may be converted to CuO at higher potentials. Our Zn X-ray data confirms our Raman finding that ZnO is the most prevalent surface species on the passive Zn electrode. Also, we have shown that ϵ–$Zn(OH)_2$ scatters light primarily by fluorescence.

STM measurement of anodized silver in alkaline media support our nucleation and growth model for the silver system. Analysis of STM data using amplitude sensitive (ADF) and wavelength sensitive (ACF) parameters are shown to be useful in interpreting digitized STM images.

REFERENCES FOR CHAPTER 10

J1) Briggs, G. W. D., M. Fleischmann, D. J. Law, and H. R. Thirsk, Trans. Faraday Soc. **64,** 3120 (1968).

J2) Smith, C. G., Ph. D. Thesis, Dept. of Chemical Engineering, University of California at Berkeley, August 1978. Lawrence Berkeley Laboratory Report LBL-8082.

J3) Mayer, S. T., and R. H. Muller, J. Electrochem. Soc. **135,** 2133 (1988).

J4) Mayer, Steve T., M. S. Thesis, Dept. of Chemical Engineering, University of California at Berkeley, December 1985. Lawrence Berkeley Laboratory Report LBL-20502.

J5) Cullity, B. D., **Elements of X-ray Diffraction**, 2nd edition, Addison-Wesley, Menlo Park, CA, 1981.

J6) Mayer, S. T., R. H. Muller, and P. N. Ross, ***In Situ* Scanning Tunneling Microscopy of Multilayer Pb Electrodeposits on Ag**, Lawrence Berkeley Laboratory Report LBL-26454.

J7) Armstrong, Michael, Ph.D. Thesis, Dept. of Chemical Engineering, University of California at Berkeley. To be published by Lawerence Berkeley Laboratory.

FIGURE CAPTIONS FOR CHAPTER 10

Figure 10-1. Scanning electron micrograph of a silver (111) surface anodized at 290 mV vs. Hg/HgO in 1M KOH for 285 seconds. Bar at bottom center equal to 943 nm in length.

Figure 10-2. Scanning electron micrograph of a silver (111) surface anodized at 290 mV vs. Hg/HgO in 1M KOH for 285 seconds. Bar at bottom center equal to 283 nm in length.

Figure 10-3. Scanning electron micrograph of a silver surface anodized by a series of three potential pulses. The first two potential pulses were for 10 minutes (50 mV to 290 mV and 290 to 310 mV). A third potential pulse from 310 to 330 mV was applied for approximately 3 minutes. Total charge passed was 41.7 mC/cm^2. Bar at bottom center is equal to 272 nm in length.

Figure 10-4. Scanning electron micrograph of a Ag surface anodized as described for Figure 10-3. Bar at bottom center is equal to 182 nm in length.

Figure 10-5. Scanning electron micrograph of a copper surface following oxidation and then reduction of the surface layers by a potential sweep of 1/2 mV/sec in 1M KOH. Maximum anodic potential 500 mV vs Hg/HgO in 1M KOH. Cathodic potential sweep halted at -750 mV (near the end of the major cathodic reduction process). Bar at bottom

center is equal to 518 nm in length.

Figure 10-6. Scanning electron micrograph of a copper surface oxidized in 1M KOH by a 1/2 mV/sec potential sweep. Maximum anodic potential 100 mV vs Hg/HgO in 1M KOH. Bar at bottom center is equal to 6.45 μm in length and corresponding to left half of figure. Area inside white box in left shown in detail in right half of the figure (blown up 10 time).

Figure 10-7. Scanning electron micrograph of Zinc (1000) surface anodized at -1.1 V vs Hg/HgO in 1M KOH for 50 sec (an active potential). Bar at bottom center is equal to 870 nm in length.

Figure 10-8. Scanning electron micrograph of Zinc (1000) surface anodized at -0.8 V V vs Hg/HgO in 1M KOH for 4 min (a passive potential). Bar at bottom center is equal to 85.5 μm in length.

Figure 10-9. Scanning electron micrograph of Zinc (1000) anodized as in Figure 10-8. Bar at bottom center is equal to 6.06 μm and corresponds to the left half of the figure. Area within white box is blown up 10x in right half of figure.

Figure 10-10. X-ray diffraction spectrum of copper anodized in 1M KOH by a 1/2 mV/sec potential sweep to a peak potential of -250 mV.

Figure 10-11. X-ray diffraction spectrum of Cu_2O and $Cu(OH)_2$ powders.

Intensity of scattering form the largest peak of Cu_{2O} is 7.5 time greater than that of $Cu(OH)_2$ in the spectral range observed.

Figure 10-12. X-ray diffraction spectrum of copper anodized in 1M KOH by a 1/2 mV/sec potential sweep to a peak potential of 100 mV vs Hg/HgO in 1M KOH.

Figure 10-13. X-ray diffraction spectrum of copper anodized in 1M KOH by a 1/2 mV/sec potential sweep to a peak potential of 600 mV vs Hg/HgO in 1M KOH. The potential was then held at this value for 1 hr. Solid lines -$Cu(OH)_2$. Dashed lines -- CuO.

Figure 10-13. X-ray diffraction spectrum of copper anodized in 1M KOH by a 1/2 mV/sec potential sweep to a peak potential of 600 mV vs Hg/HgO in 1M KOH. The potential was then held at this value for 1 hr.

Figure 10-14. A) X-ray diffraction spectrum of zinc anodized in 1M KOH by a 1 mV/sec potential sweep to a peak potential of -400 mV vs Hg/HgO in 1M KOH. The potential was held at this value as the electrolyte was removed. B) X-ray diffraction spectrum of ZnO powder.

Figure 10-15. Current transient following a potential step of a Ag thin film sputtered on mica in 1M KOH to 290 mV vs Hg/HgO in 1M KOH. Points corresponding to times at which other samples were removed from the solution for ex *ex situ* STM study are indicated and correspond to the

images shown in Figure 10-16.

Figure 10-16. Scanning tunneling micrographs of sputtered Ag oxidized in 1M KOH for various lengths of times at 290 mV vs Hg/HgO in 1M KOH. Scale for all images and for all three dimensions shown on top of figure..

Figure 10-17. Amplitude density functions (ADF) of the STM images shown in Figure 10-16 and oxidized at times corresponding to Figure 10-15. B) 30 sec. C) 45 sec. D) 60 sec. E. 75 sec. F) 120 sec.

Figure 10-18. Autocorrelation Function (ACF) of the STM images shown in Figure 10-16.

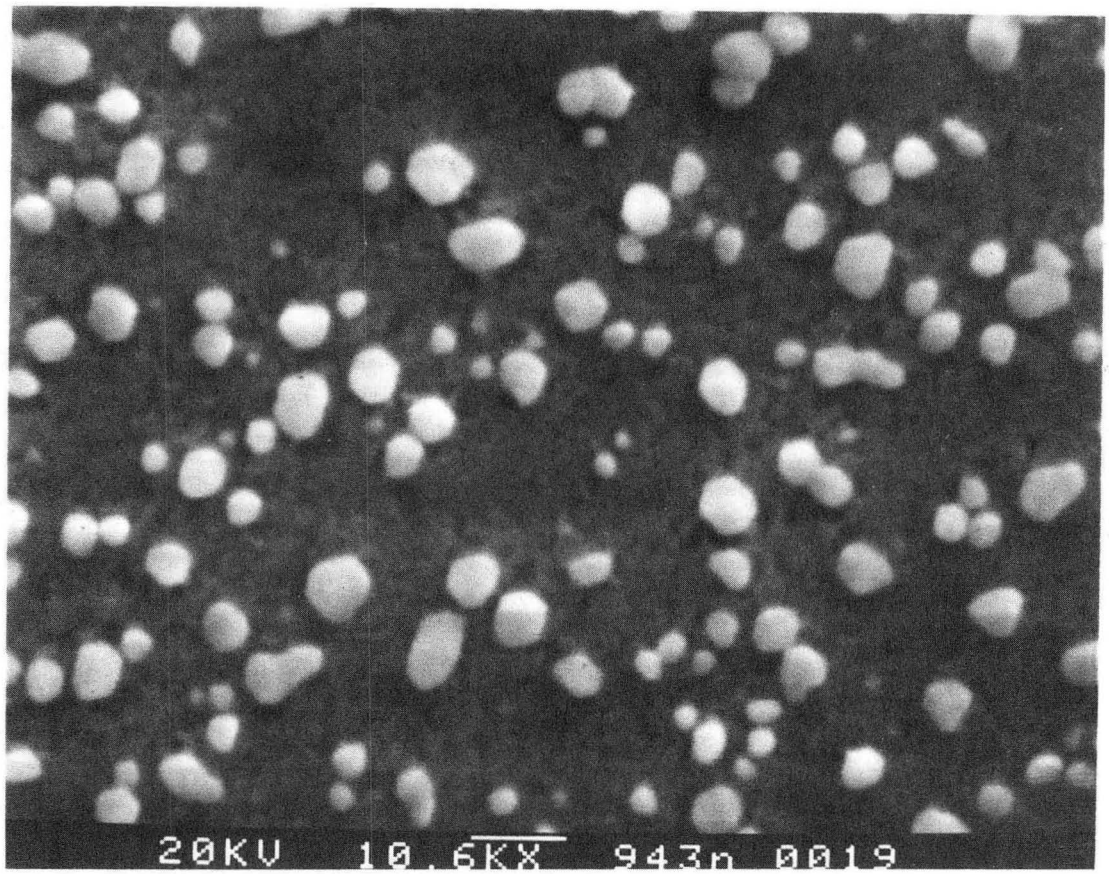

XBB 859-7232

Figure 10-1

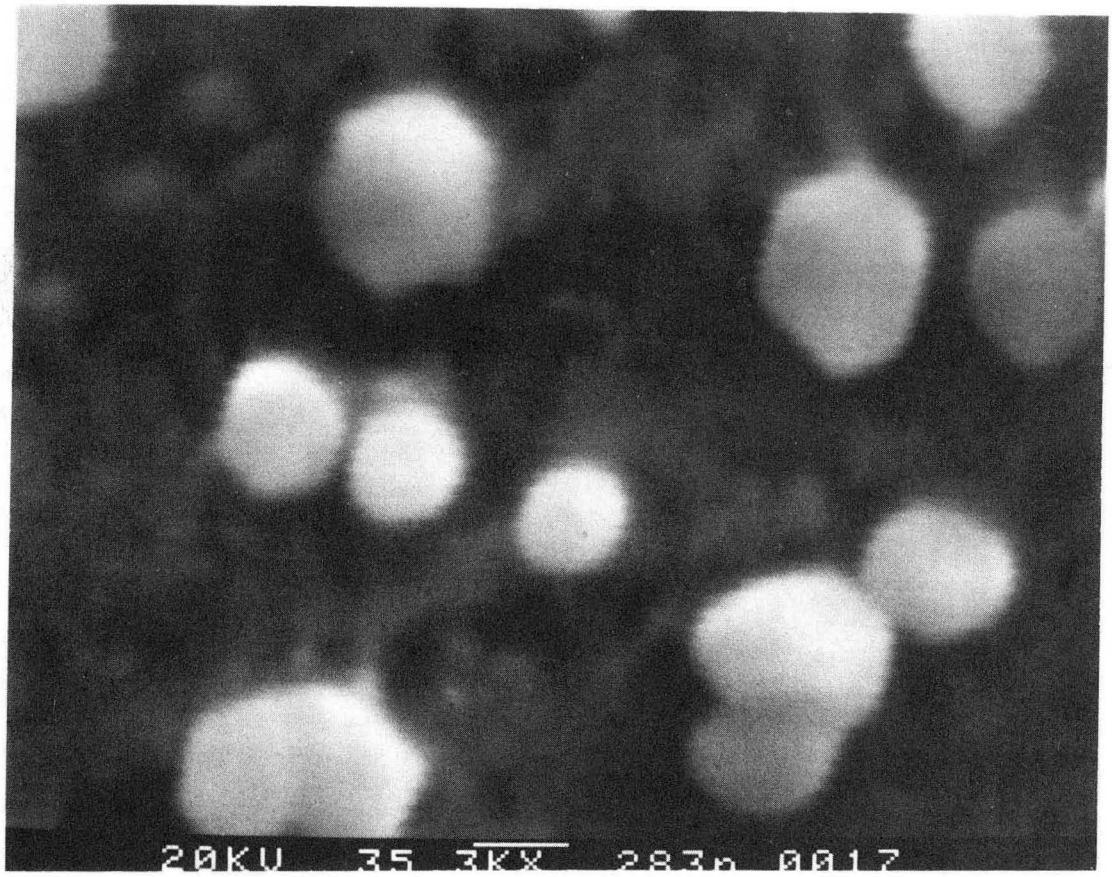

XBB 859-7233

Figure 10-2

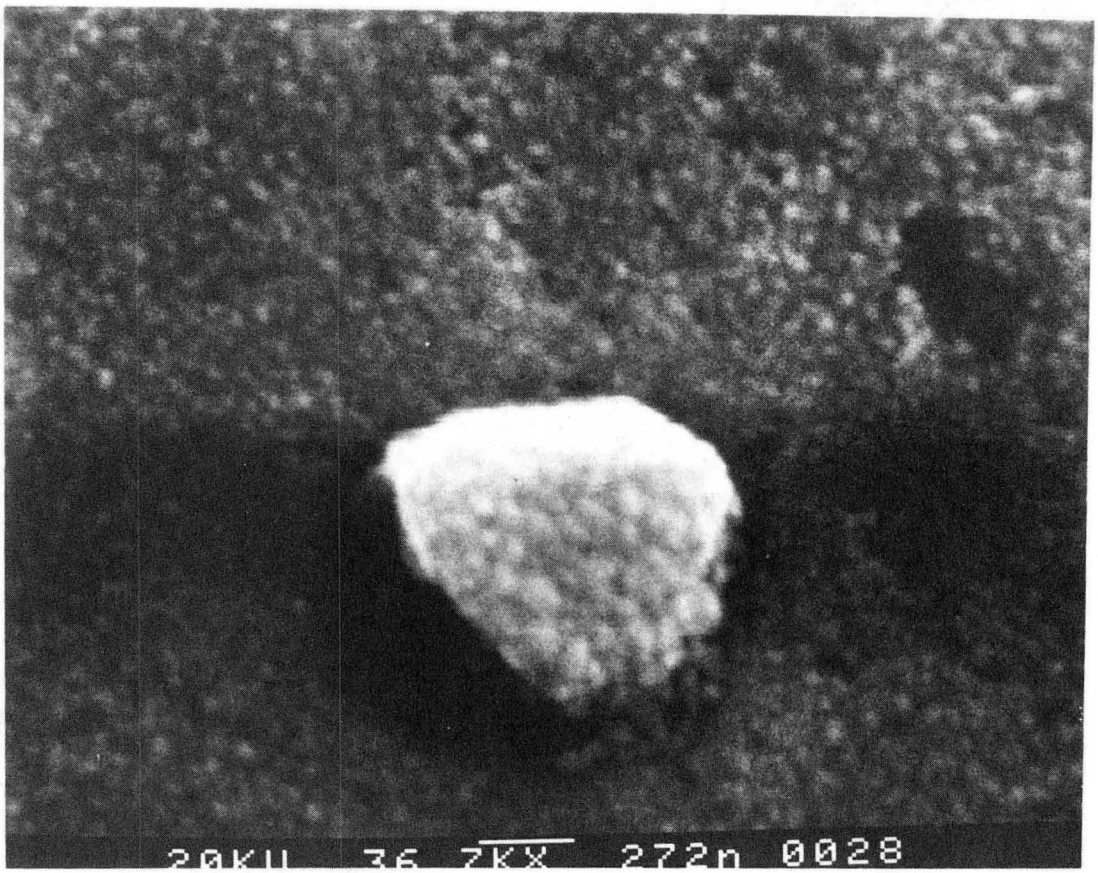

XBB 858-7130

Figure 10-3

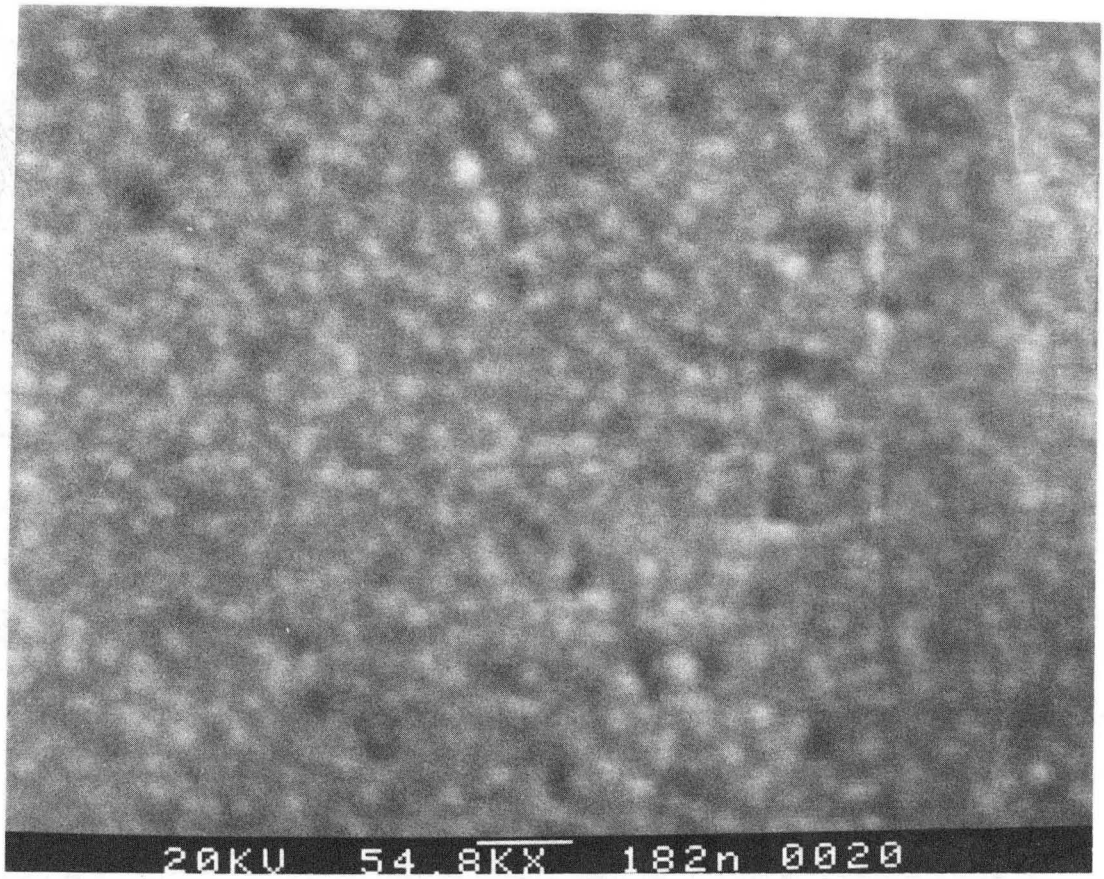

XBB 859-7236

Figure 10-4

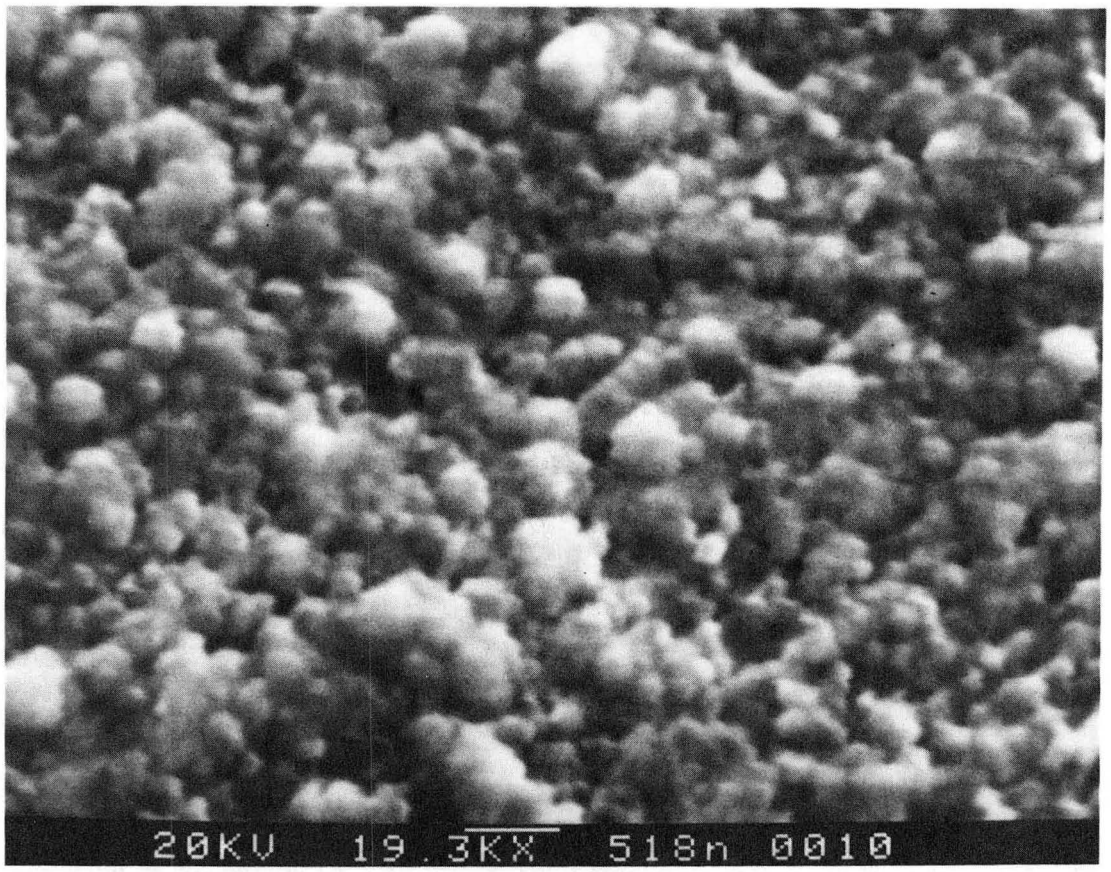

XBB 879-8197

Figure 10-5

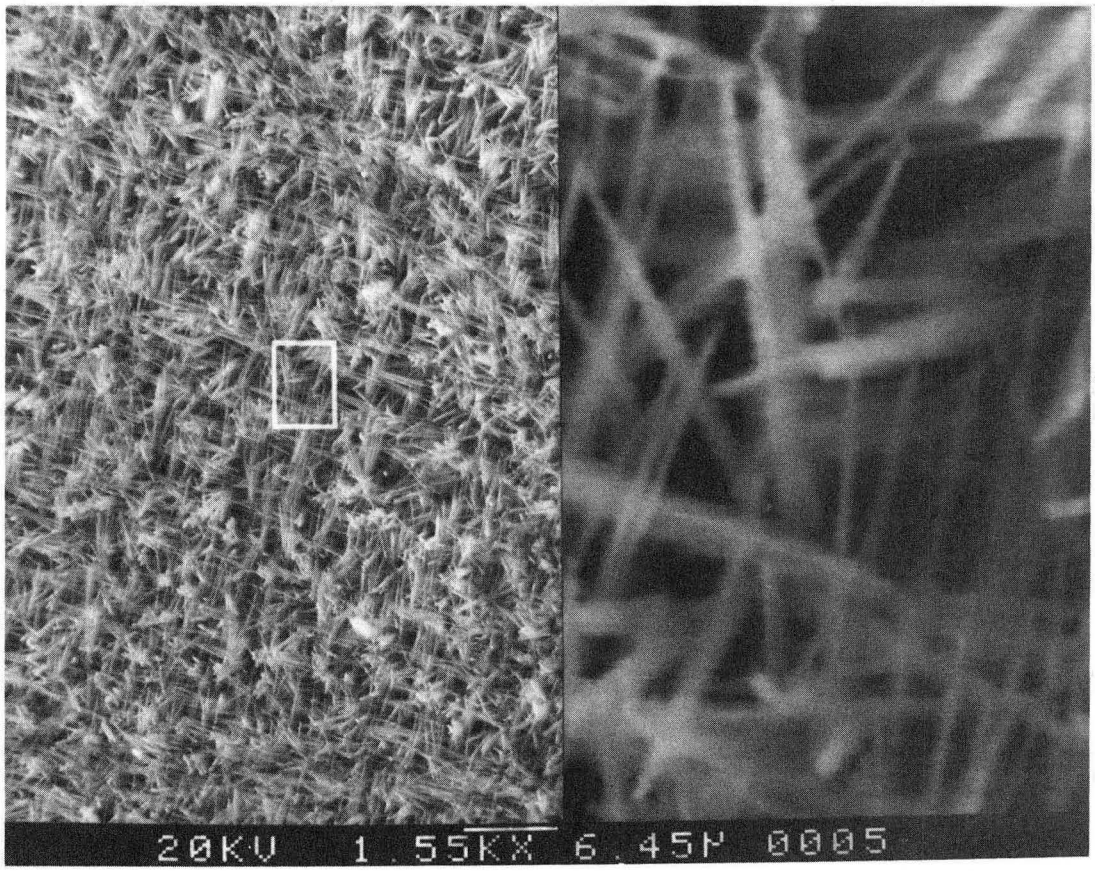

XBB 879-8192

Figure 10-6

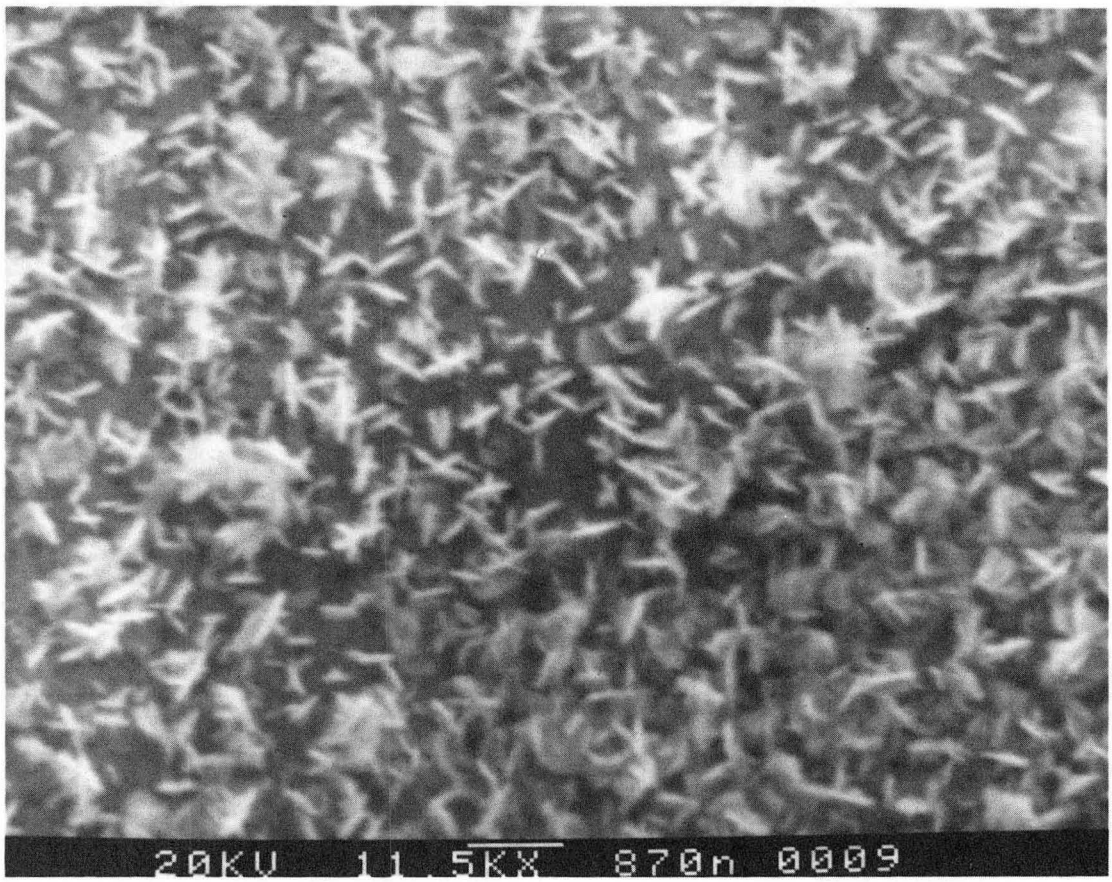

XBB 879-8185

Figure 10-7

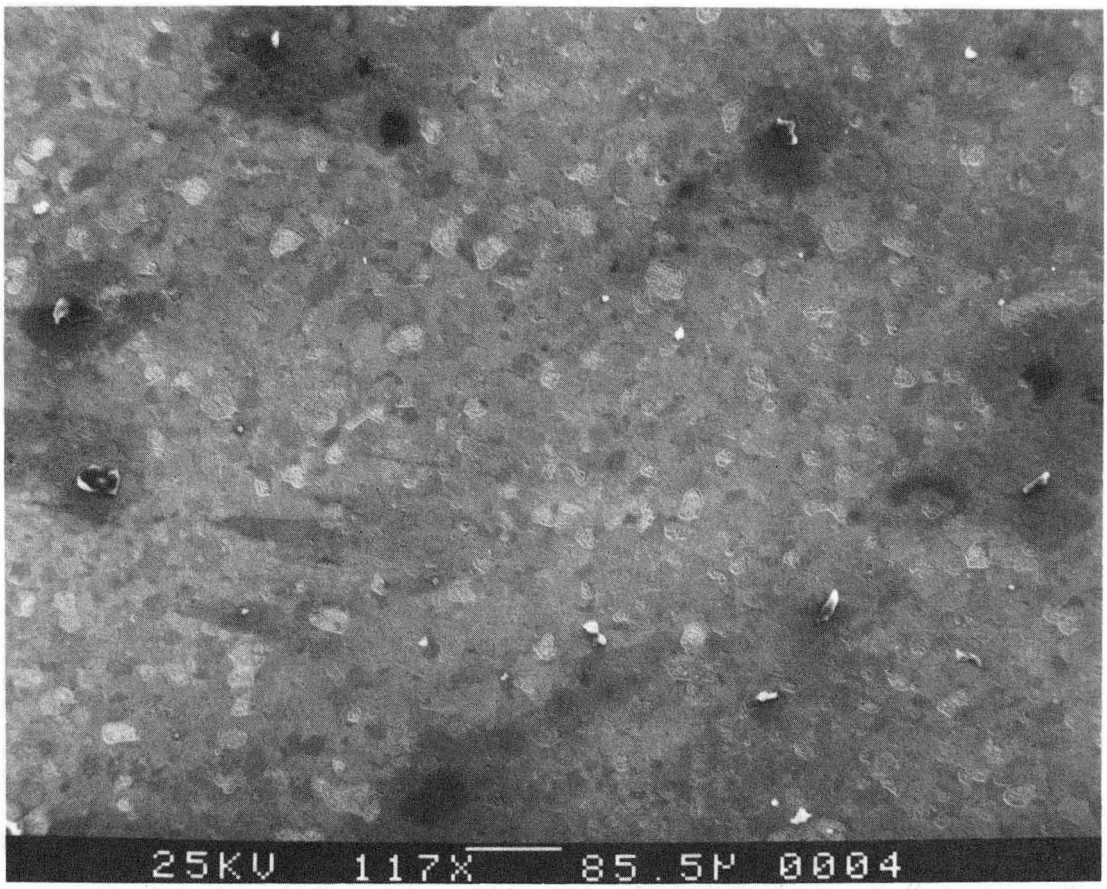

XBB 879-8187

Figure 10-8

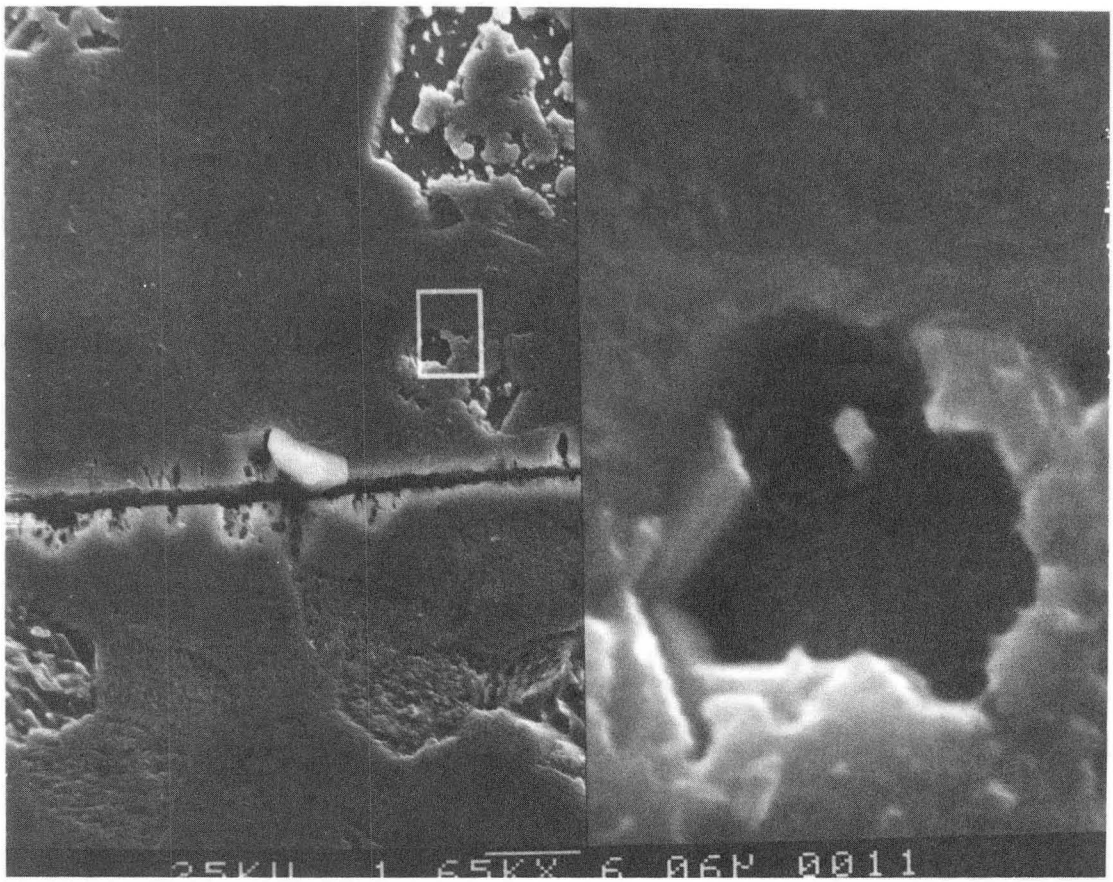

XBB 879-8188

Figure 10-9

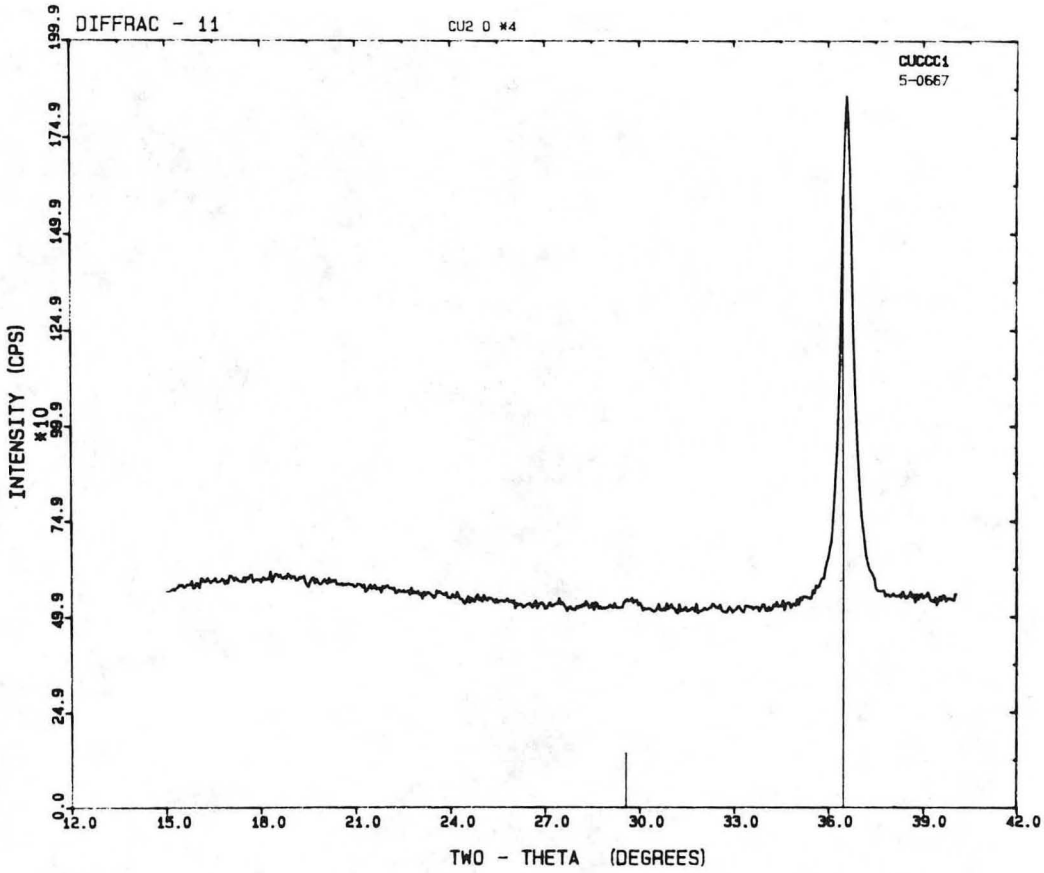

CBB 870-10455

Figure 10-10

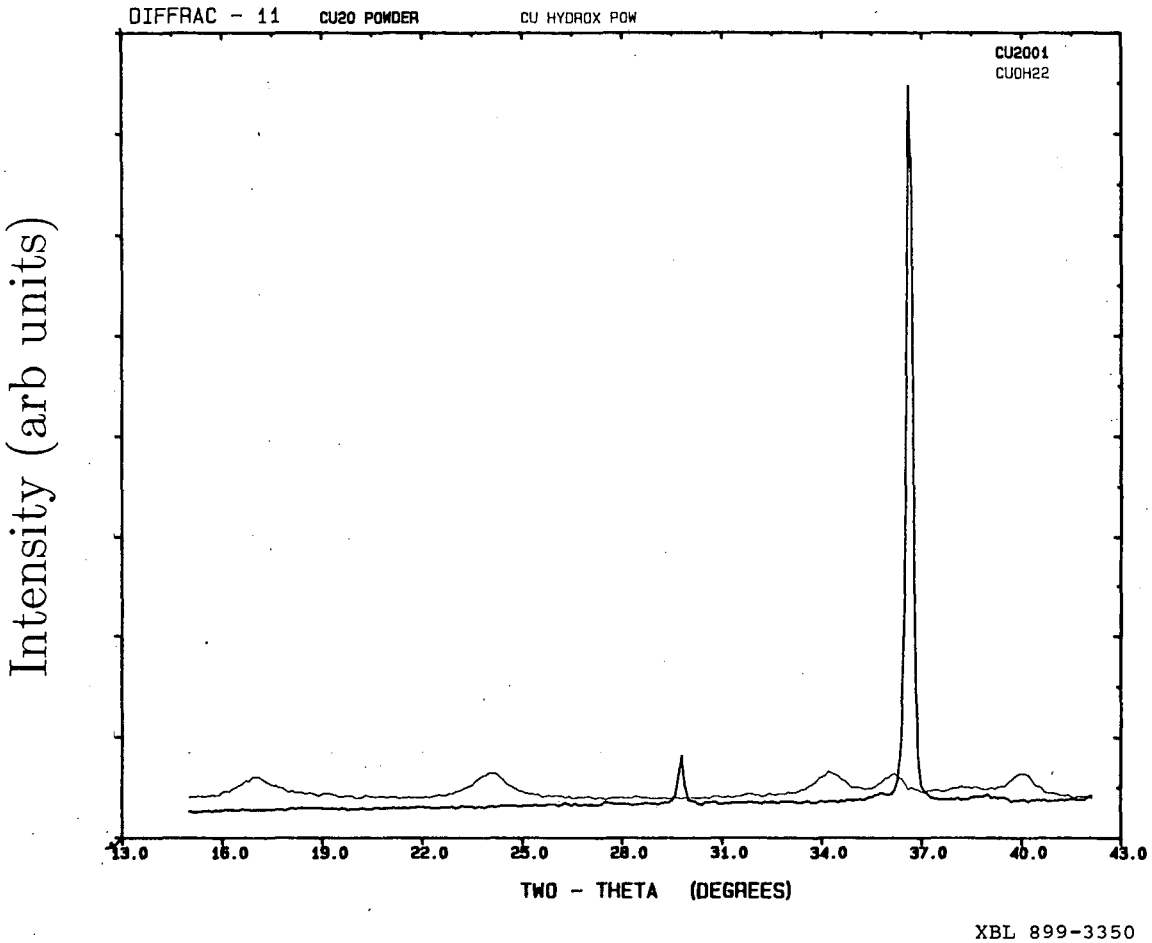
DIFFRAC - 11
CU2O POWDER
CU HYDROX POW
CU2001
CUOH22
Intensity (arb units)
13.0
16.0
19.0
22.0
25.0
28.0
31.0
34.0
37.0
40.0
43.0
TWO - THETA (DEGREES)
XBL 899-3350

Figure 10-11

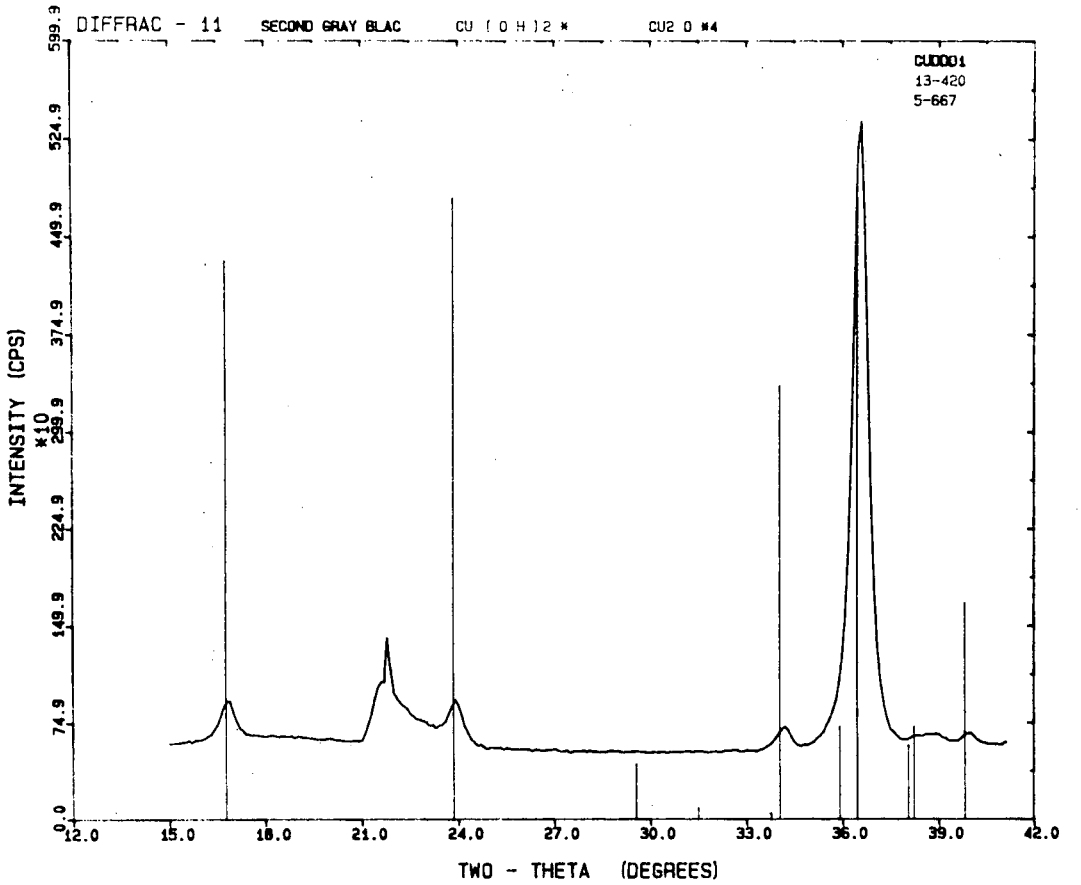

CBB 870-10461

Figure 10-12

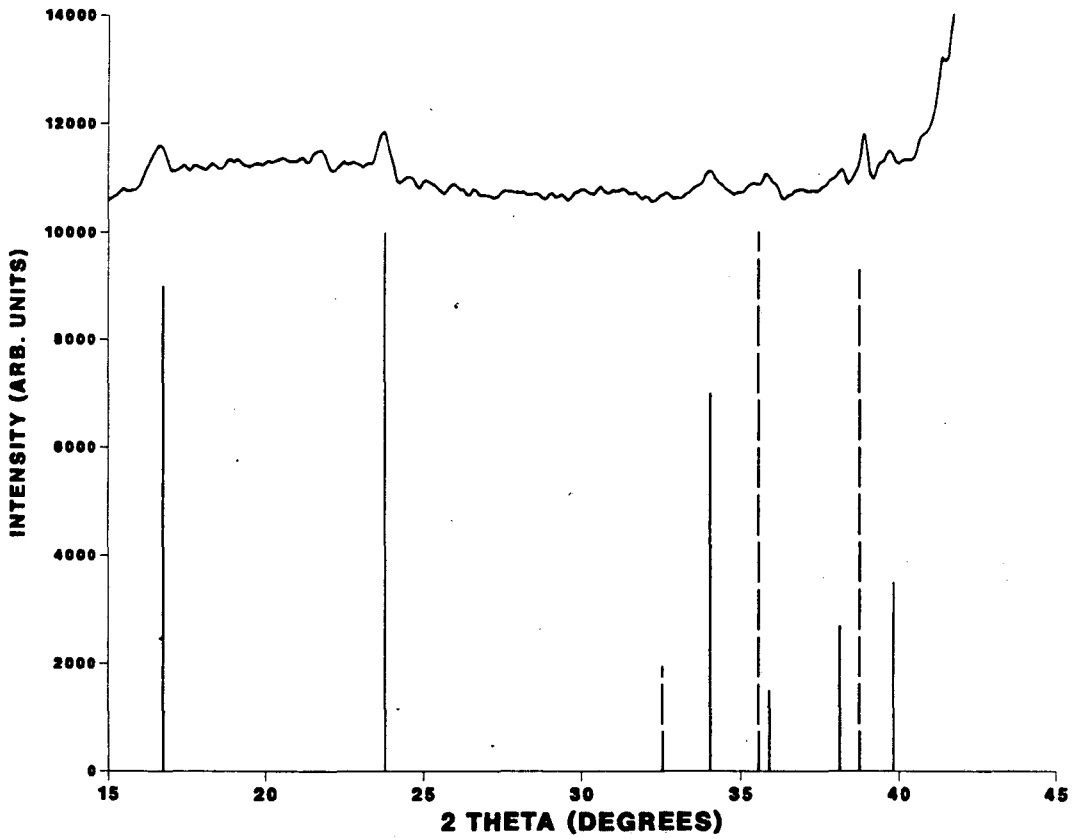

XBL 899-3352

Figure 10-13

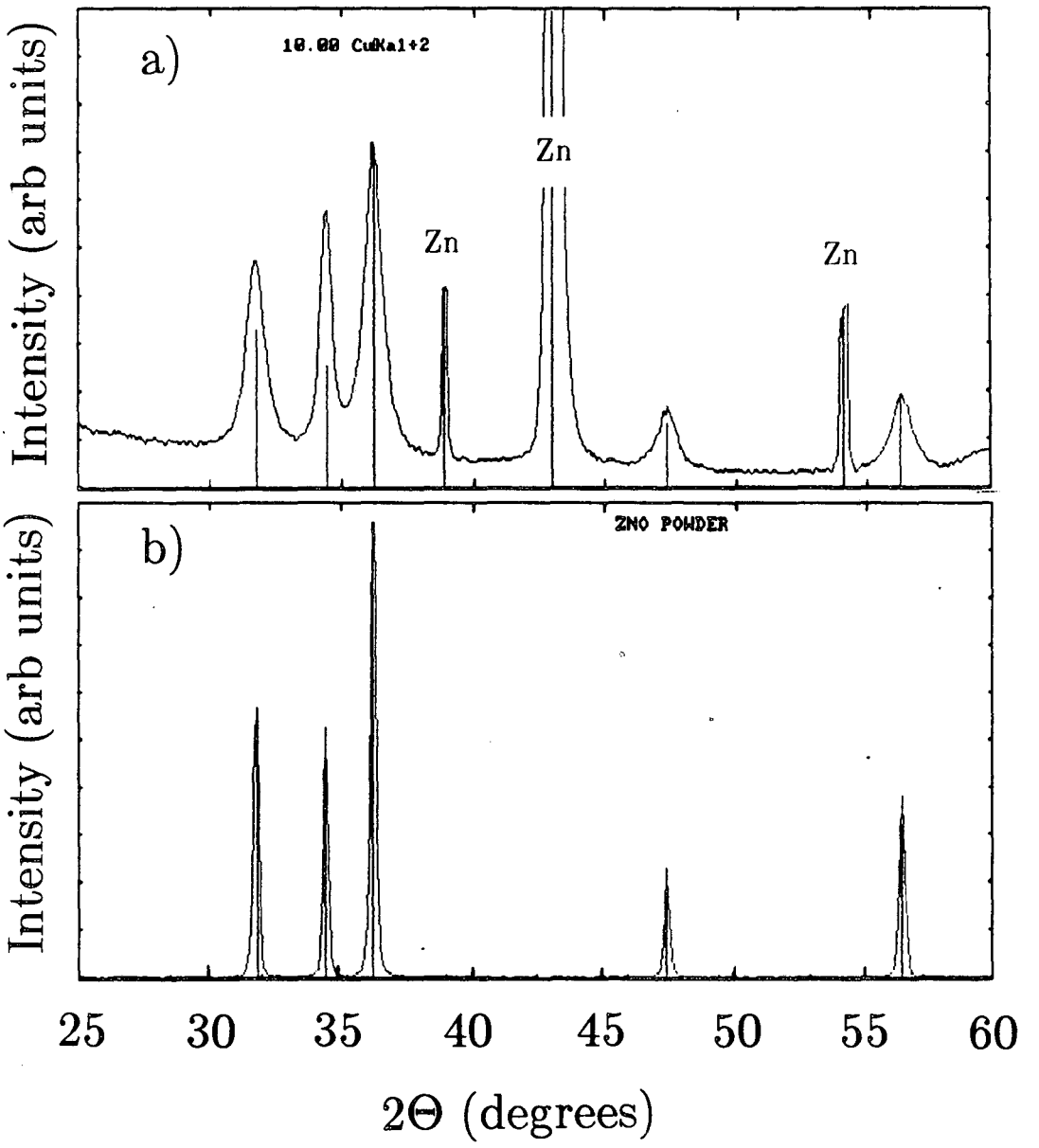

XBL 899-3351

Figure 10-14

POTENTIAL STEP OF Ag in 1M KOH to 290 mV vs. Hg/HgO

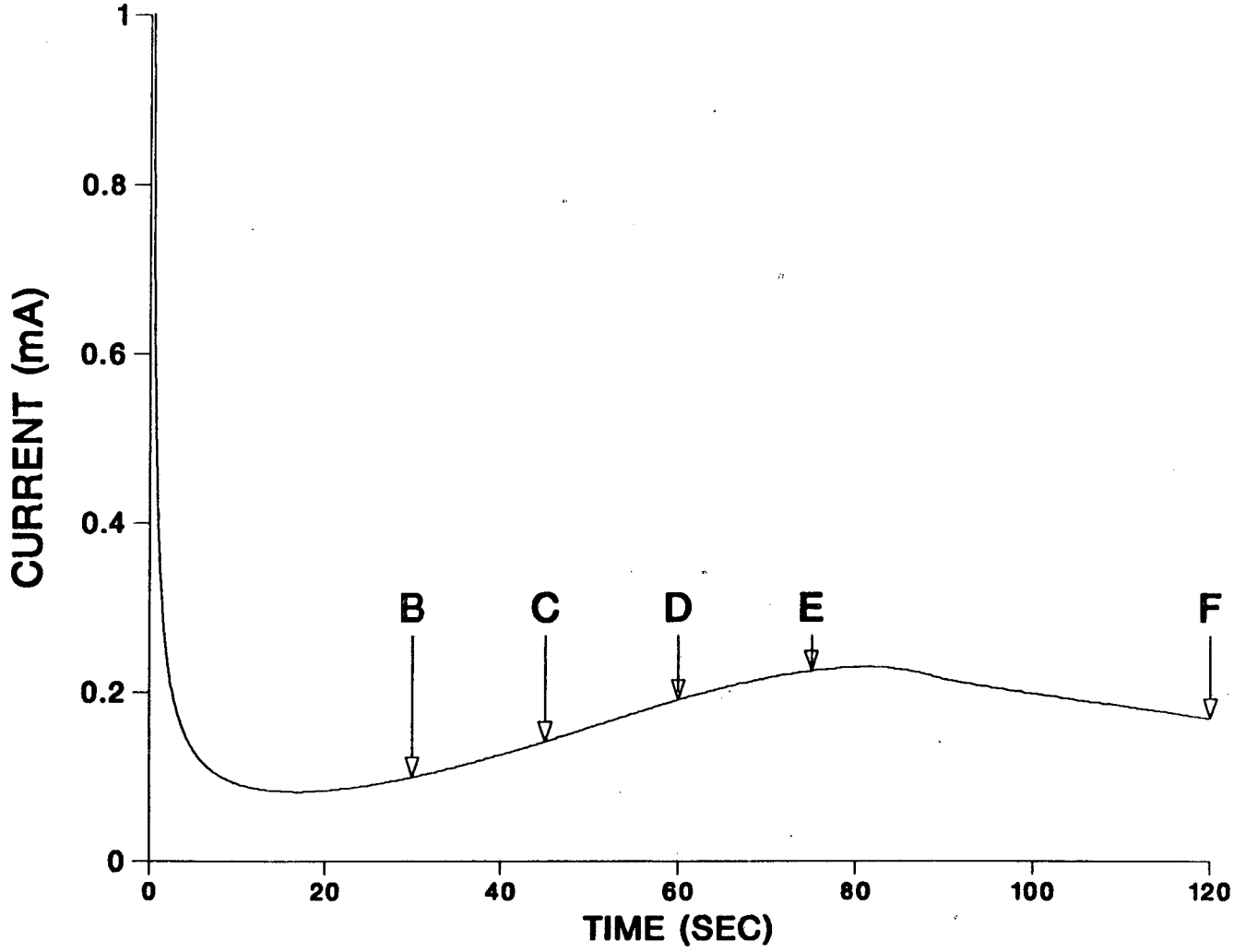

Electrode area 0.5 cm**2

Figure 10-15

XBL 891-82

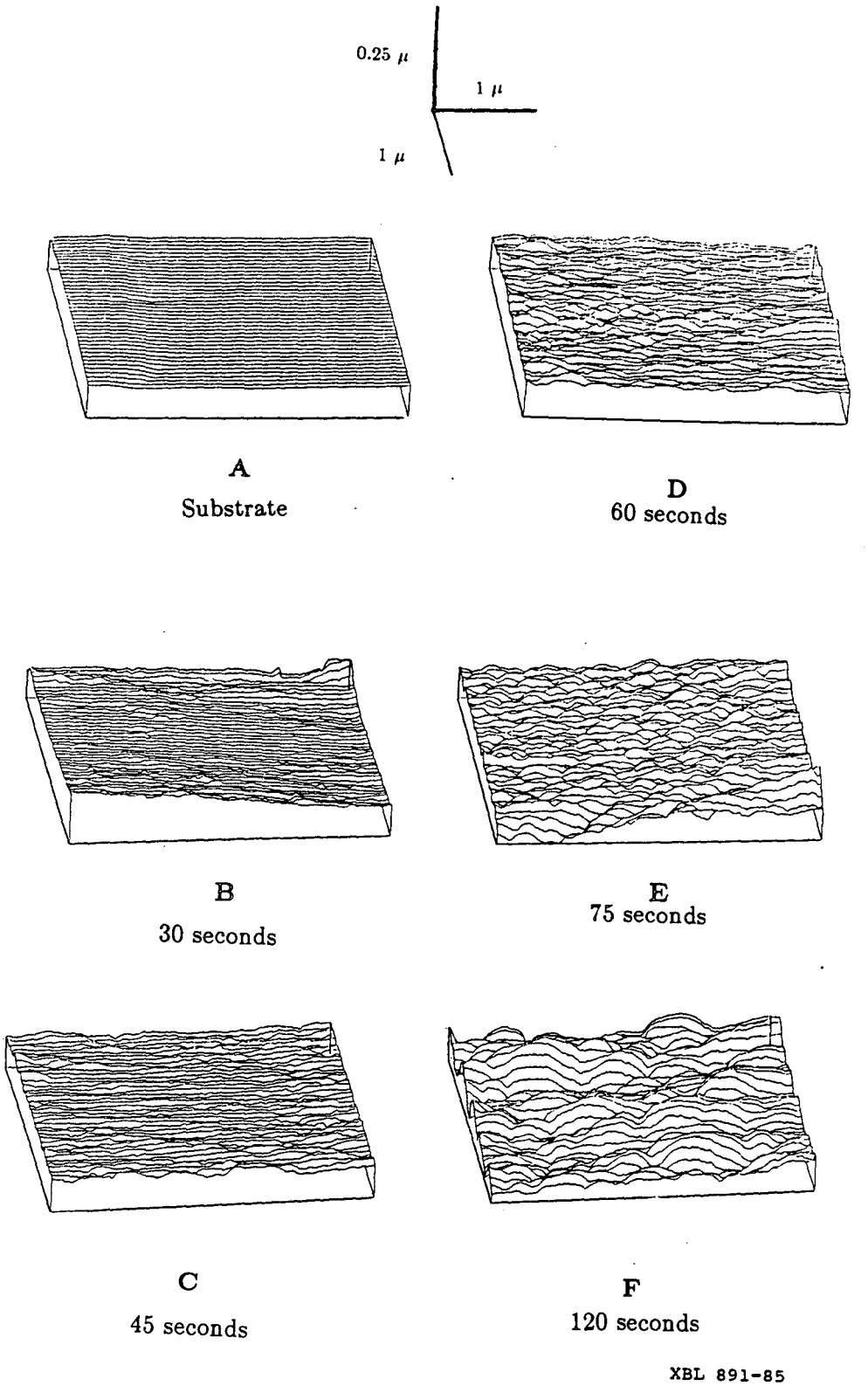
0.25 μ
1 μ
1 μ
A
Substrate
D
60 seconds
B
30 seconds
E
75 seconds
C
45 seconds
F
120 seconds
XBL 891-85

Figure 10-16

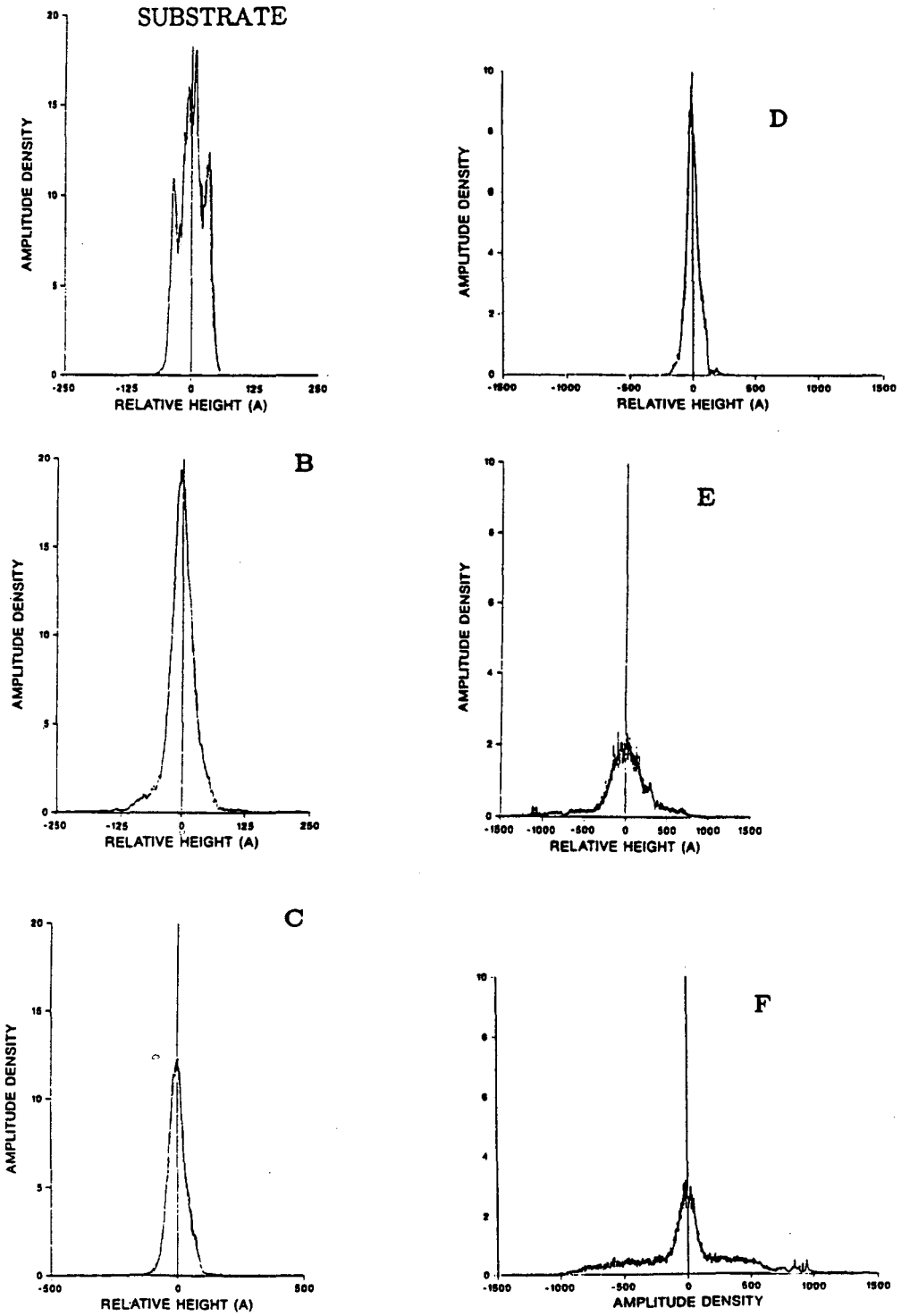

XBL 891-83

Figure 10-17

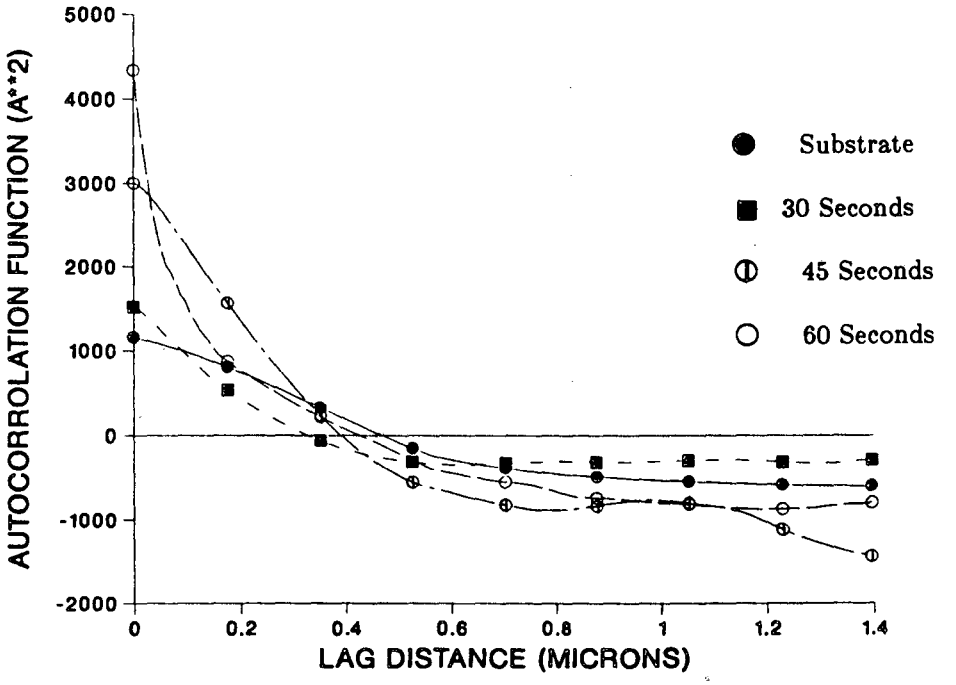

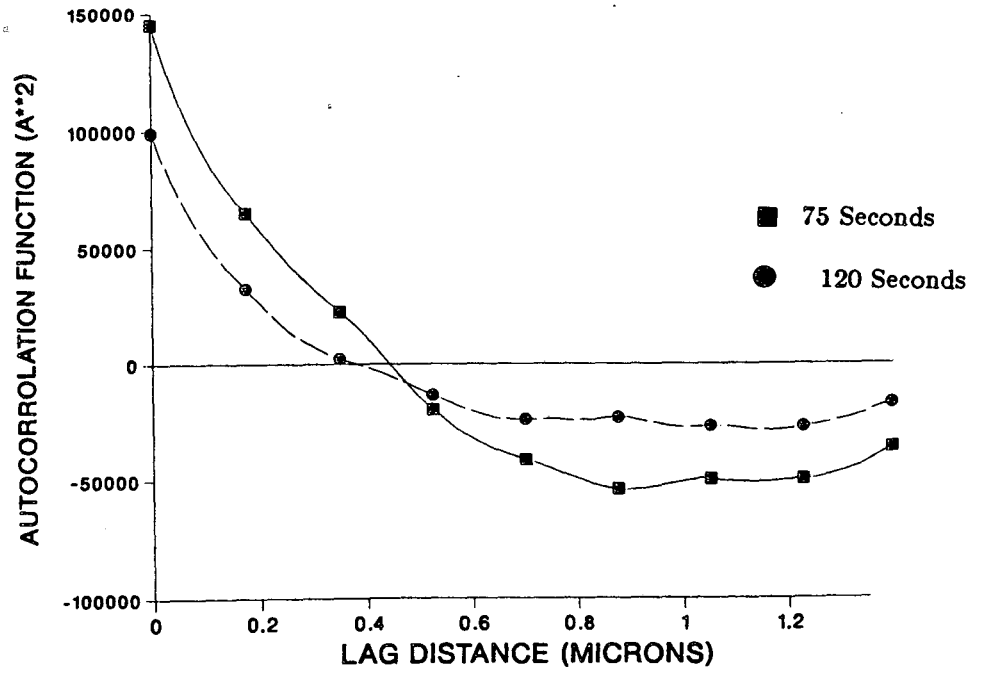

XBL 891-84

Figure 10-18

ACKNOWLEDGEMENTS

I would like to express his sincere thanks to Dr. Rolf H. Muller for his kind, inspirational, and unending support of this work. I would also like to express my gratitude to the various professional staff members at Lawrence Berkeley Laboratory. I am particularly indebted to Dr. Kirk Veirs for his help with the Raman work, Dr. Philip Ross for his discussions of the theoretical aspects of this work, and the reviewers of the thesis (Dr. Charles Tobias, Dr. Elton Cairns, and Dr. Robert Ely).

This work was supported by the Assistant Secretary of Conservation and Renewable Energy, Office of Energy Storage and Distribution of the U.S. Department of Energy under Contract no. DE-AC03-76SF00098.

INDEX

Amplitude density function (ADF) 142
and STM 472
Autocorrelation function (ACF) 143
and RMS roughness 144
and spectral power density 144
and STM 472
and vector scattering theory 149
Batteries
Cadmium/silver oxide 103
Zinc-air 107
Zinc-copper (II) oxide 109
Zinc-manganese dioxide 106
Zinc-mercury (II) oxide 105
Zinc-nickel oxide 104
Zinc-silver oxide 102
Brillouin scattering 234
Bruggeman effective media approximation 397,400
Concentration overvoltage 100
Copper
Efficiency of oxide formation 23
Passivation of 28
Pourbaix diagram of 5
Raman spectroscopy of 13,273-291
Soluble species of 284,289
Trivalent oxide species of 28
Copper oxidation
Galvanostatic measurement of 412-414
Potential-step measurements of 179-181,285-287,417-419
Potential-sweep measurements of 175-179,270-285,412-414
SEM measurements of 25
Copper species
Thermodynamics of 5
Solubility of oxides 5,6,26
Crystal growth
and screw dislocations 73
as ion sinks 84
Correlations for 74
Diffusion-controlled models of 82
Geometrical models of 78
Lattice building in 72,73
Mixed control of 84
Particle size effects on 83
Cupric hydroxide
Powder Raman spectrum of 267,269
Scanning electron microscopy of 465,466
X-ray diffraction of 467,468
Cupric hydroxide film formation
Conditions for 25
Elastic scattering measurements of 178,179
Mechanism of 179
Raman spectra of 271-287
Reflectance measurements of 24
X-ray measurements of 467,468
Cupric oxide
Relative stability vs cupric hydroxide 5,22
Powder Raman spectrum of 267
X-ray diffraction of 467,468
Cupric oxide film formation
Conditions for 25,26
Mechanism of 26
Raman spectra of 275-287
Cuprous hydroxide formation 8
Cuprous oxide film formation
Dissolution/precipitation mechanism 16-18
Elastic scattering measurement 175-181
Ellipsometry of 15,18,408-417
ESCA of 17
Mechanism of 177,178,181
Raman spectra of 270-288
Reflectance measurements of 8
Solid state mechanism of 14
Structure of 411,412
X-ray measurements of 10
Current distribution of sinusoidal profiles 87
Cyclic voltammetry
of copper 7,10,22,24
of silver 48
Effective media approximations 397
Elastic light scattering
and Raman spectroscopy 233,234
effects of insoluble particles 160,161
equipment design 151-158
Elastic light scattering theory
and aliasing 141
Interference function and 140
Intraparticle interference 136
Multiparticle interference 139
Obliquity factor 135
and radial distribution function 141,142
From random particles 132
Scalar 145,146
From semiordered particles 135
Vector 147
Wave vector in 148
Electrochemical energy storage

Solid film mechanism 99,101
Soluble material mechanism 99
Electrocrystallization, growth paths of 71
Electrode polishing 120,123
Electrolyte preparation 118-120
Electromagnetic waves, classical theory of 235-240
Ellipsometry
Coherent superposition principle and 397
Curve fitting in 393
Derivation of physical properties from 393
Derived parameters certainty 398
Effective-media approximations in 397
Film model interpretations 393
Island-film model 397
Optical models in 395
Optical path length in 395
Principles of 391-400
Sensitivity of 398
Spectroscopic vs monochromatic 392
Entropy of dissolution 100
Fresnel reflection coefficents 395
Gibbs-Thompson relation 83
Hamilton hypothesis 259,265
Hg/HgO reference electrode 123
Intensified photodiode array (IPDA) 252-256
Signal-to-noise ratio of 253-255
Laser
Ar-ion 246
Focusing and beam waist of 247-249
Plasma lines of 249
Light
Polarization states of 236,237
Time-averaged energy density 237,238
Lorentz-Lorenz effective-media approximation 397
Maxwell-Garnett effective-media approximation 397
NFSPDF ratio 163-166
Nitric acid, use as a cleaning agent 119
Nucleation
Critical free energy for 79,83
Critical nucleus size 79,83
Dissolution/precipitation mechanism of 401
Energy barriers for 77
Expectation number in 81
Inception time and 80
Instantaneous 79,81
Linear 79
of silver (I) oxide crystals 165,166
Overlap and 81
Progressive 79
Schools of thought on 76
Thermodynamics of 76
Nucleation and growth
Diffusion-controlled models 82
Geometric models 78-82
Nucleation site 76
Optical fibers 157
Ostwald ripening
of silver (I) oxide crystals 165,166,470
Oxygen and copper equilibrium potential 7
Oxygen adsorption on copper 9
Photo-counting image-acquisition systems (PIAS) 257
Raman scattering
and elastic-light scattering 233
Classical theory of 241-245
Criteria for activity 244
Depolarization ratios in 245
Discovery of 233
Equipment design for electrochemical studies 246
Optimum collection angles for 250
Optimum incident angles for 250
Polarization matrix for 241
Resonance enhancement of 242,247
Surface enhancement of (SERS) 233,247
Use of optical filters in 252
Raman spectrometer, calibration of 258
Rayleigh scattering (see elastic-light scattering)
RMS roughness
and vector-scattering theory 162
Effects of crystal number density on 171
Effects of crystal size on 171
Ellipsometry and scattering results comparison 174
Scanning electron microscopy
Equipment for 466
of silver (I) oxide nucleation 471-474
Surface preparation for 470,471
Silver
Stepwise oxidation of 45
Solubility of oxides 42,43
Silver oxidation
Ellipsometry of 46,400-408
Galvanostatic measurements of 49
Potential-step measurements of 50,166,168
Potential-sweep measurements of 403

Silver oxidation (continued)
Scanning electron microscopy of (SEM) 46,464
Silver oxidation (cont.)
Scanning tunneling microscopy of (STM) 469-474
Thermodynamics of 41
X-ray measurement of 45
Silver (I) oxide phototransformation 264
Induction time for 265
Hamilton hypothesis and 259,265
Simplex optimization 394
Single crystals, preparation of 117
Snell's law 396
Spectral power density function (SPDF) 143
and autocorrelation 144
and vector scattering theory 147
Surface-enhanced Raman scattering
of water 260
of water/KOH solutions 263
Surface spectral analysis 143
Surface stability
Capillarity and 88
Perturbation analysis of 88
Thermodynamic potential of formation
of copper oxide species 6
of silver oxide species 42,43
of zinc oxide species 59
Trivalent copper
oxide 282-283
soluble species 283
Underpotential deposition (UPD)
Epitaxy of 75
Vector scattering theory
and near-to-far SPDF ratio 163
and RMS roughness 162
Zinc hydroxide film formation
Raman spectrscopy of 297
Zinc oxidation
Ellipsometry of 418-420
Film composition of 64
Raman spectroscopy of 294-299
X-ray diffraction of 469
Zinc oxide
Rate of dissolution 63
Solution supersaturation 62
Zinc oxide film formation
Dissolution of film 422,423
Dissolution/precipitation mechanism 63
Growth law of 418,419
Raman spectra of 297
Role of space charge in 419-423
Scanning electron microscopy of 466-467
Structure of 64,65
Zinc species
Solubility of 59-62
Zincate ion
Intramolecular bonding in 59
Raman spectra of 290-293

LAWRENCE BERKELEY LABORATORY
TECHNICAL INFORMATION DEPARTMENT
1 CYCLOTRON ROAD
BERKELEY, CALIFORNIA 94720